Add 428572
428574 - 428582

DTIC
ELECTE
NOV 0 8 1995
F

DISTRIBUTION STATEMENT A
Approved for public release
Distribution Unlimited

19951107 121

DTIC QUALITY INSPECTED 5
Accession For
NTIS GRA&I
DTIC TAB
Unannounced
Justification
By
Distribution /
Availability Codes
Dist Avail and / or Special
A-1

Page: 1 Document Name: untitled

-- 1 OF 1
-- ***DTIC DOES NOT HAVE THIS ITEM***
-- 1 - AD NUMBER: D422573
Date: 5/29/95 Time: 10:53:37PM
-- 5 - CORPORATE AUTHOR: ARMY MATERIALS RESEARCH AGENCY WATERTOWN MASS
-- 6 - UNCLASSIFIED TITLE: ADVANCES IN JOINING TECHNOLOGY,
--10 - PERSONAL AUTHORS: BURKE ,J. J. ;GORUM ,A. E. ;TARPINIAN,A. ;
--11 - REPORT DATE: SEP 16, 1975
--12 - PAGINATION: 647P
--20 - REPORT CLASSIFICATION: UNCLASSIFIED
--21 - SUPPLEMENTARY NOTE: PROCEEDINGS: 'ADVANCES IN JOINING
-- TECHNOLOGY', 4TH ARMY MATERIALS TECHNOLOGY CONFERENCE, HELD 16-19
-- SEP 75, BOSTON, MASS. SPONSORED BY THE ARMY MATERIALS AND MECHANICS
-- RESEARCH CENTER, WATERTOWN, MASS. (SEE PL-26130 - PL- 26142).
--22 - LIMITATIONS (ALPHA): APPROVED FOR PUBLIC RELEASE; DISTRIBUTION
-- UNLIMITED. AVAILABILITY: 'ADVANCES IN JOINING TECHNOLOGY', 4TH ARMY
-- MATERIALS TECHNOLOGY CONFERENCE, HELD 16-19 SEP 75, BOSTON, MASS.
-- PUBLISHED BY BROOK HILL PUBLISHING COMPANY, CHESTNUT HILL, MASS.
--33 - LIMITATION CODES: 1 24

Advances in Joining Technology

Accesion For
NTIS CRA&I ☒
DTIC TAB ☐
Unannounced ☐
Justification
By ADD 422573
Distribution /
Availability Codes
Dist | Avail and / or Special
A-1

DTIC
SELECTE
NOV 0 8 1995
F

DISTRIBUTION STATEMENT X
Approved for public release;
Distribution Unlimited

DTIC QUALITY INSPECTED 8

Advances in Joining Technology

Proceedings of the 4th Army Materials Technology Conference. Held in Boston, Massachusetts, 16–19 September, 1975. Sponsored by the Army Materials and Mechanics Research Center, Watertown, Massachusetts.

Editors

JOHN J. BURKE

Associate Director, Army Materials and Mechanics Research Center

ALVIN E. GORUM

Director, Army Materials and Mechanics Research Center

ARUM TARPINIAN

Planning Directorate Army Materials and Mechanics Research Center

DTIC QUALITY INSPECTED 3

Published in cooperation with the
Metals and Ceramics Information Center
Columbus, Ohio

All Rights Reserved

Copyright © 1976
by Brook Hill Publishing Company

First Edition

Library of Congress Catalogue Card Number 76-600067

Printed in United States of America
Published by Brook Hill Publishing Company, Chestnut Hill, Massachusetts

Conference Committee

Chairman
Dr. A. E. Gorum
Army Materials and Mechanics Research Center

Executive Board
Prof. N. J. Grant
Massachusetts Institute of Technology

Prof. M. L. Williams
University of Pittsburgh

Prof. E. R. Parker
University of California at Berkeley

Program Director
Dr. J. J. Burke
Army Materials and Mechanics Research Center

Secretary
Mr. A. Tarpinian
Army Materials and Mechanics Research Center

Program Committee
Prof. C. M. Adams
University of Cincinnati

Dr. S. K. Dutta
Army Materials and Mechanics Research Center

Mr. W. S. Hyler
Battelle Columbus Laboratories

Dr. E. M. Lenoe
Army Materials and Mechanics Research Center

Dr. R. W. Lewis
Army Materials and Mechanics Research Center

Dr. B. R. Noton
Battelle Columbus Laboratories

Prof. K. J. Smith
Syracuse University

Dr. T. Vasilos
AVCO Corporation

Program Coordinator
Mr. J. Bernier
Army Materials and Mechanics Research Center

Conference Coordinator
Mrs. J. Ayoub
Army Materials and Mechanics Research Center

FOREWORD

The Army Materials and Mechanics Research Center initiated a new conference series in the fall of 1972 with the express purpose of bringing to industry, academic, and Governmental organizations the most recent advances in materials technology. This publication is the result of the fourth conference on the advances made in the technology of materials joining. The purpose of this conference was to promote an interchange of experience leading to the successful application of a broad category of materials to advanced structural and electronic design concepts.

The focus of the conference was on the relevant developments in the areas of joining metals, ceramics, polymers and composites. Consideration in this volume is given to joining methodology, factors affecting joint design, and the impact of joining methods on design concepts.

The assistance of the Technical Reports Office under the supervision of Mrs. A. V. Gallagher and the Technical Information Office under the supervision of Miss M. M. Murphy of the Army Materials and Mechanics Research Center in preparing the final manuscript is gratefully acknowledged. Special thanks go to Mr. Harold Laye for final preparation of the illustrations.

The Editors

Army Materials and Mechanics Research Center
Watertown, Massachusetts
September 1975

CONTENTS

SESSION I
METALS
C. M. Adams, *Moderator*

1 Nuclear Welding — Application for an LMFBR
G. M. Goodwin and P. Patriarca 3

2 Dynamics of Weld Cracking
E. F. Nippes 31

3 Explosive Welding and Cladding — Overview of the Process and Selected Applications
J. A. Yoblin, J. D. Mote, and L. E. Jensen 51

SESSION II
CERAMICS
T. Vasilos, *Moderator*

4 Joining of Ceramics
R. W. Rice 69

5 Joining of Turbine Engine Ceramics
M. U. Goodyear and A. Ezis 113

6 Systems for Uniting Refractory Materials
J. E. Kelley, D. H. Sumner, and H. J. Kelly 155

7 Direct Bonding of Metals to Ceramics for Electronic Applications
J. F. Burgess, C. A. Neugebauer, G. Flanagan, and R. E. Moore 185

SESSION III
POLYMERS
K. J. Smith, *Moderator*

8 Durable Surface Treatments for the Adhesive Bonding of Aluminum Alloys
T. J. Reinhart, Jr. 201

9 Polymer — Ceramic Interfaces
G. R. Kritchevsky and D. R. Uhlmann 207

PL-26130 PL-26131 PL-26132

10 Polymer — Polymer Bonding
R. Fountain 237

11 Adhesive Fracture of Epoxy and Elastomer Epoxy Resins
W. D. Bascom 265

SESSION IV
COMPOSITES
R. W. Lewis, *Moderator*

12 Improvement in Structural Efficiency of Single-Lap Bonded Joints
W. J. Renton, J. Pajerowski, and J. R. Vinson 305

13 Structural Attachment of Composite Rotor Blades
W. K. Stratton, T. S. Scarpati, and C. A. Class 317

14 Design Parameter Considerations for Composite Sandwich Bonding
J. Brentjes 339

SESSION V
STRESS ANALYSIS
E. M. Lenoe, *Moderator*

15 Thermomechanical Analysis of Welded Joints and Structures
H. D. Hibbitt 357

16 Survey of Mechanically Fastened Splice-Joint Analyses
I. U. Ojalvo 379

17 Stress Analysis of Composite Joints
D. W. Oplinger 405

SESSION VI
FRACTURE MECHANICS AND NDT
W. S. Hyler, *Moderator*

18 The Consideration of Damage Tolerance in the Design of Joints
R. L. Circle 455

19 Damage Tolerance Analysis of an Aircraft Structural Joint
S. H. Smith and F. A. Simonen 471

20 Application of NDT Techniques for Detecting Flaws in Joints
W. D. Rummel 503

SESSION VII
LIFE PREDICTION AND FACTORS INFLUENCING THE BEHAVIOR OF JOINTS
E. J. McQuillan, *Moderator*

21 A Normalization Scheme for Describing Crack-Growth Behavior
J. P. Gallagher and R. M. Bader 515

22 Fatigue Crack-Growth Behavior of Fastener-Hole Flaws
L. R. Hall 537

23 The Effect of a Corrosive Environment on the Strength and Life of Graphite–Epoxy Mechanically Fastened Joints
M. S. Rosenfeld 569

24 Detection of Adhesive Bond-Line Flaws by Neutron Radiography
D. H. Petersen and W. E. Dance 583

SESSION VIII
PANEL DISCUSSION, IMPACT OF JOINING METHODS ON MATERIALS SELECTION AND DESIGN
B. R. Noton, *Moderator*

25 Aluminum-Brazed Titanium Design
R. H. Hammer 595

26 Aerospace Adhesive Bonding
B. L. Reynolds 605

27 Aerospace Weld Bonding–Rivet Bonding
J. W. Dalley and S. W. McClaren 615

28 Ship Steel Weldments for Low-Temperature Service
H. I. McHenry 623

SESSION I

METALS

MODERATOR: C. M. ADAMS
University of Cincinnati

1. NUCLEAR WELDING — APPLICATION FOR AN LMFBR

G. M. GOODWIN and P. PATRIARCA
Oak Ridge National Laboratory
Oak Ridge, Tennessee

Many studies have predicted that the Liquid Metal Fast Breeder Reactor (LMFBR) will serve as a vital segment of our electrical energy system late in this century. This reactor concept has design requirements and service conditions that demand extremely high reliability. Fabrication of an LMFBR system is discussed, with emphasis on areas where joining innovations have been introduced. Each major component of the system, including reactor vessel, intermediate heat exchanger, steam generator, and sodium-containment piping, is treated separately. Development of special filler metals to avoid the low elevated temperature creep ductility obtained with conventional austenitic stainless steel weldments is reported. Bore-side welding of steam generator tube-to-tubesheet joints with and without filler metal is desirable to improve inspectability and eliminate the crevice inherent with face-side weld design, thus minimizing corrosion problems. Automated welding methods for sodium-containment piping are summarized; they minimize and control distortion and ensure welds of high integrity. Selection of materials for the various components is discussed for plants presently under construction, and materials predictions are made for future concepts.

INTRODUCTION

The production and utilization of energy in the United States are topics of high current interest.[1–3] Figure 1 traces the sources and consumption of energy in the United States[2] for the period from 1850 to 1990. Total energy consumed has risen steadily (with the exception of a period during the Great Depression), and trends indicate accelerated increases in demand. The contribution of nuclear power at the present time is only approximately 5% of the total energy consumed (Figure 1).

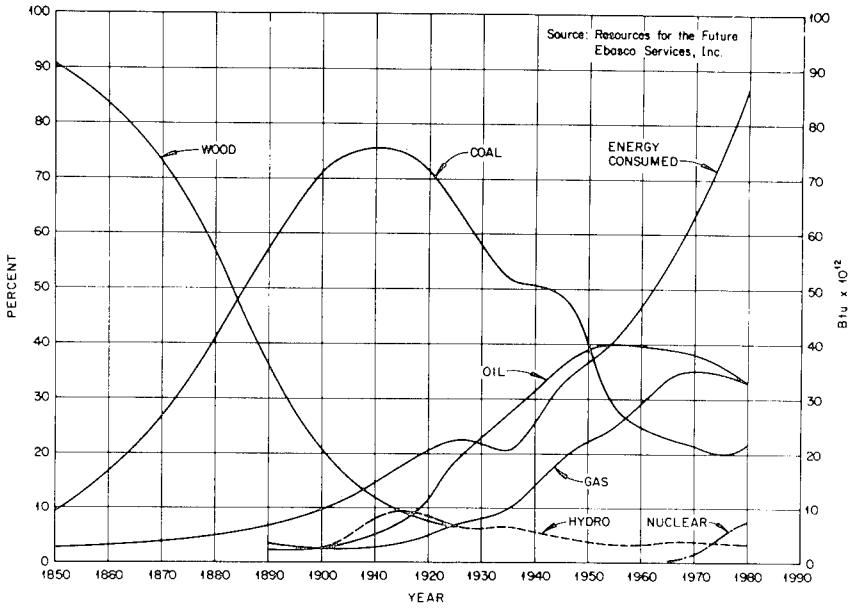


Figure 1. United States energy sources and consumption.

The projected electrical generating capacity in the United States has been forecast[3] for the years 1970–2020; total generating capacity is projected to increase tenfold during that period (Figure 2). The contribution of fossil-fueled plants could eventually decrease because of supply limitations of oil and natural gas and the many alternate uses for coal. Nuclear power can fill the large and ever-increasing gap between total demand and available supply of conventional (nonnuclear) power. The light-water reactors (LWR) will satisfy much of the near-term demand curve until limited available fuel supplies are exhausted. Being "burners" of nuclear fuel, LWRs cannot proliferate endlessly because of the fixed supply of natural fuel. Breeder reactors, on the other hand, can circumvent the problem. By transmutation of naturally abundant fertile isotopes to fissile isotopes which can be used as fuel, the breeder reactors can create more fuel than they consume, and supply fuel to satisfy projected power needs for several thousand years.[1–5] The High-Temperature Gas-Cooled Reactor (HTGR) is a "high-gain converter" which produces nearly as much fuel as it consumes. It therefore can supply significant amounts of energy as great as the breeder reactors can in the long term.

The projections shown in Figure 2 do not include possible technological breakthroughs that might make alternate energy sources, such as

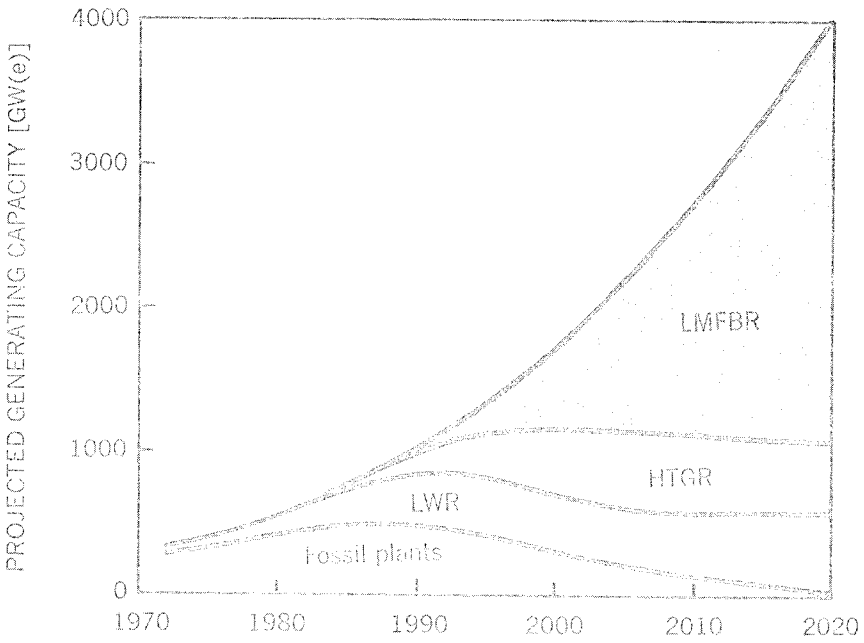


Figure 2. Projected generating capacity for the years 1970–2020.

nuclear fusion or solar energy, feasible. Although these sources are desirable, the uncertainties involved prohibit planning on their availability.

THE LIQUID METAL FAST BREEDER REACTOR (LMFBR)

The components of an LMFBR system are shown schematically in Figure 3. Flowing liquid sodium is heated by the fuel in the reactor vessel and flows through primary-system piping to intermediate heat exchangers (IHX), where heat is transferred to sodium in the secondary system and is finally pumped back to the reactor vessel. The IHX isolates the radioactive primary sodium from the secondary sodium, facilitating routine maintenance of the secondary systems. In the secondary system, heated sodium from the IHX(s) is pumped to the steam generator(s) and returns to the IHX(s). The steam produced runs a conventional turbine generator.

LMFBR demonstration plants worldwide are compared in Figure 4. At the present time, the U.S.'s Clinch River Breeder Reactor Plant

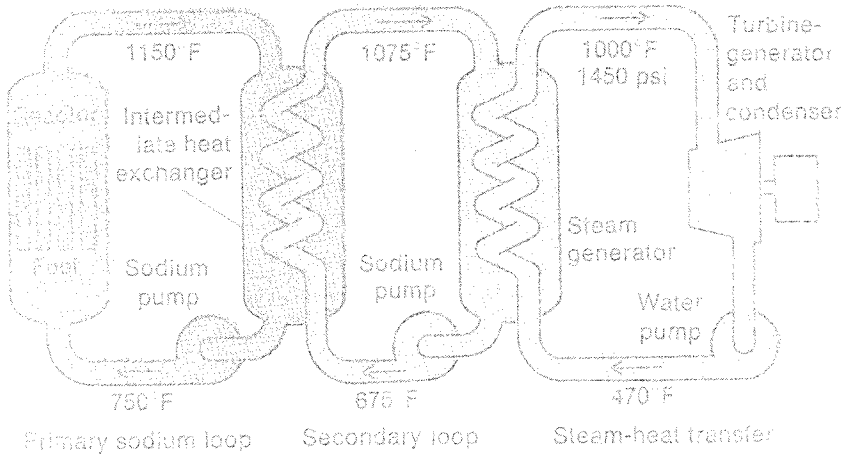


Figure 3. The Liquid Metal Cooled Fast Breeder Reactor.

	UK PFR	French PHENIX	Germany SNR	Russia BN-350	Japan MONJU	US CRBRP
Thermal output, MWt	600	563	720	1000	714	975
Electrical output, MWe	270	250	300	350[a]	300	380
Reactor						
Sodium outlet temp, °F	1044	1050	1000	932	1005	995
Sodium inlet temp, °F	752	750	700	572	734	730
Steam Generator						
Sodium inlet temp, °F	990	1022	977	842	959	936
Sodium outlet temp, °F	650	662	644	455	608	651
Feedwater inlet temp, °F	550	475	545	316	400	450
Superheat steam temp, °F	955	955	950	815	905	900
Superheat steam pressure, psig	2300	2400	2400	735	1940	1450
Number of loops	3	3	3	6[b]	3	3
Number of units or modules	9[c]	108[d]	18[e]	24[f]	9[g]	9[h]

[a] Equivalent - 200 MW(e) desalting, 150 MW(e) power.
[b] One loop on standby.
[c] Three evaporators, three superheaters, three reheaters - one each per loop.
[d] Thirty-six evaporators, 36 superheaters, 36 reheaters - 12 each per loop.
[e] Nine evaporators, nine superheaters - three each per loop.
[f] Twelve evaporators, 12 superheaters, two each per loop.
[g] Three evaporators, three superheaters, three reheaters - one each per loop.
[h] Six evaporators, three superheaters - two evaporators and one superheater per loop.

8-26-74

Figure 4. Comparison of demonstration plants worldwide.

(CRBRP) is in the design stage[6] and will be preceded by the Fast Flux Test Facility (FFTF), a materials testing reactor which does not produce steam. The discussions below are primarily aimed at the CRBRP, although many of the observations and conclusions apply equally to the FFTF and other worldwide demonstration projects.

The primary material of construction for the sodium pressure boundaries is austenitic stainless steel, with ferritic steel used in the steam generator and steam piping.

AUSTENITIC STAINLESS STEEL WELDING

Despite the wide usage of austenitic stainless steels in chemical processing and petrochemical systems, few data are available on the high-temperature behavior of stainless steel weld deposits. Creep and cyclic loadings (fatigue and creep-fatigue) data are keys to predicting the service behavior of welds. These loading conditions will force materials to strain, and good ductility — the ability to deform without fracturing — is a property of key importance. The limited creep-ductility data available show a high degree of scatter; many creep failures involve strains on the order of 1% total elongation.[7-8] As a result of the low creep-ductility problem, an extensive stainless steel welding study is in progress at the Oak Ridge National Laboratory (ORNL), involving characterization of ferrite morphology, effects of electrode coatings, and effects of slight compositional differences on properties.

Ferrite Morphology

In order to avoid the occurrence of hot cracking (fissuring) in austenitic stainless steel weldments, it is common practice to assure that the weld deposit contains a small amount of δ-ferrite. The relative amount of ferrite in the austenite matrix depends upon the composition of the weld deposit.[8,9] Also, the morphology and distribution of the ferrite phase vary with welding process and welding conditions within a given process.[10]

The microstructure present in several different types of austenitic stainless steel weldments has been carefully characterized to determine whether at least part of the observed property variations can be attributed to microstructural differences.[10] The difference in chemical composition of the filler metals used for four typical welds cause the overall mean ferrite content to vary from 3.1 to 8.2 ferrite number (FN) as measured by the quantitative television microscope (QTM). These results could not be predicted accurately from the existing Schaeffler, McKay, or similar diagrams.

Further investigation revealed substantial variations in ferrite content from weld to weld produced under identical conditions, from location to location along the center line of a particular weld, and from point to point within a particular transverse weld cross section, as shown in Figure 5.

Also, the distribution and morphology of the ferrite present varied substantially in each of the mentioned locations. The ferrite was always located at dendritic or cellular dendritic substructure boundaries, forming a more or less continuous network.

Mechanical properties tests indicated that the ferrite plays a major role in the fracture process at elevated temperatures. The fracture path almost exclusively followed the location of austenite-ferrite boundaries in the as-deposited weld metal, and the fracture surface reproduced the solidification substructure in detail.

Effects of Type of Electrode Coating

Traditionally, shielded metal-arc electrode coatings are first evaluated on such practical grounds as ease of deposition, bead contour, arc

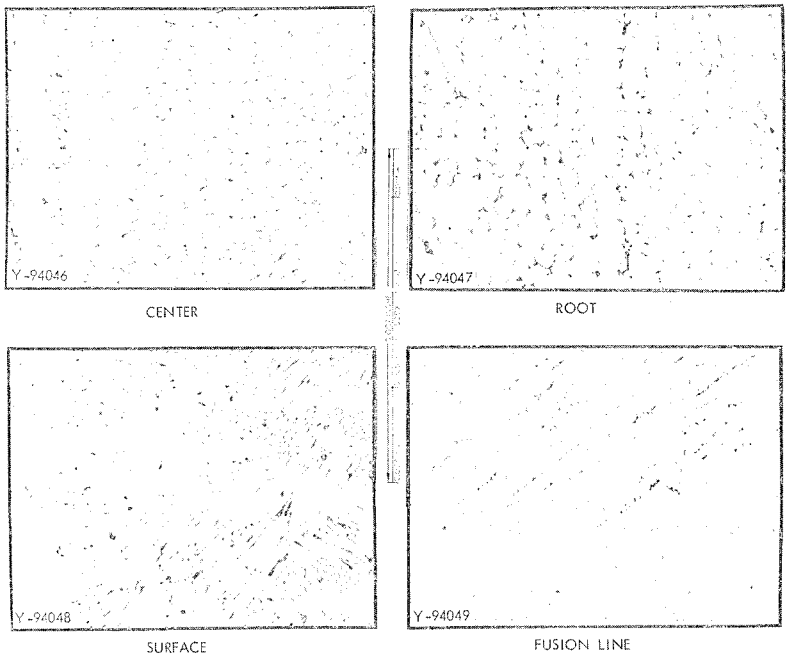


Figure 5. Variation in ferrite distribution in one cross section of a gas metal-arc weld sample. Etchant: KOH, $K_3Fe(CN)_6$.

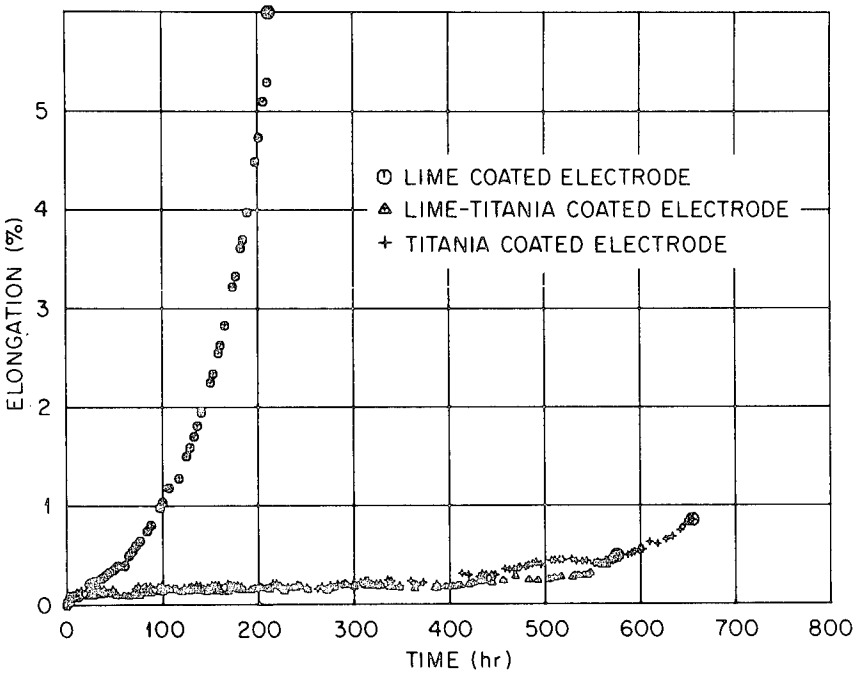


Figure 6. Elongation vs. time for experimental stainless steel deposits at 1200°F (649°C) and 18,000 psi (124 MPa).

stability, deposition efficiency, and ease of slag removal. Satisfactory bend and tensile properties of the weld are also mandatory. The collection of long-time creep data was not of major concern in the past because the applications have not required such data. The influence of particular flux coverings on the creep-rupture properties had received minimal attention. For this reason, ORNL obtained creep data at 1200°F (649°C) on the type 308 stainless steel weld metal deposited with the three most common types of E308-covered electrodes,[11] having the "lime," "lime-titania," and "titania" type of coverings. These are general classes of stainless steel electrode coating formulas that are well known and accepted throughout the welding industry. Each manufacturer has his own proprietary formulations, but the lime-type covering generally contains more calcium carbonate (limestone) and calcium fluoride (fluorspar) than the titania-type covering, and the titania-type covering contains more titanium dioxide (titania). The lime-titania covering is a compromise between the others.

Typical creep behavior for weld deposits made with each type of coated electrode is summarized in Figure 6. The weld metal deposited

from lime electrodes generally had the shortest rupture times and the greatest total elongation at each stress level. The deposits from lime-titania and titania-covered electrodes behaved nearly identically, rupturing with low ductility in long-term tests. The minimum creep rate and the tertiary creep behavior of the deposits from lime-covered electrodes differ markedly from those from the other types. The lime deposit has little steady-state or secondary creep strain, while the other electrode deposits remain in second-stage creep for relatively long periods of time, but have less third-stage creep. The total elongations of all three deposits tend to approach zero for rupture times of the order of 1000 hr.

Slight Compositional Variations

Previous work on compositional effects on stainless steel welds has usually been concerned with the influence of such elements as S, C, P, and Si on hot-cracking tendency, tensile strength, tensile ductility, and impact behavior. In a separate study at ORNL,[12] we determined the effects of various amounts of these same elements on the 1200°F (649°C) creep-rupture properties of type E308 weld deposits. Boron was also included in the experiments because it has been reported[13] to improve the creep resistance of various ferrous alloys. A series of experimental electrode batches was made by an industrial electrode manufacturer from the same heat of type 308 stainless steel core wire, but with several slightly different covering formulations to produce variations of deposit content of the elements mentioned above. In all cases, the coverings were of a typical lime-titania formulation because of its ac/dc, all-position characteristics. The adjusted deposit composition of each experimental batch of electrodes met the AWS A5.4-69 specification.

The creep behaviors of these welds were all similar at high stresses at 1200°F (649°C). Differences in creep behavior of the various deposits were apparent at low stress and the resulting longer rupture times. Table 1 shows the results of the creep tests run at 1200°F (649°C) under the relatively low 20,000 psi (138 MPa) static stress. The deposit with the highest carbon content proved to be much stronger than the standard deposit under these conditions. Lowering the carbon content below the standard did not appear to have any significant effect on the rupture life of the deposit, but it did increase rupture ductility. Adding boron to the type E308 deposit significantly improved both the rupture life and the rupture ductility. Lowering the amount of silicon in the type E308 deposit markedly increased the ductility but decreased the rupture life. There seems to be very little effect of sulfur content variations.

At a lower stress level of 18,000 psi (124 MPa) it became apparent that additions of phosphorus and boron significantly strengthen the weld deposit and resistance to creep embrittlement.

Table 1. Effect of Compositional Variables on the Creep Properties of Shielded Metal-Arc E308 Stainless Steel Welds at 1200°F (649°C) and 20,000 psi (138 MPa)

Compositional Variables	Rupture Time (hr)	Total Elongation (%)
Standard lime-titania covering*	363	2.0
Carbon, %		
Low, 0.035	346	4.0
High, 0.074	1334	1.75
Silicon, %		
Low, 0.29	127	15.7
High, 0.73	651	1.3
Phosphorus, %		
Medium, 0.023	166	9.6
High, 0.034	1329	4.35
Sulfur, %		
Low, 0.006	333	2.6
High, 0.027	292	4.05
Boron, %		
Medium, 0.004	1167	7.5
High, 0.006	1159	7.8

*0.044% C, 0.47% Si, 0.012% P, 0.016% S, 0.001% B.

Behavior of Optimized Electrode

An optimized E308 stainless steel electrode that produced deposits containing 0.007% B, 0.06% Ti, and 0.04% P was produced by an industrial manufacturer. It has been designated type 308 CRE stainless steel for the controlled residual elements it contains. We conducted an extensive mechanical properites and metallographic investigation of welds deposited in 2 3/8-in.-thick (60 mm) type 304 stainless steel plate with a double U-groove joint preparation.[14] The test specimens were taken from different locations within the weld and were categorized according to distance from the nearest plate surface regardless of the side of the midplane from which they came. They are designated L1 for surface specimens, L2 for one-third thickness specimens, and L3 for midplane specimens.

The superior elevated temperature ductility of the type 308 CRE stainless steel composition is evident in Figure 7. All the total strain data for CRE weld metal are contained in a scatter band when plotted against rupture time; comparable scatter bands are given for standard commer-

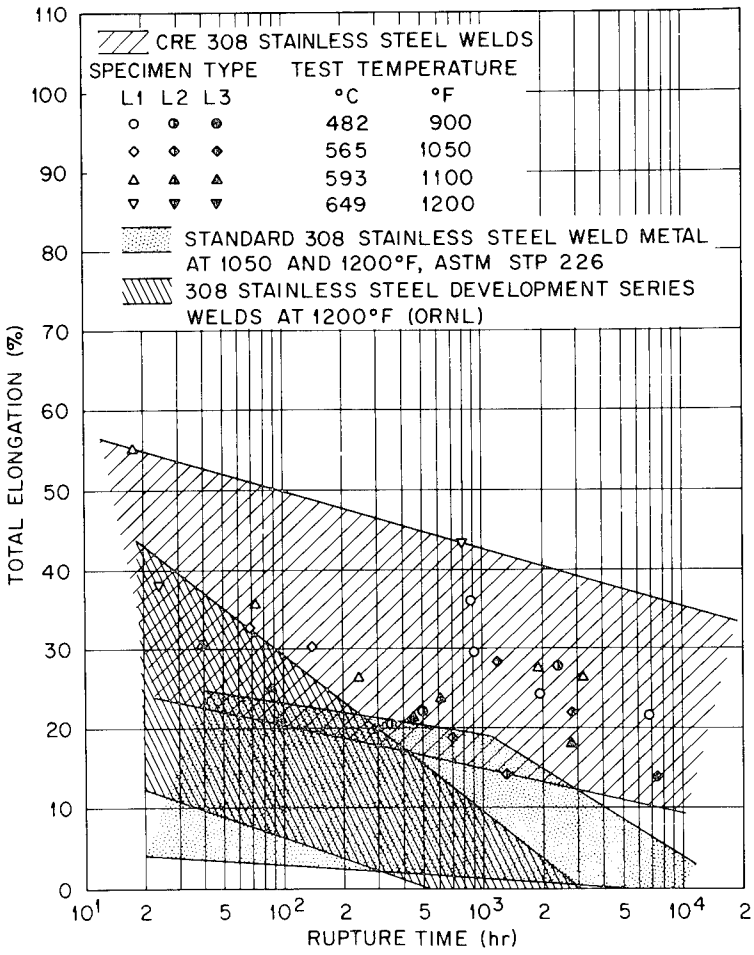


Figure 7. Ductility in creep-rupture tests of type 308 stainless steel welds.

cial weld metal and earlier developmental welds in the ORNL program. The lowest observed total creep strain for a CRE all-weld-metal specimens is 13%. Internal cracks did not develop at interphase boundaries.

The microstructure varied systematically through the thickness of the weld. In the initial passes at the center of the weld dislocation densities are highest, dislocation loops form, cell structures form, and $M_{23}C_6$ carbide precipitates on austenite-ferrite interfaces as a result of numerous thermal and mechanical cycles experienced during multipass welding. The carbide precipitate density, loop density, and dislocation

density decrease gradually toward the surfaces of the weld where less thermal and mechanical cycling occurs. Near the surface few dislocation loops and no precipiate are present, and the dislocation density is about a factor of 2.8 lower than near the center of the weld. The dislocations near the surface are generally straight, with only a hint of crude cell structure.

The systematic variations in creep properties at small and large strains and in tensile properties are at least partly attributable to these microstructural variations. Weld metal from initial passes tends to be stronger than that from the final passes.

AUSTENITIC STAINLESS STEEL COMPONENTS

The primary material of construction for the sodium containment of today's LMFBR, as mentioned earlier, is austenitic stainless steel. Thus, the metallurgical considerations discussed above for welds are relevant to the fabrication of the reactor vessel, intermediate heat exchangers, pumps, and primary and secondary sodium piping.

Reactor Vessel

A schematic of the CRBRP reactor vessel is shown in Figure 8. It is roughly 55 ft tall and 20 ft in diameter (17 × 6 m) and is constructed of type 304 stainless steel plate, nominally 2 3/8 in. (60 mm) thick. Sodium, flowing at a rate of 41.5×10^6 lb/hr (5230 kg/sec) enters the reactor at 730°F (388°C), passes through the core, and leaves the reactor at 995°F (535°C). The reactor vessel for the FFTF is nominally the same size and operates at essentially the same temperatures. It was fabricated by a commercial manufacturer (Combustion Engineering, Inc., Chattanooga Div., Chattanooga, Tennessee) using type 308 CRE coated electrodes for all structural welds. A view of one of the shell courses under construction is shown in Figure 9.

Intermediate Heat Exchangers

A schematic of one of the three intermediate heat exchangers for the CRBRP is shown in Figure 10. It is roughly 48 ft tall and 9 ft in diameter (15 × 2.7 m). It is a counterflow shell-and-tube design with the primary sodium on the shell side. Again, the FFTF uses a similar design. Figure 11 shows an IHX for FFTF under construction at a commercial manufacturer's plant.[15]

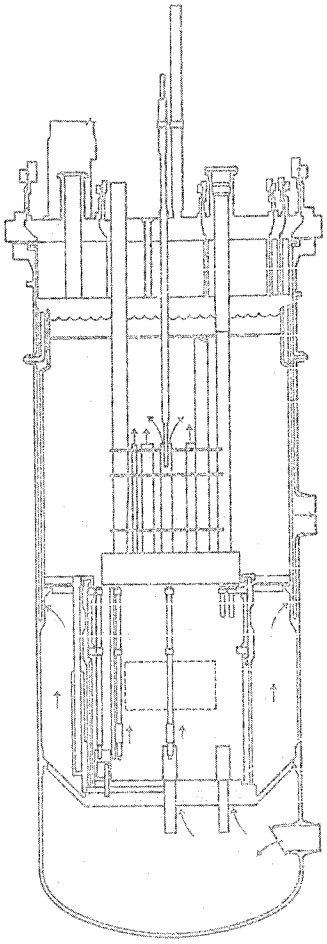


Figure 8. Schematic of CRBRP reactor vessel.



Figure 9. Fabrication of a shell course of the FFTF vessel. Combustion Engineering print.

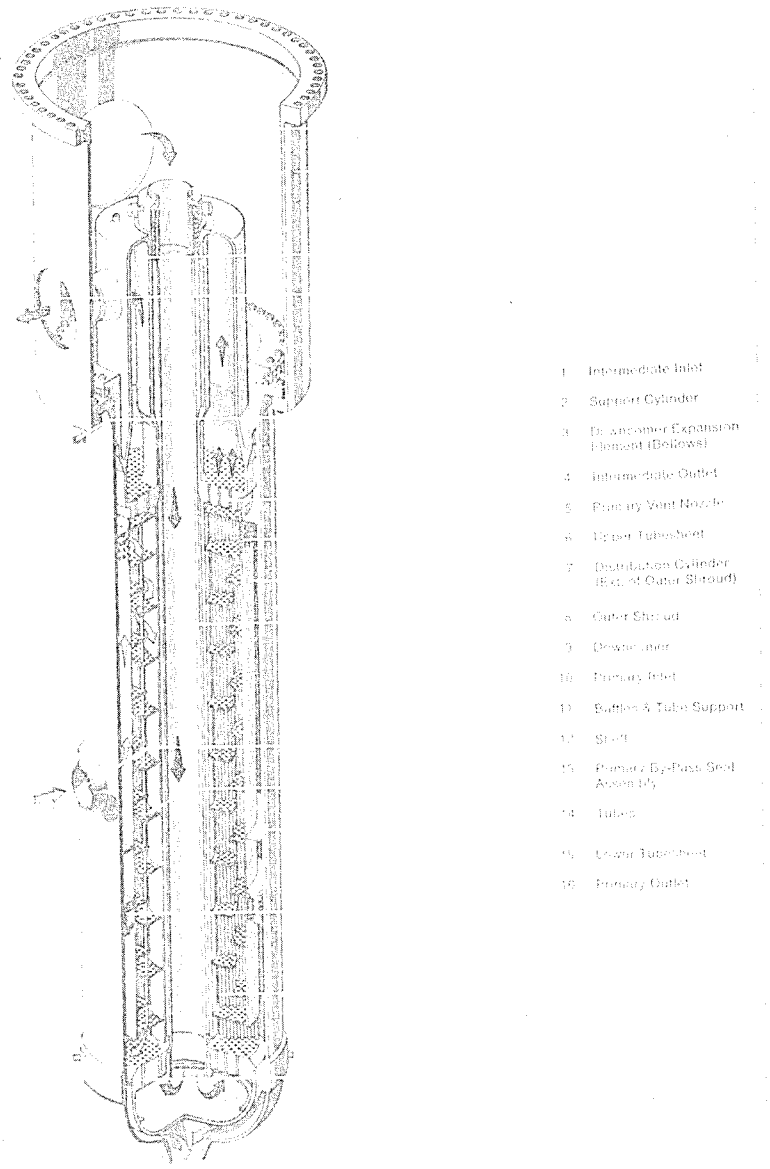


Figure 10. Schematic of CRBRP intermediate heat exchanger.

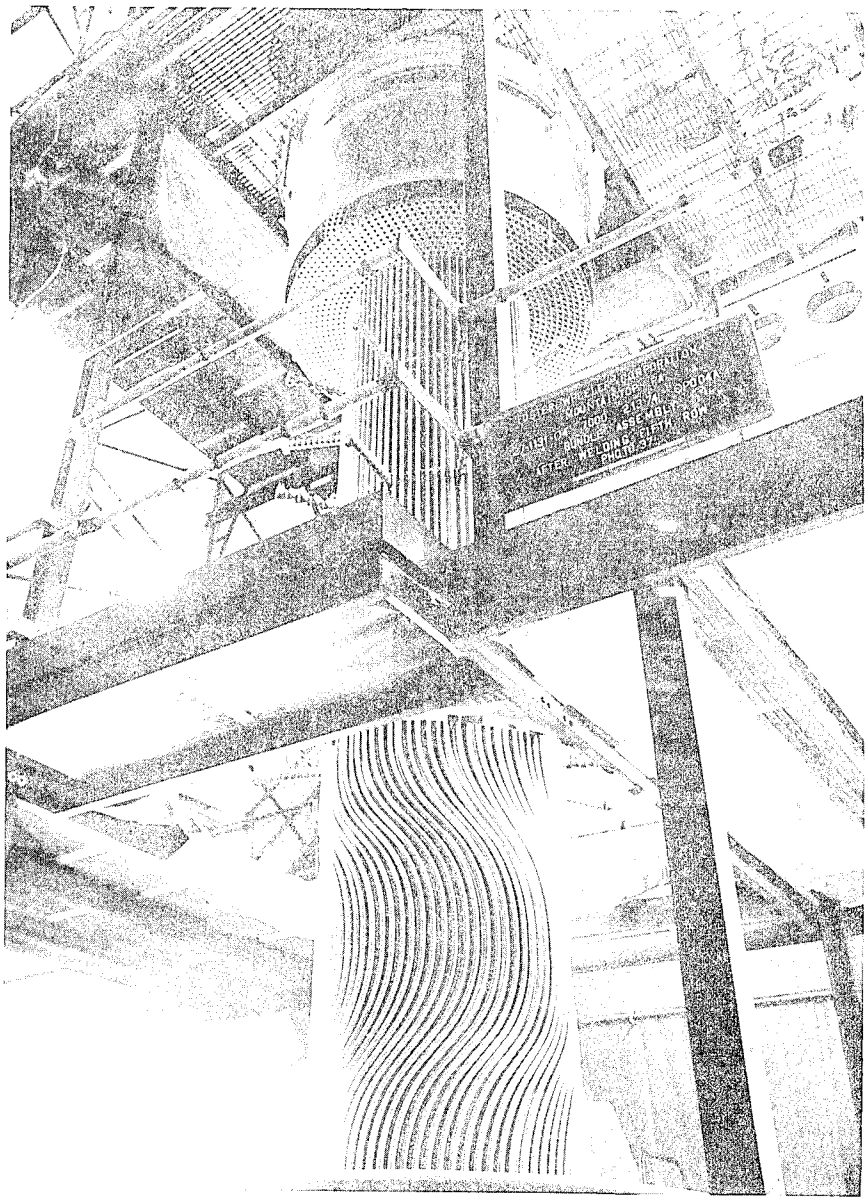


Figure 11. Fabrication of an IHX for FFTF.

A distinctive feature in U.S. designs of both IHXs and steam generators for LMFBR service is the "bore-side" tube-to-tubesheet weld. Figure 12 shows the bore-side weld compared with the conventional face-side weld. The bore-side weld is desirable to avoid the presence of the crevice between the outside of the tube and the tubesheet, and to provide a joint that is amenable to radiographic inspection. It is, however, a costly and difficult weld to produce, since the welding head must be inserted inside the bore of the tube, through a tubesheet that is over 6 in. thick for FFTF, and that will have similar thickness for CRBRP. Depending upon the type of welding equipment used and the size and wall thickness of the tubing for CRBRP, filler metal may be added to the weld joint at additional cost and with some procedural complication. Inert gas shielding is used on the outside of the tube to protect the root of the weld from oxidation. Radiographic inspection to nuclear core requirements is performed by inserting the radiation source, either a radioisotope "pill" or an X-ray tube of the pencil-anode type, into the bore of the tube and exposing film placed around the weld joint outside the tube.

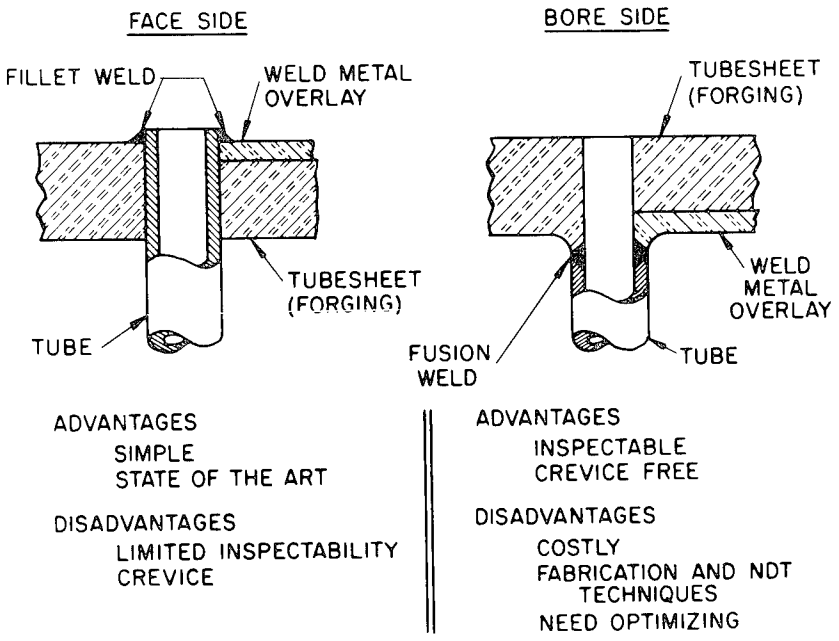


Figure 12. Tube-to-tubesheet welds for LMFBR intermediate heat exchangers and steam generators.

Pumps

A schematic of one of the six pumps (three primary and three secondary) for CRBRP is shown in Figure 13. It is approximately 57 ft tall and 12 ft in diameter (17 × 3.7 m). It is a free-surface centrifugal unit driven by a 500 hp (373 KW) variable speed motor, capable of 33,700 gpm (2.13 m^3/sec). Figure 14 shows one of the FFTF pumps under construction at a commercial manufacturer's plant.[15]

Sodium Piping

A schematic plan view of the heat transport system arrangement for CRBRP is shown in Figure 15. The primary and secondary hot-leg piping is 36 in. (0.91 m) in diameter, while the primary and secondary cold-leg piping is 28 in. (0.71 m) in diameter. Large expansion loops are included in the design to accommodate thermal expansion. Sodium piping for the FFTF is somewhat smaller; 28 in. in diameter for the hot legs, and 16 in. (0.41 m) in diameter for the cold legs.

The sodium piping for an LMFBR provides a challenging design situation. The wall thickness of the piping is in fact determined by a compromise between two contradictory considerations. Loading from the internal pressure, gravity, and particularly thermal expansion, calls for increased wall thickness, while the thermal excursions due to rapid changes in coolant temperature during normal start-ups and shutdowns, as well as off-normal conditions, makes a thin wall desirable. Thus, the wall thickness of all primary sodium piping for FFTF is a modest 3/8 in. (9.5 mm) (see Figure 16).

The use of large-diameter, thin-walled pipe demands that the pipe welds be of high integrity. Further, diametral shrinkage must be minimized in these welds to avoid the stress concentrations that result from geometric discontinuities. Both these considerations may be resolved in part by the use of automated orbital pipe welding. The reproducibility and process control that can be achieved with an automated process cannot be matched by manual techniques.[16,17] Further, by careful selection of welding process variables (heat input, number of passes, etc.), diametral shrinkage can be reduced to acceptable levels.[18,19]

Another factor that must be considered is the present and future availability of skilled construction welders to accommodate the increasing demand for their services. A potentially serious shortage is predicted,[20] but automated welding, if applied on a large scale, can achieve higher productivity than comparable manual techniques.[17]

Figure 16 shows a portion of the primary piping for FFTF under construction at a commercial manufacturer's plant (Combustion Engineering, Inc., Chattanooga Div., Chattanooga, Tennessee).

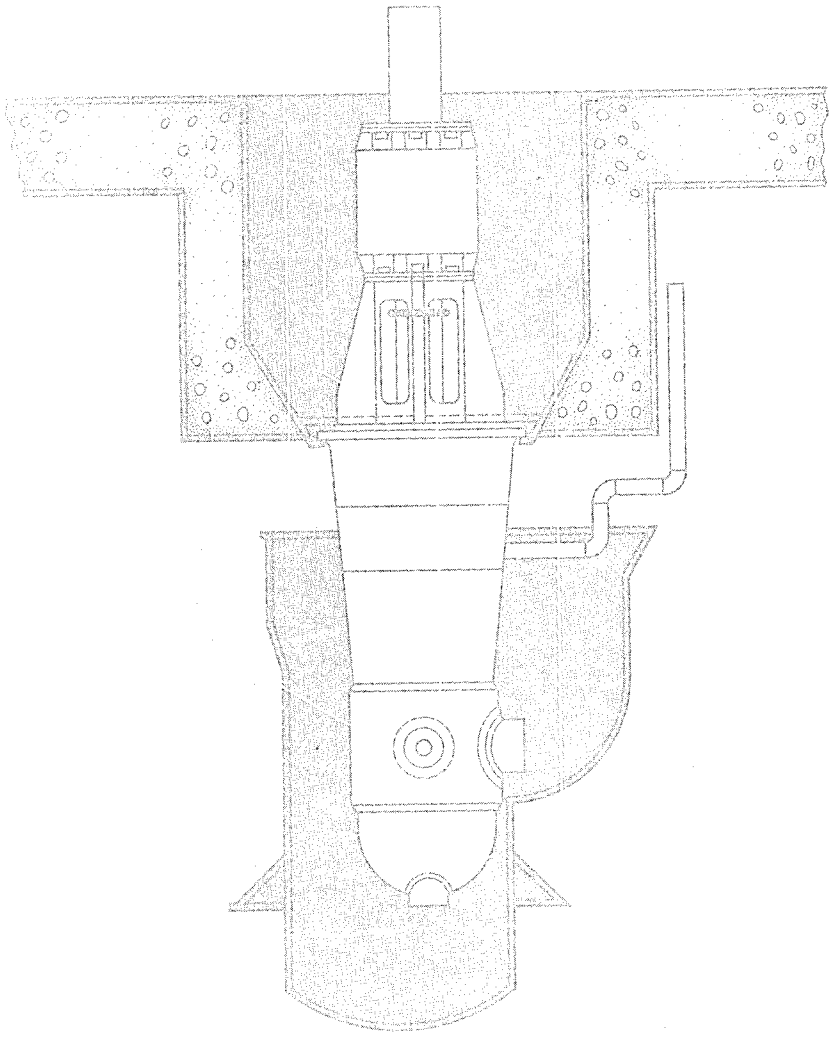


Figure 13. Schematic of CRBRP primary sodium pump.

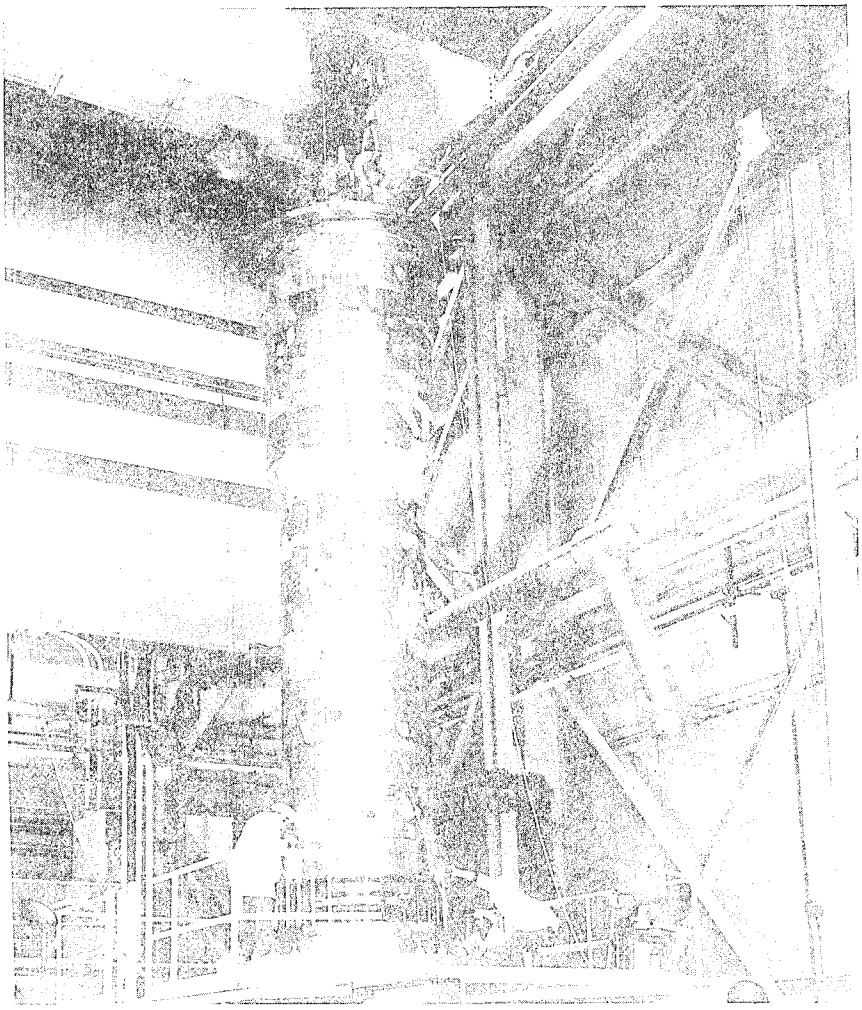


Figure 14. Fabrication of a primary sodium pump for FFTF.

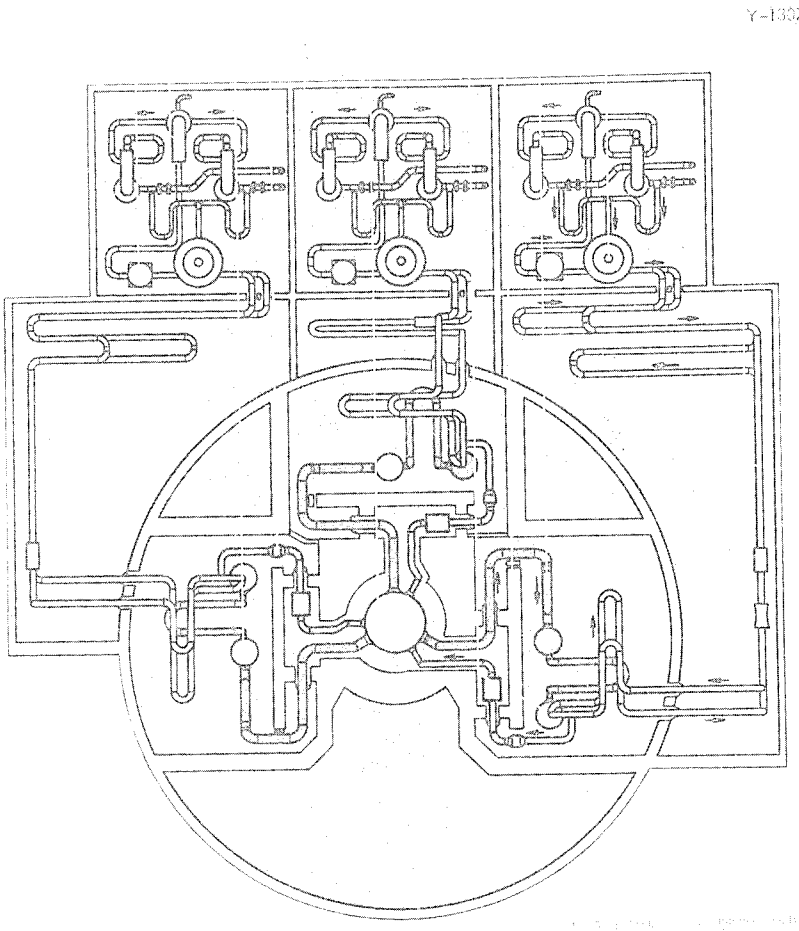


Figure 15. Schematic of CRBRP heat transport system arrangement.

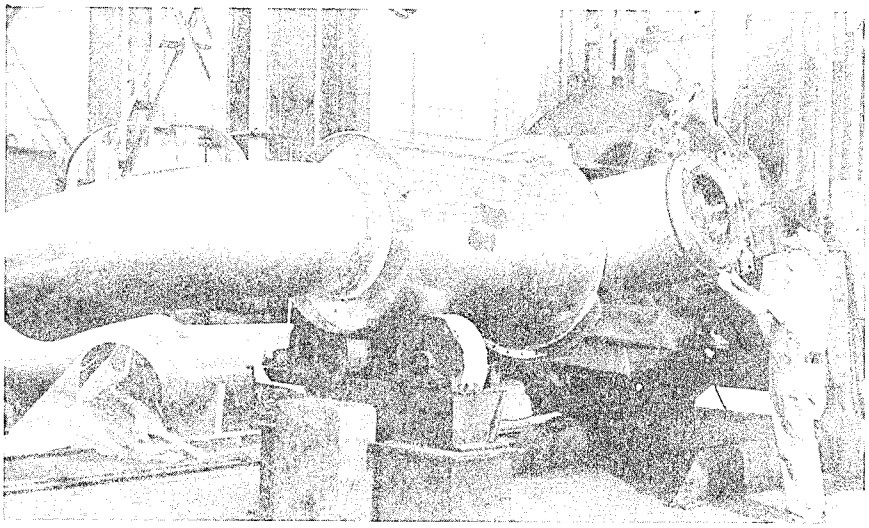


Figure 16. Fabrication of a portion of the primary sodium piping for FFTF. Combustion Engineering print.

FERRITIC STEEL WELDING

Whereas types 304 and 316 stainless steels can be welded without preheat or postweld heat treatment, ferritic steels cannot. The added requirements for process control and fabrication complications are not trivial in fabricating components for nuclear service.

However, the relative susceptibility of the austenitic stainless steels to corrosive attack in water containing chlorides and/or caustic limits the use of these materials in steam-generation systems. They can be used in dry steam (*e.g.*, superheaters) if precautions are taken to avoid carryover from the supersaturated ("wet") portions of the system. The conservative approach is to use ferritic steels for the entire steam system. Such an approach is planned for the CRBRP.

Steam Generators

A schematic of one of the nine steam generators (six evaporators and three superheaters) for CRBRP is shown in Figure 17. Each unit is approximately 65 ft in length and 4 ft in diameter (20 × 1.2 m) and each is constructed entirely of 2 1/4 CR-1 Mo steel. Since the FFTF has no steam generators, the design will be verified by model and full-scale tests

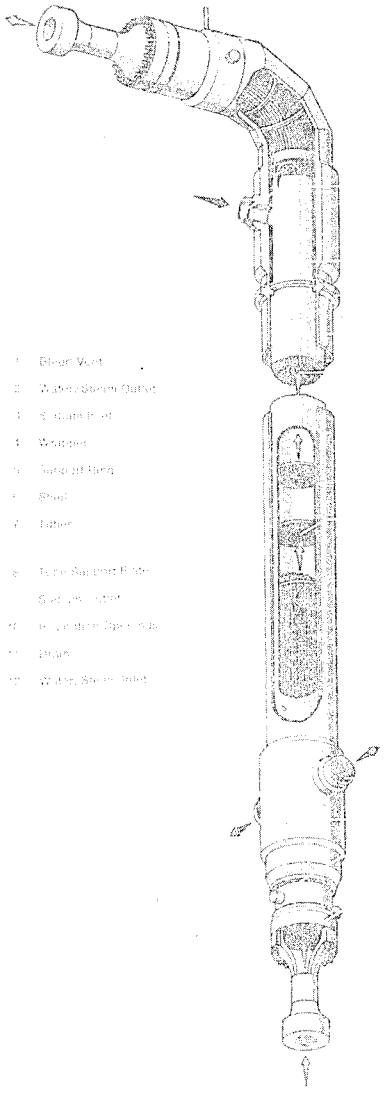


Figure 17. Schematic of CRBRP steam generator.

before CRBRP operations commence. Each unit has 757 tubes and therefore 1514 bore-side tube-to-tubesheet welds.

The desirability of bore-side welds is perhaps most vividly illustrated by the experience with the Alco/BLH steam generator.[21] This unit was performance tested at the Liquid Metal Engineering Center,[22] and subsequently destructively examined at the Oak Ridge National Laboratory.[21] It was of bimetallic construction, using type 316 stainless steel for all sodium-exposed surfaces and Inconel alloy 600 for all steam/water-exposed surfaces. Faulty tube-to-tubesheet welds, however, allowed sodium-water contact, and caustic stress-corrosion cracking progressed from the tube-to-tubesheet crevice throughout the 6-in.-thick (0.15 m) tubesheet, finally linking with the outer surface of the unit (Figure 18).

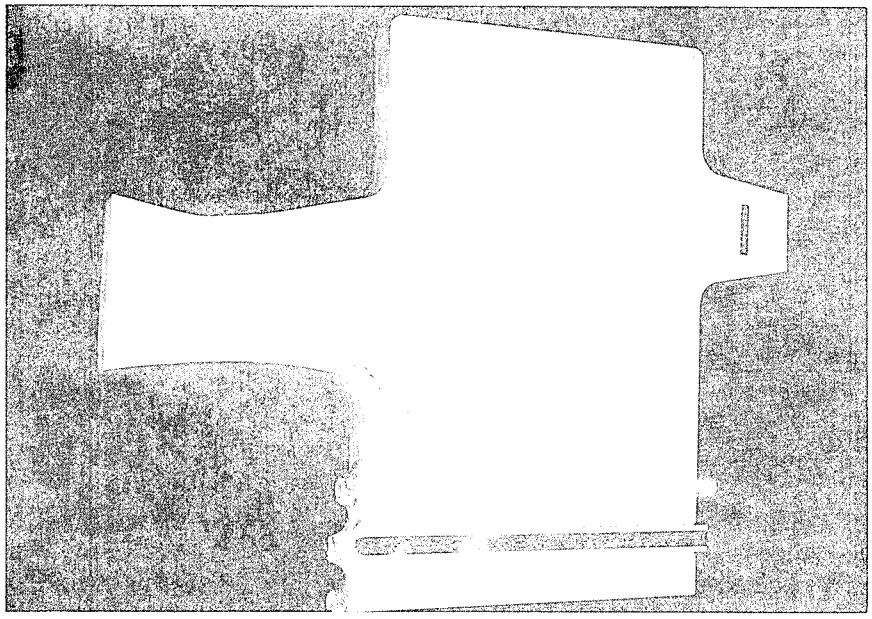


Figure 18. Section of Alco/BLH steam generator tubesheet.

TRANSITION JOINTS

The use of austenitic steels in the sodium system and ferritic steels in the steam system necessitates transition joints between these two materials, usually near the inlet and outlet of the steam generators. Although such joints have been used for many years,[23] the factors that

control their performance are poorly defined. Typically, the filler metal used has a thermal coefficient of expansion intermediate to the joined austenitic (high) and ferritic (low) steels. Thermal cycling can lead to low-ductility failure near the fusion line in the ferritic steel.[24]

MATERIALS CONSIDERATIONS

Throughout the above discussion, the materials of construction for both FFTF and CRBRP were identified without justification for their selection. Clearly, the process of materials selection is a complex one, and many different factors must be considered.[25,26]

Austenitic stainless steels have several significant advantages over other materials for use in the sodium systems of an LMFBR; high-temperature design ASME Code rules are established, a large mechanical properties data base exists, product forms are readily available, strength is adequate, and corrosion and mass-transfer resistance is suitable. However, there are persistent problems with the use of unstabilized austenitic steels, which have been known and endured for years, particularly the material's susceptibility to stress-corrosion cracking and intergranular attack.

The use of 2 1/4 CR-1 Mo ferritic steel for steam generators imposes a limitation on the maximum steam temperature that can be used. This limitation is due to the decrease in strength of that material at temperatures above 850°F (454°C). Such considerations indicate that the materials selection process will be continually reviewed, and that as service experience is gained in the demonstration plants, and as alloy development continues, alternate materials may show advantages that would lead to their use in future LMFBR plants.

SUMMARY

The energy demands of the United States are projected to increase. Nuclear power, in the form of the LMFBR, will likely be called upon to fill the gap between demand and supply.

The LMFBR is a sodium-cooled reactor system, which can produce electrical power and breed, assuring the capability for energy production to meet projected needs.

A typical system consists of a reactor vessel, intermediate heat exchanger(s), pump(s), sodium piping, and steam generator(s). The United States' effort centers around the FFTF, a non-steam-producing test reactor and the CRBRP, a large-scale demonstration reactor. The primary

material of construction for the sodium containment is austenitic stainless steel, with ferritic steel used in the steam system.

Conventional austenitic stainless steel weldments must be carefully analyzed when used in critical applications at elevated temperatures because generally they have low ductility in creep-rupture tests. The ferrite level is influenced by composition and varies with welding process, from weld to weld produced by a given process, and from location to location within a given weld. The low-ductility fracture path almost exclusively follows the austenite-ferrite boundaries.

Shielded metal-arc electrode coatings strongly influence the creep-rupture properties of austenitic stainless steel weldments. Lime-covered electrodes produced welds that were weaker but more ductile than either lime-titania or titania-covered electrode welds. Variations in the amounts of S, C, P, Si, and B affected the creep-rupture properties of austenitic stainless steel welds. An optimized electrode composition, designated "CRE" (for Controlled Residual Elements), was developed; it produced deposits containing 0.007% B, 0.06% Ti, and 0.04% P. Compared with standard commercial weld metal, the CRE material exhibits equivalent strength and superior creep-rupture ductility.

The fabrication of each major component for an LMFBR is described. Bore-side tube-to-tubesheet welds are used for both intermediate heat exchangers for FFTF and steam generators for CRBRP. Automated welding is highly desirable for critical sodium piping welds.

Austenitic-ferritic transition joints are required in current systems, and the factors that control their performance are poorly defined.

The selection of materials for a given component will be continually reviewed, and alternate materials may eventually show advantages that would lead to their use in future LMFBR plants.

ACKNOWLEDGMENTS

Research was sponsored by the U.S. Energy Research and Development Administration under contract with Union Carbide Corporation. The breadth and duration of the work described in this chapter preclude individual recognition of all who have contributed to its progress. The cooperation and counsel of staff members of Combustion Engineering, Inc., Chattanooga Division, Westinghouse-Tampa Division, Foster Wheeler Corporation, and Westinghouse Advanced Reactors Division have been invaluable. Within the Oak Ridge National Laboratory, members of many groups, including Welding and Brazing, Mechanical Properties, Metallography, Electron Microscopy, and the Reports Office have contributed.

REFERENCES

1. Culler, F. L., Jr. and Harms, W. O., "Energy From Breeder Reactors," *Phys. Today*, **25**, No. 5 (1972), 28–39.
2. "Fast Breeder Reactor Report," Edison Electric Institute, New York, Publication No. EEI 68-28, April 1968.
3. "Report of the EEI Reactor Assessment Panel," Edison Electric Institute, New York, Publication No. EEI 70-30, 1970.
4. Weinberg, A.M., "The Short Term Nuclear Option," Report of Cornell Workshops on the Major Issues of a National Energy Research and Development Program, Cornell University, Ithaca, N.Y., 1973.
5. "Report of the Liquid Metal Fast Breeder Reactor Program Review Group," Energy Research and Development Administration, Washington, D.C., Report No. ERDA-1, January 1975.
6. "Clinch River Breeder Reactor Plant," Westinghouse Electric Corporation, Pittsburgh, Pa. for the Breeder Reactor Corporation, October 1974.
7. Voorhees, H. R. and Freeman, J. W., *The Elevated-Temperature Properties of Weld-Deposited Metal and Weldments*, Special Technical Publication 226. Philadelphia: American Society for Testing and Materials (1958).
8. Schaeffler, A. L., "Constitution Diagram for Stainless Steel Weld Metal," *Metal Progr.*, **56** (1949), 680B.
9. Delong, W. T., Ostrom, G. A., and Szumachowski, E. R., "Measurement and Calculation of Ferrite in Stainless-Steel Weld Metal," *Weld. J.*, **35** (1956), 521s-28s.
10. Goodwin, G. M., Cole, N. C., and Slaughter, G. M., "A Study of Ferrite Morphology in Austenitic Stainless Steel Weldments," *Weld. J.*, **51** (1972), 425s-29s.
11. Binkley, N. C., Goodwin, G. M., and Harman, D. G., "Effects of Electrode Coverings on Elevated Temperature Properties of Austenitic Stainless Steel Weld Metal," *Weld. J.*, **52** (1973), 306s-11s.
12. Binkley, N. C., Berggren, R. G., and Goodwin, G. M., "Effects of Slight Compositional Variation of Type E308 Electrode Deposits," *Weld. J.*, **53** (1974), 91s-95s.
13. Heger, J. J., "Residual Elements in Stainless Steel — General Characteristics," in *Effects of Residual Elements on Properties of Austenitic Stainless Steel*. Special Technical Publication 418. Philadelphia: American Society for Testing and Materials (1967), 120–36.
14. King, R. T., Stiegler, J. O., and Goodwin, G. M., "Relation Between Mechanical Properties and Microstructure in CRE Type 308 Weldments," *Weld. J.*, **53** (1974), 307s-13s.
15. *Westinghouse Nuclear Engineering Digest, Vol. 3*. Westinghouse Electric Corporation, Westinghouse Nuclear Energy Systems, Pittsburgh, Pa. (1974).
16. Goodwin, G. M. and Slaughter, G. M., "Automated Welding of Stainless Steel Piping Systems," paper presented at the 55th Annual Meeting of the American Welding Society, Houston, Texas, May 6–10, 1974.
17. Goodwin, G. M. and Slaughter, G. M., "Automated Welding of Aluminum Pipes," paper presented at the 56th Annual Meeting of the American Welding Society, Cleveland, Ohio, April 21–25, 1975.

18. Downey, J. C., Hood, D. W., and Keiser, D. D., "Shrinkage Evaluation in Mechanized Weld 16-in. diam. Circumferential Pipe Joints," Aerojet Nuclear Company, Idaho Falls, Idaho. U.S. Atomic Energy Commission Contract Report No. ANCR-1121, August 1973.
19. Condron, K. J., "Final Report on Weld Shrinkage Induced by Automated Gas Tungsten Arc Welding," Bechtel Power Corporation, San Francisco, Calif., April 1973.
20. Smith, W, R. Sr., "Nuclear Construction — Some Difficulties and Challenges," paper presented at Welding and Testing Technology Exhibition and Conference (WATTec), Knoxville, Tenn., February 21, 1974.
21. DeVan, J. H. and Slaughter, G. M., "Post-Test Examination of Alco/BLH Sodium-Heated Steam Generator," Oak Ridge National Laboratory, Tenn., U.S. Atomic Energy Commission Contract Report No. ORNL-4950, May 1974.
22. "Performance Evaluation of Heat Exchangers for Sodium-Cooled Reactors," United Nuclear Corporation, Elmsford, N.Y., U.S. Atomic Energy Commission Contract Report No. UNC-5236, June 1969.
23. King, J. F., "Behavior and Properties of Welded Austenitic Stainless-to-Ferritic Steel Transition Joints — A Literature Review," Oak Ridge National Laboratory, Tenn., to be published.
24. Barford, J. and Probert, K. S., "Interfacial Effects in Dissimilar Steel Joints," paper presented at the International Conference on Welding Research Related to Power Plants, September 17–21, 1972.
25. "Report of Task Force on Alternate Structural Materials for Liquid Metal Fast Breeder Reactors," Oak Ridge National Laboratory, Tenn., to be published.
26. Patriarca, P., "ORNL Five-Year Plan for Materials for Advanced LMFBR Steam Generators," Oak Ridge National Laboratory, Tenn., November 1974.

2. DYNAMICS OF WELD CRACKING

E. F. NIPPES
Rensselaer Polytechnic Institute
Troy, New York

A plea is made for the recognition of three new zones in a weldment. Evidence is presented to show that the weld metal consists of two distinct zones – a composite zone and an unmixed zone. In addition, metallographic evidence is given to substantiate both the presence and the importance of a region adjacent to the fusion boundary within which partial melting occurs.

Two new testing procedures are described – one for hot-cracking sensitivity and the second for cold-cracking sensitivity.

At the conference, high-speed motion pictures were shown of hot cracking and time-lapse motion pictures were presented of cold cracking.

INTRODUCTION

Cracking-type defects in weldments may be classified in many ways. If one considers the temperature of formation of cracks, they may be categorized as either hot or cold cracks.

Cold cracks in steel weldments may form during cooling immediately after welding or may occur after protracted periods of time after welding. Cold cracking, or hydrogen-induced cracking, in steel weldments occurs when all of the following are present:

1. a crack-sensitive microstructure, such as martensite;
2. a diffusible hydrogen content which exceeds a critical value; and
3. stresses which exceed a critical level.

Hot cracks in weldments occur at temperatures above the effective solidus of the weld deposit and the adjacent heat-affected base metal. The effective solidus temperature of an alloy is usually much lower than its equilibrium solidus temperature because of microsegregation, which is almost always present, even in the base metal.

Cold and hot cracking may occur in both the weld deposit and the adjacent base metal and the cracks may be oriented longitudinally

and/or transversely with respect to the welding direction. Because these cracking defects are intimately associated with the weld deposit and the adjacent base metal, these regions have been subjected to careful metallographic examination at RPI.

SUGGESTED REVISIONS IN TERMINOLOGY

The junction of the weld deposit and the base metal has been generally viewed simply as a two-dimensional surface of demarcation between completely melted weld metal and completely solid base metal. The various zones of a fusion weld have been defined by the American Welding Society[1] as follows:

Bond Line: The junction of the weld metal and the base metal.

Weld Metal: That portion of a weld which has been melted during welding.

Fusion Zone: The area of base metal melted as determined on the cross section of a weld.

Heat-Affected Zone: That portion of the base metal which has not been melted, but whose mechanical properties or microstructure have been altered by the heat of welding.

Base Metal: The metal to be welded.

These definitions were found to be inadequate when the fusion boundary of heterogeneous welds were examined metallographically. For example, when filler metal is added during welding, the completely melted weld metal is not a single homogeneous region but actually consists of two distinct regions with a diffusion gradient between them.

Composite Zone

The bulk of the weld metal consists of a mixture of filler metal with base metal and has a composition intermediate between the two. This zone, which has a characteristic microsegregation pattern, has been termed the "composite zone."

Unmixed Zone

The other region, which is located between the composite zone and the bond line, is an easily masked narrow band consisting essentially of melted and solidified base metal. This region, which has also a characteristic microsegregation pattern, has a nominal composition equivalent to the base metal. Because the material in this zone experiences no mixing with the filler metal, the term "unmixed zone" has been proposed.

The equivalence between the unmixed zone in a heterogeneous weld and the overall weld metal in an autogeneous weld (in which no filler metal is added) is significant in cases where the primary purpose of adding a filler metal is to avoid some problem associated with an autogeneous weld metal. No matter how well the composition in the composite zone is modified, the problem can still persist in the narrow unmixed zone where the composition remains essentially that of the base metal. As an example, in austenitic stainless weldments, filler metals with a balanced composition may reduce the microcracking tendency of the composite zone. If, however, the base metal is sensitive to microfissuring, cracking might occur in the unmixed zone, which would have the same composition as the base metal.

Partially Melted Zone

There is a need for revision of the term presently being used to indicate the heat-affected zone, in that partial melting occurs in that portion of the base metal adjacent to the bond line. This region, which has been termed the "partially melted zone," encompasses that portion of the heat-affected base metal which has undergone any amount of localized melting. Within this region, the extent of melting is 100% at the bond line, where the peak temperature of the thermal cycle is the liquidus, and 0% at the edge of the heat-affected zone where the peak temperature of the thermal cycle is the effective solidus.

Conventional metallography does not reveal the unmixed zone or the partially melted zone. In heterogeneous welds, because the composite zone has a different composition than the base metal (and the unmixed zone), etchants attack them differently. As a result, a sharp line of demarcation generally appears at the junction between the composite and unmixed zones. This demarcation line has been mistakenly identified in the past as the bond line. Thus, welding defects which actually occurred in the unmixed or partially melted zones, were thought to have occurred in the heat-affected zone.

Figure 1 shows the striking difference between the appearance of a location along the fusion boundary, as revealed by a special solute-sensitive etchant (Figure 1A) and the identical location, as revealed by a conventional etchant (Figure 1B). In Figure 1A the special etchant has stained the iron-rich, solute-lean areas darker than the solute-rich regions. In Figure 1A, the dark-etching material at the top is the composite zone. The light-etching unmixed zone, which is in the middle of the photomicrograph, has a cellular dendritic structure. The partially melted zone, located below the unmixed zone, exhibits localized melting which may be identified as light-etching grain boundaries and scattered light-

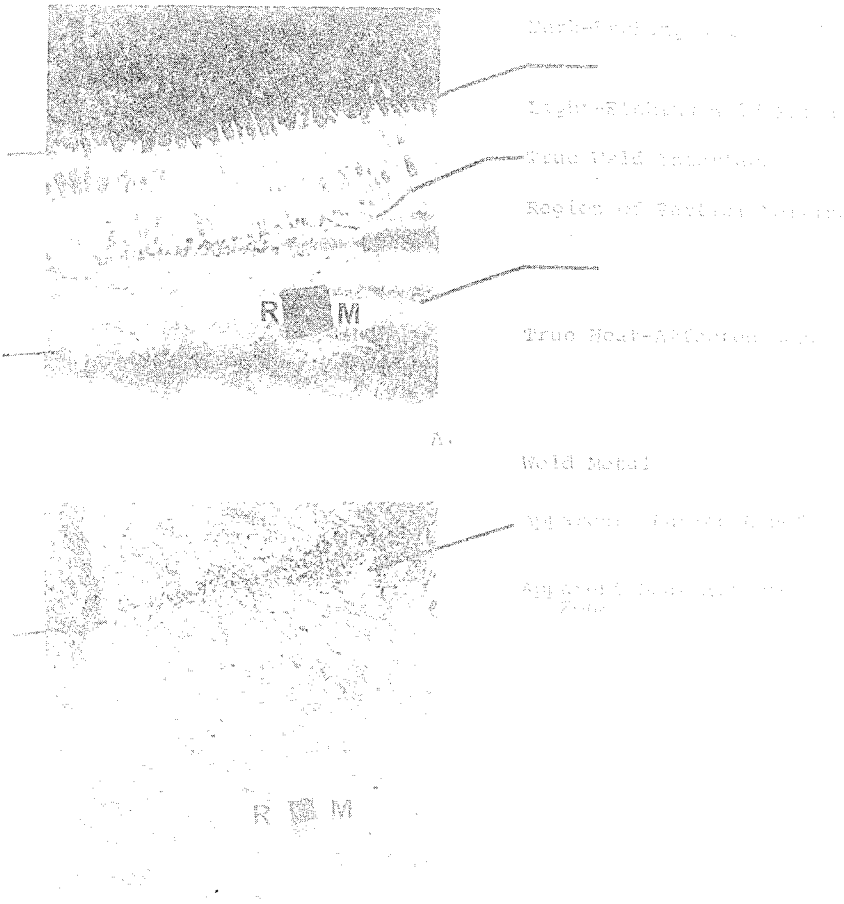


Figure 1. Fusion-boundary region in an HY-80 weldment made with E-11018M. A. Solution-sensitive etch, 250X. B. Same area shown in A, 2% nital etch, 250X. Reduced 31%.

etching dots. The true heat-affected zone is located at the bottom of the photomicrograph below the reference mark, RM, a microhardness indentation.

Figure 1B shows the identical area after repolishing and etching with 2% nital. Because this etchant attacks the unmixed, the partially melted, and the true heat-affected zones in a similar fashion, the apparent bond line corresponds to the edge of the composite zone. Note the

position of the reference mark, RM, which is actually located at the boundary between the partially melted zone and the true heat-affected zone.

The microstructure of the fusion boundary of a gas metal arc weld made in HY-130, etched with a solute-sensitive etchant, is shown in Figure 2. The crack, which has propagated along the light-etching, solute-rich, grain boundaries in the partially melted region, is a hydrogen-induced cold crack. Because the base metal and filler metal compositions were similar, the identification of the narrow unmixed zone is more difficult in this case.

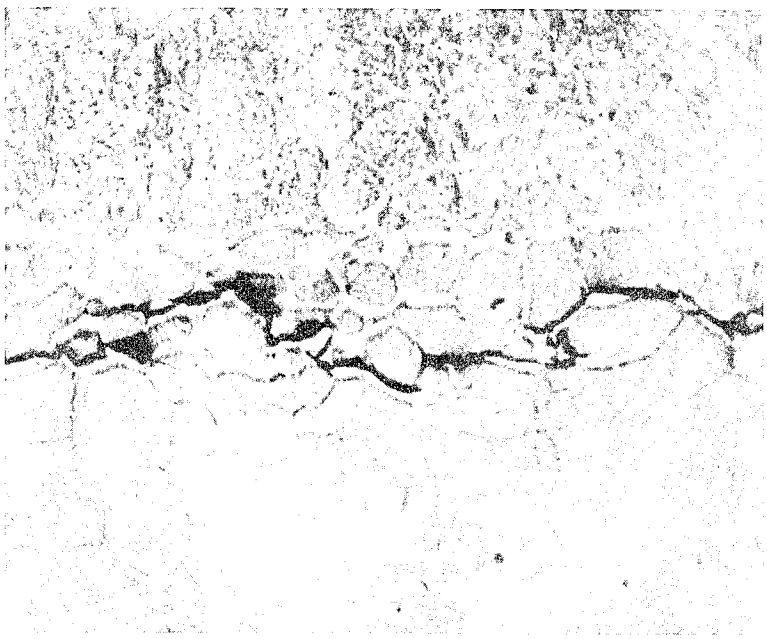


Figure 2. Fusion-boundary region of a gas metal arc weld in HY-130 steel containing underbead crack, solute-sensitive etch, 250X. Reduced 35%.

There are possibilities of interactions between inclusions and the matrix which can increase the extent of the partially melted zone. The interaction between two MnS inclusions and the HY-80 matrix, as etched with a solute-sensitive etchant, is shown in Figure 3 at 1000X. The two elliptically shaped areas, which experienced liquation and resolidification during welding, were formed by the mechanism of constitutional liquidation.[2] The dark grey material in the center of each of these

two regions is the remainder of the MnS inclusions which dissolved during the constitutional liquidation.

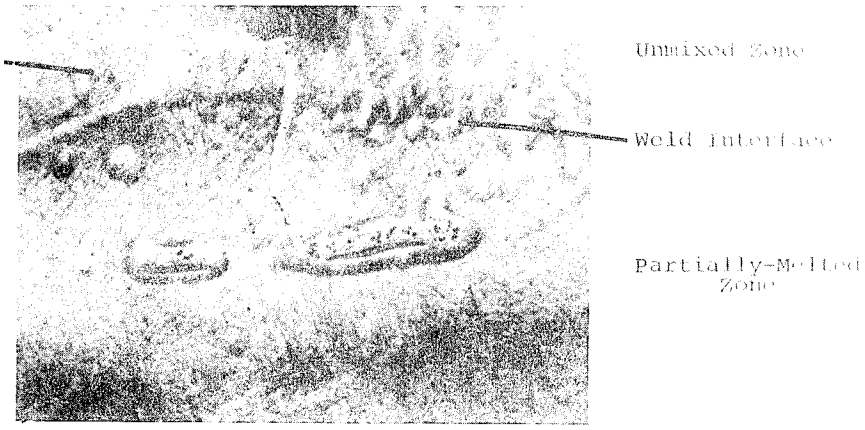


Figure 3. Constitutional liquidation of MnS in HY-80 weldment, solute-sensitive etch, 1000X. Reduced 47%.

REQUISITES FOR WELD CRACKING TESTS

A recent survey of the literature[3] reports that over 30 different weld cracking tests have been developed. The ideal cracking test, according to this report, should have:

1. Ability to show direct correlation with actual fabrication and service behavior.
2. Reproducibility, with freedom from human error.
3. Sensitivity to small changes in variables.
4. Ability to show the effects of individual welding variables.
5. Economical preparation.
6. Applicability to all welding processes.

At RPI a hot-cracking test and a cold-cracking test have been developed; these tests, which meet the majority of these criteria, will now be discussed.

HOT CRACKING TEST — THE VARESTRAINT TEST

The VARESTRAINT test, which has been described in detail[4,5] utilizes a small laboratory-scale specimen supported as a cantilever beam as shown in Figure 4. A weld is deposited on the specimen using any

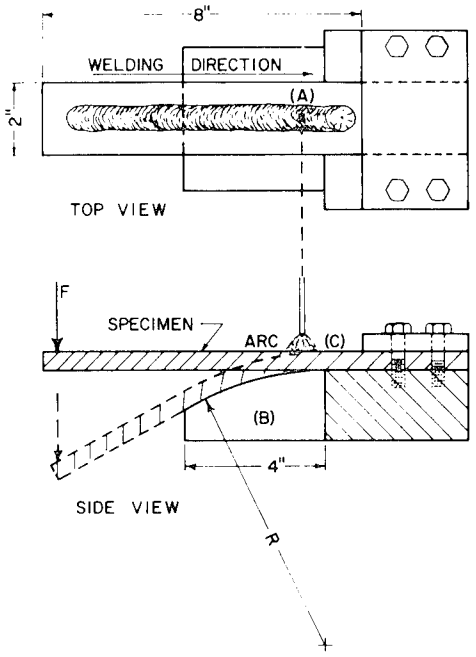


Figure 4. Schematic of VARESTRAINT test.

combination of process, joint geometry, and welding parameter of interest. As the arc passes the point marked A in Figure 4, a massive, pneumatically actuated loading yoke bends the specimen downward suddenly to conform to the radius of curvature of the top surface of the removable die block. By substituting a die block with the appropriate radius of curvature, any desired augmented strain can be applied to the outer fibers of the test specimens. The augmented strain in the outer fibers of a test specimen is equal approximately to $\frac{t}{2R}$, where t equals the specimen thickness, and R equals the radius of curvature of the die block.

Since the magnitude of the augmented strain is independent of the welding parameters, the effect of welding process, welding composition, and other parameters influencing the microstructural features of the weldment can be isolated from the mechanical effect of the externally imposed restraint.

Hot cracking is usually located at the trailing edge and alongside of what was the instantaneous position of the weld puddle at the instant of application of augmented strain, as shown schematically in Figure 5. The

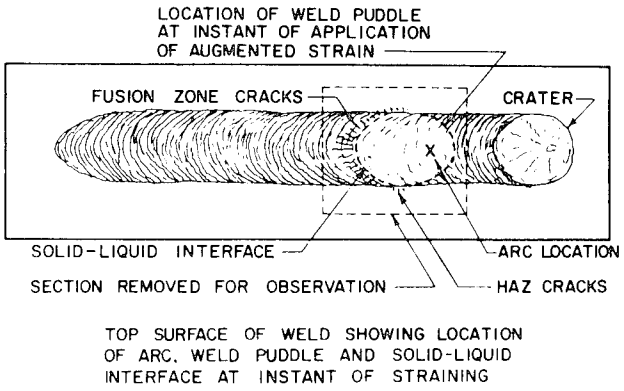


Figure 5. Hot cracks in a VARESTRAINT test specimen.

cracks invariably follow solute-enriched grain and subgrain boundaries both in the weld metal and in the partially melted zone of the base metal, as is evident in Figure 6, a photomicrograph of an 18% Ni maraging steel VARESTRAINT test specimen.

After testing, the length of each hot crack detected on the as-welded surface is measured at 60X. The total crack length plotted as a function of augmented strain provides a quantitative description of hot-cracking propensity.

Typical VARESTRAINT results are presented in Figure 7 for several materials. In addition to the total crack length, the maximum augmented strain sustained without causing cracking, called the threshold strain, can be used as an index of hot-cracking sensitivity. Although not shown in Figure 7, the maximum crack length observed in a specimen can be also used as an index.

The results of the VARESTRAINT tests have correlated well with fabricational experience. The test has proved sensitive to small changes in test variables for a variety of welding processes, and the reproducibility is normally ± 10%. The cost for evaluating the hot-cracking sensitivity of a heat of material is nominal. The test procedure has attracted considerable industrial usage. One manufacturer of nickel-base alloys subjects all heats to this test; another determines the hot-cracking sensitivity of nickel-base alloys by subjecting slabs from ingots to the test procedure.

Because the location of the weld pool, and therefore the location of the hot cracks, at the instant of loading can be programmed, high-speed cinematography of the nucleation and growth of hot cracks is made possible.

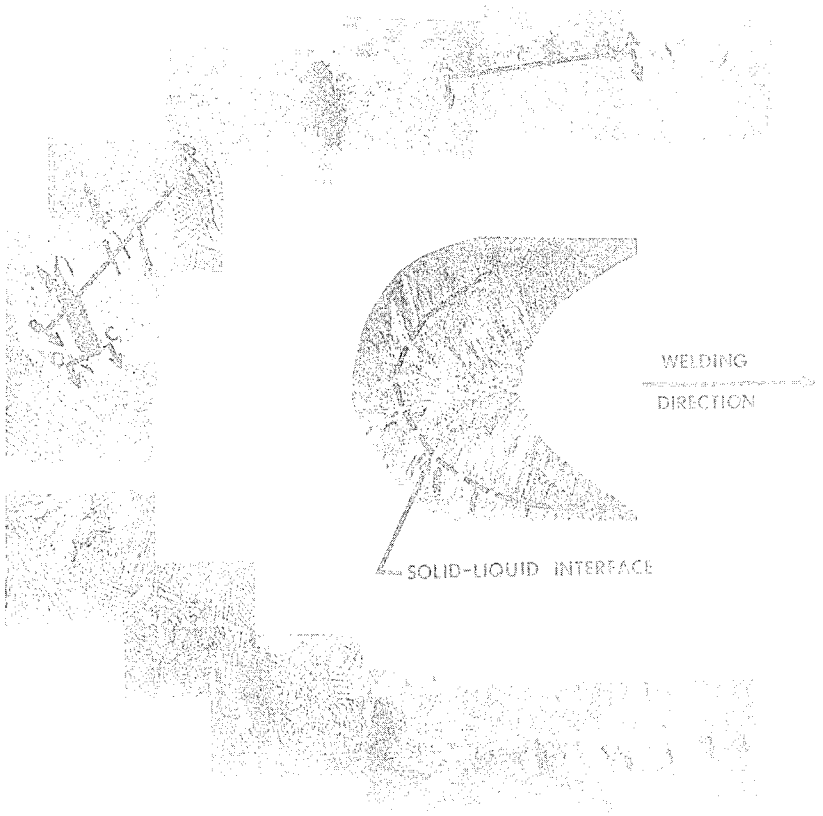


Figure 6. Location of hot cracks in a typical VARESTRAINT test in 18-Ni maraging steel, modified Wasau's etch,. 15X for central portion, 50X for montage. Reduced 36%.

THE CONSTANT-STRAIN COLD-CRACKING TEST

A direct-observation technique, originally proposed by Granjon[6] and modified at RPI,[7–9] allows direct microscopic observation of the initiation and propagation of hydrogen-induced cracks, as well as the evolution of hydrogen. The test, which imposes an augmented strain on a tranverse cross section of a small, bead-on-plate steel weldment, has been invaluable in studying the mechanism of cold cracking.

Test specimens, 2 × 1/2 × 1/2 in. were cut from 2 in. HY-80 plate in the manner shown in Figure 8. Orientation of the banding was transverse to the welding surface, and the location of the weld beads cor-

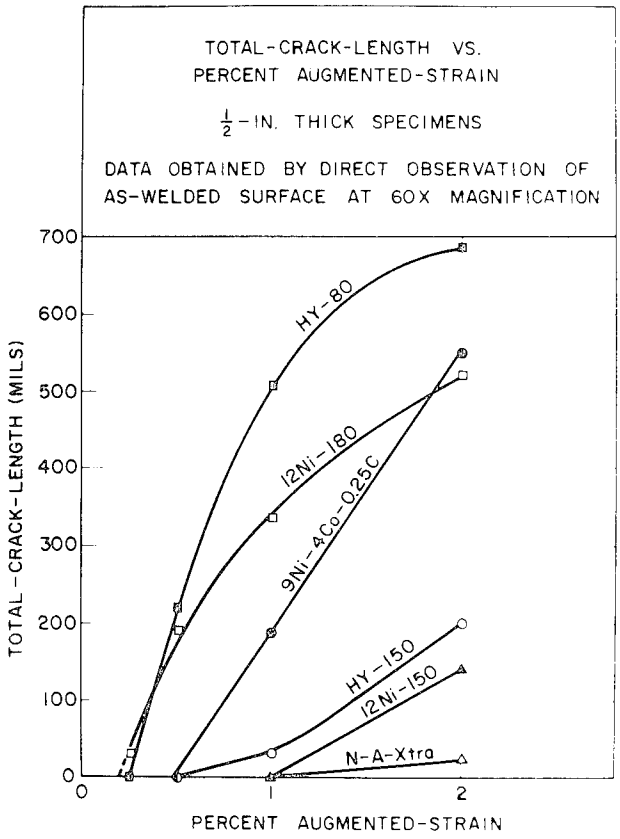


Figure 7. Total crack length vs. augmented strain for several materials.

responded to the mid-thickness of the as-received plate. The 2 × 1/2 in. surfaces were ground parallel and prepolished through 600-grit alundum paper. With the prepolished surfaces in contact, pairs of specimens were welded as shown in Figure 9. E11018M electrodes, 3/16 in. diameter, were deposited by means of an automatic stick feeder, using 165A, 22V, and 7.5 in./min. travel speed to provide an energy input of 29,000 joules/in.

The amount of diffusible hydrogen present in the weldments was controlled by intentionally contaminating the electrode coatings with water and then baking at selected temperatures to partially redry them. The diffusible hydrogen content was determined by the BWRA method[10] and reported as cc/100 gm of weld metal.

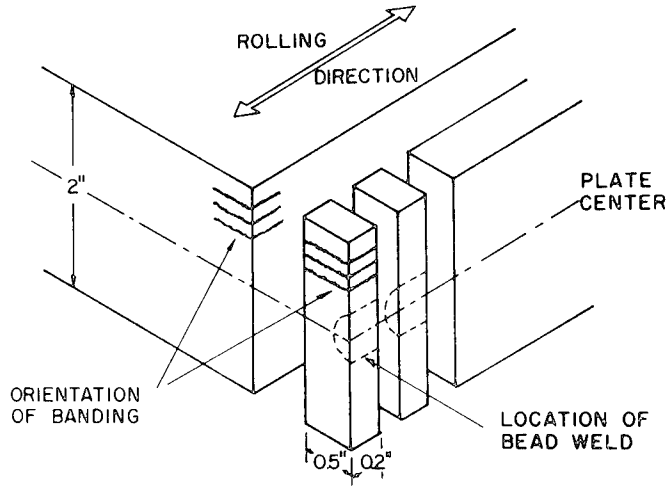


Figure 8. Schematic showing method of obtaining constant-strain cold-cracking test specimens from 2-in. Hy-80 plate.

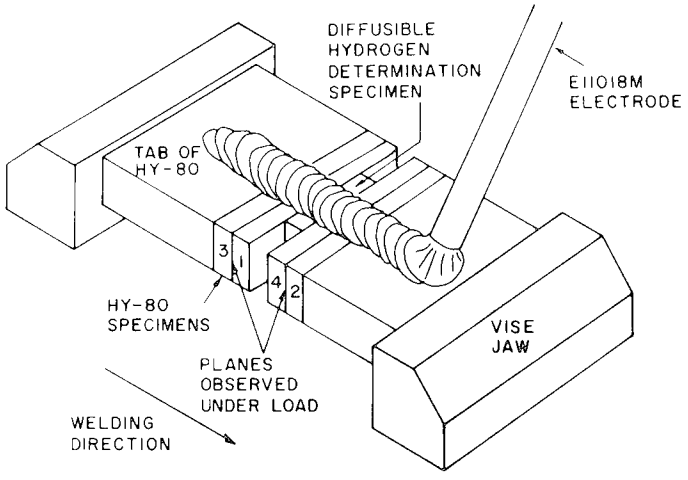


Figure 9. Schematic showing method of welding constant-strain cold-cracking test specimens.

Immediately after welding, the composite weldment was quenched in ice water and then transferred into a bath of dry ice and alcohol (−96°F) to minimize the loss of diffusible hydrogen. Each specimen to be tested was fractured from the composite weldment and then prepared

by standard metallographic techniques to allow direct observation of the cracking process under a microscope. During this preparation, the specimen was cooled frequently in the dry ice-alcohol bath to minimize hydrogen loss.

Figure 10 presents two versions of the test apparatus. The first version, shown in Figure 10A, incorporated a four-point loading system to produce a constant bending moment on the outer fibers of a transverse section of the weld bead. Figure 11 shows an overall view of the cold-cracking test apparatus showing a 35-mm camera mounted on the microscope.

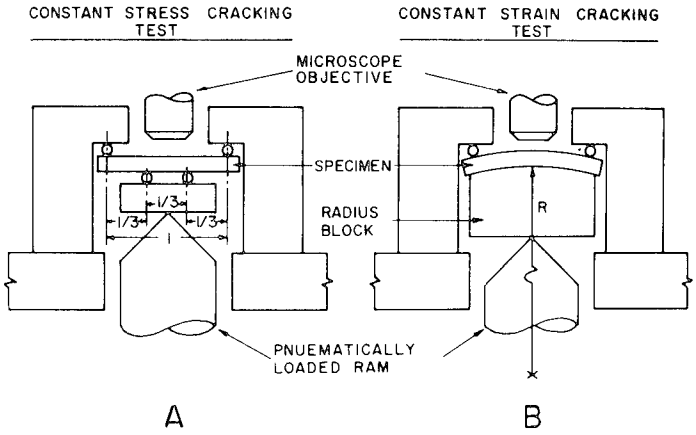


Figure 10. Schematic of constant-strain cold-cracking test fixtures. A. 4-point bending version. B. Radiused die block version.

With the four-point loading technique, it was noted that:

1. A critical value of hydrogen content was necessary for microcrack nucleation.
2. The critical value of hydrogen content was inversely proportional to the elastic stress imposed on the outer fibers of the specimen.
3. The critical value of hydrogen content at a given stress level depended on the steel.
4. Microcracks could be nucleated but failed to grow with stress up to the yield strength.
5. No microcracks were observed at any level of stress up to the yield strength in the absence of hydrogen.
6. In hydrogen-charged specimens which were notched and loaded to cause plastic flow, microcrack growth occurred intermittently for more than 24 hours.

7. Elongated MnS inclusions, particularly those that had experienced constitutional liquidation, served as nucleation sites for microcracks.

During these preliminary tests, it was discovered that when a thin layer of microscope immersion oil was placed on the specimen surface, hydrogen evolution could be observed microscopically to occur from the walls of the cracks.

The rate of the evolution of hydrogen bubbles from microscopic cracks was measured during the cracking test; these results are summarized in Figure 12. The rate of the evolution of hydrogen bubbles is shown as a function of loading time. Note that the rate of evolution increased as applied stress was increased. The rate appeared to increase with time to a maximum characteristic of the particular stress and then decrease with continued exposure to the load.

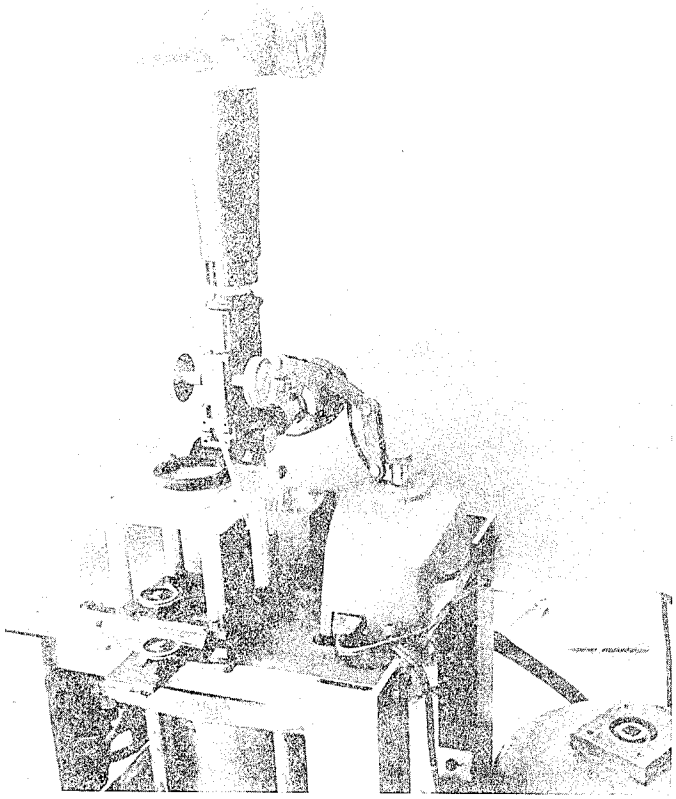


Figure 11. Overall view of constant-strain cold-cracking test apparatus, showing 35-mm still camera in position on microscope.

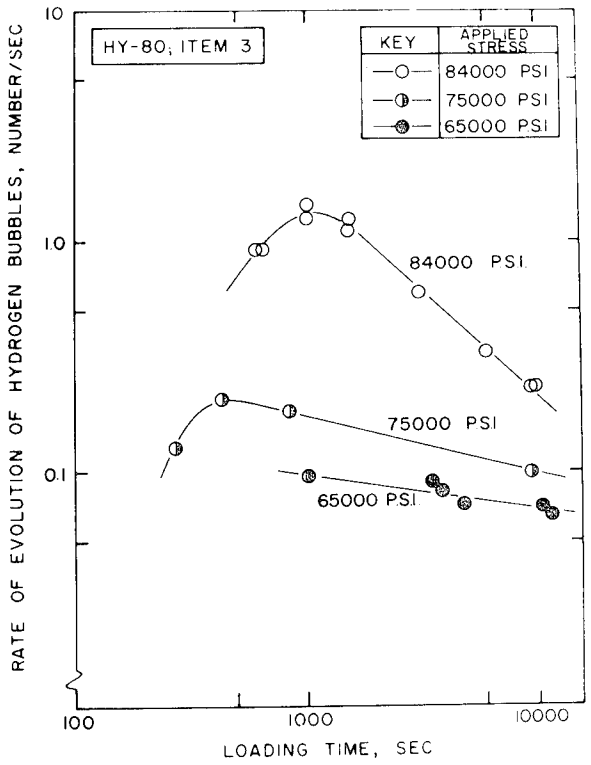


Figure 12. Rate of evolution of hydrogen bubbles vs. loading time, diffusible hydrogen 32 cc/100 g.

It appears that increasing the applied stress causes an increase in the rate of diffusion of hydrogen toward the triaxially stressed region ahead of the crack tip. This implies that the diffusion of hydrogen is stress induced.

To examine the stress-induced diffusion of hydrogen further, interrupted loading tests were performed. Figure 13 shows the results of this study. The test data shown were obtained by counting the number of bubbles evolved during three periods of loading and two intervals of two minutes during which the load was removed. Inspection of Figure 13 reveals that the bubble evolution stopped completely immediately after unloading, and that upon reloading there was an incubation period before the initial rate of hydrogen evolution was restored. This incubation time can be explained as the time required to develop a critical concentration of hydrogen by stress-induced diffusion at the crack tip.

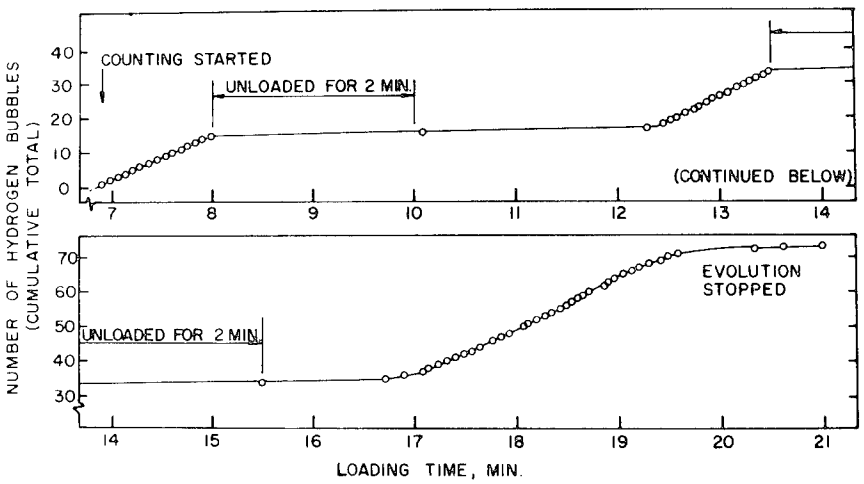


Figure 13. Result of interrupted loading test, applied stress 80,000 psi, diffusible hydrogen 32 cc/100 g.

Because the four-point loading technique was limited to elastic strains, the radiused die block testing method shown in Figure 10B was adopted. In this method, the specimen is forced to conform to a die block with a 20 in. radius of curvature. The strain in the outer fibers of the specimen is approximately equal to $\frac{t}{2R}$, where t is the specimen thickness and R is the radius of curvature of the die block.

Time-lapse motion pictures were taken at 2 frames/sec to document the principal features of crack propagation, such as: the nucleation of microcracks, the development of yielding ahead of the propagating cracks, and the evolution of hydrogen bubbles from cracks. The films demonstrate that the V-shaped zone of localized yielding ahead of the propagating crack is more extensive as the level of diffusible hydrogen is increased.

The films also show that the sites of evolution of hydrogen bubbles are usually not located at the tip of a propagating crack, but rather are located some distance behind the crack tip.

Figure 14 shows selected frames from such a motion picture, taken of an HY-80 specimen containing 32 cc of diffusible hydrogen/100 g of weld metal (29 ppmH_2) and strained 0.5%. The elapsed time after loading is indicated below each photomicrograph. Note that considerable anelastic deformation occurs in advance of the crack tip, as evidenced by the progressive roughening of the polished surface. Microcracks may be seen nucleating at inclusions in advance of the crack tip; crack growth

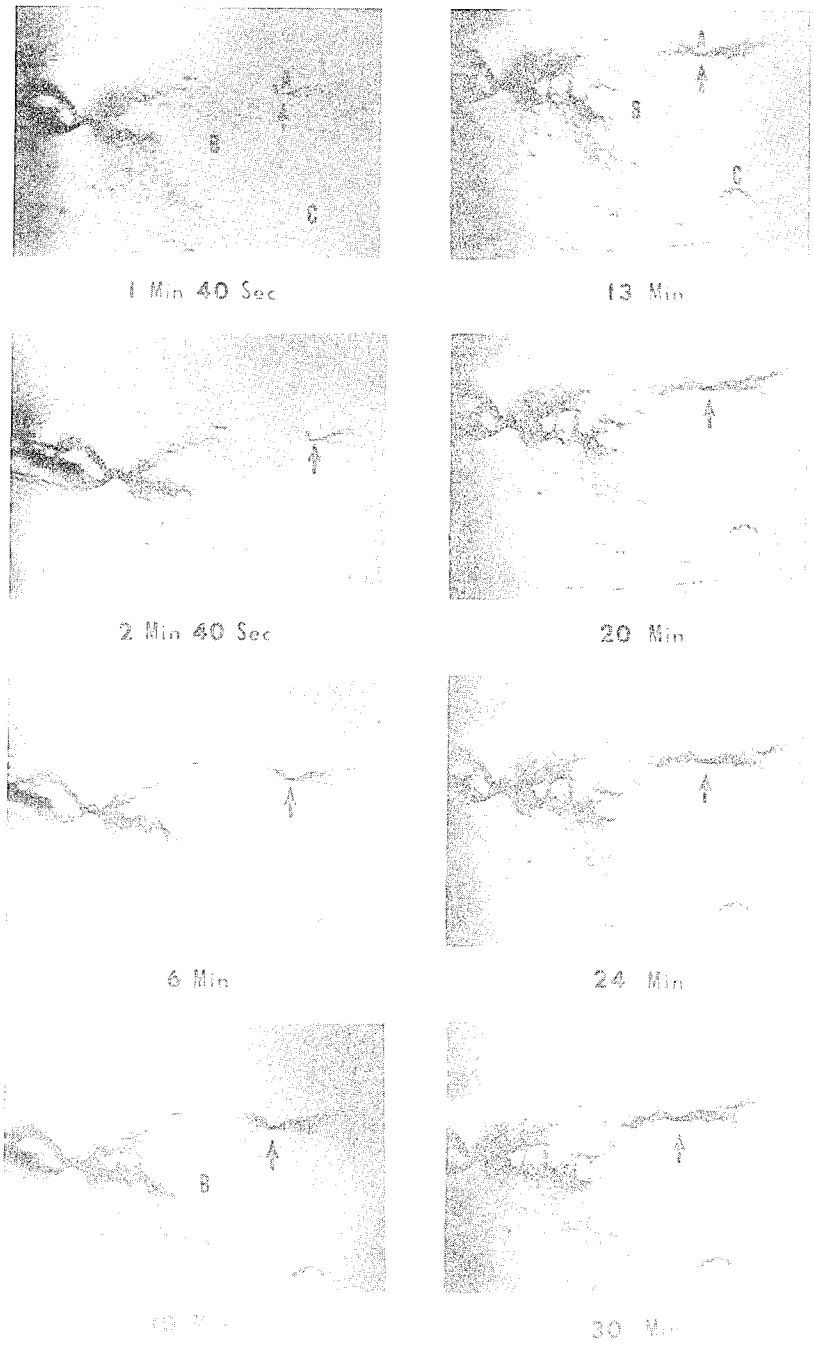


Figure 14. Selected frames from a time-lapse motion picture of growth of hydrogen-induced cracking over a period of 19 hours in HY-80. Diffusible hydrogen 32 cc/100 g. 0.5% augmented strain. As-polished, 60X. Fig. 14 reduced 21%. Fig. 14 (cont'd.) reduced 15%.

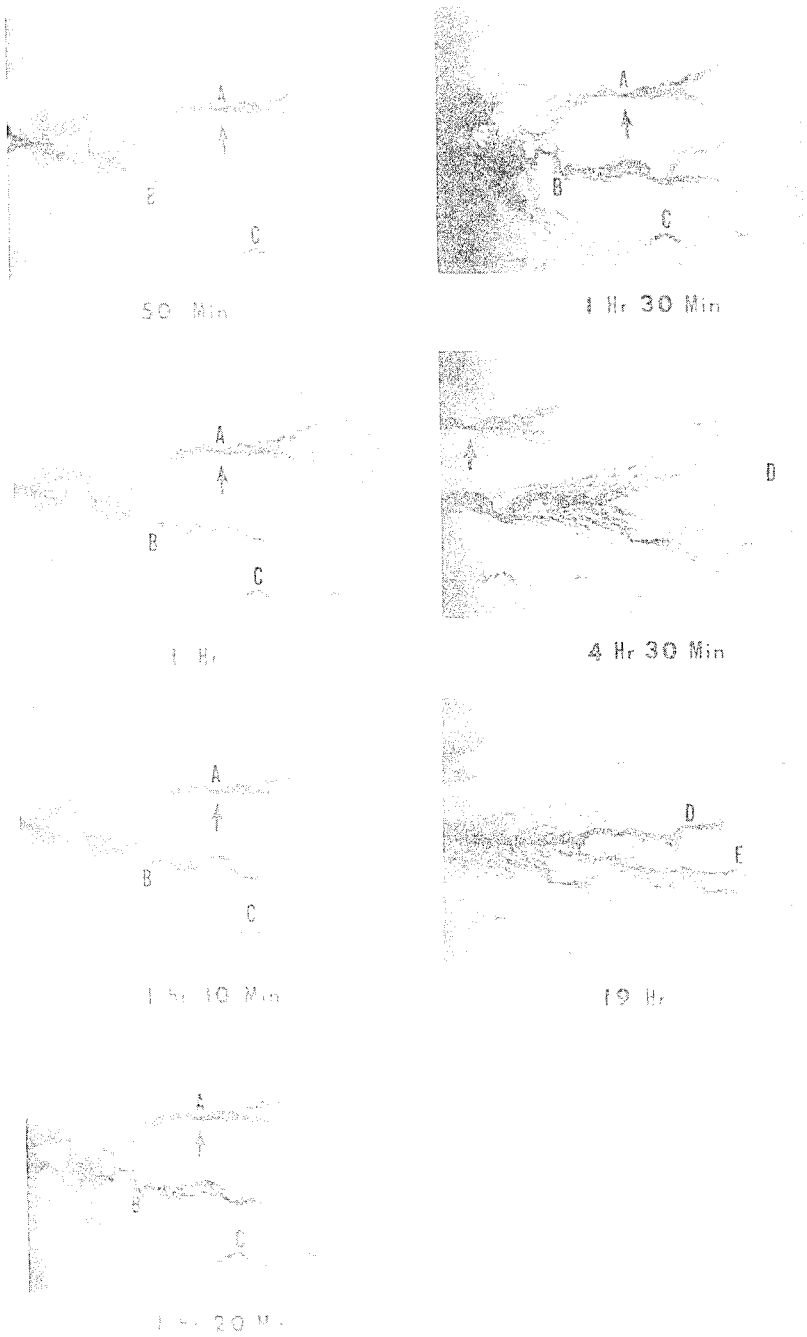


Figure 14. (Continued)

occurs from these microcracks and from the tip of the main crack until link-up occurs. This process then repeats as new microcracks form in advance of the main crack tip.

Figure 15 shows the total number of microcracks observed as a function of the diffusible hydrogen content for four lots of HY-80 steel from the same heat but with differing amounts of rare earths. Item 1, the control plate which contained no rare earths, experienced microcracking with hydrogen levels less than 5 cc/100 g (4.5 ppmH_2) and showed macrocracking with hydrogen contents 24 cc/100 g (22 ppmH_2) or greater. On the other hand, Item 3, which contained 1 3/4 lb/ton of rare earths and exhibited the best resistance of the group to hydrogen-induced cracking, showed no microcracks with hydrogen contents less than 8 cc/100 g (7 ppmH_2).

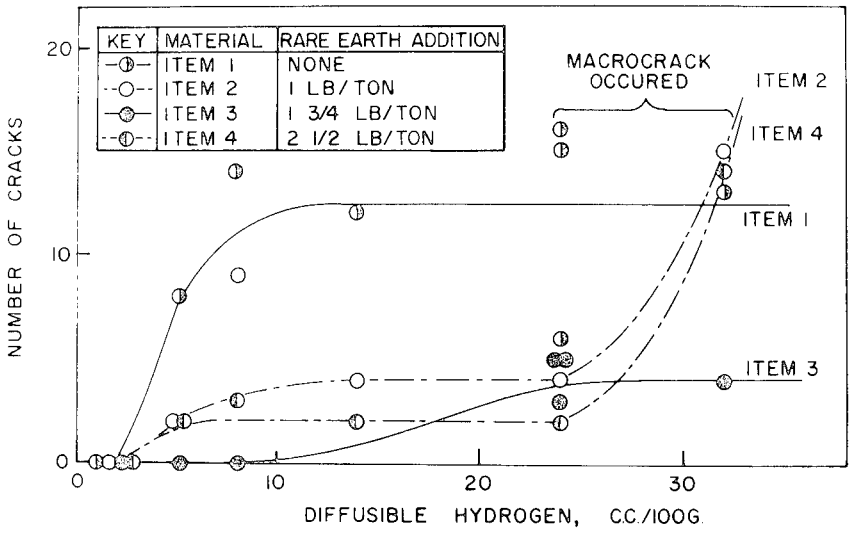


Figure 15. Number of cracks vs. diffusible hydrogen content, showing effect of rare-earth additions on cold-cracking sensitivity.

From experiments to date, the following conclusions have been drawn:

1. For a given stress level, a critical level of diffusible hydrogen exists; below this level, cold cracking does not occur.

2. Cold cracks may nucleate, but will fail to grow unless the maximum stress exceeds the yield strength.

3. When both yield-strength stresses and the hydrogen level exceed a critical value, anelastic dislocation motion occurs for an extended period of time.

4. In the absence of diffusible hydrogen, no anelastic dislocation motion is observed.

5. An interaction between the diffusible hydrogen and the dislocations exists; apparently dislocation motion facilitates hydrogen transportation to the vicinity of the crack tip.

6. Preferred sites for the nucleation of cold cracks exist: solute-enriched grain and subgrain boundaries in the unmixed zone, and constitutionally liquated sulfide inclusions in the partial melted zone.

MOTION PICTURE DEMONSTRATING THE VARESTRAINT HOT-CRACKING TEST AND THE CONSTANT-STRAIN COLD-CRACKING TEST

High-speed motion pictures, taken at 500 frames/sec, were shown of the nucleation and growth of hot cracks in VARESTRAINT specimens of a nickel-base alloy. The cracking was completed within 12 frames on the film; thus this action which originally took place in 1/40 of a sec appeared on the screen in 3/4 sec. The initial magnification on the 16 mm film was approximately 30X. The test was conducted using a gas tungsten arc bead weld made with 12V, 180A, 4 in./min, and an augmented strain of 1%.

The second portion of the film (time-lapse photographs taken at 2 frames/sec) illustrated the growth of hydrogen-induced cold cracks in HY-80 weldments. The initial sequence showed hydrogen bubbles evolving from microcracks which formed at MnS inclusions. The hydrogen evolution was intermittent and occurred from the walls of the cracks some distance behind the crack tip.

Crack growth was intermittent and hydrogen evolution occurred during the crack-arrest periods. Hydrogen evolution was also visible at certain grain boundaries in the partially melted zone. Crack propagation was accompanied by plastic deformation which distorted the polished surface near the crack. The shape of the inclusions influenced the plastic flow pattern and the crack growth rate.

SUMMARY

Evidence was presented to show that the fused metal in a heterogeneous weld consists of two distinct zones: a composite zone and an

unmixed zone. In addition, metallographic evidence was given to substantiate the presence and importance of a region adjacent to the fusion boundary in which partial melting occurs.

Two new testing procedures were described: one for hot-cracking sensitivity, and the second for cold-cracking sensitivity. Typical results of these test procedures were presented.

High-speed motion pictures were shown of hot cracking, and time-lapse motion pictures were presented of cold cracking.

REFERENCES

1. "Welding and Cutting Terms and Definitions," in *Welding Handbook, Sect. 2, Welding Processes: Gas, Arc and Resistance*, 6th ed., ed. by A. L. Phillips. Miami, Fla.: American Welding Society (1969), Appendix 1–83.
2. Pepe, J. J. and Savage, W. F., "Effects of Constitutional Liquation of 18-Ni Maraging Steel Weldments," *Weld. J.*, **46** (1967), 411s-22s.
3. Kammer, P. A., Masubuchi, K., and Monroe, R. E., "Cracking in High-Strength Steel Weldments — A Critical Review," Defense Metals Information Center, Battelle Memorial Institute, Columbus, Ohio, Report No. DMIC 197, February 1964. (AD 438 432)
4. Savage, W. F. and Lundin, C. D., "Evaluation of the Weldability of Missile Case Materials," Rensselaer Polytechnic Institute, Troy, N.Y. Air Force Materials Laboratory Contract Report No. ML-TR-65-277, July 1965. (AD 471 349)
5. Savage, W. F. and Lundin, C. D., "The VARESTRAINT Test," *Weld. J.*, **44** (1965), 433s-43s.
6. Granjon, H. P., "Studies on Cracking of and Transformation in Steels During Welding," *Weld. J.*, **41** (1962), 1s-11s.
7. Szekeres, E. S., Nippes, E. F., and Savage, W. F., "A Study of Weld-Interface in a Low-Alloy Steel," *Weld. J., Res. Suppl.*, to be published.
8. Szekeres, E. S., Nippes, E. F., and Savage, W. F., "A Study of Hydrogen-Induced Cold Cracking in a Low-Alloy Steel," *Weld. J., Res. Suppl.*, to be published.
9. Homma, H., Nippes, E. F., and Savage, W. F., "Hydrogen-Induced Cracking in HY-80 Steel Weldments," *Weld. J., Res. Suppl.*, to be published.
10. Coe, F. R., "Hydrogen in Weld Metal," *BWRA Bull.*, **8**, No. 3 (1967), 76–81.

3. EXPLOSIVE WELDING AND CLADDING — OVERVIEW OF THE PROCESS AND SELECTED APPLICATIONS

J. A. YOBLIN, J. D. MOTE, and L. E. JENSEN
E. F. Industries, Incorporated
Louisville, Colorado

Explosive welding is a viable and rapidly growing manufacturing technology. It has established itself as an important and basic process which is generating a wide variety of critical production parts. The technology is not dependent on either large pools of skilled labor or massive amounts of capital equipment; it has an outstanding safety record.

Products manufactured by explosive welding include key components for chemical process plants, oil refineries, heat exchangers, large-diameter pipeline joining, cryogenic systems, ship construction, etc.

More than fifty U.S. patents have been issued since E. F. Industries' fundamental first-in-time patent, "Explosive Welding," which issued in March, 1962. Most of these patents are owned by either E. F. Industries, Inc., of Louisville, Colorado, or by E. I. du Pont of Wilmington, Delaware. As a result of patent litigation between the two companies, EFI has licensed du Pont under its patents and du Pont has cross licensed EFI under its patents.

The science of explosive welding is highly developed; literally millions of dollars have been spent by private industry and the government to develop this technology. Although explosive welding was invented in 1958, large commercial growth has just started in the past few years and is increasing very rapidly.

INTRODUCTION

Explosive welding (DYNAWELD^{tm}) and explosive cladding (DYNACLAD^{tm}) is used by E. F. Industries, Inc., on a commercial scale to manufacture a wide variety of metallurgically bonded similar and dissimilar metals for many basic industries including:

Refineries
Chemical Processing Plants
Power Generation (fossil fuel and nuclear powered)
Cryogenics
Shipbuilding
Pipelines (oil and gas)
Electronics
General Industrial-Machinery
Heat Exchangers
Aerospace and Aircraft (commercial and military)
Desalinization Plants

The basic process and resulting products were first invented in 1958, and the resulting first U.S. patent (titled "Explosive Welding") was issued in 1962. This original pioneer patent, which is owned by E. F. Industries, Inc., is the first of more than 50 U.S. patents which have been issued. The process is not an art, but rather a precise science. Appropriate products resulting from the process are technically superior to those produced by competitive processes such as fusion welding or roll cladding. In many cases unique combinations, such as titanium to steel, have resulted in new products for which no competitive process currently exists.

In many modern industries, three metal systems commonly occur (often in the same system). These include:

1. Steel (and steel alloys)
2. Titanium (and titanium alloys)
3. Aluminum (and aluminum alloys).

No two of these three systems can be welded together by conventional techniques. Yet any combination can be explosively welded together in either flat or cylindrical configurations.

At the present time, explosive welding and cladding is a rapidly growing multimillion-dollar annual business which is also being practiced commercially in several foreign countries.

BACKGROUND

Explosive welding was invented in early 1958 by Mr. Vasil Philipchuk (now deceased) and Mr. Franklin LeRoy Bois. While Philipchuk and Bois were doing some explosive forming work they observed instances of welding between the explosively formed product and the steel die or tool. They investigated this phenomenon and determined that parts of the explosively formed product were welded to the steel die with a substantially continuous metallurgical bond. By April 1, 1958, the

inventors retained a member of the Metallurgy Department of M.I.T. as a consultant to analyze samples of welds obtained by explosive techniques. Very shortly thereafter, relatively sophisticated combinations of metal (such as aluminum to Inconel and titanium to steel) were being explosively welded and clad, and relatively sophisticated products and applications were being articulated, such as flat plate cladding, welding liners inside pipes and cylinders, explosively welding tubes and pipes to headers or tubesheets, etc.

E. F. Industries, Inc. acquired several operations (including their respective patents) involved in explosive welding and cladding. These included: Explosive Fabricators, Inc. Division of Tyco Laboratories; Explosive Metalworking Operations, Martin Marietta Corporation, Denver Division; and Explosive Welding Operation, Hexcel. In addition, Martin Marietta Corporation received a seven-year multimillion-dollar ARPA research and development contract in explosive metalworking in which they issued a subcontract to Denver University's Denver Research Institute. The last phases of this program were run while Martin Marietta's Explosive Metalworking Operation was part of EFI. E. F. Industries, Inc., has more than 21 corporate years in the field of explosive welding and cladding, and this extensive experience is enabling the technology and applications of explosive welding and cladding to be developed at an increasing rate.

Figure 1 is a pictorial schematic of the DYNACLAD^{tm} explosion cladding process. This figure illustrates the same principles which are involved in explosive welding (*e.g.*, pipelines). The main features of this process are:

1. A specific standoff between the cladder metal and the backer metal.
2. Progressive detonation of the explosive over the metal to be explosively clad or welded.
3. A specific bend angle by the cladder metal as it is forced to weld to the backer metal.
4. The formation of a jet within the included angle between the cladder metal and the backer metal. This jet actually causes the surface metal between the cladder and backer to behave as a fluid — these surfaces are scoured clean by the jet.
5. A characteristic (and visible) wavy pattern at the weld interface caused by the swirling jet as it freezes.

The cladder and backer metal are truly metallurgically joined. In many cases the strength of the weld is greater than the weaker of the two metals explosively welded together.

The list of metals which can be explosively welded is almost limitless. "Incompatible" systems such as titanium to steel, aluminum to

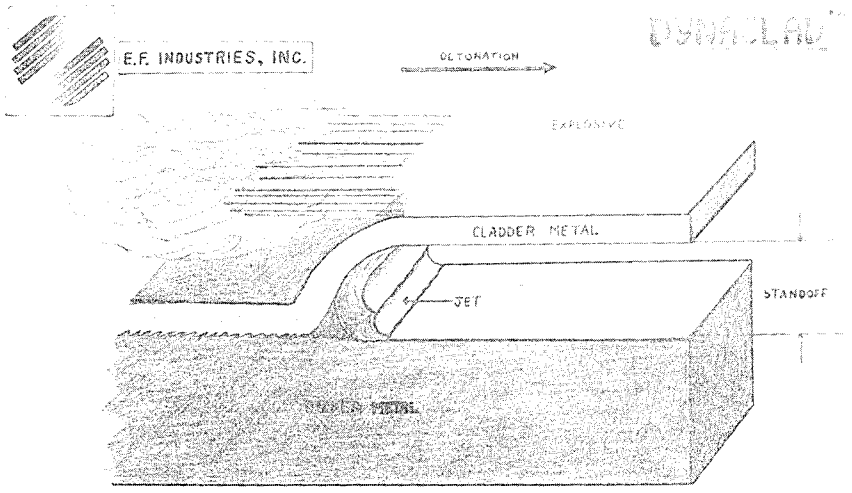


Figure 1. Explosion cladding process.

steel, and aluminum to titanium have been successfully explosion clad and welded on a commercial scale. Table 1 is a partial listing of metals which have been explosively clad. Many other combinations, including multiple clads of more than two different metals, are feasible and have been produced.

Competitive processes to explosive welding or cladding are shown in Table 2.

Certain metal systems are metallurgically incompatible to fusion welding, roll cladding, or diffusion bonding. In these cases, explosive welding and cladding offer a viable manufacturing alternative. In other cases where weld overlaying or roll cladding are feasible, large section sizes might indicate the explosive welding process to be either more cost effective, or to yield a metallurgically superior material.

Table 3 is a partial listing of products which have been manufactured using the DYNAWELD^{tm} or DYNACLAD^{tm} process.

PROCESS

Figure 2 is an engineering schematic of the explosion welding and cladding process. The schematic focuses at the collision point and shows the Collision Angle B, which is determined by the standoff distance, the explosive used (amount and detonation velocity), and the thickness and

Table 1. Partial Listing of Metals Which Have Been Explosion Welded

Steels to	Stainless Steels	Copper
	Aluminum	Nickel
	Titanium	Columbium
	Monels	Tantalum
	Copper-Nickels	Hastelloys
	Brasses	Stellites
	Bronzes	Magnesium
	Silver	Gold
Aluminum to	Steels	Titanium
	Stainless Steels	Nickels
	Copper	Silver
	Copper Alloys	Magnesium
Titanium to	Steels	Copper Alloys
	Stainless Steels	Nickel Alloys
	Aluminum	Tantalum
	Copper	Columbium

Table 2. Competitive Processes to Explosive Welding and Cladding

Fusion Welding (including weld overlaying)
Roll Cladding
Diffusion Bonding

Table 3. Partial Listing of Explosion Welded and Clad Products

DYNACLAD^{tm}	Tube Sheets (for heat exchangers)
DYNACLAD^{tm}	Plates (for pressure vessels and tanks)
DYNACLAD^{tm}	Bi-metal Tubing (for chemical plants, heat exchanger tubing, desalinization plants, etc.)
DYNACLAD^{tm}	Nozzles (for high-pressure vessel attachments)
DYNACLAD^{tm}	Cu clad Al, and Al clad Steel Strip (for electrical transition joints)
DYNACLAD^{tm}	Al clad Steel Plate and Strip (for structural transitions — marine, automotive, etc.)
DYNABOND^{tm}	Tubular Transition Joints (to join dissimilar metal tubes and pipes)
DYNAWELD^{tm}	Explosion Welded Pipelines
DYNAWELD^{tm}	Overlays (for erosion/corrosion resistant surfaces; for building up worn surfaces)

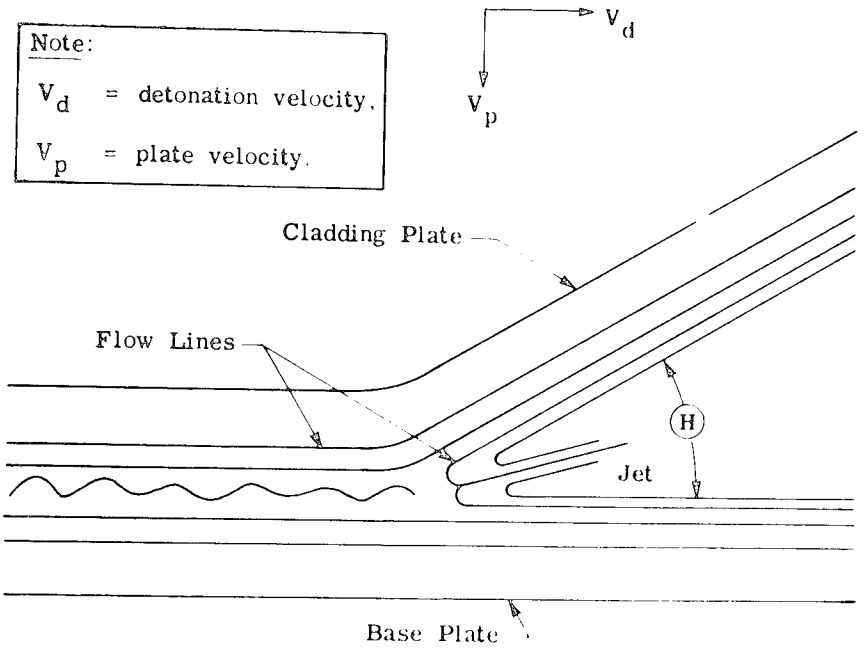


Figure 2. Engineering schematic of explosion welding process.

strength of the cladding plate. The schematic also illustrates a few imaginary flow lines in the cladding plate and in the base or backer plate. The flow lines nearest respective inside surfaces of the cladder and backer are incorporated in the jet at the collision point and turn into the jet. As the detonation front and the collision point advance, the swirling action of the jet freezes and the wavy pattern which is characteristic of the explosion welding and cladding process is formed. If too much energy (excessive amounts of explosive) is coupled with a large standoff, sufficient heat is generated in the jet to actually melt the interfacial surface of the cladder and/or the backer. This manifests itself as a melt condition, either discontinuous pockets or continuous layers, at the interface.

In situations where an undesirable compound can be formed (for example titanium/steel where a brittle iron-titanium intermetallic compound will result if melting is permitted at the interface), the explosion welding parameters are adjusted so that no melting occurs. Photomicrographs will then show a clean wavy interface free of melt pockets or zones, and tensile shear tests at the interface will confirm high strengths

in excess of ASTM code requirements. For critical applications, EFI will run shear tests on each clad plate to verify bond-strength integrity.

Figure 3 is a photomicrograph (original magnification @ 100X) of titanium (SB-265-II) explosion welded to steel (SA-516-70).



Figure 3. Photomicrograph (100X) of titanium (SB-265-II) explosion welded to steel (SA-516-70).

Figure 4 is a photomicrograph (100X) of copper-nickel (80-20) explosion welded to steel (SA-516-70).

Figure 5 is a photomicrograph (100X) of stainless steel (type 304L) explosion welded to carbon steel (SA-516-70).



Figure 4. Photomicrograph (100X) of copper-nickel (80-20) explosion welded to steel (SA-516-70).



Figure 5. Photomicrograph (100X) of stainless steel (Type 304L) explosion welded to carbon steel (SA-516-70).

The character of the waves (including amplitude and frequency) is controlled by such variables as the detonation velocity of the explosive, the standoff distance, the collision angle, the thickness of the cladder, and other properties of the cladder and the backer. In a given system (*e.g.*, a given thickness of metal A explosion welded to metal B), the character of the wave is reproducibly controlled by the appropriate manufacturing procedure. Literally thousands of explosion clad and welded products have been manufactured; once the manufacturing procedure has been established, the scrap rate is generally less than 1%.

Ultrasonic testing has been developed to the point where it is a fine nondestructive testing technique which permits 100% inspection of a clad surface. In certain cases X-ray has been used to show the frequency of the waves. In cases where the explosion welded product is machined across an interface (*e.g.*, the O.D. of a DYNACLAD^{tm} tubesheet) dye penetrant inspection is an outstanding tool.

The following series of photographs illustrates a typical sequence for explosion cladding bimetal tubesheets at E. F. Industries, Inc.

Figure 6 is a truckload of carbon-steel backer plate arriving at EFI.

Figure 7 shows each plate is inspected dimensionally and is metal stamped with the appropriate identification. Mill certifications are reviewed. In certain cases EFI may reultrasonic the steel backer plates prior to explosion welding.

Figure 8 shows a plate having one surface sand blasted to remove mill scale and other surface contaminants.

Figure 9 shows a steel backer plate being surface conditioned with disc grinders. Typically the surfaces to be clad are conditioned to the range of RMS 125.



Figure 6. Steel backer plate arriving at EFI.

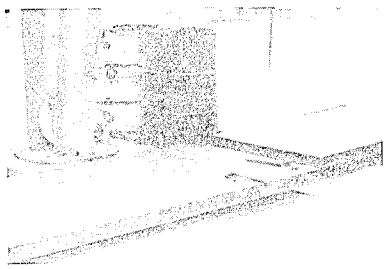


Figure 7. Incoming plates being inspected and identified.

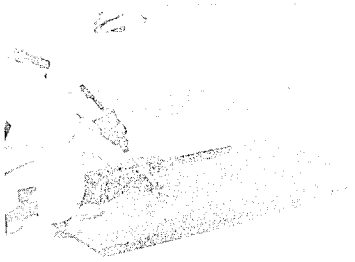


Figure 8. Sandblasting of plate surface to remove mill scale and other contaminants.



Figure 9. Backer plates being surface conditioned to approximately 125 rms.

Figure 10 is a cladder plate being surface conditioned with a disc grinder.

Figure 11 is a stack of steel backer plates whose surfaces are ready for explosion cladding.

Figure 12 is the surface of a 10-inch-thick aluminum slab which has been prepared to have a 1/4-inch-thick copper plate explosion welded to it.

Figure 13 shows the prepared interfacial surfaces of a cladder and a backer which are about to be assembled for explosive cladding.

Figure 14 shows the cladder resting on the backer, and separated from the backer by the appropriate standoff distance using small aluminum blocks (which have been machined to the correct height) as spacers (these can be seen at the corners). The production technicians are taping the edges to keep the interface space clean during transportation to the field and during field setup.

Figure 15 shows a plate being loaded onto a trailer for transportation to one of EFI's explosion welding sites.



Figure 10. Cladder plates being surface conditioned to approximately 125 rms.

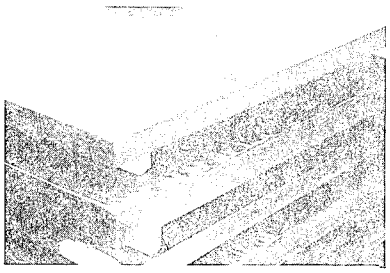


Figure 11. Prepared backer plates ready for assembly.

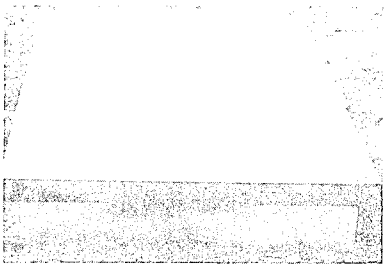


Figure 12. Ten-in.-thick aluminum backer (to be clad with 1/4-in.-thick copper).

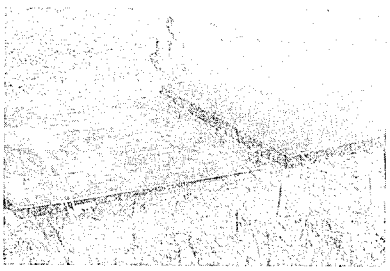


Figure 13. Cladder and backer ready for assembly.



Figure 14. Cladder and backer showing standoffs.

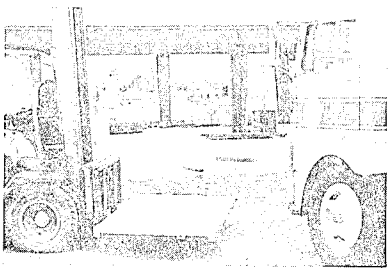


Figure 15. Loading of assembled plates onto trailer.

Figure 16 shows a trailer of assembled plates leaving for the field.

Figure 17 shows a plate being lifted from the trailer. It will be placed on the ground and the explosive will be added.

Figure 18 shows the explosive powder being placed on top of the cladder. The explosives are premixed and weighed for each plate. As a double check, the side rails are cut to a calculated height such that the proper amount of explosive will just fill the space inside the side rails.

Figure 19 shows a final assembly ready for shooting. The initiator is buried in the middle of one edge.

Figure 20 is a photograph of the shot taken from a distance.

Figure 21 shows how the force of the explosive has driven the now explosively welded bimetal plate into the ground.

Figure 22 is a photograph of the thin copper explosively welded to the 10-inch-thick aluminum slab, just after the explosion welding event.

Figure 23 shows an explosion clad plate being lifted to the trailer for return to the EFI plant.



Figure 16. Trailer load of assemblies leaves for shooting site.

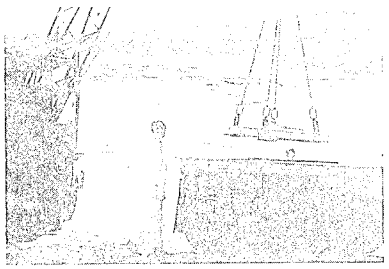


Figure 17. Unloading of assembly at shooting sight.



Figure 18. Explosive powder mix being placed on top of cladder.

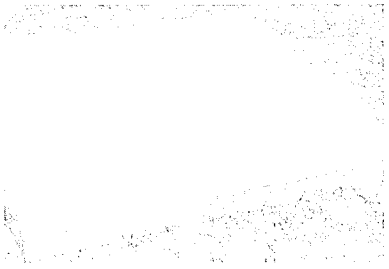


Figure 19. Final assembly ready for shooting.

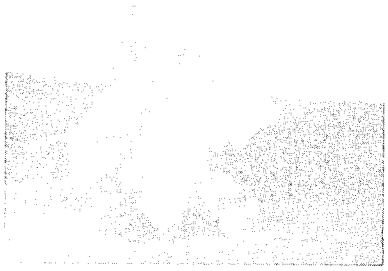


Figure 20. Explosive cladding shot.

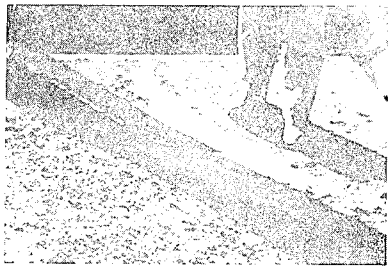


Figure 21. Explosion-clad plate after detonation.

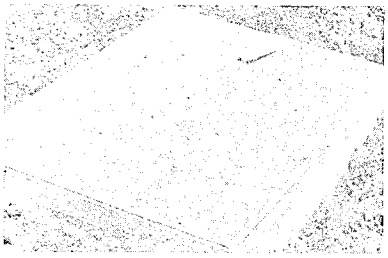


Figure 22. Explosion-clad copper on 10-in.-thick aluminum.

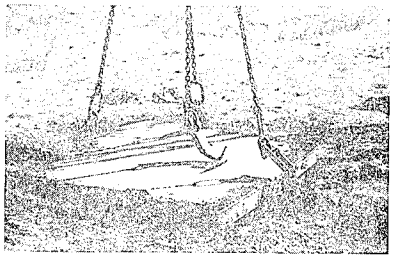


Figure 23. DYNACLAD™ plate being lifted onto trailer for return to EFI.

Figure 24 shows the copper clad thick aluminum after the explosion welded plates have been cleaned.

Figure 25 shows a circular bimetal tubesheet being cut from the explosion clad plate.

Figure 26 is a close-up of EFI's new powder torch. This cutting torch is a new Japanese invention which overcomes the problems of earlier powder torches, and is actually superior to a plasma torch in most respects. The kerf is about 3/8-inch wide and is truly vertical (not curved). Carbide precipitation is only about 0.002 to 0.003 inches, and the cut surface of the steel is readily machinable.

Figure 27 is a photograph of a batch of explosively clad tubesheet circles ready for shipment of EFI.

Figure 28 is a photograph of two sections of large-diameter steel pipe which has been explosively welded together using a collar which slips over both sections of pipe which are to be joined.

Figure 29 shows a long piece of test pipe with explosion welds joining the individual sections.

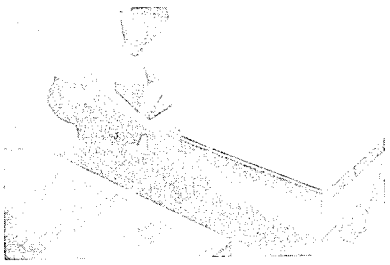


Figure 24. Copper 1/4 in. thick clad to 10-in.-thick aluminum plates.

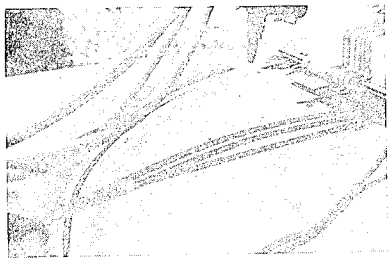


Figure 25. Bimetal tube sheet being cut from DYNACLAD^{tm} plate.



Figure 26. Special powder torch for cutting tube sheets.

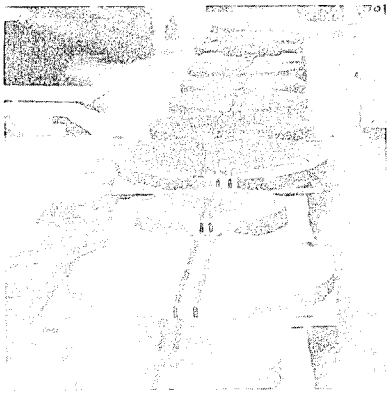


Figure 27. Explosion-clad tube sheets ready for shipment from EFI.

Figure 30 shows a section of explosion clad bimetal pipe. The inside of the pipe is copper base alloy, and the outside of the pipe is steel. The two metals are metallurgically bonded over the entire interfacial area.

Figure 31 shows a slice from the as-explosively clad bimetal pipe, as well as a room-temperature twist test which proves the quality of the bond. This pipe has been tube reduced and cold drawn to a reduction of approximately 45:1. The resulting tubing is approximately 0.75 inches O.D by 0.040-inch wall thickness. Each 10-foot-long explosion clad pipe will yield approximately 400 feet of perfectly clad bimetal tubing.

Figure 32 shows a columbium alloy cover sheet which was explosively welded to each of the columbium alloy ribs which were machined

into solid columbium backer. The application for this fin-tube construction is a very high-temperature heat exchanger.

Figure 33 is a photograph of six H-14 steel billets (each approximately 3 inches in diameter ×18 inches long) and each has had a 5/8-inch-thick copper sleeve explosion welded to its O.D. From these explosion clad composites an injector nozzle (for molten zinc) was machined. The injector nozzles needed a method of rapid heat transfer to maintain proper temperature control of the machined injector and the metallurgically bonded thick copper layer provided that.

Figure 34 shows a group of DYNABOND^{tm} tubular transition joints which were machined from explosively welded 5083 aluminum to 304L stainless steel, with a 0.030-inch interlayer of silver. These transition joints are used typically in cryogenic systems piping where an all welded system is desired. The aluminum end of the DYNABOND^{tm} joint can be conventionally welded to the aluminum piping, and the stainless steel end of the joint can be conventionally welded to the stainless piping or structure. Other DYNABOND^{tm} tubular transition joints include titanium directly to aluminum, and titanium to steel.

Figure 35 is a photograph of a titanium-faced steel blind flange. The titanium was explosion welded to the steel to provide a complete metallurgical bond to maximize the heat transfer characteristics of the flange (in addition to the obvious corrosion protection provided by the titanium face).

Figure 36 shows a high-pressure carbon steel nozzle which has had the inside surface explosion clad overlaid with 1/4 inch of stainless steel. In certain sizes, explosion clad overlaying of stainless steel is less expensive and yields a superior product compared to weld overlaying.



Figure 28. Explosion-welded steel pipe (text section).

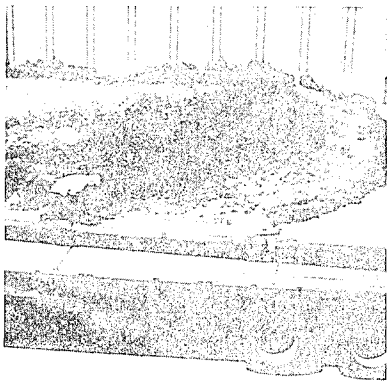


Figure 29. Explosion-welded steel pipe (long section).

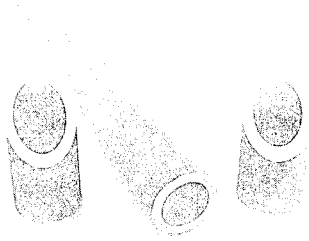


Figure 30. Explosion-clad bimetal tubing (pipe).



Figure 31. DYNACLAD^{tm} bimetal pipe and twist specimen.

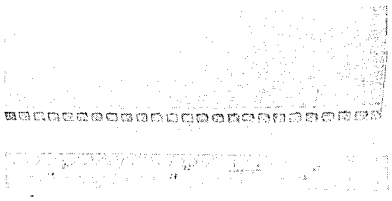


Figure 32. Columbium-alloy cover sheet explosively welded to columbium alloy ribs.

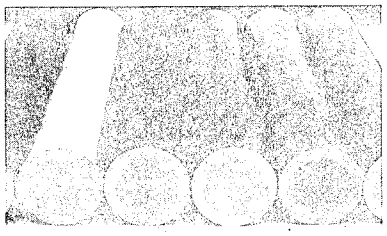


Figure 33. DYNACLAD^{tm} 5/8-in.-thick copper sleeves clad to 3-in.-diameter H-13 steel billets.

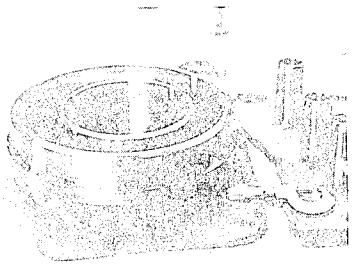


Figure 34. DYNACLAD^{tm} 5083 aluminum to 304L stainless steel transition joints.

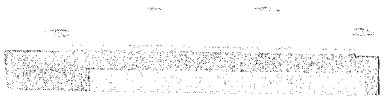


Figure 35. DYNACLAD^{tm} titanium-faced steel blind flange.

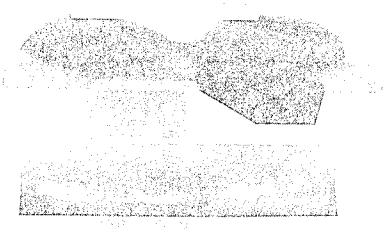


Figure 36. Carbon steel nozzle with 1/4-in. stainless steel DYNACLAD^{tm} to inside diameter.

SUMMARY

Explosion welding and explosion cladding is a basic viable manufacturing technology which lends some new dimensions to the design engineers. Certain compositions or geometries which do not lend themselves to fusion welding or roll cladding can be explosion welded or clad. In other cases, where the systems are metallurgically compatible, explosion welding or cladding may offer a more cost-effective alternative.

REFERENCES

1. Cook, M. A., *The Science of High Explosives*, rev. ed. Huntington, N.Y.: Robert E. Krieger Publishing Co., Inc. (1971).
2. Ezra, A. A., *Principles and Practice of Explosive Metalworking*. London: Industrial Newspapers Ltd. (1973).
3. Johansson, C. H. and Persson, P. A., *Detonics of High Explosives*. New York: Academic Press (1970).
4. Rinehart, J. S. and Pearson, J., *Explosive Working of Metals*. London and New York: Pergamon Press (1963).

SESSION II

CERAMICS

MODERATOR: T. VASILOS
AVCO Corporation

4. JOINING OF CERAMICS

R. W. RICE
Naval Research Laboratory
Washington, D.C.

INTRODUCTION

Joining of ceramics to other materials, particularly metals, is important for a wide variety of applications. Ceramics typically constitute critical components that must be structurally integrated with various systems predominantly, if not exclusively, of metallic construction. Ceramic–ceramic joining is also important for three general reasons, listed in approximate order of importance. First, both physical and economical limitations of producing ceramics limits the size of components that can be made; hence, construction of larger ceramic objects requires joining of smaller components. Second, some ceramic bodies — particularly those having the best properties, *e.g.*, those made by hot pressing — can only be made in relatively simple shapes, so fabrication of more complex shapes requires either extensive machining or joining. Third, some applications may require more than one type of ceramic material to be joined together to make an integral component, therefore necessitating the joining of ceramics of different compositions. Joining of ceramics to other materials, particularly metals, or to ceramics of other composition, is commonly motivated by technological needs, while joining of ceramics to make larger or more complex shapes may frequently be forced by economic considerations in addition to or instead of technological considerations.

There are three basic types of joining techniques: (1) mechanical joining through the use of mechanical interlocking or use of mechanical forces, *e.g.*, gravitational forces on the structure or from mechanical fasteners; (2) direct joining by welding, either by fusion or solid state processes in complete analogy with welding of metals; or (3) joining with other organic or inorganic materials, *e.g.*, adhesives, mortars, or cements, or brazing using either ceramic or metallic components, or both, in the braze. It is impossible to survey comprehensively all of these techniques and address all their major developments and trends. However, within the limits of the author's knowledge and his contacts in the

field, these techniques are surveyed with emphasis weighted by their importance, newness, and resultant joining capability. Substantial use has been made of previous surveys,[1–5] which, except for the shorter survey of Kutzer,[1] typically cover brazing primarily. Joining techniques will be covered in three sections: (1) adhesive, cement, mechanical, and related joining; (2) brazing; and (3) welding. Thus, in general, the sections are organized in the order of increasing temperature capability of the joining method. The basic concepts and limitations of each of the various joining techniques will be illustrated along with a number of examples, particularly those emphasizing recent applications or developments.

ADHESIVE, CEMENT, MECHANICAL, AND RELATED JOINING

Adhesive and Related Joining

Joining of ceramics with sealants, elastomers, or adhesives, *i.e.*, with organic-based materials, is one of the simplest and most widely used methods of joining ceramics not only to organic materials such as plastics but also to metals and other ceramics. Besides the general low cost, speed, and ease of this technique, it also has two important mechanical advantages. First it distributes the load, thereby minimizing stress concentrations, which can be serious for ceramic materials. Second, because of the low elastic moduli of organic materials, large strains can be accommodated without significant development of stress in the ceramic, *e.g.*, from thermal expansion differences, transient stresses, etc., although in extreme conditions ceramic failure can occur, *e.g.*, in using epoxies cured at elevated temperatures.[6] On the other hand, the strengths of adhesive, and especially sealants and elastomers, are very limited. The maximum strengths of adhesive bonds which are commonly an order of magnitude or more higher than for sealants and elastomers, are typically of the order of 5000 psi, and often are much less. The limited strengths, even of many adhesive joints, can limit their use. However, the primary and most pervasive limitation is that of temperature since these organic materials rapidly soften, weaken, and grossly degrade at temperatures from less than 100°C to at most a few hundred degrees centigrade, *e.g.*, see Weckesser.[6] To push beyond the limits of epoxies (~200°C), newer adhesives based on polyimides, polyarysulfones, polyphenylquinoxalines, or polytriazines will be needed, but upper temperatures are expected to be ~300°C or less.

Joining of ceramics to other components through the use of sealants or elastomeric materials often represent the lowest level of technology,

i.e., the least demanding applications in terms of physical parameters, such as strength, temperature, etc. Windows are an important example of this type of application where many house windows are held in place primarily or exclusively through the use of sealant materials, and automobile windshields are installed in a rubber molding which connects the windshield to the auto frame and forms a weather seal. These techniques have been extended to much more demanding applications by use of higher temperature sealants and elastomers, *e.g.*, silicone-based materials and/or insulation of the attachment area (Figures 1, 2). The extreme application is the attachment of the Space Shuttle windows having dimensions to over 3 ft and weights to over 60 lbs for some panes (Figure 2). A large-scale application of elastomer joining is of Al_2O_3 water pump seals, mostly for cars, as many as 15,000,000 annually.

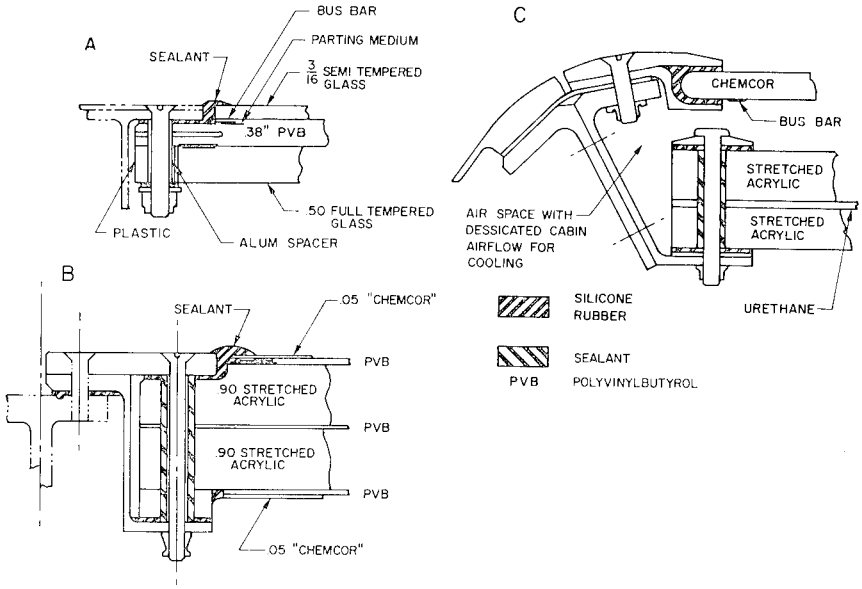


Figure 1. Schematic of attachment methods for forward-facing windows on jet aircraft. *A* and *B* represent the existing commercial jet aircraft forward-facing window designs and *C* a supersonic transport window design. Note that in all cases, the outermost layer is either tempered or chemically strengthened glass to prevent rain-erosion problems. Additional glass layers may or may not be used further down in the laminate stack. All dimensions are in inches, and most unshaded or undesignated components are metal, typically aluminum for commercial jets. Note that bus bars are for window heating for defrosting. (Information courtesy K. Wiedekamp, The Boeing Co.)

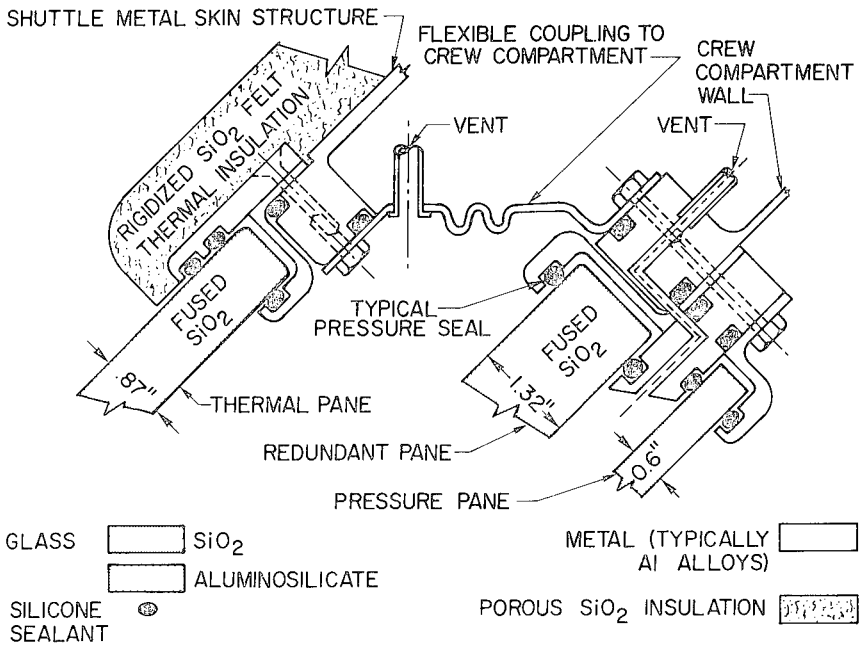


Figure 2. Space Shuttle window mounting. This schematic illustrates the design of the Space Shuttle windows which are quite large, having one dimension in excess of 3 feet and some of the panes weighing over 60 lbs. Note the extension of the SiO_2 felt insulation out over the attachment area of the outermost window to limit the temperature to the attachment. Note also that the crew compartment is a separate structure which floats inside of the main shuttle structure, attached to the latter only through flexible couplings. (Information courtesy N. Peil, NASA Headquarters.)

Because of its important advantages, adhesive joining of ceramics is used in a number of applications in which the components are used at or near room temperature. These range from the wide-scale consumer and industrial usage for products such as sandpaper and adhesively bonded abrasive wheels, to joining ferrite heads for smaller volume production of magnetic tape equipment. Examples of adhesive joining of larger parts, more demanding or newer applications are shown in Figures 1, 3–5. Almost all forward facing windows on jet aircraft (commercial jets) require glass outer layers to avoid rain erosion. The typical solution is to laminate glass to a larger plastic body which provides support for the window. In this case, a separate adhesive is not necessarily used. The glass is often directly bonded to the plastic by the laminating process,

(Figure 1) and the plastic is mechanically fastened to the aircraft. Many irdomes and windows are bonded in metal holders with epoxy, as are some radomes (Figure 3). Other radomes are often attached by a section of glass-reinforced plastic bonded directly to either the interior or exterior of the radome. While the fiber glass may be joined to the remainder of the structure in a variety of ways (see Weckesser[6]), mechanical joining by threading of the fiber glass so that it can be screwed onto a mating-metal component (Figure 3) is a common approach. Joining of piezoelectric ceramic components to themselves or to insulating ceramic is typically done by adhesive (Figure 4). Finally, Figure 5 illustrates the use of adhesive joining of metal and ceramic components in current research studying the development of ceramic sliding bearings. A new, demanding, and extensive application is the development of Space Shuttle external ceramic (low density, 9 lb/ft^3, SiO_2) insulation. Tiles 6 in. square are bonded to a thin (<0.1 in.) layer of a material similar to nylon felt for vibration isolation (since the SiO_2 has a tensile strength of only about 16 psi), and this in turn to the metal skin with a silicone rubber adhesive. Thicknesses of the (rigidized fiber) SiO_2 insulation vary from about 0.5

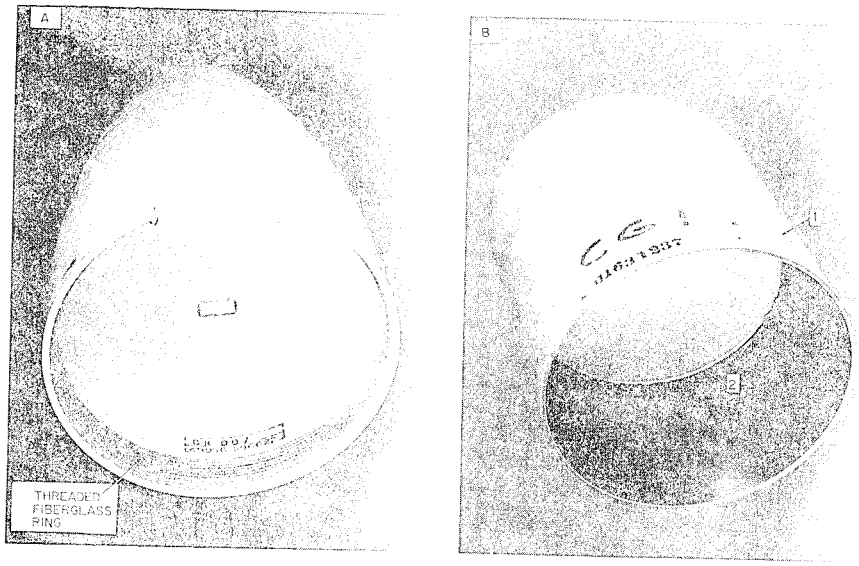


Figure 3. Attachment of ceramic radomes. *A* shows a radome which is attached by a threaded fiberglass ring bonded to the inside of the dome near the base, and *B* illustrates a smaller type of radome adhesively bonded to a metal attachment cylinder (arrow 1). Arrow 2 points out the end of the bond joint between the overlapping ceramic radome and the attachment metal cylinder.

in. to 3 in. to withstand increasing surface temperatures, which vary up to 1100°C on the outside insulation surface. Each shuttle requires over 5000 ft², *i.e.*, about 0.1 acres of such insulation.

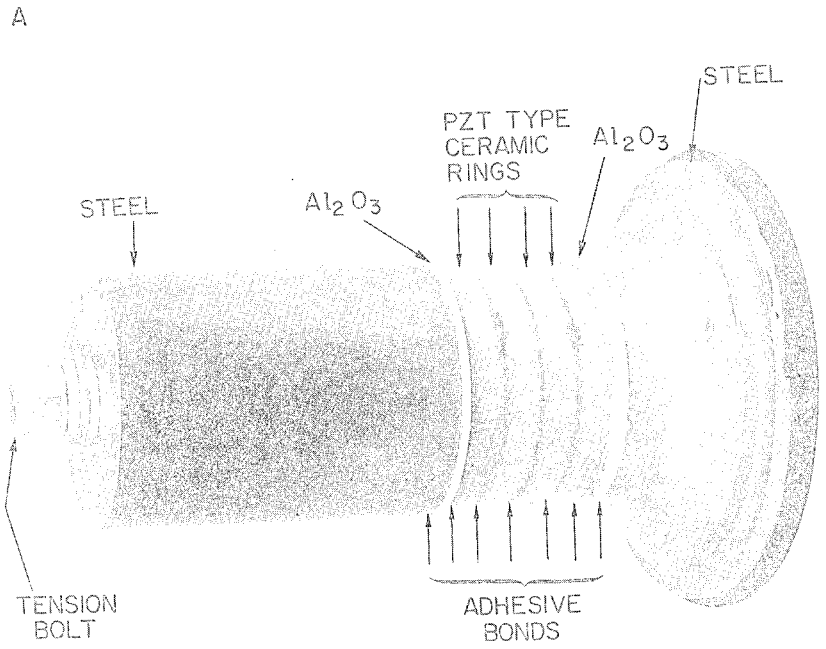


Figure 4. Adhesive bonding of sonar elements. *A* represents a fairly typical structure of an element of a sonar system in which several piezoelectric ceramic rings are bonded to one another, these in turn to an insulator, and then to a metal tail mass and a metal radiating head. Note also that a bolt through the center of the system is commonly used to apply a compressive load to the ceramic elements, which in part adds some mechanical attachment to the system. *B* illustrates the adhesive, typically epoxy, bonding of piezoelectric hollow hemispheres to make a hydrophone. Arrows indicate the bond joint of the completed left-hand element. Note also that while the wires are soldered to the electroded surfaces, they are also adhesively bonded to the surfaces to protect the soldered joints. On the right is shown a fractured element indicating much, but not all, of the failure that occurs along the bond joint.

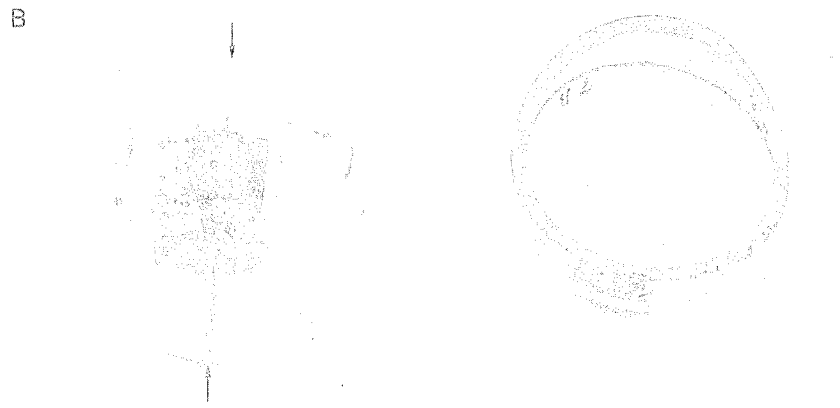


Figure 4. (Continued)

Cement and Mortar Joining

Joining of ceramics with cements or mortars is typically easy, efficient, and economical. As with adhesive joining, strength and temperature are often important limitations. Strengths often are substantially less than those obtained with adhesive joining, while the temperature capability of cements and mortars are typically greater than those of adhesives. Thermal expansion mismatch between the cement or mortar and the parts being constructed can be an important temperature limitation. The next level of temperature limitation arises from possible decomposition of the cement or mortar, *e.g.*, of lime-based mortars. A third level of limitation results from chemical interaction between the cement or mortar and the ceramic or other components. Substantial information on the types, compositions, principles, and applications can be obtained from commercial suppliers' literature and Wygants'[7] review. An outline of some applications is given below.

Mortar joining of bricks and other ceramic or ceramic-related construction materials is probably by far the highest volume usage of this type of joining. Since loads are predominantly of a compressive nature, the low tensile strengths of such joints are not a particular critical factor. While there can be substantial strength developed as a result of chemical bonding between the mortar or cement and the components involved, this need not be the case. For example, ceramic insulators which may be used in tension (as guy insulators on communication towers) have utlized cement joints wherein the necessary tensile strength is obtained primarily from mechanical interlocking as illustrated in Figure 6.

By far the most extensive high-temperature application of cements is for joining refractory bricks in furnaces. Silica, fireclay (typically

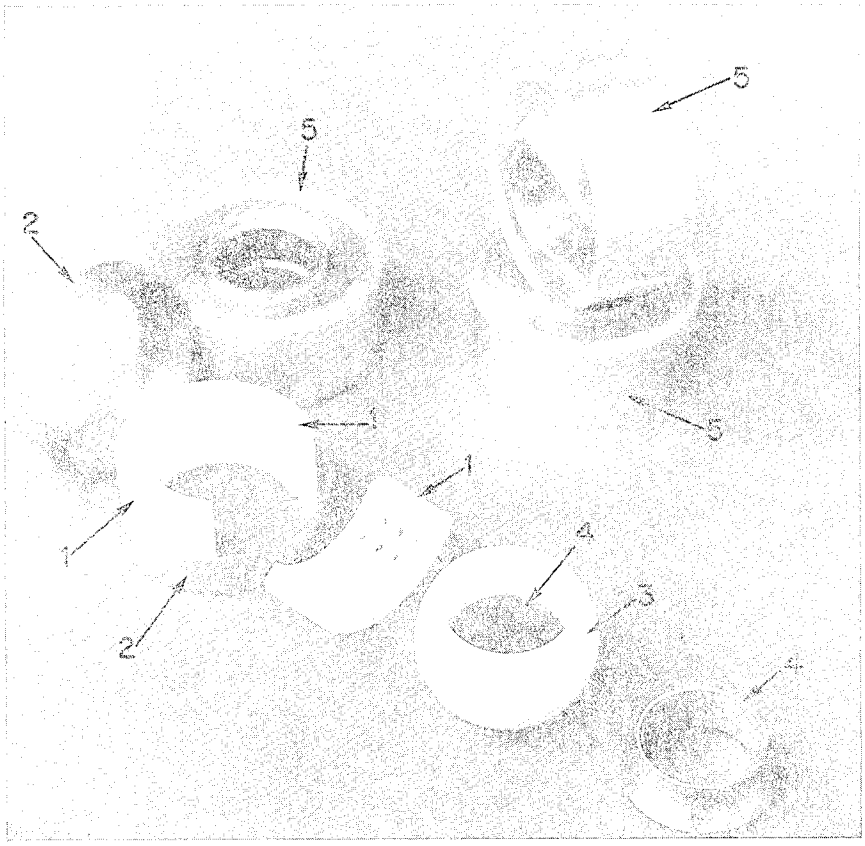


Figure 5. Adhesive bonding of experimental ceramic bearings. Such bearings are being developed for possible use in hydrofoil flap-control linkage and also for helicopter link usage. Item 1 is the ceramic outer race, which was originally a monolithic Al_2O_3 body having holes for the solid lubricant. More recent investigations have gone to ceramic coated metals for this outer race. Items 2 are the two metal caps into which the three outer race segments are bonded. Item 3 is the ball which originally was aluminum oxide, and now is hot-pressed Si_3N_4. Items 4 are the two metal inner rings that are bonded to the central ball to protect it (its edges) and provide easier and more reliable attachment to the metal shaft. Items 5 are examples of the completed bearings. Epoxy adhesive is used to bond the ceramics to the stainless steel metal components. (Photo courtesy J. Van Wycke, Boeing Company, Seattle, Washington, who is conducting this development under Naval Air Systems Command sponsorship.)

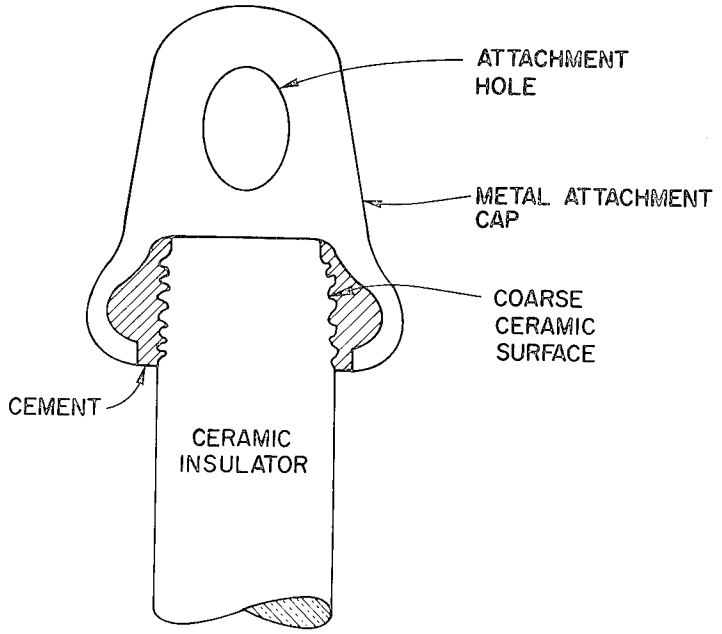


Figure 6. Schematic of joining of a metal attachment cap to a ceramic insulator. Note that the cement need not form a chemical bond to the insulator in order to provide the necessary joining, since either a rough ceramic surface or a tapering of the ceramic surface is used so that the cement provides bonding due to shear strength from friction interlocking, or compression in the joint.

about 60% Al_2O_3), and high Al_2O_3 (typically > 80% Al_2O_3) bricks are commonly mortared together, while basic (*i.e.*, magnesia and magnesia chrome) bricks are less commonly cemented. The cements used with the above refractories usually have the same general composition of the bricks they join. Mortared joints between refractories are much thinner than those used for building bricks (1/16 to 1/8 in. versus about 1/2 in. for the latter) are typically sought, *e.g.*, by dipping bricks in cement slurries, or by grouting. During curing, these cements generally bond or sinter to the refractory, and therefore to some extent represent either diffusion or fusion brazing with ceramics, or solid-state welding as discussed respectively in later sections.

Used on a far more limited scale are the technical cements such as Sauereisen and Astrocerams,[8] cements familiar in the laboratory for thermocouple and furnace cementing. The development of new cements is not particularly active, but some research and development continues,

e.g., on systems that can bond either grain or bulk bodies.[9,10] New developments tend to be in specialized areas, such as a recently announced zirconia-alumina cement for glass tank refractories.[11]

Mechanical Joining

Mechanical joining is basically very simple and efficient, and in principle should be capable of both high temperature and high strength. However, the typical lack of ductility in ceramics until quite high temperatures are reached severely limits the temperature range over which the method is applicable because of the resultant severe stress concentrations which can cause ready, catastrophic failure in the ceramic. Such failure also severely limits the tensile stresses that can typically be sustained by mechanical joints. In mechanical joining applications involving tensile loads, grommets or shims of suitable soft materials — usually of soft metals such as lead or copper — may be used to minimize stress concentrations, but flow of such materials limits stresses that can be supported. Some information on mechanical joining is also given by Kutzer.[1]

Despite the above limitations, there are a variety of applications for mechanical joining of ceramics, usually where tensile stresses can be kept low. Thus, for example, large numbers of a wide variety of ceramic insultators, terminals, etc., are mechanically mounted by metal clamps, screws, etc. A particularly large-scale example of such low-stress mechanical joining of ceramics is that of furnace refractories using mechanical interlocking or metal brackets, *e.g.*, for furnace roofs (Figure 7). Since threads can often be formed in ceramic bodies, this is sometimes used as a joining technique (some ferrite adjustment slugs are threaded so they can be screwed in or out for magnetic adjustment). Threading can sometimes be supplemented by other means, especially adhesive joining (two parts screwed together may have adhesive on their mating surfaces, and possibly on the threads). Some radomes may also involve mechanical joining (Figure 3). Some windows also partly involve mechanical joining, *i.e.*, the sealant or elastomer in contact with the pane is mechanically clamped (Figures 1, 2). Substantial tensile loads can be carried if the tensile stresses are kept low — some guy insulators for antennas etc., attached to guy cables by shackles and pins may carry considerable load, but usually at limited stresses, such as a few hundred to a few thousand psi in the ceramic. Also, with careful design substantial temperatures can be accommodated for some systems, such as the nose cap and leading edges (Figure 8) of the Space Shuttle.

Some older and a number of newer applications of mechanical attachments involve close tolerances. The use of ceramics in spark plugs

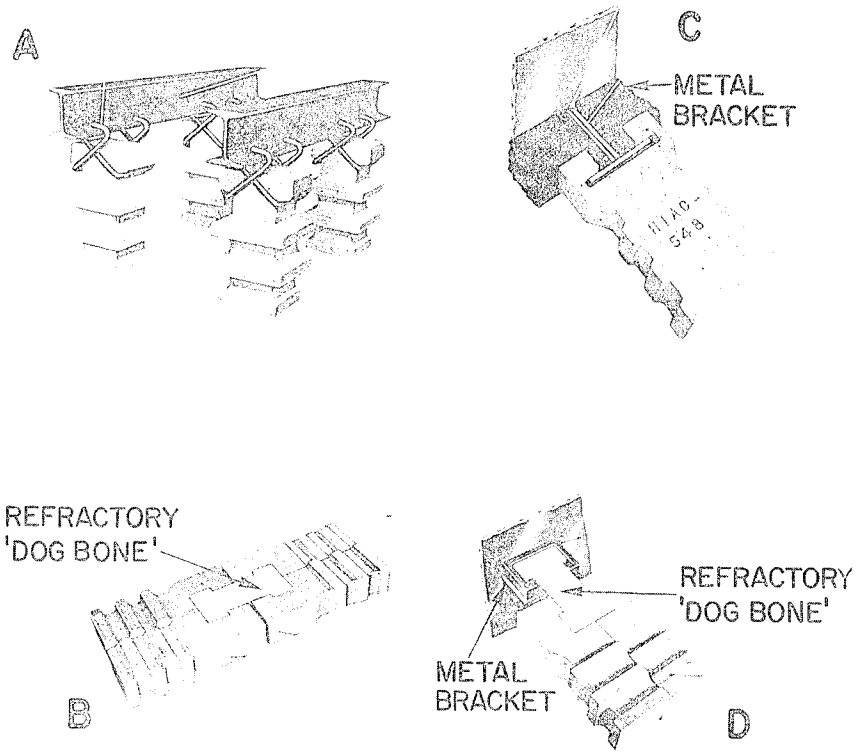


Figure 7. Mechanical attachment of refractory furnace bricks. *A* illustrates the metal hangers that are commonly used to suspend refractory bricks to form the ceiling of a furnace. *B* represents techniques commonly used to join two different layers of bricks, e.g. in the wall of a furnace and Figure C and D illustrate the use of either a metal C or a ceramic D attachment of bricks to metal wall brackets. (Photos courtesy General Refractories Company, Baltimore, Maryland.)

for cars, aircraft, etc., is a long-standing and important example. Press, and especially shrink, fitting are old but growing methods that often demand even closer tolerances. Thus, for example, soft Cu or Au plated Fe alloy rings have been shrunk onto ceramics, *e.g.*, for microwave or optical window mounting.[4] More recently, many Al_2O_3 water pump seals machined to 0.002 in. tolerances are pressed into Kovar, Invar, or stainless steel bands, so the resultant compressive stresses allow the Al_2O_3 to withstand more severe thermal stress (Figure 9B). An extension of this

now under commercial evaluation is to press the Al_2O_3 seal into a cap-shaped piece of metal instead of a band so the encapsulated Al_2O_3 can be attached to the shaft via the metal cap by standard metal-joining techniques (Figure 9C). More demanding is the press fitting of ceramics, such as of ZrO_2 nozzles for metal extrusions dies, and Al_2O_3 liners for pumps for corrosive or abrasive fluids, (the latter often requires Al_2O_3 tolerances of 0.0005 in.).

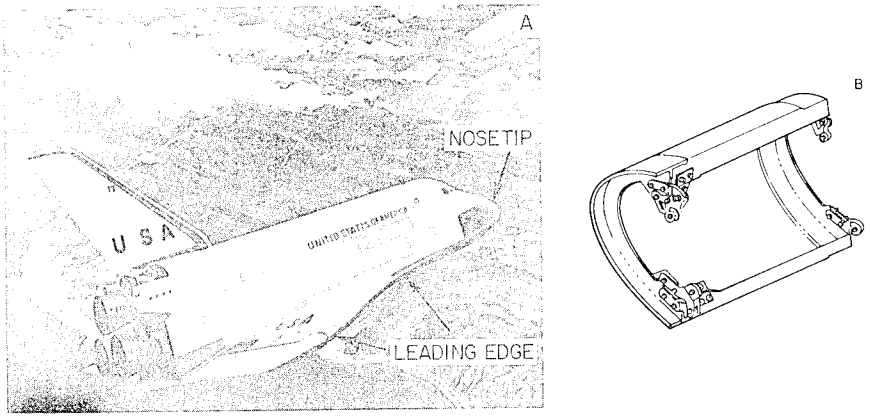


Figure 8. Mechanical attachment of carbon-carbon composite Space Shuttle leading edges. *A* is a photo of the Space Shuttle returning for landing with the carbon-carbon nose cape and leading edge sections (44 per wing) indicated. (Photo courtesy N. Peil, NASA Headquarters.) *B* is a sketch of a carbon-carbon leading edge section and half of its mechanical mounting. Note the carbon-carbon T shaped strip overlapping the joint on the left-hand edge and attached to the main leading edge segment by the mechanical mounting device. The mechanical mounting serves two purposes: (1) suitably easy removal for replacement, and (2) standoff from the Al skin and structure to allow enough temperature drop. To accomplish the temperature transition from about 650°C on the carbon-carbon to about 175°C on the aluminum, the metal attachment members on the carbon-carbon are super alloys, and Ti on the Al structure.

BRAZING AND SOLDERING

Introduction

The American Welding Society defines soldering as those processes carried out below 800°F (~425°C) and processes carried out above this

temperature as brazing. The latter are also sometimes referred to as silver soldering or hard soldering. Based on this definition, most ceramic joining processes are by brazing instead of soldering, but the latter term is often used for sealing with glasses, even if done at over 425°C. However, soldering with either metals or glasses is generally accomplished in a fashion similar to those described below for brazing. Further, a number of the brazing processes described can be used to apply a metal layer to the ceramic (referred to as metallizing), with metal soldering or brazing subsequently used to join the metallized ceramic and another metal component. Thus, while the following discussion concentrates on brazing, many of the techniques are applicable to soldering.

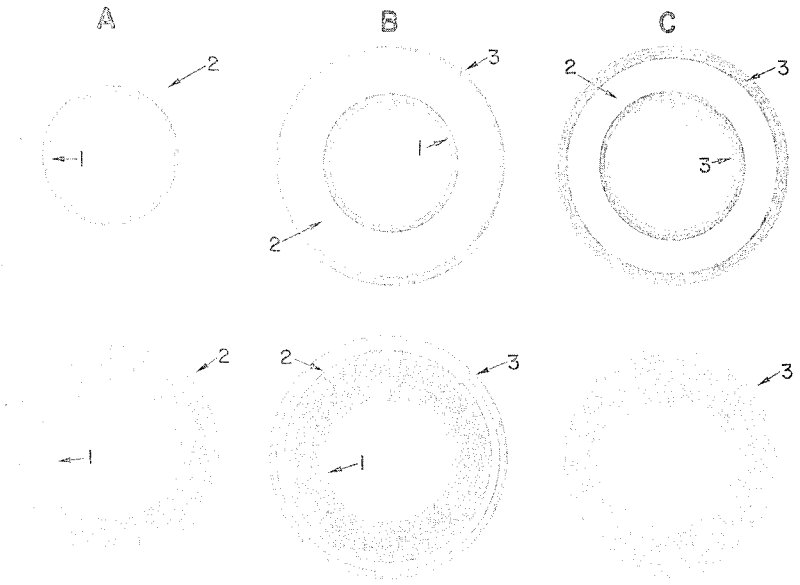


Figure 9. Al_2O_3 water pump seals. *A*, *B*, and *C* are photographs of each side of three different types of Al_2O_3 water pump seals for automobiles. *A* and *B* represent present practice wherein the Al_2O_3 body, Item 2, is attached to the shaft via a rubber or elastomeric material, Item 1. In *B*, the Al_2O_3 (Item 2) is pressed into an outer metal band (Item 3) to provide compressive stresses to give greater thermal shock resistance. *C* shows a new form of the seal now under commercial evaluation wherein the Al_2O_3 is pressed into a metal cap, Item 3, to provide both compressive stresses for better thermal shock resistance and direct metal attachment to the shaft. (Samples courtesy J. Abar, Crane Packing Company, Morton Grove, Illinois.)

There are basically two types of ceramic brazing: those using metallic materials and those using ceramic materials. Metal brazing will be discussed first, and ceramic brazing will be discussed at the end of this section. There are basically three metal-brazing methods that are not necessarily fundamentally different processes in terms of mechanisms of bonding but are differentiated by practice. The three techniques can generally be referred to as noble-metal brazing, active metal brazing, and refractory metal brazing. For greater details on brazing with metals, the reader is referred to articles by Clarke *et al.*[2] Reed,[4] Hitch and Bube,[5] and especially Pattee *et al.*[3] A British symposium[12] on ceramics for electronic tubes also provides useful information. It should be noted that metal brazing of ceramics is one of the most common methods of joining ceramics, especially for high–technology applications, *e.g.*, for vacuum and electronic applications. The basic advantage is that a variety of materials can be joined together by relatively simple procedures involving generally available facilities to produce vacuum-tight joints, that have modest to quite substantial strengths and resistance to various chemical environments. The main limitations are in finding braze compositions that meet increasingly severe demands for a wider variety of materials. This field is fairly mature, but a reasonable, though not extensive amount of research and development continues, with much of it focused on further understanding of the processes and applying them to a wider range of materials and environments.

Noble-Metal Brazing

Noble-metal brazes are most commonly based on silver or platinum and their alloys with other noble metals, and frequently include base metals such as Cu or Ni. In the past, such brazing was done by raising such alloys to their melting point normally in air. There is growing evidence that under such oxidizing conditions, some noble-metal oxides may be formed, and certainly some formation of base-metal oxides probably occurs which could react with the ceramic. However, if such oxides are formed, they may be more important in aiding wetting than in actual bond formation.

Formation of noble-metal oxides and resultant wetting of ceramics is indicated by Bruin *et al.*[13] They reported brazing of several oxides — MgO, Al_2O_3, ZrO_2, UO_2, BeO, ferrite, and SiO_2 — or glasses as well as graphite to themselves or various combinations with one another using Pt, Pd, Au, or Ag with little or no pressure. Temperatures of 800–1100°C (below the melting point of the metal) were often maintained for several hours. While Pt migration into pores of graphite did occur, as expected, no bulk reaction of any of the noble metals and the ceramics occurred.

However, they report that a surface reaction did occur with the oxides, leading to a liquid phase well below the melting point of the metal. This liquid phase, which was observed at the interface of metal grids (Pt) in contact with oxide (MgO) particles in an electron microscope (hence in vacuum), wet the oxide. Copley and Riner[14] have also recently shown evidence of noble-metal oxide formation in wetting oxide materials.

Bruin *et al.* report that the above noble-metal seals could be vacuum tight. While absolute joint strengths were not given, a relative test indicated that strengths 50–100% of those achieved by epoxy bonding were achieved. Testing of noble-metal brazes often resulted in failure in the ceramic; though this can in part result from boundary stresses, it generally indicates a reasonable to good level of strength. The strengths with noble metals were equal to or greater than strengths obtained using other (transition) metals (discussed below). These authors specifically noted that the best brazes were obtained below the melting point of the metal, *i.e.*, solid-state or diffusion brazing in contrast to earlier practice of melting noble-metal braze alloys.

Klomp's[15] work in which he bonded sapphire, alumina, or glass to one another using both noble (Pt) and several base metals (Fe, Ni, Cu, Al, and Pb) appears to be consistent with that of Bruin *et al.* Carefully cleaned 100 μm thick rolled foils of these metals were placed between hollow tubes of the various above ceramics to be joined. The parts were then heated to approximately 90% of the melting point of the metal, at which time a pressure ranging from about 4 to 1200 psi was applied. Subsequent examination of the bonded surfaces indicated no reaction between the various metals and Al_2O_3. Strengths were found to increase linearly with the temperature of the process and hence with the melting point of the metal, from approximately 3400 psi for lead to approximately 36,000 psi for platinum.

As noted earlier, an important thrust of metal brazing is applying this in new environments and to new materials, *i.e.*, to other than the traditional oxides. Bruin's brazing to graphite noted above is an example of use of newer materials. Applications in medical electronics are examples of new environments, *e.g.*, a heart pacer electrical feed through using an 82-18 Au-Ni braze to join 316 stainless steel and Al_2O_3. Figure 10 is an example of the size part that can be brazed by noble metal on other metal brazes.

Active Metal Brazing

Active metal brazing is most commonly based on the use of Ti, but may also be based on Zr, Nb, or Y, particularly for Al_2O_3, since this is one of the most extensively brazed materials. It seems appropriate to

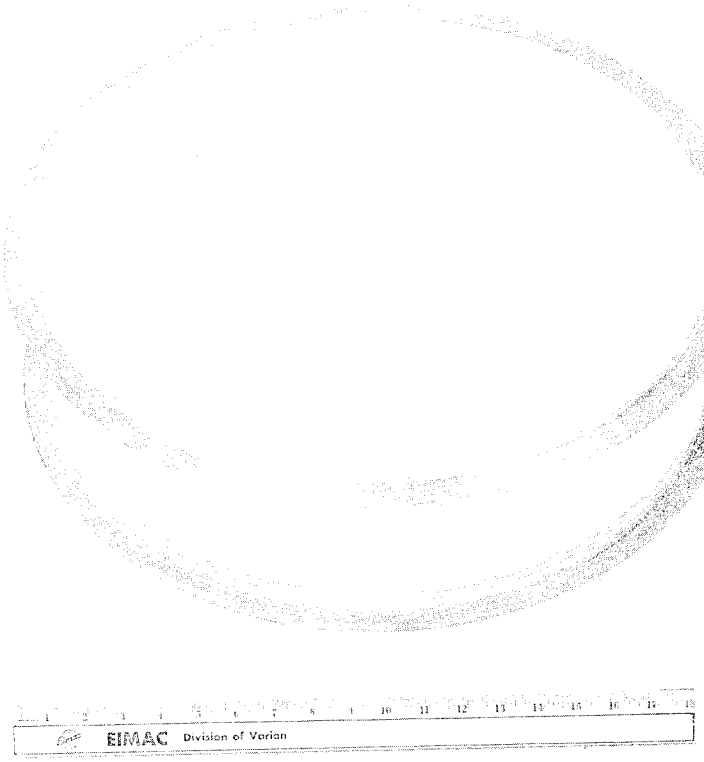


Figure 10. Example of noble-metal brazing to ceramics. Cu flanges are brazed to a large (nearly 18 in. dia) Al_2O_3 cylinder using a Cu-Ag eutectic braze. This is illustrative of the size of components that can be handled by metal brazing.

extend this definition to include metals that might be active or reactive with other oxides or other ceramic materials in general — transition metals, such as Fe, Co, and Ni for other oxides. Basically, two procedures have been used with the traditional titanium-based active brazing process. The first, and most common, has been to incorporate the titanium (or Zr) into the brazing alloy to aid wetting. The second procedure has been to coat the ceramic surface to be brazed with the active metal, or a compound that will decompose to produce the active metal, such as titanium hydride fired in vacuum. Such coating of a ceramic with a metal layer is referred to as metallization. Appropriate braze alloys will then wet the Ti metallized layer.

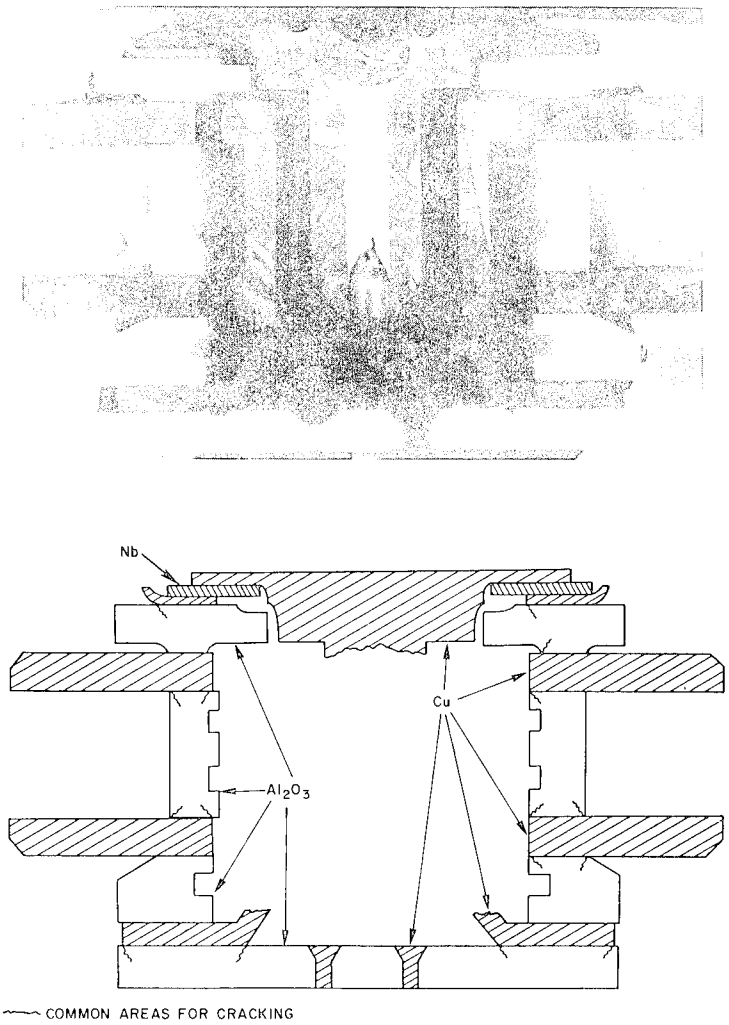


Figure 11. An example of a small brazed microwave tube consisting primarily of copper and Al_2O_3 joining formed with a titanium-based active metal braze. The upper photo is an actual cross section of one of these small tubes, having dimensions of the order of 1/2 in., and the bottom is a schematic indicating the different materials in the cross section. Note also in the bottom sketch, that the many areas in which cracking may occur as a result of stresses in the joint are illustrated. The possible cracks are shown at a much higher angle relative to the metal than is observed in reality for clarity of illustration. (Photos and sketch information courtesy of D. Viechnicki, Army Materials and Mechanics Research Center, Watertown, Mass.)

Pattee *et al.*[3] have also reviewed techniques of applying active metals using molten salts, *e.g.*, mixtures of alkali halide to deposit the active metal onto ceramic surfaces for subsequent brazing with other alloys. Zr, Hf, and U as well as Ti have been coated on ceramics at temperatures as low as 600°C. Some of these processes can be carried out in air. For example, a thin Ti sheet previously coated with a mixture of alkali or alkaline earth halides is protected from oxidation by melting and flowing of the salts over the Ti, which is then deposited on the ceramic surface.

An example of the use of active metal brazing is the microwave tube shown in Figure 11. Such electronic applications are one of the most important uses of metal-brazing techniques. However, care must be taken to select the proper alloys so very brittle intermetallic compounds, or compounds having significantly different thermal expansion from the ceramic are not formed. These, particularly the latter, can lead to joint stresses that result in cracking in the ceramic (Figure 11B). Mechanical testing of such joints will thus cause failure in the ceramic, which may be erroneously interpreted as a sign of high strength. Such cracking from joint stresses can apparently lead to release of gases from pores in the ceramic into the tube interior, which in the case of small tubes can actually lead to failure by raising the gas level too high.[16] This need not occur immediately, since variable stresses and stress corrosion can lead to crack growth and hence pore connection to the interior over a period of time.

Bruin *et al.*[13] also investigated joining of various oxides (MgO, Al_2O_3 and BeO and SiO_2) together by using various transition metals such as Ni, Ti, Fe, and Cu below their melting point, in conjunction with their noble-metal brazing discussed above. Electron-probe analysis clearly shows that substantial diffusion of the metal into the various ceramics occurs, typical at temperatures of 1000–1200°C. The relative strengths of resultant joints was indicated to be about 50% of those obtained with epoxy, *i.e.*, about equal to or less than strengths obtained with noble-metal brazing as discussed above. Also, as Reed has noted in his survey,[4] other active metals such as indium have been used to form vacuum-tight seals from about 200°C (soldering). More recently Heidt and Heimke[17] have studied diffusion bonding of Al, Cu, and Ta to sapphire, reporting that only the latter involves a thin layer of reaction.

As with other metal-brazing processes, reactive metal brazing is a well-established field, and hence not one of great research activity. Research and development is directed toward adapting the technique to new environmental requirements (for devices using alkali metal gases), and new materials. Thus, for example, Takamori and Akanuma[18] investigated 130 metals and alloys for brazing graphite. First wetting, then a

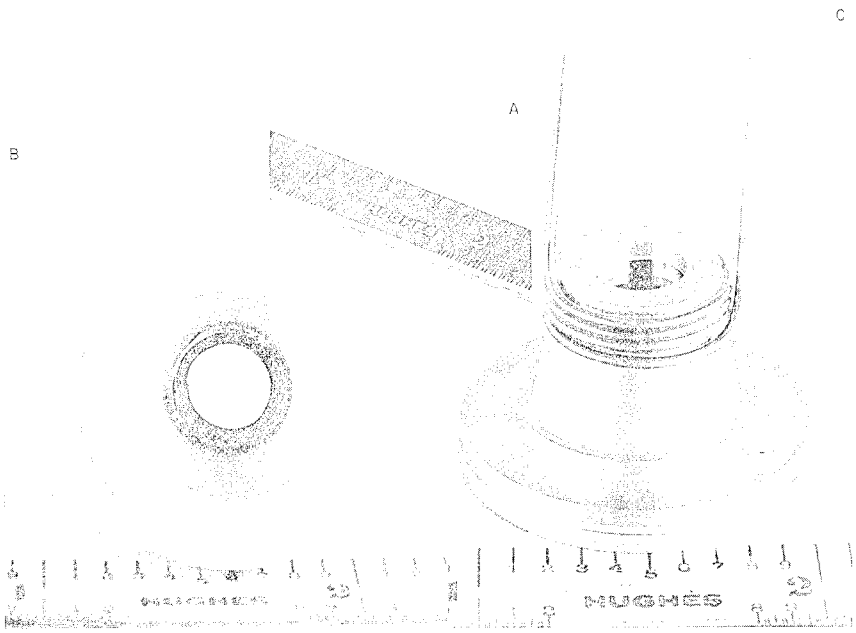


Figure 12. Brazed diamond window for the Pioneer Venus spacecraft. Diamond was selected as the IR spectrometer window to provide the necessary 3–20 μ wavelength transmission and withstand the conditions expected in the Venus atmosphere (temperatures to 550°C with pressures of 100 atmospheres containing H_2SO_4). The diamond (Type 1A oriented 5 1/2° to the {111} plane) window, 18 mm in diameter and 2.5 mm thick, is brazed into Mallory Metal 2000 (95% tungsten) alloy holder using a TiH-Cu-Ag eutectic braze. The braze is coated with Au for chemical protection, and the W holder is mounted in stainless steel. The brazing was done by EIMAC Corp. San Carlos, Calif. for Hughes Aircraft Co., which is building the Pioneer craft for NASA under the Pioneer-Venus Program-NAS2-8300. *A* is a picture of the diamond itself; *B* shows the front or outside view of the window and mounting assembly; *C* shows the back side of the diamond in its assembly. Note the heater coils to maintain the window at least 5°C above the outside temperature during its descent to impact on Venus' surface. (Photos courtesy M. Bafico, Hughes Aircraft Co.)

relative strength test were used to narrow the candidates down to 5 showing good results: Ag-Cr, Ag-Ti, Ag-Zr, Au-Cr, and Cu-Cr. All of these involve a good carbide former, and analysis of systems with Si showed formation of SiC. Another example, involving both new materials and extreme conditions is the brazing of diamond in a W holder for

the Pioneer Venus vehicle[19,20] (Figure 12). More recently Scott *et al.*[21] have investigated the effect of Cr, Ti, and V on wetting of diamond by copper alloys, finding wetting within the solubility limit for only Cr and Ti, the latter giving wetting at 1150°C at addition of more than 0.1 at. % Ti. Again, these are good carbide formers and thin (0.02 μm) carbide layers were observed. Optimum strengths were produced at lower concentrations than for optimum wetting, but compromise strengths of about 20,000 psi were achieved.

Also, as with noble-metal brazing, there is some trend toward solid-state, or diffusion brazing (below the liquidus temperature). Thus, recently, Elssner and colleagues,[22–24] have bonded Al_2O_3 and hot-pressed Si_3N_4 to themselves using Nb and Zr, respectively. A thin wafer of the metal is placed between prepared parts to be joined and then heated in vacuum (10^{-6} torr) to temperatures of the order of 1300–1600°C. With some pressure (a few hundred psi) held on the parts, usually for a few hours, some rather impressive joint strengths (to 40,000 psi) have been obtained. Bernard *et al.*[25] have also recently reported various methods of diffusion brazing of Al_2O_3 with Nb, obtaining strengths to 14,000 psi.

Refractory Metal Brazing and Metallization

Though some brazing is done with refractory metals, as noted above, they have in the past been more commonly used to coat or "metallize" a ceramic with subsequent brazing to the metallized layer, which may sometimes be plated (*e.g.*, electroplated) with another metal before brazing. However, this important distinction will not be carried through the following discussion. The term brazing will be used to refer to the metallizing process itself. Also, since in the past almost all refractory metal brazing was done with either tungsten or, much more commonly, with Mo, only these two processes are considered in this section. This distinction between reactive and refractory metal brazing is arbitrary, and is made even less distinct by the recent use of Ta and Nb noted above. This terminology nonetheless represents a large amount of practice. Further, since Mo is very often used in combination with limited quantities of Mn (and sometimes of Ti) it is frequently referred to as the moly-manganese process.

The high temperatures, 1400–1600°C, and the hydrogen atmosphere required for the typical application of this process are constraints on its utilization. However, the refractoriness of the resultant brazes, their high strength and good reliability make this one of the most common ceramic brazing techniques, especially for Al_2O_3 and BeO. Further, the green metallization — especially the W — can be cofired on a green ce-

ramic. The metal may be applied to the ceramic surface by a variety of processes, but most commonly it is applied as a powder by spraying or silkscreening or other similar processes. For such powder-applications processes, the fine metal (typically 200 mesh or less) is mixed with appropriate binders and solvents. The metals may also sometimes be applied by deposition processes such as vacuum deposition, sputtering, or by the application of oxides or other salts which will be reduced to the metal by the hydrogen firing. The use of metals as oxides along with other metals such as Mn along with Fe (both added as oxides) can lower the brazing temperature, to 1000°C or less if strengths such as < 15,000 psi are acceptable, but this can also reduce the reliability of vacuum tightness, which is often important to many brazing applications. Examples of the variety of moly-manganese brazes are shown in Figure 13.

Strengths of refractory brazes depend on the braze composition, its microstructure and thickness, and brazing conditions, as well as the substrate grain size and composition which may be substantially interrelated. Moly brazing of Al_2O_3 bodies can frequently result in strengths of 15,000–30,000 psi at the highest brazing temperatures, 1500–1600°C. These strengths typically decrease with increasing Al_2O_3 content: strengths for 94% Al_2O_3 are often 25,000–30,000 psi; 20,000–25,000 psi for 96% Al_2O_3; and only 15,000–20,000 for 99.6% Al_2O_3 with optimum processing. In addition to the increases of braze strength with decreasing Al_2O_3 content, strengths also frequently increase with increasing grain size of the Al_2O_3 body. Also, as noted above, processing at lower temperatures will typically reduce strength to the 10,000–15,000 psi level or below. While moly brazing is most commonly applied to Al_2O_3 it has been applied to some other oxides, BeO (Figure 13) and steatite, giving strengths of the order of 10,000 psi in the former.

The glassy phase of Al_2O_3 has generally been recognized as an important factor in the refractory metal brazing process, as indicated by the trends with Al_2O_3 content. It has generally been felt that much of the braze strength is due to the migration of glass into the sintering metal, providing strength from interlocking of the metal with part of the glass and the remainding glass bonded to the Al_2O_3. In fact, in some cases, glass powder or oxide powders that will react to form glasses are added to the refractory metal powder. The role of addition of Mn or, less frequently, of Ti is controversial, with some investigators feeling that as these metals oxidize, they react with the ceramic and lower the viscosity of the glassy phase. Recently Twentyman,[25] based on a survey of the literature, has proposed a model to explain the processing parameters and strengths of such refractory metal brazing involving glassy phase. He views the metalizing and the ceramic as two joined capillary systems, competing for the glassy phase based on the concept that pores in

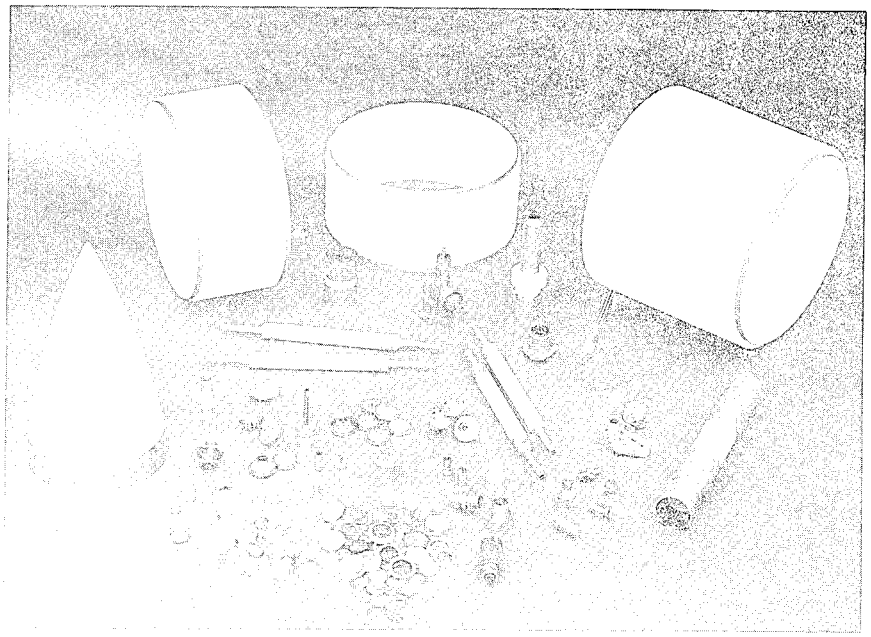


Figure 13. A variety of shapes, sizes, and complexities of parts joined using moly-manganese brazing. Both BeO and Al_2O_3, the latter in either single-crystal form (note sapphire windows in the center foreground) or polycrystalline form are represented in this photo. (Photo courtesy S. Jepson, EIMAC Division of Varian Corp., San Carlos, Calif.)

both the metal and the ceramic can cause glass migration due to their capillary action. Based on the relative capillary pressure of the glass in the sintering metal and the alumina, he determines three classes of brazing conditions. The first is large-grained Al_2O_3 with glassy patches larger than the pores in the unsintered metal. So long as there is an adequate supply of glass in the Al_2O_3 and the temperature is high enough to give good enough flow and wetting of the glass, good bonds are obtained — except at very high temperatures where excessive migration of the glass can flood and coat the surface of the metallization. The second condition is when the glass patches in the Al_2O_3 are approximately equal to the pores in the unsintered metal powder. This typically requires higher temperatures, but there is a reasonable temperature range over which the metal will become partially, but not fully, filled with glass to give a good bond. The third category is very fine-grained Al_2O_3 with glassy patches smaller than the pores in the unsintered metal, which provide the worst situation: requiring temperatures that either may not be reached by some

apparatus, or may be sufficiently high to cause distortion of the Al_2O_3; or excessive sintering of the metal powder so glass migration into the metal is prevented. Twentyman views the Mn or Ti effecting the process by altering the pore structure in the metal and by dissolving in the glass, the net result of which may or may not be beneficial. Twentyman and Popper[27,28] report experiments that support Twentyman's model for the situation when you have alumina bodies containing a glassy phase, or add glass or other ceramic components to the metal powder. While the glass phase plays an important role in the quality (strength of the bond obtained) and may enhance the sintering of Mo,[29] it may not be necessary. Clark *et al.*[30] have reported Mo metallization of BeO(99.5%), suggesting that direct BeO-Mo bonding occurred.

The above brief summary of a partial survey of research shows the same trend as with other metal brazing, *i.e.*, refining understanding of the process and extension to other materials, such as BeO, and more extreme conditions. Use of Mo-Mn metalized sapphire windows (brazed to Kovar with Cu) for a variety of applications such as cryogenic conditions[19] and the Pioneer Venus space craft[20] are examples of the latter. There are also important microcircuit applications (Figure 14).

Brazing with Ceramics

Ceramics can also be joined to themselves or to metals by brazing with ceramics instead of metals. This can often work with metals without wetting problems since the oxide coating on metals will typically allow them to be wetted by other oxides. Glasses are a common ceramic braze (or solder) material, but mixtures of glasses and crystalline phases, or all crystalline phases, often as eutectics, may be used. Ceramic brazes, which can generally be applied in and processed in the same fashion as metal brazes, *i.e.*, in the solid (diffusion brazing) or fluid state, have similar advantages and limitations as metallic brazes. Thus, good environmental compatibility, often better than with metals, can be achieved, but this may often not equal that of the ceramic component itself. Because their plastic flow is often more limited, ceramic brazes are usually less tolerant of thermal expansion mismatches between either component and the braze than metallic brazes, but, on the other hand, may allow a better match of thermal expansion with the ceramic component. Although not as extensively developed, and limited somewhat by suitable phase information, the greater range of ceramic brazing compositions, and their greater ceramic and environmental compatibility offer considerable potential for future development.

A variety of compositions and techniques exist for brazing with glasses, or glass-containing compositions. These may be referred to by a

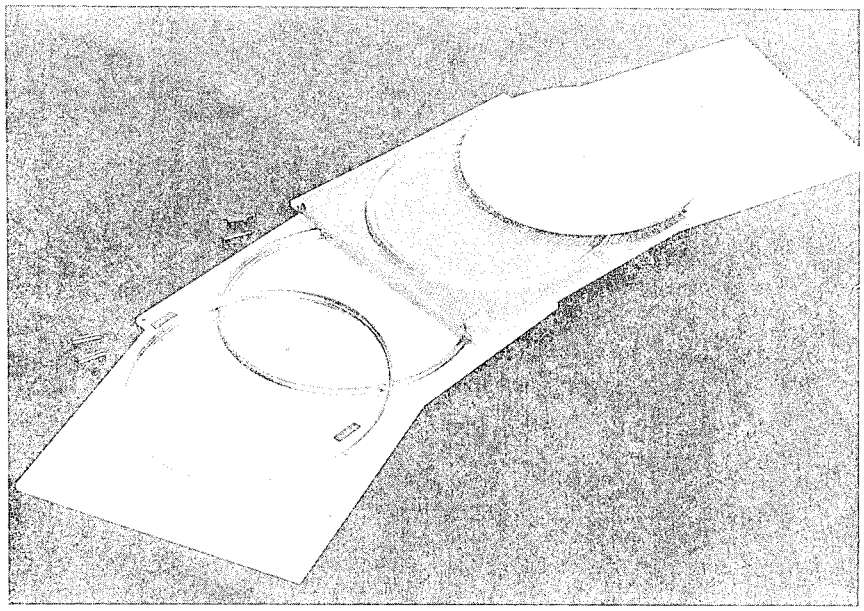


Figure 14. Components for a large microelectronic package. Starting from the lower left, the first two large white squares are ceramic substrates with metal seal rings sitting on them. Next is the substrate with 300 conductor lines which are plated molymanganese metalization. The seal ring is now brazed to the substrate insulated from the conducting lines with a layer of Al_2O_3 and the metal sealing lid is sitting on top, offset from its final placement after a hybrid circuit or large semiconducting chip up to 3 in. in dia is bonded in place. The lid provides complete hermetic sealing. The fourth large square white object, upper right, is the ceramic thermal radiator. Depending upon the selection of Al_2O_3 or BeO for the substrate and/or radiator, such packages are designed to dissipate between 20 and 50 watts of power. Many electronic packages use noble metal thick filming conductors, where, for example, high sealing temperatures required in this package are not involved in the processing.

variety of terms including brazes, solders, or adhesives.[31] Reed[4] has, for example, discussed some of the established glass brazing, noting that strengths in the 5,000 psi range are often obtained in joining to Kovar or a refractory metal such as Mo.

A major trend in brazing or soldering with ceramics, especially glasses, is in the microelectronics area. The large-scale usage of fritted conducting ink in microelectronic circuitry in recent years can probably be classed as this type of joining, and hence as one of its most significant

applications and development. Such inks are typically mixtures of noble metals — Au, Pt, or alloys of these with other noble metals in powder form that are mixed with glass frit and organic additives to form a paste. Circuit patterns are formed by printing, then fired onto ceramic substrates, most commonly Al_2O_3 (Figure 14). The primary mechanism of bonding as shown by Hitch[32] and corroborated by Becher *et al.*[33] is for the glass to form a strong bond with the alumina, with the remainder of the glass entrapped between the sintered metal particles, *i.e.*, along their grain boundaries. Since much of the glass joins to the alumina interface, good adhesion of the metal to the alumina subtrate is obtained by its mechanical interlocking with the glass which is joined to the substrate. Another important and related area is the use of glasses to seal microelectronic packages, usually at temperatures of less than 500°C, with the drive to get still lower sealing temperatures. Some of these sealing glasses, such as Pb, Zn borosilicate glasses, are heat treated at 450–500°C after sealing for crystallization to give greater strength.

An interesting technique of solid-state brazing of glass to a metal semiconductor with the use of an electrical field has been reported.[34–36] A glass, such as borosilicate, or a glass ceramic part is placed in good physical contact (due to good surface finish) with a metal or semiconducting part, which is the positive terminal of a DC circuit. The negative terminal need only be placed in physical contact with the opposite side of the glass, *e.g.*, the point contact of a wire for a small part, and does not form a strong bond to the glass. With voltages of 200–2000V for thin glass pieces (a fraction of a mm), heating to 300–600°C (several hundred degrees below the softening temperature) is reported to result in a hermetic seal in times from less than one minute to several, with the time varying inversely with temperature. Fused quartz has been reportedly joined to silicon at 850°C by this technique, which apparently depends on ionic (Na) transport. This process has apparently not yet seen any significant application. Whether this is due to possible thickness limitations, surface finish (2 μm) requirements, other problems, or lack of awareness, is not known. However, the process would appear to be worthy of further investigation.

Turning next to more refractory ceramic brazes, these may contain glass phase, but often will not, especially for high-temperature applications. Thus, for example, Clark *et al.*[2] note that a technique based on a eutectic of manganese pyrophosphate and MgO was in the development stages. In this technique the eutectic is mixed with MgO in the ratio of 30:70 to make a sealant powder that could be pressed around metal pins, then fired at 1180°C for 30 minutes in air, argon, or vacuum, producing impermeable joints. They also noted that it might be feasible to replace the MgO with BeO. Klomp and Bolden[37] have reported joining Al_2O_3 to

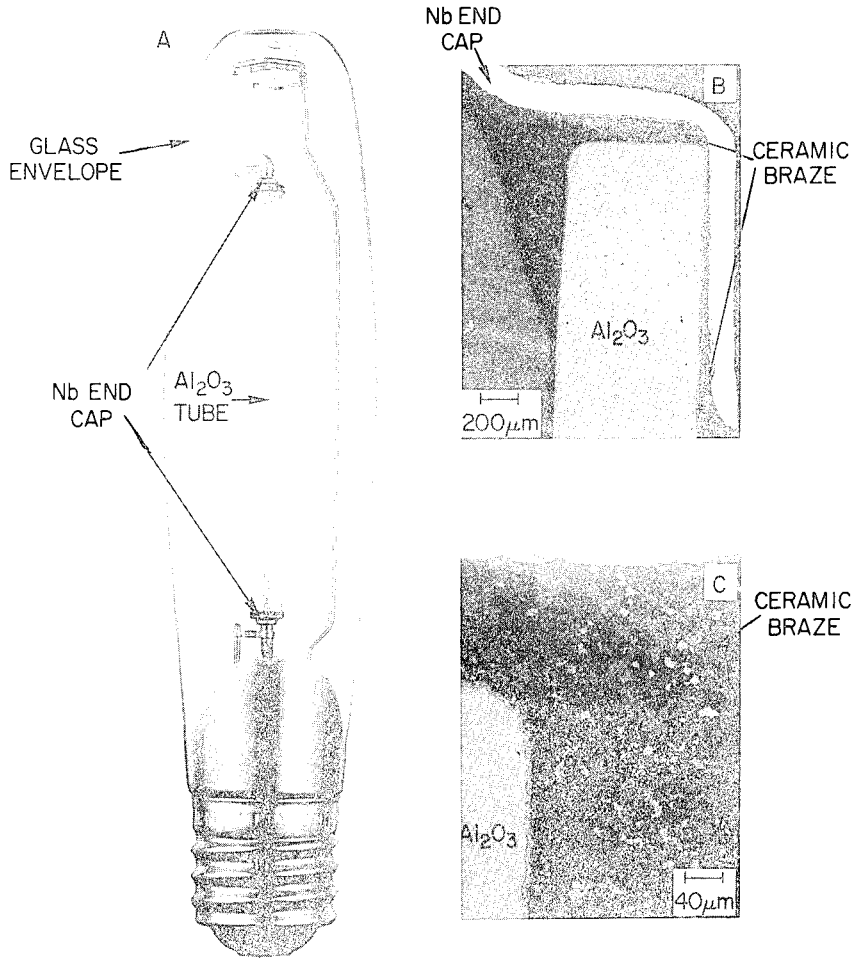


Figure 15. Ceramic brazing in modern high-pressure Na vapor lamps. *A* Commercial lamp. *B* and *C* Micrographs of a cross section through the Nb to Al_2O_3 (Lucalox®) braze. Note that the bright layer on the inside of the Nb cap in *B* is due to a thin W coating to promote adhesion. The braze originally was a CaO-Al_2O_3-MgO composition; more recently BaO has been substituted for part of the CaO and Al_2O_3. Note the dark grains in a glassy (gray) matrix and the layer of grains of reaction material at the Al_2O_3-braze interface. (Photos courtesy J. Burke and C. McVey, General Electric Company.)

itself or to Kovar using Al_2O_3-MnO-SiO_2 or Al_2O_3-CaO-MgO-SiO_2 mixtures (not eutectics) in the 1100–1400°C range in hydrogen. Seal strengths of at least 10,000 psi, and frequently 20,000–25,000 psi were

reported. Similar compositions are used to seal the metal (Nb) electrode end caps onto the Al_2O_3 envelope of modern high-intensity Na vapor lamps (SiO_2 deleted to avoid Na attack, Figure 15). This illustrates a switch from metals to ceramic brazes as environmental extremes increase, *e.g.*, higher temperatures and pressures of Na vapor in this case. Turning again to eutectics, recently metal-nonmetal eutectic systems have been used to join metals to ceramics, *e.g.*, Cu to Al_2O_3 for electronic applications as discussed by Neugebauer and Burgess.[38] Also DeLuca[39] has patented a process of joining sapphire to sapphire with a eutectic mixture of Al_2O_3 and ZrO_2.

Finally, there is the growing need for joining nonoxide ceramics to themselves or other components as their usage increases. This is an area in which ceramic brazes may often have even more applicability. Little work has been done, but isolated examples indicate promise. Thus, for example, Samsonov[40] has briefly reviewed brazing of LaB_6 to Ta using $MoSi_3$ or WC, or to Mo using $MoSi_2$ or Cr_7C_3 with either 1% NaF or CaF_2 at about 2000°C. The use of $MoSi_2$ with Mo was noted as being more limited because of lower stability of molybdenum silicides than those of Ta.

WELDING OF CERAMICS

Introduction

Welding is really the oldest technique of joining a major type of ceramics, namely, silicate glasses. The frequent joining of two or more glass shapes to one another in the practice of glass blowing, though not referred to as such, is really welding since it is clearly analogous with the welding of metals. However, the welding of ceramics in general, and in particular very refractory single-phased crystalline materials, is relatively new and offers considerable opportunity. Because of the potential and newness of their techniques, they are reviewed in greater detail in comparison to their application.

Basically the requirements for welding ceramics are that the ceramics be compatible, both chemically and mechanically with one another and with the welding environment. The details, emphasis, and limitations of these requirements depended on the method of welding used. The two basic methods of welding ceramics, solid-state and fusion welding, in complete analogy with welding of metals are reviewed below and more recent developments discussed. The summary is drawn primarily from a report by Rice,[41] but some brief mention of welding can be found in the reviews by Pettee *et al.*[3] and Reed.[4]

Solid-State Welding

Solid-state welding is done by heating the components while they are held together, usually under pressure. Often an intervening layer of powder is sandwiched between the two parts. The powder is of the same composition as the two bodies being joined if they are identical, or of one or the other or a mixture of both if two bodies of different composition are being joined. In the extreme, a series of thin layers of powder grading from one composition to the other may be used (see Kelly[42]). Bonding occurs by reaction if the materials to be welded are dissimilar and/or sintering, which will most commonly be due primarily to diffusion. The components must of course be able to withstand the pressures needed to bring about adequate bonding, as well as having suitably matched coefficients of thermal expansion. Besides being chemically compatible with each other, they must be compatible with the environment. Thus, for example, solid-state welding of CeO_2 components would not be practical using graphite tooling because of easy reduction of CeO_2 when heated near graphite. When dissimilar materials are being joined, bonding will depend on the reaction or interdiffusion of both components. With similar materials, it depends primarily on the sintering ability of the materials. Thus BN and Si_3N_4 which are difficult to sinter, would be difficult to solid-state weld in their pure form. However, they can be solid-state welded with additives in the same fashion that they are hot pressed. Another basic problem that affects a few materials is the occurrence of phase changes that can lead to cracking and other problems on cooling.

A wide variety of oxide and nonoxide materials have been solid-state welded to themselves, one another, or other materials such as metals. Tables 1 and 2 list several of the materials that have been solid-state welded. A considerable amount of welding has involved single crystals on either one or both sides of the joint, most commonly Al_2O_3 or MgO (Figures 16, 17). Kimura[43] recently appears to have significantly reduced if not totally eliminated the residual porosity and impurities that can be trapped in the joint in solid-state welding MgO crystals together (Figure 17). A potentially important application of solid-state welding is the work to join a hot-pressed Si_3N_4 rotor hub and a monolithic reaction sintered Si_3N_4 ring and blade body for gas turbine applications. Earlier work[44] showed some success of hot pressing a previously hot-pressed rotor into the ring and blade body. Recent work[45] has focused on hot pressing Si_3N_4 powder to form the rotor inside of the reaction sintered ring and blade. Even graphite appears to have been solid-state welded under pulse magnetic pressure, which apparently gave a weld of approximately 35% of the original graphite strength — a weld strength of prob-

Table 1. Summary of Oxide Solid-State Ceramic Welding[1]

Materials Welded	Type*	Temperature (°C)	Pressure (1000 psi)	Time (min)	Ambient Weld Strengths (1000 psi)
MgO-MgO	C to C	1750–1950	3–5	5	7–17
Al_2O_3-Al_2O_3	C to C, C to P, P to P	1700	1	30–40	—
Al_2O_3-Al_2O_3	C to C	1900–2000	0.1–1	60–70	—
Al_2O_3-Al_2O_3, Al_2O_3 + 1 wt % MgO	C to C	1400	2	60	—
Al_2O_3 + 1 wt % MgO					
Al_2O_3-Al_2O_3	C to C	1600	0.6	180	—
Al_2O_3-Al_2O_3	P to P	—	—	—	up to 54
Al_2O_3-Al_2O_3	P to P	1300–1400	8–10	20–30	30–45
Al_2O_3-Al_2O_3	P to P	1500	0.7	60	—
Al_2O_3-Al_2O_3 + H_3PO_4 or AlF_3	P to P	900–1200	0.7	60	20–50 estimated
NiO-NiO	P to P	1000	10	90	—
MgO-MgO	P to P	800–1100	10–12	30	1–15
MgO-MgO	P to P	1300–1400	5	15	—
CaO-CaO (with 2 wt % LiF)	P to P	1000–1100	5	15	—
CeO_2-CeO_2	P to P	1000	—	—	—
Al_2O_3-Nb	P to P	—	—	—	up to 11.7
Al_2O_3-Cu	P to P	1000	0.3	10	10–28
Al_2O_3-Ni, Fe, etc.	P to P	1250–1300	0.3	10	7–28
Al_2O_3-Ni	C or P to P	1200	—	—	—
Al_2O_3-Nb	P to P	1500	2.1	17	11–13
Al_2O_3-ZrC, ZrN, or ZrB_2	P to P	1750	3	60	—
ZrO_2 or ZrB_2	P to P	1800	3	60	—

*C = crystal, P = polycrystal.
[1]See Rice[41] for details.

Table 2. Summary of Nonoxide Solid-State Ceramic Welding[1]

Materials Welded	Type*	Temperature (°C)	Pressure (1000 psi)	Time (min)
LiF-LiF	C to C	840–860	0	
B_4C-Si				
TaC-TaC	P to P			
(ZrC, NbC, TaC)-(Nb, Ta, Mo, W)	P to P	1200–2000†	0.7	5–60†
ZrC-ZrB_2				
ZrN-ZrB_2	P to P	2100	4	30
ZrC-ZrN				
TiC-TiB_2				
TiC-TiN				
TiB_2-TiN	P to P	2100	4	60
TiC-ZrB_2				
C-C	P to P	(see text)		

*C = cyrstal, P = polycrystal.
†See Ref. 42.
[1] See Rice[41] for details.

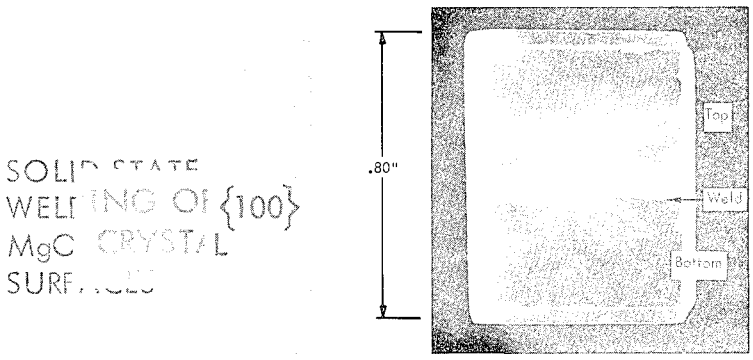


Figure 16. Earlier solid-state welding of MgO crystals. *A* is a top view looking down through the welded crystal joint and *B* is a side view in which the high lighting accentuates scattering from the surface and in the weld region (Rice[41]). However, there is some porosity and second-phase material in the weld region, which results in significant etching of the weld similar to etching of normal polycrystalline grain boundaries.

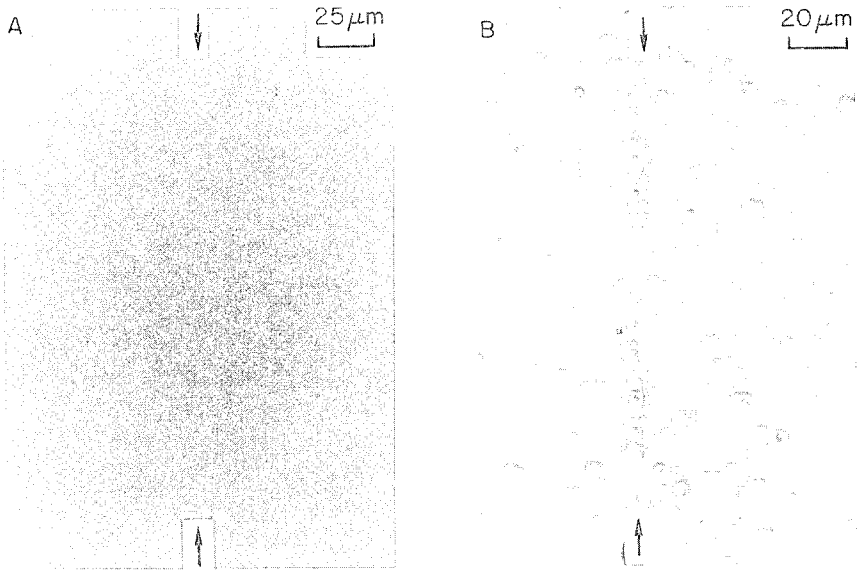


Figure 17. Microstructure of more recent solid-state welding of MgO crystals. *A* is an optical photo of the surface of the welded samples with the weld indicated by the arrows. *B* is an etching of this sample indicating very little preferred etching of the weld showing the high quality of the joint. (Photos courtesy S. Kimura, Tokyo Institute of Technology, Tokyo, Japan.)

ably about 1000–3000 psi which was apparently limited by cracking. Another technique of joining materials in the solid state has been reported by Messier and Wong, who report joining to pieces of Al_2O_3 by chemical vapor deposition to fill the gap between the materials. A special technique important for microelectronic parts is bonding of green bodies, *e.g.*, substrate tapes. Solvent is put on the bodies to be joined to soften their binders, then the bodies are pressed or rolled together. On subsequent firing, an excellent solid-state weld is formed.

Fusion Welding

Fusion welding of ceramics is achieved by filling the joint between parts with molten material obtained by melting the edges of the components in contact, or with melt from a filler of similar materials just as in welding of metals. In the fusion welding of dissimilar materials, their melts must also be compatible with one another. While compatibility of welding environment depends somewhat on the fusion techniques used, an overall requirement is that the materials melt. A number of ceramic

materials such as BN and SiC sublime without melting and, at normal pressures, cannot be fusion welded. Some, such as MgO, can have quite high vapor pressures at their melting points, making it difficult if not impossible to fusion weld them. Also, because of the higher temperatures involved in fusion than in solid-state welding, problems of phase transformations may be more serious since the higher temperature range may present more phase transformations than the lower temperatures at which solid-state welding can be conducted. Thus, for example, the phase transformation of BeO at approximately 2100°C probably makes the success of fusion welding of this material doubtful.

Many have not felt fusion welding to be feasible (see Pattee *et al*[3]) because of resultant thermal stress fracture. However, it has now been demonstrated that there are techniques to prevent such fracture. Supplemental heating around the weld zone to reduce the thermal gradients from welding below the level that can cause cracking is the most common method. For some materials and situations, a simple slower heat-up and post cool using the welding energy in a diffused or lower power mode, is suitable. While such thermal stress precautions encumber fusion welding of ceramics in comparison to welding of metals, it is still a very useful technique.

Primary methods of fusion welding and their capabilities and limitations are briefly outlined as follows. The most versatile welding technique can be referred to as optical or electromagnetic beam welding. This is primarily laser welding; however, arc image furnaces have been used. Its main advantage is that it can be used with any environment, and while there may be some variability of coupling between different materials, it can basically be used with all materials. In materials that are completely opaque to the wavelength or wavelengths used, the very shallow absorption of the laser energy may lead to some greater vaporization. However, overall, this is essentially the most versatile technique, particularly as lasers of increased power become available. Trial laser welds with several oxide materials have shown promise (Table 3), and an arc image furnace has been used to weld "T" sections of Al_2O_3 tubing.[46]

Electron-beam welding, while typically encumbered by the need for a vacuum chamber, is the next most versatile technique. Many have assumed that this will not work for dielectrics because of charge buildup. This is not so. The combination of high-temperature conductivity and electron emission, and nearby supplemental heaters prevents such charge buildup. Substantial electron-beam welding of Al_2O_3 has been conducted (Figures 18–20, Table 3), and trials with some other oxides and a few carbides show considerable promise. No attempts of electron-beam welding involving fluorides or refractory nitrides or borides either

Table 3. Sample of Fusion Welding of Polycrystalline Ceramics[1]

Welded Parts	Weld Method	Representative Weld* Strengths Achieved (1000 psi)
Al_2O_3-Al_2O_3	Electron beam	15–30
Al_2O_3-Ta	Electron beam	5–10
Al_2O_3-Al_2O_3	Laser	25
ZrB_2-ZrB_2	Arc	20–60
TaC-TaC	Arc	20–30
ZrB_2 + C or SiC to itself	Arc	~10
W-graphite	Arc	3–5
ZrB_2-Mo, Nb, or Ta	Arc	15–30
ZrB_2 + SiC-Mo or Ta	Arc	15–30
ZrB_2-graphite	Arc	~2
Fireclay, brick to itself	Arc (with feed material)	0.2–1.5

[1]See Rice's[41] survey for details.
*These strengths generally represent only preliminary trials, and may often be limited by the quality of the bodies to be welded.

to themselves or refractory metals are yet known, but several of these should be successful. Al_2O_3 weld strengths of 30,000 psi or more (Table 3) can be achieved in welding fine (1–10 μm) grain bodies. Welds of larger (60 μm) grain bodies are usually highly cracked, apparently due to the larger resultant weld grain size (apparently not inhibited by MgO), and associated cracking from thermal expansion anisotropy.

The next more versatile method of fusion welding is arc welding. This of course is restricted to electrically conducting materials. However, many dielectrics may be suitably conducting at elevated temperatures, achieved by supplemental heating and/or use of higher voltages. Thus, even some Al_2O_3 may be, and probably most ZrO_2 bodies are amenable to arc welding. However, thus far arc welding has been tried only on some carbides, borides, and refractory metals to graphite (Table 3). For such conducting materials, arc welding is one of the most versatile techniques.

Typical examples of experimental arc welds of carbide or boride materials to themselves or refractory metals are shown in Figure 21. While it would commonly be best to use a supplemental heating furnace to avoid thermal stress failure in arc welding such materials, this has generally not been done in prior investigations. Instead, arc powers in-

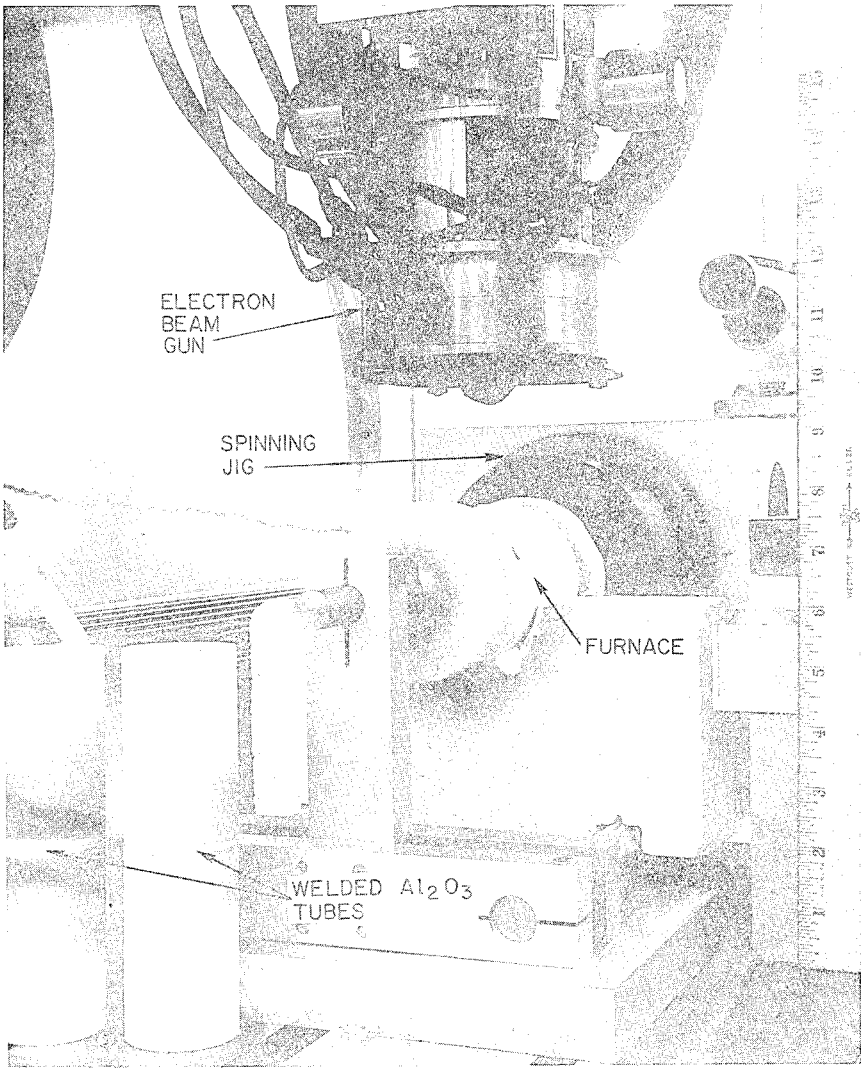


Figure 18. Electron-beam welding of ceramics. This is a photograph looking into the electron welding set-up for welding of Al_2O_3 tubes, two of which are shown in the foreground. The darker region around the central area of the tubes is metal deposited from the elements of the supplementary heating furnace. Note that only the central region of the tubes were provided with supplemental heating. Note also the inch scale at the right hand of the photo.

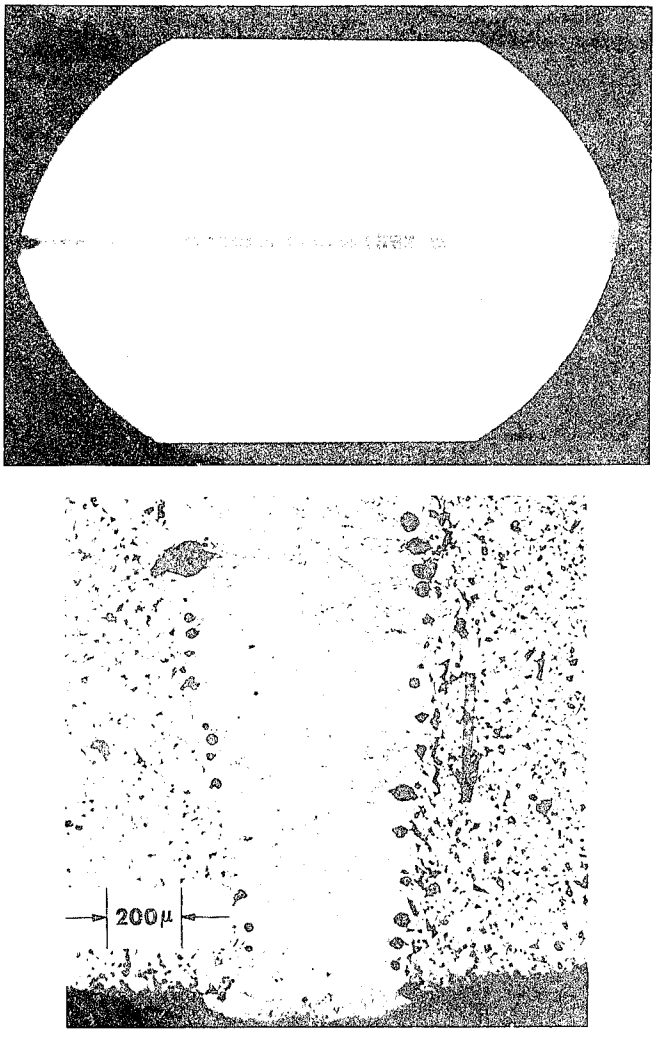


Figure 19. Electron-beam-welded Al_2O_3. *A* shows a top view of 1.5 in.-long pieces of hot-pressed Al_2O_3 welded together, starting at the left and welding toward the right. Note that very shallow cracking along the surface of the weld is accentuated in this photo. Samples cut from such specimens typically had strengths of about 30,000 psi. *B* is the microstructure of a cross section of approximately the bottom third of a weld of commercial 99% Al_2O_3. Note the columnar grain structure of the weld, which was characteristic of many welds of Al_2O_3 of other materials. This photo also shows some of the bubbles that can often be a problem in welding commercial ceramics, presumably due either to vaporization of less refractory additives or impurities or to expansion of gas trapped in the voids of the ceramic.

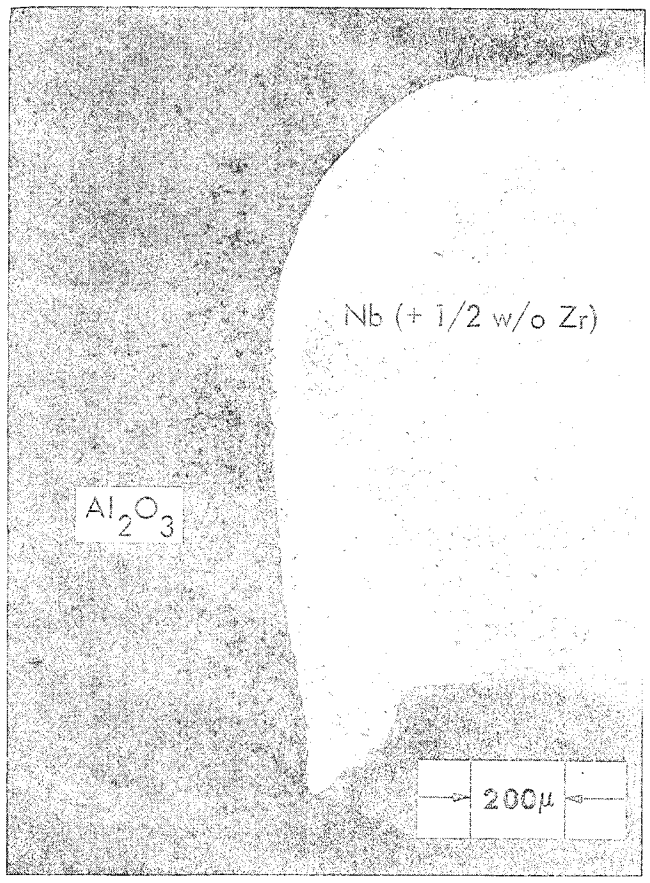


Figure 20. Sample cross-sectional micrograph of an electron-beam weld of Al_2O_3 to a metal. In this case the metal is an alloy, as indicated.

sufficient to cause melting, and hence welding, have been used quite satisfactorily to pre and post heat samples to avoid excessive thermal stresses on the small parts (up to 1 in.) that have been welded by this technique. This can present problems for a hand-held torch, since the added heat due to the pre and post heat as well as the higher welding temperatures for many of the very refractory ceramics and the longer times that may be involved can lead to considerable difficulty in holding the torch. An additional problem that can be encountered particularly in arc welding extremely refractory materials such as TaC, which melt above tungsten, is that the tungsten tip may melt — which can limit welding and lead to contamination and other problems. This has been

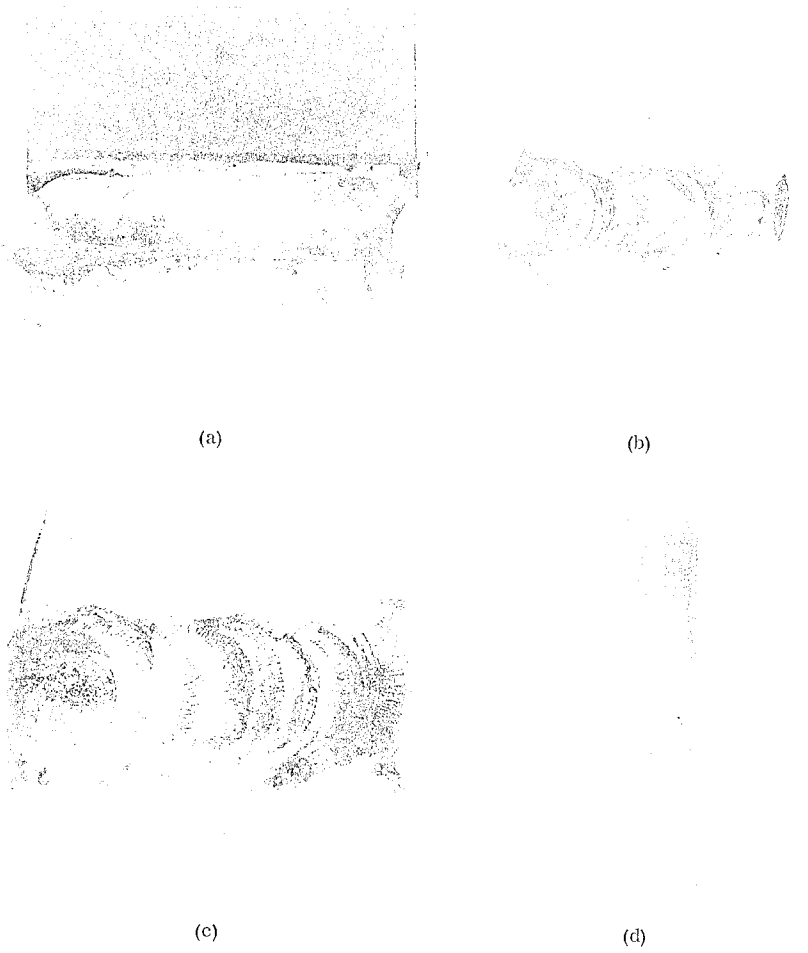


Figure 21. Examples of arc welding of ceramic materials. *A* is an approximately 1 in.-long tungsten-graphite weld, graphite on top. *B* is an approximately 0.6 in.-long TaC-TaC weld. *C* is an approximately 0.6 in.-long ZrB_2-ZrB_2 weld, and *D* is an approximately 0.5 in.-long ZrB_2-Ta(Ta on top) weld.

successfully solved in trials by replacing the tungsten tip with a TaC tip which showed no serious problems of thermal shock failure. Welding of refractory metals to graphite may be limited to metals having lower rates of carbon solubility.

A number of investigators have done some limited torch welding of various ceramic materials — usually less refractory ones. This has usually been done without extra supplemental heating. The flame intensity, or distance of the torch from the part, or the speed of motion has simply been varied to provide pre and post heating. Closure of thermal couple tubes and repair of furnace refractories have been typical of applications of such torch welding. As noted above, plasma torches have probably also been used for some limited welding trials, either as a typical heat source for welding or by filling joints between materials by flame spraying; however, specific information and details are not available. No known use of induction headed torches or newer types of special electrical torches for welding is known, but these may be promising.

COMPARISON OF JOINING METHODS — SUMMARY AND CONCLUSIONS

Table 4 presents a general summary comparison of the various joining techniques. While this cannot adequately convey the full potential and limitations of each method, it gives the general trend. The following comments amplify on this. As noted earlier, the primary advantage of adhesive, cement, and mortar, and to some extent mechanical joining, is their ease, versatility, and low cost. Strength and temperature are commonly important limitations of these methods. Though some mechanical joints and some cement joints may be able to withstand substantial temperatures, most cannot. While all of these techniques can provide sealing (*e.g.*, vacuum sealing) under some conditions, this can often be more difficult with these techniques. However, the significant number of low-stress, low-temperature joining requirements make these — especially adhesive and cement joining — very important.

Brazing techniques, particularly the active metal and the moly-manganese technique are the most widely used for more demanding applications, *e.g.*, in the electronics industry. They are quite versatile, and can readily produce vacuum tightness, good strengths, and substantial temperature capability and can often be developed to resist a variety of chemical environments. They are quite amenable to mass-production operation, and thus can be done quite economically. Significant successes of brazing with both noble and active metals below the melting point, *i.e.*, diffusion bonding, indicates new opportunities. There also appears to be substantial further development of brazing with ceramics.

Welding offers the ultimate in temperature capability and generally in strength and chemical inertness. Solid-state welding, because of its lower temperatures, can typically produce the greatest strengths (over

Table 4. Summary of Joining Techniques

	Technique					
Requirement	**Adhesive**	**Cement**	**Mechanical**	**Brazing**	**Welding diffusion**	**fusion**
Strength (numbers in 1000 psi)	low, e.q. < 5	usually low, often below 1	low-medium e.g. 1–10	good, e.g. 10–40	often best e.g. 20–60 +	good e.g. 10–50
Compatibility with severe environments	generally poor[1]	poor-medium	poor-medium	medium-good	medium-good	generally best
Vacuum tight	question-able[2]	generally not	generally not	usually	frequently[3]	usually
Cost	low	low	low-medium	medium-high	medium-high	low-high[4]

[1]e.g. due to temperature and some chemical limitations.
[2]e.g. due to outgassing of organic constituents.
[3]may not always be as reliable as brazing or fusion welding.
[4]can depend substantially on the number of parts, material, and type of weld, e.g. low for considerable arc welding, but would be high for small numbers of electron beam welds.

60,000 psi). However, obtaining vacuum tightness and, particularly, inertness, may sometimes be more difficult with this technique. It is also typically much slower, and would generally be more costly, and is usually limited in the size and especially the shapes to which it can be applied.

Fusion welding offers a variety of techniques applicable to one or more classes of materials, and though somewhat incumbered in comparison to metals by the common requirement for pre and post heating of a substantial area around the weld, offers much of the potential versatility that metal welding does. However, this need not be a serious impediment in many cases since a tunnel kiln type of pre and post heat furnace can often be used. Thus, with the welding device at the center, the through-put of parts would not be affected by the pre and post heat, except for start-up and shutdown times, which may often be less than an hour total. While some fusion welding methods require a greater capital outlay, some — arc welding of conductive material such as carbides and borides or torch welding of less refractory materials — do not involve any large investment in equipment. Laser welding is potentially the most versatile, and continued industrial development of lasers is significantly reducing the capital investment required. Operation in any atmosphere, and production of a narrow weld are important advantages. Electron-beam welding, though typically limited by the need for vacuum and related vaporization and operation problems and related costs, is versatile and provides good coupling and a narrow weld. Plasma torches, especially some newer plasma-type torches that offer a fine beam, may be extremely promising for future welding of ceramics because of moderate cost and versatility. Thus, there is an increased array of joining techniques that can be considered for joining ceramics to themselves or other materials to meet a wider range and greater extremes of ceramic applications. Because of the versatility and advantages, welding of ceramics should see increasing application, though not yet significantly used.

Ceramics play, and will continue to play, an ever increasing role in our technological society. This will place even greater emphasis on the increasing demand for more economical and more versatile joining techniques, and especially on those techniques that can produce joints capable of greater operational ranges. There is clearly substantial growth in available joining technology to meet these demands. However, joining often is not adequately considered in design and development, in part because of the lack of knowledge of the different techniques, their procedures, advantages, limitations, and development. It is hoped that this chapter, along with its companion chapters on joining of ceramics, will provide much of the needed information and hence enhance the utiliza-

tion of ceramics to better meet the ever increasing technological demands of our society.

ACKNOWLEDGMENT

The author wishes to acknowledge commentary from W. Bascom of the Naval Research Laboratory on adhesive joining, A. Foessel of General Refractories on cement and mortar joining, and S. Jepson of EIMAC Division of Varian Corp. on metal brazing of ceramics, as well as K. Wiedekamp of the Boeing Co. for information on aircraft window mounting, N. Peil of NASA for information on Space Shuttle applications, J. Abar of Crane Packing Co. for information on Al_2O_3 water pump seals, and M. Bafico of Hughes Aircraft for information on Pioneer-Venus windows.

REFERENCES

1. Kutzer, L. G., "Joining Ceramics and Glass to Metals," *Materials in Design Engineering* (Jan. 1965), 106–10.
2. Clarke, J. F., Ritz, J. W., and Girard, E. H., "State-of-the-Art Review of Ceramic-to-Metal Joining," Technical Report AFML-TR-65-143, May 1965.
3. Pattee, H. E., Evans, R. M., and Monroe, R. E., "Joining Ceramics and Graphite to Other Materials," Report NASA SP-5052, 1968.
4. Reed, L., "A Review of Ceramic-to-Metal Structure," in *Nuclear Applications of Nonfissionable Ceramics*, ed. by A. Boltax and J. H. Handwerk, Am. Mic. Soc., Inc., Hinsdale, Ill. (1966), 329–46.
5. Hitch, T. T. and Bube, K. R., "Basic Adhesion Mechanisms in Thick and Thin Films," NAVAIR SYSCOM Report PRRL-75-CR-3, January 31, 1975.
6. Weckesser, L. B., "Thermal-Mechanical Design Principles," in *Radome Engineering Handbook*, ed. by J. D. Walton Jr., New York: Marcel Dekker, Inc. (1970), 41–126.
7. Wygant, J. F., "Cementitious Banding in Ceramic Fabrication," in *Ceramic Fabrication Processes*, ed. by W. D. Kingery, Cambridge, Mass.: Massachusetts Institute of Technology Press (1958), 171–88.
8. Cprnely, K. W., "Refractory Cements," *Materials in Design Engineering* (Nov. 1961), 12–13.
9. Williams, E. L., Jr. and Wilson, H. H., "Low Temperature Cementation Effects in Nickelous Nitrate-Water-Magnesium Oxide System," *J. Amer. Ceram. Soc.* 50 No. 1 (1971) 629–30.
10. O'Hara, M. J., Duga, J. J., and Sheets, H. D., Jr., "Studies in Phosphate Bonding," *Amer. Ceram. Soc. Bull.*, 51, No. 7 (1972), 590–95.
11. Ceramic Industry Newsletter, "New cement for glass tank refractories," in *Ceramic Industry Magazine* (July 1975), 7.

12. Popper, P., ed., "Symposium on the Use of Ceramics in Valves," Special Publication No. 48, Henry Blacklock & Co., Ltd., Manchester 8, England (1965).
13. DeBruin, H. J., Moodie, A. F., and Warble, C. E., "Ceramic-Metal Reaction Welding," *J. Mat. Sci.*, **7** (1972), 909–18.
14. Copley, G. J. and Rivers, A. D., "The Wetting of Three Component Silicate Glasses on Platinum," *J. Mat. Sci.*, **10** (1975), 1291–99.
15. Klomp, J. T., "Bonding of Metals to Ceramics and Glasses," *Amer. Ceram. Soc. Bull.*, **51**, No. 9 (1972), 683–88.
16. Viechnicki, D. J., "Microstructural Investigation of High Alumina Ceramics of the Vacuum Envelope of the M1140 Fuze A2 Tube," Report AMMRC TR 75-14, June 1975.
17. Heidt, G. and Heimke, G., "A Study of the Nature of Solderless Metal-Ceramic Bonds by Reflectivity Measurements," *J. Mat. Sci.*, **10** (1975), 887–95.
18. Takamori T. and Akanuma, M. "Possible Braze Compositions for Pyrolytic Graphite," *Amer. Ceram. Soc. Bull.* **48**, No. 7 (1969), 734–35.
19. Jepson, S., EIMAC Division of Varian Corp., private communication.
20. Bafico, M., Hughes Aircraft, private communication.
21. Scott, P. M., Nicholas, M., and Dewar, B., "The Wetting and Bonding of Diamonds by Copper-Base Binary Alloys," *J. Mat. Sci.*, **10** (1975), 1833–40.
22. Elssner, G., Riedel, S., and Pabst, R. "Fractography and Fracture Paths in Ceramic-Metal Composites," *Practical Metallography*, **12**, No. 5 (1975), 234–43.
23. Elssner, G. and Pabst, R., "Adhesive Joints of Ceramic Materials and Refractory Metals," *Proc. Brit. Ceram. Soc.*, No. 25, *Mechanical Properties of Ceramics II* (1975), 179.
24. Pabst R. and Elssner, G., "Parameters Affecting the Bond Strength of Metal/Ceramic Adhesive Joints," Proceedings of a Conference Held September 1975 in Cambridge, England, to be published as a Volume of Science of Ceramics.
25. Bernard, J., Bourrasse, A., and Ragot, P., "New Types of Metal-to-Ceramic Seals for High Temperature Applications," Report of a "Symposium on Special Ceramics," British Ceram. Res. Asso., Penkhull, Stoke-on-Trent, England (July, 1974), 3.
26. Twentyman, M. E., "High-Temperature Metallizing, Part 1. The Mechanism of Glass Migration in the Production of Metal-Ceramic Seals," *J. Mat. Sci.*, **10** (1975), 765–76.
27. Twentyman, M. E. and Popper, P., "High-Temperature Metallizing, Part 2. The Effect of Experimental Variables on the Structure of Seals to Debased Aluminas," *J. Mat. Sci.*, **10** (1975), 777–90.
28. Twentyman, M. E. and Popper, P., "High-Temperature Metallizing, Part 3. The Use of Metallizing Paints Containing Glass or Other Inorganic Bonding Agents," *J. Mat. Sci.*, **10** (1975), 791–98.

29. Bean, L. W., "The Sintering of Molybdenum Metallizing," *BCS Trans. & J.*, **70** (1971), 121–22.
30. Clark, D. E., Hench, L. L. and Bates, S. R., "Molybdenum Metalizing on Beryllia," *Amer. Ceram. Soc. Bull.*, **53**, No. 6 (1974), 473–77.
31. Robbins, W. P., "High-Temperature Bonds with New Ceramic Adhesives," in *Product Engineering* (September 3, 1962), 75–77.
32. Hitch, T. T., "Phase Morphology and Adhesion in Thick Film Conductor Inks," in Proc. Intnl. Soc. Hybrid Micro-electronics, ed. by W. H. Liederback, ISHM, Park Ridge, Ill. (1971), 7.7.1–11.
33. Becher, P. F., Bascom, W. D., Bitner, J. L., and Murday, J. S., "Fracture Mechanics Approach to Thick Film Adhesion Testing," to be published in Proc. Intnl. Soc. Hybrid Micro-electronics, ISHM, (1975).
34. Wallis, G. and Pomerantz, D. I., "Field Assisted Glass-Metal Sealing," *J. Appl. Phys.*, **40**, No. 10 (September 1969), 3946–49.
35. DeNee, P. B., "Low Energy Metal-Glass Bonding," *J. Appl. Phys.*, **40**, No. 13 (December 1969), 5396–97.
36. Walis, G., "Direct-Current Polarization During Field-Assisted Glass-Metal Sealing," *J. Amer. Ceram. Soc.* (October 1970), 563.
37. Klomp, J. T. and Bolden, Th. P. J., "Sealing Pure Alumina Ceramics to Metals," *J. Amer. Ceram. Bull.*, **49**, No. 2, (1970), 204–11.
38. DeLuca, J. J., "Bonding of Sapphire to Sapphire by Eutectic Mixture of Aluminum Oxide and Zirconium Oxide," U.S. Patent No. 3,859,714, January 14, 1975.
39. Neugebauer C. and Burgess, J., "Direct Bonding of Metals to Ceramics for Electronic Applications," this volume.
40. Samsonov, G. V., "High-Temperature Compounds of Rare Earth Metals with Nonmetals," Consultants Bureau, N. Y. (1965), 86–87.
41. Rice, R. W., "Welding of Ceramics," NRL Report 7085, July 6, 1970.
42. Kelley, J. E., Summer, D. H., and Kelley, H. J., "Systems for Uniting Refractory Materials," this volume.
43. Kimura, S., Kim, H., and Yasuda, E., "Fabrication of MgO Bicrystals," *J. Amer. Ceram. Soc.*, **57**, No. 10 (October 1974).
44. McLean, A. F., Fisher, E. A., and Bratton, R. J., "Brittle Materials Design, High Temperature Gas Turbine," Tech. Report AMMRC CTR, April, 1974, 74-26.
45. Goodyear, M. U. and Ezis, A., "Joining of Turbine Engine Ceramics," this volume.
46. Stablein, P. F. and Araoz, C., "Technique for Fusion Bonding Ceramics," *Rev. Sci. Instr.*, **34**, No. 11, (November 1963), 1275–76.

5. JOINING OF TURBINE ENGINE CERAMICS

M. U. GOODYEAR and A. EZIS
Ford Motor Company
Dearborn, Michigan

Techniques have been developed for bonding silicon nitride ceramic components for turbine engine applications. Both reaction-sintered and theoretically dense hot-pressed materials have been bonded. Slip-casting techniques for bonding reaction-sintered silicon nitride components suitable for stationary engine parts are discussed. Both the processing procedures and casting parameters are correlated with the bond density and bond integrity, and the results are shown both analytically and microstructurally. Various hot-press bonding techniques to join reaction-sintered and hot-pressed silicon nitride component parts suitable for fabricating the highly stressed turbine rotor are discussed. Results of a bonding parameter study, including bond-strength data and interface microstructures are presented. It is concluded that the bond between a reaction-sintered blade ring and hot-pressed hub in a turbine rotor assembly can be made as strong as the weaker of the two parent materials. Typical silicon nitride turbine engine components manufactured through bonding technology are illustrated.

INTRODUCTION

Ford Motor Company has undertaken a program sponsored by the Advanced Research Projects Agency, to demonstrate that brittle materials can be successfully utilized in demanding high-temperature structural applications. The major goal of the program is to show by a practical demonstration that efforts in design, materials, fabrication, and testing can be drawn together and developed to establish the usefulness of ceramic materials for engineering applications. The gas turbine engine, utilizing uncooled ceramic components in the hot gas flow path shown in Figure 1, has been chosen as the vehicle for this demonstration. The use of ceramics in the gas turbine engine makes possible an increase in the turbine inlet temperature to 2500°F, which will produce significant improvements in engine efficiency and specific power.

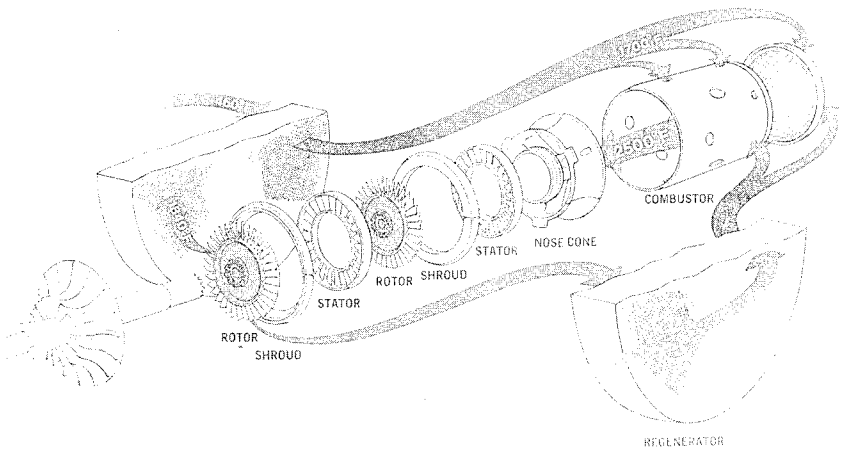


Figure 1. The all-ceramic flow path of Ford's vehicular turbine engine.

The design criteria for the vehicular turbine engine under development at Ford requires many complex shaped ceramic components. Due to the complex shapes and the stringent material properties required for the engine environment, new fabrication techniques must be developed to produce engine hardware that satisfy all requirements. Silicon nitride (Si_3N_4) has been chosen as a primary candidate material because of its good thermal and physical properties. Theoretically dense, high-strength Si_3N_4 can be prepared by hot-pressing techniques, but complex shaped blade configurations cannot be readily formed. However, techniques have been developed to form complex shaped reaction-sintered Si_3N_4 prototype components by both injection molding and slip casting, but these parts, because of their lower strength, cannot be used throughout the engine. Therefore, fabrication of useful complex shaped ceramic turbine hardware appears promising if technology can be developed to bond various component parts together.

This chapter describes joining techniques used to bond various Si_3N_4 materials for turbine engine components. Both slip-cast bonding and hot-press bonding techniques are described.

Slip-cast bonding is used for joining of silicon metal components into desired shapes and nitriding the whole into a homogeneous reaction-bonded silicon nitride component.

The hot-press bonding technique is utilized to fabricate a duodensity turbine rotor. This concept consists of a reaction-sintered Si_3N_4 blade ring bonded to a hot-pressed, theoretically dense Si_3N_4 hub section to produce an integral turbine rotor.

REACTION-SINTERED BONDING

Introduction

Silicon nitride can be fabricated by either reaction sintering (reaction bonding) or hot pressing. Reaction sintering produces a silicon nitride in the low- and medium-density ranges (*i.e.*, from 1.75 to 2.90 gm/cm^3), with a much more versatile fabrication capability than the high-density, hot-pressed grade. Reaction-sintered silicon nitride is manufactured by compacting finely divided silicon powder into the required component shape utilizing fabrication techniques currently employed by the powder metallurgy, ceramic, and plastic industries. After compaction, the silicon is converted to silicon nitride by reacting the mass with nitrogen at temperatures up to 2660°F. Due to the insignificant dimensional change during the reaction, components can be made to close tolerances without the usual dependence on expensive corrective diamond grinding of the final product. Machining, if necessary, can be performed on a seminitrided compact prior to complete conversion to silicon nitride by using ordinary machine-shop techniques with high-speed steel or carbide tipped tools. A further advantage is the material's ability to be joined by adhesive bonding, slip-cast bonding, or flame-spray welding in the green, or presintered condition, which upon reaction sintering produces a homogeneous joint of high integrity.

Forming Methods

There are many techniques available for compacting silicon powders into usable shapes, including isostatic pressing, flame spraying, injection molding, warm die molding, slip casting, extrusion, and thin-film forming.[1,2] Forming-method selection depends on design requirements such as strength, size, and shape of the component to be manufactured. Each forming process has its strong and weak points in these areas, and many times it is necessary to combine several forming processes to produce a single article. Currently, at Ford Motor Company, injection molding and slip casting are being emphasized as fabrication techniques for ceramic gas turbine engine components.[3,4]

Injection Molding. Injection molding is applied in the forming of complex shapes of close manufacturing tolerances such as rotor blade rings, stators, and nose cones on a low-unit-cost, high-volume basis (see Figure 2). The moldable compound is formulated by adding polymeric materials (20–40% by volume) to the silicon, which when heated produces a viscous material that can be forced under moderate pressures into a metal die cavity to form the desired part. The molded object, once

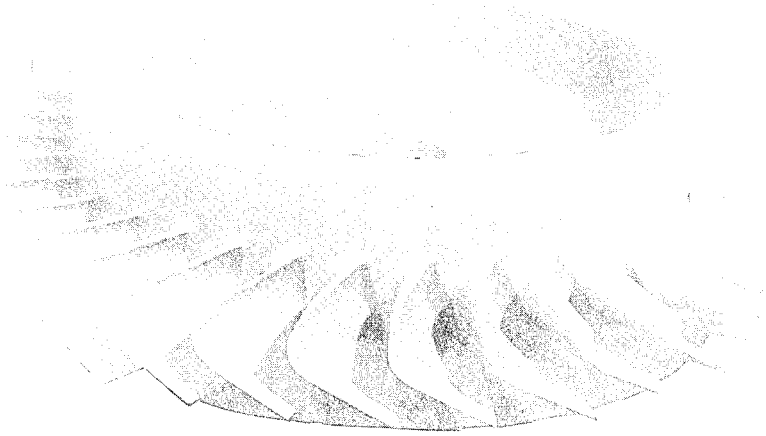


Figure 2. Injection-molded turbine rotor blade ring.

solidified by cooling, is extracted from the mold and reheated under controlled conditions to remove the polymeric vehicle. Subsequent reaction with nitrogen converts the component to silicon nitride. Typical densities fall into the 2.2–2.6 gm/cm^3 area; however, recent developments at Ford Motor Company indicate that densities up to 2.75 gm/cm^3 with bend strengths exceeding 40,000 psi may be achieved.[4]

Slip Casting. Finely divided silicon is suspended in a suitable liquid vehicle (slip) and poured into an absorbant mold (casting) which represents the negative of the object being formed. The mold absorbs much of the liquid fraction of the slip through capillary action, leaving a coherent casting. The casting is subsequently dried and reaction sintered to give the component its final properties. Figure 3 schematically describes the basic slip-cast process.

There are two types of slip-casting techniques: (1) casting of solid parts, and (2) drain casting of hollow parts. Solid castings are made by continuously replacing the absorbed liquid fraction with additional slip until a solid article is formed. Hollow castings are made by pouring the excess slip out of the mold after the article has reached the desired wall thickness. Figure 4 shows prototype silicon nitride turbine components formed by solid casting, while Figure 5 shows other ceramic turbine parts formed by drain casting. The majority of the components shown do not represent as-cast hardware; machining or grinding to final dimension was necessary.

The major advantage of slip casting is the ability to form shapes of high density with good mechanical properties using inexpensive, short

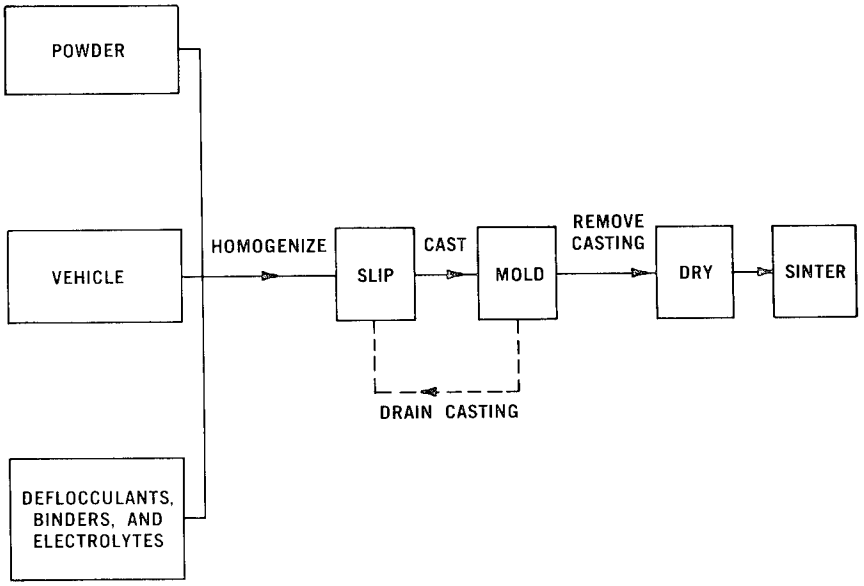


Figure 3. The slip-casting process.

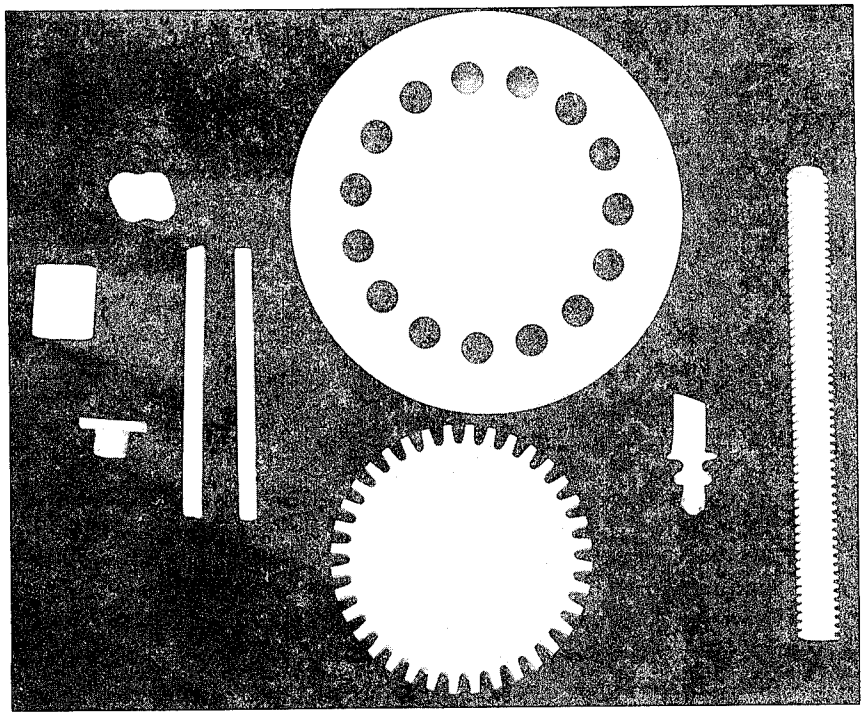


Figure 4. Typical solid-cast articles of silicon nitride.

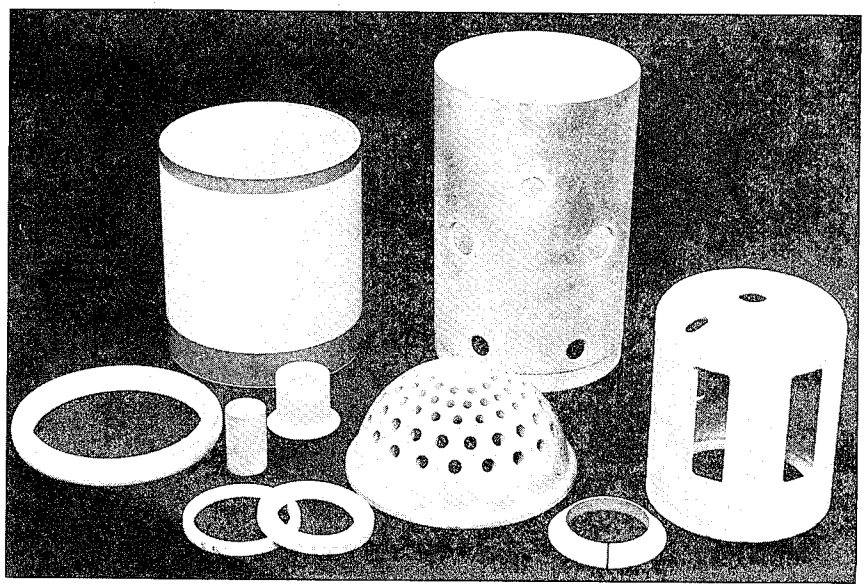


Figure 5. Silicon nitride turbine components formed by drain casting.

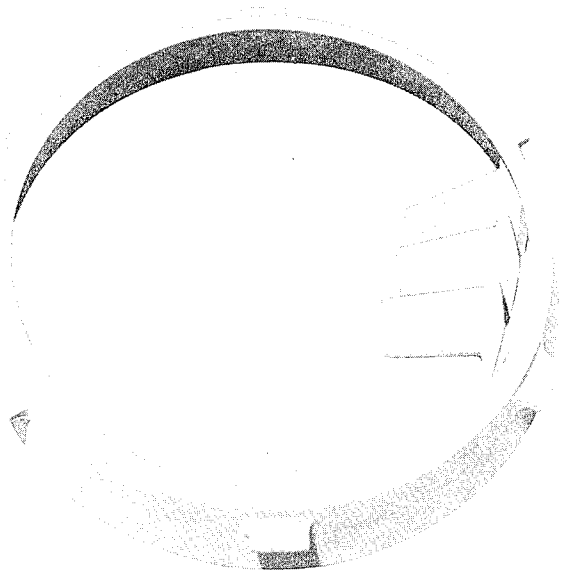


Figure 6. Injection-molded vanes and slip-cast shroud for the inverted channel 2nd stage stator.

lead-time tooling. Green densities of 1.96 gm/cm^3 have been achieved for silicon metal castings, which is equivalent to theoretically dense (3.18 gm/cm^3) reaction-sintered silicon nitride if complete nitridation were possible. However, present state-of-the-art nitriding techniques limits fully nitrided densities to approximately 2.9 gm/cm^3 (cross sections of less than 1/8 in. thickness).

The major disadvantages of slip casting are its lack of fabrication flexibility, which restricts the use of the process to components of relative simple geometry, and its relative unsuitability for mass production of many of the ceramic turbine components. In addition, due to the nature of the process, control of dimensional tolerance is difficult, and machining is usually required to produce a finished component.

Combining Forming Techniques. Part geometry and design requirements often dictate the marriage of two forming processes to produce a final component. For example, a second-stage stator design proposed earlier in Ford's program could not be injection molded into one piece because of the blade overlap necessary to provide adequate aerodynamic turning. As an alternative, an "inverted channel" stator design was proposed. Individual blades were injection molded and bonded to a channeled slip-cast outer shroud ring (Figure 6); the whole was then reaction sintered, producing a homogeneous silicon nitride stator (Figure 7). Injection molding was used to fabricate the individual blade segments

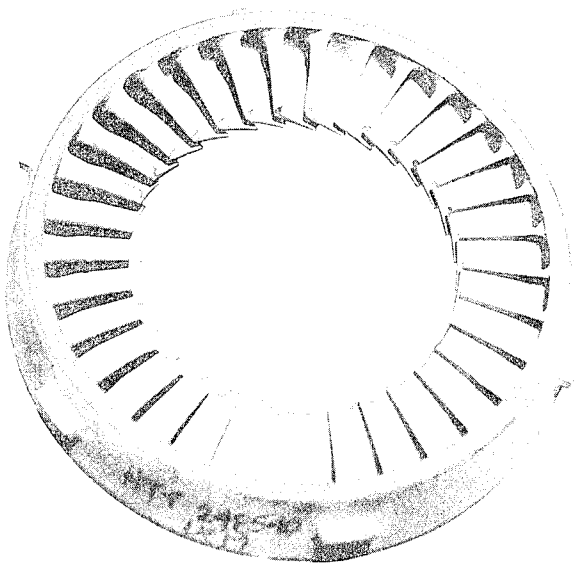


Figure 7. Inverted channel 2nd stage stator.

because of the intrinsic capability of this process to produce complex shapes. However, the outer shroud, which required higher design strengths, was slip-cast because higher densities could be attained by the slip-casting process. The slip-cast Si_3N_4 material has a transverse strength of 40,000–50,000 psi, providing a considerable strength increase over the lower density (2.2 gm/cm^3) injection molding Si_3N_4 (17,000–20,000 psi). In the fabrication process described, the bonding operation becomes the critical step. A homogeneous material free of voids and stress concentrations is required, and the bond strength must equal or exceed the strength of the parent material.

Slip-Cast Bonding

As mentioned, there are several techniques available for the bonding of silicon bodies. Flame-spray welding and adhesive bonding were ruled out because of limitations in bond density, part complexity, and service requirements. Therefore, a technique especially suitable for turbine applications was developed and is referred to as slip-cast bonding (SC bonding). This process is defined as follows: a low-viscosity, chemically suspended silicon slurry is introduced into a casting volume which is defined by the walls of the porous presintered silicon components. The slurry solidifies by extraction of the vehicle through the porous silicon structures by capillary action, producing a coherent mass of silicon within the casting volume which when nitrided results in a homogeneous silicon nitride body.

The joining volume is generally small; therefore, to avoid gas entrapment and premature bridging the bonding slip must have high fluidity or low viscosity. In addition, the slip must completely wet the surfaces of the structures to be joined, the density of the bond must be readily controllable, and the green shrinkage (*i.e.*, shrinkage after the bonding material is thoroughly dried) must be low to prevent bond "pull away" or bond cracking.

To understand the controlling parameters of SC bonding one must understand the fundamentals of metal-powder slip casting as used in the manufacture of hardware. These fundamentals are detailed elsewhere;[5–9] however, the critical areas that must be controlled are the properties of the metal powder, the properties of the liquid media and the rheological additives. Notice should be taken of the fact that many of the variables are closely related and difficult to treat independently.

Suspension Mechanisms. Basically, there are two mechanisms by which a stable suspension is achieved, and they are categorized as either physical or chemical. Physical suspensions are generally used for high specific gravity powders or for powders that have a preponderance of

large particles (>10 microns). These powders require special gelling additives which physically hold the particles in suspension. High-viscosity slips and low-density castings are generally associated with physical suspensions. Chemical suspensions are those whose rheological properties are largely controlled by ionic interactions between the liquid and solid phase. To produce a chemical suspension, the powder particles must fall within a size range where surface forces such as London-van der Waals, rather than gravity, govern their behavior.[10] For most metals, a chemical suspension can be obtained if the bulk of the particles fall in the size range of 1–10 microns. In addition to size, the surface of each particle must be receptive to the formation of an electrical double layer. This may be accomplished by the selection of an appropriate vehicle (usually aqueous) and an appropriate deflocculating agent or agents. The electrical double layers produce repulsive forces between particles; when properly controlled they will prevent particle agglomeration and produce a stable, well-dispersed suspension. The nature of chemical suspensions provides for low-viscosity slurries and high-casting densities; therefore, for SC bonding a chemically suspended slip was required.

A chemical suspension for silicon in this study was produced by using finely divided silicon metal, 0.01–0.06 wt% of an alkaline deflocculant, distilled water as the polar vehicle, and electrolytes such as nitric acid and ammonium hydroxide.

Powders. The as-received silicon metal was a nominal 325-mesh grade, which was too coarse for establishing a chemical suspension. The powder was comminuted by dry milling in a porcelain mill with high-density alumina balls. After comminution, the powders underwent an on-the-shelf aging process for a minimum of 14 days. This allowed the freshly cleaved silicon-metal surfaces to attain a pseudoequilibrium state by forming an oxide layer. Table 1 summarizes the chemistry of the

Table 1. Chemical Analysis of Slip-Cast Silicon Metal

Element	Percentage
Fe	0.75
Al	0.25
Ti	0.06
Ni	0.04
Mn	0.03
V	0.02
Ca	0.01
Zn	0.01
Si	Balance

milled powder and Figure 8 represents its particle size distribution. (Determined by X-ray sedimentation, Micron Data Company, Grimsby, Ontario, Canada.) The characterized silicon metal powder will be referred to as 6.0 micron powder (mean particle size by weight on the distribution curve shown in Figure 8).

pH-Viscosity Relationship. The viscosity values of chemically suspended slips are very sensitive to the ionic atmosphere surrounding the metal powder particles. To illustrate this, a slip having a specific gravity of 1.71 was prepared using the following: 70.59 wt% of 6.0 micron silicon powder, 29.37 wt% of distilled water, and 0.04 wt% of an alkaline deflocculant. The mixture was allowed to homogenize and attain chemical equilibrium[5] by rolling the slip for 20 days in a 5-gallon polyethylene bottle at 24 rpm. The slip was equally divided into smaller lots, the pH was varied using small additions of concentrated HNO_3 and the viscosity of the slip at each acid level was measured. The pH and viscosity values before adjustment were 10.0 and 50 centipoise, respectively. The pH was not increased above 10 because higher values resulted in chemical instability. Figure 9 summarizes the resultant pH-viscosity relationship. The minimum viscosity was established for pH values greater than 9.4; the viscosity increased as the pH was lowered from this range. The relationship such as the one shown in Figure 9 is only characteristic of the subject slip. The amount and type of deflocculant, the specific gravity of the slip, and the silicon particle size and particle-size distribution can all

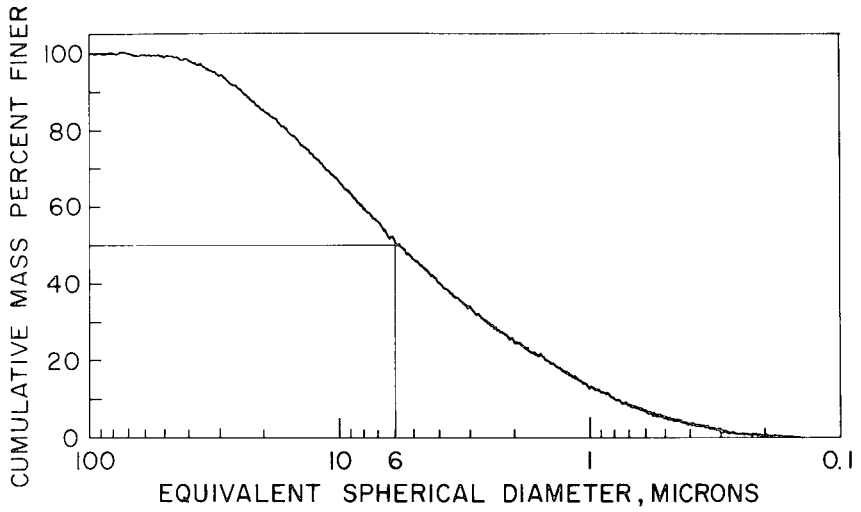


Figure 8. Particle-size distribution of slip-cast 6.0 micron silicon metal powder.

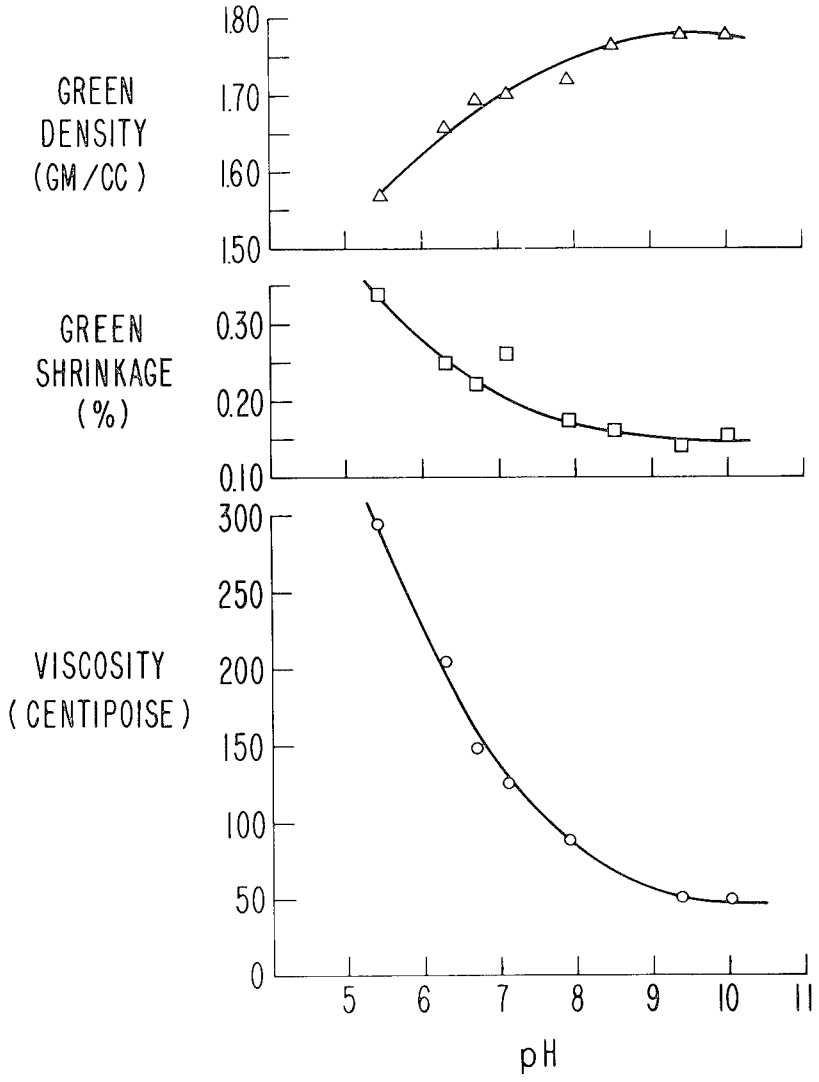


Figure 9. Viscosity, green density, and green shrinkage vs. pH for an aqueous 6.0 micron silicon metal slip with a specific gravity of 1.71.

alter this relationship. For example, a 5.5 micron slip[5] having 0.02 wt% of an alkaline deflocculant, and having a specific gravity of 1.73 yields a pH-viscosity relationship shown in Figure 10. The pH and viscosity values before making adjustments were 6.0 and 125 centipoise, respectively. The pH was again lowered by using small additions of HNO_3; however, the pH was raised by using small additions of concentrated NH_4OH.

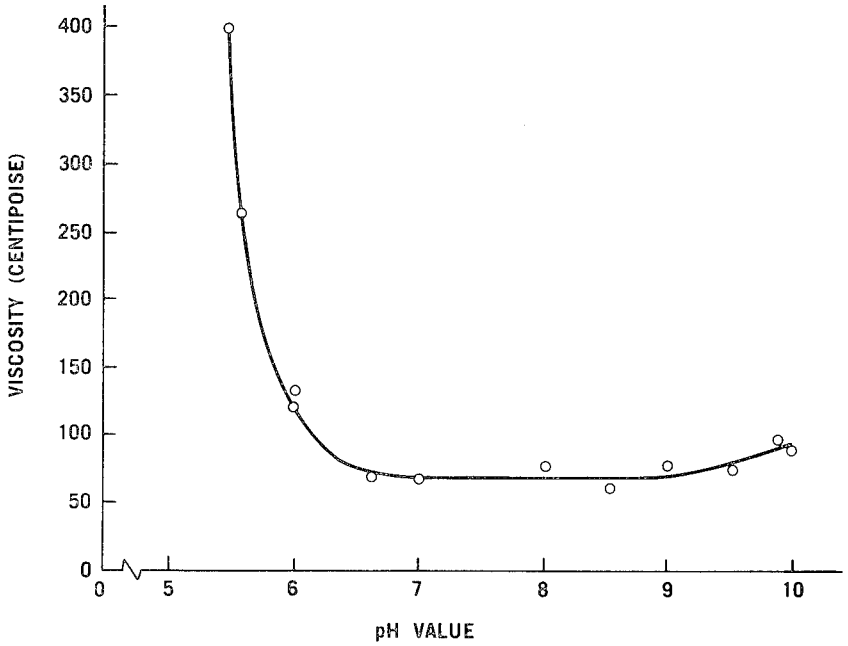


Figure 10. Viscosity-pH relationship for an aqueous 5.5 micron silicon metal slip with a specific gravity of 1.73.

All viscosity measurements were made with a RVE-100 Brookfield viscometer using a Number 2 spindle at 50 rpm.

A Sargent-Welch Model LS pH meter with a glass combination electrode was used to measure the ion concentration (pH) in all slips. The internal element for the glass electrode was a nonpolarizable cartridge of thallium amalgam. The reference electrode utilized a similar internal element and incorporates a porous-platinum-plug liquid junction. Mention should be made that very little is known about the true meaning and mechanisms of pH in nonaqueous solutions; however, ionic-concentration measurements in a metal-powder slip made with standard pH equipment are reproducible and are essential as a process control.

Density. Physical properties of the green casting are controlled by the pH-viscosity relationship discussed above. The green density of specimens cast from various positions on the pH-viscosity curve is also shown in Figure 9. This figure illustrates that the highest casting density was produced from slips of minimum viscosity and that the density decreases as the viscosity of the slip increases. The corresponding density for silicon nitride can be determined by assuming that the silicon will

gain approximately 60% in weight during reaction sintering. The theoretical weight gain is 66.67%; however, the entire gain is not realized because of silicon volatilization during the nitriding process. Therefore, the calculated maximum silicon nitride density shown in Figure 9 is 2.85 gm/cm^3; the lowest is 2.50 gm/cm^3. These results demonstrate the flexibility inherent in the silicon-metal slip-casting system. Thus, a given slip-casting system can be chemically controlled to produce a bond joint of a predetermined density.

The green densities shown in Figure 9 are only representative of the 6.0 micron silicon metal previously characterized. By varying one or more of the controlling parameters, different results can be obtained. For example, the choice of particle size and particle-size distribution greatly influences the final density. The highest calculated silicon nitride density for the 5.5 micron silicon-metal slip represented in Figure 10 was 2.74 gm/cm^3 (corresponds to minimum viscosity) whereas the lowest was 2.40 gm/cm^3 (corresponds to maximum viscosity).

All green density measurements were conducted on argon heat-treated specimens according to the standard ASTM immersion-density procedures.

Green Shrinkage. Green shrinkage is the result of complete extraction of the liquid vehicle from the casting and can be defined as the dimensional change (percent) between the dry mold dimension and the corresponding dry part dimension. Green shrinkage is required in the slip-casting process because the casting, upon consolidation and during drying, must be released from the mold walls to facilitate extraction. However, in a bonding application, if release occurs, the result is bond "pull away" and bond cracking. Therefore, the most effective bonding slip would allow for little or no green shrinkage.

Investigators have shown that green shrinkage is dependent upon particle size and particle size distribution.[6] For example, a casting composed of too many fines may crack on drying due to excessive shrinkage, whereas a casting with a high coarse fraction may not have sufficient shrinkage to allow extraction from the mold. From these observations, bonding slips apparently should have a high coarse fraction to minimize or eliminate green shrinkage. As mentioned earlier, the silicon particle size also determines the mechanism for suspension. Silicon-metal powders having large coarse fractions are difficult to suspend chemically and yield low casting densities. Therefore, the coarse fraction must be maintained within the limits as defined by a chemical suspension. These limits, together with the quantity and the type of coarse fractions, must be determined empirically.

For metal slip-cast systems such as Mo and $MoSi_2$, the green shrinkage is dependent upon the pH value of the slip.[11,12] Maximum

shrinkage values correspond to the maximum density values, and as the pH is altered from this point, the density and the green shrinkage decrease. These observations have been explained on the basis of deflocculation optimization and arise as a result of the powerful solvate layers that develop around the particles when minimum viscosity (maximum density) has been achieved.

Green shrinkage values in this investigation were determined using two types of molds (Figure 11). The "dog bone" mold was used for screening all candidate slips. Castings were made and allowed to dry in the mold; if the casting fractured at the neck, the slip was considered unsuitable for bonding purposes. If no cracking was evident, the slip was used to cast 1″ × 1″ × 6″ indexed bars as shown in Figure 11. All bar castings, once solidified, were removed from the mold and thoroughly

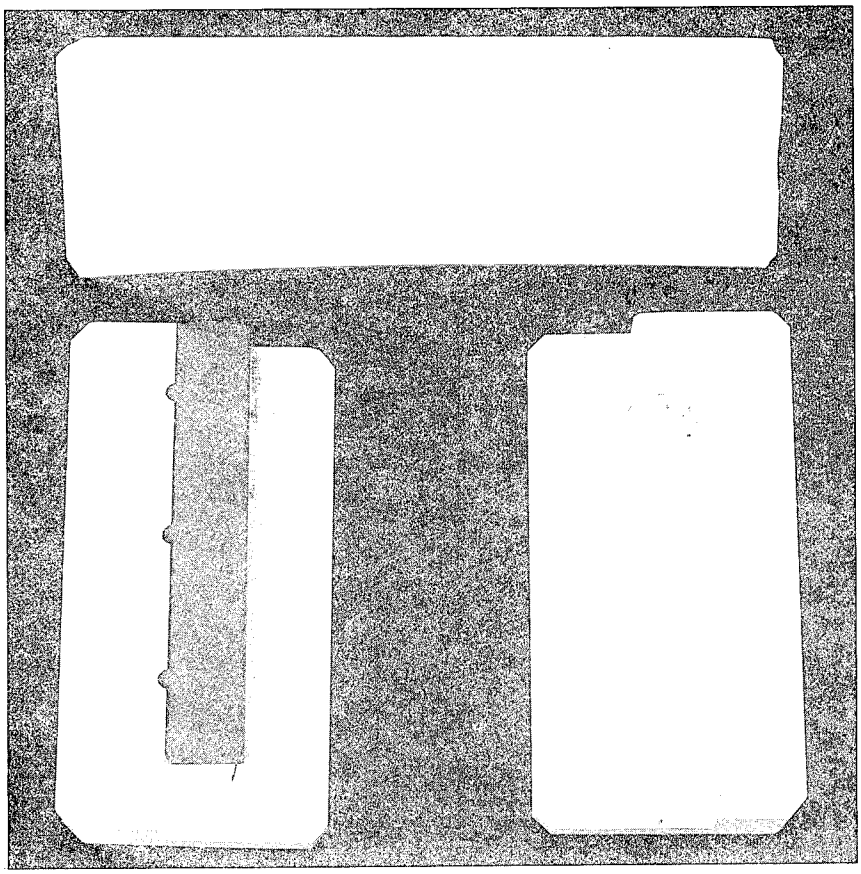


Figure 11. Plaster molds used to determine green shrinkage.

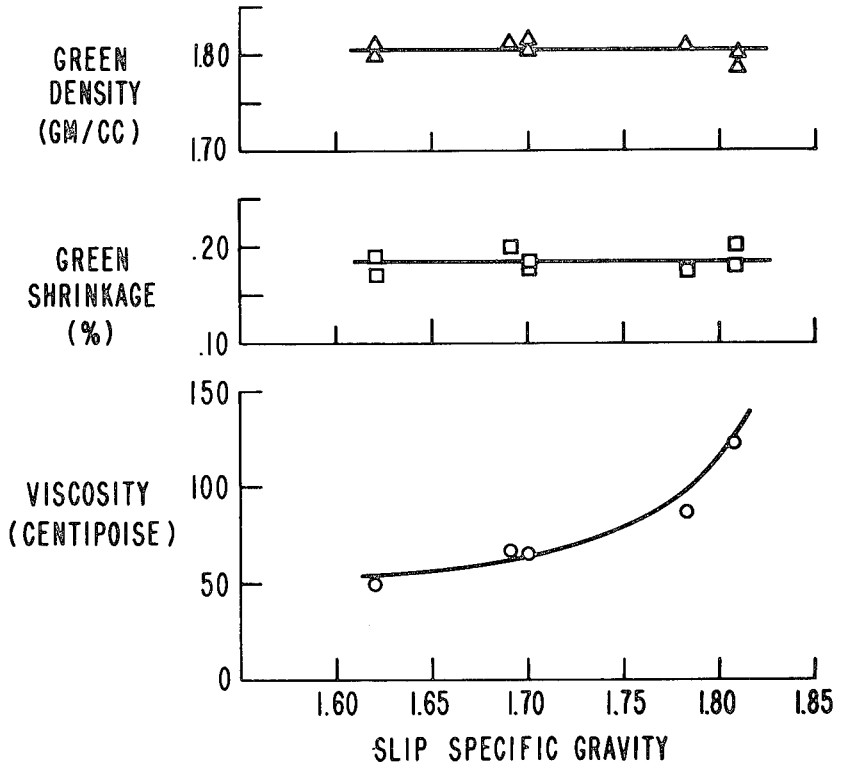


Figure 12. Effect of slip dilution on the viscosity of an aqueous 6.0 micron silicon metal slip (pH = 8.0) and on the resultant green-casting density and green shrinkage.

dried. Linear green shrinkage was determined by measuring with an optical comparator the index length on the bar and on the mold and calculating the difference.

To illustrate the effects of pH on green shrinkage, the 6.0 micron silicon-metal slip was selected. Measurements were conducted at various pH levels and the results are shown in Figure 9. These data show that the lowest linear green shrinkage corresponds to maximum green density or minimum viscosity. Deviation from this pH level results in castings with higher green shrinkage. These results are not consistent with the observations on the Mo and $MoSi_2$ slips previously referenced. The explanation for these differences is beyond the scope of this chapter.

For bonding purposes, silicon-metal slips were utilized at pH levels that produced minimum viscosity, maximum density and minimum green shrinkage.

Slip Dilution. As previously indicated, one of the requirements for a bonding slip was high fluidity or low viscosity. The most effective method for reducing a slip's viscosity is by increasing the water-to-metal ratio; that is, diluting the slip with additional vehicle. Previous results (Figure 9) demonstrated that changes in slip viscosity, when induced chemically, produce corresponding changes in casting density and casting green shrinkage.

To determine if viscosity changes through slip dilution also affect casting properties, the following study was conducted: a 6.0 micron silicon-metal slip containing 0.031 wt% of an alkaline deflocculant, having a water-to-metal ratio of 0.302, and having a specific gravity of 1.81 was formulated. Four additional slips with specific gravity levels of 1.78, 1.70, 1.69, and 1.62 were prepared by diluting the original slip with distilled water. Minimum viscosities were established by adjusting the pH of each slip to approximately 8.0; consequently, the resultant castings represent the maximum green density for each specific condition. The viscosity, green shrinkage, and green density were determined for all slips; these results are summarized in Figure 12. This figure shows that slip dilution substantially reduces the viscosity of the slip and has little effect on the green density or the green shrinkage of the casting.

These results are significant in their application to SC bonding. By using slip-dilution techniques, requirements such as high fluidity and low casting rates can be met without sacrificing the green density or increasing the green shrinkage of the bonding material. However, care must be exercised to avoid over dilution, which may produce slips that are unstable or result in incomplete suspension of the metal particles.

Bonding Operation

The importance of slip parameter control in SC bonding has been demonstrated. However, to assure a homogeneous bond joint, other factors must also be considered. These include the condition or state of the elements that are to be bonded, the configuration of the bonding cavity and the technique of bond slurry introduction.

Presintering. Early attempts to join or bond components to form a consolidated silicon nitride mass were conducted on green, prenitrided or fully nitrided segments. Results were unsatisfactory due to inadequate, inhomogeneous, or unreliable bonding. Green (unfired) component bonding is difficult due to the fragile nature of the components. Bonding in the prenitrided or nitrided state is not reliable because of the difficulty in obtaining cohesive bond between silicon nitride and silicon metal grains.

By replacing the prenitriding operation by a heat treatment or presintering operation, a material with machining properties comparable to prenitriding was obtained. Presintering is conducted by heat treating the silicon compact in a nonnitrogen atmosphere such as argon. Temperatures to 2000°F with holding times to 8 hours (depending upon the density of the silicon compact) are generally used.

As mentioned, argon heat treating imparts strength to the green compacts, but more importantly, it does so without a second phase formation; that is, the compact chemistry has not changed. Consequently, all bonding or joining operations were conducted with silicon metal structures that had been argon sintered.

Bonding Cavity Design. The bonding cavity, where possible, was designed to avoid premature bridging and gas entrapment. Premature bridging is a condition where sections of the bond become isolated from the slurry reservoir during the slip-cast solidification process and produces large pores or low-density regions in the bond joint. Premature bridging can be eliminated by utilizing cavity designs that control the casting direction. For example, V-type cavities are preferable to parallel wall cavities. To avoid gas entrapment, the bond joint cavity should be accessible for bottom fill. This allows the slurry to be introduced into the bottom of the cavity enabling the rising column of slip to progressively displace the air in the cavity. In addition, the slurry must perfectly wet all surfaces of the casting volume. To insure this, all argon-sintered silicon components used for joining were "washed" or saturated with distilled water just prior to the bonding operation. Another consideration was the casting volume size. The casting volume should be as small as possible to minimize the amount of bonding material that would be subjected to drying shrinkage. This is necessary when using any bonding slip that exhibits green shrinkage, even though the green shrinkage has been minimized by control of slip rheological and physical properties.

Bond Testing and Evaluation

All bonds were evaluated metallographically or mechanically. Mechanical evaluation was conducted on argon-sintered bars of the configuration shown in Figure 13 and were manufactured to be representative of the silicon compacts that were to be bonded. The notch in the bar represents the bonding cavity and was filled with a predetermined bonding slurry. Once the bond material solidified and dried, the bar was reaction sintered to form Si_3N_4, and flexure strength tests (four-point loading) were performed to evaluate the bond strength. The bonding joint was placed in tension by orienting the specimen with the joint plane perpen-

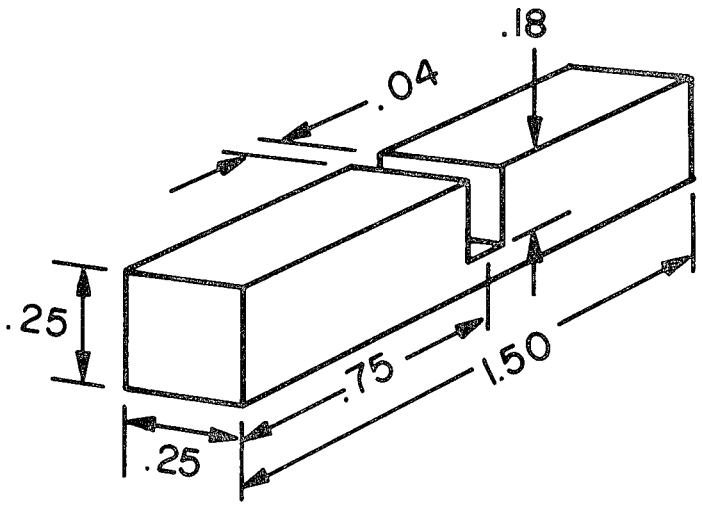


Figure 13. Bonding fracture specimen.

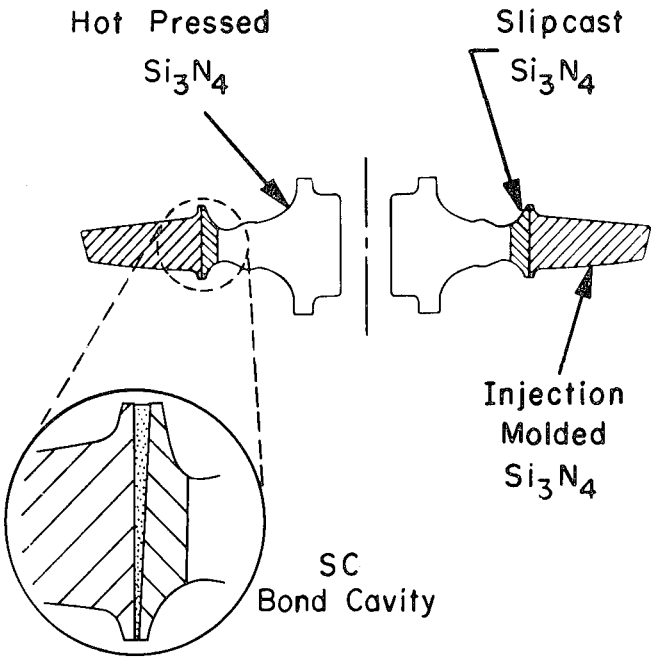


Figure 14. Tridensity turbine rotor.

dicular to the applied tensile stress. For the bond to be acceptable, the flexural strength must equal or exceed the flexural strength of the parent material.

An early rotor concept[13,14] (tridensity) utilized a low-density (2.2 gm/cm^3) injection molded blade ring that was joined to an intermediate-density (2.7 gm/cm^3) slip-cast reinforcing ring and subsequently bonded to a hot-pressed rotor hub (Figure 14). The slip-cast reinforcing ring was needed because higher strengths were necessary to carry both the hot-pressed bonding load and the centrifugal rim loads during spin testing. SC bonding was used to join the blade ring to the reinforcing ring. The operation involved argon sintering the injection-molded blade ring and then machining the inner diameter to a predetermined value. The slip-cast reinforcing ring was machined with a 3° outside taper from an argon-sintered drain-cast cylinder. When mated, the components formed a "half-V" casting cavity that was accessible to bottom fill. After the bonding operation, the reinforced blade ring was reaction sintered and subsequently diffusion bonded to a hot-pressed silicon nitride hub. To evaluate the bond integrity, spin testing and metallographical analysis were used. Figure 15 shows the resultant SC bond achieved between the injection-molded blade ring and the slip-cast reinforcing ring. Although some density gradients in the bond region are evident, high bond integrity was demonstrated.

HOT-PRESS BONDING

Introduction

The duodensity turbine rotor concept is the primary fabrication technique being developed at Ford Motor Company for the high-temperature turbine engine, and a sectioned view of the rotor is shown in Figure 16. This concept utilizes the high strength of the hot-pressed Si_3N_4 in the hub region where stresses are highest but temperatures are moderate and, therefore, creep problems caused by the use of an MgO densification aid are minimized. Reaction-sintered Si_3N_4, which can be readily formed into complex airfoil shapes by injection molding, is utilized for the blade rings. This material does not contain the MgO densification additive and therefore exhibits better creep resistance at the higher engine operating temperatures. Although the reaction-sintered material is of lower strength, it is adequate for the turbine blades because the stress levels in this region are lower.

This concept relies on the ability to bond the two Si_3N_4 components (blade ring and hub) by hot-pressing techniques into an integral turbine

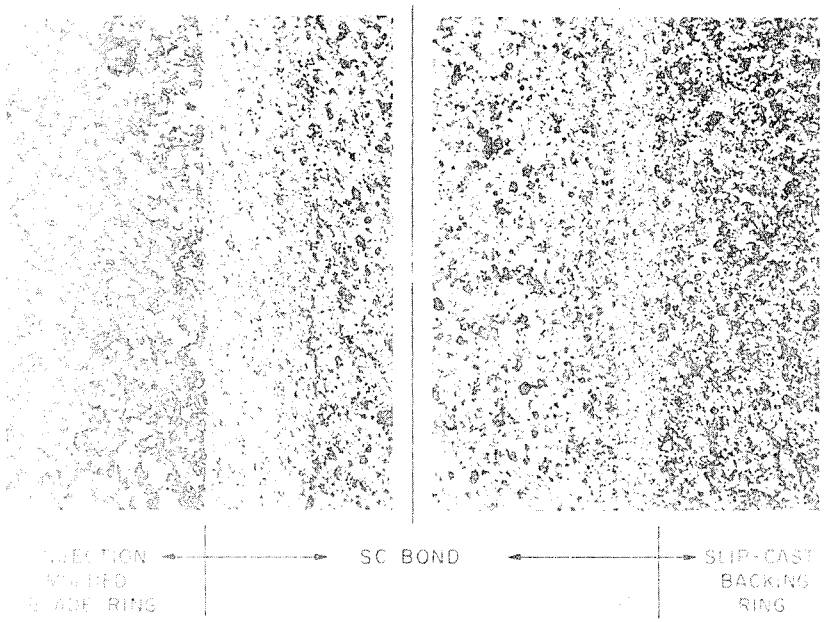


Figure 15. Typical cross-sectional photomicrograph of a SC bond as found in the tridensity rotor. 150 X.

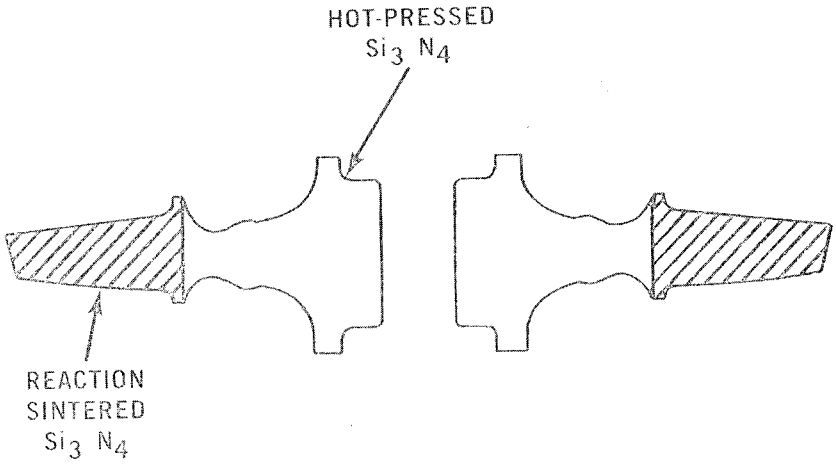


Figure 16. Duodensity ceramic turbine rotor concept.

rotor. Since the hot-press bonding of Si_3N_4 component parts is critical to the success of the duodensity turbine rotor, studies were initiated to evaluate the effect of fabrication parameters on the degree of bonding. The results of the parametric study were incorporated into the development of fabrication techniques to achieve complete bonding between the blade ring and the hub.

Hot-Press Bonding Parametric Study

The significant bonding parameters along with a range of values for each parameter are summarized in Table 2. Each of the first three parameters — temperature, pressure, and time (at temperature and pressure) — may be varied over a fairly wide range while still achieving some degree of bonding. For this investigation, several levels were selected for each parameter. The Si_3N_4 slip was a slurry of Si_3N_4 powder with various magnesium oxide concentrations dispersed in a lacquer vehicle. This slurry was painted on the bond surface to act as a bonding agent.

Since over 700 experiments would have been required to evaluate all possible parametric combinations, a statistically designed study was initiated to minimize the number of experimental runs. A factorial experiment was made with the four parameters at two different levels as indicated in Table 2. Thus, only 16 experimental runs were required to evaluate the effect of each parameter on bond strength.

Table 2. Bonding Study Parameters Considered Important for Bonding Si_3N_4 Component Parts With Investigated Parameters Indicated

Bonding Study Parameters						
Temperature, °C	1550	**1600**	1650	1700	**1750**	1800
Pressure, p.s.i.	500	**1000**	1500	2000	**2500**	3000
Time, Hours	0.5	**1**	2	**3**	4	
Si_3N_4 Slip, %MgO	**No Slip**	1	**2**	5		

Initial experiments[4] on bonding reaction-sintered Si_3N_4 disks to hot-pressed Si_3N_4 disks yielded bonds with strengths greater than the strength of the reaction-sintered Si_3N_4 portion. The strength of the bond could not be evaluated since failure always occurred in the reaction-sintered region; therefore, the use of two hot-pressed Si_3N_4 disks was necessary.

Procedures. The studies involved the hot-press bonding of two theoretically dense Si_3N_4 disks as shown in Figure 17. Bonded samples were prepared at each of the various processing parameters as indicated in Table 2. Each bonded specimen was characterized with respect to microstructure and bond strength.

Room temperature flexural strength measurements were made to evaluate the bond strength. The strength measurements were conducted on test bars 1/8 × 1/8 × 1 1/4 inches long in 4-point loading. The top span was 0.375 inches and the bottom span was 1.125 inches. The cross-

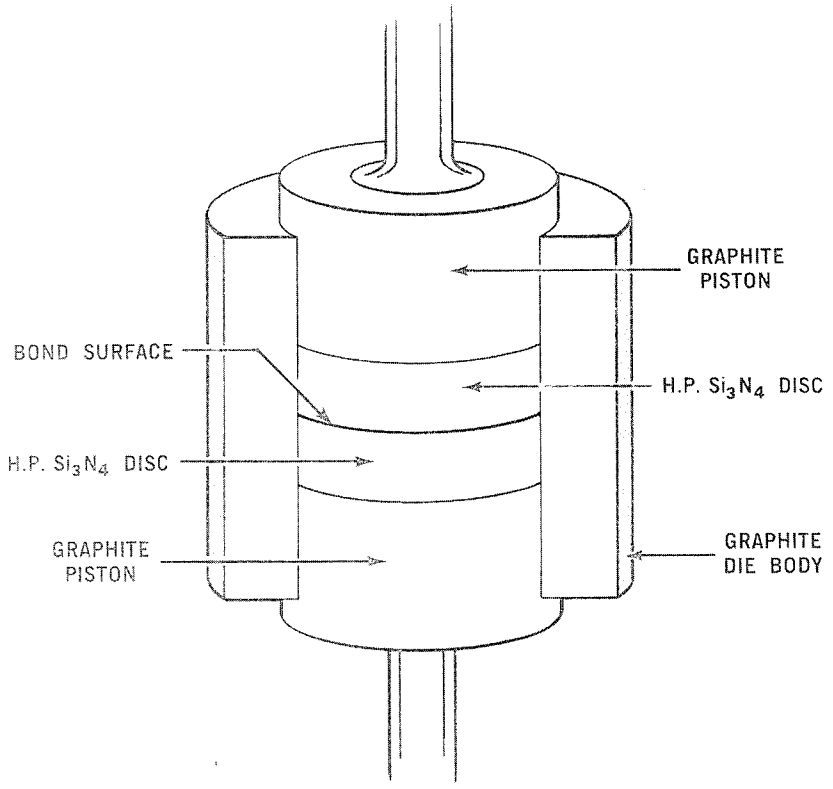


Figure 17. Hot-pressing system for bonding silicon nitride disks.

head speed on the Instron was 0.1 inches per minute. The test samples were positioned such that the point of maximum tensile stress occurred in the bond region.

Results. The flexural strength values as related to the processing parameters, summarized in Table 3, are averages of 10 values for each hot-press bonding condition. A first-order interaction factorial analysis of the data in Table 3 is summarized in Figure 18. For the first case, temperature is the main factor. The effect of the remaining three factors — pressure, time, and slip — cancel one another because all levels of each are present at both the upper and lower limits of temperature. This is also true for each remaining case where, in turn, pressure, time, and slip are main factors.

The results show that temperature was the most effective factor on bonding. A 74% increase in bond strength (from 30.4 to 52.9 ksi) was achieved by increasing the temperature 150°C (from 1600 to 1750°C). Similarly, a 37% (35.2 to 48.1 ksi) and 23% (37.4 to 46.0 ksi) increase in bond strength was exhibited by pressure and time, respectively. An 11% decrease in bond strength from 44.0 to 39.3 ksi resulted when a 2 wt% MgO-Si_3N_4 slip was used at the bond surface. It was anticipated that

Table 3. Summary of Flexural Strength Measurements of the Bond for Various Hot-Press Parameters

Hot-Press Run	Temperature (°C)	Pressure (psi)	Time (Hr.)	Slip (%MgO)	Flexural Strength (ksi) Average	Std. Dev.
HP-225	1600	1000	1	None	18.5	7.31
HP-250	1750	1000	1	None	31.9	5.91
HP-235	1600	2500	1	None	31.8	6.83
HP-241	1750	2500	1	None	58.0	7.97
HP-226	1600	1000	3	None	50.8	4.66
HP-229	1750	1000	3	None	54.4	6.76
HP-231	1600	2500	3	None	45.8	7.54
HP-240	1750	2500	3	None	61.0	6.21
HP-227	1600	1000	1	2	11.5	6.32
HP-230	1750	1000	1	2	48.7	4.22
HP-228	1600	2500	1	2	40.4	5.98
HP-255	1750	2500	1	2	58.4	7.50
HP-248	1600	1000	3	2	22.7	7.74
HP-252	1750	1000	3	2	43.4	8.12
HP-247	1600	2500	3	2	22.7	4.18
HP-253	1750	2500	3	2	67.6	2.17

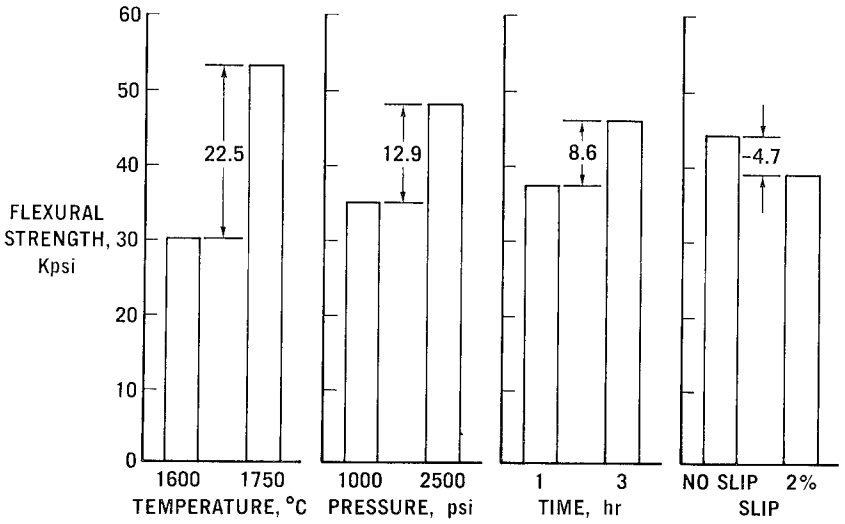


Figure 18. First-order interaction factorial analysis of bond strength parameters.

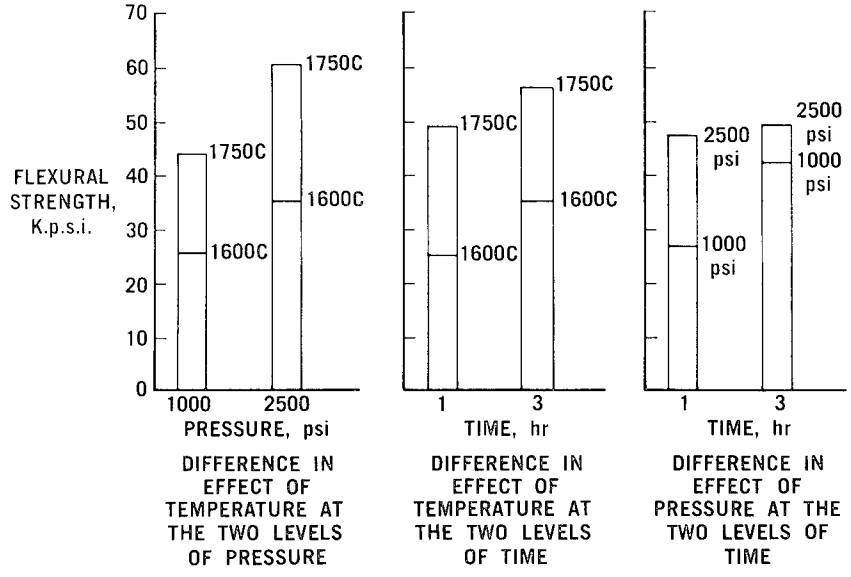


Figure 19. Second-order interaction factorial analysis of bond strength parameters.

slips with a MgO additive would enhance bonding and permit greater flexibility in the fabrication parameters without sacrificing bond integrity. However, the results indicate that the temperatures associated with the lower pressures were insufficient to densify the Si_3N_4 powder in the slip.

A second-order interaction factorial analysis of the data in Table 3 is illustrated in Figure 19. The first two cases represent the difference in effect of temperature at the two levels of pressure and time, respectively, and indicate that the temperature increase has about the same effect on bond strength at both levels of pressure and time. The third case represents the difference of pressure at the two levels of time, indicating that higher pressures are less effective on bond strength at longer processing times.

Figures 20 and 21 show typical microstructures (500 X) of the bond region for two hot-press bonded specimens having bond strengths of approximately 30 and 60 ksi, respectively. As expected, the degree of porosity at the bond surface was directly related to the bond strength of the samples. From these results, all visible traces of porosity must be eliminated when examined metallographically at 500 X to insure bond strengths adequate for turbine engine applications.

Fabrication of Duodensity Turbine Rotors

The fabrication of the integral duodensity turbine rotor involves developing hot-press bonding assemblies that enable the transfer of pressure to the component parts, which are the reaction-sintered blade ring and the fully dense hot-pressed hub.

Reaction-Sintered Blade Rings. The reaction-sintered Si_3N_4 blade ring component is produced by injection molding and a typical silicon metal blade ring is illustrated in Figure 2. A detailed description of the injection molding process is summarized in the previous section.

Si_3N_4 Powder for the Hot-Pressed Hub Components. The Si_3N_4 hub component was prepared by hot pressing alpha Si_3N_4 powder. The silicon nitride powder was manufactured by Advanced Materials Engineering (AME) in England and is designated high alpha grade. The phase identification, performed by X-ray diffraction, showed the silicon nitride powder to be approximately 85% alpha and 15% beta. Spectrographic analysis showed iron, calcium, and aluminum to be the major impurities at the 3000–7000 ppm level. The powder particle size was reported to be minus 100 mesh.

The Si_3N_4 powder was wet ball milled in rubber-lined mills with Coors AD-99 alumina oxide balls and tertiary-butyl alcohol for 168

Figure 20. Microstructure of bonded sample with a bond strength of 30,000 psi. 500 X.

Figure 21. Microstructure of bonded sample with a bond strength of 60,000 psi. 500 X.

hours. Magnesium oxide was added to the Si_3N_4 powder prior to milling in concentrations ranging from 2 to 5 wt%. Spectrographic analysis indicated alumina contamination of approximately one percent from the milling operation. The particle size of the comminuted Si_3N_4 powder was approximately 1–2 microns.

Hot-Press Bonding Fabrication Techniques. To form an integral turbine rotor, the reaction-sintered Si_3N_4 blade ring is bonded to the theoretically dense Si_3N_4 hub and is accomplished by hot-pressing techniques. Figure 22 illustrates the hot-pressing facility at Ford Motor Company. The temperature capability of equipment is in excess of 2000°C. The hydraulic rams are rated at 100 tons and pressure can be applied from both the top and bottom positions.

Development of hot-press bonding techniques have led to the design of a graphite system illustrated in Figure 23. To restrain the blade ring during the hot-pressing operation, force is applied to the blade ring periphery through the graphite wedge components. A compression rig was designed to apply pressure to the hub component independent of the graphite wedge assembly. The compression rig is illustrated in Figure 24. The large stainless steel plate transmits pressure from the top hydraulic ram of the press to the outside cooling ram which connects to the outside graphite wedge assembly. The smaller hydraulic piston exerts pressure on the center cooling ram which transmits pressure to the hub component. The force to each component (the blade ring periphery and the hub component) can be individually monitored and controlled.

Early experiments demonstrated that a restraint system was necessary to reinforce the blade ring, otherwise, deformation and tearing of the rim (as shown in Figure 25) was experienced. After evaluating several reinforcement systems, a blade-fill technique utilizing slip-cast Si_3N_4 was chosen. This system, when subjected to the high hot-pressing temperatures, prevents blade tearing because expansion mismatches have been eliminated between the blade-fill material and the blade ring. The sequence of the blade-fill preparation is shown in Figures 26, 27, and 28. The Si_3N_4 blade ring is first coated with boron nitride as shown in Figure 26. This is necessary to prevent bonding of the blade fill to the blade ring, and eases the removal of the fill after hot-press bonding. The blade cavities are filled next with a silicon metal slip. The slip cast inserts must be completely independent of one another as indicated in Figure 27. The blade ring is again coated with boron nitride and a second application of slip-cast silicon metal is made to completely encase the silicon nitride blade ring. The entire assembly is nitrided by using a standard nitriding cycle to convert the silicon metal fill material to silicon nitride. The second fill encasement also prevents reaction of the Si_3N_4 blades with the

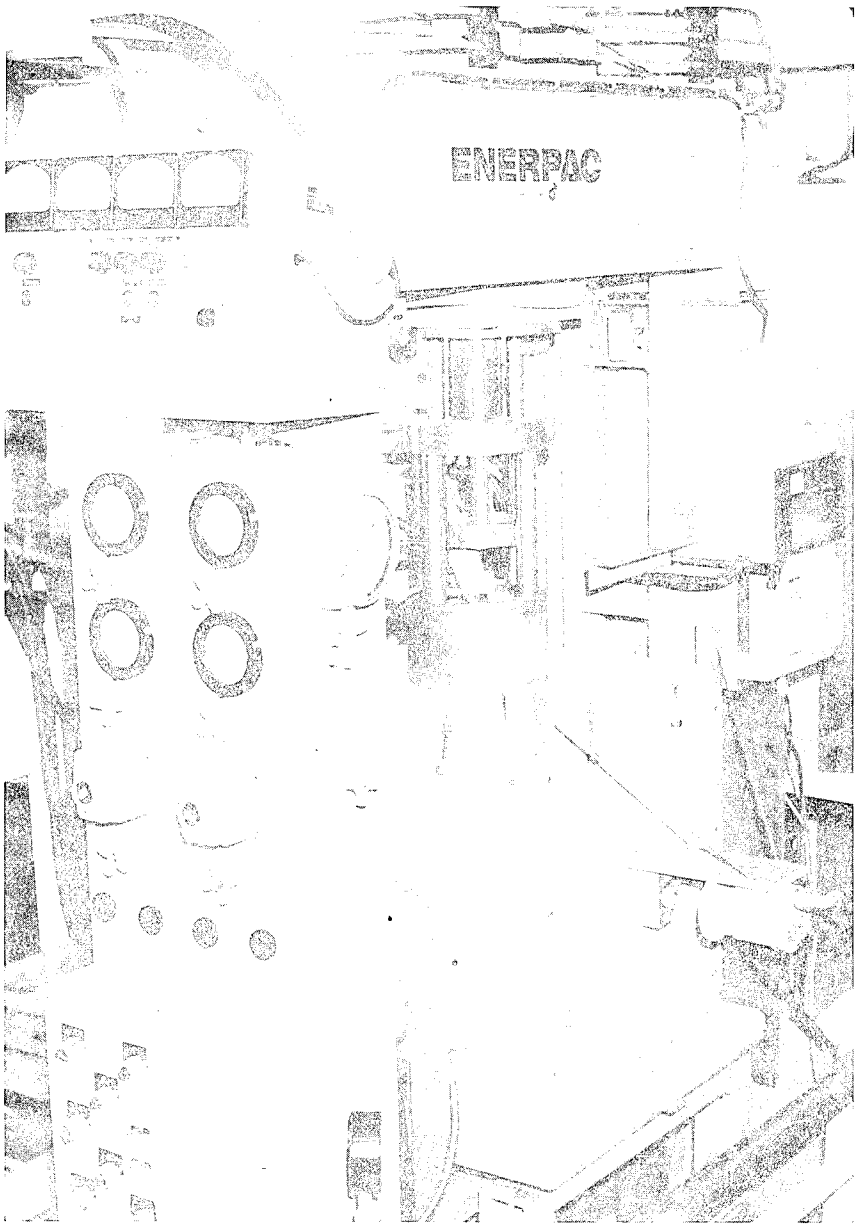


Figure 22. Hot-pressing facility at Ford Motor Company.

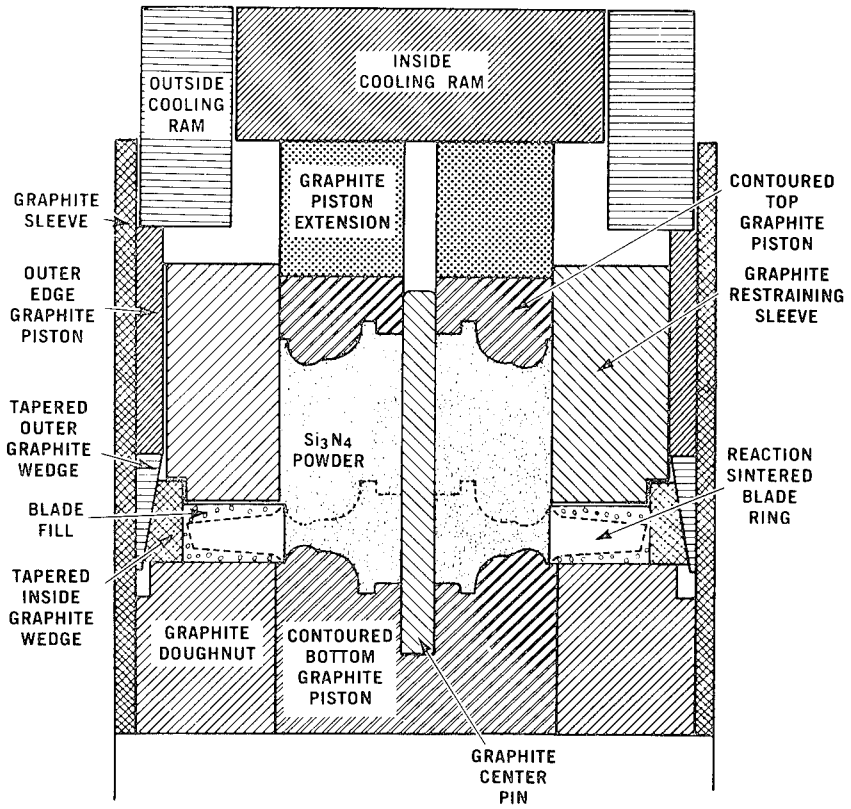


Figure 23. Hot-press bonding assembly for simultaneously forming and bonding a silicon nitride rotor hub to a blade ring.

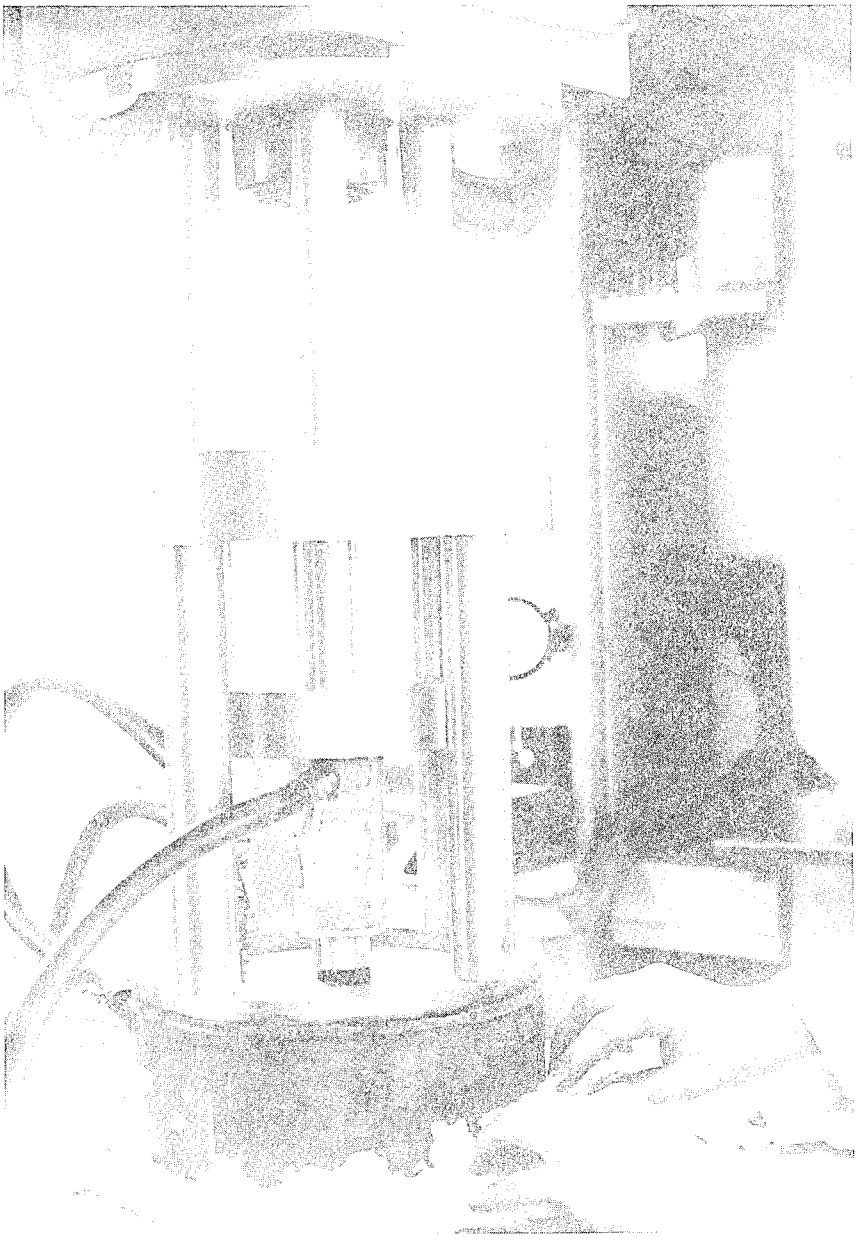


Figure 24. Compression rig for applying and monitoring two independent pressures.

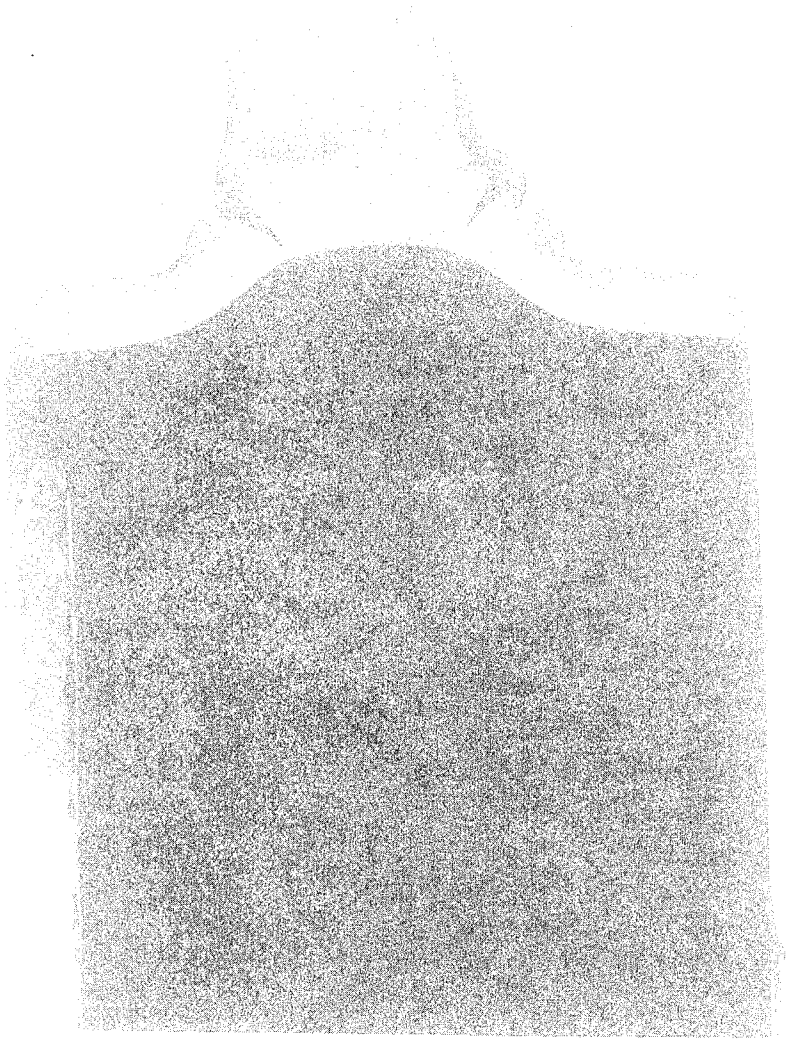


Figure 25. Deformation of reaction-sintered Si_3N_4 blade ring when not reinforced.

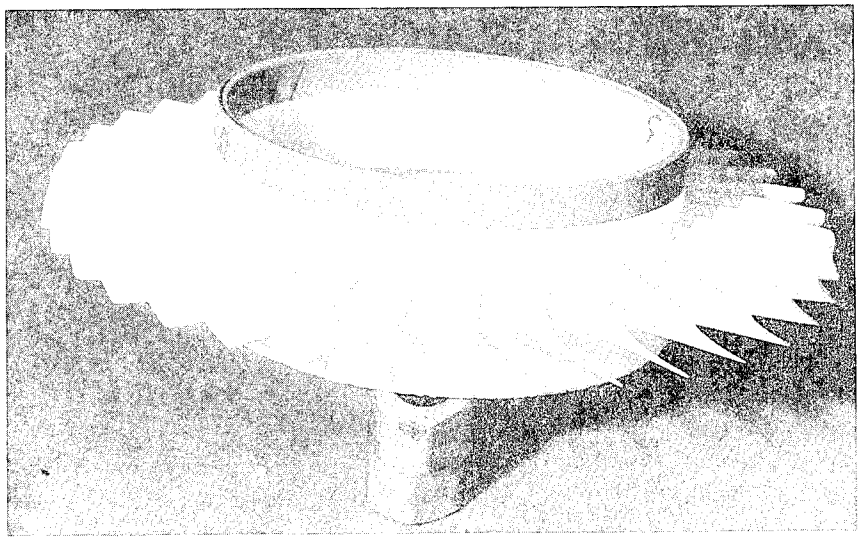


Figure 26. Reaction-sintered Si_3N_4 blade ring showing boron nitride coating.

carbonaceous atmosphere encountered during the hot-press bonding operation. If unprotected, this reaction would degrade the blade ring by forming SiC. An encased blade ring with a hot-pressed Si_3N_4 hub is shown in Figure 28. Once the blade ring has been completely encased for reinforcement, it is assembled in the graphite system for hot-press bonding as shown in Figure 29.

Early attempts at bonding the blade ring and hub involved first hot pressing the contoured hub to theoretical density followed by hot-press bonding the contoured hub and blade ring together. The inside diameter of the blade ring and the outside diameter of the dense Si_3N_4 contoured hub were machined to within 0.001 of an inch and fitted into the graphite assembly. The two component parts were hot-pressed bonded at 1750°C and 2500 psi for 2 hours. Although excellent bonding was produced near the blade centerline axis, bonding at the outer extremities of the rim was poor. This was a result of insufficient pressure at these extremities and was caused by the geometry of the contoured graphite piston in this region. Slight convex bowing of the blade rim was also observed due to the higher concentration of pressure at the blade centerline axis. Cracking of the blade ring rim was frequently observed because of misalignment problems of the blade ring and preformed hub during hot-press bonding.

A substantial improvement in the hot-press bonding fabrication process was made by hot pressing the Si_3N_4 powder directly to the blade



Figure 27. Reaction-sintered Si_3N_4 blade ring with first blade-fill material.

ring. The rig for this fabrication technique is illustrated in Figure 23 and, as shown, only the encased blade ring needs to be fitted in the graphite wedge assembly. A predetermined amount of processed Si_3N_4 powder, with a MgO additive, was placed in the hub cavity and hot pressed to theoretical density while simultaneously bonding to the Si_3N_4 blade ring. Final densification of the Si_3N_4 powder is indicated by the dashed outline. To insure complete densification and bonding, fabrication is accomplished at 1750°C and 2500 psi for 3 hours. This technique eliminates many misalignment problems and related blade-rim cracking problems previously encountered with the preformed hub. In addition, only one hot-pressing operation is required whereas the former technique required two independent hot-pressing operations. After hot-press bond-

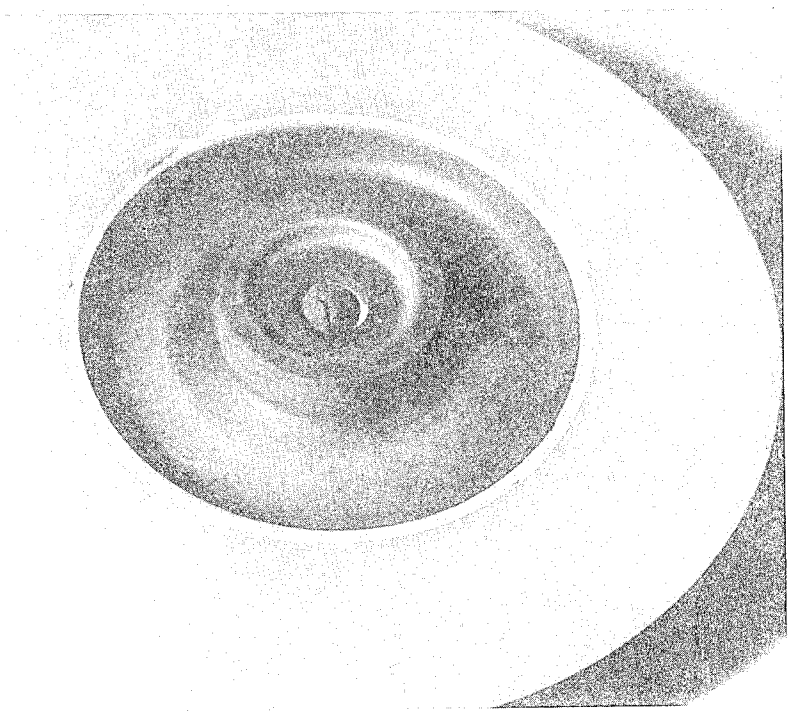


Figure 28. Reaction-sintered Si_3N_4 blade ring with second blade-fill material.

ing, the second and first blade-fill materials are removed and the fabricated trubine rotor is cleaned by vapor blasting.

A hot-press bonded duodensity turbine rotor fabricated by this technique is shown in Figure 30. The hub portion is hot pressed to the design contour and surface finish; therefore, no profile machining is required. However, machining of the bore and curvic teeth (not shown) are necessary to facilitate connection of the ceramic turbine rotor to a metal shaft. The convex bowing of the blade rim previously encountered has been eliminated, as shown in Figure 31, when Si_3N_4 powder rather than a preformed hub is used.

Bonding between the reaction-sintered blade ring and hot-pressed hub is considered excellent, as evidenced by the microstructure in Figure 32 (500 X). Migration of the magnesium densification aid across the bond surface is required to produce a bond and is directly related to the magnesium oxide concentration in the Si_3N_4 powder. Magnesium migration during hot-press bonding was substantial for the 5 wt% MgO-Si_3N_4 powder compositions which caused densification and deformation of the

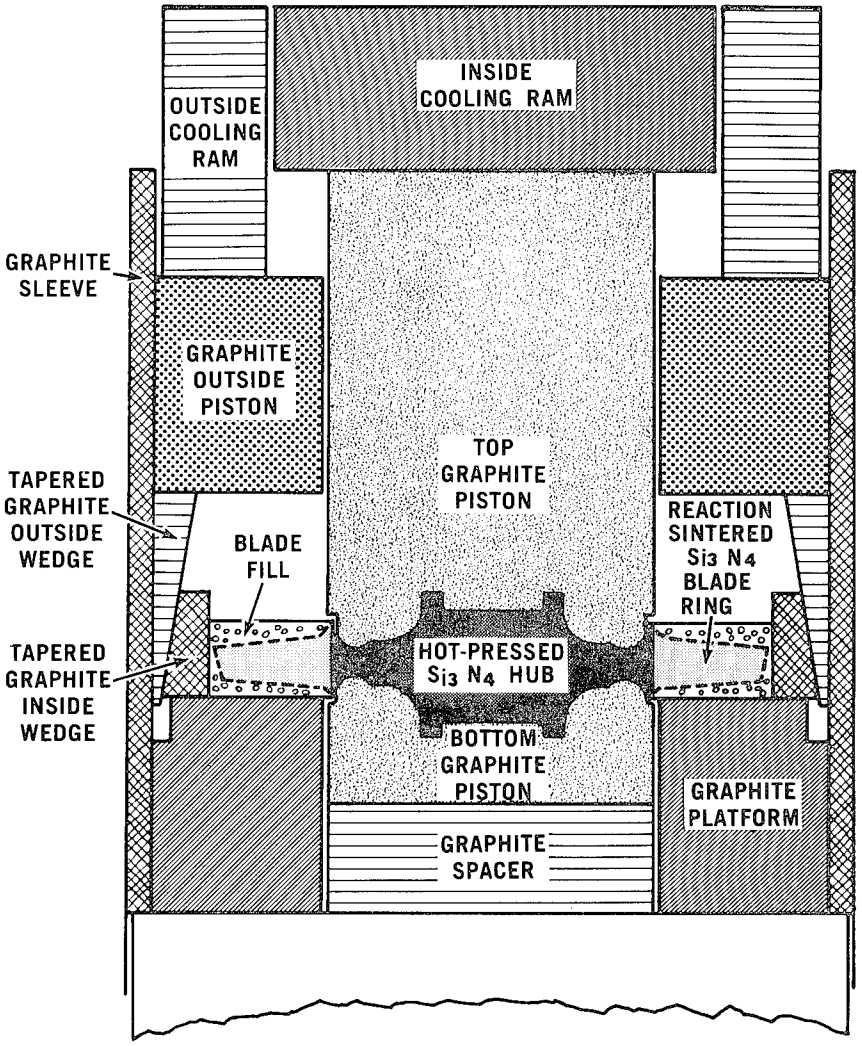


Figure 29. Hot-press bonding assembly for reaction-sintered blade ring and preformed hub.

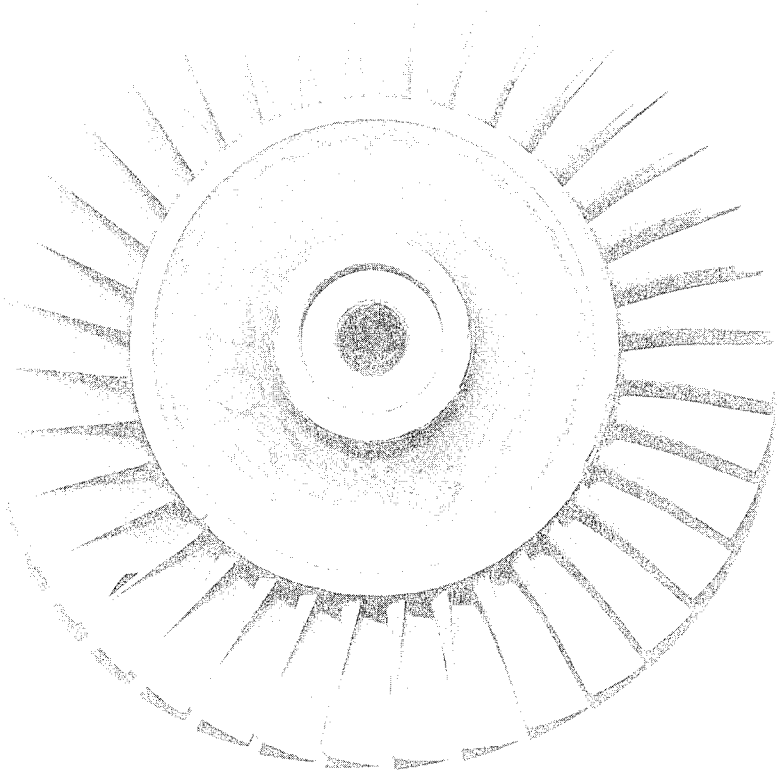


Figure 30. Hot-press bonded, duodensity Si_3N_4 turbine rotor.

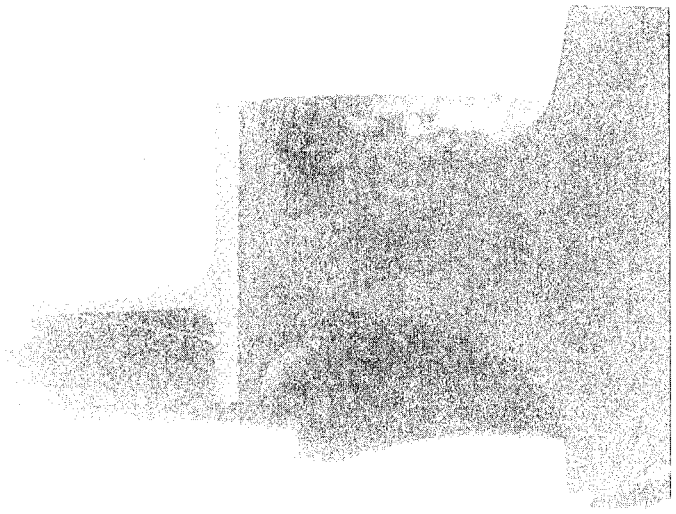


Figure 31. Sectioned hot-press bonded, duodensity Si_3N_4 turbine rotor.

rim of the blade ring. The migration of the magnesium was reduced considerably with a 2 wt% MgO-Si_3N_4 powder composition. Correspondingly, both densification and deformation of the reaction-sintered rim were reduced without sacrificing bond quality as established by microstructural examination. Although the degree of bonding appears to be independent of the MgO concentration in the 2–5 wt% range, close control of the amount of the MgO additive is required to prevent the densification and deformation of the blade ring rim.

Spin testing[14] provides a method of evaluating ceramic turbine rotors to establish their maximum room temperature strength. It also provides a means of qualifying turbine rotors for subsequent engine testing. Hot-press bonded, duodensity, Si_3N_4 turbine rotors tested in the spin pit have exceeded 54,000 rpm before a blade failure occurred. Failure of the turbine rotor is detected electrically and photographed to record the failure mode. The duodensity turbine rotors tested to date are of a previous design, and the failure speed when corrected for the present design turbine rotor corresponds to an equivalent failure speed of approximately 70,000 rpm. This speed exceeds the maximum engine speed by approximately 9 percent. All spin-test failures to date have been related to either a blade failure or failure of the spin-test support spindle. Failure at the bond interface during spin testing has not been observed. These results coupled with the microstructural examination of

bonded rotors indicates an adequate bond can be achieved to meet the program objectives.

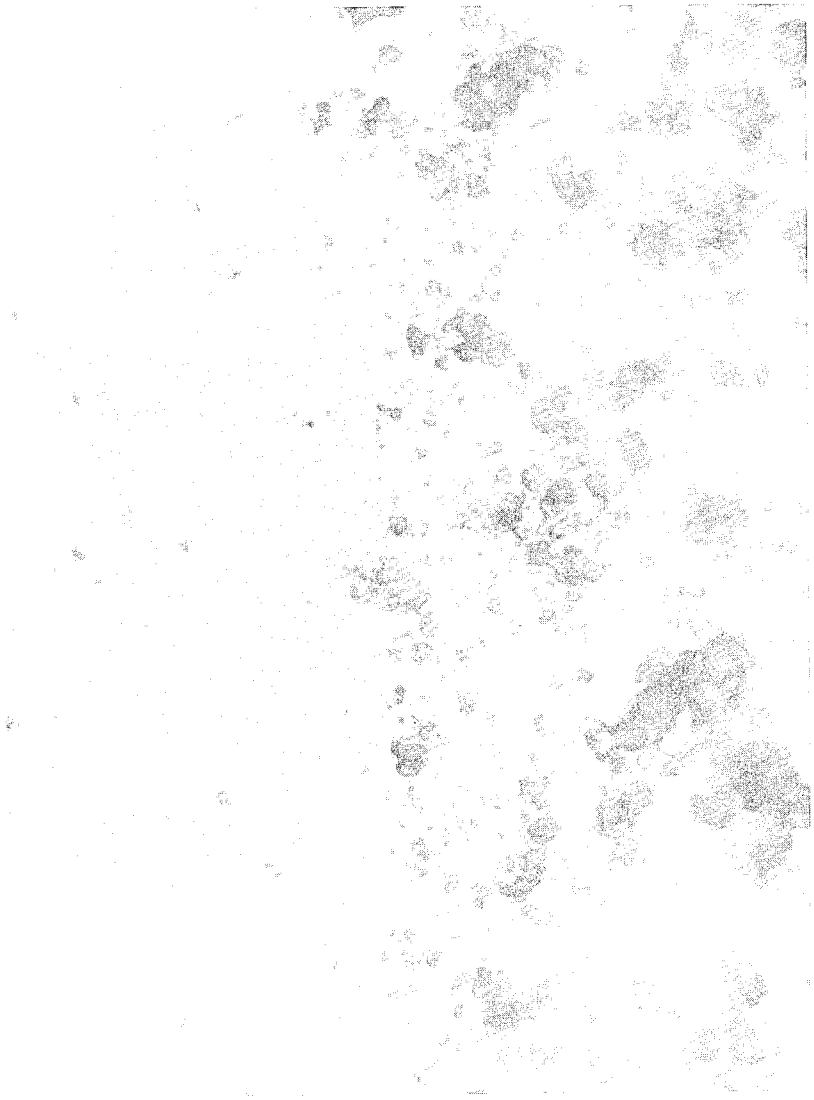


Figure 32. Microstructure of bond interface between hot-pressed Si_3N_4 rotor hub and reaction-sintered Si_3N_4 blade ring. 500 X.

CONCLUSIONS

Processing methods have been developed for bonding both reaction-sintered and hot-pressed Si_3N_4 components for turbine engine applications.

Slip-cast bonding can be used successfully to bond reaction-sintered silicon nitride units into a homogeneous component. The inverted channel stator and the tridensity rotor are illustrative of the turbine engine components that have been manufactured using SC bonding. The conclusions drawn from this portion of the investigation are:

1. The controlling parameters for SC bonding are closely related to the fundamentals of metal-powder slip casting. These parameters include the properties of the metal powder, the properties of the liquid media, and the rheological properties of the slip.
2. Chemical control of the silicon metal slip is used to produce a bond joint of a desired density.
3. Green shrinkage, if not minimized, will produce bond "pull away" and bond cracking. Silicon metal castings experience minimum green shrinkage when slips are adjusted to pH levels that produce minimum viscosity.
4. High-fluidity slips are needed for SC bonding applications and can be produced by using slip dilution techniques.
5. All joining operations are conducted only on silicon metal structures that have been argon sintered, but are not yet nitrided.
6. To achieve joints of high integrity, the bonding cavity must be designed to avoid premature bridging and gas entrapment.
7. Slip-cast bonding, when controlled properly, is capable of producing high-quality joints.

Fabrication techniques were developed which enabled a contoured Si_3N_4 hub to be simultaneously hot pressed to theoretical density and bonded to a reaction-sintered blade ring to form an integral, duodensity turbine rotor. Several conclusions of this investigation are summarized below:

1. A parametric hot-press bonding study indicated temperature is the most effective parameter for bonding Si_3N_4 components together.
2. Migration of magnesium across the bond interface is essential for bonding a hot-pressed hub and reaction-sintered blade ring. The quantity of magnesium migration is critical to prevent deformation of the blade ring rim and yet achieve good bonding.
3. The development of a slip-cast Si_3N_4 restraint system for the blade ring periphery was achieved which prevented deformation and tearing of the blade ring rim during hot-press bonding.

ACKNOWLEDGMENTS

The author's wish to acknowledge G. J. Chaundy, W. B Copple, J. M. Nicholson, L. V. Reatherford, J. R. Secord, and E. A. Fisher for their assistance and ideas throughout this project; and Ms. L. Tracy for her efforts in preparing the manuscript. This work was partially supported by the Advanced Research Projects Agency, and the Army Materials and Mechanics Research Center under contract No. DAAG-46-71-C-0162.

REFERENCES

1. Fisher, E. A., "Technical Ceramic Fabrication Processes," ASME publication, 75-GT-110 (March 1975).
2. Caws, R. B., Graham, R. P., and Stoddart, D. E., "Silicon Nitride Materials for Gas Turbine Components," ASME publication, 73-GT-47 (April 1973).
3. McLean, A. F., Fisher, E. A., Bratton, R. J., and Miller, D. G., "Brittle Materials Design, High Temperature Gas Turbine," Interim Report, July 1, 1974 — December 31, 1974, Ford Motor Company, Dearborn, Michigan, Army Materials and Mechanics Research Center, Contract Report No. AMMRC CRT 75-8 (March 1975).
4. McLean, A. F., Fisher, E. A., and Bratton, R. J., "Brittle Materials Design, High Temperature Gas Turbine," Interim Report, January 1, 1974 — June 30, 1974, Ford Motor Company, Dearborn, Michigan, Army Materials and Mechanics Research Center, Contract Report No. AMMRC CTR 74-59 (September 1974).
5. Ezis, A., "The Fabrication and Properties of Slip-Cast Silicon Nitride," in *Ceramics for High Performance Applications*, Burke, J. J., Gorum, A. E., and Katz, R. N., eds., Chestnut Hill, Mass.: Brook Hill Publishing Company (1974), 207–22.
6. Kingery, W. D., *Ceramic Fabrication Processes*, Cambridge, Mass.: The M.I.T. Press (1958).
7. Hausner, H. H., and Poster, A. R., "Slip Casting of Metal Powders and Metal-Ceramic Combinations," in *Powder Metallurgy*, Leszynski, W., ed., New York: Interscience Publishers, Inc. (1961), 461–506.
8. Hausner, H. H., "Slip Casting of Metal Powders," in *Consolidation of Metal Powders*, Vol. 1, Hausner, H. H., Roll, K. H., and Johnson, P. K., eds., New York: Plenum Press (1967), 221–38.
9. St. Pierre, P. D. S., "Slip Casting Metals," General Electric Corporate Research and Development, Schenectady, New York, Report No. 59-Rl-2281M (October 1959).
10. Overbeek, J. T. G., *Colloid Science, Vol. 1, Irreversible Systems*, Krieyt, H. R., ed., New York: Elsevier Publishing Company (1952).

11. Dobrovol'skii, A. G., and Dem'yanchuk, V. G., "Production of Molybdenum Parts by Slip Casting," *Poroshkovaya Metallurgiya*, No. 8(56) (August 1967), 1–6.
12. Dobrovol'skii, A. G., and Nazarchuk, N. V., "Slip Casting of Molybdenum Disilicide," *Poroshkovaya Metallurgiya*, No. 5 (May 1966), 1–8.
13. U.S. Patent No. 3,887.441, June 3, 1975. "Making a Triple Density Article of Silicon Nitride," Goodyear, M. U., Ezis, A., and Styhr, K. H., to Ford Motor Company.
14. Styhr, K. N., "Spin Testing of Ceramic Turbine Rotors," in *Ceramics for High Performance Applications*, Burke, J. J., Gorum, A. E., and Katz, R. N., eds., Chestnut Hill, Mass.: Brook Hill Publishing Company (1974), 415–24.

6. SYSTEMS FOR UNITING REFRACTORY MATERIALS

J. E. KELLEY, D. H. SUMNER, and H. J. KELLY
Albany Metallurgy Research Center, U.S.D.I.
Albany, Oregon

A study to determine the feasibility of joining refractory hard metals to each other and to oxide ceramics by a vacuum hot press-diffusion bonding method is presented. Very satisfactory joins were made in the systems ZrC–ZrB_2, ZrN–ZrB_2, ZrC–ZrN, and ZrC, ZrN, ZrB_2-Al_2O_3. Each of these join assemblies contained a mixture layer, 50 wt% each of the two end compounds. The mixture layer, sandwiched between each end compound, enhanced bonding and smoothed out the thermal expansion gradient between the two end members. Joins of ZrO_2 to ZrC, ZrB_2, and ZrN also were made, but five intermediate grading layers were required to prevent destructive cracking of the ZrO_2 portions.

Strength and thermal shock tests showed the join areas of the ZrC, ZrN, ZrB_2 joins to be stronger and more shock resistant than the parent materials. These tests were not made on the oxide joins because of the brittle nature of the oxide portions of the joined assemblies.

Also included in the joining tests was one each of TiC–TiB_2, TiC–TiN, TiB_2–TiN, and TiC–ZrB_2 joins. Each of these were well bonded, showing that the vacuum hot-press method can be used for a variety of systems.

INTRODUCTION

This report describes a Bureau of Mines' program to study methods of joining dissimilar refractory materials. The purpose of the program is to investigate fabrication methods and bonding mechanisms for making graded joints of refractory metal carbides, borides, nitrides, and oxides with each other and with refractory metals. This is in anticipation of the need for more refractory electron-tube envelopes, and for monolithic refractory shapes that would be serviceable in two different environments.

Thus, hardware that requires a dual composition of oxidation-resistant materials in one portion and capacity to withstand a reducing environment in another portion could be easily fabricated.

The work described in this report includes joining studies on ZrC, ZrN, ZrB_2, and ZrO_2 and an evaluation of the properties of these materials and the graded joints resulting from their union.

Fabrication of graded joints was accomplished by vacuum hot pressing preformed cylinders of the materials together with a wafer between which contained a 50-50 weight percent mixture of these materials. Porembka[1] showed that metals and ceramics could be bonded by this method whereby the thermal expansion gradient between the two materials was smoothed out at the joint by the graded composition. Zimmer[2] also describes the compositional grading process for joining dissimilar metals which have greatly differing thermal expansions. Diffusion bonding of carbides to refractory metals by hot pressing butt joints has been investigated by Burykina and Evtushenko.[3] By taking advantage of diffusion-bonding effects and compositional grading, we have successfully fabricated satisfactory graded joints between ZrC, ZrN, and ZrB_2. The works of Porembka and Zimmer include graded joining of dissimilar metals and metals to ceramics, whereas our work adds a different class of materials, namely, the refractory hard metals. These studies, together with the work of Burykina and Evtushenko on diffusion welding of refractory carbides to refractory metals, provide important insight into the problems of joining the major classes of high-temperature materials.

CHARACTER OF MATERIALS AND PRODUCTS

Starting Materials

It has been noted that the compositions and properties of most of the refractory hard metals vary greatly from one source to another. Therefore, it was felt desirable to carefully characterize the materials in this work. (ZrC and ZrB_2 were purchased from the Hermann Starck Company. ZrN was purchased from Cerac, Inc. The ZrO_2 was prepared in this laboratory.)

Analyses. *Spectrographic And Gaseous Impurities.* An impurity analysis was made to determine the metallic and gaseous impurities. Results of the analysis are shown in Table 1. Some of the metallic impurity levels are shown as a range of values.

Compound Identification. An X-ray diffraction examination made on ZrC and ZrB_2 showed only ZrC and ZrB_2 present. The primary con-

Table 1. Impurity Analysis of Materials, Percent

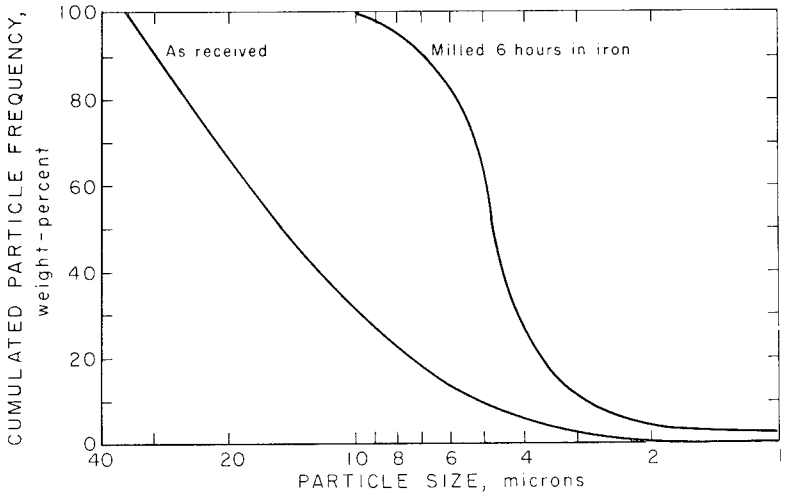
	ZrN[1]	ZrC[2]	ZrB_2[3]	ZrO_2[4]
Al	0.06	—	—	0.001–0.01
B	0.005	0.3–3	—	—
Ca	0.001	—	—	—
Co	0.004	—	0.1–1	—
Cr	0.03	0.01–0.1	0.03–0.3	—
Cu	0.006	0.00003–0.0003	—	—
Fe	0.2	0.003–0.03	0.14	0.1–1
Hf	0.03–0.3	—	—	—
Mn	0.002	—	—	0.03–0.3
Mo	0.1	0.01–0.1	—	—
Ni	0.05	—	0.01–0.1	—
Pb	0.001	—	—	—
Si	0.02	0.001–0.01	0.003–0.03	0.1–1
Ti	0.03	0.01–0.1	0.11	0.0003–0.003
V	0.03	—	—	—
W	0.02	—	0.57	—
Y	—	—	—	1–10
Zn	0.005	—	—	—
C	1.35	—	0.13	142 ppm
O	0.82	0.58	0.85	26.2
N	—	0.89	0.11	<10 ppm

[1]Milled 2 hours in WC mill.
[2]Milled 6 hours in iron mill, leached.
[3]Milled 4 hours in WC mill.
[4]As received.

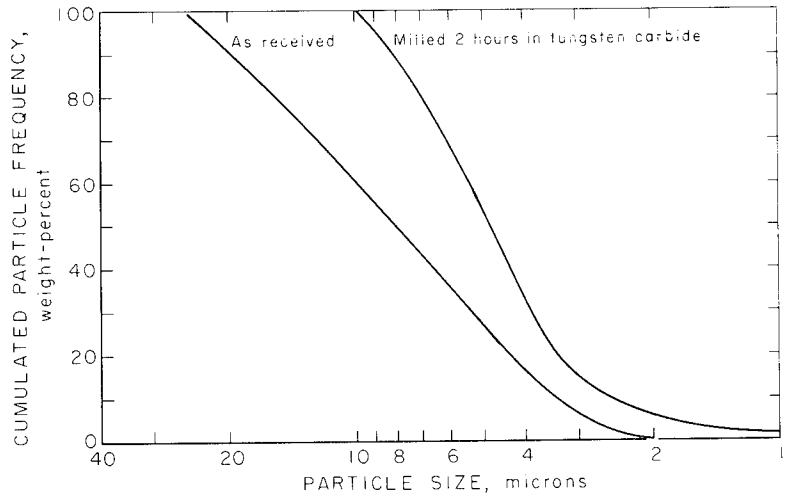
stituent for ZrN was ZrN with monoclinic ZrO_2 reported as a barely detectable trace. The only constituent found for $(ZrO_2)_{0.9} \cdot (Y_2O_3)_{0.1}$ was cubic ZrO_2 solid solution.

Particle-Size Distribution. Because it was necessary to reduce the particle size of the commercial powders, particle-size analyses before and after milling were made. Thus, in subsequent grinding operations the particle-size distribution can be reproduced to insure similarity in all products. The ZrC was milled 6 hours in an iron vibratory mill, then leached in 4N HCl to remove the iron contamination.

Maximum particle size of the ZrC powder was reduced from 35 microns to 10 microns. A reduction in maximum particle size of the ZrB_2 powder from 45 microns to 15 microns was achieved by milling for 4 hours in a tungsten-carbide lined vibratory mill. A comparable reduction in particle size in the ZrN powder, from 25 to 10 microns resulted from

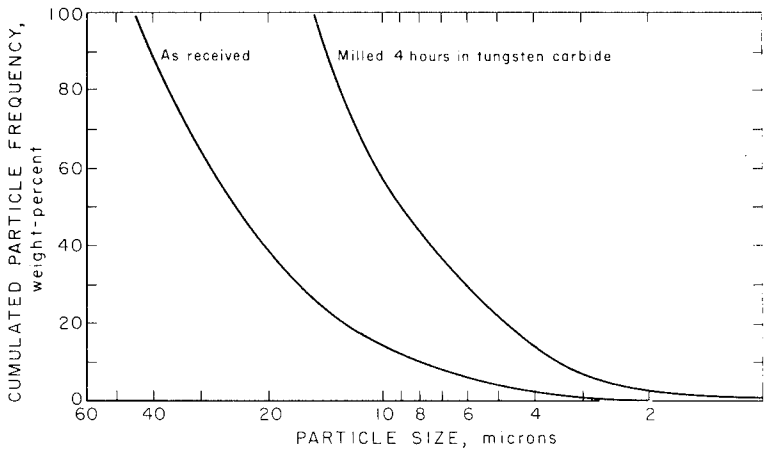


(a)

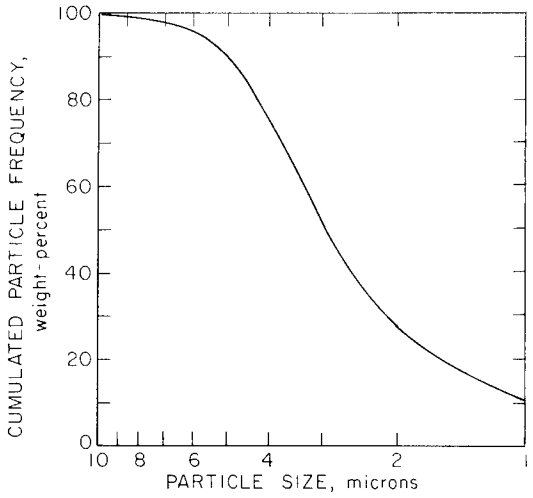


(b)

Figure 1. Particle-size distribution: (a) ZrC, (b) ZrN, (c) ZrB_2, (d) $(ZrO_2)_{0.9} \cdot (Y_2O_3)_{0.1}$.



(c)



(d)

Figure 1. (Continued)

a 2-hour grind in the tungsten carbide mill. Figures 1(a), (b), (c) show particle-size distribution for ZrC, ZrN, and ZrB_2 before and after milling. Figure 1(d) shows particle size distribution for $(ZrO_2)_{0.9} \cdot (Y_2O_3)_{0.1}$.

Pycnometric Density. Densities of the as-received ZrC, ZrN, ZrB_2, and ZrO_2 powders were determined on a Beckman Model 930 air comparison pycnometer. Helium rather than air was used for ZrC because of the pyrophoric nature of finely divided ZrC. The density values for the powders are as follows:

ZrC - 6.46 ± 0.02 gm/cm^3
ZrN - 7.15 ± 0.02
ZrB_2 - 6.09 ± 0.02
ZrO_2 - 5.77 ± 0.02

In this report, all density values which are expressed in percent of theoretical are relative to these pycnometric densities.

Vacuum Hot-Pressed Products

Physical and Mechanical Properties. *Density*. Bulk density measurements were made on specimens of ZrC, ZrN, and ZrB_2 which had been vacuum hot pressed at 2100°C and 4000 psi. Each specimen was carefully measured and weighed after sectioning into a cubical shape on a diamond thin-sectioning machine. The bulk density and percent of theoretical density values are as follows:

ZrC - 6.33 ± 0.01 gm/cm^3 = 97.9 percent of theoretical
ZrN - 6.57 ± 0.01 gm/cm^3 = 91.9 percent of theoretical
ZrB_2 - 6.03 ± 0.02 gm/cm^3 = 99.0 percent of theoretical
ZrO_2 - not determined

Thermal Expansion. One very important property influencing the success of any joining operation is thermal expansion. Coefficients of thermal expansion were therefore measured for vacuum hot-pressed ZrC, ZrN, ZrB_2, ZrC • ZrN, ZrC • ZrB_2 and ZrB_2 • ZrN. (ZrC • ZrN represents 50 wt% ZrC + 50 wt% ZrN.) No measurements were made on ZrO_2 because of specimen fabrication difficulties. The thermal expansion measurements were made by observation of the relative displacement of the ends of the specimens as they were heated in a graphite resistance tube furnace. Observation and measurements of thermal expansion were made with two tandem mounted telescopes fitted with filar micrometer eyepieces.

This assembly can detect displacements as small as ± 0.00002 inches at a focal distance of 22 inches. However, experimental reproducibility was within ± 0.0005 inch on a 3-inch specimen. The furnace is

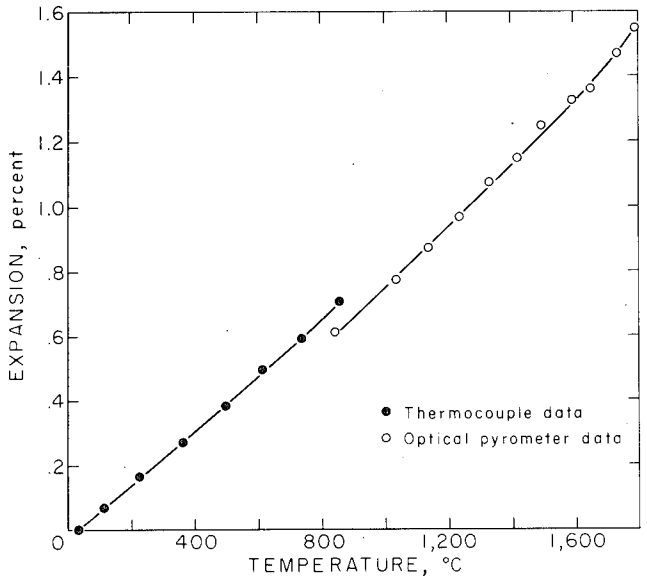
very similar to the apparatus described by Miccioli and Shaffer.[4] Because of limitations in measuring temperature with a thermocouple, the thermal expansion tests were done in two steps. First, from room temperature to about 800°C, the temperature was sensed with a Pt versus Pt 10 Rh thermocouple; from 800°C up an optical pyrometer was used. Expansion versus temperature curves are shown in Figures 2(a) through 2(f). Data from these curves were analyzed on an IBM 1410 computer for best fit and the results yielded the coefficients of thermal expansion, shown in Table 2.

Thermal Shock Resistance. Thermal shock tests were made on disc-shaped specimens of vacuum hot-pressed ZrC, ZrB_2, ZrN, ZrC • ZrN, ZrB_2 • ZrN, and ZrC • ZrB_2. The specimens, 1/2-inch diameter and 1/16-inch thick, were sawed from hot-pressed cylinders using a diamond thin-sectioning machine. Each disc was alternately heated and cooled in an R. F. furnace until visible cracks occurred. Each of these thermal cycles consisted of a 20-second heat-up to 1400°C and a 20-second cool-down to 600°C. For determinations of relative thermal shock resistance, the number of thermal cycles to failure was recorded. Although the results were not considered to be quantitative, a definite pattern of thermal shock resistance was determined. ZrB_2 was the most resistant to shock, followed in order of decreasing resistance by ZrC, ZrB_2 • ZrN, ZrB_2 • ZrC, ZrN, and ZrN • ZrC. The average number of thermal cycles to failure for each material is shown in Table 3.

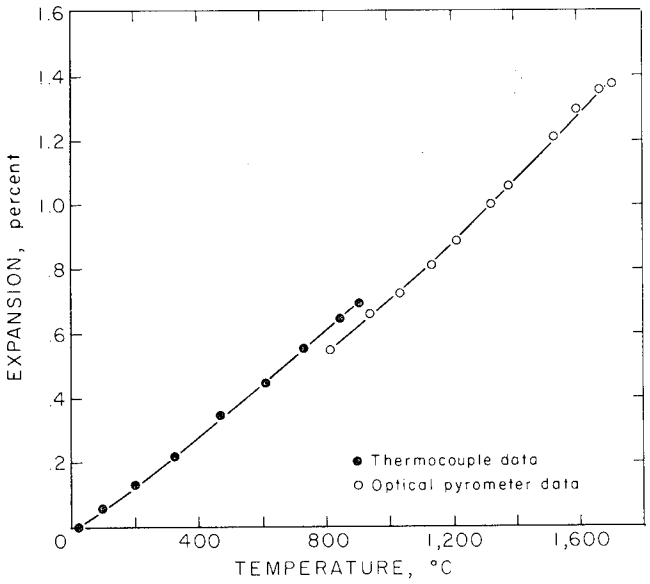
Table 2. Average Thermal Expansion Coefficients

Material	Temperature range, °C	α, × 10^{-6}/°C[1]
ZrB_2	20–911	7.683 ± 0.022
ZrB_2	818–1718	9.492 ± 0.032
ZrN	23–916	8.395 ± 0.017
ZrN	840–1796	9.715 ± 0.032
ZrC	23–931	7.164 ± 0.052
ZrC	862–1770	9.417 ± 0.047
ZrC • ZrN	23–927	7.504 ± 0.018
ZrC • ZrN	734–1727	9.706 ± 0.030
ZrC • ZrB_2	23–949	7.359 ± 0.024
ZrC • ZrB_2	855–1808	9.525 ± 0.034
ZrB_2 • ZrN	23–919	8.006 ± 0.052
ZrB_2 • ZrN	837–1793	10.579 ± 0.033

[1] α = average coefficient of thermal expansion.

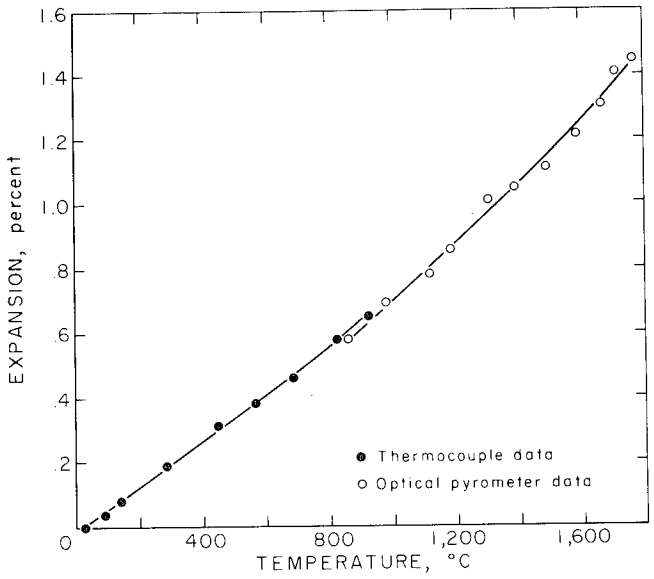


(a)

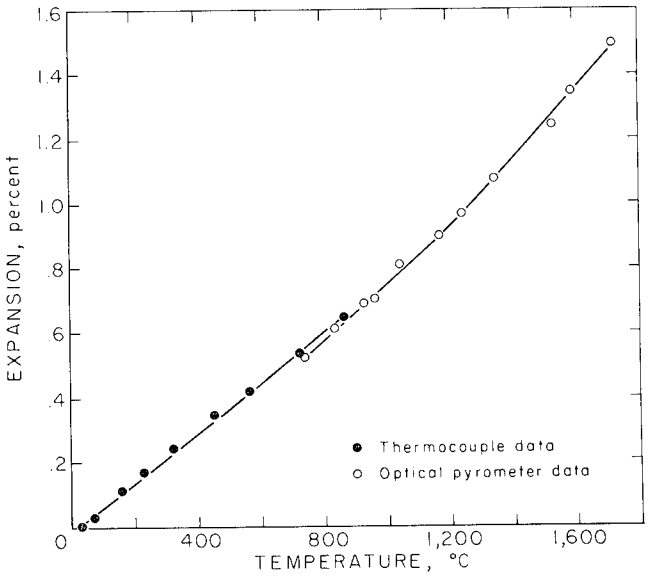


(b)

Figure 2. Thermal expansion curve for: (a) ZrN, (b) ZrB_2, (c) ZrC, (d) ZrC • ZrN, (e) ZrC • ZrB_2, (f) ZrB_2 • ZrN.

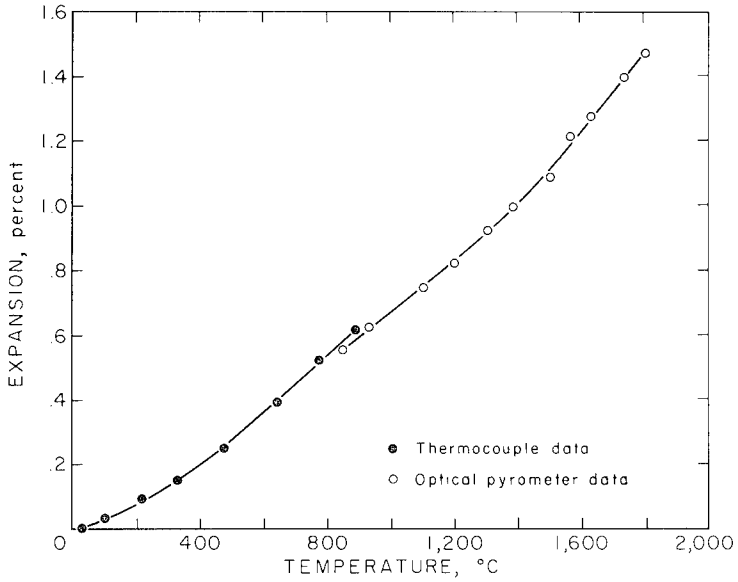


(c)

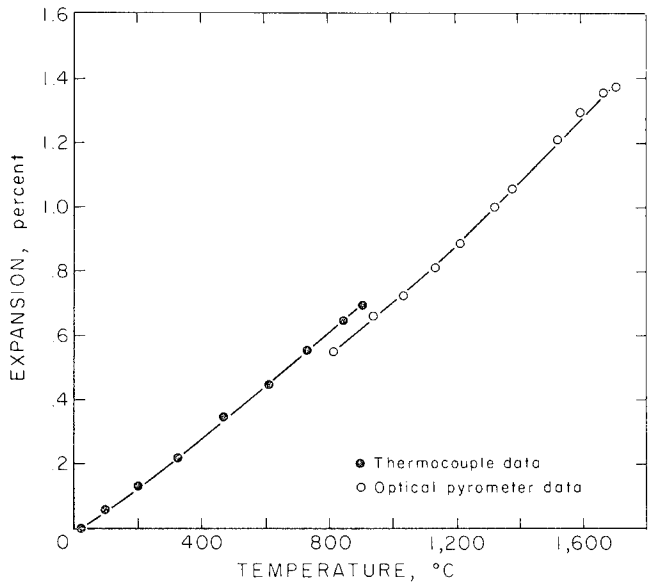


(d)

Figure 2. (Continued)



(e)



(f)

Figure 2. (Continued)

Table 3. Thermal Shock Data

Material	Average number of thermal cycles to failure
ZrB_2	109
ZrC	102
ZrB_2 • ZrN	94
ZrB_2 • ZrC	58
ZrN	20
ZrN • ZrC	10

Strength. Modulus of rupture measurements were made on vacuum hot-pressed cylinders of ZrC, ZrB_2, ZrN, ZrN • ZrC, ZrB_2 • ZrN, and ZrB_2 • ZrC to provide a comparison of transverse strength of the materials. A "single-point" loading jig with 0.25-inch diameter bearings and a 1.25-inch span was used on a universal testing machine which loaded at a strain rate of 0.025 inch per minute. Five specimens, 1/2-inch diameter and 1 5/8 inches long, were tested for each composition. The strength values, expressed as rupture moduli, are shown in Table 4.

Chemical Properties. *Melting Point*. The congruent melting temperatures of ZrC, ZrN, and ZrB_2 were measured, and the liquidus temperatures were determined for the binary mixtures containing 50 wt% of each compound. A self-resistance furnace, which is described by Adams and Beall[5] was used for heating the specimens, and the temperature was measured with an optical pyrometer. Melting was noted when an 0.050-inch diameter black-body hole in the specimens was observed to change brightness as seen through the optical pyrometer. Melting point values were: ZrC, 3380° ± 50°C; ZrB_2, 3220° ± 50°C; and ZrN, 2980° ± 50°C. For comparison, Cronin[6] found the melting point of ZrC to be 3532°C and 2982°C for ZrN. Kieffer and Kolbl[7] reported the melting point of ZrC to be 3250°C. Schwarzkopf and Kieffer[8] claim 3040° ± 50°C as the melting point of ZrB_2. Liquidus temperatures for the binary mixtures were determined by noting the optical pyrometer readings at the first sign of liquid formation in the specimen black-body holes. Those values were:

ZrC • ZrB_2 - 2980° ± 50°C
ZrC • ZrN - 3410° ± 50°C
ZrB_2 • ZrN - 2660° ± 50°C

Oxidation Behavior. A study of the oxidation behavior of vacuum hot-pressed ZrC, ZrB_2, ZrN, ZrC • ZrB_2, ZrC • ZrN, and ZrB_2 • ZrN in

Table 4. Strength of Vacuum Hot-Pressed Products

Material	Rupture modulus, psi
ZrC	14,700
ZrN	29,100
ZrB	26,600
ZrC • ZrN	23,000
ZrB_2 • ZrN	27,600
ZrB_2 • ZrC	21,000

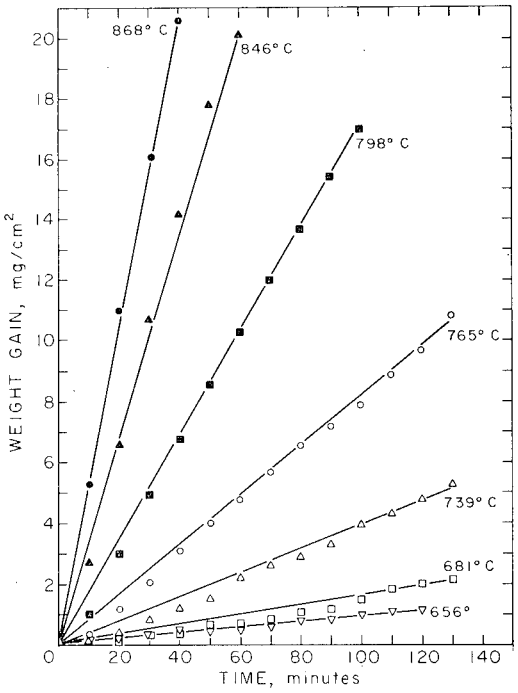
air was made to provide additional information on the limitation of the joins formed between these materials. Isothermal weight-gain measurements were taken on cubical shaped specimens 2 mm on a side. The specimen weight was continuously monitored through a heating cycle in air by recording the output signal from a Cahn electrobalance on a strip-chart recorder. The weight-gain versus time curves at constant temperature were then analyzed on the computer. Detailed analysis of the weight-gain curves was made for ZrC and ZrB_2 to yield oxidation rate constants and activation energies. Such a detailed study was not continued for ZrN and the binary mixture compositions because the weight-gain curves were complex; apparently a result of several interacting mechanisms. The oxidation rate constants and activation energies therefore were not computed because the rate-controlling mechanisms were not determined.

Best fit curves representing data from the computer stepwise regression analysis of weight-gain versus time tests are shown in Figures 3(a) through 3(f). Activation energy curves for oxidation of ZrC and ZrB_2 are shown in Figures 4(a) and 4(b), respectively.

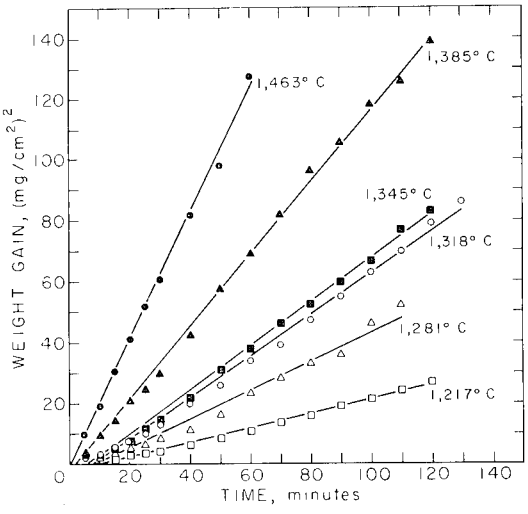
A linear oxidation rate was found for vacuum hot-pressed ZrC in air with an activation energy of minus 39.8 kcal/mole. The computer-analyzed data for ZrC between 656°C and 868°C can be expressed in an Arrhenius-type equation which describes the temperature dependence of oxidation rate as follows:

$$\ln k_1 = 16.858 - \frac{20.03}{T}$$

where k_1 is the linear rate constant and T is absolute temperature. Table 5 shows the ZrC linear rate constants for each isothermal test. One test at slightly above 868°C was discarded because of catastrophic oxidation of the specimen. These ZrC specimens were 95.2% of theoretical density.

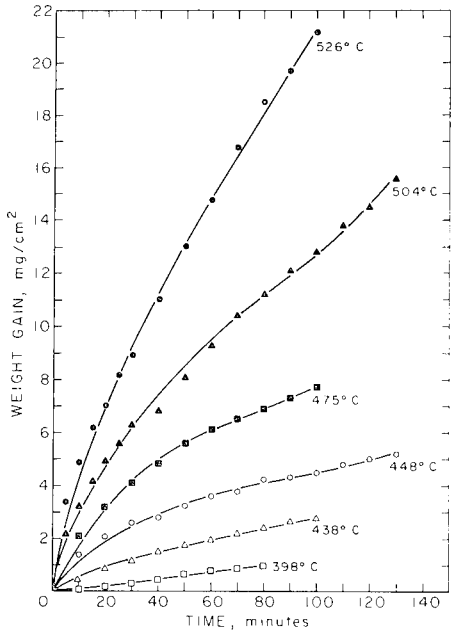


(a)

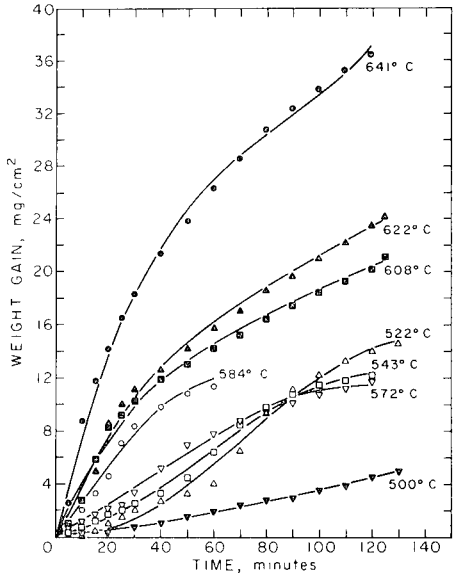


(b)

Figure 3. Weight-gain plot for: (a) ZrC in air, (b) ZrB_2 in air, (c) ZrN in air, (d) ZrN • ZrC in air, (e) ZrN • ZrB_2 in air, (f) ZrC • ZrB_2 in air.

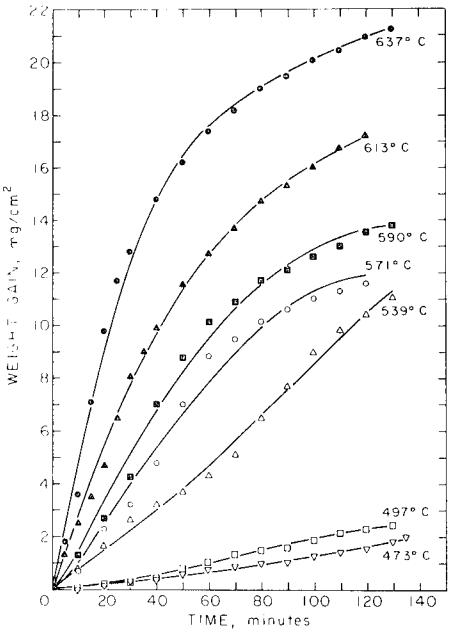


(c)

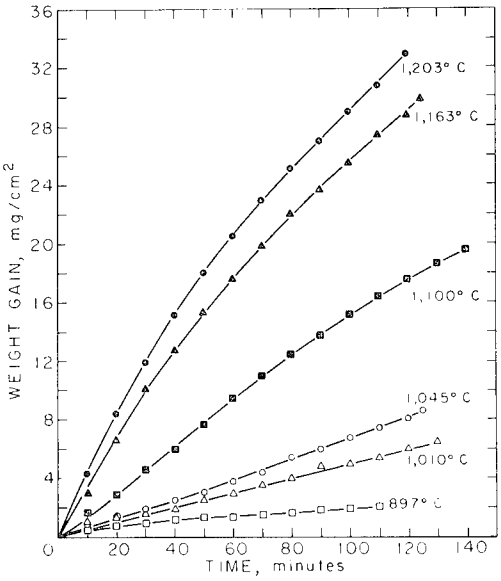


(d)

Figure 3. (Continued)

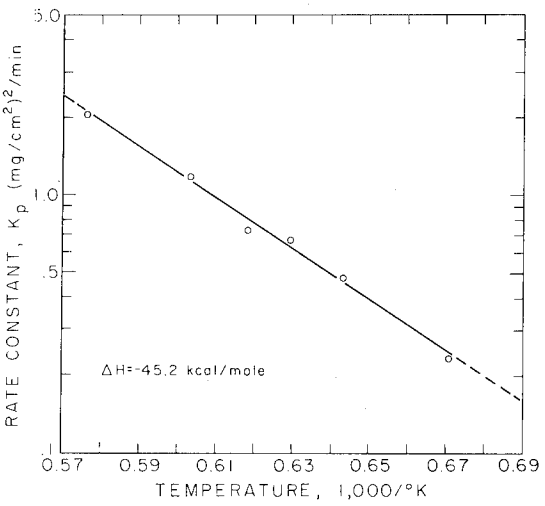


(e)

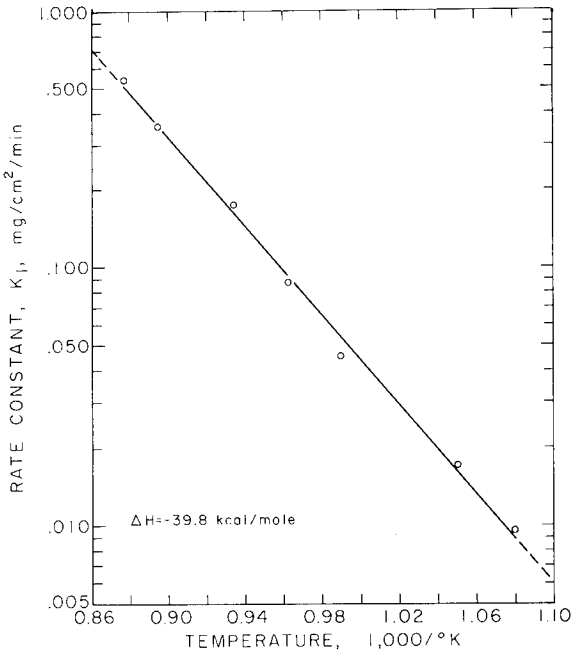


(f)

Figure 3. (Continued)



(a)



(b)

Figure 4. Arrhenius plot for: (a) ZrC in air, (b) ZrB_2 in air.

Table 5. Oxidation Rate Constants for ZrC from 656°C to 868°C

Temperature, °C	Linear rate constant, k_1 mg/cm²/min
656	9.62×10^{-3}
681	17.62×10^{-3}
739	42.38×10^{-3}
765	84.30×10^{-3}
798	174.70×10^{-3}
846	359.90×10^{-3}
868	519.40×10^{-3}

A parabolic oxidation rate was found for vacuum hot-pressed ZrB_2 in air, and the activation energy was determined to be minus 45.2 kcal/mole. The Arrhenius equation describing the temperature dependence of oxidation rate for ZrB_2 is:

$$\ln k_p = 13.867 - \frac{22.78}{T}$$

where k_p is the parabolic rate constant and T is absolute temperature. Parabolic rate constants for the temperature range 1217–1463°C are shown in Table 6. Catastrophic oxidation occurred in ZrB_2 at slightly above 1463°C. The ZrB_2 specimens had a density of 95.6% of theoretical.

COMPATIBILITY OF MATERIALS

Prior to the joining tests, a series of compatibility runs were made to determine if any undesirable reactions would occur between the components of the join assemblies. Two series of tests were made; the first by pressureless sintering, and the second by vacuum hot pressing.

Cold-Pressed and Vacuum-Sintered Bodies

Cylindrical bodies containing equal parts of ZrC + ZrB_2, ZrC + ZrN, and ZrB_2 + ZrN were cold pressed in a 1/2-inch-diameter steel die and ram set at 20,000 psi. The powders were well mixed in a vibratory mill, then dampened with benzene prior to cold pressing. The benzene acted as a binder and was easily removed by heating just before vacuum sintering. Following the cold pressing, the bodies were vacuum sintered in an induction furnace at 2000°C for 80 minutes. Specimens for X-ray

Table 6. Oxidation Rate Constants for ZrB_2 from 1217°C to 1463°C

Temperature, °C	Parabolic rate constant, k_p $(mg/cm^2)^2/min$
1217	0.235
1281	0.474
1318	0.678
1345	0.723
1385	1.192
1463	2.083

diffraction and metallographic examination were removed from each body by sectioning on a diamond thin-sectioning machine. The extent of compatibility of the mixtures was determined from the results of the X-ray diffraction and metallographic examinations. These results are shown in Table 7. The results of the compatibility tests indicated that no adverse reactions would occur at the test conditions. These results also indicated that higher densities were desirable in the ZrB_2 • ZrN and ZrC •ZrN systems. Therefore, a series of bodies for compatibility tests were fabricated by vacuum hot pressing.

Vacuum Hot-Pressed Bodies

Cold-pressed cylindrical bodies, as described above for pressureless sintering tests, were vacuum hot pressed in a 1/2-inch-diameter graphite die and rams. The die and charge was heated in an induction furnace hot press in a 10^{-5} torr vacuum. These bodies were heated to 2100°C, held at 2100°C for 30 minutes, then cooled to room temperature in 2 hours. A pressure of 4000 psi was applied to the bodies during the heating period, but was released during cool-down. Following the fabrication, the vacuum hot pressed bodies were sectioned for X-ray diffraction and metallographic examinations, and density measurements. The results of these examinations showed no adverse reactions which would preclude the use of the compound mixtures in join assemblies.

X-Ray Diffraction and Metallographic Examinations. *Fifty Percent ZrC + Fifty Percent ZrN.* Two phases were noted by X-ray diffraction. The primary constituent was a ZrC-ZrN solid solution, and a minor constituent was ZrC. The ZrC • ZrN phase was a striking maroon color. Two other phases were seen and were identified as ZrC and ZrN. Figure 5 shows microstructures of the hot-pressed mixtures and photograph A

Table 7. Results of Compatibility Tests on Cold-Pressed and Vacuum-Sintered Bodies

	50ZrC-50ZrN	50ZrN-50ZrB_2	50ZrC-50ZrB_2
X-ray	Single-phase solid solution of ZrC and ZrN	Primary constituents: ZrB_2 and ZrN in equal amounts	Primary constituents: ZrC and ZrB_2 in equal amounts
Metallography	Single-phase, very porous	Two-phase, in equal amounts, fairly porous	Two-phase, very dense
Density	69.7 percent of theoretical	89.6 percent of theoretical	97.0 percent of theoretical

shows the ZrC • ZrN phase, where the rounded light-gray grains are ZrC.

Fifty Percent ZrN + Fifty Percent ZrB_2. Two phases were reported as the primary constituents, ZrN and ZrB_2 in equal amounts. Part B in Figure 5 shows the ZrB_2 phase as light gray grains. Most of the ZrB_2 grains are longer in one direction than another. The ZrN grains are the white phase in this photograph. Some very small dark grains were identified as ZrO_2.

Fifty Percent ZrC + Fifty Percent ZrB_2. Equal amounts of ZrC and ZrB_2 were reported as the primary constituents. The ZrC appears as a light gray phase and the ZrB_2 as a darker gray phase in part C of Figure 5. This mixture hot pressed to a very dense structure. It appears that sintering of the ZrC was enhanced by the presence of ZrB_2.

FABRICATION OF GRADED JOINTS

The fabrication procedure for making graded joints consisted of two steps. The first was the prefabrication of the individual joint components; namely, one cylindrical body of each of the two compounds being joined, and a disk-shaped wafer consisting of a mixture of equal parts of those two compounds. The second was vacuum hot pressing the two cylindrical bodies with the mixture wafer between them in a three-component assembly.

Prefabrication of Joint Components

Powders for the end components of each join were dampened with benzene just prior to cold-pressing into 1/2-inch-diameter cylinders. The mixture wafers, 1/8-inch thick, were also cold pressed following a thorough mixing of the powders in a vibratory-mill. Benzene was added as a binder to give the bodies green strength after cold pressing. All of the components were cold pressed in a steel die and ram set at 20,000 psi pressure.

Vacuum Hot Pressing Joint Components

Joining of the three-component assembly was accomplished by vacuum hot pressing in a graphite die and ram. Each component was loaded, one on top of the other, into the 1/2-inch-diameter die and then the whole unit was inserted into the hot-press furnace. A cut-away graphite



Figure 5. Microstructures of hot-pressed mixtures. 500X.

die containing the three components is shown in Figure 6. Each joined body was hot pressed in vacuum at 4000 psi for 30 minutes at 2100°C. Heating and cooling rates were approximately 20°C/minute. The finished body length was 1 1/2 inches.

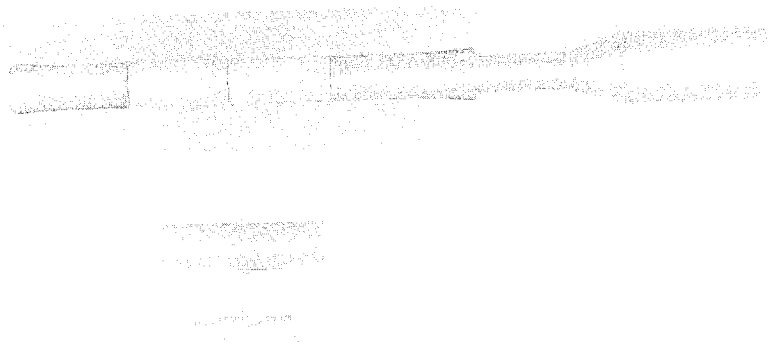


Figure 6. Upper, cut-away view of loaded graphite hot-press die; lower, joined body.

JOINT EVALUATION

A series of joined bodies in the ZrC, ZrB_2, and ZrN systems were fabricated for strength tests, thermal shock tests, and for metallographic examination.

Strength

Qualitative strength tests were made on joined bodies in each of the three systems studied. The modulus of rupture testing method described earlier was used; however, because of the inhomogeneous nature of the three component bodies, the stress distributions were complex and led to widely scattered strength values. However, these tests were useful in demonstrating that the joins were sound, because most of the failures were in the parent materials, rather than at the join interfaces.

Thermal Shock

A series of qualitative thermal shock tests were made on joined bodies of each of the three systems containing ZrC, ZrB_2, and ZrN. These tests were performed to show which portion or component of the join assembly was the most susceptible to thermal shock damage.

Method. Each specimen was heated very rapidly to 1500°C in the self-resistance "melting-point" furnace which was described earlier.

Then the power was shut off and the specimen allowed to cool rapidly. The rapid heating and cooling cycles were repeated until the specimen fractured. It was then noted which portion was damaged.

Results. In the ZrB_2-ZrC system, the carbide end fractured first. Neither the boride nor the graded zone failed. The nitride portion of the ZrB_2-ZrN system was the first to fail, and again, the boride and the graded zone survived. Zirconium carbide was the first to fail in the ZrC-ZrN system, and none of the other portions failed.

Microstructure Examination

Metallography specimens of the graded join bodies were prepared by making longitudinal slices through the specimens on a diamond thin-sectioning machine, thus exposing the cross section through the join. The specimens were then mounted in bakelite and polished by normal techniques. A microstructure study was then made.

ZrC–ZrN System. The join interface between ZrC and the ZrC • ZrN mixture layer is shown in Figure 7, part A. This join is well bonded as indicated by the wide diffusion zone produced by solution of ZrC by the ZrC • ZrN phase. It appears that a very smooth compositional gradient exists at the join. ZrC is the light gray phase at the left of the photograph, and the darker gray phase to the right is ZrC • ZrN solid solution. The large white angular grains are undissolved ZrN.

Figure 7, part B, shows the ZrC • ZrN–ZrN join interface. The gray matrix on the left is the ZrC • ZrN solid solution and the white material is ZrN. It can be seen that some porosity has been formed at the interface, possibly from partial decomposition of the ZrN. The extent of diffusion appears to be small across the interface.

ZrN–ZrB_2 System. Figure 7, part C, shows the ZrN–ZrN • ZrB_2 join interface. On the left is the ZrN portion and the ZrN • ZrB_2 two-phase region is on the right. Diffusion across the interface appears to be fairly extensive.

The two-phase region to the left in Figure 7, part D, is the ZrN • ZrB_2 portion and the white grains on the right are ZrB_2. A dark gray material in the ZrB_2 area was identified as ZrO_2. Black, round areas are voids. It is interesting to note that the voids in ZrB_2 have assumed a spherical shape, and are all nearly the same size. There appears to be good diffusion across the interface.

ZrC–ZrB_2 System. The join interface between ZrB_2 and ZrB_2 • ZrC is shown in Figure 7, part E. The light colored grains appearing on the left side of the field are ZrB_2 and the mixture layer is on the right. In the

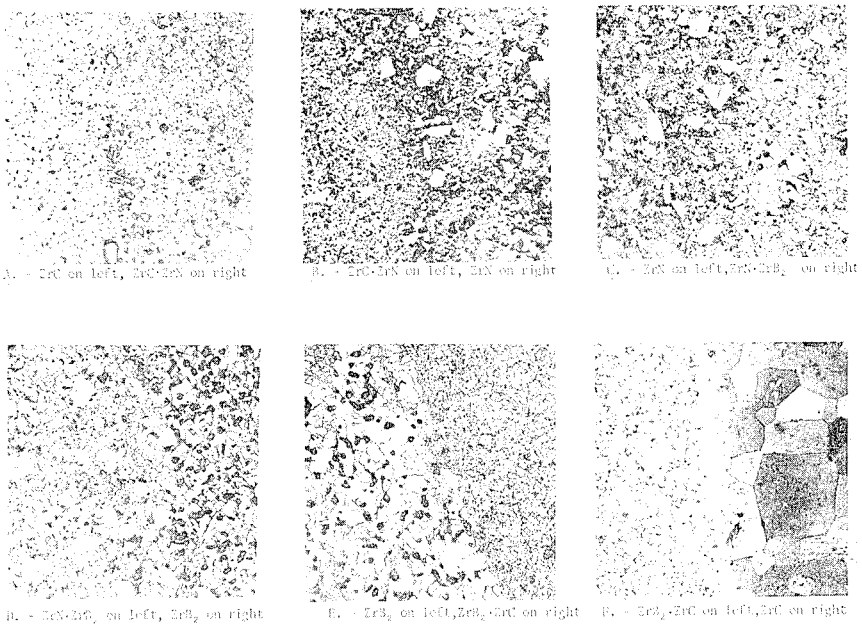


Figure 7. Join interfaces. 250X.

ZrB_2 • ZrC portion, the light colored phase is ZrC and ZrB_2 is the gray matrix. The extent of diffusion across this interface appears to be small.

Figure 7, part F, shows the ZrB_2 • ZrC–ZrC join interface. The ZrB_2 • ZrC area is on the left of the figure, and the very large grains on the right are ZrC. Visual inspection shows a small amount of diffusion across this interface. The original grain size of the ZrC was less than 10 microns, but it can be seen in the figure that a tenfold increase in grain size has occurred. The grain-size distribution can be seen in Figure 8. The fine-grained material at the upper left-hand corner of this photograph is ZrB_2 • ZrC. Grain-size decreases from about 100 microns at the join interface to the original 10 microns about 500 microns away from the interface. It is also noted that there are very few voids in the ZrC phase near the join interface. It is possible that the grain growth was accelerated by small amounts of boron which diffused across the join into the ZrC. This hypothesis is supported by the fact that the structure of the ZrC in the ZrC • ZrB_2 composition was nearly void-free, as noted in Figure 5c.



Figure 8. $ZrC–ZrB_2$ • ZrC interface, showing extent of ZrC grain growth. 40 X.

OTHER SYSTEMS

Several series of joining tests were made to demonstrate that the hot-press joining method would be useful in systems other than zirconium, and in systems containing an oxide as one component of the joined couple. Successful joins were obtained in systems of TiC, TiN, and TiB_2, and in systems of Al_2O_3 with ZrC, ZrN, and ZrB_2. All of these join specimens were sectioned and visually examined and evaluated.

Titanium Compounds

One each of the following joins were made: TiC–TiN, $TiN–TiB_2$, $TiC–TiB_2$, and $TiC–ZrB_2$. These joins were made by hot pressing the

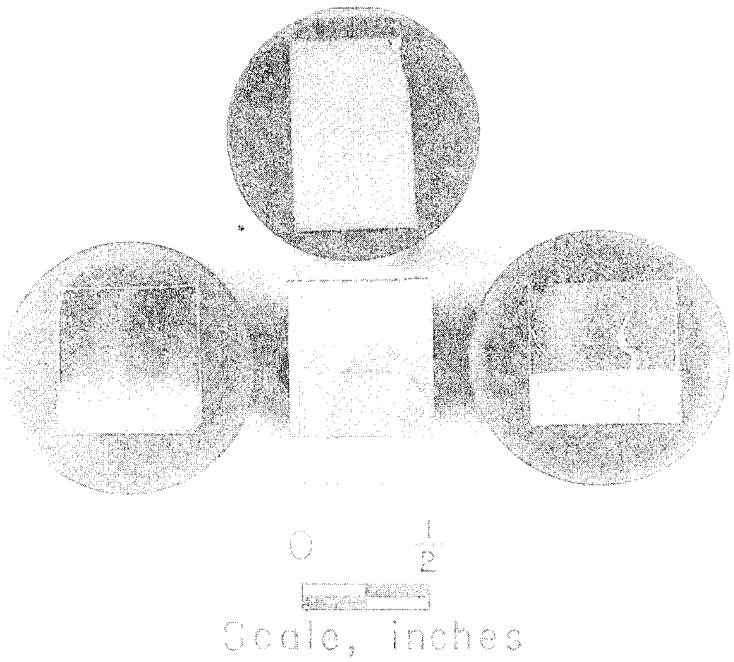


Figure 9. Titanium compound joins: left, TiC–TiB_2; center, TiC–TiN; upper center, TiB_2–TiN; right, TiC–ZrB_2.

component parts, including a 50-50 mixture wafer between the two end portions, at 2100°C and 4000 psi for one hour in a graphite die and ram. An argon atmosphere was used. Bonding in each case was excellent; however, the titanium compounds were found to be more prone to cracking than were the zirconium compounds, as can be seen in Figure 9. It is interesting to note that no grain growth was noted at the TiC interface with either TiB_2 or ZrB_2, as was seen in the ZrC–ZrB_2 system.

Joins to Oxides

Of special interest from an electronic application standpoint is the type of join which mates an electrical conductor to an electrical insulator. The hot-press fabrication method was used to successfully join ZrC, ZrB_2, and ZrN (all electrical conductors) to Al_2O_3 and ZrO_2.

Alumina. Bodies of alumina were hot-press joined to ZrN, ZrC, and ZrB_2 with a 50-50 mixture layer between ends. Each joined body was hot pressed at 1750°C and 3000 psi in a graphite die for one hour. An argon



Figure 10. Joins to alumina: left, ZrC–Al_2O_3; center, ZrB_2–Al_2O_3; right, ZrN–Al_2O_3.

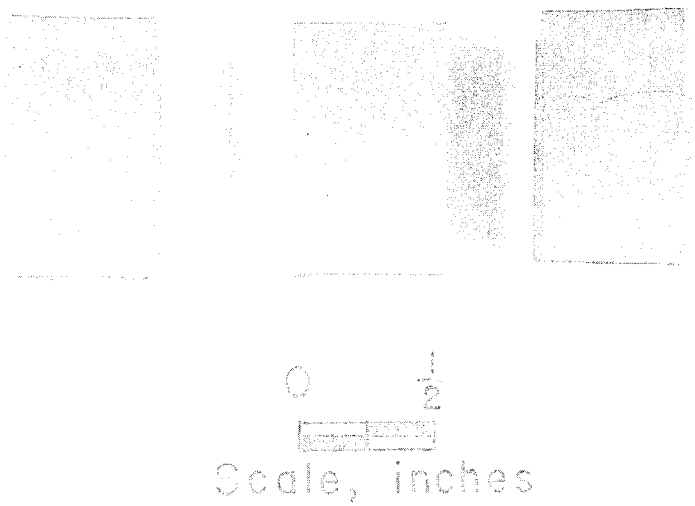


Figure 11. Joins to zirconia; left, ZrC–ZrO_2; center, ZrB_2–ZrO_2; right, ZrN–ZrO_2.

atmosphere was used. Very strong bonding of the components resulted, and visual examination of sectioned samples showed no evidence of adverse reactions between the compounds. The alumina joins are shown in Figure 10, where the alumina end of the assemblies is toward the top of the picture.

Zirconia. Hot-press joining of ZrC, ZrN, and ZrB_2 to ZrO_2 (yttria-stabilized) was accomplished, but with much more difficulty than in any of the other systems. The major problem was thermal shock damage to the ZrO_2 component of the joins. Sandwich-type joins were made which contained one, three, and five intermediate mixture layers between the ends. Extreme cracking destroyed all specimens containing one and three mixture layers, but most of the specimens containing five layers survived. These join bodies were hot pressed in graphite at 1800°C for one hour in argon. Figure 11 shows a specimen of ZrC joined to ZrO_2, ZrB_2 to ZrO_2, and ZrN to ZrO_2. The ZrO_2 sections are toward the top of the picture. Composition of the intermediate layers had the proportions 85-15, 75-25, 50-50, 25-75, and 15-85.

CONCLUSIONS

The results of this research indicate that diffusion bonding of refractory hard metals is a promising method for joining dissimilar materials. Fabrication of graded joins by vacuum hot pressing a mixture layer between two end materials proved to be very satisfactory for the joining of nitrides, carbides, and diborides of zirconium and titanium. Joint evaluation showed the joins to be as strong or stronger than the end materials. Also, sound joins of ZrC, ZrN, and ZrB_2 were made to alumina and zirconia. Microstructure examinations showed bonding to be promoted by mechanical interlocking of phases and by diffusion of one component into another.

Experience gained in this work indicates that multicomponent refractory hard metal and/or refractory oxide hardware can be fabricated as a monolithic body without the use of low-melting brazes or solders, or mechanical fastening devices.

REFERENCES

1. Porembka, S. W. Jr., "Joining Ceramics to Metals for High Temperature Service," *Battelle Tech. Rev.*, **13**, No. 9 (1964), 2–7.
2. Zimmer, F., "New Ways to Bond Dissimilar Materials," *Met. Prog.*, **83**, No. 1 (1963), 101–104, 147–48.

3. Burykina, A. L. and Evtushenko, O. V., "Vacuum Diffusion Welding of Metalline Carbides to High-Melting Metals," *Sov. Powder Met. Metal Ceram.*, No. 1 (1965), 66–72.
4. Miccioli, B. R. and Shaffer, P. T. B., "High Temperature Thermal Expansion Behavior of Refractory Materials: I. Selected Monocarbides and Binary Carbides," *J. Amer. Ceram. Soc.*, **47** (1964), 351–56.
5. Adams, R. P. and Beall, R. A., "Preparation and Evaluation of Fused Hafnium Carbide," U.S. Bureau of Mines Report No. RI-6304, 1963.
6. Cronin, L. J., "Refractory Cermets," *Bull. Amer. Ceram. Soc.*, **30** (1951), 234–38.
7. Kieffer, R. and Kolbl, F., "Tungsten Carbide-Free Hard Metals," *Powder Met. Bull.*, **4** (1949), 4–17.
8. Schwarzkopf, P. and Kieffer, R., *Refractory Hard Metals, Borides, Carbides, Nitrides and Silicides*. New York: The Macmillan Company (1953), 283.

7. DIRECT BONDING OF METALS TO CERAMICS FOR ELECTRONIC APPLICATIONS

J. F. BURGESS and C. A. NEUGEBAUER
General Electric Company
Schenectady, New York

G. FLANAGAN
General Electric Company
Syracuse, New York

R. E. MOORE
General Electric Company
Pittsfield, Massachusetts

The direct bonding of metals to ceramics is possible utilizing a gas-metal eutectic. The mechanism of direct bonding of copper foil to ceramics in a slightly oxidizing atmosphere is presented. It involves the formation of eutectic melt between copper and oxygen at a temperature slightly below the melting point of copper, which serves to bring the foil into intimate contact with the substrate. Metals to which this technique is applicable include Cu, Fe, Ni, Co, Ag, Cr, Mo, and Al. A brief review of other metal-ceramic bonding techniques is given for comparison.

The process for fabricating direct bonded copper structures is given, and properties of the bond are discussed. The use of the direct bonding process in a number of electronic applications such as hybrid packages and power device heat sinks is indicated.

INTRODUCTION

Strong bonding of metals to ceramics generally does not take place unless an intermediary layer is present, or forms due to diffusion or reaction. The adhesion of the metal to this intermediary is better than to the ceramic directly. However, an intermediary layer is undesirable in many applications. This is true, for instance, where high heat conductivity is required. The presence of an intermediary layer generally re-

duces heat conductivity, especially if the layer is nonmetallic. Further, in high-frequency applications, where the current flows in a thin skin at the metal-ceramic boundary, intermediary layers are undesirable because they are generally more resistive than the metal to be bonded. Finally, intermediary layers are often less corrosion resistant and lead to premature failure.

Unfortunately, strong direct metal to ceramic bonds are not common, either because the bond is inherently weak, or because of the difficulty of bringing the metal into intimate contact with the ceramic. In this chapter, a new method of direct bonding of metals to ceramics will be given. For a better perspective, a short summary of the mechanisms of presently used metal-ceramic bonding techniques is given below.

BONDING MECHANISMS INVOLVING INTERMEDIARY LAYERS

Some of the more pertinent literature in this area has been reviewed by C. I. Helgesson,[1] and a short review was recently given by Loasby *et al.*[2] Commonly used intermediary layers are glass layers, where the glass is intentionally added or is originally present in the ceramic itself, or polycrystalline semiconducting compounds formed by the reaction between the metal or metal oxide and the ceramic itself.

Glassy Intermediary Layers

Glassy phases are usually present in the grain boundaries of impure (<99.8%) ceramics. Thus, Al_2O_3 or BeO ceramics usually contain glassy mixtures of MgO, SiO_2, and CaO concentrated in the grain boundaries. When a metallizing mixture is applied to such a ceramic, and the temperature is raised to sintering temperatures, the glass from the ceramic penetrates into the (porous) metal layer and locks it to the ceramic after cooling by mechanical forces.

More commonly, glass is intentionally added to the metallizing mixture to form the intermediate layer. This is particularly true if the ceramic is pure. For example, to take advantage of the high thermal conductivity of BeO ceramic, glass must be kept out of the grain boundaries. Therefore, the common metallizing mixtures, such as Mo-Mn, when used on beryllia, contain up to 20% SiO_2. Thus the composition of a typical mixture is 71.5% Mo, 10.7% Mn, and 17.8% SiO_2, fired on BeO at 1300°C. The manganese diffuses into the glass.

Another commonly practiced method of bonding through an intermediary glass phase involves glass frit additions to the finely divided metal in the metallizing mixture. Thus, the majority of the so-called

"thick film" conductor pastes contain a glass frit, generally chosen for low melting point and thermal expansion match, in addition to dispersed metal (normally noble metals) in an organic carrier. The glass frit melts and reacts with the ceramic (usually Al_2O_3), and it also forms a network within the metal conductor. Thus, the bond between the metal and the ceramic is due to mechanical locking by the reacted glass. It should be noted that the bond strength of glass frit compositions is best on alumina; for beryllia, cracking of the glass and spalling is generally observed.

Polycrystalline Intermediary Layers

Such layers are usually compounds formed between the metallizing mixture and the ceramic. In one method, the metal oxide is applied to the ceramic, and sintered with the ceramic to form a mixed oxide compound. For instance, such a compound is formed between copper oxide and alumina, possible $CuAlO_2$, when they are sintered together at 1150°C in air. Subsequent reduction gives an adherent metal layer bonded on the mixed oxide phase. This method is also applicable to cobalt, nickel, iron, and silver.

The widely used moly-manganese process also falls into this category. In this process, a mixture of molybdenum and manganese oxide is fired on alumina (not beryllia) at 1400°C in an atmosphere of wet hydrogen. The hydrogen reduces the molybdenum oxide to the metal, but not the manganese oxide, which reacts with the alumina to form the intermediate layer compound $MnO \cdot Al_2O_3$. The molybdenum, which is unable to diffuse deeply into pure Al_2O_3, will diffuse readily into the manganese aluminate spinel. This leads to good adhesion of the Mo layer. When MoO_3 alone is used, some penetration of alumina by MoO_3 occurs, especially in hydrogen atmospheres at high humidities. A compound between Mo and Al_2O_3, perhaps $Al_2(MoO_4)_3$,[3,4] is formed to provide the intermediary bonding layer.

DIRECT BONDING

Direct bonding here implies the absence of a readily identifiable intermediate phase between the metal and the ceramic. It does not exclude, however, the presence of a transition layer one or two monolayers thick, such as oxygen bridges between the metal and ceramic.

A method of direct bonding which does not depend on any kind of intimate bond between metal and ceramic is that involving mechanical locking or keying.

In this process the metal is screened on the ceramic in the form of an organometallic paste. The paste decomposes on heating in air, with the result that metal particles are now locked in pores in the ceramic surface to give a mechanical bond. Films of noble metals, such as platinum, are typically applied in this way. However, poor adhesion is obtained in the mechanical locking process. Clearly, in order to get good adhesion by direct bonding it is required that:

1. The metal must be brought into intimate contact with the ceramic over the entire area on an atom to atom basis.

2. The metal must form a strong bond with the ceramic, be it by van der Waal's or chemical bonding, without extensive reaction or diffusion of the two phases into each other.

To get intimate contact between metal and a ceramic surface, the metal could be brought into the liquid state by melting. The liquid will replicate the ceramic surface where it wets it, and if a strong bond is formed, good adhesion is obtained after cool-down. For instance, when copper is melted in hydrogen on an alumina substrate, a molten droplet is formed with a melting angle of approximately 120°, which after cool-down to room temperature adheres strongly to the ceramic. The problem with simply melting the metal, of course, is that one or more droplets are formed, and the metal member to be bonded entirely loses its shape. This can be avoided by the gas-metal eutectic method.

DIRECT BONDING BY THE GAS-METAL EUTECTIC METHOD

The basic idea here is to form a liquid skin around the metallic member to be bonded. The liquid must wet both the metallic member and the ceramic, and form a strong bond after cool-down. The melting point of this liquid should be near the melting point of the metal member itself, say within 50°C, so that the metal member becomes soft and pliant and conforms easily to the shape of the substrate surface. Further, the predominant constituent of this liquid should be the same element as makes up the metallic member, and any additional constituent should be present in only small amounts or be easily removable after bonding. The thickness of the molten skin must be kept small in comparison to the thickness of the member to be bonded.

Ideal for use as the skin material are eutectics formed by the flow gas in a bonding system with the metal member itself. Such a eutectic exists, for instance, between copper and oxygen, at 0.39 wt% oxygen.[5] The melting point of this eutectic is 1065°C, as compared to 1083°C for pure copper. Thus, if the oxidizing conditions in the flow gas are chosen properly, one may have the molten copper-oxygen eutectic mixture and

solid copper (containing a small amount of dissolved oxygen) coexist together, in the temperature interval $1065° < T < 1083°C$. It is this copper-oxygen eutectic skin which is in effect used as a glue to bond the solid copper member to the ceramic, without the Cu member losing its shape. Thus, in order to bond copper foil to ceramic, the process is as follows:

The Cu foil is laid on top of the ceramic in a furnace containing a flow gas atmosphere consisting primarily of an inert gas, such as argon or nitrogen, with a small addition of oxygen, typically of the order of a few hundredths of a percent. Copper initially reacts during the heat-up period with the oxygen in the flow gas. A small amount of oxygen dissolves in the copper, but most of it reacts to form Cu_2O around the foil. When 1065°C or above is reached, a liquid phase of or near the eutectic composition forms a skin around the copper. The thickness of this molten skin depends on the O_2 partial pressure and the oxidation time. If the partial O_2 pressure in the flow gas is less than $1.5 \cdot 10^{-6}$ atm (the equilibrium partial pressure over Cu_2O at 1065°C), Cu_2O will not form and the eutectic phase also will not form. The formation of a molten layer between the Cu foil and the substrate serves to bring the copper in intimate contact with the ceramic, by wetting it over the entire interface. Once in intimate contact with the ceramic, copper forms a strong bond with it. The temperature must remain below 1083°C, the melting point of copper, since otherwise the foil loses its structural integrity and liquid drops are formed. Similarly, if the partial pressure of oxygen is too high, all copper present is converted into eutectic melt. Thus, an intermediate O_2 partial pressure is required where both phases are present simultaneously. On cool-down below 1065°C, the eutectic segregates into Cu and Cu_2O. Evidence of this is shown in Figure 1, which is a micrograph through a section of bonded copper foil, and indicates the presence of a second phase. This oxide phase may now be reduced in hydrogen at low temperature, without loss of adhesion. The bonding process is schematically illustrated in Figure 2.

Copper has been bonded successfully by the gas-metal eutectic methods on alumina, beryllia, silica, various other spinels, other metals, and to itself. It does not bond, however, to boron nitride or carbon. The bond strength to oxygen-containing ceramics can be in excess of 20,000 psi. Removal of the copper by etching in nitric acid or ferric chloride solution leave no copper residue. Since the copper itself does not melt during bonding, precut or stamped foils of copper of the desired shapes can be bonded. In addition, holes previously cut into ceramic substrates can be covered hermetically, and the copper can overhang the ceramic. Bonds between copper and other metals, and between two copper members, can also be made by this method. A photograph of various

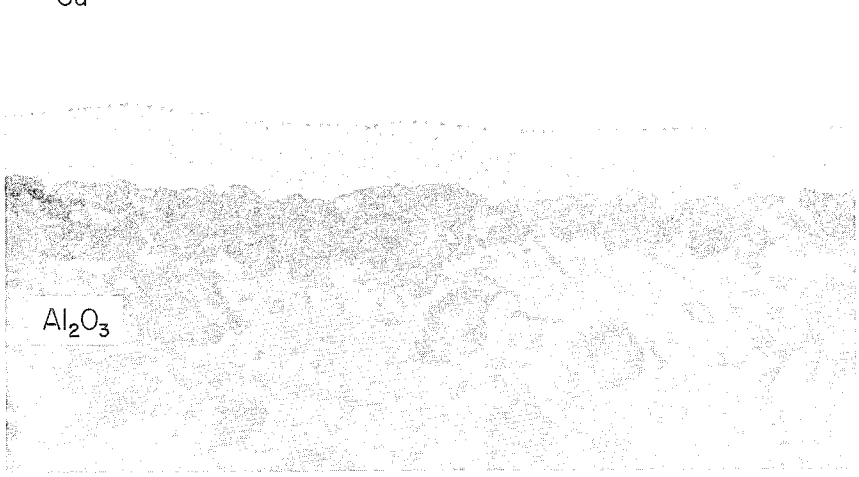


Figure 1. Micrograph of section through direct copper bond to alumina, showing the precipitated Cu_2O from the eutectic.

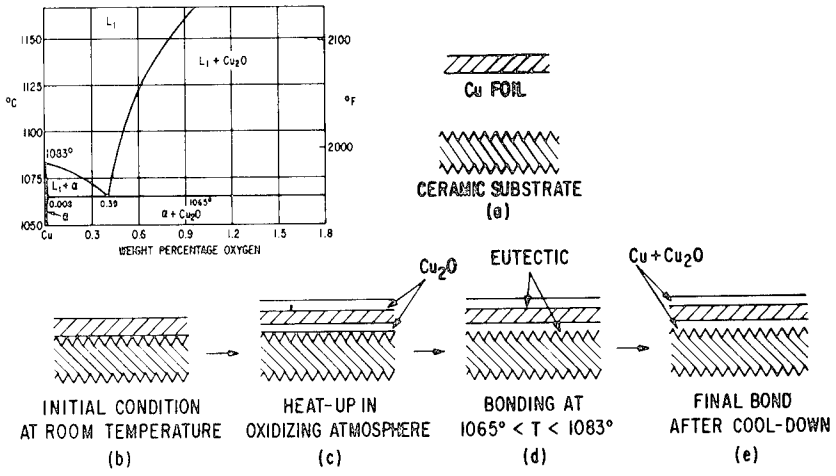


Figure 2. Eutectic phase diagram and schematic of bonding process.

direct bonded copper structures prepared in this laboratory are shown in Figure 3.

PROPERTIES OF DIRECT BONDED COPPER STRUCTURES

Some properties of direct bonded copper on ceramic structures are listed in Table 1.

APPLICATION OF DIRECT BONDED COPPER IN HYBRID PACKAGING

The use of directly bonded Cu foil to ceramics for the construction of hybrid packages offers advantages because:

1. Foils from 1 to 250 mils or more in thickness can be bonded on Al_2O_3, BeO, or metal without the use of an intermediary layer and without losing the structural integrity of the foil.
2. Several layers of Cu foil and ceramic can be bonded in one single firing step. This allows fabrication of conductor crossovers and intercon-

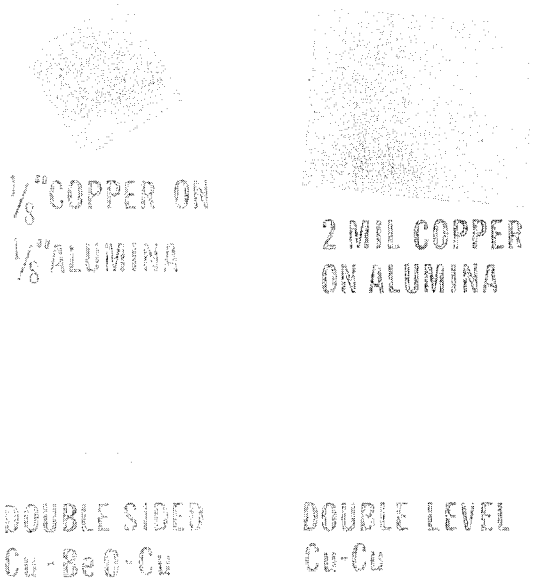


Figure 3. Direct bonded copper structures.

Table 1. Some Properties of Direct Bonded Copper on Ceramic Structures

Electrical conductivity is at least within 5% of pure copper, in the as-bonded condition.
The hardness of the copper in the as-bonded condition is much higher than after hydrogen reduction, because of dispersion hardening due to precipitated Cu_2O from the eutectic.
The Cu-ceramic bond strength routinely exceeds 20,000 psi.
In spite of the expansion coefficient difference, repeated thermal cycling from 77°K to 600°K does not cause mechanical failure.
Brazing, soft and hard soldering, resistance and electron-beam welding are possible to the bonded copper without causing bond failure.
Holes in the ceramic can be sealed hermetically by direct bonded copper.

nections among various conductor layers; the inclusion of a Cu backplate for heat sinking; and external package leads in one single step.

3. Since the Cu-ceramic bond does not require an intermediate interfacial layer, better heat sinking is possible.

4. Thick film conductor screening and firing steps can be entirely eliminated.

5. The Cu-ceramic bond is exceptionally strong.

6. Fabrication costs are considerably below conventional methods because of process simplicity and lower materials cost.

Figure 4 illustrates the use and versatility of the copper-foil bonding process in fabricating electronic packages, including heat sinking, conductor crossovers and interconnections, and top to bottom straps. Copper foil and ceramic pieces are previously cut to the desired dimensions and are appropriately located on the ceramic substrate before the furnace pass for one-step bonding. Alternatively, the pattern can be etched after bonding. This latter technique is particularly suitable for fine and complex geometries.

Figure 5 gives a sequence of steps to fabricate a hermetic ceramic package. Pieces of copper and ceramic are cut to the appropriate size and are bonded directly to give a lead frame, conductor pattern, pellet bonding pad, conductor crossover, and heat sink. The window frame for lid attachment is fired on by means of a glass ceramic frit at $500 < T < 700$°C. Pellet bonding and lid attachment complete the package.

When the direct bonded copper foil covers a hole previously cut into the ceramic, a hermetic seal is formed. This allows for the mounting of pins or tabs from the backside by soldering, welding, or plating on copper. Figure 6 illustrates a sequence of steps to fabricate a package in

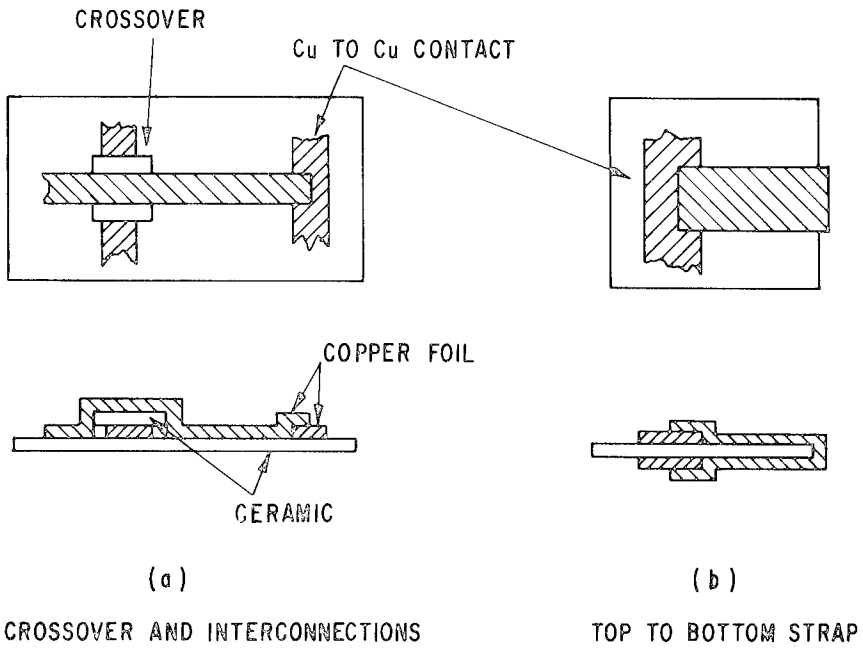


Figure 4. Using direct bonded copper in constructing electronic packages.

this manner. After direct bonding of a copper foil to a predrilled ceramic substrate, the conductor pattern and window frame are photoetched. After nickel plating, the pins are mounted and the pellet is attached. Lid attachment completes the hermetic package. Figure 7 is a photograph of a hybrid circuit fabricated by this process.

APPLICATION TO OTHER METAL-CERAMIC SYSTEMS

For the direct bonding of metal by the gas-metal eutectic method, the following prerequisites must be fulfilled:

(a) a eutectic must exist between the metal and the flow gas;

(b) the percentage of the gas component in the eutectic must be low and/or easily removable after bonding;

(c) the eutectic temperature must be at least 10 degrees or so below the melting point of the metal to give a realistic temperature range for bonding;

(d) the metal must be pliant at the bonding temperature so that it conforms to the substrate shape.

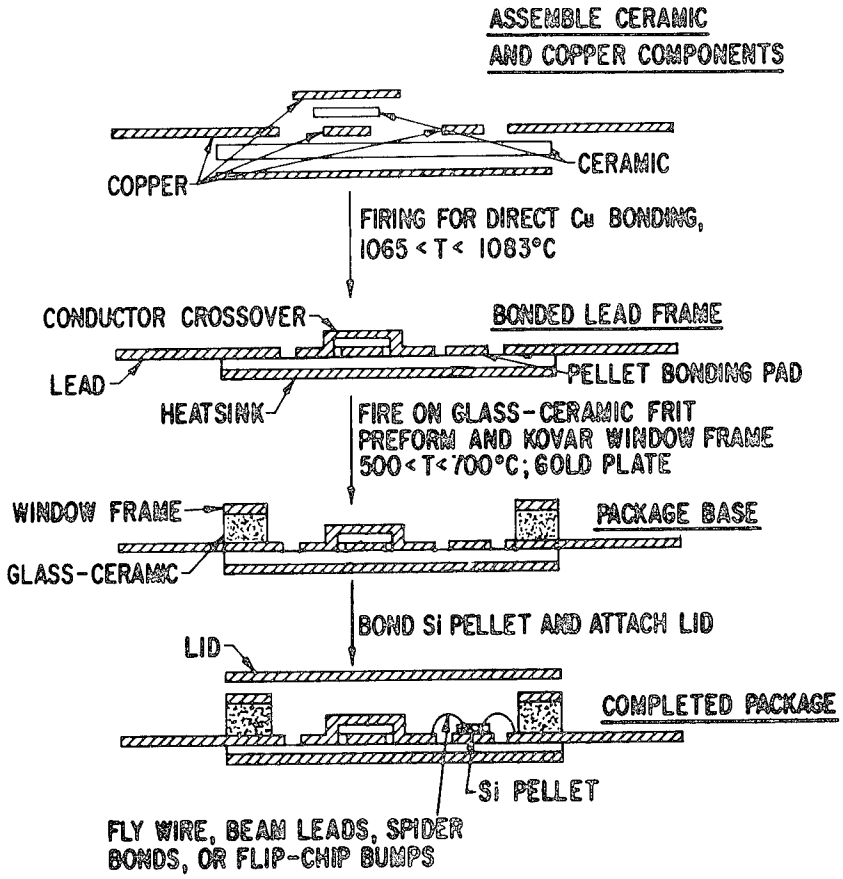


Figure 5. Process steps to fabricate electronic package by direct bonding process.

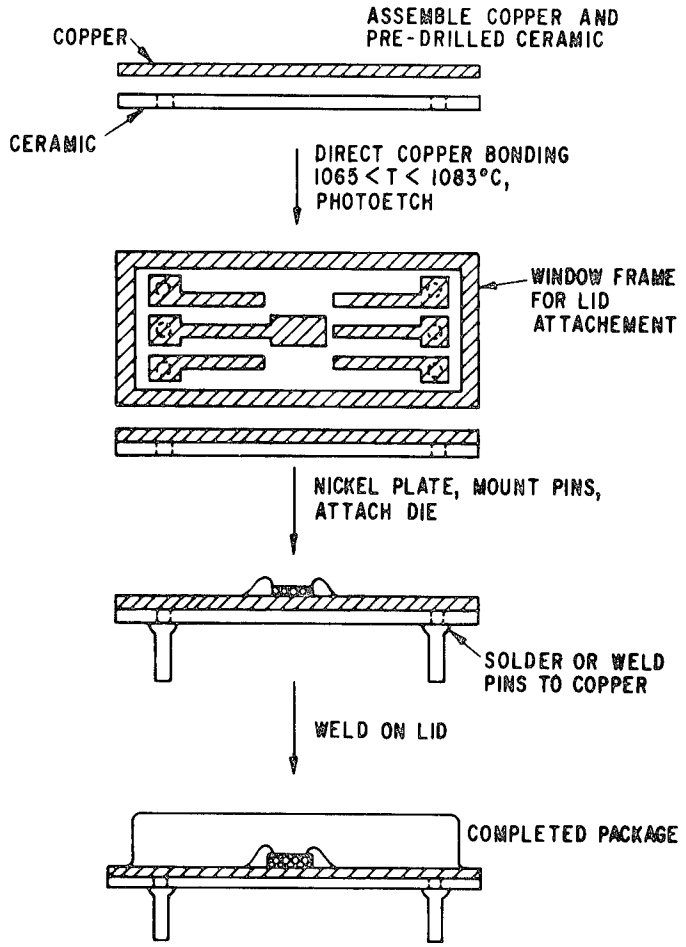


Figure 6. Process steps to fabricate electronic package by direct copper bonding process.

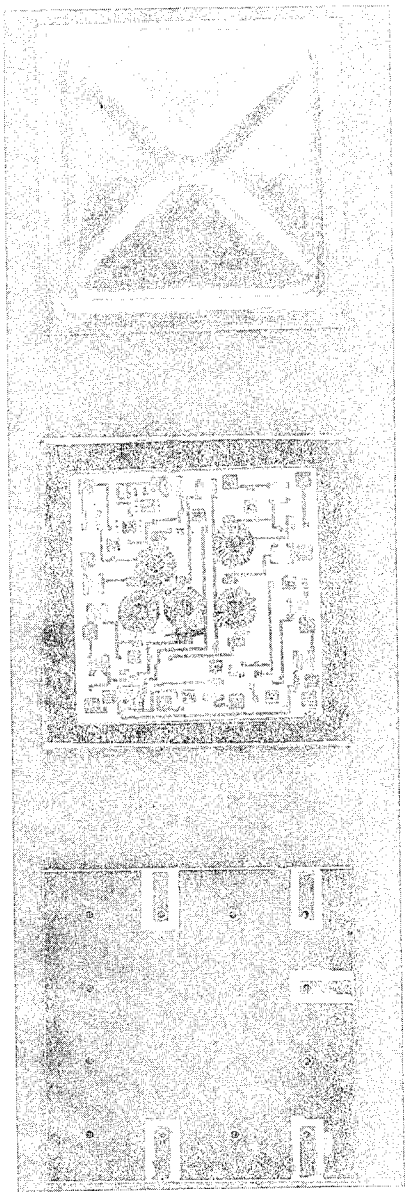


Figure 7. Example of hybrid circuit fabricated by process illustrated in Figure 6.

Inspection of phase diagrams of metals with the more common gases reveals a number of possibilities. In particular, oxygen, sulfur, and phosphorus form eutectics with several metals. These are listed in Table 2, in addition to the eutectic temperature, the melting point of the metal, and the percentage of the gas component in the eutectic.

The flow gas would contain small amounts of oxygen, hydrogen disulfide, phosphine, or silane, as appropriate. However, in some cases a constituent of the flow gas such as silicon may not be easily removable, and the bond in such a case could not, strictly speaking, be called "direct."

Table 2. Metal-Gas Eutectics for Direct Bonding

Eutectic	Eutectic Temp. °C	Weight % Nonmetal	Melting Point of Metal
Copper-oxygen	1065	0.39	1083
Iron-oxygen	1523	0.16	1535
Nickel-oxygen	1438	0.24	1452
Cobalt-oxygen	1451	0.23	1480
Copper-sulfur	1067	0.77	1083
Silver-sulfur	906	1.8	960
Chromium-sulfur	1550	2.2	1615
Silver-phosphorous	878	1.0	960
Nickel-phosphorous	714	11.0	1452
Copper-phosphorous	714	8.4	1083
Molybdenum-silicon	2070	5.5	2625
Aluminium-silicon	577	11.7	660

REFERENCES

1. Helgesson, C. I., *Ceramic to Metal Bonding*. Cambridge, Mass.: Boston Technical Publications (1968).
2. Loasby, R. G., Davey, N., and Barlow, H., "Enhanced Property Thick-Film Conductor Pastes," *Solid State Tech.*, **15**, No. 5 (1972), 46–50, 72.
3. Pincus, A. G., "Mechanism of Ceramic-to-Metal Adherence," *Ceram. Age*, **63**, No. 3 (1954), 16–20, 30–33.
4. Butts, A., ed., *Copper, The Science and Technology of the Metal, Its Alloys and Compounds*. New York: Reinhold Publishing Corporation (1954), 475.

SESSION III

POLYMERS

MODERATOR: K. J. SMITH
Syracuse University

8. DURABLE SURFACE TREATMENTS FOR THE ADHESIVE BONDING OF ALUMINUM ALLOYS

T. J. REINHART, JR.
Air Force Wright Aeronautical Laboratories (AFSC)
Wright-Patterson Air Force Base, Ohio

INTRODUCTION

Adhesive bonded components have been utilized successfully in many high-performance applications in aerospace and ground vehicle structures for many years. Each year millions of pounds of adhesives are utilized in the transportation industries in bonding hood and deck lid components and in fabricating bonded clutch and brake facings. Aircraft manufacturers utilized adhesives for many bonding applications including control surfaces, fuselage bulkheads, and wing panel and skin stiffeners, flooring, and, of course, in the fabrication of helicopter rotor blades.

Adhesive bonding has proved to be more economical, lighter in weight, and better performing in many applications when compared to other forms of mechanical fastening such as bolting or riveting. It provides cost and weight savings over riveting, increased fatigue life and improved corrosion resistance.

Until comparatively recent times, however, adhesives have rarely been found in primary structural load-carrying applications. There are many reasons for the existence of this situation. Some of these reasons are as follows: high apparent variability in bond strength; lack of structural redundancy; lack of rational joint design and analysis procedures; sensitivity of joint strength to test-method geometry; lack of confidence in existing nondestructive inspection techniques; and last, but not least, variability in performance under service environment.

The pressure to continue to expand the applications of adhesive bonding into primary structural applications is derived from the potential cost and weight savings that can be achieved. Bonding is an efficient process from the standpoint of structural efficiency and cost.

Highly loaded airframe structural members can and have been efficiently joined using adhesive bonding. Careful selection of structural design concept and the utilization of optimized materials and processes are necessary to obtain the maximum efficiency of adhesive bonding.

The interdependence of the many steps that go into the development of a bonded component — design, analysis, materials and process selection, fabrication and inspection — will demand competent execution in each phase to insure that maximum durability and reliability be achieved.

METAL SURFACE PREPARATIONS

One of the most critical steps in the process selection is the selection of the prebond surface preparation for the metallic adherend involved. In this discussion we shall concentrate on aluminum alloys because over 95% percent of the bonding in our (USAF) aircraft involves these materials.

There are several aspects that must be considered in the selection of a surface preparation for aluminum alloys. It is highly desirable that the surface preparation impart high wettability (of the adhesive being considered) to the alloy. The surface preparation should possess high cohesive strength to prevent failure along weak boundary layers. In addition, any surface preparation intended for use in structural adhesive bonding applications must possess extreme stability to chemical and physical change under exposure to aggressive environments such as combined heat, humidity and stress.

Since the two most serious structural maintenance problems involved in Air Force aircraft are fatigue and corrosion of metallic elements, our selected surface preparation must also possess inherent resistance to corrosion or its corrosion resistance must be somehow enhanced, prior to the bonding step.

One of the most serious problems that had to be solved was that, in the past, we had no really discriminating test for use in the evaluation of the adequacy of our surface preparation. This was amply demonstrated by the fact that our service experience has been varied. In some aircraft systems bonded structure has provided excellent service performance, while others have experienced disbond and bond-line corrosion. Traditional test methods, such as lap shear and peel, used to evaluate adhesive bonding systems could not discriminate between good and poor surface preparations.

Extensive work performed in the failure analysis of bonded components has revealed that service delaminations are the result of combined low stress, moisture and heat working on an unstable metal oxide layer.

Moisture has been shown to enter the bond-line by diffusion through the adhesive as well as along the scrim cloth and adherend adhesive interfaces. This work has enabled us to determine that the prebond metal surface preparation is the single most critical aspect affecting adhesive bond durability.

Work by Ripling and Mostovoy in the development of the wedge-opening crack-growth test for adhesives, modified and adopted by researchers at Boeing, has resulted in a test that can quickly discriminate between desirable and undesirable adherend surface preparations. Experience has shown that the wedge opening beam test can, in less than an hour, reveal unsuitable metal surface preparations. A reasonable correlation has been made between service experience and the wedge-opening test utilizing specimens cut from components removed from service.

In addition to the specific chemical treatment utilized in the prebond treatment of the adherend, surface characteristics such as the amount of surface contamination, surface roughness, and the physical history of the surface, *i.e.*, shot peened, machined, ground or chemical etched all will play an important role in determining the optimized procedures that will be selected.

Since *all* of our service failures of adhesive bonded components have involved *adhesive* failure of one kind or another; that is, within the oxide layer on the aluminum alloy or between the oxide layer and the base alloy metal, we are convinced that these few hundred angstroms of the bond (polymer, oxide layer, metal) are critical to the strength and durability of the adhesive bonded joint. It has been shown that even in the highest quality of bonded joints, if the metal surface preparation utilized is not hydrolytically stable, the interface is very sensitive to moisture attack. It is also known that certain forms of the oxide film on the metal surface can be very prone to water attack. Considering that the stability of the oxide layer on the aluminum is one of the weakest links in the chain, investigations have concentrated on the identification and characterization of the oxide layers produced by the various treatments.

The first factor to consider is that there are four common, naturally occurring forms of aluminum oxide that can be formed. These are:

Bayerite ($\beta Al_2O_3 \cdot 3H_2O$)
Boehmite ($\alpha Al_2O_3 \cdot H_2O$)
Diaspore ($\beta Al_2O_3 \cdot H_2O$)
Corundum (αAl_2O_3)

It has been determined that of these oxides, boehmite ($\alpha Al_2O_3 \cdot H_2O$) had the stability and the cohesive and adhesive properties necessary to act as a wettable surface layer for adhesive bonding of aluminum

alloys. Boehmite forms in hot acid treatments and in acid electrolytic anodization processes.

Since bayerite ($\beta Al_2O_3 \cdot H_2O$) is the predominant, naturally occuring oxide and since we find it is not the strongest material to bond to, it must be removed prior to any step involving prebond surface treatment. Therefore, subsequent to the initial cleaning process that removes any scale, dirt, grease, grime, or other contamination, it is required that the aluminum alloy be deoxidized; that is, we dissolve off the unwanted oxide prior to forming the specific oxide desired for bonding.

The old standby FPL or sulfuric acid sodium dichromate etch has been utilized to produce the boehmite ($\alpha Al_2O_3 \cdot H_2O$) with varying degrees of success for many years. Certain production problems have been encountered in obtaining reproducible bonding with the FPL etch. First, it is a complex chemical solution requiring strict chemical control because it is sensitive to the levels of the many variables involved and the bath is easily contaminated. Good and poor surface preparations are separated by a hairline in using this process. The FPL etch produces a thin coating or layer of boehmite (100–400 Å), which in itself possesses poor stability to moisture or other corrosive attack, primarily because moisture has easy access to the base metal under the thin oxide layer. However, in conjunction with optimized FPL procedures and corrosion-inhibiting primers, very strong and durable bonded joints can be prepared. Optimized FPL etch procedures involve very hot etch baths (180°F and up), control of the dissolved aluminum and copper in the bath, and immediate rinse upon removal from the etch bath. It has been found that the FPL etch treatment followed by a seal in a boiling water solution of sodium dichromate produces a much thicker oxide layer that demonstrates significant resistance to moisture attack. It has also recently been found that the FPL bath can easily be poisoned by small amounts of various chlorides and other contaminants. Anodization techniques, as previously mentioned, also strongly favor the boehmite formation. We have had experience with several different processes.

Sulfuric acid anodizing provides perhaps the best form of corrosion protection for aluminum and is also very receptive to many epoxy adhesives. In the development of the adhesive bonding system for the C-5 this process was investigated extensively. A serious weakness was disclosed which prevented its use in the bond lines of this aircraft. The problem involved a separation of the anodic oxide layer from the base metal during adhesive peel testing at low temperatures. It is understood that recent work by some researchers has shed some light on this problem, and its solution may not be too far away.

Chromic acid anodizing has been utilized as a prebond surface preparation treatment for aluminum alloys for many years. This surface

treatment method was investigated extensively by Lockheed-Georgia Company on the C-5 program and was selected for use on all production bonding on the C-5 aircraft. Service performance of bonded structure on the C-5 to date has been very good. The chromic acid anodize does not provide the inherent corrosion or salt spray resistance provided by the sulfuric acid process. However, in combination with a corrosion inhibiting primer, outstanding corrosion resistance is obtained. There are many versions of the chromic acid anodize process; some use a chromate rinse and others a water rinse. Good results have been achieved with these procedures.

Phosphoric acid anodizing is a process recently developed by the Boeing Company under the direction of the late Dr. B. Bethune. The inherent simplicity of this process and the demonstrated durability and reproducibility of adhesive bonds formed using this procedure make it a natural for future production considerations. Bonds prepared using this process consistently outperform all other known methods of surface preparation in tests involving combined heat, humidity, and stress.

Data presented by Dr. Bethune at a recent SAMPE symposia and data generated by the AFML confirm that phosphoric acid anodizing is perhaps the best prebond surface treatment for aluminum alloys developed to date. Oxide layers produced by anodization are in general thicker (2000–4000 Å) and more uniform than those provided by the FPL etch. However, the most significant factor associated with the phosphoric acid-oxide films is their outstanding resistance to hydration by water. This resistance to hydration precludes the weakening of the oxide and the resulting delamination of the bonded structure under stress. The phosphoric acid anodize layer itself again, as in the chromic process, does not provide maximum corrosion protection and, therefore, must be combined with a corrosion-inhibiting primer for optimum results. Our work has shown that the anodizing treatments as compared to FPL etch provide enhanced environmental durability, but do not change the initial unexposed mechanical properties of the bonded specimens. Likewise, initial unexposed climbing drum peel values do not change. The other strong advantage we see for the anodizing processes is their relative simplicity compared to FPL etch, very low scatter and very good reproducibility in the bonded joint test data.

CONCLUSIONS

From our failure analysis work we have concluded that service bond delaminations are the result of combined low stress, heat, and moisture working on an unstable metal oxide surface preparation.

Serious bond-line corrosion is a secondary effect to interfacial failure and occurs after disbond.

The surface preparation of aluminum prior to bonding is the single most critical aspect affecting bond durability. Anodizing surface preparations (specifically, chromic and phosphoric) in conjunction with corrosion-inhibiting primers provide superior environmental durability compared to FPL etch.

Anodizing surface preparations (specifically, phosphoric acid anodize) are suited to production applications due to their inherent simplicity, relative insensitivity to operating variables and parameters and low cost.

SUMMARY

Recent work in the area of prebond surface preparations for aluminum alloys and specifically, work designed to reveal exactly what the chemical nature and stability of the surfaces produced has produced extensive improvements in the state of the art of adhesive bonding. In addition, the development of test techniques that duplicate our service failures have led to an understanding of our past service problems. We now understand better the characteristics required in good surface preparation for the prebond treatment of aluminum alloys.

Anodizing surface preparations in combination with corrosion inhibiting primers have produced, in the laboratory, bonded specimens with greatly reduced scatter and variability in properties data as well as greatly increased resistance to environmental degradation and corrosion. As a result of these advances in the state of the art, the USAF is expending considerable effort to develop, design, and test aircraft structure utilizing adhesive bonding in primary structural applications.

9. POLYMER-CERAMIC INTERFACES

G. R. KRITCHEVSKY and D. R. UHLMANN
Massachusetts Institute of Technology
Cambridge, Massachusetts

An understanding of the nature of a polymer-ceramic interface necessitates a thorough understanding of the surfaces of these materials. Surface characteristics are discussed in terms of surface chemistry and physical methods for studying the surface. The effects of environmental conditions and surface treatments upon wetting and adhesion, silane coupling agents, and models of their methods of coupling are reviewed. Although a combination of these models seem to describe the bonding in a thermoset composite fairly well, the theories do not well describe the behavior of thermoplastic systems. The need for silanes with the ability to entangle with as well as bond to the polymer is suggested. These would be analogs to the new titanium-based coupling agents, which are also reviewed.

INTRODUCTION

Areas of technology involving polymer-ceramic interfaces have been ones of intense activity in recent years. These areas are typified by the use of glass fibers in epoxy- or polyester-matrix composite materials, but also include areas such as the use of polymeric adhesives to bond ceramics and broad field of polymers filled with particulate ceramics. Perhaps more important than past activity in the field is the substantial growth which seems to be destined for materials based on polymers and ceramics used in combination. If this destiny is to be fulfilled, it will be important to achieve improved understanding of the chemistry and structure of polymer-ceramic interfaces and of the interactions which are critical to their behavior.

The present chapter will be concerned with the salient features of polymer-ceramic interfaces and with the modifications which can be made to improve adhesion and provide composite materials with improved engineering properties. The general nature of surfaces and their importance in the joining of materials has been reviewed in other

chapters of this book, and need not be repeated here. It seems appropriate, however, to begin with a few specific comments on the surface characteristics of polymers and ceramics.

This area has been one of renewed interest in recent years because of the development of new techniques which, particularly when used in combination, offer the promise of providing important new insight into surfaces and surface phenomena. These techniques include ESCA and Auger spectroscopy, ion microprobe mass spectrometry, fast Fourier transform spectroscopy, and scanning electron microscopy.

From results obtained on polymers and ceramics, one principal fact seems to have emerged — viz., that the surfaces of these materials usually differ both in chemistry and structure from the bulk. Such differences render hazardous any attempt to discuss surface-related phenomena in terms of the bulk characteristics of the materials. Lacking detailed characterization of the surfaces, however, resort must often be made to such rough approaches.

Two examples will suffice to illustrate the differences between surface and bulk characteristics and the importance of these differences to scientific understanding and technological applications. The first is provided by electron microscope observations of heterogeneities — termed nodules — in a number of nominally glassy polymers (see References 1 and 2 for summary and discussion). These nodular structures, observed on a scale of 30–200 Å in volume fractions approaching 50%, were interpreted as regions of locally high order in the materials. The existence of these structures seemed inconsistent with the model of random (Gaussian) coils as the morphology of bulk amorphous polymers; and their observation led to the suggestion of alternative structural models — with important implications for the rheological and mechanical properties of the materials.

The results[3,4] of small-angle neutron scattering studies of several polymers in which nodules were reported indicate, however, radii of gyration of the molecules in bulk polymers which are within experimental error identical to those of the same polymers in θ solvents (where the molecular configuration is generally agreed to be that of a random coil). Further, small-angle X-ray scattering (SAXS) studies[5,6] of a number of these polymers have indicated levels of inhomogeneity in the materials which are little more than those corresponding to thermal density fluctuations frozen in at the glass transition. Such fluctuations are expected for all materials; and the SAXS studies have therefore been taken as indicating random, amorphous structures.

The electron microscope observations were, however, made by competent investigators; and the question must be asked: if the nodular structures are not representative of the bulk material, what do they rep-

resent? The tentative answer, advanced previously in several papers,[5,7] is that the nodules represent surface features of the polymers. These features, and the structural inhomogeneity which they indicate, may well be significant to many surface-sensitive properties of the materials; and their characterization may provide a notable area of investigation in the coming years.

The second example is provided by the chemistries of oxide glasses exposed to various environments, and in particular by the chemistry of soda-lime-silicate glass exposed to an SO_2-SO_3 atmosphere. Such exposure has been known for many years to produce glasses with improved chemical durability. The standard explanation for this behavior[8] appeals to the depletion of sodium ions from the surface regions. The depletion was associated with the formation of sodium-sulfur-oxygen complexes, whose vaporization leads to the indicated depletion of alkali ions. On this basis, a gradient in sodium ion content with distance into the sample from the surface would be expected.

Such a gradient in sodium ion concentration has been observed in recent ESCA studies[9] in which successive layers of material were removed by bombardment with rare gas ions. Not expected, however, was the marked depletion of calcium ions from the surface region which was also observed. The origin of this depletion has not been explained in satisfactory detail, but may well involve the formation and vaporization of calcium-sulfur-oxygen complexes or even sodium-calicum-sulfur-oxygen complexes. In any case, it seems clear that the notable increase in chemical durability produced by the sulfur treatment is associated with the marked depletion of sodium and calcium in the near-surface region.

The general subject of chemical differences, and structural differences as well, between the bulk and surface regions of polymers and ceramics could readily occupy our entire chapter. For reasons of space, however, we shall simply note that such differences constitute a complicating factor which should be kept in mind, and that the interpretation of many results may require modification as new information becomes available on the surface chemistry and structure of the materials investigated.

INTERFACES AND ADHESION

Perhaps the most salient features of polymer-ceramic interfaces are the nature of the adhesive bonds formed between such disparate materials, and the dependence of such bonds on chemistry, preparation techniques, and environmental factors. In many uses of composite structures formed from these materials — *e.g.*, in automobile windshields — the

desideratum is not the greatest achievable strength of the adhesive bond, but rather a controlled degree of adhesion. The ability to provide adhesive bonds of desired strength, like that to provide bonds of the highest possible strength, depends ultimately upon the understanding and control of the chemistry and structure of polymer-ceramic interfaces. As shall be seen from the discussion to follow, our understanding in this area leaves much to be desired; and the area should be a fruitful one for research over the coming decade.

Wetting

A number of factors have been suggested as important in the development of good adhesive bonds. Among these, wetting of the adherend by the adhesive has received perhaps the widest attention. Such a wetting is often discussed in terms of the critical surface tension, γ_c, introduced by Zisman and his co-workers.[10] This factor is usually defined by the relation:

$$\text{Cos } \theta = 1 + b(\gamma_c - \gamma_L) \tag{1}$$

where θ is the contact angle of the liquid (adhesive) on the adherend surface and γ_L is the surface energy of the liquid-vapor interface.

The critical surface tension of a given surface is then evaluated by determining the contact angle made by various liquids (of known γ_L) brought in contact with the surface, and plotting cos θ vs. γ_L. Such a plot for a variety of liquids on polytetrafluorethylene at 20°C is shown in Figure 1. From the data shown there, a γ_c value of 18.5 ergs cm^{-2} is

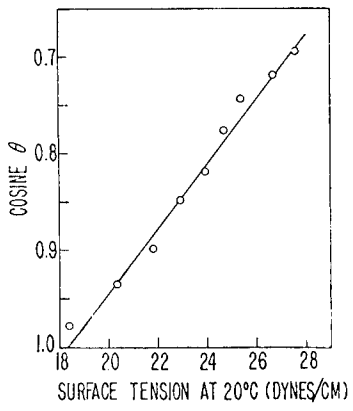


Figure 1. Critical surface tension of polytetrafluorethylene determined by contact angles of a series of n-alkanes.[10]

inferred. The work of adhesion can be related to γ_c and γ_L, and on the basis of equation (1) displays a maximum at

$$\gamma_L = \frac{1}{b} + \frac{1}{2}\gamma_c \tag{2}$$

The work of adhesion at this maximum increases with increasing γ_c.

For complete wetting, the adhesive must have a surface tension lower than the critical surface tension of the adherend. Although the surfaces of most glasses and crystalline ceramics have high critical surface energies (in the range of hundreds of ergs cm^{-2}), they tend to be hydrophilic and adsorb one or more layers of water. For smooth, clean surfaces of aluminum, iron and silica (both of which are surface oxides) as well as SiO_2, the equilibrium thickness of surface water approaches 20 molecular layers at ambient temperatures and humidities.[11]

In the treatment of the wetting of high energy surfaces such as these and other oxide ceramics, specific attention must be directed to changes in the surface energy of the solid upon exposure to the environment. In terms of the simple model discussed above, the development of hydrated surface layers lowers the γ_c and decreases the ability of the adhesive to wet the surface — and it has been shown that a layer of water only one molecule thick has a very strong effect upon wetting.

Water is adsorbed on the surface of oxides such as SiO_2, FeO_3, and Al_2O_3 in the form of hydroxyl groups (R-OH) and as molecular water bonded to the surface hydroxyls. The chemical characteristics of the hydrated surfaces are quite different for different oxides, depending significantly upon the acid-base character of the surface and hence upon the ionic-covalent character of the metal-oxygen bond. For a given material, however, the surface behavior may be dominated by the chemistry and perfection of the surface sites.

The interaction between ceramic oxides and organic adhesives has been discussed by Bolger and Michaels[12] in terms of the ionic character of the hydrated oxide surface and the organic functionality of the adhesive. The ionic nature of the oxide surface was described by its isoelectric point (IEP), *i.e.*, the pH of the aqueous solution in which the surface exhibits no net charge. The IEP is highest for metals of low valence such as the alkaline earths and lowest for metals of high valence such as Si, W, and Ti. For the case of nonpolar adhesives, this analysis predicts that both hydrogen bonding and ionic bonding would be negligible and dispersion forces should be predominant. It also predicts that certain organic functional groups such as carboxylic acids and amines should form bonds to the oxide surfaces (both high-IEP and low-IEP) which are relatively insensitive to water. The analysis also describes the role of standard etching treatments with oxidizing agents in terms of their ef-

fects on the surface characteristics of the oxides, including a decrease in the IEP of the surfaces.

It has been noted by several authors that the surface chemistries of multicomponent oxide glasses differ significantly from those of the single-component oxides; and these differences significantly affect the adsorption and wetting behavior. For example, powders of multicomponent oxide glasses adsorb much more water than an SiO_2 powder of similar surface area.[13] The adsorbed layers on such glasses are generally quite alkaline; this indicates an exchange of alkali and alkaline earth ions for protons from the water, which can place the surface of the glass in tension. Adams *et al.*[14] showed that the glass surface could be put under compression, thereby strengthening the glass fiber and the composite, by exchange of surface Na^+ with larger cations such as K^+ or Ba^{+2}.

Adsorbed water is capable of surface diffusion. Mould and Southwick[15] and Charles and Hillig[16] showed that oxide glasses are weaker in a wet environment than in a dry environment at temperatures above about 75°K, and proposed that water at the tip of the crack hydrates cations which then hydrolyze siloxane bonds and thereby propagate the cracks.

The roughness of the solid surface is an important parameter which affects the wetting behavior. Thermodynamically, the effect may be described in terms of the ratio, r, of the true surface area to the surface area of a smooth surface. In these terms, the contact angle θ_r of a liquid on a surface of roughness r can be related to that on a smooth surface as:

$$\cos \theta_r = r \cos \theta \tag{3}$$

It is apparent from this relation that spreading (wetting) is promoted by roughening the surface. Such roughening can readily be effected for ceramics in plate form, but is not easy to accomplish for fiber geometries.

Surface Condition and Surface Treatment

Johannson[17] showed the effects of cleaning on the contact angles of water with an E-glass (a lime-alumino-borosilicate glass) surface. The contact angles of water upon an E-glass surface with no prior treatment are between 45° and 60°. Heat cleaning reduces this angle to 16°, allowing better wetting and formation of a better bond. Cleaning with acid produces a surface that is completely wet ($\theta = 0°$); but upon aging overnight the contact angle increases to about 16°. This likely reflects the adsorption of water.

The adhesion between oxides and polymers is usually found to have low stability in wet environments. The vulnerability of the ceramic-

polymer interface to water attack results from flaws near the interface created by incomplete wetting that can become migration paths for adsorbed water to the interface. Such water will hydrolyze interfacial metal-oxygen bonds and cause adhesive failure. A range of finishes on the glass have been tried to improve wet strength of glass-resin composites. Originally, it was expected that these finishes would provide a water-resistant barrier at the interface. Finishes containing chromium, zirconium and nickel complexes, silanes, and titanium halides have all been explored in some detail. Of these, the chrome complexes such as Volan and the silanes have proved the most generally useful.

Volan can be represented as a chromium chloride coordinated with methacrylic acid (Figure 2), and is useful with polyester-glass and epoxy-glass composites. The reaction of Volan with a glass surface is thought to take place between the chromium on the Volan and the surface SiOH on the glass. It is thought to react with the resin through its unsaturation which enters into copolymerization with the resin.

The titanium halides have been found to decrease the strength of glass fibers to which they are applied, while the nickel and zirconium complexes generally represent poorer adhesion promoters than the chromium complex. In contrast, the silanes can significantly increase the wet strength of polymer-ceramic bonds, and can also significantly increase the bond strength in a dry environment.

For purposes of comparison, silane-coated glass surface has a contact angle with water of about 20°; after heat treatment at 125°C, this increases to about 70°. Heat treatment at this temperature causes the silane coating to cross link; hence the small contact angle of the as-coated silane is likely due to water soaking into the open silane structure. Presumably resin can also soak into an as-deposited silane coating. The chemical structure of this and other silanes can be represented as X_3 –

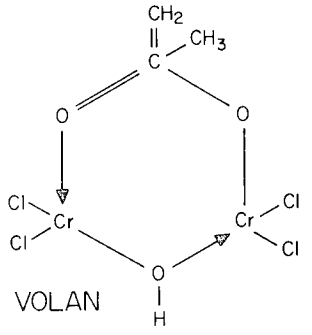


Figure 2. Volan.

$S_i(CH_2)_n - Y$ where X is a hydrolizable group, n varies from 0 to 3, and Y is an organofunctional group that is capable of bonding to the resin.

In general the silanes seem to decrease the γ_c's of glass surfaces, such that the silane-treated surface will not readily be wet by the adhesive or resin coating. It has been shown, however, that some silanes known to be effective as coupling agents — such as vinyl trimethoxy silane and γ (methacryloxy)-propyltrimethoxy silane (γ_c = 25 and 28 ergs cm^{-2}, respectively) produce low-energy surfaces, while some silanes that are ineffective as coupling agents, such as bromophenyl trimethoxy silane, produce relatively high-energy surfaces (γ_c = 43.5 ergs cm^{-2}).

The critical surface tensions of silane-coated surfaces can be reasonably well related to the polarity of the organofunctional group on the silane, *i.e.*, the Y group, as well as to the solubility parameter of this group. Hence, the chemical structure of the organofunctional group not only influences bonding to the resin, but also determines how well the resin will wet the silane-coated ceramic material. Similarly, if one is interested in bonding a ceramic to a resin through a nonpolar organic group which would produce a small γ_c if the silane were applied directly to the ceramic, it may be advantageous to blend the silane into the resin where it would not strongly affect the wetting of the ceramic by the resin.

It might be expected that if a freshly prepared ceramic surface could be coated with a layer of resin before it had a chance to adsorb a layer of water or any other impurity, a high-strength bond would be formed because the ceramic would have a high-energy surface. To explore this hypothesis, A. O. Smith Corp.[18] formed a clean glass surface by cleaving a glass in the liquid resin. The strength of the bond was found, however, to be poor and similar in quality to bonds with chemically cleaned or water-contaminated surfaces or surfaces without silane coupling agents. This result suggests that one or more of the contaminants adsorbed upon the glass surface upon exposure to the atmosphere enters into the bonding and is necessary for a strong bond. If this is so, it seems likely that adsorbed water is the important "contaminant" for bonding.

By starting the resin cure in a vacuum and releasing the vacuum when the resin is fluid, complete wetting can be obtained even if the calculated contact angle is greater than 0°. The vacuum technique is effective by decreasing the pressure of the voids at the interface, so that when atmospheric pressure is restored to a fluid resin, the volume of the air bubbles is reduced by a factor inversely proportional to the vacuum achieved.

The driving force for the displacement of air from the interface is the decrease in surface area resulting when the air coalesces into spherical bubbles. The opposing force is the work of displacement for the air.

In addition to thermodynamic considerations, the displacement of air from the interface is also affected by the viscosity of the resin. If the resin does not become fluid at the temperature of the cure, the air cannot be displaced even if $\theta = 0$.

Silanes do inhibit the wetting of a surface, although it has been shown[19] that after primary bonding considerations are provided for, the surface with a silane coating that is better wetted by the resin will form a stronger and more permanent bond.

In a study of air entrapment in adhesive films, Bascom[20] reports that as an adhesive joint is cured with heat, the air coalesces into bubbles at the surface which are then displaced into the liquid adhesive. If the contact angle is greater than 0°, however, the air will not be displaced from the interface. Air at the interface is detrimental to bond life because it serves as a stress concentrator and leads to crack initiation.

A clean glass surface in contact with an uncured layer of adhesive normally exhibits a transluscent or transparent interface; but after curing the interface often becomes opaque. This is due to cracks and crazes at the interface, which are usually associated with thermal stresses developing upon cooling because of the differences in thermal expansion between the resin and the glass. When a good coupling agent such as an appropriate silane is used, the interfacial region is translucent in appearance. The silane must therefore provide some relief for the thermal stresses. It should be noted, however, that a certain amount of interface debonding is beneficial in absorbing energy when the composite would fracture in a brittle manner without such debonding.

The presence of some water at the interface is necessary for the silane to be effective. Specifically, unless there is sufficient water present to hydrolyze silane-alkoxy groups, the silane is completely ineffective as a coupling agent. Erickson[21] deposited silane from two organic-based (nonaqueous) solvents, a freon-based solvent and xylene, both of which he dried before use. He then exposed dried glass fibers to varying degrees of humidity, coated them with chloro-silanes from dilute solution and measured the strength of the composite formed. From both solvents, the coverage of silane corresponds to approximately one monolayer in thickness.

It was found that at relative humidities of 50% and below the composite strength is significantly less than at higher humidities. Unless all three alkoxy groups on the silane need to be hydrolyzed and moved to the glass surface, it is not clear why such a small decrease in the water content on the surface should so drastically affect the composite strength.

Plueddemann *et al.*[22] made two series of fumarate-based silanes. The first series had an allyl fumarate capable of reacting with the resin, with the number of alkoxy groups on the silane varying from one to

three. The second series employed a group of dialkyl fumarate-based silanes. Their results, shown in Figure 3, indicate that silane molecules with more alkoxy groups and with the ability to form more than one bond to the glass surface provide better coupling, provided there is no interference from the brittleness or inflexibility of the silane.

Surface Chemistry and Silane Coupling Agents

Although organo-silanes have been used successfully as glass-resin coupling agents for the past 15 years, there is no satisfactory general explanation for their method of coupling. A number of suggestions have been offered, which if combined seem to account for the most of the observed phenomena.

The marked effect of these coupling agents on adhesion suggests that understanding the nature of silane coupling may provide improved understanding of the mechanism of adhesion in general. A satisfactory model for the action of the silane must be capable of describing several characteristics of the interface, including:

1. The surface chemistry. If the coupling agent bonds chemically to the glass and resin, the coupling agent must have functional groups capable of reacting with functional groups on the glass and the resin. These reactions must be describable by a satisfactory theory.

2. Morphology of the polymer at the surface. An acceptable theory must predict the structural differences which are seen or inferred between bulk polymer and interfacial regions.

3. Differential shrinkage at the interface. The theory must also describe the development and relaxation of the stresses which arise on cooling from the temperature of cure and are associated with differences in the coefficients of thermal expansion between resin and glass.

4. The action of water. Perhaps the most difficult task for the theory of coupling agent adhesion is the prediction of the role of water, both in forming and destroying the bond.

The model with the strongest support is the chemical bonding theory. This theory states that a successful coupling agent is one that has the ability to bond chemically to the glass surface through covalent siloxane bonds. In addition, the silane must have a functional group capable of reacting chemically with the resin (if such bonding occurs, the coupling agent becomes part of the resin).

If the silane is not capable of chemical reaction with the resin, the strength of the resulting bond is about half that which results if such bonding were possible. The partial increase in strength which is observed with silanes which bond only to the glass or ceramic may be due to a physical adsorption or entanglement of the silane in the resin, and

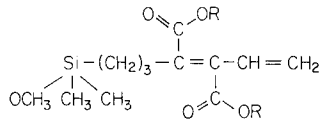
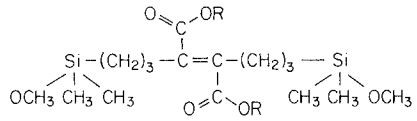
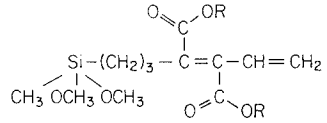
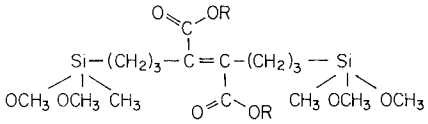
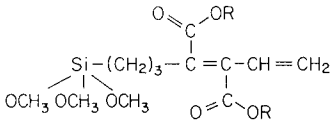
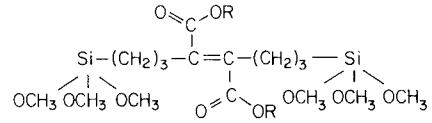
	Flexural Strength	
	DRY (psi)	WET (psi)
 $CH_3OSi(CH_3)_2(CH_2)_3$ Allyl fumarate	 91,500	90,800
 $[CH_3OSi(CH_3)_2(CH_2)_3]_2$ Fumarate	 81,500	66,300
 $(CH_3O)_2SiCH_3(CH_2)_3$ Allyl fumarate	 96,700	90,700
 $[(CH_3O)_2SiCH_3(CH_2)_3]_2$ Fumarate	 82,300	79,900
 $(CH_3O)_3Si(CH_2)_3$ Allyl fumarate	 82,100	70,100
 $[(CH_3O)_3Si(CH_2)_3]_2$ Fumarate	 87,900	79,200

Figure 3. Flexural strengths of a series of fumarate-based silanes.[22]

should decrease after a period of time as physically adsorbed silane diffuses away from the interface. Such a bond would be less stable toward water attack than a bond formed with a reactive silane.

Studies of glass-coupling agent-resin interfaces using laser Raman spectroscopy[23–25] suggest that chemical bonding does occur at such interfaces. Fibers of both E-glass and SiO_2 were immersed in a 2–3% solution of vinyltriethoxysilane [$(CH_3\ CH_2\text{-}O)_3 - Si\text{-}CH = CH_2$] and dried. By comparing the Raman spectra of the treated fibers with spectra of both the silane and the polysiloxane, it was found that the silane polymerized as it absorbs on the glass.

In assessing these results, it should be noted that the silanes are usually applied from aqueous solutions at a pH of about 4. Under these conditions, hydrolysis to silane triols is very rapid but polymerization is slow. Precipitation occurs after a few hours, at a point where about 1/3 of the silanol is still in monomeric form and the remaining 2/3 consists of dimers, trimers, and tetramers.

For the silane-sized E-glass and the silane-sized SiO_2, an absorption band appears at about 1085 cm^{-1}. This band is not present in the Raman spectra of the polysilane, the uncoated glass or the silica, and has been related to Si-O bonding at the glass-silane interface.

If a sample of polyvinyl siloxane is allowed to react with chlorine, the 1600 cm^{-1} absorption of the C = C unstaturation disappears completely, indicating essentially complete reaction of the vinyl group. If, however, the coated glass is reacted with chlorine, the C = C vibration decreases in magnitude. This indicates that a portion of the vinyl groups are not available for reaction, presumably because the polymeric nature of the silane coating shields some of the vinyl groups from reaction.

After the glass fibers were coated with silane, methyl methacrylate was polymerized onto the surface. From the ratio of siloxane vinyl groups to Si-O groups one should be able to estimate the fraction of unsaturated siloxane that has reacted with the methyl methacrylate. This should depend upon the fraction of surface chemically bound to the resin but is also a function of a number of mers in the siloxane polymer. Such estimates were developed by the authors of the laser Raman study; but the results are subject to considerable uncertainty. It should also be noted here that commercially produced fiber glass is normally coated with a finish that contains a majority of binder and lubricant and only enough silane to form a one monolayer coverage.

A second model for the role of silane coupling agents is known as the restrained boundary-layer theory. According to this model, in order to transfer stress uniformly, the boundary layer between the high-modulus reinforcement and the low-modulus resin should have a modulus intermediate between the two. Although the silane coating itself may be

only several monolayers thick, the polymer adsorbed on the coating is packed more tightly about the reinforcing filler than in the bulk polymer. The spatial orientation of polymer molecules has been suggested[26] to extend as much as 1500 Å into the polymer from filler particles of TiO_2 in an epoxy resin.

In other work, silane coupling agents have been used to orient liquid crystals[27]. The two silanes employed were (see Figure 4) N-Dimethyl-N-octadecyl-3-aminopropyltrimethoxysilyl chloride (DMOAP) and N-Methyl-3-aminopropyltrimethoxyl silane (MAP). Linear liquid crystals were observed to orient perpendicular to DMOAP coated surfaces but parallel to MAP coated surfaces. Helical liquid crystals, however, orient parallel to a DMOAP surface and perpendicular to a MAP surface. It has also been shown[28] that the crystalline morphology in the regions adja-

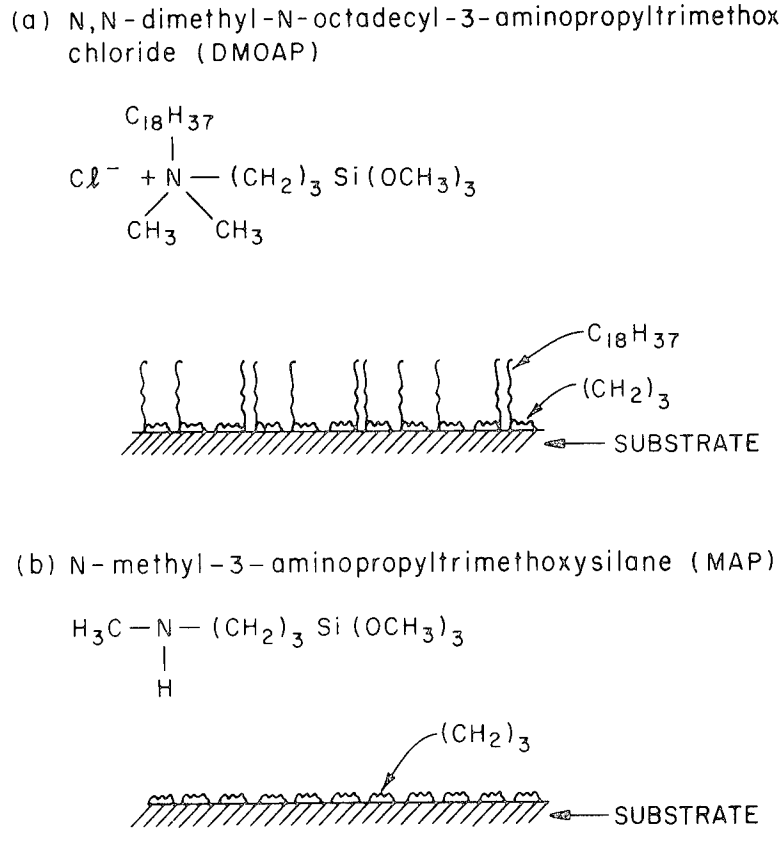


Figure 4. Orientation of two liquid crystals on a substrate.[27]

cent to silane-treated glass fibers in Nylon 6 is markedly different from that in the bulk polymer.

While the concept of distinct boundary layers is thus supported by experimental data, the specific restrained boundary-layer model cannot satisfactorily account for the different thermal stresses which are produced upon cooling in the resin and the glass or other reinforcing filler.

Another model of some merit is the so-called deformable layer theory. According to this model, the differential stresses which arise on cooling are taken up by the polysiloxane. The siloxane polymer seldom extends, however, more than 10 to 20 monomer units, which would be too thin a layer to absorb these stresses. This difficulty is somewhat mitigated by considerations such as the following: When an amine cured epoxy is placed in contact with a silane, the silane can preferentially absorb amine, thereby creating a thicker stress-absorbing interface layer with a gradation in properties.

The reversible hydrolyzable bond model combines the principles of the chemical bonding theory with the ability of deformable layers to accommodate thermal stresses and the rigid interface of the restrained layer theory. According to this model, once the silane is hydrolyzed into a silanol it is able to compete with the water molecules at the surface because it has a very strong ability to hydrogen bond. The silanol can either bond directly to the metal or silicon at the surface through an oxane bond or it can bond through an intermediate water molecule by a hydrogen bond (see Figure 5). Both of these are reversible reactions. If both the glass and the resin have rigid surfaces, a bond may break, but the reactive groups from the broken bond will have no place to go. Hence either the original bond may reform, or if the sample is under stress a new bond may be formed with an adjacent group. This process would serve as a method of relaxation for the stresses introduced upon cooling the composite. The model can also explain the ability of silanes to form strong bonds to metal oxides even though these bonds are known to have poor hydrolytic stability.

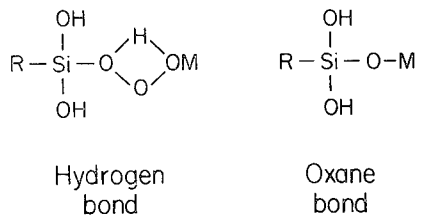


Figure 5. Two models for silane bonding on a metal or glass surface.[22]

The bonding of an epoxy resin through a hydroxyl group to a hydrophilic surface can be explained by the same mechanism. The equilibrium for bond retention is less favorable here than for a silanol; but if the concentration of the hydroxyl groups at the surface is sufficiently large, a water-resistant bond can be formed. Ester and amide groups can also hydrogen bond; but equilibrium conditions are not favorable for bonding. Hydrocarbons and nonpolar resins in general can bond to a hydrophilic surface only by weak dispersion forces and cannot compete with water for a specific surface site. Therefore one would expect a silane to improve adhesion to a nonpolar resin to a larger extent than to a polar resin.

This seems to explain the results of Vanderbilt,[29] who measured the wet and dry flexural strengths of polymers bonded to heat-cleaned and silane-treated glass. He found no improvement in the dry strength and a small improvement in the wet strength of the epoxy composite with silane treatment. In contrast, silane treatment of a polyester composite produced a substantial increase in the dry strength and a large increase in the wet strength. After silane treatment, the dry and wet strengths of all the composites are nearly 80,000 psi, implying that the bond strength is not affected by water when the silane is present and is not dependent upon the resin. Hence it is likely that breakage of the glass-silane bond is the limiting factor in the measurements of composite strength.

If bonding takes place to a polymer surface that is not rigid, it is more difficult to form a hydrolytically stable bond. According to the reversible hydrolyzable bond theory, if small areas of the polymer can pull away from the interface as their surface bonds are hydrolyzed, the bond on a macroscopic level will fail. This hydrolyzed polymer surface will have retracted from the glass and will not be available for bonds to reform. In order to bond to a flexible material, it must be possible to make the surface rigid. This is sometimes done by putting a rigid primer on the surface of the polymer. A method that is more convenient involves using excess silane which will diffuse into the polymer and possibly serve to cross link or orient the polymer surface. Peroxide or other cross-linking agents can also be used.

The basic concept of the reversible hydrolyzable bond model is that the interface is characterized by dynamic bonding. In the presence of water, the bonds are in equilibrium with respect to breaking and reforming. The silanes are not the only materials which can form hydrolytically stable bonds, but other materials do not form hydrogen bonds that are as strong and the equilibrium favors water in the other cases. It is thus a question of the degree, not the type of bonding which is involved.

To investigate the physical nature of the adsorbed siloxane film, Schrader *et al.*[30] carried out experiments in which γ-aminopropyl trieth-

oxy silane [$(NH_2\text{-}CH_2\text{-}CH_2\text{-}Si(O\text{-}CH_2\text{-}CH_3)_3$] was deposited from aqueous solution on Pyrex and E-glass surfaces. Attempts were made to extract the APS from the surface, and the amount of silane remaining on the glass surfaces was monitored by radioactively tagging the gamma carbon. From the variation of silane remaining on the surface with time of extraction, three distinct types of APS adsorbed on the surface were inferred. The first was physically adsorbed and was not removed by washing the surface with benzene; it was, however, hydrolyzed and remained by cold water. This fraction comprised about 98% (about 270 monolayers) of the adsorbed silane. The second fraction (about 10 monolayers) was removed by boiling the sample for 3–4 hours in water. Electron microscopy after a short period of boiling revealed islands of silane present on the surface, which may be associated with hydroscopic sites on the surface of the glass. The remaining APS (about 1 monolayer) is not removed by boiling water. It seems very likely that this final fraction is so tightly bound either because it is cross linked within itself or because it is multiply bound to the glass surface. The latter explanation seems more plausible.

To determine the location of bond failure, glass surfaces were coated with APS and an epoxy interlayer as an adhesive.[30,31] The sample was then pulled in a wet environment until failure occurred and the location of the failure was monitored. A nearly equivalent amount of radioactivity was seen on both fracture surfaces, and it was concluded that the APS is adsorbed as dimers, with both the amine of the other half dimer bound to the resin. The failure was then suggested to occur at the siloxane linkage between the dimer halfs. This suggestion is not, however, well established. Why, for example, should dimers be more stable than monomers or trimmers? And why should the processes of adsorption and fracture occur with such regularity?

Schrader *et al.* also prepared samples in which the amount of APS on the surface was varied by depositing it slowly from organic solvents. The joint life was found to decrease slowly with decreasing APS on the surface until the chemically adsorbed fraction ($\leq$ 10 monolayers) is reached, beyond which a fast linear decrease in bond life with decreasing APS is observed (Figure 6).

It seems, however, that there are two differently bonded types of silane; and the plot of joint life versus initial APS on the surface can be better approximated by two intersecting straight lines. The two lines intersect at about 3 monomers per 100 Å, which is the value calculated for one monolayer coverage. After one monolayer is exceeded, the joint life increases slowly with increasing APS on the surface. A dimer may then have been chosen as having the best joint life because this was the largest amount deposited in the study. After boiling water extraction,

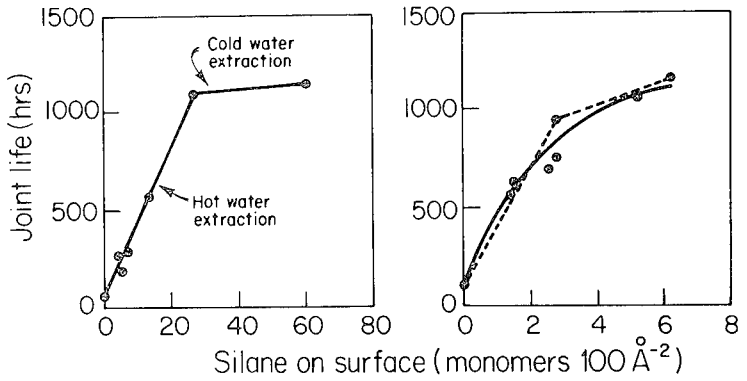


Figure 6. Bond life as a function of silane remaining after extraction and amount of silane deposited from dilute solution.[30]

Schrader *et al.* found about half a monolayer (about 0.25 nanomoles-cm^{-2}) of APS remaining on the surface that could not be removed by the boiling water.

In a study of boiling water extraction of 3 (methacryloxy) propyltrimethoxy silane from E-glass surfaces, Johannson[17] finds that the amount remaining after extraction is independent of the amount initially deposited and equal to 0.5 mmole per 100 m^2, corresponding to a single monolayer coverage. These results provide insight into the manner of deposition of APS on the surface. Silane molecules in the layer closest to the surface have more than one of their alkoxy groups hydrolyzed and are multiply bonded to the glass. The amine group also has an attraction for the glass, and since there are hydroscopic groups on the glass surface and its isoelectric point varies from point to point, some areas of the surface will preferentially attract the amine end of the silane and the silane will be deposited "upside down." The silanol ends of these molecules cannot bond to the resin.

When the bond is pulled apart, the silanes attached to the glass through the amine stay on the glass as the silanes bonded to the glass by siloxane bonds fail by pitting the glass surface. Failure thus occurs cohesively within the glass. The chunks of silane and glass freed from the glass surface remain bound to the resin by fewer than one third the number of bonds that were once made to the glass. Schrader *et al.* find one tenth of the initial radioactivity remaining on the resin surface. When the fraction of APS remaining on the resin is plotted versus the amount initially applied to the glass, a fairly steady value of 7% APS is noted. Exceptionally high values are observed when a monolayer or double layer of silane is initially applied to the surface (Figure 7). Data

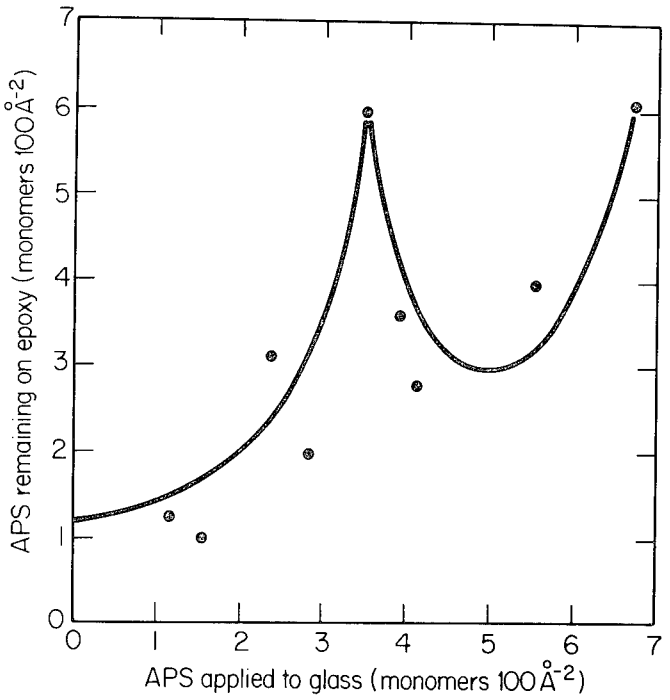


Figure 7. γ-Aminopropyltriethoxy silane remaining on epoxy surface after bond failure.

are not available to determine whether a three-deep layer of APS would also produce better bonding to the resin. It seems, however, that integral layers of coupling agents produce better bonding to the resin; and this should be explored further, taking into account the diffusion of silane into the resin when it is present in excess. Possibly this is happening with the thicker layers, with the diffused silane serving to increase bond life by stiffening the resin near the interface. Fillers can exert a catalytic influence, either positive or negative, on the curing of resins. For polyester, epoxy, and urethane systems, fillers generally lower the cure exotherm of the resin. It has been shown that fillers which allow high exotherms produce composites with the best mechanical properties.

Silane finishes on A-glass, E-glass, and silica have been shown[32] to restore and in some cases increase the cure exotherm above its value for the unfilled resin. It seems that the silane restores reactivity, but it is not necessary that the silane react with the resin to be effective.

Turning to particulate fillers, Ranney *et al.*[33] show that the modulus of an elastomer blend is increased by about 78% by APS when clay, talc, or SiO_2 are used as fillers, by about 52% when TiO_2 or $CaCO_3$ are used,

and by about 30% when no filler is employed. In the last case, the APS likely enters into the resin cure; when the fillers are used, the different improvements may be due to the fact that the APS can adsorb on the surface with either the amine or the siloxane group oriented towards the resin. The group oriented toward the resin will naturally affect its cure. The influence of filler chemistry on orientation of the silanes remains, however, to be satisfactorily elucidated.

Another source of the different effects of different fillers in the presence of silanes may be the following: in the case of SiO_2 and other silicate fillers (which produce a 78% improvement in modulus), the silane bonds chemically to the filler; while in the case of TiO_2, $CaCO_3$ and nonsilicate fillers (that produce a 52% improvement), the silane does not bond to the filler but creates a type of interlocking cage around the particles.

The surface treatments and cleaning solutions applied to glass surfaces prior to bonding will affect the concentrations of the individual cations found on the surface; and the bulk composition will normally be quite different from the surface composition. Wong[34] used Auger spectroscopy to monitor differences between surface and bulk as a function of various acid leaching treatments. He finds that leaching increases the surface available for bonding; but it could also help adhesion by changing the isoelectric point of the surface (IEPS). The silanes have IEPS's of about three and are effective with materials that have an IEPS between two and nine, but are poor coupling agents with surfaces that are alkaline. This approach should be applied to the aminotrialkoxysilanes to determine whether by making the filler surface more acidic one could cause more of the coupling agent to be deposited "right side up."

The reaction between the silane coupling agent and the resin can take several different forms. If the silane has a vinyl organofunctional group, the reaction will tend to be copolymerization and will depend upon the relative reactivities of the vinyl group on the silane and the unsaturatedgroups in the resin. For example, the double bond of the methacryloxy group is 40 times as reactive as a vinyl double bond. Therefore the bonding of a methacryloxy silane to a resin with unsaturated groups will be much better than the corresponding reaction with a vinyl silane. Silanes that have groups such as mercaptosilanes can act as chain transfer agents and thereby bond into the resin. Other silanes with epoxy functionalities can initiate polymerization in the resin.

Since many of the silanes must compete with resin groups to bond, Ranney and Pagano[35] believe that the extent of reaction of the silane vinyl group can be influenced by varying the level of peroxide curing agent. Looking at the modulus of an ethylene propylene diene polymer as a function of silane concentration, one sees that the modulus increases but levels out by about 1% silane with 3% peroxide present.

Increasing the peroxide concentration to 5% increases the modulus as expected; but more importantly, the modulus is just beginning to level out at 2% silane coupling agent (Figure 8).

Hence, at lower levels of curing agent, the resin is not able to take advantage of increased amounts of silane. Increasing the peroxide allows higher levels of silane to be effective, presumably by entering into the cross linking and thereby increasing the bonding. This increase will not continue indefinitely; and it would be interesting to determine the physical basis of the leveling-off of the modulus as a function of silane concentration. What, for example, are the characteristics of the silane coverage when additional peroxide is no longer effective? Can the resin-silane bond be any stronger than if one full monolayer equivalent of silane has reacted with the resin?

A new group of silanes has been introduced which may be useful for studying the relationship between curing agent and coupling agent. These are the silyl peroxides,[36,37] and have the general formula, X_N-$Si(OOY)_{4-N}$. They are unique as silanes since they need not be hydrolyzed to be effective. These silanes still need some reactive functional

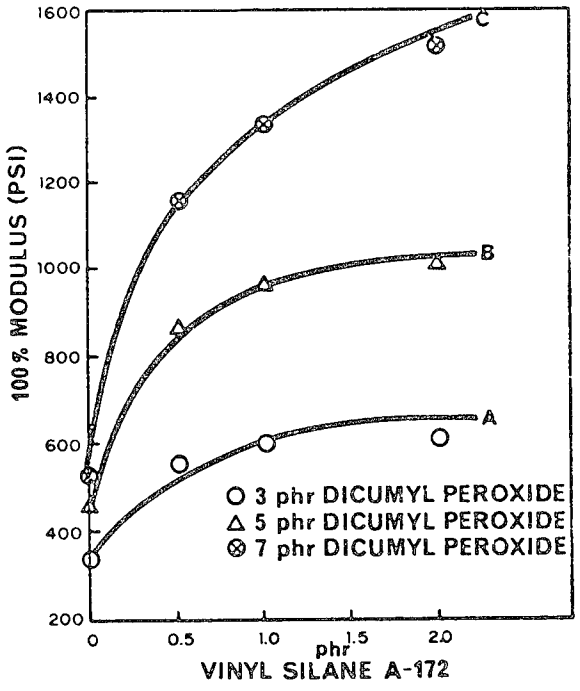


Figure 8. Composite modulus vs. silane and peroxide concentrations indicating more effective use of silane at higher peroxide levels.[35]

group to bond to the resin, but bonding to the glass or to another silane molecule is by temperature-induced decomposition of the peroxy group. The silyl peroxy group is much more thermally stable than the corresponding carbon peroxy (trimethylbutylperoxy) silane.

An interesting matter that remains unexplained and even uncertain is that bonding seems to follow different rules depending upon the size of the interface. For example, Trivisono[38] found that the addition of film-forming resins to silane compositions improve adhesion to the surface of glass blocks but not to glass fibers.

Swanson and Price[39,40] studied a number of silanes applied as integral blend additives in polyurethane adhesives. They find that the peel strength to aluminum as a function of aging time at a fixed temperature and humidity decreases from an initial value, then increases and finally levels off. The initial bond strength is attributed to chemical bonds between the oxide layer on the aluminum substrate and isocyanate groups that have not yet reacted with the curing agent. This initial bond strength is therefore greater when there is an excess of isocyanate. As water diffuses into and through the urethane, it has several effects. First it serves to hydrolyze the silane so it can bond to the substrate. Water also hydrolyzes the isocyanate-oxide bonds at the interface causing interfacial failure. After the silane molecules have been hydrolyzed, the bond strength increases as the hydrolyzed coupling agent orients itself toward the oxide surface and forms covalent bonds.

In this work, the silane was mixed with the isocyanate prepolymer and allowed to age at elevated temperatures prior to curing. In some cases, the viscosity increased beyond the range where the prepolymer was useful. Primary amino and mercapto functional silanes were reacting toward the isocyanate and yet did not have an adverse effect on the viscosity. With these silanes, the bond strength increased dramatically upon aging. Aging allows the the coupling agent to react without having to compete with curing agent for isocyanate. It is also possible that in the absence of aging, a hydroxyl functionality on the curing agent will react with the alkoxy group on the silane, making the silane too bulky to diffuse through the urethane.

As the ratio of prepolymer to curing agent is varied, one will see a variation in the amount of free isocyanate and in the initial bond strength at low temperatures (150°F). At higher temperatures the isocyanate will be cross linked as biuret linkages, and at even higher temperatures as allophanate linkages, lowering the bond strength. At any temperature, increased amounts of curing agent will promote formation of moisture-stable bonds to the oxide surface through OH groups on the curing agent. Hence for the silane to be most effective, it must be allowed time to remove its bulky alkoxy groups by hydrolysis but not enough time or

the right pH to allow silane polymerization which would also prevent migration to the interface.

This study indicates a few of the complications that arise in the reaction processes when a coupling agent is involved. Most studies on other polymer systems do not allow for these complications, and focus primarily on mechanical strength. It seems likely that future work will explain some of the mysteries associated with the use of silane coupling agents in terms of such unexpected chemistry.

When silane coupling agents are used, they are either put directly onto the filler, usually from dilute solution, or blended with the polymer resin. In both cases, diffusion is important. In the integral blend method, the silane must get to the surface to be effective; and in the direct application method, the amount of silane that migrates from the interface and the distance it travels will affect the bond and the properties of the composite.

Of the bonds formed by coupling agents discussed above, the silanol bond has been seen to provide the greatest stability in wet environments. If the bond to a glass or ceramic filler must stand up to other chemical environments, however, some other type of coupling agent may be preferred. The effectiveness of silanes as ceramic-polymer coupling agents is a matter of degree, not the type of bond. Other chemicals with hydroxyl groups can form the same type of bond to a ceramic surface; but the silanol bond competes favorably against hydroxyl bonds for surface sites.

BONDING IN THERMOPLASTICS

The silane coupling agents developed for thermosetting resins have also been shown to be effective in many cases with thermoplastics. With the thermoset, it is widely agreed that the alkoxy groups on the silane are removed, the inorganic reinforcement reacts with the remaining hydroxyl, and the organofunctional group reacts with the thermoset (thereby producing a specificity for a particular silane). This latter reaction does not necessarily apply to thermoplastics, which are polymerized prior to reinforcement.

In bonding to a thermoplastic, a silane with a functional group capable of entanglement with the polymer would usually be desired. A reactive group on the silane is unnecessary, since well-polymerized thermoplastic would have few or no reactive groups (residual unsaturation) with which the silane can react.

When examined in more detail, however, thermoplastics can be divided into two groups in discussing their reactivity with coupling agents. These are termed reactive and nonreactive thermoplastics. The reactive

thermoplastics are polymers which contain chemical functional groups capable of reacting with the functional group as the coupling agent. These thermoplastics include polymers such as polyamides, polycarbonates and nylon, whose reactive functionality is found in the backbone of the chain, and polymers such as polymethyl methacrylate and polyvinyl chloride, whose reactive functionality is found in a pendant group. In all cases, the reactive functionality consists of polar species rather than residual unsaturation. Hence these polymers are expected to show improvements in properties through the use of presently available silanes that can approach — but should not equal — the improvements obtainable with thermosetting polymers, where the organofunctional group of the silane can be polymerized into the matrix resin.

The nonreactive thermoplastics include polymers such as polyethylene, polypropylene, and polystyrene. Such hydrocarbon polymers are not capable of reacting with a silane functional group. For these polymers, entanglement interactions should be required for effective bonding with silanes; but the bonding obtained in these cases should be less effective than that obtainable with reactive thermoplastics.

As an example of the effects which have been observed, consider general purpose polystyrene, which has a flexural strength of about 9500 psi. When reinforced with heat-cleaned fiberglass (E-glass) cloth, the flexural strength is increased to about 24,000 psi.[42,43] The addition of almost any silane increases the strength to some extent. If A-174, the methacryl silane is used, the flexural strength is doubled to about 48,000 psi. In contrast, use of β-carboxyethyltriethoxy silane (which is equivalent to A-174 but lacks unsaturation) results in composites having flexural strengths of only about 23,000 psi.[42] An explanation for these observations remains to be provided, since according to the previous argument, polystyrene is a nonreactive polymer and should not be sensitive to a particular functional group.

As a second example, consider the case of nylon. The flexural strength of this polymer is doubled by reinforcement with fiberglass, and can be doubled again by use of a silane.[42,43] With nylon, many silanes give very good improvements in properties with fiberglass. Comparing the effectiveness of A-1100 (γ aminopropyltriethoxy silane) and Y-2967 [bis(beta-hydroxymethyl) gamma aminopropyltriethoxy silane], it is found that the Y-2967 provides better strengths in wet environments. This should be expected since the Y-2967 silane has both the amino functionality of A-1100 and also a hydroxyl reactive group which should be effective in bonding with nylon. This hydroxyl group can compete with water in wet environments.

As a further example, consider the case of polycarbonate.[43] In general, the behavior of this polymer with silane coupling agents is that which would be expected for nonreactive thermoplastics. Some im-

provement in flexural strength is noted when A-1100 and epoxy-functional silanes are used with fiberglass; but the observed improvements are only about 10–20%. For this material, a significantly greater improvement in properties might be obtained by using a silane which is capable of entanglement.

Polyvinyl chloride[43] shows significant improvements in dry flexural strength (from 23,000 to 36,200 psi) when A-1100 silane is used with fiberglass. In this case, the amine is very likely coupling to the unsaturation produced by dehydrochlorination of the PVC at molding temperatures.

Polypropylene[43] — also a supposedly nonreactive thermoplastic — shows a significant increase in flexural strength when silanes are used with fiberglass (from 13,000 to 22,000 psi with A-1100, and from 13,000 to 20,000 psi with A-174). While these represent significant improvements in strength, they are appreciably smaller than the improvements which can be obtained with thermosetting polymers. If a peroxide is added to the polypropylene, however, greater improvements in strength can be obtained — to the range of 32,000 psi in the case of A-174 silane, for example.

The improvements in strength seen upon the addition of dicumyl peroxide to polypropylene are significant (60%), particularly when compared with the improvements of 10–20% seen by Ranney and Pagano[35] in an ethylene propylene-diene rubber. The 60% improvement in strength upon addition of peroxide to polypropylene implies that there must be some peroxide-initiated bonding between the silane and the polymer. Since polypropylene should not have significant amounts of residual monomer or unsaturation, the free radicals produced may be bonding to the chain ends of the polymer. Since other factors may be operative, this suggestion must be regarded as highly tentative. While the observed effect is a large one, it may be associated with constituents present in small concentrations. For this reason, as well as the potential for optimization and other applications, the area seems to be deserving of further investigation.

Relatively little attention has been directed toward the development of a silane coupling agent for which entanglement plays an important role in the performance. Of the available silanes, the most attractive for purposes of entanglement appears to be a triethoxyoctyl silane. The results obtained with this silane have not, however, been particularly encouraging. It seems, therefore, that the presence of a reactive group in addition to the long chain is required for effective coupling.

Taken in toto, the above results indicate that there are groups in many thermoplastics which are capable of reacting in a specific manner with organofunctional groups in silanes. The observed behavior is, how-

ever, not well correlated with the simple grouping into reactive and nonreactive thermoplastics. The mechanism of bonding in many of these cases remains to be elucidated satisfactorily; and more detailed studies of the relevant chemistries seem clearly indicated. In some cases, it appears that entanglement can play an important role in increasing the mechanical properties; and this approach also merits further attention.

More generally, it should be noted that the number of reactive groups in thermoplastic polymers — particularly those designated as nonreactive — is considerably smaller than the number in familar thermosetting resins. In this light, it should not be surprising that the increases in strength observed when silanes (or even silanes and peroxides) are used with thermoplastics are usually smaller than those found with thermosets. It is also not surprising that the effects of silane treatment are not applicable to all thermoplastics. Indeed, it *is* surprising that some of the silane-filler-thermoplastic combinations achieve as good properties as are observed.

A new family of coupling agents has become available which have organofunctional groups capable of both entanglement and reaction with the thermoplastic. Rather than being silicon based, however, these coupling agents are based on titanium. They are known as titanate coupling agents.[44]

The titanates usually have three organofunctional groups and one alkoxy group — in contrast to the silanes which have three alkoxy groups and one organofunctional group. With only a single alkoxy group, the titanates cannot polymerize, nor can they form a cross-linked layer on the ceramic surface. When attempting to couple between a ceramic and a thermoplastic, the principal difficulty lies in achieving a bond to the plastic rather than to the ceramic; hence it seems sensible to formulate a coupling agent directed to this objective (as done with the titanates). Some of the titanates also have incorporated a pyrophosphato group, which provides a mechanism for absorbing moisture on the filler surface and converting part of the pyrophosphato to an alcohol. This mechanism leads to improved composite wet properties. Some of the titanates also incorporate a transesterification mechanism which can be controlled so that the viscosity of the resulting composite can be fairly well chosen. This results in both mixing of filler into the composite system and allows high filler loadings to be achieved. With 40% by weight of inorganic filler in polypropylene, the impact strength is improved by a factor of 7.5 over unfilled polypropylene and by a factor of 5 over 40% filled polymer without the coupling agent. The flexural modulus and the tensile strength are, however, decreased upon addition of the coupling agent. In filled polystyrene, the titanates are used to improve melt flow, allowing composites with higher loadings of filler to be injection molded.

Adding titanate to high-density polyethylene improves melt flow and mechanical properties and allows useful properties to be obtained with loadings of calcium carbonate as large as 75%.

CONCLUDING COMMENTS

The discussion of the present chapter has been concerned with bonding between ceramics — particularly glasses — and polymers. Attention has been focused upon the factors which influence adhesion between these materials, and upon the effects of various additives — particularly the organosilanes — on bonding and composite properties.

The field has been one of intense activity during the past two decades, and this activity has led to significant improvements in technology. Marked variability is, however, noted in many of the results; and understanding has lagged far behind technological advance. The phenomena of concern are complex; and their satisfactory elucidation seems to require a combined approach based on chemistry, mechanics, and materials engineering.

Fortunately, the past few years have seen dramatic advances in instrumentation for characterizing surfaces. These advances lead to the authors' confidence that a Conference on Joining held in 1985 will be marked by vastly improved understanding of polymer-ceramic materials, and a greatly expanded role in our society of materials based on polymers and ceramics used in combination.

ACKNOWLEDGMENTS

Financial support for the present work was provided by the National Science Foundation, and by the Army Materials and Mechanics Research Center. This support is gratefully acknowledged.

REFERENCES

1. Geil, P. H., "Morphology of Amorphous Polymers," Case Western Reserve University, Cleveland, Ohio. U.S. Army Research Office, Durham Contract Report No. TR-260, November 1973. (AD 776 983)
2. Yeh, G. S. Y., "Morphology of Amorphous Polymers," *Crit. Rev. Macromol. Chem.*, **1** (1972), 173–213.
3. Kirste, R. G., Kruse, W. A., and Schelten, J., "Die Bestimmung des Trägheitsradius von polymethylmethacrylat im Glaszustand durch Neutronenbeugung," *Makromol. Chem.*, **162** (1972), 299–303.

4. Benoit, H., "Determination of Polymer Chain Conformation in Amorphous Polymers," *J. Macromol. Sci., Phys.*, to be published.
5. Renninger, A. L., Wicks, G. G., and Uhlmann, D. R., "On the Structure of Glassy Polymers. I. Small Angle X-Ray Scattering from Polycarbonate," *J. Polym. Sci., Polym. Phys. Ed.*, **13** (1975), 1247–61.
6. Renninger, A. L. and Uhlmann, D. R., "On the Structure of Glassy Polymers. II. Small Angle X-Ray Scattering for Poly(methyl methacrylate)," *J. Polym. Sci., Polym. Phys. Ed.*, **13** (1975), 1481–90.
7. Uhlmann, D. R., Renninger, A. L., Kritchevsky, G., and Vander Sande, J., "Electron Microscopy and Small Angle X-Ray Studies of Amorphous Polymers," *J. Macromol. Sci., Phys.*, to be published.
8. Holland, L., *The Properties of Glass Surfaces.* London: Chapman and Hall (1966).
9. Anderson, P. R., "Effects of Sulfate Treatment on Soda-Lime-Silicate Glass," to be published.
10. Fox, H. W. and Zisman, W. A, "The Spreading of Liquids on Low Energy Surfaces. I. Polytetrafluoroethylene," *J. Colloid Sci.*, **5** (1950), 514–31.
11. Bowden, F. P. and Throssell, W. R., "Adsorption of Water Vapour on Solid Surfaces," *Nature*, **167** (1951), 601–02.
12. Bolger, J. C. and Michaels, A. S., "Molecular Structure and Electrostatic Interactions at Polymer-Solid Interfaces," in *Interface Conversion for Polymer Coatings*, ed. by P. Weiss and G. D. Cheever. New York: American Elsevier Publishing Company (1968), 3–60.
13. Bascom, W. T., "The Surface Chemistry of Moisture-Induced Composite Failure," in *Composite Materials*, Vol. 6, *Interfaces in Polymer Matrix Composites*, ed. by E. P. Plueddemann. New York and London: Academic Press (1974), 79–108.
14. Adams, R. G., Milletari, S. J., and Roth, A., "The Influence of Ion Exchange Strengthening on the Performance of Finished Fiberglass Fabrics in Composites," in *Proceedings of the 26th Annual Technical Conference, February 9–12, 1971*, The Society of the Plastics Industry, Inc., Reinforced Plastics/Composites Division, Washington, D.C. (1971), Sect. 8-D, 1–10.
15. Mould, R. E. and Southwick, R. D., "Strength and Static Fatigue of Abraded Glass Under Controlled Ambient Conditions: I, General Concepts and Apparatus," *J. Amer. Ceram. Soc.*, **42** (1959), 542–47 and "II, Effect of Various Abrasions and the Universal Fatigue Curve," *J. Amer. Ceram. Soc.*, **42** (1959), 582–92.
16. Hillig, W. B. and Charles, R. J., "Surfaces, Stress-Dependent Reactions, and Strength," in *High Strength Materials*, ed. by V. F. Zackay. New York: John Wiley & Sons, Inc. (1965), 682–705.
17. Johannson, O. K., Stark, F. O., Vogel, G. E., and Fleischmann, R. M., "Evidence for Chemical Bond Formation at Silane Coupling Agent Interfaces," *J. Compos. Mater.*, **1** (1967), 278–92.

18. "Effect of Glass Surface Chemistry on Wetting, Bond Strength and Bond Life of an Epoxy Resin," A. O. Smith Corp., Milwaukee, Wisc., U.S. Navy Bureau of Weapons Contract Report, July 1962. (AD 278 592)
19. Plueddemann, E. P., "Adhesion through Silane Coupling Agents," *J. Adhes.*, **2** (1970), 184–201.
20. Bascom, W. D., "Structure of Silane Adhesion Promoter Films on Glass and Metal Surfaces," *Macromolecules*, **5** (1972), 792–98.
21. Erickson, P. W., "Silane Treatment of Glass Fabric from Nonaqueous Solvents," in *Proceedings of the 24th Annual Technical Conference, February 4–7, 1969*, The Society of the Plastics Industry, Inc., Reinforced Plastics/Composites Division, Washington, D.C. (1969), Sect. 19-B, 1–10.
22. Plueddeman, E. P., Clark, H. A., Nelson, L. E., and Hoffman, K. R., "New Silane Coupling Agents for Reinforced Plastics," *Mod. Plast.*, **39**, No. 12 (1962), 135–40, 144–46, 187–93.
23. Koenig, J. L. and Shih, P. T. K., "Raman Studies of the Glass Fiber-Silane-Resin Interface," *J. Colloid Interface Sci.*, **36** (1971), 247–53.
24. Shih, P. T. K. and Koenig, J. L., "Raman Studies of the Hydrolysis of Silane Coupling Agents," *Mater. Sci. Eng.*, **20** (1975), 137–43.
25. Shih, P. T. K. and Koenig, J. L., "Raman Studies of Silane Coupling Agents," *Mater. Sci. Eng.*, **20** (1975), 145–54.
26. Kwei, T. K., "Polymer-Filler Interaction. Thermodynamic Calculations and a Proposed Model," *J. Polym. Sci., Pt. A*, **3** (1965), 3229–40.
27. Kahn, F. J., "Orientation of Liquid Crystals by Surface Coupling Agents," *Appl. Phys. Letters*, **22** (1973), 386–88.
28. Bessell, T. and Shoetall, J. B., "The Crystallization and Interfacial Bond Strength of Nylon 6 at Carbon and Glass Fibre Surfaces," *J. Mater. Sci.*, **10** (1975), 2035–43.
29. Vanderbilt, B. M., "Water Resistance of Fibrous Glass Reinforced Thermoset Plastics," paper presented at the 22nd Annual Technical Conference of the Society of Plastic Engineers, March 7–10, 1966.
30. Schrader, M. E. and Block, A., "Tracer Study of Kinetics and Mechanism of Hydrolytically Induced Interfacial Failure," *J. Polym. Sci.*, Pt. C, No. 34 (1971), 281–91.
31. Schrader, M. E., Lerner, I., and D'Oria, F. J., "Radioisotope Study of Coupling Agents in Reinforced Plastics," *Mod. Plast.*, **45**, No. 1 (1967), 195–97, 268, 272, 276, 280, 282.
32. Plueddemann, E. P., "Mechanism of Adhesion through Silane Coupling Agents," in *Composite Materials*, Vol. 6, *Interfaces in Polymer Matrix Composites*, ed. by E. P. Plueddemann. New York and London: Academic Press (1974), 173–216.
33. Ranney, M. W., Berger, S. E., and Marsden, J. G., "Silane Coupling Agents in Particulate Mineral Filled Composites," in *Composite Materials*, Vol. 6, *Interfaces in Polymer Matrix Composites*, ed. by E. P. Plueddemann. New York and London: Academic Press (1974), 131–72.

34. Wong, R., "Recent Aspects of Glass Fiber-Resin Interfaces," *J. Adhes.*, **4** (1972), 171–79.
35. Ranney, M. W. and Pagano, C. A., "Silane Coupling Agent Effects in Ethylene Propylene Diene Terpolymers," *Rubber Chem. Technol.*, **44** (1971), 1080–92.
36. Fan, Y. L. and Shaw, R. G., "Silyl Peroxides: Adhesion Promoters and Crosslinkers," *Rubber World*, **164**, No. 3 (1971), 56–62.
37. Fan, Y. L., "Silyl Peroxide — Some Chemical and Physical Effects on Adhesion Promotion," *J. Adhes.*, **4** (1972), 261–73.
38. Trivisono, N. M., Lee, L. H., and Skinner, S. M., "Adhesion of Polyester Resin to Treated Glass Surfaces," *Ind. Eng. Chem.*, **50** (1958), 912–17.
39. Swanson, F. D. and Price, S. J., "The Evaluation of Silane Coupling Agents as Integral Blend Additives in Urethane Adhesives," in *Materials '71*, Proceedings of the 16th National SAMPE Symposium and Exhibit, Anaheim, Calif., April 21–23, 1971. Azusa, Calif.: Society of Aerospace Material and Process Engineers (1971), 45–57.
40. Swanson, F. D. and Gregornik, N. W., "The Bulk of Effect of Particulate Fillers in Epoxy Resin Compositions," in *Materials Review for '72*. Proceedings of the 17th National SAMPE Symposium and Exhibit, Los Angeles, Calif., April 11–13, 1972. Azusa, Calif.: Society of Aerospace Material and Process Engineers (1972), III-B-Four 1–9.
41. Hartlein, R. C., "New Coupling Concepts for Glass Reinforced Thermoplastics," *Ind. Eng. Chem. Prod. Res. Dev.*, **10** (1971), 92–99.
42. Sterman, S. and Marsden, J. G., "Effect of Silane Coupling Agents in Improving the Properties of Filled or Reinforced Thermoplastics," in *Proceedings of 21st Annual Technical Conference, February 8–10, 1966*, The Society of the Plastics Industry, Reinforced Plastics Division, Chicago, Ill. (1966), Sect. 3-A, 1–10.
43. Sterman, S. and Marsden, J. G., "Theory of Mechanisms of Silane Coupling Agents in Glass Reinforced and Filled Thermoplastic and Thermosetting Resin Systems," Union Carbide, Adhesion Promoters Division.
44. "Ken-React, Titanate Coupling Agents for Filled Polymers," Kenrich Petrochemicals, Inc., Bayonne, N.J.

10. POLYMER–POLYMER BONDING

ROGER FOUNTAIN
Textron's Bell Aerospace Company
Buffalo, New York

Polymer–polymer bonding is reviewed by emphasizing joint strength relative to adhesive selection, adherend surface preparation, and the development of cohesive adhesive strength within the bond line. The adhesive/adherend systems discussed range from thermoplastics and elastomers to thermosets. Only by careful adherend surface preparation with adhesive selection, application, and cure can high-performance bonds be developed.

INTRODUCTION

The bonding of polymers with polymeric adhesives form the beginning of modern adhesive technology. Although ancient uses of polymer bonding are known, such as the sealing of documents with molten wax, the First World War opened up adhesive technology through bonding doped fabric to wooden airframe structures with animal glue.[1] Since that time, polymer–polymer bonding has mushroomed due to the development of synthetic polymers resulting in lightweight, smooth surface high-strength joints. The current types of adhesives include chemically reactive types such as polyimides, epoxies, phenolics, polyesters, and polyurethanes; evaporation or diffusion types such as solvent-based elastomers, vinyl resins, and acrylics; and hot-melt types such as polyamides, ethylene vinyl and ethyl acrylates, and ethylene acrylic acid salts (ionomers). These adhesives are used to bond together polymeric adherends including wood, paper, fabrics, cork, leather, rubber, composites, and plastic sheets. This broad spectrum of adhesives and adherends gives some idea of the extensive use made of polymer–polymer bonding in current-day products such as high-speed aircraft using structural thermoset adhesives (composite to composite bonding) or cereal box-top sealing using hot melts (cardboard to cardboard). Generally, joint design, adhesive selection, adherend preparation, and cohesive adhesive strength development are the required steps to produce a reliable polymer–polymer bond.

DISCUSSION

General

Initial design considerations for adhesive material joining should include physical and chemical adhesive and adherend characteristics plus the operational environment that the joints will see in use. Maximum bond integrity will be realized when everything in the bonding process is monitored, particularly factors pertaining to the adherend surfaces. Several features to be considered for high-strength joints are:

1. Adherend surface condition — porosity, cleanliness, "wettability" (free energy of surface higher than interfacial energy).
2. Physical and mechanical properties of adherends and cured adhesive — e.g., shear strength and thermal coefficient of expansion.
3. Rheological and physical properties of adhesive — *e.g.*, viscosity and film thickness.
4. Compatibility of adhesive with adherends.
5. Methods of applying and curing adhesive including volatile by-product removal.

Adherend surfaces require conditioning before strong bond attainment. Most solid surfaces are microscopically rough and contain adsorbed moisture, gases, and other substances. A strong tenacious bond requires the displacement of these adsorbed materials. Also, surface porosity is encountered in adherends such as wood, paper, fabrics, and rubber. Adhesive selection and application has to take these factors into account.

Five separate components form the bonded joint: first adherend and interface, adhesive film, second interface, and adherend. Recently the concept of interface has been replaced by interphase,[2] where no drastic change from one material to another exists. Adhesive bonding is advantageous for joining porous materials, nonmetallics, and dissimilar substances. For porous adherends, the adhesive must be formulated to prevent excessive absorption into the adherend and so prevent starved glue lines. Porosity can be advantageous however, since volatiles during cure can escape into the adherent without void or blister formation. Nonporous materials, such as plastic sheet and molded polyester glass fiber, require the selection of an adhesive of similar composition. Fillers are often needed to form an escape path for volatiles and to control bondline thicknesses. In bonding dissimilar substrates, the different thermal expansion coefficients for all materials has to be considered. For porous materials, the surfaces generally require sealing and sometimes chemical activation through priming, the adhesive being chemically compatible with both primers. Nonporous materials are normally bonded by using

adhesives containing "mixed polarities." For example, rubber and phenolic adherends may be bonded with rubber-base adhesives containing isocyanates.

Joint Design and Adhesive Selection

Joint design aims at obtaining maximum strength for a respective area. Joint design selection may also be determined by limitations in production facilities, costs, or the desired final appearance of the part. The strength of an adhesive joint is determined primarily by the mechanical properties of the materials involved, residual internal stresses, degree of true interfacial contact, and the geometry of the joint. Elimination of stress concentrations concerns the design engineer since such stresses reduce the strength and useful life of the joint. Localized stresses are not always apparent, and may occur as a result of differential thermal expansion of the adhesive and adherends or from the shrinkage of the adhesive during the cure cycle. Expansion problems may be overcome by using a filled adhesive, since filler addition can lower the thermal expansion coefficient.[3] Volatiles trapped in the adhesive may also set up internal stresses, particularly at the interface. Internal stresses decrease as the thickness of the adhesive layer decreases, and the tendency to trap volatiles in the adhesive layer is reduced. Entrapment of air at the interface occurs if the adhesive has high viscosity, little flow during cure, or poor substrate wetting.

An adhesively bonded joint can be loaded in compression, tension, shear, cleavage, or peel (Figure 1). When loaded in pure compression, a joint is less likely to fail than when loaded in any other fashion, but such joints are limited in application. Structural adhesives are strong in shear and weak in cleavage and peel. Loading a joint in pure tension is generally impractical because, under high stress, the applied forces can become misaligned resulting in generation of the relatively weak cleavage and peel forces. The usual practice in designing adhesive joints is to minimize the peel and/or compression for maximum strength and applying a thin, uniform adhesive layer over the largest practical bond area (Figure 2).

The most popular theory of adhesion only considers the equilibrium thermodynamics situation of wetting and adsorption. Kinetic effects and methods of measuring adhesion are ignored. Adhesion is considered similar to the adsorption of gases onto the adherend (Figure 3) provided the surface tension thermodynamics of wetting are satisfied. This approach resulted in the Bondability Index[4] for elastomers: the higher the index, the higher the bond strength, *i.e.*, polar groups bond to polar groups better than polar groups bond to nonpolar groups, etc. Figure 4 shows

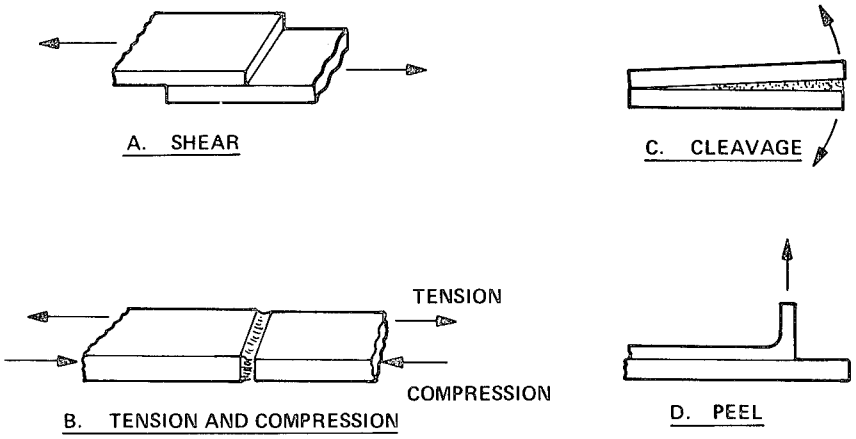


Figure 1. Five most common types of stresses in adhesive joints.

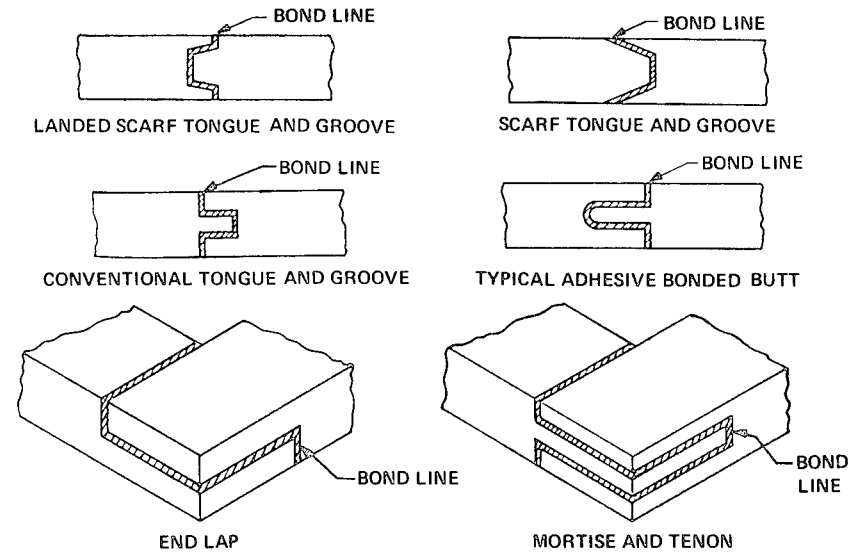


Figure 2. Types of joints minimizing tensile stresses.

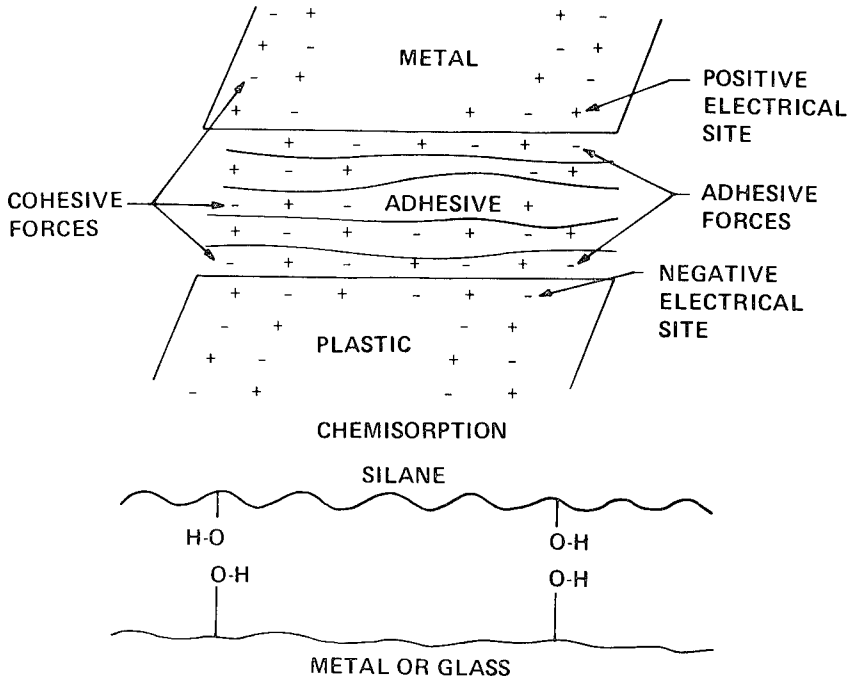


Figure 3. Physical adsorption.

the index for a polar adherend. However, more recently, the method of testing appears more important to bond strength.[5,6,7] Peeling (180°) styrene butadiene (SBR) elastomeric adhesives from Mylar adherends was found rate dependent (Figure 5). Extrapolation of the data to zero rate gave the thermodynamic work of adhesion which was orders of magnitude lower than for the work of adhesion at higher rates of peel. This characteristic applied also to shear and tension testing.[6,7] Peel testing, over a wide range of peel rate, showed that the adhesive's behavior towards peel strength was modulus dependent relative to its glass transition temperature since the adhesive obeyed the Williams Landel Ferry relationship, *i.e.*, approximately, rate α 1/Temperature °K. Thus, although an adhesive has high static bond strength, its behavior under dynamic loading may be entirely different due to its apparently high dynamic modulus. Figure 6 shows this effect on a nylon fabric tested with an isocyanate tire cord adhesive. Static peel testing gave a high bond strength of over 100 lb/in. width. However, the bond failed during a flexing test (ASTM D430 Method B) after only a few hundred cycles at 5 cycles/second due to the high stiffness of the adhesive and fabric under

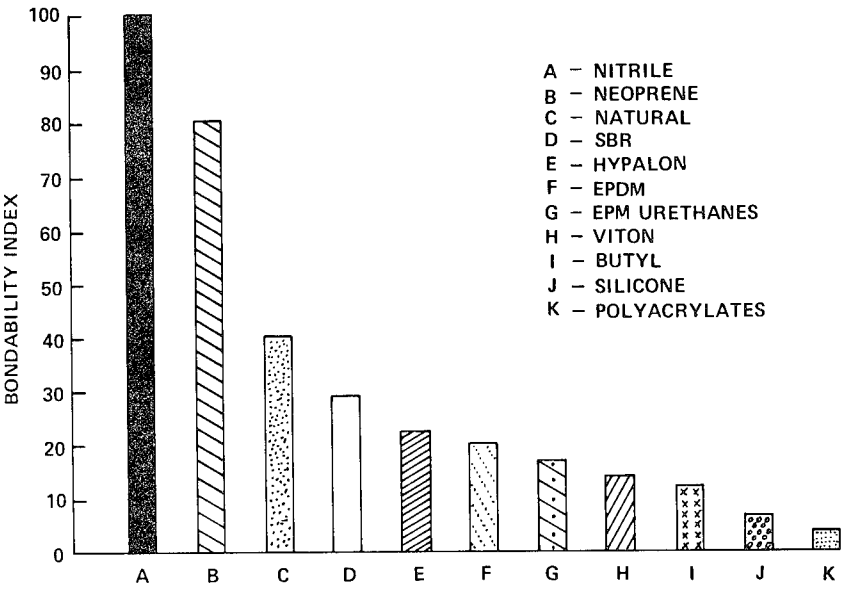


Figure 4. Bonding elastomer to polar adherends.

these conditions. Others[8] have also found that thermodynamic wettability is insignificant in determining interfacial bond strengths in fiber–epoxy composites.

Testing is another problem area. Single lap shear testing is common for structural adhesives due to its low cost and simplicity of manufacture and testing. However the loads are situated at the end of the joint and contain more than just shear stresses (Figure 7). To overcome this problem, torsional shear testing can give pure shear data[9] but is expensive. Other cheaper methods that reduce the peel stresses are grooved (notched) double and stepped lap joints. The latter, though, produces a thick joint.[10]

Several basic requirements should be considered when selecting an adhesive. The type of material to be bonded is important — whether the adherends are wood, paper, fabric, leather, plastic, or elastomer. Next, physical properties of the adherends such as size, flexibility, porosity, and heat distortion temperature should be considered. If final assembly is structural, the strength of the adherend itself is important. Assembly steps, such as surface preparation, adhesive application, and curing or setting methods, should be reviewed with the performance requirements. Service conditions must be considered. Is the bond under tensile,

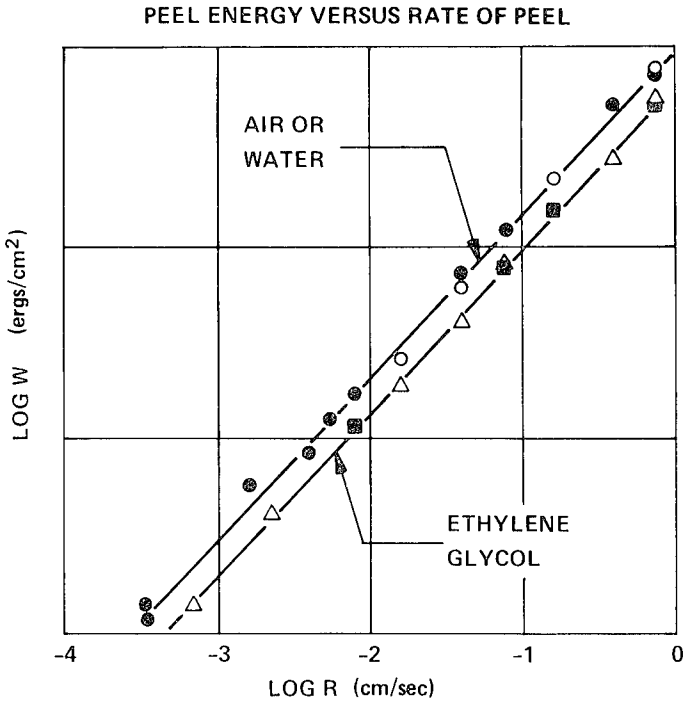


Figure 5. Kinetic effects.

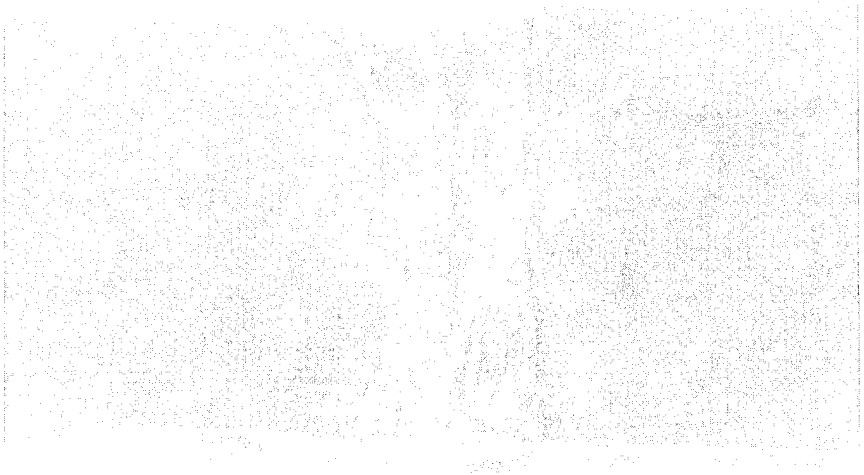


Figure 6. Demattia flex test result — isocyanate rubber-based adhesive-bonded nylon fabric.

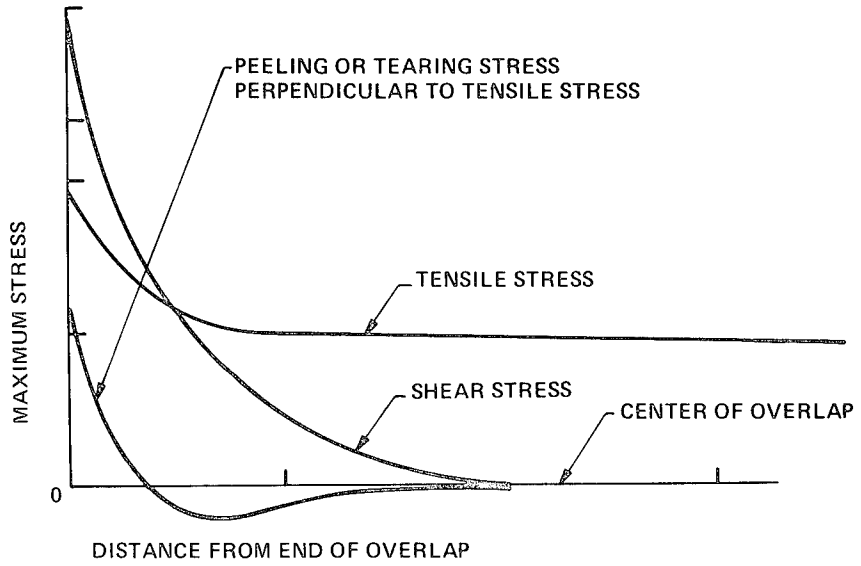


Figure 7. Simple stresses in single lap joint.

shear, peel, or cleavage loading? Whether the type of loading is continuous or intermittent should also be considered. Identification of environments such as heat, cold water, humidity, chemicals, oil, or solvents in many special applications is fundamental in the selection of adhesives. Finally, cost considerations reflect adhesive and process choice. The cost of the adhesive itself per unit is usually minor compared with the cost of the process.

Joint strength is the measure of performance. The specification should cover the requirements under environmental conditions. Any evaluation program should include the temperature range, moisture conditions, and any other condition related to the performance of the assembly. Epoxy, epoxy phenolic, vinyl phenolic, nitrile phenolic, and neoprene phenolic adhesives are usually chosen for structural bonding where high strength over a wide range of temperature is required. In both the heat reactive or catalyst-cured adhesives, strengths from 2000 to 5000 psi are possible. The choice of the resin or elastomeric part of the material is dependent on the elasticity required in service.

For structurally bonding composites, the heat-up rate is important since it determines the gel time and temperature for both the adhesive and adherend matrix. Ideally, the adhesive should gel at a higher temperature than the matrix so that adhesive flow can be realized over the

set adherend matrix. Thus, for bonding a boron–epoxy laminate to another laminate both in the prepreg state with a 3°F/min. heating rate in an autoclave at 50 psi, the gel point for the epoxy matrix was 290°F, and 300°F for the epoxy adhesive. The determination of the desired gel points for the total system was complicated further by the apparent temperature dependence of the energy of activation (ΔE) of cure for dicyandiamide epoxies (Figure 8). Autoclave cure for this system should take place in the higher ΔE range of matrix cure (above 250°F) to enable the adhesive to flow during and after adherend solidification.

Evaporation or diffusion adhesives achieve their strength by drying or crystallizing. The loss of the solvent or water carrier leaves a dry film. The strength of the film is controlled by the ratios of elastomer, resin, plasticizer, and pigment. Evaporation-type adhesives can be compounded to be used with any substrate. Since these compounds are not usually chemically reactive or cured, high constant loading may cause cold flow; their use is therefore limited to low load assemblies. Higher resin compounds give less cold flow but tend to be brittle. Evaporation adhesives also show a higher degree of variation over a wide temperature range. Usually the maximum strength for these types of adhesives will be about 800–1000 psi at 80°F.

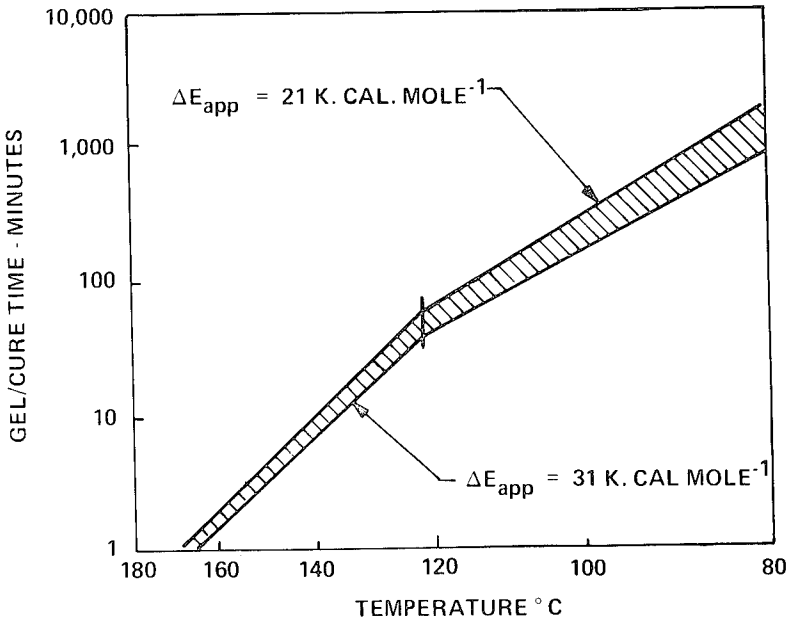


Figure 8. Gel/cure time versus temperature for three batches of an epoxy resin used in boron/epoxy prepreg tape.

Rubber adherends can be compounded for greater adhesion promotion by (a) keeping blooming additives to a minimum, (b) using silica and channel black rather than thermal or furnace blacks, (c) using naphthenic oils at less than 25 phr for processing and compensating with extra black loadings, and (d) reblending the stock directly before the bonding operation. Elastomer to tire cord bonding uses adhesives such as resorcinol formaldehyde containing lattices with isocyanate or aminimide adhesion promoters.[11] For high-temperature performance, room-temperature curing (RTV) poly-siloxanes are used as the elastomeric adhesive. Phenol laminates are bonded with an RTV to polycarbonate to produce canopy and windshield edge attachments.[12] The RTV had a double lap shear strength of 475 psi and a flatwise tensile strength of 350 psi, both at 280°F.

Hot-melt adhesives (cooling type) are replacing solvent-based adhesives in many nonstructural applications. The strength of the hot-melt adhesive is determined by the strength of the compounded polymers and resins. These are normally thermoplastic-based compounds with 100 percent solids and good cohesive strength. Application requires more specialized equipment than the evaporation type of adhesive (Figure 9), but hot melts offer the advantages of having no solvent and a very fast set. Recently polyamide hot melts have given some structural significance to this fast growing field of adhesives.[13] The tensile bond strength of one such polyamide bonded to an elastomer gave 650 psi, which is equivalent to most RTV and rubber cement systems that have primed adherend surfaces. The common hot melts consist of ethylene vinyl acetate copolymer compounded with polyterpene tackifiers, waxes and antioxidants. Their tensile bond strength with elastomers is in the order of 200–400 psi.

Film type adhesives can be either thermoplastic or thermosetting. In either case, heat and pressure are normally used for the application. A few of the thermoplastic films may be used with solvent activation. The thermosetting films are used for high-strength bonds over a wide temper-

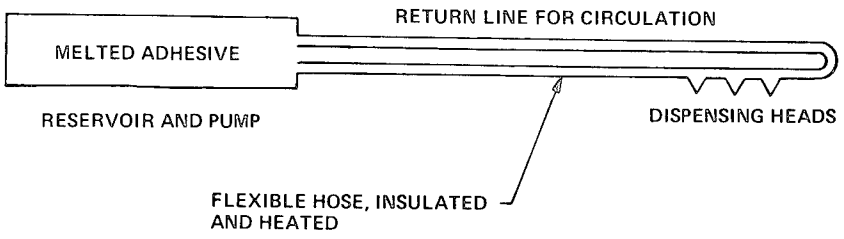


Figure 9. Setup for hot-melt adhesive dispensing.

ature range. The bond strength from the thermoplastic film again is related to the tensile strength of the polymer. The softening range and melting point will dictate its application area. From an engineering standpoint, these are the simplest adhesives to apply.

Pressure-sensitive adhesives are not used in a permanent bond, especially where higher loading strengths are required. Their relatively low strength and high tack make them valuable where the substrate can be bonded, easily removed, and rebonded. Pressure-sensitive adhesives are ordinarily applied to one of the substrate materials from a solution or a hot melt. When substrates with large dimensional variations are bonded, a sealing tape extruded on a carrier may simplify the operation. Once the adhesive is chosen, the surface of the adherends have to be treated before a tenacious bond can be prepared.

Surface Preparation of Adherends

Once an adhesive which is physically and chemically compatible with the adherends has been selected, the adherends usually require surface preparation prior to bonding. This ensures a clean surface capable of thermodynamic and chemical reaction with the adhesive. For polymer adherends, the process includes the following steps: solvent cleaning, physical abrasion or chemical etch, solvent cleaning, priming or immediate bonding. Vapor degreasing is preferred over solvent-soaked cloth cleaning. The latter, although commonly used, is fraught with danger. Cheesecloth and many commercial solvents such as trichloroethylene contain oily residues (Figure 10) which are left behind on the adherend after cleaning. Contaminated solvent cleaning results in premature adhesive failure as shown in Figure 11 for nylon bonded to rubber.

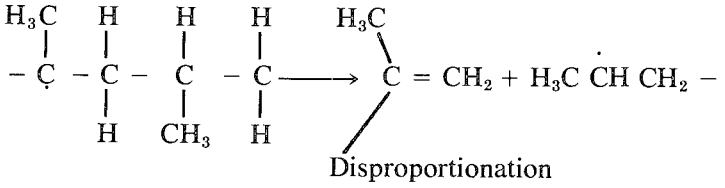
In all abrasive methods, a hard sharp material is brought into contact with the adherend surface and causes part of it to ground out, exposing clean material. For composites, hand sanding and glass shot grit blasting are commonly used to create the bonding surface. Although abrasion increases the bonding area, too much can lead to fissures and cracks in the adherend. High peaks and valleys on the adherend surface give rise to poor adhesive wet-out. This will result in not only bonding over a smaller surface area but also in gas and solvent penetration into the joint interface resulting in poor environmental resistance.[3] Contamination of composites also exists between the fiber and matrix. Boron fibers may contain traces of nitrogen, carbon, oxygen (oxide), sulfur, and iron, the latter elements also being epoxy matrix contaminants.[14] The importance of the fiber surface on epoxy matrix adhesion is demonstrated in Figure 12.[15] An increase in the fiber direction length of surface "crystallites" on graphite fibers decreases the number of reactive sites

for adhesion and hence the interlaminar shear strength of the total cured composite.

Chemical etching is usual for difficult-to-bond adherends such as polyethylene, polypropylene, and polytetrafluroethylene (TFE). The surface fluorine atoms of TFE are removed by treatment with metallic sodium and liquid ammonia. The excess etching solution is removed from the TFE with a butanol and water rinse. Acetals are equally difficult to bond and require concentrated sulfuric or hydrochloric acid immersion followed by air drying to achieve optimum bond strength. In order to improve the surface wetting and mechanical strength for adhesion promotion of nonpolar plastics and elastomers, photochemical degradation techniques have been developed[16] using surface sensitizers such as benzophenone. Irradiation from uncooled mercury lamps causes the sensitizer to vaporize and attack the adherend surface by free radical hydrogen elimination, *e.g.*, for polypropylene:

$$H_3C\text{-}R\text{-}H \xrightarrow[\gamma_0]{\text{Benzophenone } (\phi \text{ co } \phi)} H_3C\text{-}R^{\circ} + \phi\,\overset{\overset{OH}{|}}{\underset{\circ}{C}}\,\phi$$

This may result in disproportionation and hydroperoxide formation.[16]



Hydroperoxide Formation

$$R^{\circ} + O_2 \longrightarrow R - O_2^{\circ} \xrightarrow{R'H} R\,O_2H + R'$$

After solvent cleaning and abrading or etching, the polymeric adherends may be primed with a polymer that is flexible and has high adhesion to both adhesive and adherend. Its prime function is to lower internal stresses across the interface by absorbing expansion or impact stresses.[17] Also, it forms a barrier to environmental gas or solvent interface attack. Acrylate automotive sealers use a silane primer when bonded to glass fiber-reinforced polyester laminates.[3] These primers are often

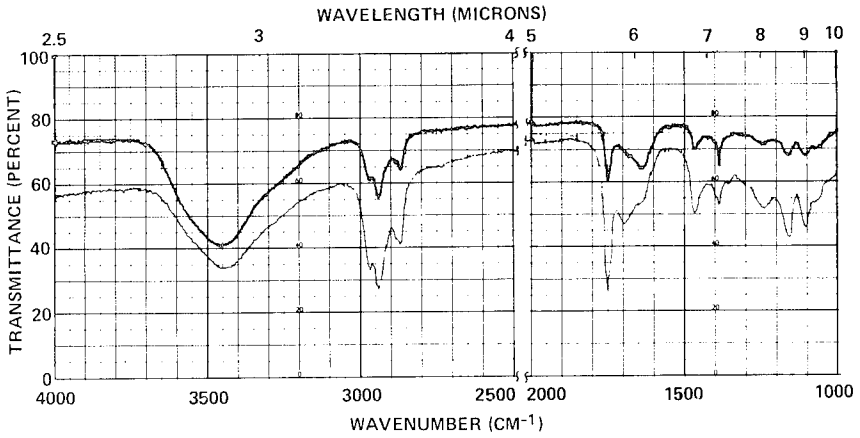
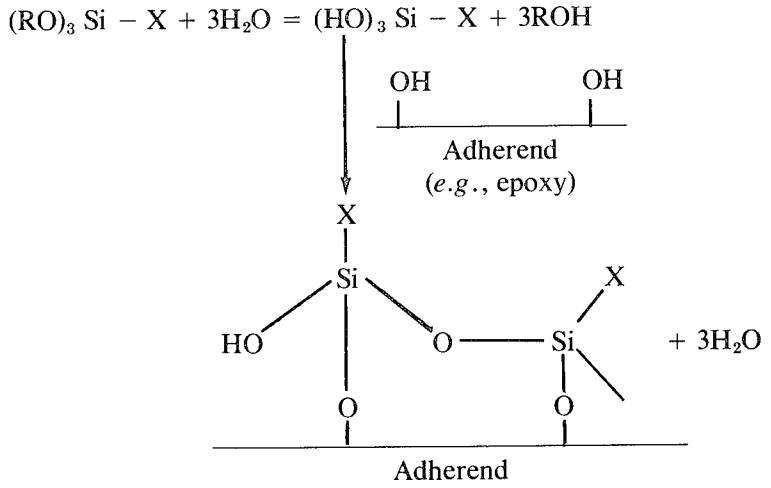


Figure 10. Infrared spectrum of trichloroethylene residue from nylon fabric clean.

called coupling agents due to their chemical reactivity towards both primer and adherend. This is illustrated below.



The X function is usually an adhesive reactant group (such as $\rangle$CH = CH_2 which is sensitive to polyester adhesive cure).

Coupling agents then may be multifunctional for primary thermoset and thermoplastic mixed systems. An example is Dow Corning's XZ85069 silane in which the X chain is multifunctional containing halogen, vinyl, and amine groups.



Figure 11. Nylon fabric — adhesively failed peel joint due to fabric contamination.

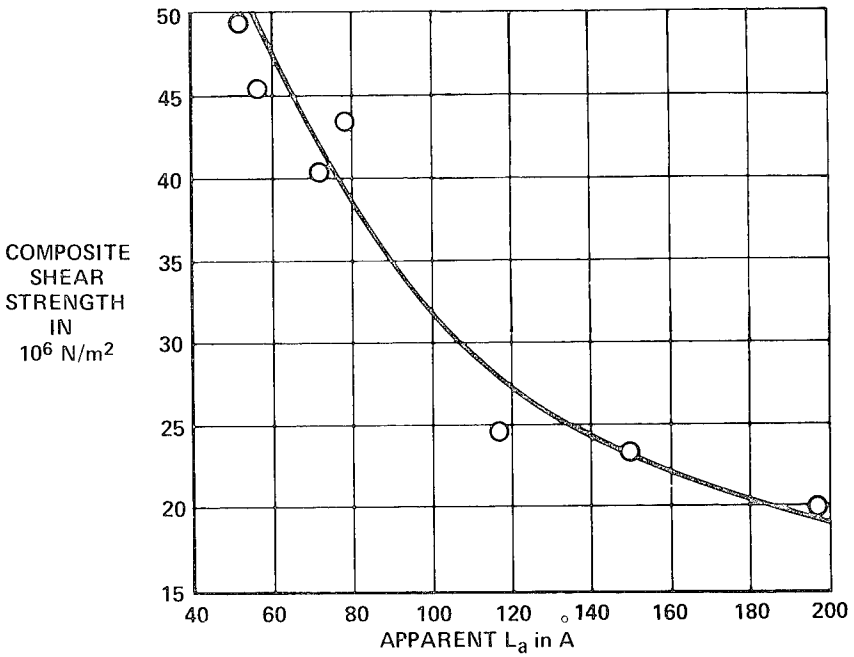


Figure 12. Relation between composite shear strength and the L_a found through the Roman spectrum of various graphite fibers.

$$(CH_3O)_3\,Si\,(CH_2)_3 - \overset{\overset{HCl}{|}}{NH} - (CH_2)_2\,NHCH_2 - O - CH = CH_2$$

With silane primers however, care has to be taken in the application, since their ability to bond to the adherend depends upon hydrolysis and condensation reactions. If the humidity is low the drying time will be long. Figure 13 shows the effect of incomplete primer hydrolysis on the tensile bond strength of silicone rubber bonded specimens for the 50% relative humidity condition using a General Electric polysiloxane primer. The bond strength increased with an increasing degree of primer hydrolysis.

Polymers of low bondability index such as butyl and ethylene propylene rubbers usually require at least one coat of primer, and, to prevent solvent preparation of solvent based adhesives, the primer should be prebaked. The enhancement of bond strength rendered by a two-coat relative to a one-coat system is shown in Table 1 for rubber bonded nylon. For nonstructural applications however, the need for this somewhat elaborate priming practice is disappearing with the increased use of hot melt adhesives.[18]

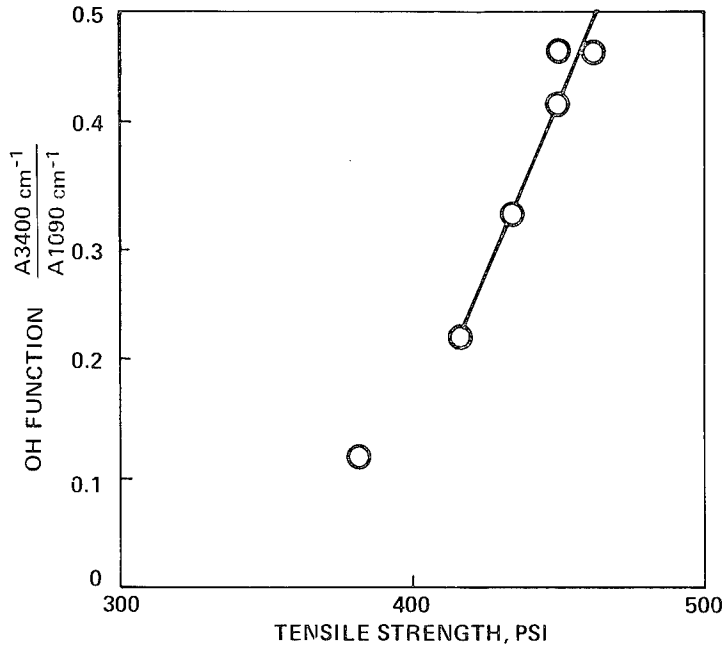


Figure 13. Relationship between primer hydrolysis (determined by infrared spectroscopy) and bond strength.

Adhesive Application and Bonding

Having obtained clean or primed adherend surfaces, the next step is to apply the adhesive to the adherends and bond the whole system together forming a joint. Methods for applying adhesives are numerous, ranging from manual brushing, rolling, pasting, and dipping operations to machine rolling, coating, and spraying. A relatively new method for applying adhesive to wood, plastic, leather, and paper surfaces is flow or curtain coating (Figure 14). Basically, a pump delivers liquid adhesive to a reservior which has a slit at its base from which adhesive is delivered onto the adherend passing underneath on a conveyor belt.

Thermoplastic hot-melt adhesives are applied with the equipment in contact with the adherend (extrusion or wheel applicator) or by spraying as in the packaging industry. Figure 9 illustrated the concept. Adhesive application for polymeric structural adherends usually consists of applying adhesive-coated cloth onto the adherends followed by autoclave curing of the adhesive and often the composite itself. The cure (adhesive cross linking) takes place under elevated temperature and pressure.

Table 1. One-Coat Adhesive versus Primer with Adhesive (Two Coats) for Neoprene-Bonded Nylon Cord

Type	Cure Cycle	180° Peel Strength, lb/in.	Failure Mode, % Adhesive
10% Adhesive Pickup One-Coat System	30 min. at 320°F	55	70%
21% Pickup Two-Coat System	30 min. at 320°F	90	30%

Bond strength develops as the adhesive solidifies. This is why, for example, the pressure-sensitive types do not achieve high strengths because they are used well above their glass transition temperatures. In the case of fabric bonding, high pressure during cure can be detrimental to bond strength. During 800 psi, a low-viscosity adhesive, that gave excellent wet-out on the fabric, resulted in half the peel strength of the fabric coated with a poor-wetting, high-viscosity adhesive (paste). The reason was simply that under the high pressure the low-viscosity adhesive flowed away from the bonding surface into the fabric. More of the paste adhesive remained on the bonding surface at this pressure.

Many adhesives, such as epoxies or polysiloxanes, cure at room temperature through the use of organometallic catalysts. In this case, roller pressure, to ensure adhesive adherend contact, is all that is required for joint strength development. This method is often used for bonding cured polymeric adherends where post cure of them during adhesive bonding would cause their degradation. However, for rubber and composite bonding, cocure of both adhesive and adherend is desired. For elastomeric bonding, satisfactory bonding requires mold pressures of about 200 psi during the curing cycle. Molds should be well fitting while allowing adequate venting. The design should be such that the spew and bond lines do not coincide since, if this does occur, pressure at the bond edge may be inadequate for good bonding. If multicavity molds are used, simple jigs should be designed for loading the coated adherends. If the latter are loaded into the hot mold by hand, the first ones may be overheaded and cross linking may commence, thus resulting in RC (rubber/cement) failure. Similarly the molds should be placed in the press as soon as possible after loading. Again it must be emphasized that for successful bonding, it is essential that the elastomer compound

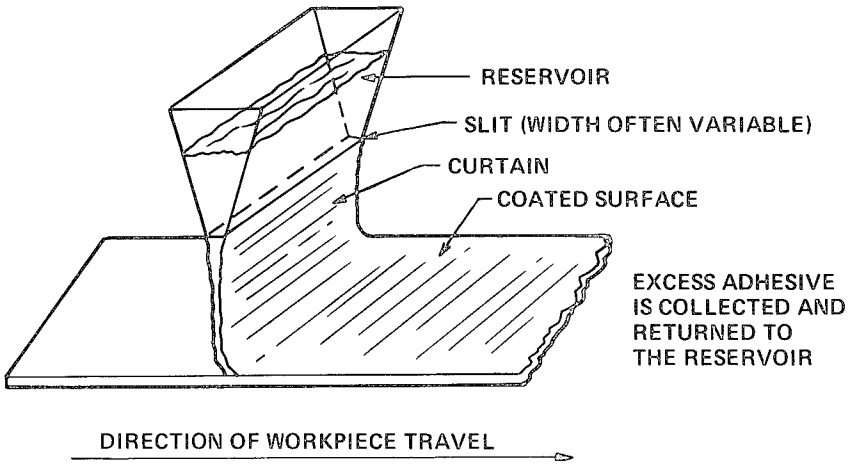


Figure 14. Essential principles of a curtain coater.

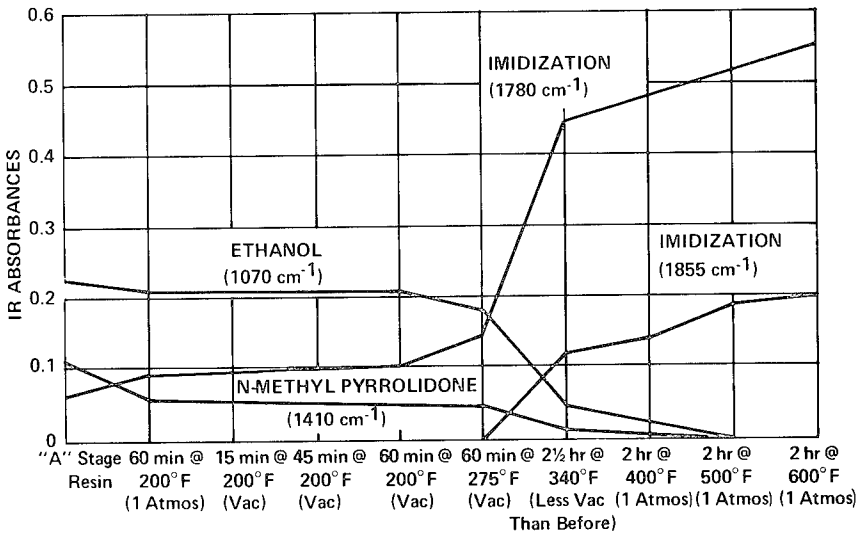


Figure 15. Boron/polyimide prepreg-cure cycle-use of infrared spectroscopy for studying cure mechanisms. (Solvent outgassing occurred simultaneously with final cross-linked polymer formation.)

should be completely free from precure at the time the elastomer–cement interface is formed. In general, best bonds are produced when the cure is slightly longer than the technical optimum.

Cocuring of boron and graphite epoxy composite laminates with a structural epoxy adhesive led to a problem of outgassing resulting in low bond strengths.[19] Outgassing was caused by absorbed water, carbon dioxide from decomposing resin, and ammonia from the curing agent which was common to both adhesive and matrix. Placing a low-temperature step in the cure cycle eliminated the problem. The problem of outgassing is especially pertinent in cocuring boron–polyimide laminates since the polyimide adherend contains ethanol and N-methyl pyrrolidone solvents, with water being formed during imidization. This problem may again be minimized by developing stepwise cures during bonding[20] which minimize bond-line void formation (Figure 15).

Assuming adhesive selection, adherend surface preparation, and bonding has been correct, joint strength will depend largely on the cohesive strength of the adhesive that has been developed during its solidification (cure). Poor cohesive adhesive strength may be caused by undercure or catalyst poisoning and are discussed in the next section. These are problems relatively rare in bonding to metals. They are prevalent in polymer–polymer bonding because of the complex chemical nature of the adherend.

Cohesive Strength of the Adhesive Relative to Polymeric Adherends

Catalyst cure retardation is a common feature of poor adhesive cohesive strength. Catalytic cure is a feature of room-temperature curing adhesives. For example, a 3M Company XA 3549 epoxy polyurethane adhesive was used to room-temperature bond an acrylonitrile butadiene styrene (ABS) overflow to a melamine lavoratory. The two-component adhesive consisted of an isocyanate curing agent and a linear epoxy polyurethane. On combination of the components a two-hour set-up time resulted, which was too long for production requirements. The addition of small temperature-dependent amounts of tributyl tin dilaurate shortened the work life (gel) to the production-desired 15 minutes (Figure 16).

Inhibition of organometallic catalysis in the RTV cure of adhesives causes incomplete cure and is illustrated by the following examples. Polyester adhesives, cobalt naphthenate catalyzed with a hydroperoxide and styrene curing system were used to room-temperature bond glass fiber polyester (FRP) reinforced ribs to FRP integral tub/shower units. Upon converting the whole system to fire retardancy by $Al_2O_3 \cdot 3H_2O$ and dimethyl methyl methyl phosphonate addition to the polyester, cure

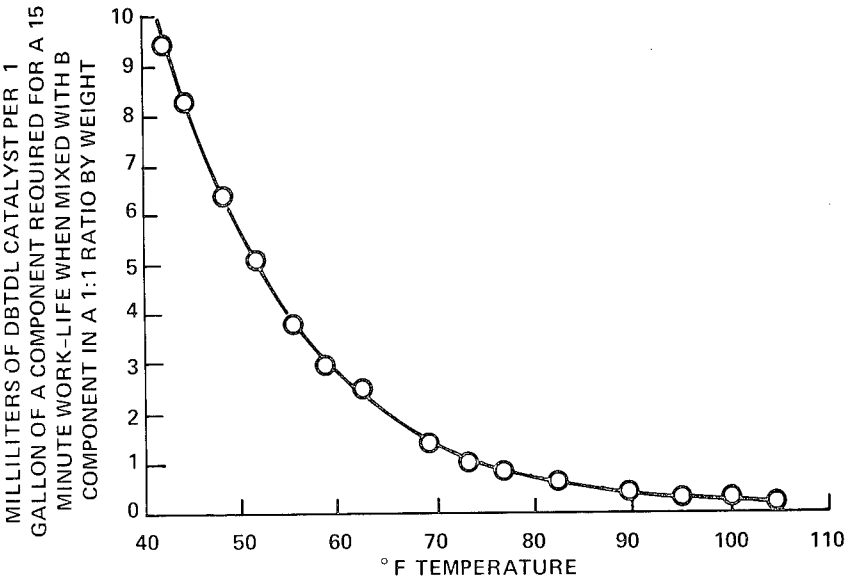


Figure 16. Effect of temperature upon catalyst addition to the adhesive for a 15-minute work life.

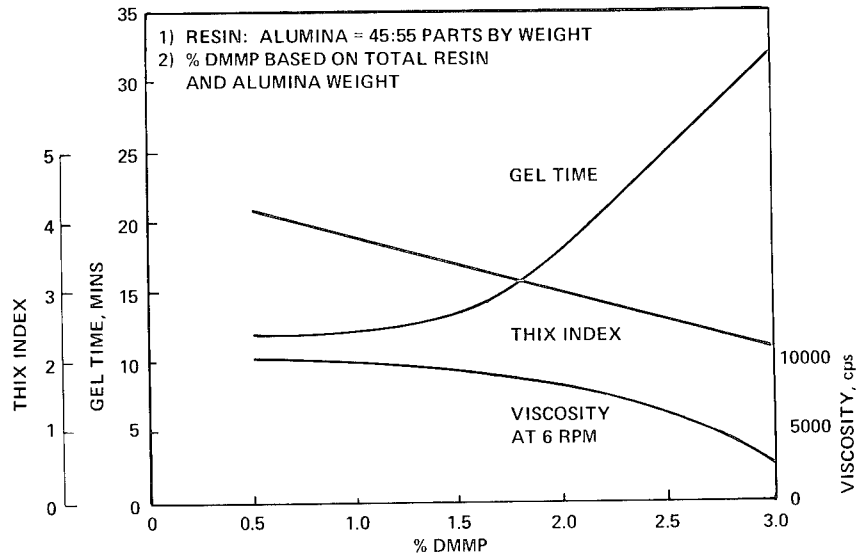
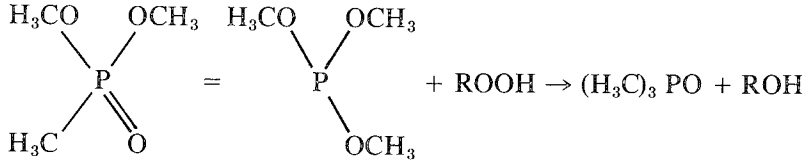


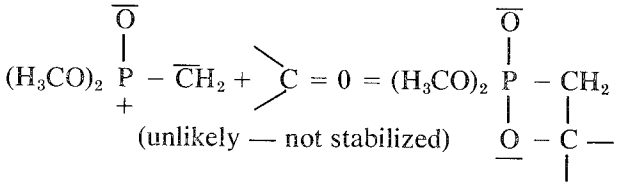
Figure 17. Percent DMMP versus gel time, viscosity, and thix index.

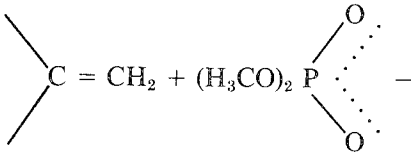
retardation was experienced in the adhesive and adherends causing a low-strength product.

Dimethyl methyl phosphonate (DMMP) retards the room-temperature cure of FRP system as shown in Figure 17 for gel time. Figure 17 also shows that the DMMP aids the spraying operation by acting as a viscosity depressant. There are several possible reasons for DMMP retarding the gel time and cure of the polyester. One possibility is for the DMMP to tautomerize to a phosphite[21] followed by reaction with the hydroperoxide catalyst, methyl ethyl ketone peroxide (MEKP).

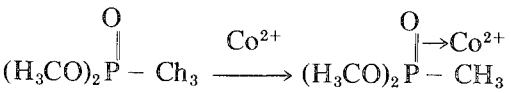


Another would be for the DMMP to react with a carbonyl group from the catalyst or the polyester itself.[22]





However, unpublished visible spectroscopy work by the writer and previous organometallic catalytic polymerization studies[23] indicated that cure retardation by the DMMP was caused by chelation of the cobalt from the 6% cobalt naphthenate promoter solution to the phosphonate. Thus the active cobalt concentration for free radical promotion was depleted with the consequence of cure retardation.



To solve the problem therefore, an extra addition of 0.2% by weight of the 6% cobalt naphthenate solution was made to the FRP formulation giving a 15-minute gel time with a 60-minute "cure." The minimum

amount of cobalt naphthenate required to do this was determined by differential scanning calorimetry.

Adherends can also cause poor adhesive cohesive strength via catalytic poisoning of the curing system. In this case, a cured epichlorohydrin ethylene oxide (ECO) elastomeric boot was being bonded to a FRP radome to give the radome rain-erosion protection. The adhesive chosen for high-temperature resistance was the General Electric RTV 630 polysiloxane system. Infrared spectroscopy and photoelectron spectroscopy (ESCA) showed that the rubber adherend contained the ECO curing agent on the surface of the rubber.[24] This material reduced the cure in the adhesive by chelating with the adhesive's platinum catalyst.[25] Oxidation of the ECO surface removed most of the ECO excess curing agent and enabled the adhesive to cure, thus increasing the bond strength between the adhesive and the ECO adherend (Figure 18). Undercure also happens with incorrect molding conditions. In bonding boron–epoxy composites with an epoxy adhesive, below specification lap shear bond strength was shown to be due to incomplete consumption

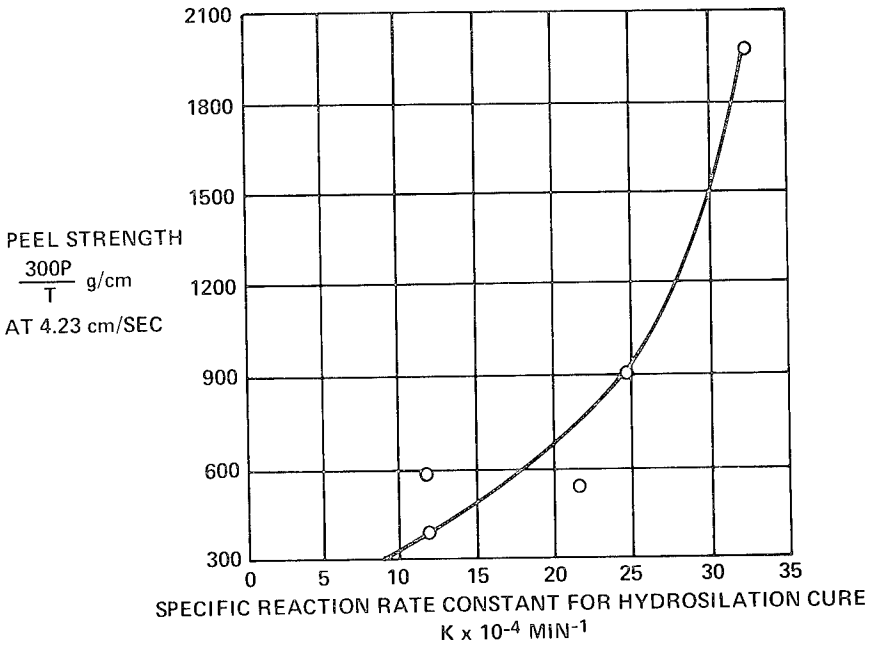


Figure 18. Correlation between peel strength and the cure of the adhesive.

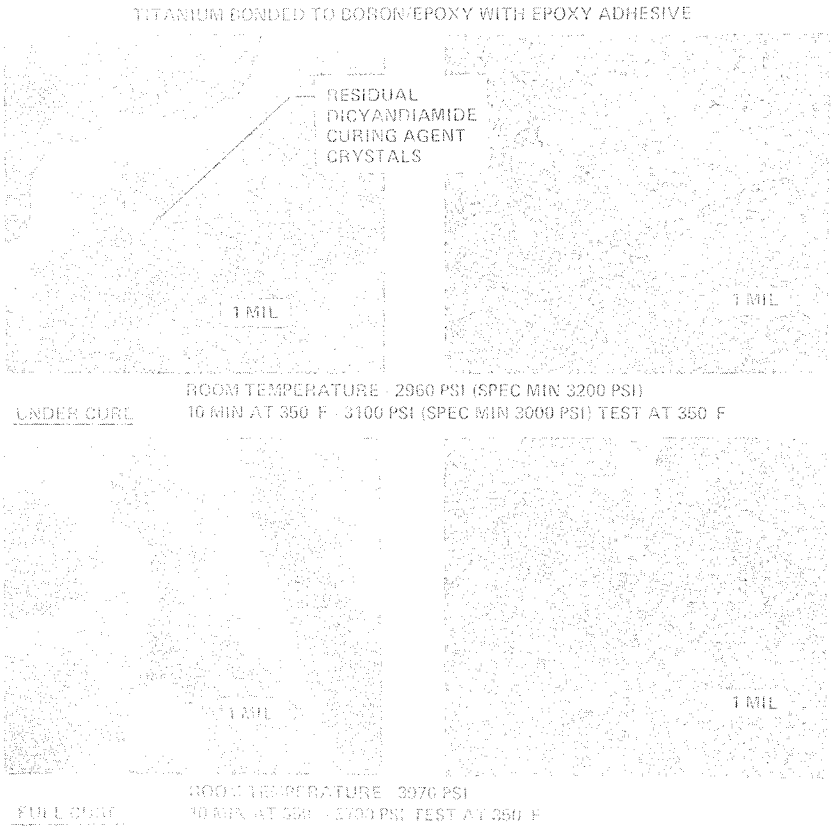


Figure 19. Double lap shear failures.

of the adhesive's dicyandiamide curing agent (Figure 19). Increasing the post-cure temperature eliminated the problem. Low cohesive strength in the adhesive may also be due to the molecular weight distribution in the as-received state of the prepreg tape.[26] For example, the presence of higher molecular weight species in a structural epoxy adhesive appeared to improve single lap shear strength. Figure 20 shows the molecular-weight species for one batch of the adhesive as determined by gel-permeation chromatography. Five batches were analyzed this way; bonded, cured, and tested in lap shear at 420°F. Figure 21 shows the results. The higher the low to high molecular weight ratios the lower the bond strength. The opposite effect is seen with boron–polyimide composites (Figure 22), the higher initial imidization, the lower the matrix–fiber bond strength. This indicates two competing mechanisms for developing bond strength. The polyimide matrix bond strength increased with better

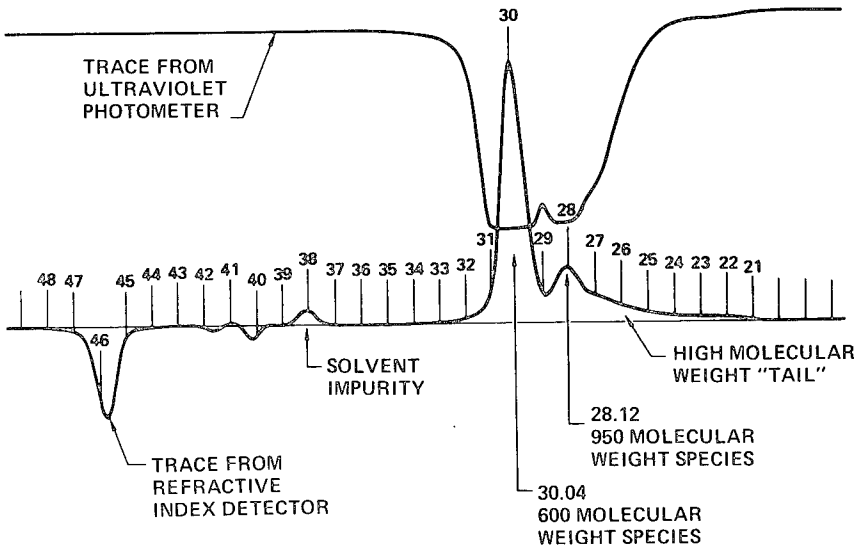


Figure 20. Gel permeation chromatogram of one batch of epoxy resin.

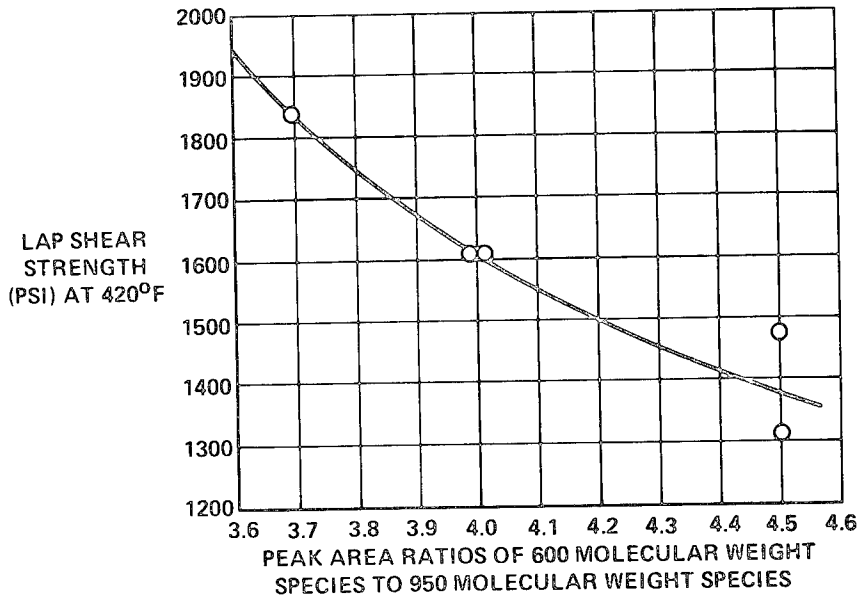


Figure 21. Lap shear strength versus molecular weight distribution in epoxy adhesive.

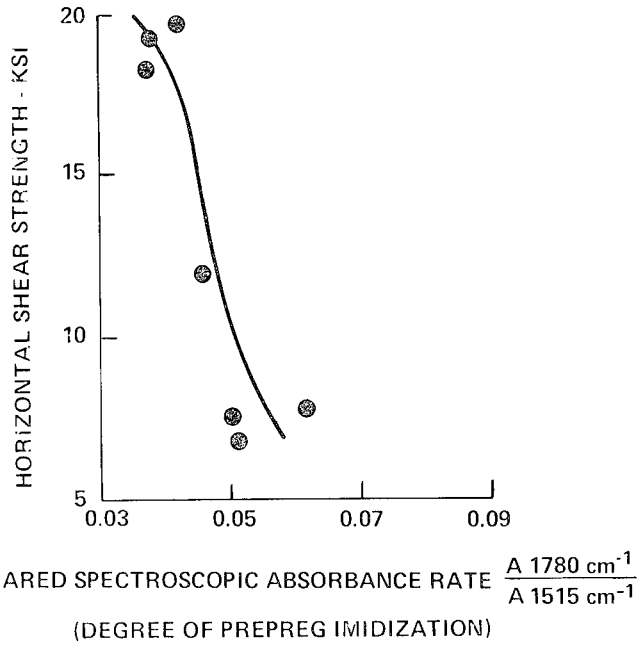


Figure 22. Correlation between strength and prepreg cure advancement.

wet-out due to the lower degree of initial imidization. However the initial high molecular weight species of the epoxy tended to reduce wet-out but increased its cohesive strength for a given cure since the more advanced the initial cure, the higher the bond strength.

Gent and Petrich[5] showed that adhesive undercure explained difference in stress–strain behavior in 180° peel testing of rubbery adhesives bonded to Mylar. If the adherend is flexible and elements of the adhesive treated as independent entities,

$$P = h \int_0^{fm} f \, de$$

where

P = peel force
f = tensile stresses in adhesive layer elements
e = fractional extension of stretched adhesive element
h = adhesive layer thickness

and

fm = maximum stress attained.

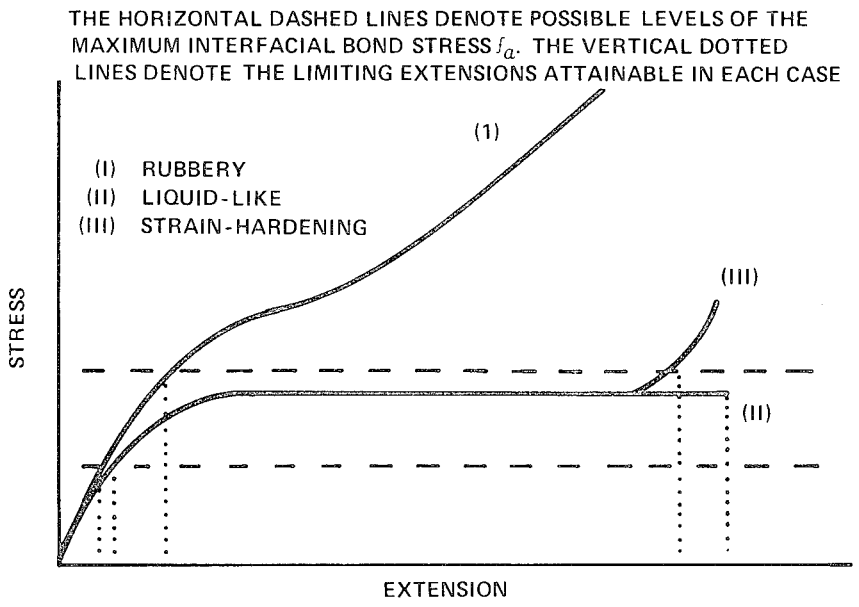


Figure 23. Stress-strain relations for rubbery liquid-like and strain-hardening materials.

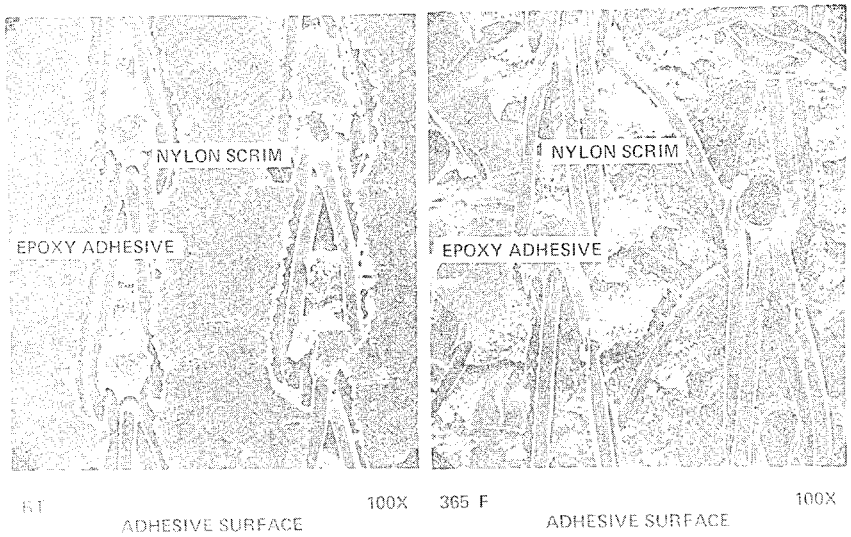


Figure 24. Scanning electron photomecrographs of batch 78 failed metal — metal lap shear specimens (reduced 52%).

For an undercured adhesive, the adhesive will fail cohesively below the adhesive bond stress limit due to its yielding capability (Figure 23). A cured adhesive would exceed the maximum stress limit and fail adhesively. This phenomenon is apparent in certain structural adhesives.[26] At room temperature they fail adhesively, but at 420°F above their glass transition region, they fail cohesively at a lower stress level under a higher strain (Figure 24).

REFERENCES

1. Wake, W. C., "Adhesives," Royal Institute of Chemistry, Lecture Series No. 4, 1966.
2. Sharpe, L., "Some Thoughts About the Mechanical Response of Composites," *J. Adhes.*, **6** (1974), 15–21.
3. Schneberger, G. L., "Polymer Structure and Adhesive Behavior," *Adhes. Age*, **17**, No. 4 (1974), 17–23.
4. Bright, W. M., "The Adhesion of Elastomeric Pressure-Sensitive Adhesives: Rate Processes," in *Adhesion and Adhesives, Fundamentals and Practice*. New York: John Wiley & Sons, Inc. (1954), 130–38.
5. Gent, A. N. and Petrich, R. P., "Adhesion of Viscoelastic Materials to Rigid Substrates," *Proc. Roy. Soc., London*, Ser A, **310** (1969), 433–48.
6. Gent, A. N., "Adhesion of Viscoelastic Materials to Rigid Substrates. III. Energy Criterion for Failure," *J. Polym. Sci.*, Pt. A-2, **9** (1971), 659–68.
7. Gent, A. N. and Schultz, J., "Effect of Wetting Liquids on the Strength of Adhesion of Viscoelastic Materials," *J. Adhes.*, **3** (1972), 281–94.
8. Hawthorne, H. M. and Teghtsoonian, E., "Graphite Fibre–Epoxy Matrix Interface Interactions," *J. Adhes.*, **6** (1974), 85–105.
9. Humpidge, R. T. and Taylor, B. J., "Apparatus for Measuring the Shear Strength of Adhesive Joints at High Temperatures and Methods for Constructing the Adhesive Joints," *J. Sci. Instrum.*, **44** (1967), 457–60.
10. Hart-Smith, L. J., "Design and Analysis of Adhesive-Bonded Joints," in *Proceedings of the Conference on Fibrous Composites in Flight Vehicle Design*, Air Force Flight Dynamics Laboratory, Wright-Patterson AFB, Ohio, Report No. AFFDL-TR-72-130, December 1972. (AD 907 042L)
11. Takeyama, T. and Matsui, J., "Recent Developments with Tire Cords and Cord-to-Rubber Bonding," *Rubber Chem. Technol.*, **42** (1969), 159–256.
12. Voss, D. L., "Polycarbonate for Advanced Aircraft Transparencies," paper presented at Symposium on Aircraft Transparencies, sponsored by Air Force Materials Laboratory and the University of Dayton, held at Dayton, Ohio, June 24–26, 1969.
13. Dexheimer, R. D. and Vertnik, L. R., "Metal Bonding with Polyamide Hot Melt Adhesives," *Adhes. Age*, **17**, No. 18 (1974), 31–34.

14. Kardos, J. L. and Fountain, R., "Aging Characteristics of Reinforced Epoxy Composites," Washington University, St. Louis, Mo., February 1973.
15. Tuinstra, F. and Koenig, J. L., "Characterization of Graphite Fiber Surfaces with Raman Spectroscopy," *J. Composite Mater.*, **4** (1970), 492–99.
16. Bragole, R. A., "Adhesive Bonding of Polyolefins," *Adhes. Age*, **17**, No. 4(1974), 24–27.
17. Sheratte, M. B., "Polymers for High Impact Application," McDonnell Douglas Corporation, Douglas Aircraft Company, Long Beach, Calif., Report No. MP51,097, September 1968.
18. Litz, R. J., "Developments in Ethylene-Based Hot Melt Adhesives," *Adhes. Age*, **17**, No. 8 (1974), 35–38.
19. Jones, J. F., Bartels, T. T., and Fountain, R., "The Processing and Aging of Boron/Epoxy Composite Materials," *Polym. Eng. Sci.*, **14** (1974), 240–45.
20. Fountain, R. and Haas, T. W., "Application of Infrared Spectroscopy to the Cure of Polyimide Laminates," *J. Appl. Polym. Sci.*, **19** (1975), 1767–70.
21. Swern, D., ed., *Organic Peroxides*, Vol. 3, *Alkyl and Acyl Hydroperoxides*. New York: John Wiley & Sons, Inc. (1972).
22. Boutagy, J. and Thomas, R., "Olefin Synthesis with Organic Phosphate Carbanions," *Chem. Rev.*, **74** (1974), 87–99.
23. Fountain, R. and Kardos, J. L., "High Temperature Elastomeric Bonding for Rain Erosion Boots for Aircraft and Radomes," paper presented at the International Rubber Conference sponsored by the Institution of the Rubber Industry, Brighton, England, May 1972.
24. Fountain, R. and Kardos, J. L., "The Use of X-Ray Photoelectron Spectroscopy (ESCA) to Characterize Cure Inhibition in a Polysiloxane Adhesive," *J. Polym. Sci., Pt. B*, **12** (1974), 161–65.
25. Fountain, R. and Kardos, J. L., "Hydrosilation Cure Inhibition in Polysiloxane Adhesives," *J. Appl. Polym. Sci.*, to be published.
26. Fountain, R., "Characterization and Control of a Structural Epoxy Adhesive," *Polym. Eng. Sci.*, **14** (1974), 597–603.

11. ADHESIVE FRACTURE OF EPOXY AND ELASTOMER EPOXY RESINS

W. D. BASCOM
Naval Research Laboratory
Washington, D.C.

The fracture behavior of a diglycidyl ether bisphenol A (DGEBA) epoxy resin modified with a carboxy-terminated butadiene acrylonitrile (CTBN) has been studied in both mode-I (cleavage) and combined mode-I and -II (cleavage and shear) stress conditions. The CTBN reacts with the DGEBA monomer to form a dispersed phase of 2–5 μ elastomeric particles. The presence of these particles results in increases in mode-I fracture energy of almost 40 X over the unmodified epoxy. Considered from a continuum point of view, the role of the elastomer particle is to enlarge the size of the crack-tip deformation zone.

Studies of the mode-I adhesive fracture of the CTBN-epoxy resins revealed a very strong bond-thickness effect. Adhesive toughness was found to be a maximum when the bond thickness was about the same size as the crack-tip deformation zone, i.e., ≈20 mils. A study of the effect of temperature on mode-I adhesive fracture gave further evidence of the involvement of the deformation zone in the bond-thickness effect.

The CTBN-epoxy resin exhibited an anomalous behavior in combined-mode adhesive fracture tests in that the combined-mode toughness was nearly a factor of 10 lower than the corresponding mode-I toughness. This result has important implications to the use of fracture criteria for adhesive joint design since it had been previously thought that mode-I fracture testing would be sufficient as this is usually the lowest energy mode for most polymers and metals. The results of this study show that this is clearly not the case for adhesive fracture; and consequently, combined-mode testing is required.

INTRODUCTION

The successful use of adhesive bonding to fasten load-bearing structures in aerospace vehicles has encouraged design engineers to consider

structural adhesives for automobile and rail car construction and even for advanced ships such as the hydrofoils and surface-effect vehicles. The advantages of adhesive bonding over conventional mechanical fasteners are lower fabrication costs, smoother skin surfaces, better fatigue resistance, and reduced weight. In addition, adhesive bonding is mandatory in joining composite materials, which cannot tolerate the high stress concentrations encountered with mechanical fasteners. These advantages are especially important in aircraft design and easily outweigh the deficiencies of adhesive bonding, namely, low resistance to peeling forces and, in the case of metal bonds, poor moisture resistance. However, these trade-offs are not realistic for automobile and advanced ship construction so that the future use of adhesives in these technologies will depend on improving peel strength and most especially moisture resistance. Peel resistance is essentially a problem in the fracture toughness of adhesive resins, which is the general topic of this report.

The base resins from which essentially all structural adhesives are formulated are the thermosetting polymers; *i.e.*, epoxies, polyesters, phenolics, etc. These materials offer the required tensile strength to bond load-bearing structures. Equally important, the monomers and oligomers are liquids or semisolids that can be easily applied to adherend surfaces. However, the thermosets are relatively brittle materials having fracture toughnesses 2–3 orders of magnitude less than that of the metals and composites they are called upon to bond. Consequently, all structural adhesives are highly formulated resins; generally complex mixtures of the base resin with elastomers, plasticizers, and inorganic particulate fillers. Indeed, structural adhesive formulation is very much an art that is rarely revealed even in the patent literature.

Despite the complexity (and secrecy) of adhesive formulations they have a common morphological feature; a discontinuous elastomeric phase dispersed in a matrix of the thermoset resin.[1] In this configuration the elastomer imparts a high toughness without a serious loss in the tensile strength and modulus of the matrix resin. Morphologically, these adhesives are closely related to the high-impact polystyrenes and other resins having a low modulus phase dispersed in a high modulus matrix. In fact, there are several similarities in the fracture behavior of all these multiphase resins, as was demonstrated by McGarray and coworkers [2,3] in their studies of polyester and epoxy polymers modified with carboxy-terminated butadiene-acrylonitrile (CTBN) elastomers.

About 20 years ago the Navy recognized that in order to design adhesive-bonded structures there was a need to develop reliability criteria for adhesive joints. The peel and lap shear tests normally used to characterize adhesive strength are too dependent on specimen geometry to be useful for design purposes. Instead, it was judged that fracture toughness is the appropriate criterion for adhesive failure for essentially

two reasons: first, that the adhesive resins are generally brittle materials that fail by crack initiation and propagation rather than by flow and yielding; second, even if the adhesive resin does exhibit yielding, it does so within the confines of a thin (≈0.025 cm) bond line which is small compared to the overall joint dimensions so that the joint fails in a linear elastic, brittle, fashion. The accomplishments of this Navy-sponsored program have been described in the publications of Mostovoy, Ripling, Corten, Patrick, and Bersch[4–14] and include the methodology they developed for adhesive fracture testing and data for epoxy resins and various commercial structural adhesives. Recently, in work at the Naval Research Laboratory, these techniques of Mostovoy *et al.* were employed in a study of adhesive fracture behavior using CTBN-modified epoxy resins as model structural adhesives in an effort to get at the micromechanics of failure.[15–18] The results of that study are reviewed here.

FRACTURE ENERGY AND FRACTURE DESIGN CRITERIA

A few comments are in order about the concept of fracture energy and its use in engineering design. The depth of the discussion is necessarily limited and the reader is referred to the voluminous literature on these subjects for more detailed treatment.[19–21] Modern fracture mechanics began with the Griffith criteria for fracture based on equating the strain-energy content with the energy to create new surface area at the instant of crack propagation. Thus, for a tensile-loaded, edge-notched bar,

$$\sigma_c = \sqrt{\frac{2E\gamma}{\pi a}} \tag{1}$$

where σ_c is the stress at crack initiation, a is the notch depth, and γ is the surface fracture energy. Except for exceedingly brittle materials, the experimentally determined values of γ are orders of magnitude greater than can be accounted for by just the rupture of chemical bonds at a crack tip. Actually, crack initiation involves a number of energy-consuming processes within the immediate vicinity of the crack tip, including viscoelastic and plastic deformation. Irwin[21] demonstrated that the Griffith equation is formally correct if the surface energy term, γ, redefined by Irwin as the strain energy release rate, $\mathcal{G}_c$, is taken to include all the crack tip, energy dissipative processes so that,

$$\sigma_c = \sqrt{\frac{E\mathcal{G}_c}{\pi a}} \tag{2}$$

where $\mathcal{G}_c$ is an index of fracture toughness and in the ideal, brittle limit,

$\mathcal{G}_c = 2\gamma$. The deformation processes are limited to a small volume at the crack tip and the dimensions of this region, *e.g.*, the volume radius (r_c), are also critical conditions for the onset of fracture. Analytical relationships exist between $\mathcal{G}_c$ and these dimensions, but their explicit forms depend upon the model assumed for failure and yielding in the deformation zone, *e.g.*, for elastic–plastic failure,

$$\mathcal{G}_c \approx 6\pi\, \sigma_y\, \varepsilon_y\, r_c \tag{3}$$

where σ_y and ε_y are the yield stress and strain, respectively.

Neither $\mathcal{G}_c$ nor r_c are true material constants. In general, they are time and temperature dependent; especially for polymers. Additionally, they are dependent on material thickness such that in passing from the plane-strain conditions (uniform triaxial stresses) at the crack tip at large thicknesses to plane-stress conditions in thin sections the overall change in fracture toughness is given by:

$$\mathcal{G}_{(\text{plane strain})} = \frac{\mathcal{G}_{(\text{plane stress})}}{(1 - \nu^2)}$$

where ν is Poisson's ratio.

The fracture energy of isotropic solids is a function of the stress state so that it is necessary to define a strain-energy release rate for each of the three principal modes of failure (Figure 1); opening mode $\mathcal{G}_{Ic}$, in-plane shear $\mathcal{G}_{IIc}$, and torsional shear $\mathcal{G}_{IIIc}$.

The quantity most often used to predict failure by unstable crack growth is the stress-intensity factor, K; a measure of the stress in the vicinity of a crack tip. For an isotropic material, the general expression for K is

$$K = \alpha P \sqrt{a} \tag{4}$$

where P is the applied load, a the flaw size, and α is a function determined by the stress conditions and the geometry of the structure. The

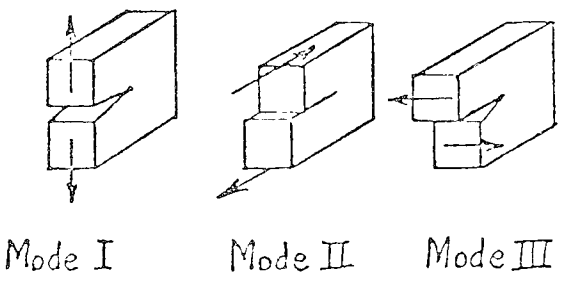


Figure 1. Principal fracture modes.

exact form of α must be determined by a stress analysis of the structure. The strain-energy release rate is related to K by

$$\mathcal{G}_I = \frac{\pi K_I^2 (1-\nu^2)}{E}$$

for the case of mode-I loading and plane-strain conditions. Thus, for a critical value of $\mathcal{G}_{Ic}$ there is a corresponding critical value of K_{Ic}.

In order to predict the failure stress P_c, the explicit form of equation (4) must be determined analytically, K_c must be determined experimentally, and the size of the most severe flaw (internal crack, surface scratch, etc.) must be known. The field of the fracture mechanics is devoted to developing stress analyses and the test methodology of fracture-toughness determinations and flaw detection.

The application of fracture mechanics to adhesive-joint design is complicated by the fact that the explicit form of equation (4) is generally not known. The problem is that solutions of (4) require analyses for the stress distribution at the crack tip and until recently such analyses have not been available for a flaw in an adhesive layer. Erdogan and coworkers[22] have addressed the problem and the application of their results to a simple butt joint in tensile loading has been described by Hilton and Gupta.[23] The analytical difficulties become more severe in complex geometries such as lap shear and scarf joints.

These difficulties can be avoided if the design analysis is based on the strain-energy release rate, $\mathcal{G}$, rather than on the stress-intensity factor. The general expression for $\mathcal{G}$ is given by:

$$\mathcal{G} = \frac{P^2}{2b} \frac{\partial C}{\partial a} \tag{6}$$

where b is the material thickness in the vicinity of the crack and $\partial C/\partial a$ is the change in the compliance, C, of the structure with crack length, a ($C = \delta/P$ where δ is the displacement through which the load P travels). Since $\partial C/da$ is a "global" property of the specimen, equation (6) is independent of the crack-tip stress distribution. In order to develop equation (6) in explicit form for a specific structure, $\partial C/da$ must be determined and this can be obtained experimentally[24] although the procedures are tedious and often inaccurate. Alternately, there are analytical solutions to equation (6) for simple geometries, and in recent years dC/da has been determined by computer-controlled finite-element analyses. Once the proper expression for $\mathcal{G}$ has been obtained, the load P_c for fracture in the adhesive bond line can be computed from an experimentally determined $\mathcal{G}_c$ and the flaw size, a. However, $\mathcal{G}_c$ of a resin in an adhesive joint is different from the $\mathcal{G}_c$ of the resin in bulk. This distinction was clear from the work of Mostovoy *et al.*[9–12] In this report,

a strong dependence of adhesive $\mathcal{G}_c$ on bond thickness and bond angle will be discussed, and it will also be shown that the temperature dependence of $\mathcal{G}_c$ differs for adhesive and bulk resin.

DETERMINATION OF ADHESIVE FRACTURE ENERGY

Mostovoy *et al.*[5–13] devised a tapered-beam test specimen for mode-I fracture energy, $\mathcal{G}_{Ic}$. The explicit form of equation (6) for a cantilever beam is

$$\mathcal{G}_{Ic} = \frac{4P_c^2}{b^2E}\left(\frac{2a^2}{h^3} + \frac{1}{h}\right) \tag{7}$$

where E is the elastic modulus, a is the crack length, and h is the beam height measured normal to the crack tip. Equation (7) requires that the load and crack length be measured simultaneously. However, if the beams are tapered as in Figure 2 so that m = constant, then $\mathcal{G}_c$ is independent of crack length,

$$\mathcal{G}_{Ic} = \frac{4P_c^2}{b^2E}m \tag{7a}$$

and only the load at crack initiation need be measured. Two such

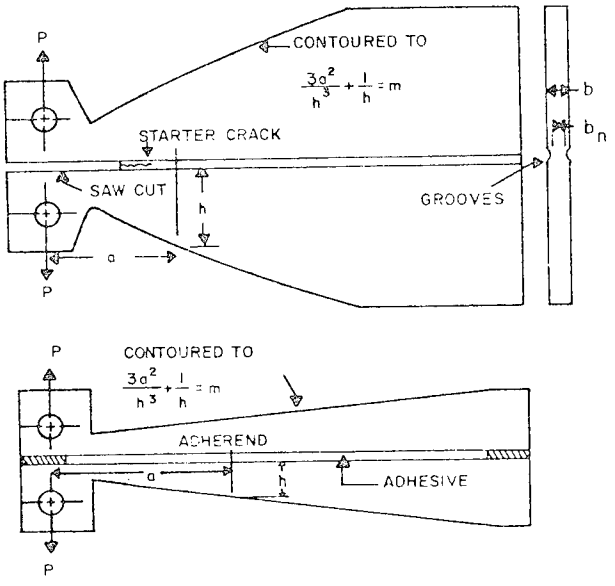


Figure 2. Tapered double-cantilever beam specimen for bulk (A) and adhesive (B) $\mathcal{G}_{Ic}$ testing.[10]

constant-compliance beams are illustrated in Figure 2 for $m = 3$ cm^{-1} and $m = 90$ cm^{-1}. It is important in these tests to avoid inelastic bending of the beam arms, and for this reason the bulk polymer specimens are made quite stiff ($m = 3$ cm^{-1}). Due to the much higher modulus and yield strength of the metal adherends compared to the resin, the adhesive specimen need not be as steeply tapered as the bulk specimen, *i.e.*, $m = 90$ cm^{-1} in Figure 2B.

Equation (7a) has an interesting property in that for the tapered DCB specimen the load-displacement curve should show crack growth at constant load as in Figure 3A. This will be the case if the fracture energy is independent of the crack velocity. Actually most of the polymers being considered here are strain-rate sensitive, *i.e.*, $\mathcal{G}_{Ic}$ decreases with increasing crack rate, so that once the crack is initiated it propagates spontaneously until the strain energy in the specimen is insufficient to continue propagation. At that point the crack arrests. The result is a peaked load-displacement curve as in Figure 3B, with the peaks corresponding to an initiation energy $\mathcal{G}i_{Ic}$, and the valleys to an arrest energy, $\mathcal{G}a_{Ic}$.

The bulk polymer fracture specimens can be prepared either by cutting plate stock into the appropriate shape or by casting and curing in silicone rubber molds. Grooves are then machined along each side to guide the crack through the center plane. A saw cut is made at the loading end and a starting crack is formed by tapping with a sharp blade at the end of the saw cut. In a glassy polymer this produces a short, "natural" crack having a very small crack-tip radius. Erroneously high $\mathcal{G}i_{Ic}$ values are obtained if the starting crack is blunt, *e.g.*, if the blade forms a V-notch without initiating a crack.

The adhesive fracture specimens are assembled as shown in Figure 4. The two metal halves are clamped together with PTFE spacers at each end to establish the desired bond thickness. One side of the bond is closed with pressure-sensitive tape and the liquid polymer is poured into the resulting cavity. After heat curing, the tape is removed and any excess resin is machined or abraded off. When testing commercial structural film adhesives, the specimen is prepared by placing strips of the film between the tapered beams. These films usually contain a support or skrim cloth which establishes the bond thickness without any need for spacers. The bonding pressure recommended by film-adhesive suppliers may not be attainable using spring loaded clips as in Figure 4, so vacuum bagging can be used, or mechanical jigging as described by Mostovoy and Ripling.[14] Details concerning the tapered DCB specimen and its use in adhesive testing can be found.[5–18] In all of the work discussed here, the adherends were 5086 or 2024 aluminum alloys. The choice of alloy had no effect on the results.

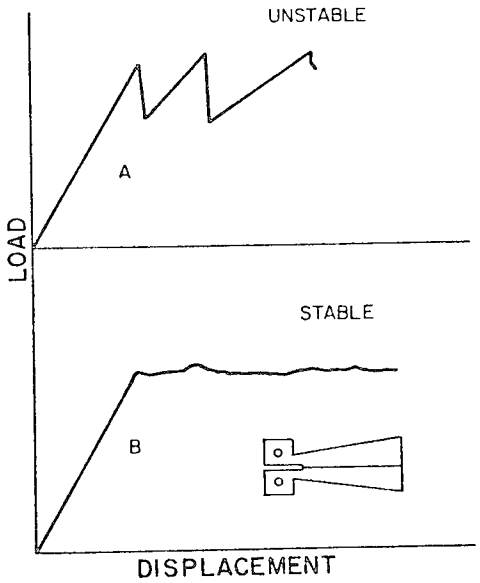


Figure 3. Load-displacement curves for unstable (A) and stable (B) crack propagation of tapered double-cantilever beams.[16]

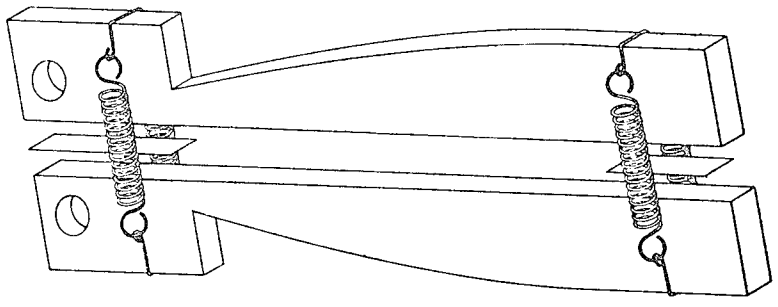


Figure 4. Schematic of tapered double-cantilever beam adhesive fracture test specimen.[16]

It is important to test adhesive fracture under stress conditions other than mode-I loading. In fact, most adhesive joints are designed to minimize peeling (mode-I) loads in favor of shear loads. A specimen designed by Ripling, Mostovoy, and Patrick[5] for pure shear (mode-II) and a scarf joint described by Trantina[25–27] for mixed-mode (combined tensile and shear forces on the bond line) are illustrated in Figure 5. These specimens are prepared and assembled in much the same way as the mode-I specimen. The side arms on the mixed-mode specimen are clamped with spring clips to hold the two halves together during sample preparation. The mode-II fracture energy can be calculated from:

$$\mathcal{G}_{II} = \frac{P_c^2}{b^2 h E} \tag{8}$$

where h is the beam height as shown in Figure 5A.

Trantina developed a finite-element stress analysis for the combined-mode specimen of Figure 5B from which the adhesive fracture energy can be computed. He presented his results in terms of the dimensionless parameter, f,

$$f = \frac{K b W}{P} \tag{9}$$

where K is the stress-intensity factor, P the tensile load, and b and W the specimen thickness and width, respectively. This parameter is tabulated for various crack length to width ratios (a/W) and crack angles (ϕ) in Reference 27. The fracture energy (total critical strain-energy release rate) is calculated from the critical stress-intensity factor, using

$$K_{(I,II)c}\phi^2 = \mathcal{G}_{(I,II)c}\phi \tag{10}$$

where E is the tensile modulus of the aluminum. It should be noted that Trantina's analysis was for a monolithic specimen with edge cracks at various angles (ϕ). He presumed the bond thickness to be too thin to affect the analysis. This assumption has been demonstrated to be correct by showing that the compliance derivative, dC/da, of the 45°-specimen is identical within experimental error to that of a specimen constructed entirely of aluminum with edge notches sawed at 45° to the loading direction.[28]

MODE-I ADHESIVE FRACTURE

Unmodified Epoxies

Some perspective as to the magnitude of polymer fracture energies relative to other materials is offered in Figure 6. The $\mathcal{G}_{Ic}$ values of

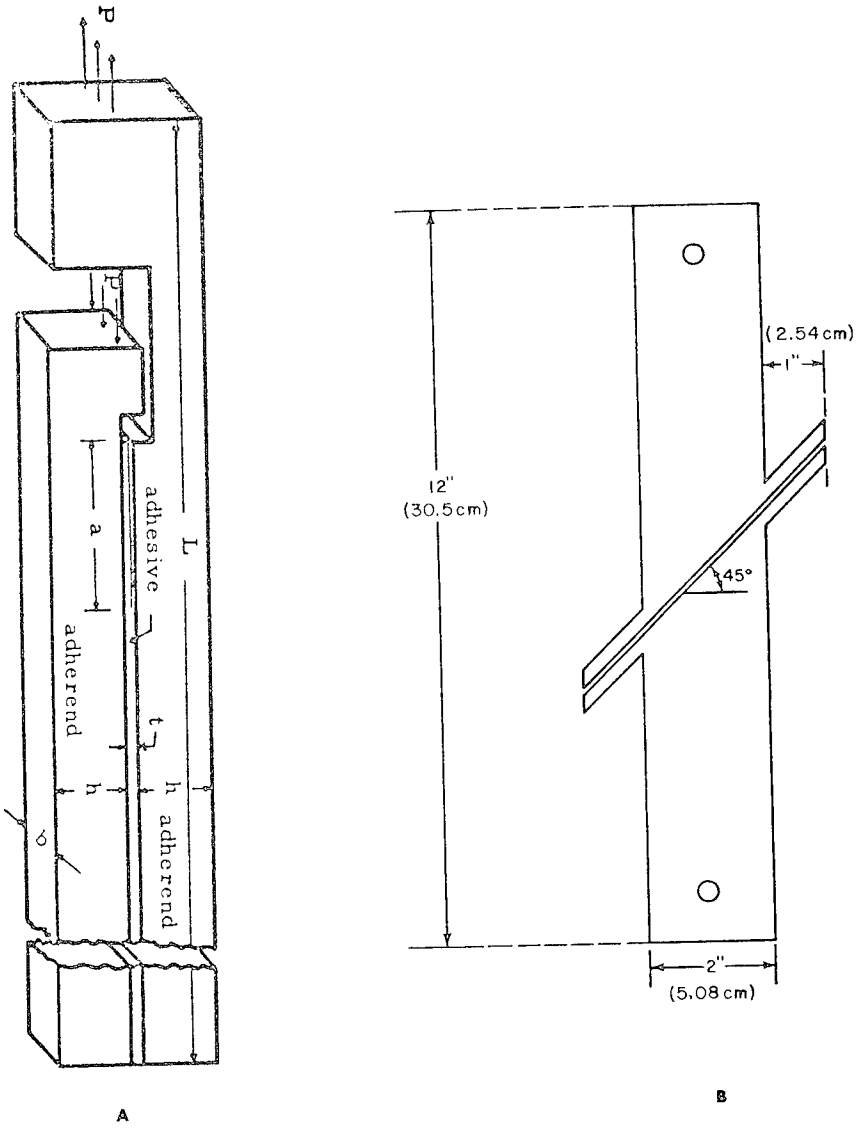


Figure 5. Test specimens for mode-II (A) and mixed-mode (B) adhesive fracture.[5,15]

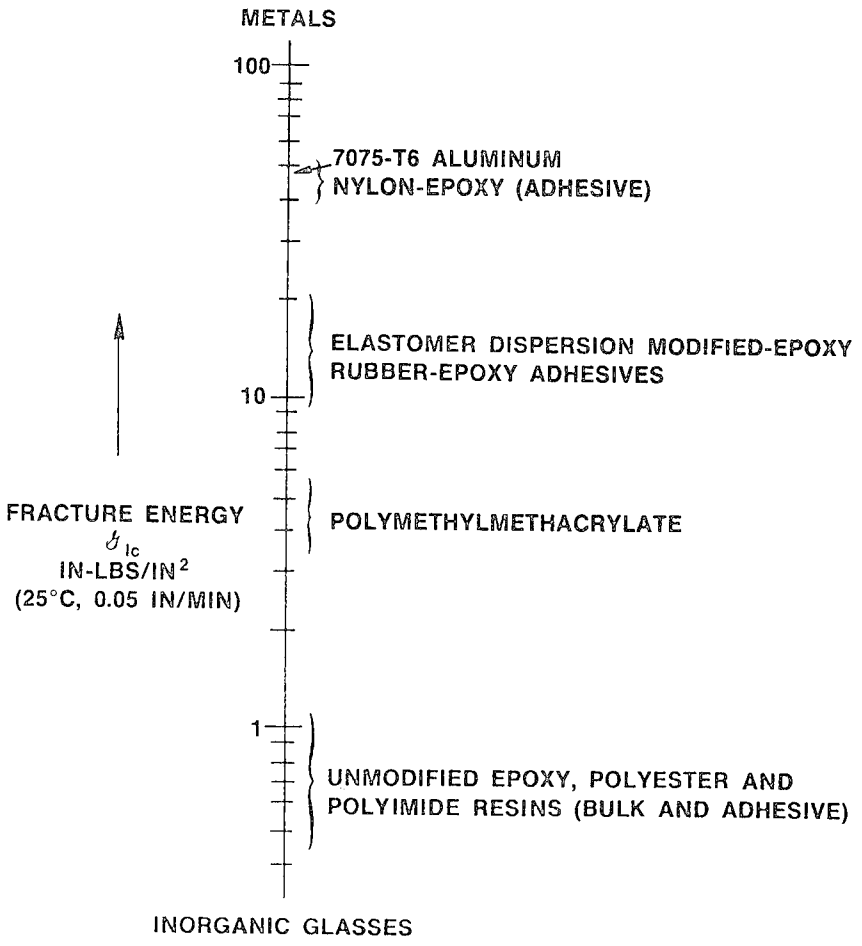


Figure 6. Relative ranking of fracture energies (1 in.-lb/in.^{2} = 175.3 J/M^2).

various polymers in bulk and as adhesives are scaled between the very brittle inorganic glasses and the relatively tough metals. Note the large gain in fracture energy by the addition of an elastomer to an epoxy and the even greater values obtained for the nylon–epoxy adhesive formulations which actually approach the metals in toughness.

A comparison is made in Table 1 of the bulk and adhesive fracture energies of a few epoxy resins based on diglycidyletherbisphenol A (DGEBA) and cured with various agents. The values range between 50 and 200 J/m^2 with no systematic dependence on the type of curing agent

Table 1. Adhesive Fracture Energies of Unmodified Bisphenol — A Diglycidyl Ether Resins

(25°C, 45% RH, 0.13 cm/min)

Curing Agent	$\mathcal{G}_{Ic}$ (J/m^2) Adhesive	Bulk
Hexahydrophthalic Anhydride[15]	116	136
Hexahydrophthalic Anhydride[12]	105	210
"Nadic" Methyl Anhydride[18]	124	86
Piperidine[16]	121	154
Tetraethylpentamine[12]	58	88
M-Phenylenediamine[18]	177	148

or whether the energies were determined in bulk or in an adhesive specimen.

Mostovoy, Ripling, and Bersch[11] found an inverse correlation between $\mathcal{G}_{Ic}$ and resin tensile modulus for DGEBA cured with various amounts of tetraethylenepentamine and post-cured at different temperatures. These variations would be expected to affect the tensile properties of the resin and an inverse relation between $\mathcal{G}_{Ic}$ and E might be expected from equation (3) if the substitution $\varepsilon = \frac{\sigma_y}{E}$ is made:

$$\mathcal{G}_{Ic} \approx 6\pi \frac{\sigma_y^2}{E} r_c \tag{11}$$

but only under the fortuitous condition that σ_y and r_c are relatively constant. Actually, the relation between E and $\mathcal{G}_I$ of Reference 11 was nonlinear in contrast to the linear dependence of equation (11). They also found an inverse relation between $\mathcal{G}_{Ic}$ and both tensile modulus and tensile strength for DGEBA cured with hexahydrophthalic anhydride which is clearly unexpected from equation (11). Much more work is required to establish the interrelationship between resin tensile properties and fracture energy, but, even at best, these can only be approximate correlations since the inelastic deformation processes that determine fracture energy can only be crudely modeled by the elastic properties of the resin.

Judging from the magnitude of the fracture energies in Table 1, it is clear that inelastic dissipative processes dominate crack initiation. The rupture of chemical bonds can account for no more than 10 J/m^2, less than 10% of the measured energies.[29] Most of the fracture energy involves viscoelastic and plastic deformation of the resin structure at the crack tip. Post-failure scanning electron microscopy (SEM) examination

of bulk and adhesive resin fracture surfaces reveal clear evidence of plastic deformation in the region of crack initiation. These regions of deformation appear as fingernail-shaped markings across an otherwise smooth surface. An example is shown in Figure 7 from a bulk test of the DGEBA-piperidine resin. Similar evidence of plastic deformation of epoxy resins in the region of crack initiation has been presented by Patrick *et al.*[30] Intuitively, plastic yielding and flow of these highly cross-linked resins is difficult to accept in view of their usual brittle behavior in tensile tests. Nonetheless, the stress magnification at the tip of a crack is sufficient to induce plastic flow. The stress conditions in this region are uniformly triaxial, and probably induce void formation similar to the crazing of crack tips in thermoplastic polymers[31] although there is no published evidence to this effect.

Quantitative description of the crack-tip deformation must involve the time–temperature dependent viscoelastic-plastic properties of the resin. Although some progress has been made in this direction, the results are complex and at best approximate.[32,33] For the present it is necessary to rely on the simpler models, recognizing their limitations. One of the more useful of these is the elastic-plastic model which assumes that within the deformation zone there is a wedge of material at yield stress, σ_y, but at the failure strain, ε_f (Figure 8). Surrounding this wedge the material is at the yield stress and strain, ε_y, out to the elastic-plastic boundary which envelopes a volume with a diameter of $2r_c$.

The arrest fracture energies, *i.e.*, the "valleys" in the load-displacement curve of Figure 3B are important from an engineering point of view in that the difference between initiation and arrest energies reflects the tendency for a crack to propagate spontaneously. The physical significance of fracture arrest is less understood than is initiation. Presumably, crack arrest for the tapered DCB specimen occurs when the strain energy driving the crack is reduced by elastic and inelastic resin deformation (and perhaps by kinetic energy losses) to a level insufficient to continue crack motion. Whether this critical level is characteristic of the material is problematical. Nonetheless, $\mathcal{G}_{Ic}$ arrest values for bulk and adhesive resin fracture have been found to be as reproducible as the initiation energies.

Elastomer-Modified Epoxies

The addition of carboxy-terminated butadiene acrylonitrile (CTBN) elastomers to epoxy resins increases the fracture energy by factors of 30–40 over the unmodified resin. In Table 2, $\mathcal{G}_{Ic}$ values are listed for the DGEBA–piperidine resin with increasing amounts of a 3500 number average M.W. CTBN. In the concentration range up to 15%, the elas-

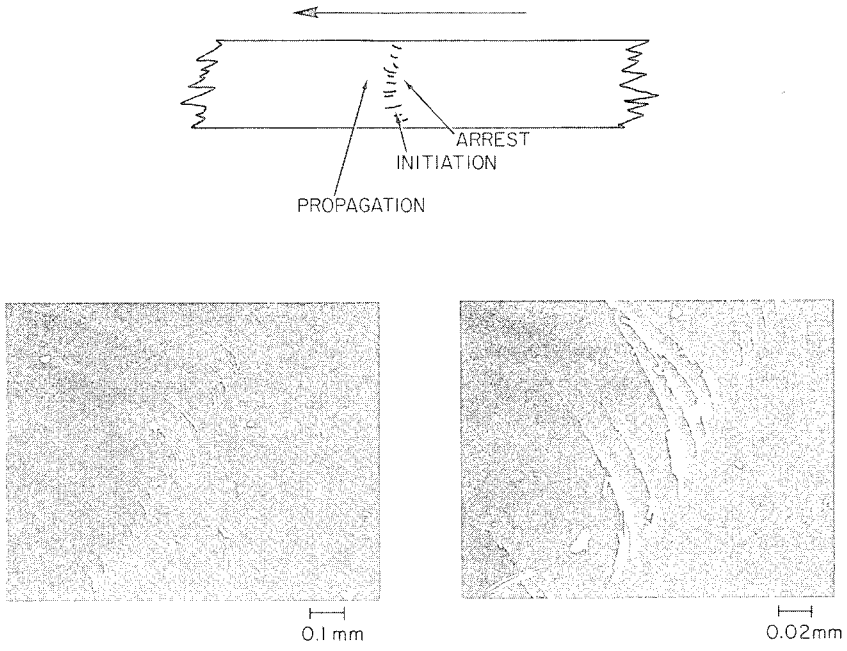


Figure 7. SEM evidence of plastic flow at crack initiation on a fracture surface of an unmodified epoxy resin.[16]

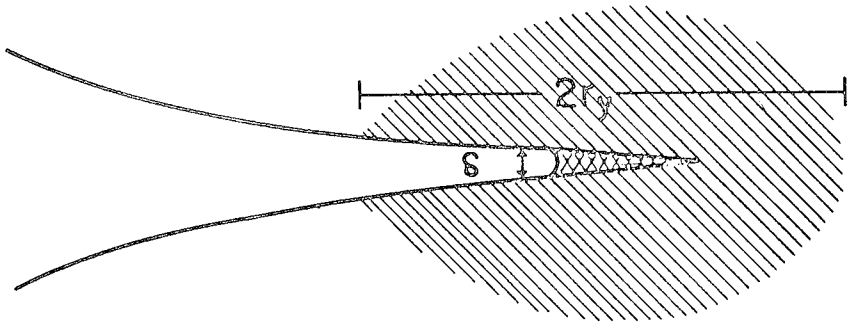


Figure 8. Schematic of the crack-tip deformation zone of an elastic-plastic material.

Table 2. Bulk Fracture Energy and Deformation Zone Size for CTBN–DGEBA–Piperidine Epoxy Resins[16]

CTBN Concentration (wt%)	Fracture Energy, $\mathcal{G}_{1c}$ (J/m^2)	Deformation Zone Size, $2r_c$ ($cm \times 10^{-3}$)
0	121	0.8
4.5	1050	12.4
10	2720	21
15	3430	33
20	3590	70

tomer precipitates out early in the resin cure as spherical particles with diameters of 2–5 μm.[2,3,34,35,36] These particles can be seen in the fracture surface of an elastomer-epoxy resin shown in Figure 9. At concentrations above 15% the elastomer does not precipitate out but instead forms a more or less homogeneous blend, and with increasing elastomer the fracture energy declines sharply.

One of the merits of elastomer-epoxy dispersions is that the large gain in toughness is accomplished with relatively little loss in the high tensile strength, modulus, and thermo-mechanical resistance of the epoxy matrix resin. This is illustrated in Figure 10 for the DGEBA-piperidine system. Above 15% CTBN, resin composition passes from a dispersion to a blend and there is an abrupt decline in strength. It is for just this retention of properties that the dispersed elastomer morphology is sought in formulating structural adhesives.

As with the unmodified epoxy resins, the CTBN-epoxy material also exhibited fingernail markings on the fracture surfaces at the positions of crack initiation. These markings are much broader on the modified resin than on the simple epoxy, and are found to be composed of holes left by the deformed elastomer as illustrated in Figure 11. Beyond these regions of crack initiation (see Figure 9) the surface is very rough but the elastomer particles are relatively undeformed, indicating that the strain rate of the propagating crack was too fast to allow significant plastic deformation.

Considered from a continuum point of view, the role of the elastomer particles is to allow a much larger volume for plastic deformation at the crack tip. In plain-strain mode-I fracture, there is a more or less symmetrical dilatation of the particles accompanied by plastic flow of the epoxy matrix. This deformation gives rise to a stress whitening which is responsible for the large fingernail marking in Figure 11, and just prior to crack initiation there is a uniform whitish zone at the crack



Figure 9. Region of fast crack propagation on a CTBN-epoxy fracture surface.[16]

tip shown schematically in Figure 12. Relaxation of the stress removes the zone except for a slice ahead of the crack (Figure 11). Buchnall and Smith[37] observed this stress-whitened zone at crack tips in elastomer-modified, high-impact polystyrene and McGarry *et al.*[2,3] have described it for a CTBN-modified epoxy resin. The importance of the deformation zone size in determining the toughness of the CTBN–epoxy resins can be judged from equation (11) and the data in Figure 10. Of the three variables that determine fracture energy, σ_y, E, and t_c, the tensile strength actually decreases the change in modulus is too small to account for nearly a fortyfold increase in $\mathcal{G}_{Ic}$, all of which clearly indicates the commanding role of the zone diameter in the enhanced toughness. Calculation of $2r_c$ gives values of 10 μm for the unmodified DGEBA– piperidine resin and 350 μm for the resin with 15% CTBN. The similarity between the stress-whitened patterns of Figure 12 and the schematic of the idealized crack-tip deformation zone of Figure 8 gives some confidence in applying the elastic–plastic model of fracture [*i.e.*, equations (3) and (11)] to these elastomer-modified resins.

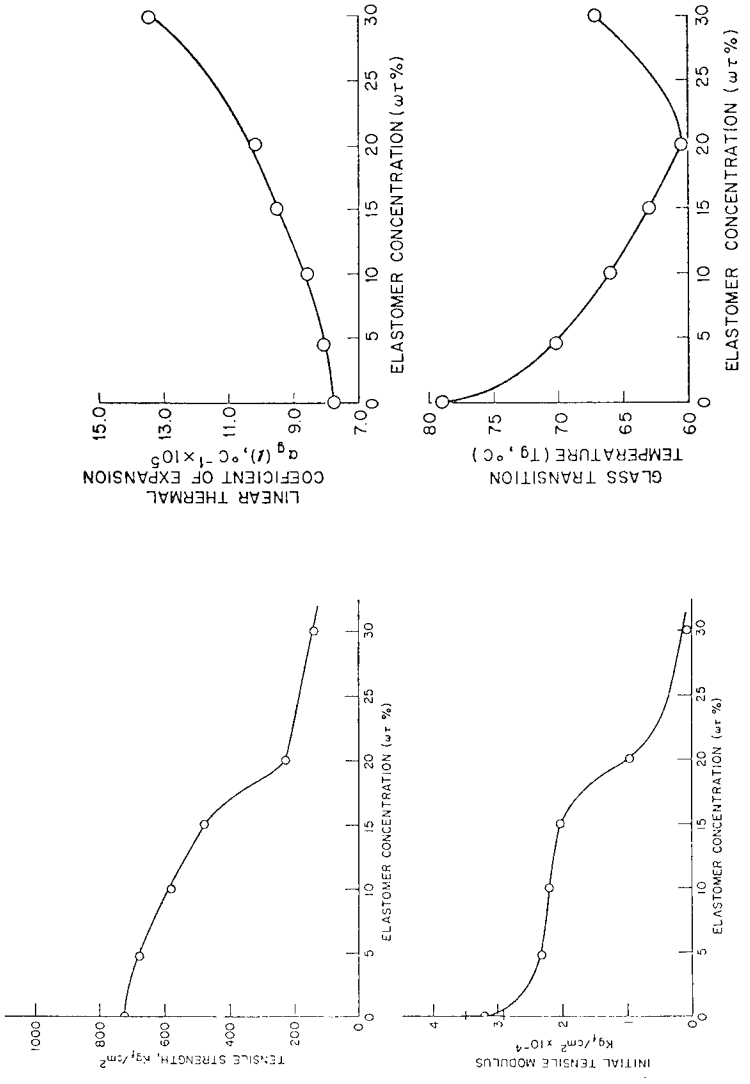


Figure 10. Effect of CTBN elastomer on mechanical and thermo-mechanical properties of the DGEBA-piperidine epoxy resin.[16]

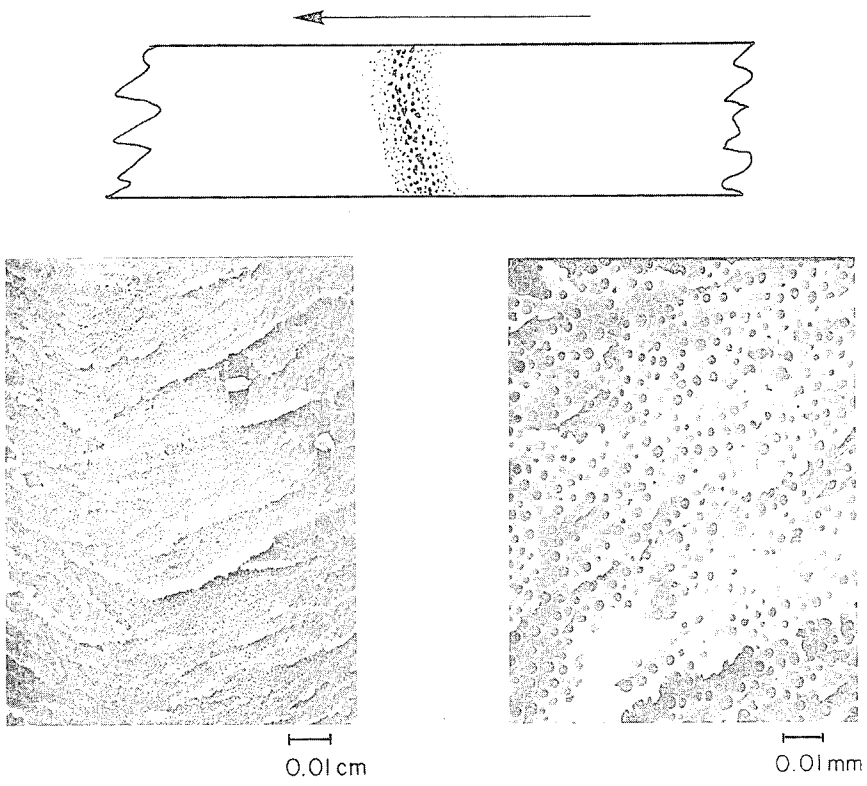


Figure 11. Region of crack initiation on a 15% CTBN–DGEBA–piperidine resin fracture surface.[16]

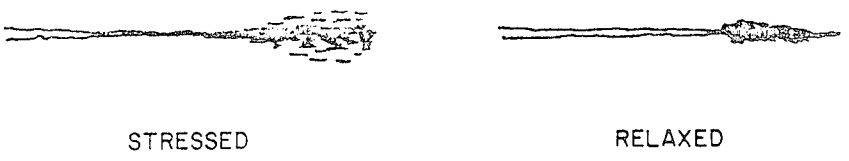


Figure 12. Schematic of stress-whitened deformation zone in CTBN–epoxy resins under stress and after removal of load.[16]

The fracture behavior of the CTBN–epoxy resins as adhesives is dominated by strong bond-thickness effects. The reason for this is not hard to discover when it is realized that the plastic deformation zone, $2r_c$, for many of these resin formulations is actually larger than the usual 5–10 mil (0.013–0.025 cm) bond thickness of most adhesive joints. Figure 13 shows the effect of bond thickness on $\mathcal{G}_{Ic}$ for the 15% CTBN–DGEBA–piperidine resin. The important features in this figure are the maximum in fracture energy at about 0.05 cm and the stable-unstable transition in the mode of crack propagation. At the maximum, the deformation zone size, $2r_c$, is approximately equal to the bond thickness. As the bond thickness is reduced, there is a change in the locus of failure from center-of-bond to the resin–adherened boundary as illustrated schematically in Figure 14. The entire resin layer becomes stress whitened in the thin-bond failure, and SEM post-failure examination revealed complete dilatational deformation of the resin (as shown in Figure 15) and that failure had occurred near the boundaries and left islands of resin on both fracture surfaces. Separation occurred outside of the roughness of the adherend but close enough to replicate the tool markings on the metal.

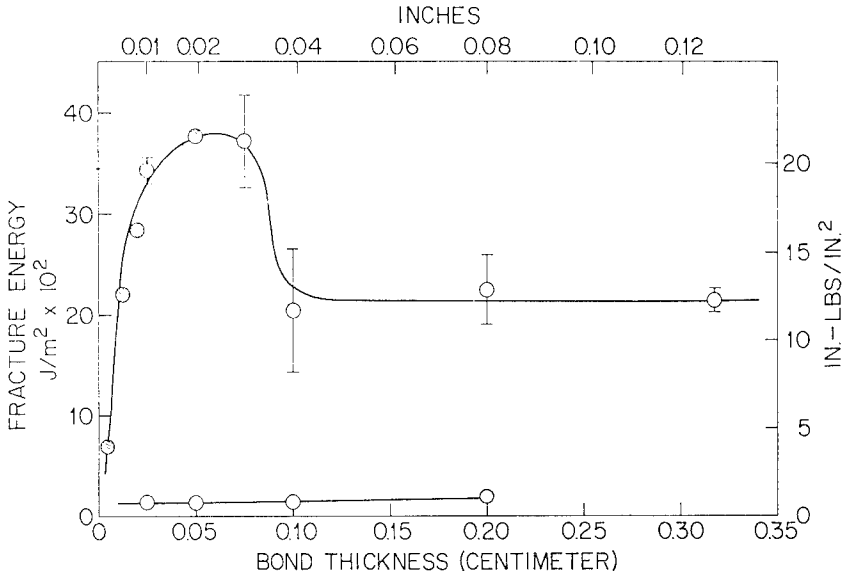


Figure 13. Effect of bond thickness on adhesive $\mathcal{G}_{Ic}$ for an unmodified epoxy resin and for a CTBN-epoxy resin (upper points). Shaded circles indicate stable crack propagation (25°C and 0.13 cm/min loading rate).[16]

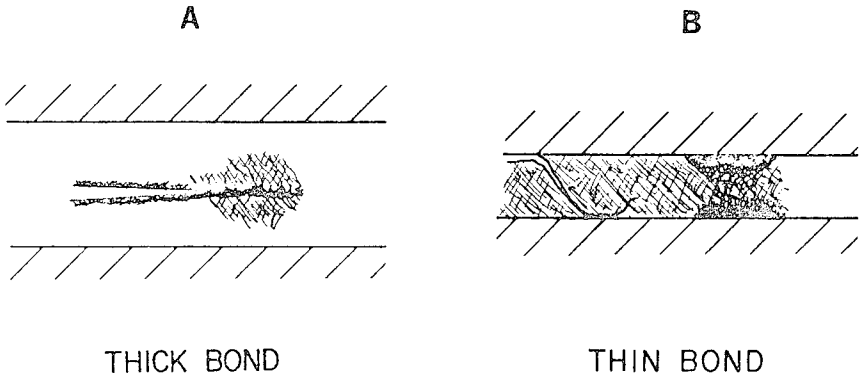


Figure 14. Appearance of stress-whitened zone in a CTBN–epoxy adhesive layer when bond thickness is greater (A) or less (B) than $2r_c$.[16]

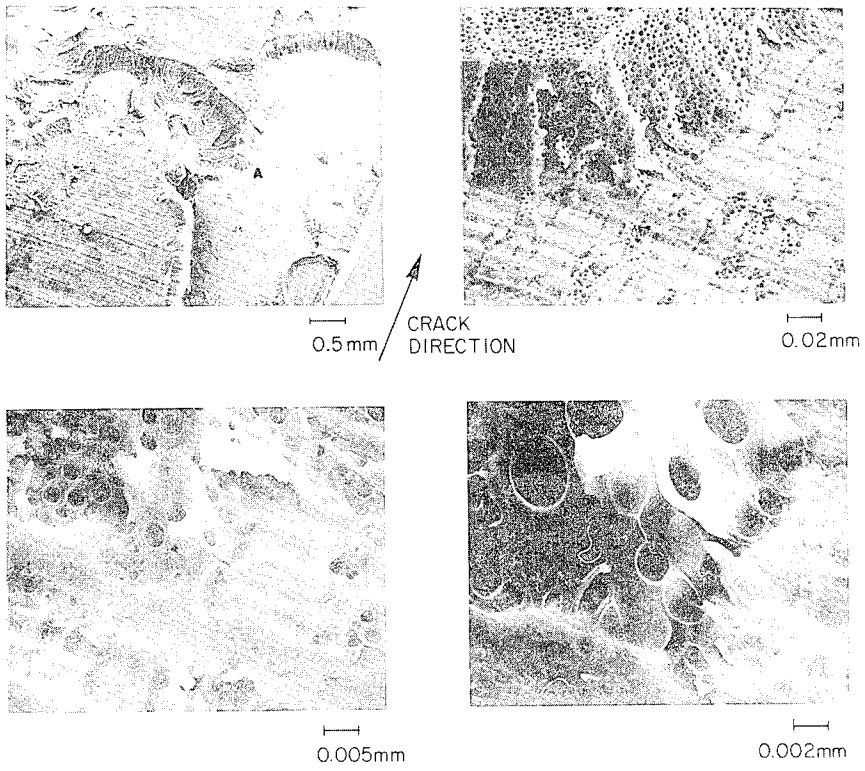


Figure 15. SEM post-failure appearance of a "thin" bond adhesive fracture of a 15% CTBN–DGEBA–piperidine resin.[16]

The decline in adhesive $\mathcal{G}_{Ic}$ as the bond thickness is reduced from the maximum point can be viewed as the result of increasing constraint on the plastic deformation of the resin; in effect, a reduction of $2r_c$ in equation (11). Note that the bond thickness for optimum adhesive-joint performance is not at the maximum but at a somewhat thinner bond where the mode of crack propagation is stable with less chance of catastrophic fracture. In Figure 13 this optimum point would be at about 0.01–0.03 cm (5–10 mils), which is the usual range of thickness specified in adhesive bonding technology.

The decline in toughness for bond thicknesses greater than at the maximum is not fully understood. In this region failure is center-of-bond and the fracture markings are broad, fingernail-shaped features very similar to those seen on bulk specimens of the resin (Figure 11). Some evidence has been presented that the decrease in $\mathcal{G}_{Ic}$ in the thick-bond region is the result in a change from plane-strain conditions at the maximum to conditions approaching plane-stress as the bond is thickened.[18]

Effect of Temperature on $\mathcal{G}_{Ic}$

In the work of Mostovoy and Ripling[38] the temperature dependence of mode-I adhesive fracture energy was investigated for unmodified epoxy resins and the results had the general shape given in Figure 16. At the high-temperature end the toughness increases sharply as the glass transition temperature (Tg) is approached. An increase in fracture energy near Tg is associated with an increase in molecular mobility allowing greater plastic deformation at the crack tip. At the lower end of the

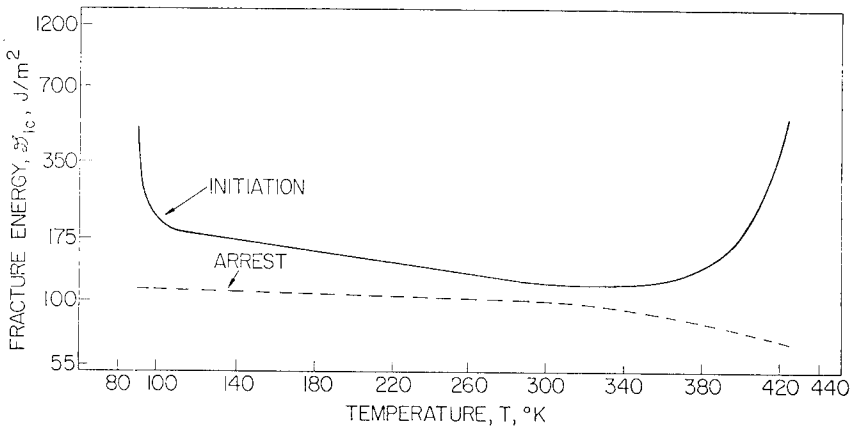


Figure 16. Typical adhesive fracture energy vs. temperature curve for unmodified epoxy resins in bulk and as adhesives.[38]

temperature spectrum (≈90°K) the steep rise in $\mathcal{G}_{Ic}$ may be related to some second-order structural transition, although this seems unlikely at such a low temperature since there are distinct β-transitions at higher temperatures which do not affect $\mathcal{G}_{Ic}$. More likely, the high toughness near 90°K is due to the plasticizing effect of the LN_2 coolant as was described by Olf and Peterling[39] in the fracture of polymers.

The effect of temperature on the bulk fracture energy of the 15% CTBN–DGEBA resin given in Figure 17 indicates a rise in $\mathcal{G}_{Ic}$ as the temperature approaches the *Tg* characteristic of the epoxy matrix. The fact that it is the matrix *Tg* that dictates this thermomechanical response is evidence that it is the viscoelastic (plastic) response of the matrix that governs energy dissipation at the crack tip and that the function of the elastomer particles is to enlarge the volume in which this dissipation occurs relative to the unmodified epoxy.

The effect of temperature on the adhesive $\mathcal{G}_{Ic}$ of the 15% CTBN–DGEBA–piperidine resin is given in Figure 18 as a function of bond thickness. Note that the maximum in $\mathcal{G}_{Ic}$ and the stable-unstable transition in crack propagation shifts to higher bond thicknesses as the temperature is increased. As indicated earlier, this maximum occurs when the crack-tip deformation diameter $2r_c$ is about equal to the bond thickness. Accordingly, the shift in the maximum point with temperature reflects the effect of temperature on $2r_c$. Zone diameters were calculated for the 15% CTBN–resin at the various test temperatures of Figure 17, using equation (11) and the resin tensile strengths and moduli.[18] In Table 3 these zone sizes are compared with the corresponding bond thickness (h_{max}) at maximum $\mathcal{G}_{Ic}$. The agreement is nearly quantitative at the higher temperatures but becomes less satisfactory even at 25°C. Part of this discrepancy can be attributed to the fact that the tensile strength

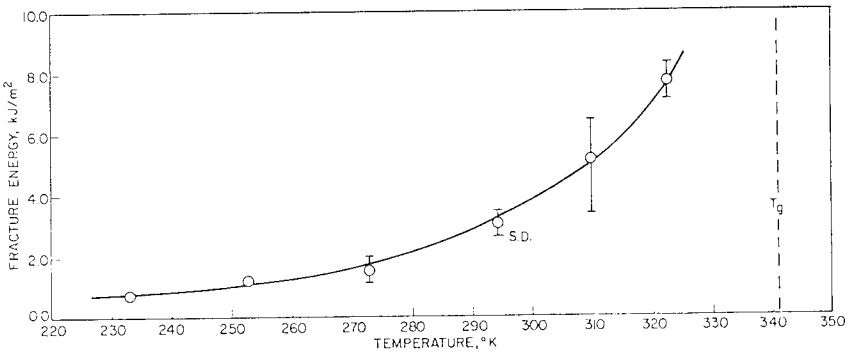


Figure 17. Bulk $\mathcal{G}_{Ic}$ vs. temperature for a 15% CTBN–DGEBA–piperidine epoxy resin.[18]

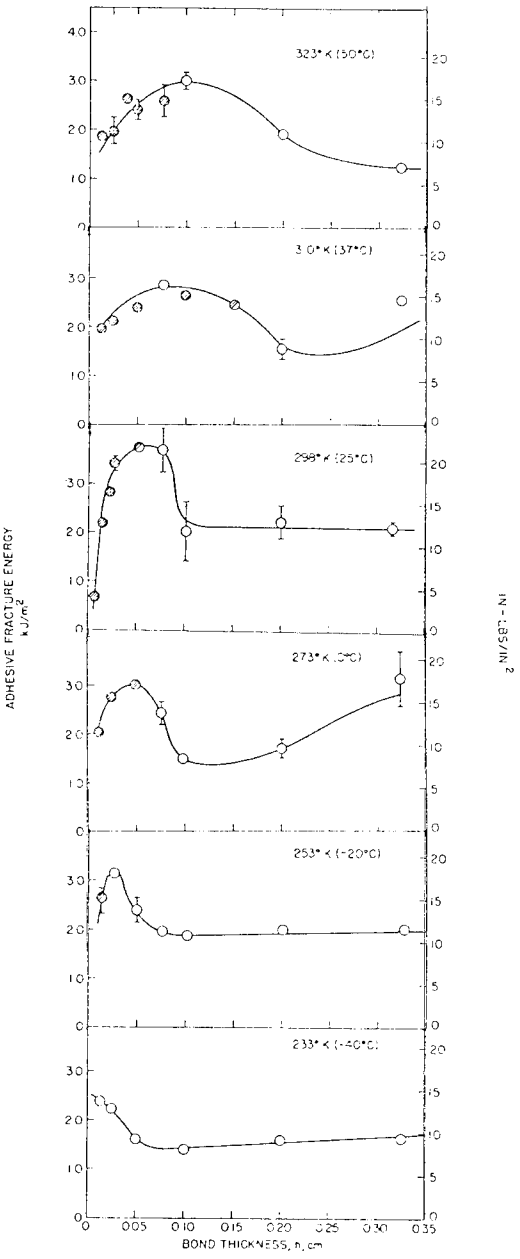


Figure 18. Adhesive $\mathcal{G}_{1c}$ vs. bond thickness and temperature for a 15% CTBN–DGEBA–piperidine epoxy resin.[18]

Table 3. Comparison of Bond Thickness, h_{max}, at Maximum Fracture Energy With Crack-Tip Deformation Zone Diameter, $2r_c$[18]

Temp, °K	h_{max} (cm)	$2r_c$ (cm)
323	0.10	0.12
310	0.075	0.078
298	0.060	0.033
273	0.050	0.013
253	0.025	0.008
233	< 0.01	0.004

increasingly underestimates the true yield strength as the temperature decreases, and the error is aggravated by the use of σ_y^2 in computing r_c. Nonetheless, the shift in $\mathcal{G}_{Ic\ (max)}$ and the transition from stable to unstable propagation toward smaller bond thicknesses is clearly associated with a decrease in $2r_c$ with temperature.

It is evident from the data in Figure 18 that a comprehensive picture of the effect of temperature on adhesive fracture requires fracture measurements as a function of bond thickness. To illustrate this point, a plot of adhesive $\mathcal{G}_{Ic}$ versus temperature is given in Figure 19 for 0.025-cm (10 mil) bond thickness. Plotted in the same figure (broken line) are the data of Mostovoy and Ripling for a commercial "rubber-modified epoxy" structural adhesive that had also been tested at 10-mil bond thickness. Note that in both cases the toughness was maximum at room temperature. In a study of six other commercial modified-epoxy adhesives, including a nylon-epoxy composition, Mostovoy and Ripling found that the optimum toughness was at or very near room temperature. Clearly, the CTBN–epoxy serves as a relatively simple model for structural adhesives both in the magnitude and temperature dependence of adhesive $\mathcal{G}_{Ic}$.

The decrease in $\mathcal{G}_{Ic}$ above and below room temperature when measured at constant bond thickness can be understood in terms of equation (11). At temperatures below 25°C the decline in adhesive toughness must be attributed to a decline in the deformation zone size r_c, and not to changes in σ_y or E which increase as the temperature is lowered.[18] Above room temperature the decline in toughness with increasing temperature (Figure 19) is due to the fact that at constant bond thickness the r_c term in equation (11) cannot increase and, as yield strength and modulus decrease with increasing temperature, the adhesive $\mathcal{G}_{Ic}$ decreases. This trend is in distinct contrast with the bulk toughness for which there is no constraint on development of the deformation zone and $\mathcal{G}_{Ic}$ increases progressively as Tg is approached.

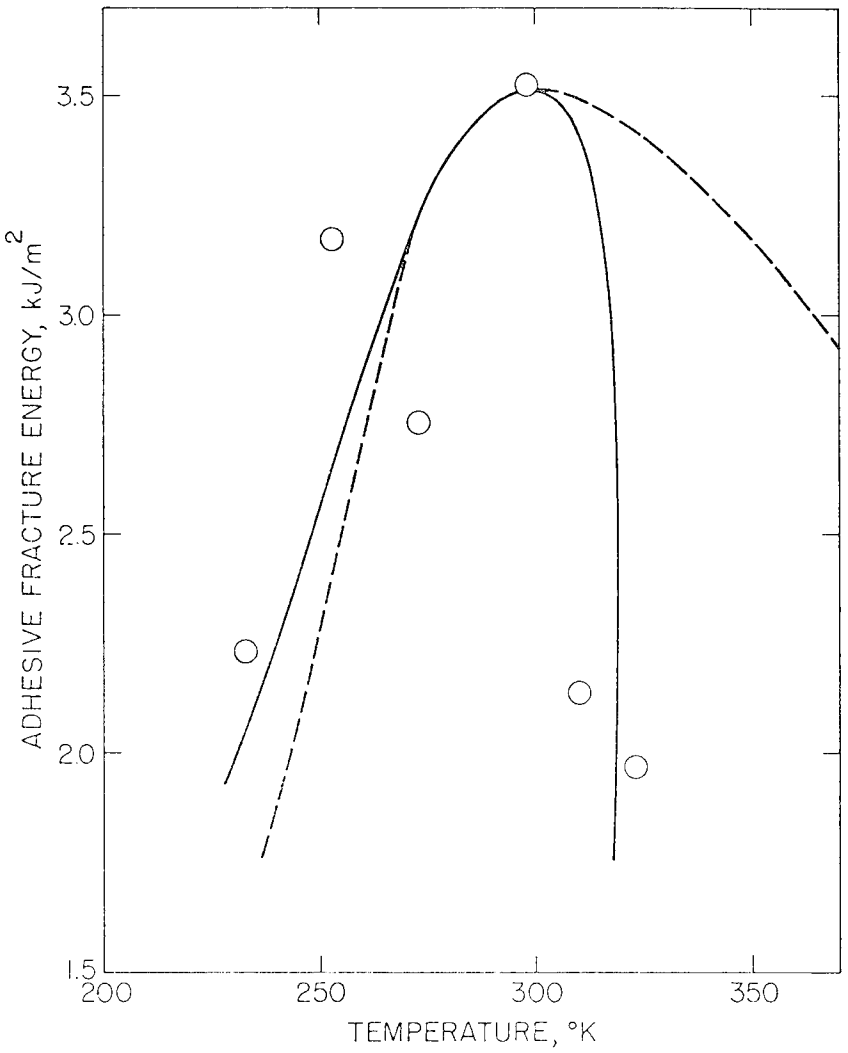


Figure 19. Adhesive $\mathcal{G}_{Ic}$ vs. temperature at constant bond thickness (0.025 cm) for a 15% CTBN–DGEBA–piperidine resin, ○, and an elastomer-epoxy commercial structural adhesive, (----).[18]

COMBINED-MODE FRACTURE

Unmodified Epoxies

It has been determined both experimentally and theoretically[40,41] that mode-I is the lowest energy fracture mode. Thus, a crack always propagates along a path normal to the direction of greatest tension. In other words, a crack in an isotropic plate will propagate in mode-I fracture regardless of how the initial flaw is oriented with respect to the applied load. Such is not necessarily the case in adhesive fracture, since flaw propagation is constrained to the resin layer regardless of the orientation of the bond line — except, of course, when the adherend has a lower toughness than the resin (*i.e.*, bonding composite materials). Consequently, attention must be given to adhesive fracture in combined stress conditions.

Ripling, Mostovoy, and Patrick[5] determined the mode-II adhesive fracture of a DGEBA–TEPA resin using the specimen illustrated in Figure 5A. Trantina[26] determined the mixed-mode adhesive fracture behavior of the same epoxy resin using the scarf-joint specimen in Figure 5B, and Bascom *et al.*[15] used the same specimen design to study the mixed-mode adhesive fracture behavior of a DGEBA–HHPA and a DGEBA–piperidine resin. The fracture energies are listed in Table 4 with the notation $\mathcal{G}_{IIc}$ and $\mathcal{G}_{(I,II)c}$ ϕ for mode-II and mixed-mode fracture respectively. The mode-I values are also presented and are comparable to the $\mathcal{G}_{(I,II)c}$ ϕ values, with the latter generally higher. The shear-energy values were better than a factor of 10 greater than either the mode-I or mixed-mode values. However, observations by Ripling *et al.* and at this laboratory[28] suggest that failure of the shear specimen does not occur by simple mode-II fracture. Instead, microcracking occurs in the resin layer principally near the loaded end of the specimen and along planes at an angle to the shear direction. These microcracks subsequently extend to the inter-

Table 4. Effect of Fracture Mode on Adhesive Fracture Energy of DGEBA–Resins[5,10,15,16]

Resin	Fracture Energy (J/m²)		
	$\mathcal{G}_{Ic}$	$\mathcal{G}_{IIc}$	$\mathcal{G}_{(I,II)c}$ 45°
TEPA–DGEBA	70	1450	130
HHPA–DGEBA	116	—	140
Piperidine-DGEBA	121	—	255

faces and are joined by failure along the boundaries. Consequently, the high apparent $\mathcal{G}_{IIc}$ values reflect not only the stress to initiate microcracks (in some mixed-mode fashion) but also includes the stresses needed to join the microcracks and overcome the frictional resistance of the jagged surfaces to slide past each other. Presumably, the values in Table 4 for $\mathcal{G}_{IIc}$ are much too high. The most that can be said is that $\mathcal{G}_{IIc}$ is greater than the energy needed to initiate the microcracking.

An interesting feature of the fracture of adhesive specimens in combined loading (*i.e.*, scarf joints) is that the locus of failure is invariably near the interface. This was the case even though the same resins exhibited center-of-bond failure in the mode-I double-cantilever beam tests. The locus of failure as determined by Trantina[26] is presented schematically in Figure 20. The precrack formed by wedging open the side arms was usually center-of-bond along $\overline{A\,B}$ as would be expected for cleavage. As the specimen was loaded, the crack jumped toward the interface along $\overline{B\,C}$ and then, at a still higher load, propagation occurred along the boundary, $\overline{C\,D}$. Bascom *et al.*[15] examined this apparent interfacial failure of the scarf joint in detail. They determined by C-14 radioactive labeling of the resin (DGEBA–HHPA) that a residual layer was invariably left on the adherend so that failure was not truly interfacial.

As might be expected, they found that the surface roughness of the adherend had a significant effect on $\mathcal{G}_{(I,II)c}$ In Table 5 the fracture energies for $\phi = 45°$ are given for aluminum adherends with different surface roughnesses. Clearly, the interrelationship is complex between roughness and fracture energy. Bascom *et al.*[15] concluded that the deep surface scratches markedly retarded crack initiation (from point C in Figure 20) to give high $\mathcal{G}_{(I,II)c}$ values (*e.g.*, milled surfaces), but that surfaces with many sharp asperities (600 grit surfaces) created stress concentrations in the interfacial region which aid crack initiation. The surface roughness of the polished surfaces was too shallow to influence the fracture energy. Post-failure SEM examination of the polished adherends revealed parabolic markings as shown in Figure 21. These markings indicate microcracking of the resin ahead of the main crack front, as shown schematically in Figure 22. The microcracks (voids) appear to have propagated more or less perpendicular to the applied load, indicating localized mode-I failure. It should be noted that these features are observed in a region of the fracture surface where the crack is propagating unstably, *i.e.*, along the plane defined by $\overline{C\,D}$ in Figure 19, and do not necessarily reflect the micromechanics of crack initiation. Further study is needed of crack initiation close to resin–adherend boundaries, especially in connection with the mixed-mode fracture of modified epoxy resins as described in the next section.

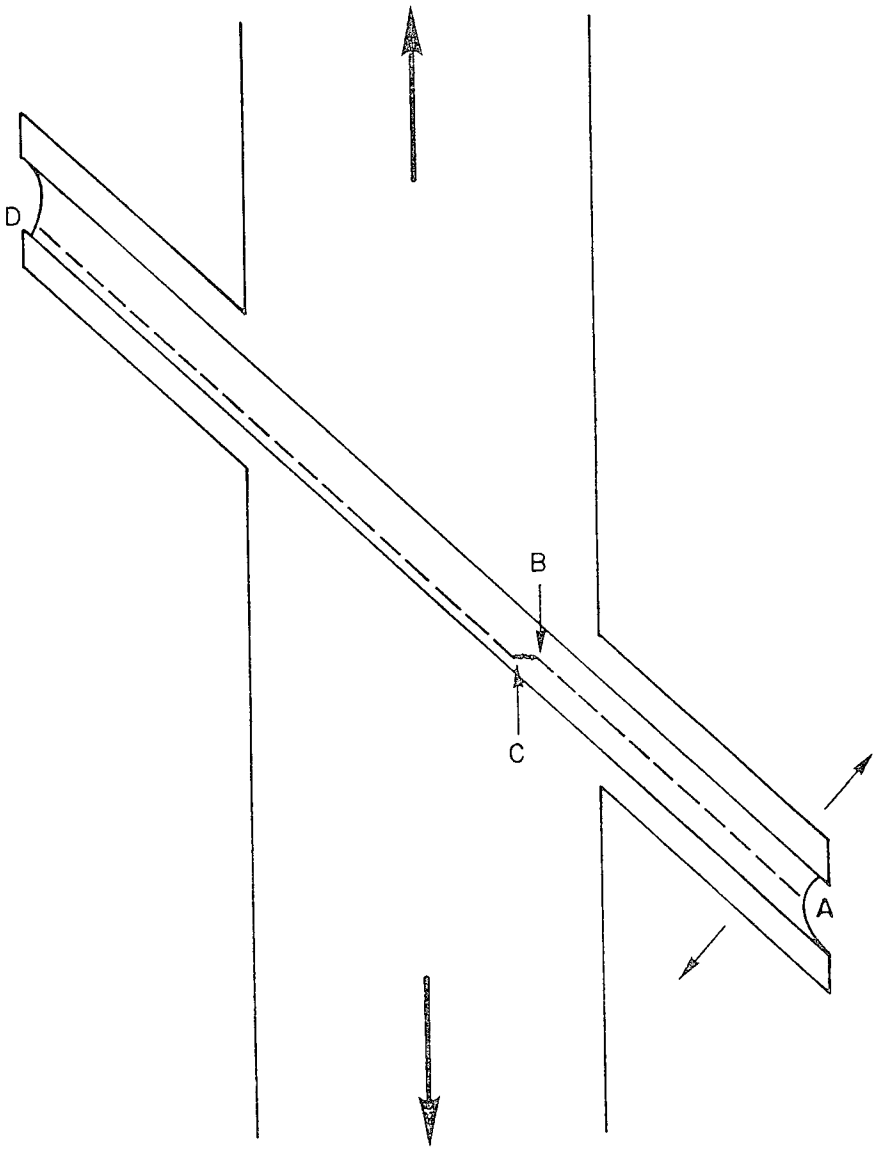


Figure 20. Schematic of the locus of failure in combined-mode tests of unmodified epoxy resins.[15]

Table 5. Effect of Roughness on Combined-Mode Adhesive Fracture

Surface Treatment	Roughness* (μm)	h_r(Å)	$\mathcal{G}_{(I,II)c}$ 45° (J/M^{-2})
Milled + etched	1.17	2150	290 ± 90
180 grit + etch	1.07	8950	123 ± 27
600 grit + etch	0.36	2600	82 ± 33
Polished	0.08	640	140 ± 63

*Center-line-average (CLA).
h_r = thickness of residual film on adherend.

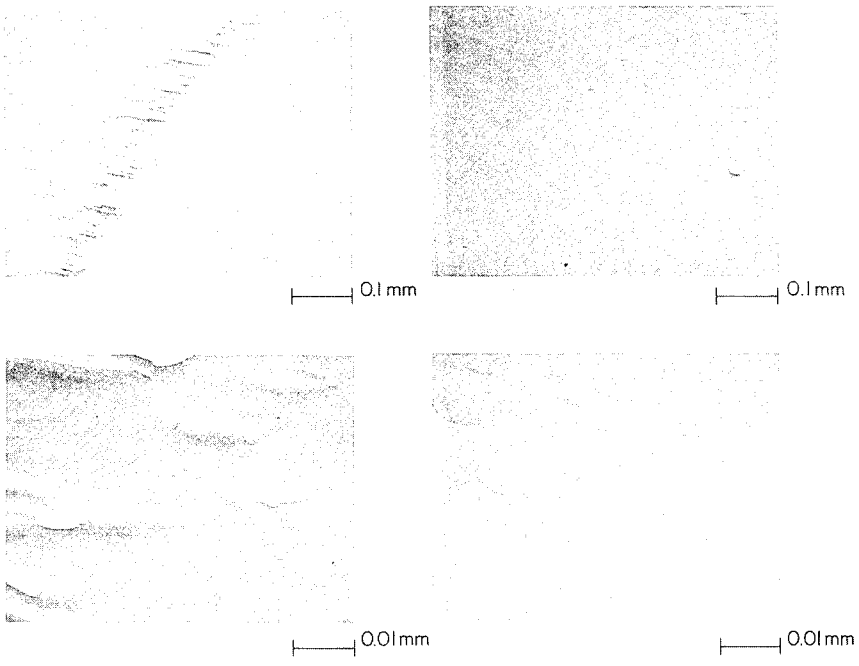


Figure 21. Parabolic markings observed (SEM) in combined mode fracture of an unmodified epoxy resin from polished adherends.[15]

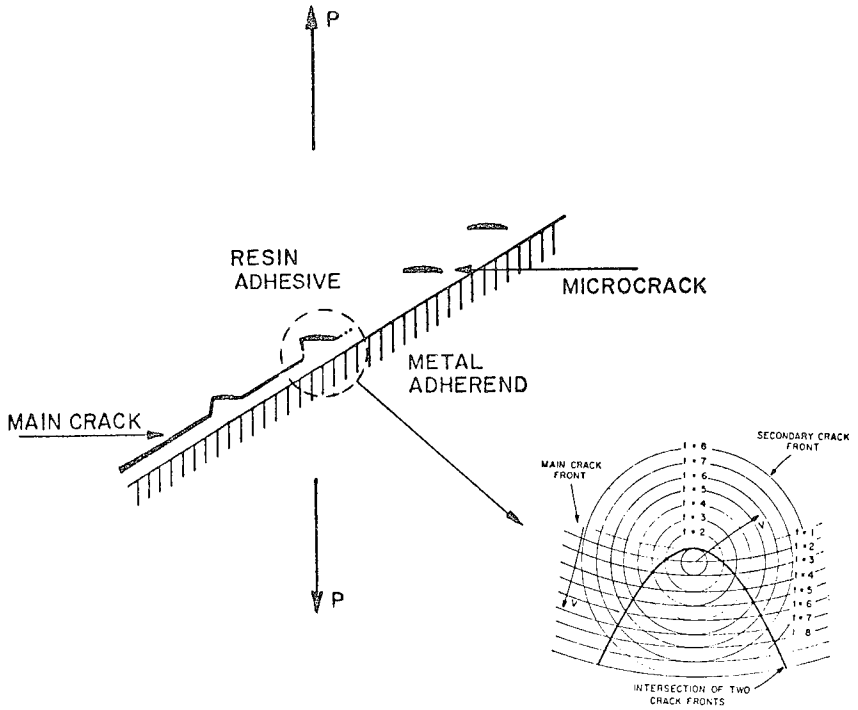


Figure 22. Schematic of parabolic fracture marking formation by the interaction of advance microcracks with the main crack front.[15]

Elastomer-Modified Epoxies

The mixed-mode adhesive fracture of the CTBN–elastomer epoxy compositions and the commercial structural adhesives differ radically from the mixed-mode behavior of unmodified-epoxy resins. In Table 6 the adhesive $\mathcal{G}_{Ic}$ and $\mathcal{G}_{(I,II)c}$ 45° for these resins are compared, and the mixed-mode energies are seen to be lower by more than a factor of 10 in some instances for the modified epoxies and commercial adhesives. This difference is in distinct contrast to the unmodified epoxy resins for which $\mathcal{G}_{Ic} < \mathcal{G}_{(I,II)c}$ Such low fracture energies for the modified resins in combined stress loading raised questions about the validity of Trantina's analysis of the scarf-joint specimen in that the assumption was made that it could be modeled by an isotropic metal plate with edge notches, *i.e.*, that a 10-mil adhesive bond line was too thin to affect the stress analysis. As mentioned in the Introduction, experimental compliance calibrations[28] have established that Trantina's analysis is correct.

Table 6. Mode-I Versus Mixed-Mode Adhesive Fracture Energy[17]

Adhesive Resin	Fracture Energy (J/M^2) Cleavage $\mathcal{G}_{Ic}$	Cleavage + Shear $\mathcal{G}_{(I,II)c}$ 45°
Unmodified Epoxy*	116	136
CTBN–Epoxy†		
10% Elastomer	3500	110
30% Elastomer	2200	110
Commercial		
Elastomer–Epoxy	2300	870
Nylon–Epoxy	6100	750
ME 329‡	630	55
AF 243§	860	220

*Hexahydrophthalic Anhydride–DGEBA
†Piperidine–DGEBA
‡Obtained from the Reliabond Co.
§Obtained from the 3M Co.

The low combined-load adhesive fracture energy of the modified resins is probably attributable to differences in the micromechanics of crack initiation between mode-I and mixed-mode adhesive fracture. The principal difference is that in mode-I the crack is initiating center-of-bond, whereas in mixed-mode the stress condition forces initiation toward the resin-metal boundary. Although this focusing of failure into the interfacial region is more or less clear cut for the unmodified-epoxy resins (*i.e.*, Figure 20), the situation is more complex for the modified resins since the deformation zone (seen as stress-whitened resin) tends to be spread across the entire bond thickness. Nonetheless, the stress whitening observed after fracture in the region of crack initiation is usually most intense along one boundary, which suggests that separation began near the interface. Perhaps this focusing of the deformation zone against the boundary tends to reduce the fracture energy by constraining zone development in the sense that reducing bond thickness to less than $2r_c$ lowers toughness in open-mode fracture. Clearly, there is a need to examine the micromechanics of stress-focused, interfacial failure.

The effects of bond angle and bond thickness on mixed-mode adhesive fracture have been investigated.[28] In Figure 23 the results are presented for epoxy, elastomer–epoxy, and a commercial adhesive using 30°, 45°, and 60° scarf-joint specimens. All resins except the DGEBA–TEPA exhibited a maximum at $\phi = 45°$. Curiously, both the modified

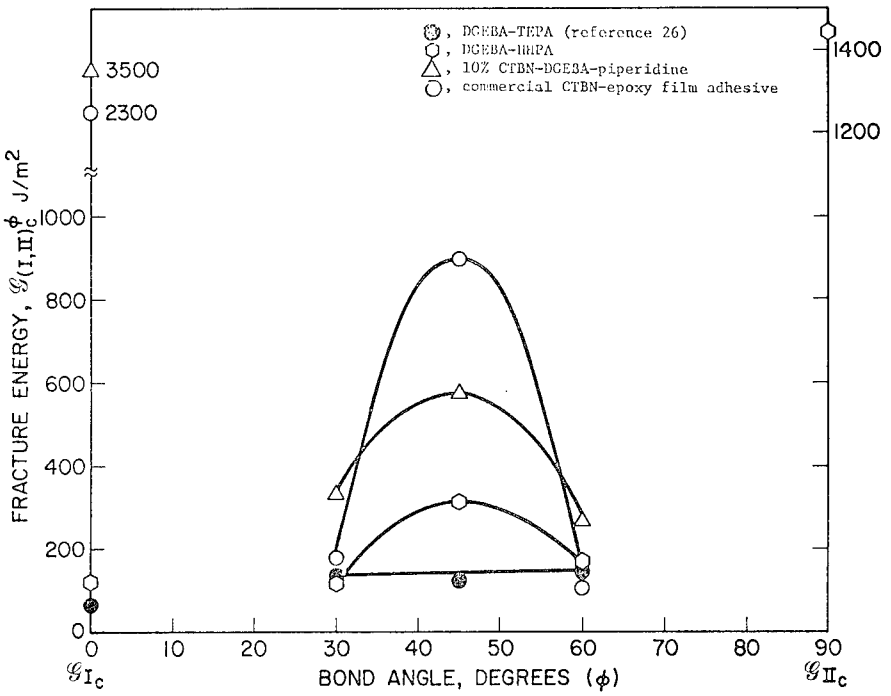


Figure 23. Effect of bond angle on adhesive fracture energy, 0.025-cm bond thickness, 25°C and 0.13 cm/min loading rate.

and unmodified resins had nearly the same adhesive toughness at 30° and 60° bond angle.

In other words, the high opening-mode toughness built into the resin by formulation is essentially lost at 30° and 60° and only partially retained at 45°. Further work is underway on the effect of bond angle on adhesive fracture, using a test specimen that is shaped like the pure mode-II specimen (Figure 5A) but altered for simultaneous application of tensile forces normal to the shear-load direction at the crack tip. Thus far, work with this joint confirms the general trend of the data in Figure 23.

The effect of bond thickness on the mixed-mode (ϕ = 45°) fracture of a commercial elastomer-epoxy adhesive very similar in composition to the 15% CTBN–DGEBA is shown in Figure 24. A maximum in $\mathcal{G}_{(I,II)c}$ 45° between 0.025 and 0.050 cm was observed similar to the results with mode-I testing (Figures 13 and 18). Presumably, the same explanation

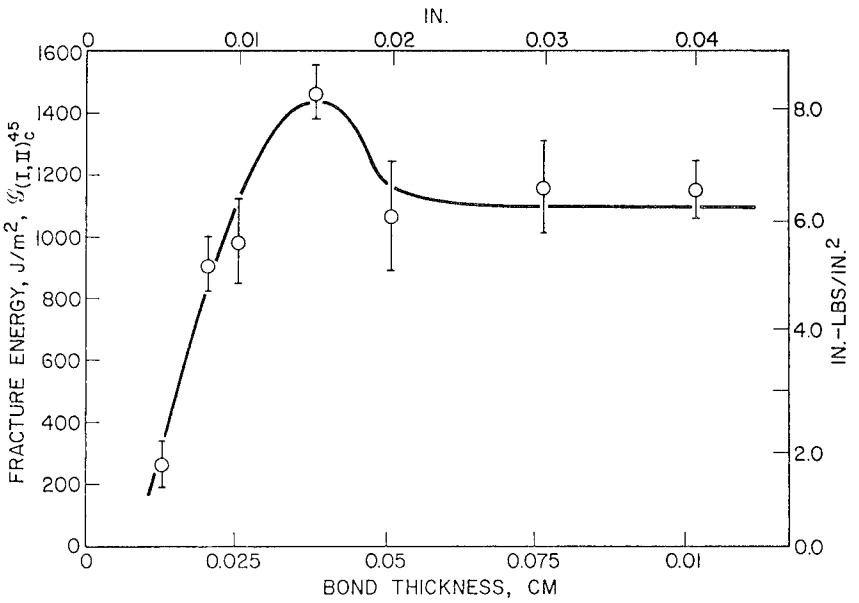


Figure 24. Bond thickness vs. fracture energy for combined-mode test specimens bonded with a commercial CTBN–epoxy film adhesive (D = 45°, 25°C, 0.13 cm/min loading rate).

offered for the bond thickness effect on $\mathcal{G}_{Ic}$ applies here, namely, a constraint on crack-tip deformation in bonds of less than 15 mils and deviations from plane-strain conditions in the thicker bonds.

SUMMARY

The high opening-mode toughness (peel strength) required of structural adhesives can be attained by the in situ formation of an elastomeric, dispersed phase in a thermosetting resin matrix. Compositions of this type have been the basis for structural adhesive formulation for better than a decade and offer high toughness with a minimum of trade-off in the desirable thermomechanical properties of the matrix resin. The enhanced toughness of the modified-resin compositions compared to the thermoset resin alone can be associated with crazing of the elastomer particles in the triaxial stress field at a crack tip and the inability of the crack to advance through this crazed region. This crazing can be viewed as an enlargement of the crack-tip deformation zone diameter ($2r_c$) as defined in the elastic-plastic model of linear elastic fracture.

The fracture behavior of CTBN-epoxy resin compositions was found to simulate the commercial structural adhesive resins. Using these "model" adhesives, the adhesive fracture energy was shown to have strong bond-thickness and bond-angle dependencies and a temperature dependence quite different from that of bulk resin. These effects were shown to be related to the fact that $2r_c$ is of the same order of magnitude as the bond thickness, which leads to various interactions of the stress fields in and around the deformation zone with the resin-metal boundaries. These interactions deserve further study in order to better understand the mechanism of adhesive fracture. Undoubtedly, the resin morphology and composition play important roles in the micromechanics of fracture and work to identify such factors would aid in optimizing adhesive resin formulation.

The dependence of adhesive fracture energy, $\mathcal{G}_c$ (K_c), on joint geometry imposes specific requirements in developing adhesive failure criteria. First, the bond thickness effects observed in both mode-I and mixed-mode studies indicate the need to test adhesives for the effect of bond thickness on $\mathcal{G}_c$ and its temperature dependence. Second, the mixed-mode study clearly show that mode-I data do not represent the worst-case situation as is generally true of isotropic materials. Hopefully, some analytical expression, born of a more detailed study of adhesive fracture micromechanics, can be found to relate $\mathcal{G}_{Ic}$ and $\mathcal{G}_{(I,II)c}\phi$. Until then, adhesive fracture testing will be incomplete without mixed-mode data.

ACKNOWLEDGMENT

The author wishes to express his appreciation to Mr. Robert L. Cottington, Mr. Charles M. Henderson, Mr. Jack L. Bitner, Mr. Carter O. Timmons, Dr. Paul Peyser, Dr. Robert L. Jones, and Dr. Donald L. Hunston for their very capable technical work and advice during the course of these studies. We also wish to thank Mr. Charles Bersch of the Naval Air Systems Command for his advice and encouragement.

REFERENCES

1. Bolger, J. C., "Structural Adhesives for Metal Bonding," in *Treatise on Adhesion and Adhesives*, Vol. 3, ed. by R. L. Patrick. New York: Marcel Dekker, Inc. (1973), 1–78.
2. Sultan, J. N., Liable, R. C., and McGarry, F. J., "Microstructure of Two-Phase Polymers," *Appl. Polym. Symp.*, No. 16 (1971), 127–36.
3. Sultan, J. N. and McGarry, F. J., "Effect of Rubber Particle Size on Deformation Mechanisms in Glassy Epoxy," *Polym. Eng. Sci.*, **13** (1973), 29–34.

4. Corten, H. T., "Overview: Fracture Control of Adhesively Bonded Components," *J. Adhes.*, **3** (1971), 103–06.
5. Ripling, E. J., Mostovoy, S., and Patrick, R. L., "Application of Fracture Mechanics to Adhesive Joints," in *Adhesion*, ASTM Special Technical Publication 360. Philadelphia: American Society for Testing and Materials (1963), 5–19.
6. Mostovoy, S. and Ripling, E. J., "Fracture Toughness of an Epoxy System," *J. Appl. Polym. Sci.*, **10** (1966), 1351–71.
7. Mostovoy, S. and Ripling, E. J., "Influence of Water on Stress Corrosion Cracking of Epoxy Bonds," *J. Appl. Polym. Sci.*, **13** (1969), 1083–1111.
8. Patrick, R. L., Brown, J. A., Verhoeven, L. E., Ripling, E. J., and Mostovoy, S., "Stress-Solvolytic Failure of an Adhesive Bond," *J. Adhes.*, **1** (1969), 136–41.
9. Mostovoy, S. and Ripling, E. J., "Fracture Toughness and Stress Corrosion Cracking Characteristics of an Anhydride-Hardened Epoxy Adhesive," *J. Appl. Polym Sci.*, **15** (1971), 641–59; and "Effect of Joint Geometry on the Toughness of Epoxy Adhesives," *J. Appl. Polym. Sci.*, **15** (1971), 661–73.
10. Ripling, E. J., Mostovoy, S., and Corton, H. T., "Fracture Mechanics: A Tool for Evaluating Structural Adhesives," *J. Adhes.*, **3** (1971), 107–23.
11. Mostovoy, S., Ripling, E. J., and Bersch, C. F., "Fracture Toughness of Adhesive Joints," *J. Adhes.*, **3** (1971), 125–44.
12. Ripling, E. J., Mostovoy, S., and Bersch, C. F., "Stress Corrosion Cracking of Adhesive Joints," *J. Adhes.*, **3** (1971), 145–63.
13. Patrick, R. L., Gehman, W. G., Dunbar, L., and Brown, J. A., "Scanning Electron Microscopy of Fracture Surfaces," *J. Adhes.*, **3** (1971), 165–75.
14. Mostovoy, S. and Ripling, E. J., "Fracturing Characteristics of Adhesive Joints," Materials Research Laboratory, Inc., Glenwood, Calif., Naval Air Systems Command Contract Report, December 1972. (AD 762 457)
15. Bascom, W. D., Timmons, C.O., and Jones, R. L., "Apparent Interfacial Failure in Mixed-Mode Adhesive Fracture," *J. Mater. Sci.*, **10** (1975), 1037–48.
16. Bascom, W. D., Cottington, R. L., Jones, R. L., and Peyser, P., "The Fracture of Epoxy- and Elastomer-Modified Epoxy Polymers in Bulk and as Adhesives," *J. Appl. Polym. Sci.*, **19** (1975), 2545–62.
17. Bascom, W. D. and Timmons, C. O., "Mixed-Mode Fracture of Structural Adhesives," in *Adhesion Science and Technology*, Vol. 9B, ed. by L. H. Lee. New York: Plenum Press (1975), 501–11.
18. Bascom, W. D. and Cottington, R. L., "Effect of Temperature on the Adhesive Fracture Behavior of an Elastomer-Epoxy Resin," *J. Adhes.*, **7** (1976), 333–46.
19. Liebowitz, H., ed., *Fracture: An Advanced Treatise*, Vols. I–VII. New York and London: Academic Press (1968).
20. Tetelman, A. S. and McEvily, A. J. Jr., *Fracture of Structural Materials*. New York: John Wiley & Sons, Inc. (1967).

21. Irwin, G. R., "Fracture," in *Encyclopedia of Physics*, Vol. 6, *Elasticity and Plasticity*, ed. by S. Flugge. Berlin: Springer-Verlag (1958), 551–90.
22. Arin, K. and Erdogan, F., "Penny-Shaped Crack in an Elastic Layer Bonded to Dissimilar Half Spaces," *Int. J. Eng. Sci.*, **9** (1971), 213–32.
23. Hilton, P. D. and Gupta, G. D., "Stress and Fracture Analysis of Adhesive Joints," ASME Paper 73-DE-21, 1973.
24. Gray, T. G. F., "An Experimental Introduction to the Griffith Concept of Fracture," *Bull. Mech. Eng. Educ.*, **10** (1971), 151–58.
25. Trantina, G. G., "Fracture Mechanics Approach to Adhesive Joints," *J. Composite Mater.*, **6** (1972), 192–207.
26. Trantina, G. G., "Combined Mode Crack Extension in Adhesive Joints," *J. Composite Mater.*, **6** (1972), 371–85.
27. Trantina, G. G., "Combined Mode Crack Extension in Adhesive Joints," University of Illinois, Urbana, Naval Air Systems Command Contract Report No. T/AM-352, November 1971. (AD 741 687)
28. Bascom, W. D. and Timmons, C. O., unpublished research.
29. Berry, J. P., "Brittle-Like Fracture," in *Fracture Processes in Polymeric Solids*, ed. by B. Rosen. New York: Interscience Publishers (1964), 157–290.
30. Patrick, R. L., "The Use of Scanning Electron Microscopy," in *Treatise on Adhesion and Adhesives*, Vol. 3, ed. by R. L. Patrick. New York: Marcel Dekker (1973), 163–229.
31. Kambour, R. P., "A Review of Crazing and Fracture in Thermoplastics," *J. Polym. Sci.*, Pt. D, **7** (1973), 1–154.
32. Knauss, W. G., "On the Steady Propagation of a Crack in a Viscoelastic Sheet: Experiments and Analysis," in *Deformation and Fracture of High Polymers*, ed. by H. H. Kausch, J. A. Hassell, and R. I. Jaffee. New York and London: Plenum Press (1973), 501–41.
33. Schapery, R. A., "A Theory of Crack Initiation and Growth in Viscoelastic Media," *Int. J. Fract.*, **11** (1975), 141–59.
34. Rowe, E. H., Siebert, A. R., and Drake, R. S., "Toughening Thermosets with Liquid Butadiene/Acrylonitrile Polymers," *Mod. Plast.*, **47**, No. 8 (1970), 110–17.
35. Siebert, A. R. and Riew, C. K., "The Chemistry of Rubber Toughened Epoxy Resins, I," *Amer. Chem. Soc., Div. Org. Coat. Plast. Prepr.*, **31**, No. 1 (1971), 522–60.
36. Riew, C. K., Rowe, E. H., and Siebert, A. R., "Rubber Toughened Thermosets," *Amer. Chem. Soc., Div. Org. Coat. Plast. Prepr.*, **34**, No. 2 (1974), 353.
37. Bucknall, C. B. and Smith, R. R., "Stress-Whitening in High-Impact Polystyrenes," *Polymer*, **6** (1965), 437–46.
38. Mostovoy, S. and Ripling, E. J., "Effect of Temperature on the Fracture Toughness and Stress Corrosion Cracking of Adhesives," *Appl. Polym. Symp.*, No. 19 (1972), 395–408.

39. Olf, H. G. and Peterlin, A., "Crazing and Fracture in Crystalline, Isotactic Polypropylene and the Effect of Morphology, Gaseous Environments, and Temperature," *J. Polym. Sci., Polym. Phys. Ed.*, **12** (1974), 2209–51.
40. Irwin, G. R., "Analysis of Stresses and Strains Near the End of a Crack Traversing a Plate," *J. Appl. Mech.*, **24** (1957), 361–64.
41. Erdogan, F. and Sih, G. C., "On Crack Extension in Plates Under Plane Loading and Transverse Shear," *Trans. ASME, Ser. D, J. Basic Eng.*, **85** (1963), 519–27.

SESSION IV

COMPOSITES

MODERATOR: R. W. LEWIS
Army Materials and Mechanics Research Center

12. ON IMPROVEMENT IN STRUCTURAL EFFICIENCY OF SINGLE-LAP BONDED JOINTS

W. J. RENTON
Advanced Technology Center, Inc.
Dallas, Texas

J. PAJEROWSKI and J. R. VINSON
University of Delaware
Newark, Delaware

Recent experiments have shown that significant improvements can be made in the structural efficiency of single-lap joints through several modifications.

Tests have been conducted in which the adherends were linearly tapered from full panel thickness to practically zero thickness over the length of the bond line in the load direction. Further, tests were conducted to examine the effects of introducing small grooves on the adhesive side of the adherends, perpendicular to the load direction. Similarly, grooves only over the thicker half of the tapered adherend were investigated, because these grooves do introduce stress concentrations.

In each case, significant improvements in joint efficiency were made under either static or fatigue loadings. Additionally, specific observations are made pertaining to the residual strain effect due to joint fabrication on the fatigue life of the joint.

Second, studies were made on the effects of using hybrid adherends and their effect on joint efficiency. Recently, much discussion has centered on the placement of several layers of Kevlar-49 or fiberglass material, on the outer surface of graphite panels, to improve impact resistance. What is the effect of such hybrid construction on the shear and normal joint stresses in bonded-lap joints? The effects are discussed, for the cases in which the outer hybrid layers increase or decrease and A and D matrices of the adherends, versus a nonhybrid construction.

INTRODUCTION

In lap joints, stress concentrations in the adhesive and adherends arise due to the difference in elastic moduli of the constituents and the abrupt thickness change which occurs at the ends of the overlap. Mylonas and deBruyne[1] among others, have suggested that tapering the outer surface of the adherends would result in a more uniform state of shear stress in the adhesive while minimizing the tear stress it experienced. This result is directly attributed to minimizing the in-plane and transverse strain discontinuity at the ends of the joint. Recently, Cherry and Harrison[2] have shown mathematically that for identical adherends, a linear taper will result in the adhesive shear stress attaining a near-uniform distribution, while if the adherend thickness is much less than the overlap length, the adhesive tensile stresses will be negligible.

The initial segment of this chapter presents static and constant amplitude fatigue-test data comparing four adherend geometries. The constant thickness adherend lap joint, a linearly tapered adherend lap joint, and two linearly tapered joints that are fully and partially notched (Figure 1) along the adhesive–adherend interface are discussed.

Next, the problem of premature fatigue failure of the constant thickness aluminum adherends is looked at. Reasons for the existence of this problem are advanced. Finally, the effect of the addition of several layers of a foreign lamina to the outer surface of a composite laminated structure, for impact toughness and its ensuing effect on the adhesive stress distribution of a bonded joint, is discussed.

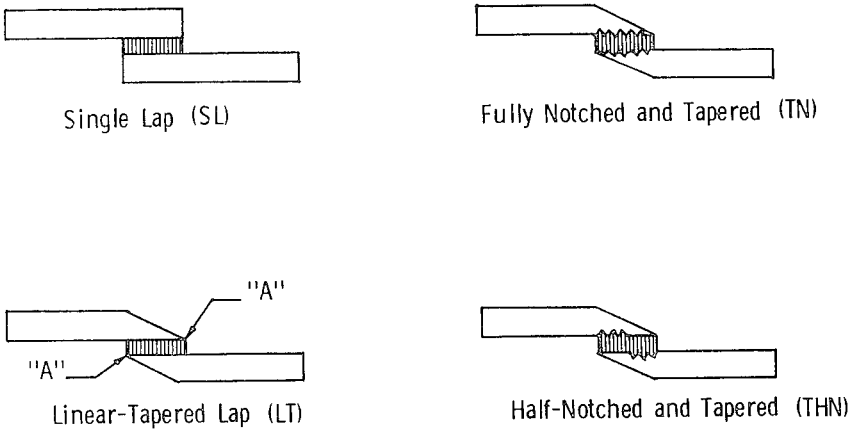


Figure 1. Typical lap-joint configuration.

Static and Fatigue-Test Results

The test specimens were composed of 7075-T6 bare adherends and EA951 Nylon–epoxy adhesive of 0.50- and 0.80-in. overlap length. All tests were run at room temperature, within a relative humidity range of 10–55 percent. The crosshead rate for the static tests was 0.05 in./min. The fatigue results are for a stress ratio (R) of +0.10 and a 30 Hertz cycling rate. All specimens were fabricated using a platen press, after the surfaces were prepared with an FPL etch.

The static test results are summarized in Table 1. Failure of the standard and tapered lap joints occurred in the adhesive. The tapered and grooved specimens failed in a combined adhesive–adherend mode with the adherend usually failing along a notch at the centerline of the overlap. Figure 2 shows typical failed specimens.

Any improvement in the static load-carrying ability of the various joint configurations is best reflected by its joint efficiency. Joint efficiency is defined as the ratio of the joint strength (*i.e.*, the load-carrying ability of the joint) versus the strength of the sheet material. Results indicate that with a high-strength adhesive such as EA951 and with proper design, one can achieve 80–90 percent efficiency for each of the lap-joint geometries looked at. Modest improvement in efficiency for a similar overlap length is seen to exist for the tapered, and/or tapered and

Table 1. Static Test Results

Type of Joint	Overlap Length (in.)	Avg. Adhesive Thickness (in.)	Avg. Ult. Joint Load (LB)	Joint Efficiency (%)	Type of Failure
Single Lap	0.540	0.0045	2600.0	52.5	Adhesive
Singla Lap	0.800	0.0055	3769.0	82.5	Adhesive
Tapered	0.540	0.0070	2612.0	52.7	Adhesive
Tapered	0.730	0.0020	4237.0	85.0	Adhesive
Tapered and Grooved	0.540	0.0040	3642.0	73.0	Adherend and Adhesive
Tapered and Grooved	0.800	0.0030	4518.0	91.0	Adherend and Adhesive
Tapered, Grooved along ½ overlap	0.800	0.0070	4160.0	84.0	Adherend and Adhesive

Strain Rate = 0.05 in./min.
Specimen Width ≅ 1.00 in.

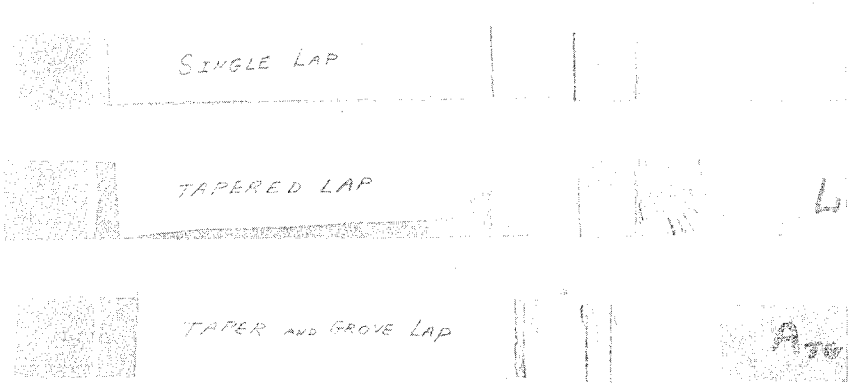


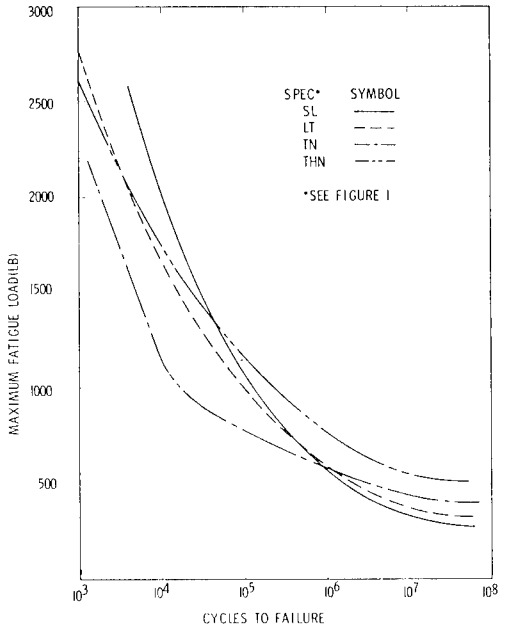
Figure 2. Typical static failure specimens.

grooved configurations. This is realistic, as the tapering effect at the unloaded adherend ends (*i.e.*, location A, Figure 1), results in a reduction in stiffness mismatch. This effectively reduces the shear and tension strain discontinuities at these ends, resulting in a more uniformly loaded adhesive. Moreover, for a ductile adhesive the improvement in load carrying ability, sought by tapering the adherends, is enhanced by the adhesive's ability to load up fully along the total adhesive bond line.

The fatigue-test results are summarized on the S–N curves of Figure 3. The curves represent best-fit regression analysis of the various test data. More than 60 test points are represented on the curves. The low-cycle, high-load specimens failed in the adhesive. Those specimens exceeding a life of 80,000 cycles failed in the adherend at the edge of the overlap. In this region, the sheet experiences maximum tensile stress and moment, which is directly proportional to the size of the load-path discontinuity at the edge of the joint.

Table 2 summarizes the improvement seen in the load-carrying ability of tapered adherend configurations at 4×10^6 cycles. Specifically, the results indicate that the efficiency of the standard lap joint subject to a fatigue loading can be improved by approximately 20% by tapering and/or inserting grooves at the interface. This improvement is primarily due to the reduced stiffness of the adherends in the overlap region, allowing the joint to reorient itself, when loaded, into a scarf-type geometry (Figure 4). This is the most efficient joint configuration, resulting in a reduction in moment and peak tensile stresses in the adherends.

Overall, results would indicate that a tapered and/or grooved specimen can definitely improve the static and fatigue efficiency of a single-lap



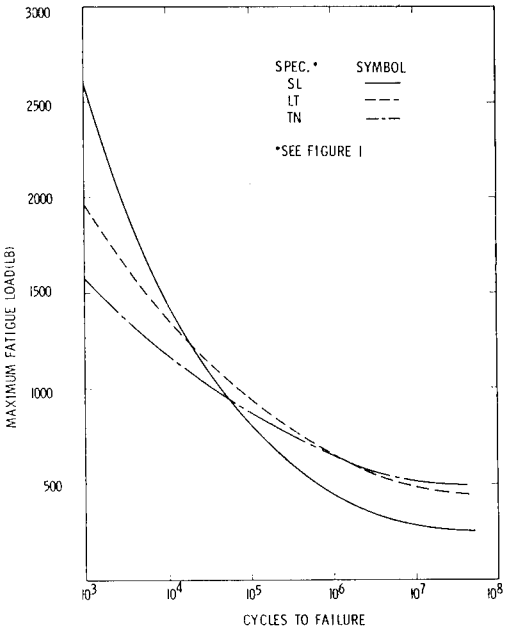


Figure 3. Fatigue-test results.

Table 2. Summary of Fatigue-Test Results at 4×10^6 Cycles

Type of Joint	Overlap Length (in.)	Joint Efficiency (%)
Single Lap	0.540	33.5
Single Lap	0.800	38.4
Tapered	0.540	52.5
Tapered	0.730	39.7
Tapered and Grooved	0.540	52.2
Tapered and Grooved	0.800	41.3
Tapered, Grooved, along ½ overlap	0.800	54.5

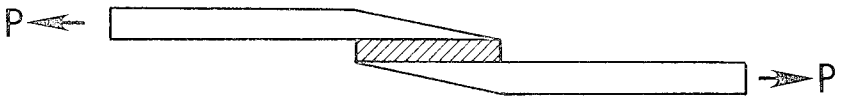
$R = +0.10$
Cycles = 30 Hz
All failures in adherends adjacent to overlap.

joint. The addition of properly shaped grooves (V-notches were used in these tests) over a selected length of the overlap may further improve the joint's efficiency. Moreover, the proper selection of taper and grooves could conceivably allow the joint to respond to load as a true scarf joint, resulting in significant increases in joint efficiency, without the problems associated with fabrication of scarf joints.

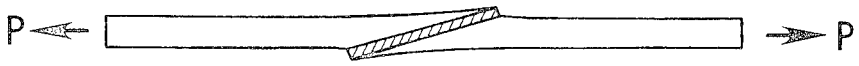
Residual Strains

An existing problem in bonded joints of sufficient magnitude to warrant comment, is that of residual strains. They arise due to the high-temperature cure requirements of certain adhesives. The residual strains occur due to the differential thermal contraction and conductivity between the adhesive and/or the adherends. Upon completion of the elevated temperature cure cycle, the adhesive cools down and begins to acquire a significant stiffness and strength capability, long before reaching room temperature. For an adhesive that cures at 350°F, this capability occurs with some significance at 180–200°F. The net result is that a sizable nonuniform residual strain is locked into the adherends, reaching a peak at the edge of the overlap (point A in Figure 1).

The residual strain effect for identical adherends is thought to be minimal, yet the data presented in Table 3 suggests otherwise. The data in columns 1–3 emphasize that based on the applied load, and with the inclusion of the bending stresses per the Goland-Reissner[3] analysis, a significant reduction in the life of the aluminum sheet does occur for



BEFORE LOAD IS APPLIED



DURING LOAD PROCESS

Figure 4. Tapered joint reorientation during the load process.

Table 3. The Influence of Residual Strains on the Fatigue Life of Bonded Joints

Spec.	(1) Max. Sheet Stress (P/A + MC/I) ksi	(2) Expected Cycles to Failure ($\times 10^6$)*	(3) Actual Cycles to Failure ($\times 10^6$)	(4) Actual Max. Sheet Stress for (3) (ksi)*	(5) Residual Stress (4)–(1) (ksi)	Type of Failure
0.50″ Single Lap	22.1	>10.0	0.806	42.0	19.9	Adherend
	27.6	>10.0	0.668	42.0	14.4	Adherend
	37.3	>10.0	0.167	46.0	8.7	Adherend
	64.5	0.020	0.012	66.0	−1.5	Adhesive
0.80″ Single Lap	42.6	0.500	0.211	45.0	2.4	Adherend
	57.5	0.070	0.053	56.0	−1.5	Adhesive
	27.5	>10.0	0.567	43.0	15.5	Adherend
†0.50″ Single Lap	30.0	>10.0	0.700	41.0	11.0	Adherend
	44.6	0.400	0.200	49.0	4.4	Adherend
	52.0	0.100	0.100	51.0	−1.0	Adhesive
	25.0	>10.0	2.00	38.0	13.0	Adherend

$R = +0.10$
*Values from Goodman Curve for 7075-T6 Sheet
†From Data, 2024-T3 Sheet[4]

both the data in this report and that of Wang.[4] Metallurgical data specifies that during the adhesive cure cycle the heat treatment of the aluminum is changed from T6 to T73. Yet, available fatigue data suggest that there is no loss in fatigue life of the aluminum. Column 5 estimates the potential magnitude of the locked-in stress in the adherend necessary to cause failure at the cycles specified in column 3.

Is the magnitude of the residual strain realistic? A simple calculation suggests it is. If, for example, the temperature level at which residual strains begin to be locked in is 180°F, then the peak residual tensile strain in the aluminum sheet, at room temperature, is approximately 14.4 ksi. A sizable sum in fatigue.

In the high-load, low-cycle region, the adhesive becomes the initial item to fail. As the test data move into this region, the disparity between the actual and expected cycles to failure for the sheet becomes minimal. Therefore, it is in the high-cycle regime that the residual strain effect is most detrimental. The resulting residual strain distribution throughout the sheet cross section must be self-equilibrating. Therefore, it is not uniform. The exact distribution is unknown.

The residual strain effect accompanying fabrication of dissimilar materials can be even more detrimental due to the addition of a thermal mismatch problem between the adherends. Initial efforts were made to quantify the residual strains resulting from the fabrication of a fiberglass to aluminum single-lap joint. A 350°F cure adhesive was used. The effort was partly successful. Strain gages were placed along the periphery of the joint monitoring the residual strain buildup which occurred during the fabrication process. Results indicated: (1) that the transverse residual strains were an order of magnitude larger than their longitudinal counterparts (this was supported by the transverse warpage evident in Figure 5), (2) that peripheral gages were unable to quantify the peak residual strains occurring in the overlap end region.

The significance of the problem is self-evident. Yet a reliable, accurate means to resolving this problem is presently unavailable. Definitely, work in this area should prove highly rewarding.

Hybrid Composites

The desirability of using laminated composite materials in numerous structural applications has led to the use of hybrids to resolve specific structural design requirements. Frequently, several layers of a foreign material are laminated in a prescribed manner within a base material. Such an application is frequently used to improve the fracture toughness of a brittle lamina (*i.e.*, graphite). Therefore, the question to be resolved

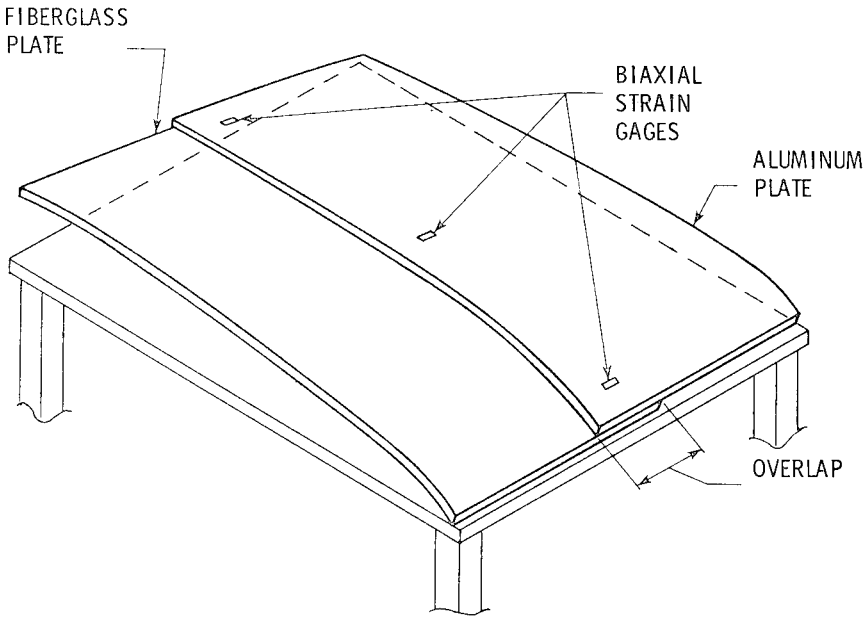


Figure 5. Dissimilar adherence warpage specimen.

is: what is the influence on the stress distribution in an adhesively bonded joint when the composition of the adherends is altered by substituting for several plys of the base material, another laminated material system?

To answer the question qualitatively, a single-lap joint will be analyzed using the closed form analytical routine BOND4. The analysis (BOND4), has been shown by Sharpe and Muha,[5] through their experimental investigation, to characterize the state of stress in the adhesive most accurately of the many models they investigated. The results presented are generally applicable to all bonded joint configurations. The load is held constant. Figures 6 and 7 show the adhesive shear and normal stress distributions for two limiting cases (solid lines). Curve 1 is for two identical fiberglass adherends. Curve 2 represents two geometrically similar adherends with the material properties being those of graphite in place of fiberglass. With the adhesive properties being invariant, all other adherend material combinations for the like geometrical constraints of thickness and overlap length will have peak stresses that fall within these bounds (*i.e.*, the all-glass adherend joined to the all-graphite adherend shown by the — — — lines).

The fundamental adherend parameters being varied are the in-plane and flexural stiffnesses. Basically, the larger the ratio of the in-plane

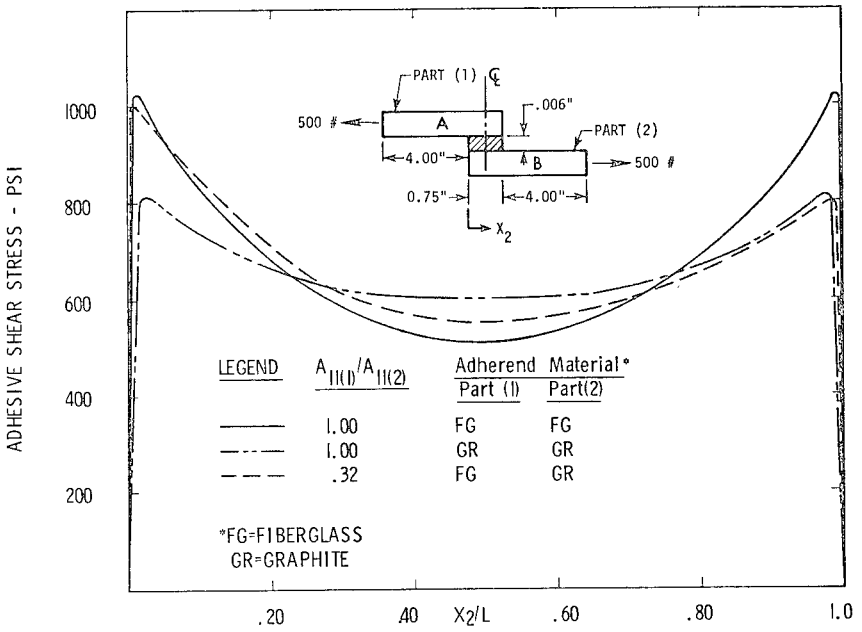


Figure 6. The influence of the ratio of in-plane stiffness to the effective shear factor ($A_{11(2)}/G_{\text{eff}} \circ \eta$), for values of (1, 3 and 3) $\times 10^4$ associated with curves 1 to 3, respectively.

stiffness (A_{11}) to the adhesive shear modulus factor ($G_{\text{eff}} \circ \eta$), the more uniform is the adhesive shear stress, with the stress peaks approaching a minimum value. Similarly, the larger the ratio of the flexural stiffness (D_{11}) to the adhesive tension modulus factor ($E_{\text{eff}} \circ \eta^3$), the less significant are the peel stresses in the adhesive. η is the adhesive thickness and G_{eff} and E_{eff} are the adhesive effective shear and tension moduli. The maximum values of adhesive shear and normal stress will occur at the edge of the overlap adjacent to the adherend with the minimum in-plane and flexural stiffness, respectively.

All-graphite adherends, being most rigid, represent a lower bound for this study as pertains to peak adhesive stress. Substituting all-glass adherends, results in the peak shear stress increasing 27 percent and the peak normal stress increasing 61 percent. The problem is to determine if, by the substitution of several plys of fiberglass for graphite, the adhesive can withstand a fraction of these increased stresses for its design load versus life spectrum, assuming a base design with all-graphite laminates. The fractional stress increase would be proportional to the number of plys of fiberglass replacing graphite in each case.

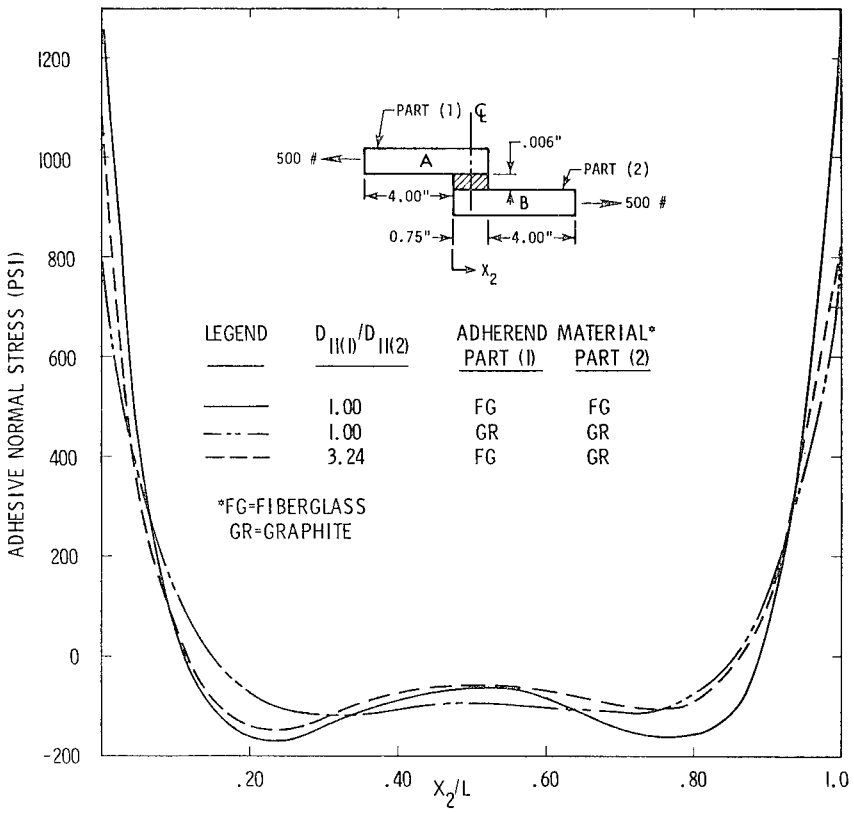


Figure 7. The influence of the ratio of the flexural stiffness to the effective tension factor ($D_{11(2)}/E_{\text{eff}} \circ \eta^3$), for values of (37.4, 115 and 115) $\times 10^9$.

Normally, an efficiently designed adhesive joint cannot withstand these increased stress levels without failing prematurely. To avoid this, several alternatives are available to the designer to lessen the peak stresses. First, increasing the overlap length can many times reduce the peak stress to an acceptable level. Second, a less stiff adhesive can be used to increase the ratios ($A_{11}/G_{\text{eff}} \circ \eta$) and ($D_{11}/E_{\text{eff}} \circ \eta^3$). This effectively reduces the peak stresses. Third, increasing the thickness of the adherends with the addition of several plys of new material reduces the peak stresses. Additionally, such adjustments in the design can alleviate the introduction of excessive moments at the ends of the overlap due to the insertion of the layers of the foreign lamina.

The strain mismatch problem associated with the formation of a hybrid construction has not been accounted for in this discussion. This

should be a point of concern in all designs. Finally, for the instance when one must join two dissimilar adherends, the use of a hybrid design could conceivably alleviate an adverse peak adhesive stress situation by enabling one to match the in-plane and flexural stiffness of the adherends. This is an optimum condition.

SUMMARY

Ways to increase the efficiency of adhesive bonded joints have been ascertained for static and fatigue loads. The effect of incorporating residual strains into the joint during fabrication was discussed. A full understanding of the magnitude and distribution of these strains is lacking. Finally, the effect of hybrid construction on the peak adhesive stress in bonded joints was looked at qualitatively.

REFERENCES

1. Mylonas, C. A., and deBruyne, N. A., "Static Problems," in *Adhesion and Adhesives*, ed. by N. A. de Bruyne and R. Houwink. Amsterdam and New York: Elsevier Publishing Company (1951), 91–143.
2. Cherry, B. W. and Harrison, N. L., "The Optimum Profile for a Lap Joint," *J. Adhes.*, **2** (1970), 125–28.
3. Goland, M. and Reissner, E., "The Stresses in Cemented Joints," *J. Appl. Mech.*, **11** (1944), 17–27.
4. Wang, D. Y., "Influence of Stress Distribution on Fatigue Strength of Adhesive-Bonded Joints," *Exper. Mech.*, **4** (1964), 173–81.
5. Sharpe, W. N. Jr. and Muha, T. J. Jr., "Comparison of Theoretical and Experimental Shear Stress in the Adhesive Layer of a Lap Joint Model," in *Proceedings of the Army Symposium on Solid Mechanics, 1974: The Role of Mechanics in Design-Structural Joints*. Army Materials and Mechanics Research Center, Watertown, Mass., Report No. AMMRC-MS-74-8 (September 1974), 23–44. (AD 786 543)

13. STRUCTURAL ATTACHMENT OF COMPOSITE ROTOR BLADES

W. K. STRATTON, T. S. SCARPATI, and C. A. CLASS
Boeing Vertol Company
Philadelphia, Pennsylvania

The decision to convert completely to composite rotor blades for all new helicopters dictated the development of a root-end-retention concept which made maximum use of the inherent properties and characteristics of fiberglass.

A trade-off study was conducted which evaluated many variations of three basic structural concepts against stringent criteria for safety, reliability, maintainability, structural efficiency, and manufacturing simplicity.

The vertical-wraparound concept was selected for development on the UTTAS and Heavy-Lift helicopters. This chapter presents reasons for the selection along with the initial results of fabrication and test. The methods of automated lay-up for the vertical-wrap concept, which provides extremely low fabrication and labor costs, are described.

The results of static and fatigue testing of full-scale specimens are also discussed. This includes the data on fail-safety testing in which major portions of the root-end specimens were purposely damaged to levels beyond that of 23mm HEI, then fatigue tested for the equivalent of hundreds of flight hours without propagation of damage.

INTRODUCTION

The development of composite rotor blades at the Boeing Vertol Company began in 1958. Development continued through the 1960s, leading to the successful design, fabrication, and flight testing of fiberglass and later boron-composite advanced-geometry rotor blades. In 1969 a decision was made that all new helicopters would be equipped with composite rotor blades. Furthermore, the company initiated an active program to modernize existing helicopter fleets with such blades. The major reasons behind these decisions reflect the many advantages

over metals that composites offer when applied to helicopter rotor blades:

1. The capability to tailor configuration, geometry, and structural material to achieve the most aerodynamically and structurally efficient rotor blade.
2. An order-of-magnitude improvement in safety, damage tolerance, and survivability.
3. The capability to fabricate blades with a high degree of contour repeatability to achieve an improvement in vibration levels.
4. The promise of improved reliabilty and maintainability which reduce the cost of ownership over the aircraft's life cycle.

With the decision made to pursue composite rotor blades for production applications, a proper retention system had to be selected which was in keeping with the cost, safety, and strength objectives defined for the production blades themselves. This choice posed one of the most difficult aspects of composite-rotor-blade development.

Fatigue capability is the primary design consideration in the development of a rotor-blade root-end retention. It must be designed to withstand very high steady loads, dominated by blade centrifugal force, and variable phasings of both alternating and steady torsional and bending loads.

The second major consideration affecting root-end-retention design dictates that the concept make the most efficient use of the inherent structural and fail-safe properties of composites. Composites are most efficient when the major loads are aligned with the principal fiber direction. This provides a favorable load path in the composites while transferring loads to a single-point metal hub. Metal components within the root end which are not fail-safe or easily replaceable should be avoided.

The design of a rotor blade must also account for kinematic, geometric, and configurational compatibility with the remainder of the aircraft. Such factors include blade folding, hub and control-system geometry, static and rotating clearances, lead-lag dampers and their attachment, vibration-absorption devices, and hub and control-system loads. For new aircraft these considerations do not present a major problem; the hub-attachment geometry is flexible and can be traded against its impact on blade-retention-system design. On existing aircraft this flexibility may not be there. Geometry and permissible envelope are fixed and are generally inflexible to significant deviations. It therefore becomes an additional design objective that a root-end-retention concept be selected which can be used on both new and existing aircraft so that service history, experience, and test data accumulate quickly and are significant to all products.

The search for the most efficient structural attachment for composite blades started virtually simultaneously on three aircraft, each with a specific design requirement. The Heavy-Lift Helicopter required a new, articulated rotor blade; the new UTTAS needed a hingeless rotor blade; the CH-47 Chinook helicopter required a replacement blade that could be attached to an existing, single-pin hub fitting. Each dictated a separate but coordinated trade-off study.

TRADE-OFF STUDY EVALUATION CRITERIA

The criteria for selection included the specific and general requirements for each blade application. The general criteria for the evaluation of the composite-blade-retention concepts can best be grouped into four categories.

Structural Efficiency

Consideration of the structural efficiency of a concept includes the strength and weight of the joint, the effective use of materials, the directness of load paths, and the state of knowledge of allowable stresses and analytical methods. Special consideration must be given to metal components in the joint, the bond-line interface of the composite and metal components, and use of the composite material in its most efficient orientation.

A good design will avoid having a metal or metal/composite bond in the primary load path. When a metal component becomes a major structural element in a root-end retention, it inherently becomes the structurally limiting element or weak link in the load path. Metals are not as strong as composites on an equal-weight basis and are subject to all the ills which have driven rotor blades to composites — fretting, notch sensitivity, manufacturing defects, etc. The bonded interface of the composite spar to the metal element requires sophisticated analytical modeling. There is also a lack of proven allowable stresses and methodology for low-stress, high-cycle fatigue analysis and long-term durability of bonded joints.

Composites are not homogeneous or isotropic; strength and stiffness exist only where the designer places the reinforcing fibers. The structural advantage of composites is realized only when the fibers can carry the load; resin can carry only a fraction of the load that fibers can. When a retention-system concept calls for a significant loading at angles to the fibers, additional reinforcing material is necessary, thus reducing some of the overall structural efficiency of composites.

Safety

Evaluation of a concept's safety includes consideration of the failure mode and fail-safe factors of the joint, the inherent redundancy of load paths, the requirement for a failure-detection system, and the safe operating life after a failure.

Metal in the retention system has a distinct effect when evaluating the safety of that system. If the concept is one in which most or all of the load is in a metal component, the rapid crack-propagation rate of metal becomes a significant design consideration. To satisfy the fail-safe objective, redundancy and its potential weight penalty or a failure-detection system is required.

Reliability and Maintainability

These criteria evaluate a joint concept's component reliabilty, repairability, replaceability, and ease of inspection. When evaluating the reliability and maintainability, careful attention must be paid to concealed and nonreplaceable fittings. Since metal fittings are normally stressed closer to their allowable endurance limits, a situation may occur wherein the metal component has a limited retirement life. If retirement of the fitting necessitates retirement of the blade, the cost to the user becomes prohibitive. Metal components and their bond lines must be minimized and they must be easily inspectable and repairable or replaceable. The requirement for a failure-detection system has a significant impact on the reliability and maintainability rating of a retention concept.

Manufacturing Simplicity and Cost

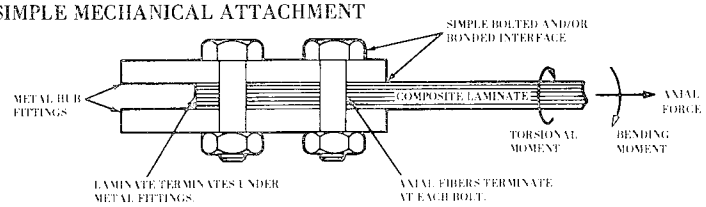
These criteria evaluate the concept for the number of individual elements and degree of complexity, the simplicity of lay-up, and considerations which affect the overall cost of the total blade. When evaluating the cost of a root-end concept, special note must be paid to the automation potential of the lay-up. A concept for a root end which dictates complicated hand lay-up should be avoided; complex machined parts, close tolerances, and hand fit-up for secondary bonding are all cost-driving elements that should also be avoided.

BASIC ROOT-END-RETENTION CONCEPTS

There are three basic structural concepts that can be used to form a composite laminate-to-metal joint in a vibratory load field dominated by a strong axial load such as centrifugal force. These concepts are (Figure 1):

- FIBER DIRECTION IS PREDOMINANTLY AXIAL (0^{o}) FOR LAMINATES IN ALL CONCEPTS
- CONCEPTUAL REPRESENTATIONS ARE SCHEMATIC

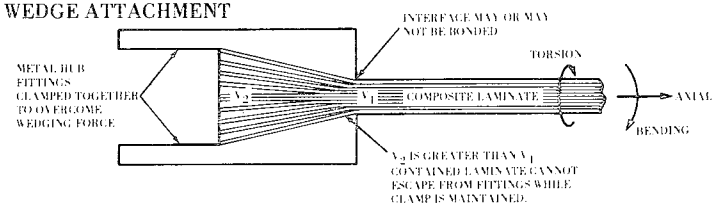
SIMPLE MECHANICAL ATTACHMENT



LOADS ARE TRANSFERRED TO METAL BY:

- BOND-LINE SHEAR
- BOLT BEARING AGAINST LAMINATE
- SOCKET ACTION OF LAMINATE AGAINST FITTINGS.

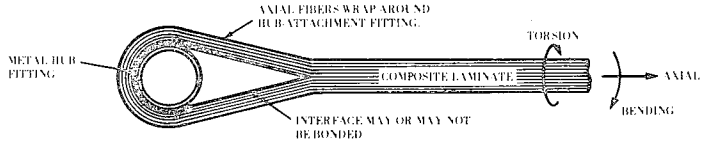
WEDGE ATTACHMENT



LOADS ARE TRANSFERRED TO METAL BY:

- BEARING OF WEDGE AGAINST METAL FITTING
- SOCKET ACTION OF LAMINATE AGAINST FITTINGS
- BOND-LINE SHEAR.

WRAPAROUND ATTACHMENT



LOADS ARE TRANSFERRED TO METAL BY:

- BEARING OF WRAP AGAINST PIN
- SOCKET ACTION AGAINST FITTING AND PIN
- BOND-LINE SHEAR.

Figure 1. Structural concepts for composite-to-metal interfaces in a high-axial-load field.

1. A simple mechanical interface in which the laminate is treated as if it were a metal and is attached by bolts and/or adhesives.

2. A wedge concept wherein the laminate is captured between two metal elements so that the enclosed volume of laminate is greater than the exit from the cavity.

3. A wraparound concept in which the laminate is wrapped and formed around a metal retention fitting.

These three basic structural concepts can be used to design many advanced and different blade-retention concepts, depending upon the specific capabilities and requirements of the joint.

A summary of a few of the more popular concepts is presented in Figure 2. These are the remaining concepts which evolved from a general design trade study of blade-retention concepts. Some designs were eliminated quickly because of obvious deviations from the criteria. Each remaining concept is fully capable of being used on a helicopter rotor blade. Sufficient analysis and design of each concept have been conducted to demonstrate feasibility and to define critical loadings, stresses, and relative weights. Each of the concepts shown in Figure 2 has been analyzed and evaluated against the criteria cited previously during a final trade study which ultimately led to the concept for final design and fabrication.

Boeing Vertol's successful composite blades have been designed around two of these concepts. These included the fiberglass Advanced-Geometry Blade (AGB) developed by Boeing Vertol and test-flown under Army contract on the CH-47 helicopter in 1969 (Figure 3); the all-boron-composite AGB developed and flown on the CH-47 under Air Force contract (Figure 4); the fiberglass-boron Boeing Vertol 222 tilt-rotor blades developed and wind-tunnel-tested under NASA contract (Figure 5); and the fiberglass blade in production for the Messerschmitt-Boelkow-Blohm BO-105 helicopter (Figure 6). Both Advanced-Geometry Blades (fiberglass and boron) and the 222 tilt-rotor composite blade used the cylindrical-wedge concept; the BO-105 employs a single-pin, vertical-wrap root end with external fitting.

All the concepts shown in Figure 2 terminate in a single- or double-vertical-pin connection to the rotor hub since all helicopters built at Boeing Vertol are subject to the requirement that the rotor blade be capable of folding about this attachment. This was a significant factor in the trade study and ultimate selection.

DISCUSSION OF TRADE-OFF STUDY RESULTS

The final results of the study showed that the vertical-pin wrap is the preferred concept, with the two-pin version being the better where

aircraft geometry and design considerations will permit. This vertically wrapped concept satisfies all the objectives initially stated. There are no critical metal fittings and therefore no critical bond line to develop. The load transfer is direct to the attachment pin.

The primary loading and resultant failure mode, as established by over 100 tests of the BO-105, is slow breakdown of the resin with no primary-fiber breaks. Thus, there is no failure in the critical load path. The multipin concept adds to this alternate load paths, insures inherent fail-safety, and eliminates the need for a failure-detection system. All metal elements in the root are repairable or replaceable; manufacturing is simplified since there are no complicated fittings to be machined. Vertical wrapping of the lay-up is more complicated than horizontal wrapping. However, aggressive action during the development programs identified means to simplify both manual and automated lay-up.

The vertical-pin wrap was therefore selected as the primary root-end concept. The multipin concept was selected for the HLH and, more recently, for the CH-46. The single pin was selected for the CH-47 because of its adaptability to the current CH-47 hub and for the UTTAS because of its proven characteristics for a hingeless, single-rotor helicopter, based upon the flight-proven BO-105 helicopter.

The cylindrical wedge or coke-bottle concept rated relatively low in this study in spite of our experience with it. The major reason for this rating is the metal fitting. The safety, maintainability, and reliability of the highly stressed, captured inner socket are unacceptable for a production application to helicopter rotor blades. To insure fail-safety, a highly sensitive failure-detection system would be necessary to protect this critical fitting properly. Furthermore, a totally satisfactory means of replacing the metal fitting was never identified. Thus, the effective life of the blade would be dependent upon the less reliable metal. By the time the required fail-safety and life could be achieved, there would be a significant weight penalty compared to the other concepts.

Although the mechanically fastened concept is a very cost-effective design, it has the distinct disadvantage of interrupting the fibers in the joint area rather than keeping the loads aligned with them. This concept is inherently redundant and repairable with generally straightforward load paths. Aggressive programs to develop mechanical attachments for the use of composites on fixed-wing structure have provided a background in the required design allowables. However, detailed analysis revealed extensive structural risk as well as uncertainty and problems in material selection. The load transfer into the plates must occur through the bond line, with some load transferring through the bolts. Uncertainty as to load sharing forces a conservative assumption of 100-percent bolt-bearing transfer. Fiberglass alone could not be used as the spar material

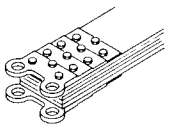
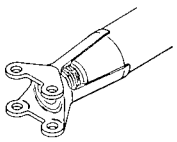
CONCEPT / CRITERION	MECHANICAL RETENTION 	WEDGE 
STRUCTURAL EFFICIENCY	• LAMINATE IS POSITIVELY CONTAINED • STRUCTURAL BOND IN PRIMARY LOAD PATH • LAMINATE IS LOADED IN SHEAR TEAR-OUT MODE AND REQUIRES HIGH-MODULUS FIBERS TO SUPPLEMENT FIBERGLASS	• LAMINATE IS POSITIVELY CONTAINED; • STRUCTURAL BOND IN PRIMARY LOAD PATH • LOAD REACTION INDUCES HIGH STRESSES ACROSS FIBERS IN WEDGE
SAFETY	• ALL LOADS ARE TRANSFERRED INTO METAL FITTINGS • HOWEVER, CONCEPT HAS INHERENT REDUNDANCY AND VISIBLE FAILURE PROPAGATION • ACTIVE FAILURE-DETECTION SYSTEM NOT REQUIRED FOR FAILSAFETY	• INTERNAL FITTING HAS HIGH STRESS LEVELS, RAPID CRACK RATE • CONCEPT REQUIRES FAILURE-DETECTION SYSTEM FOR FAILSAFETY
MAINTAINABILITY	• ALL ELEMENTS ARE INSPECTABLE AND REPAIRABLE	• OUTER FITTINGS ARE INSPECTABLE AND REPAIRABLE, INNER FITTINGS ARE NOT
MANUFACTURING SIMPLICITY	• LAYUP IS AUTOMATABLE AND EXTREMELY SIMPLE • MAJOR COST IS IN MACHINING AND DRILLING, BONDING, AND BOLTING OF ASSEMBLY	• LAMINATE LAYUP IS AUTOMATABLE BUT MODERATELY COMPLEX • MAJOR COST IS IN MACHINING OF ROOT-END FITTINGS

Figure 2. Summary of root-end-retention concepts and trade study.

since its modulus is so different from that of the metal fittings that effective bond–joint transfer would not be obtained. The shear-tearout properties of the fiberglass material are not sufficiently developed to permit fiberglass alone in this configuration. High-modulus fiber material — graphite or boron — would be necessary, at least as local doubler material under the metal fittings, to improve the spanwise-strain compatibility and improve the bearing and tear-out characteristics of the total laminate. The high-modulus fiber composites have the distinct disadvantage of failing across the fibers when they do fail; in this characteristic, they

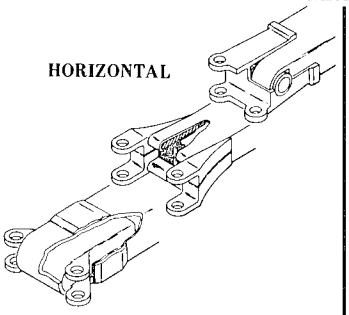
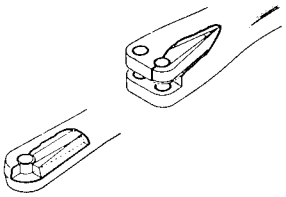
CONCEPT / CRITERION	WRAPAROUND: HORIZONTAL	WRAPAROUND: VERTICAL
		
STRUCTURAL EFFICIENCY	• MAJOR LAMINATE STRESSES ARE IN DIRECTION OF PRIMARY FIBER ORIENTATION • LAMINATES ARE ALL POSITIVELY CONTAINED • STRUCTURAL BONDS IN PRIMARY LOAD PATH BETWEEN LAMINATE AND METAL FITTINGS	• MAJOR LAMINATE STRESSES ARE IN DIRECTION OF PRIMARY FIBER ORIENTATION • LAMINATES ARE ALL POSITIVELY CONTAINED • NO STRUCTURAL BONDS IN PRIMARY LOAD PATH
SAFETY	• ALL PRIMARY LOADS ARE TRANSFERRED INTO METAL FITTINGS • CONCEPTS HAVE INHERENT REDUNDANCY AND GENERALLY VISIBLE FAILURE MODES • ACTIVE FAILURE-DETECTION SYSTEM NOT REQUIRED FOR FAILSAFETY	• NO METAL FITTINGS REQUIRED TO TRANSFER LOADS FROM LAMINATE TO HUB ATTACHMENT • FIBERGLASS FAILURE MODES PREVAIL • INHERENT FAILSAFETY WITHOUT ACTIVE FAILURE DETECTION SYSTEM
MAINTAINABILITY	• EXTERNAL FITTINGS ARE INSPECTABLE, REPAIRABLE, AND REPLACEABLE • INTERNAL FITTINGS ARE INSPECTABLE ONLY	• ALL ELEMENTS INSPECTABLE AND REPAIRABLE
MANUFACTURING SIMPLICITY	• LAMINATE LAYUP IS SIMPLE AND AUTOMATABLE • MAJOR COST IS IN MACHINING OF FITTINGS	• LAYUP IS AUTOMATABLE BUT MODERATELY COMPLEX • MAJOR COST IS IN LAYUP

Figure 2. (Continued)

resemble metals. Since this failure mode acts to degrade the centrifugal-force load path (which is the catastrophic failure mode of a rotor blade), high-modulus material reduces the safety rating of this concept compared to an all-fiberglass joint.

The horizontal-wrap concepts seemed to offer an efficient means for load transfer and for low-cost spar fabrication; however, the metal structure became complex, heavy, and expensive. The criticality of the bond line between the laminate and metal fittings is also a problem in this concept. Although the concepts are inherently redundant, the loads must

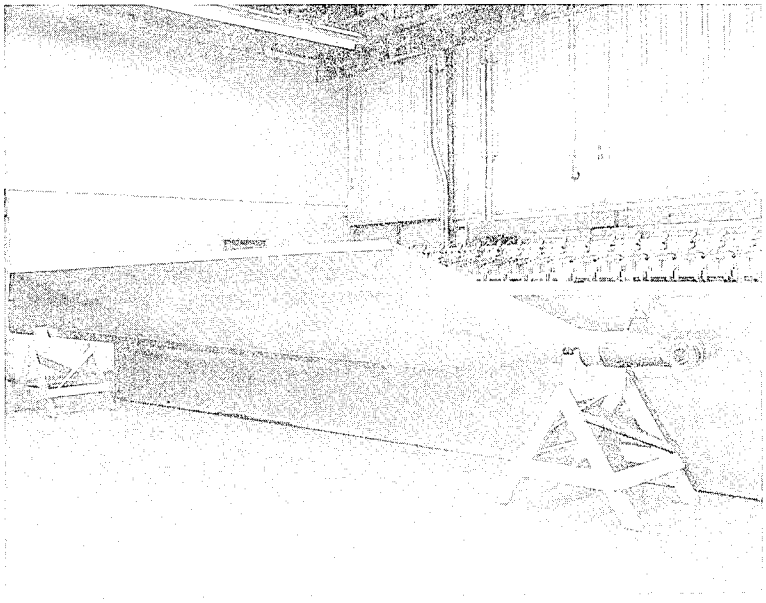


Figure 3. Boeing Vertol's fiberglass advanced-geometry rotor blade.

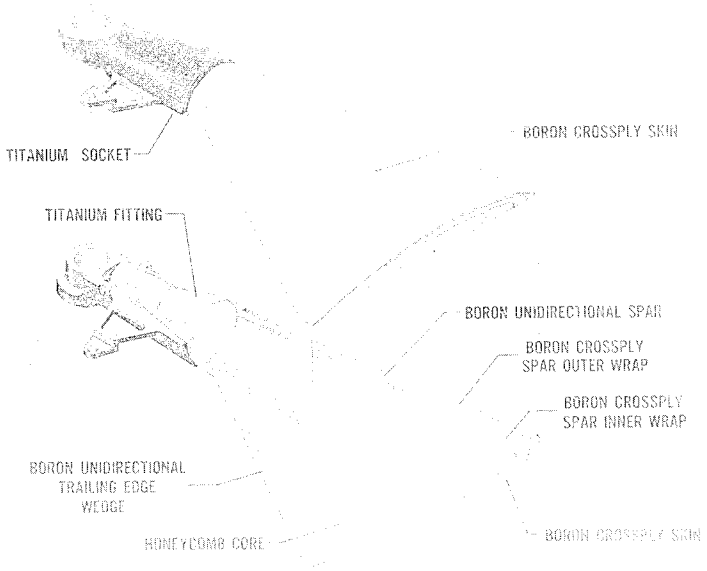


Figure 4. Attachment joint for the boron advanced-geometry rotor blade.

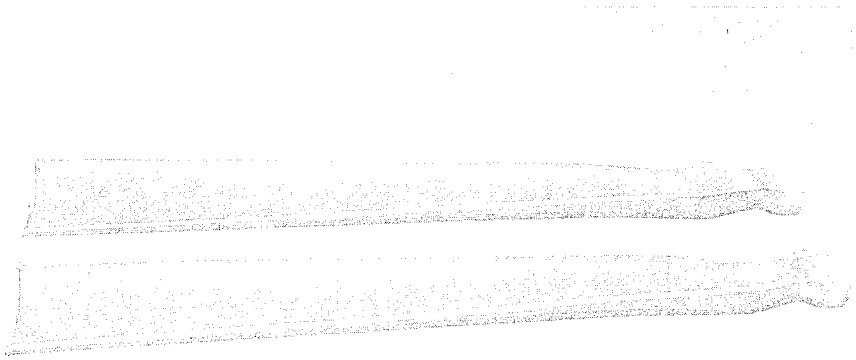


Figure 5. Fiberglass and boron blade for the Boeing Vertol 222 tilt-rotor.

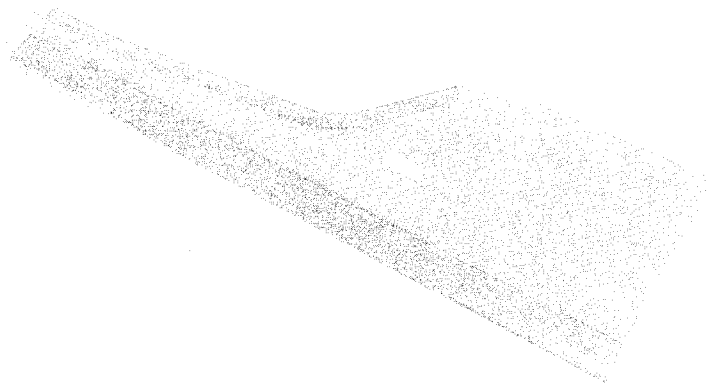


Figure 6. Root section of the fiberglass blade for the MBB BO-105 helicopter.

be transferred into the metal fittings and consequently the failure characteristics, reliability levels, and crack-propagation rates of the metal prevail. It is in this regard that the following requirement impacts the results of the study. If the pin attachment to the hub could be made through horizontal pins rather than vertical pins for folding, then the requirement for the fittings would be eliminated. The horizontal wrap would then have the same advantage as the selected vertical-wrap concept.

In the following sections the results of the fabrication and development testing of vertically wrapped concepts are presented, including the automated lay-up technique which eliminates the lay-up complexity of vertical wrapping.

DEVELOPMENT OF THE SELECTED RETENTION CONCEPT

The vertical-wrap concept can be used for either single or multilug configurations. Figure 7 shows the typical construction of each configuration. The unidirectional (0-degree) material of the spar is laid in equal-width packs from the blade tip, around the root, and symmetrically back to the blade tip. In the shank area, the pack transitions from the horizontal to the vertical to form a natural lug and then back to the horizontal again.

This lay-up technique, which requires the individual pack transitioning, is relatively simple and definitely automatable. However, it is more restrictive and inherently must be laid at slower rates than the lay-ups for the flat, mechanically retained configuration and the horizontal wrap. This is because each pass of the vertical strap forms only a portion of either the upper or lower spar unidirectional width, whereas the complete width of the upper or lower spar half of both the horizontal wrap and mechanically retained configuration can be laid per machine pass.

In itself, this requirement does not pose a serious cost concern. With no root-end fittings to machine, the overall concept is very cost-competitive. Each configuration of vertical loop can be laid automatically at rates of 25 pounds per hour with production-rate tape lay-up equipment. The Army/Goldsworthy/Boeing Vertol Automatic Tape Lay-up System (ATLAS) has already demonstrated (Figure 8) a rate of 9 pounds per hour during ATLAS demonstrations at partial speeds; the normal rate for hand lay-up is 0.3 pound per hour. Figures 9 and 10 show typical UTTAS and HLH hand-laid straps.

Lay-up rates of 9 to 25 pounds per hour are satisfactory to reach the cost objectives for production composite blades. However, the desire still existed to reduce the complexity of lay-up, eliminate the necessity for multiaxis lay-up equipment with numerical-control capability, and in-

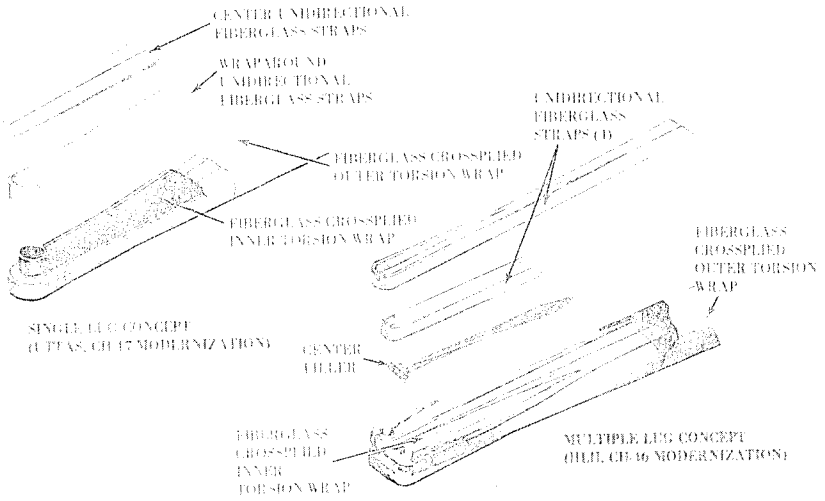


Figure 7. Construction details of spars and root ends.

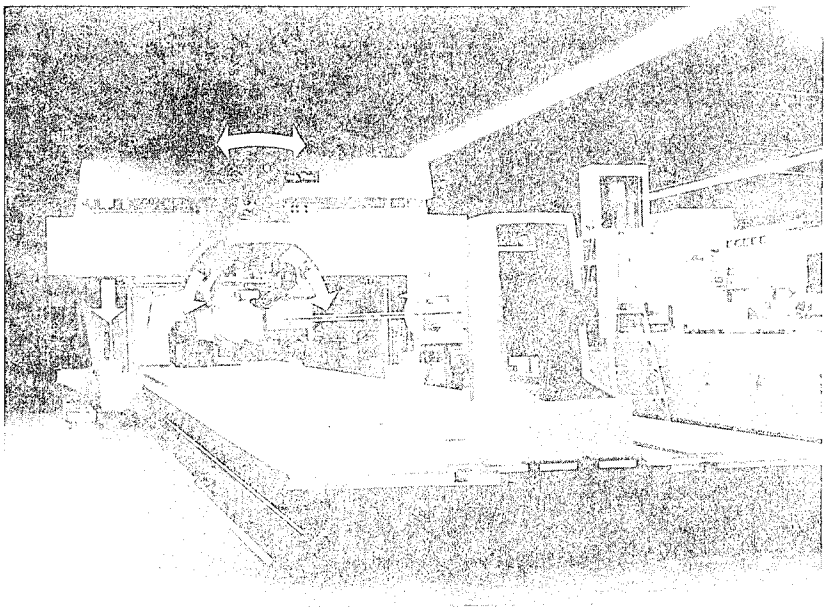


Figure 8. The automatic tape lay-up system (ATLAS).

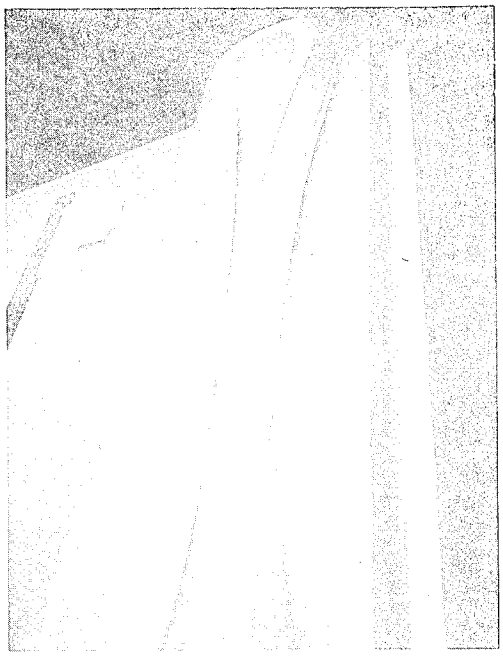


Figure 9. Hand-laid fiberglass straps for UTTAS blade.

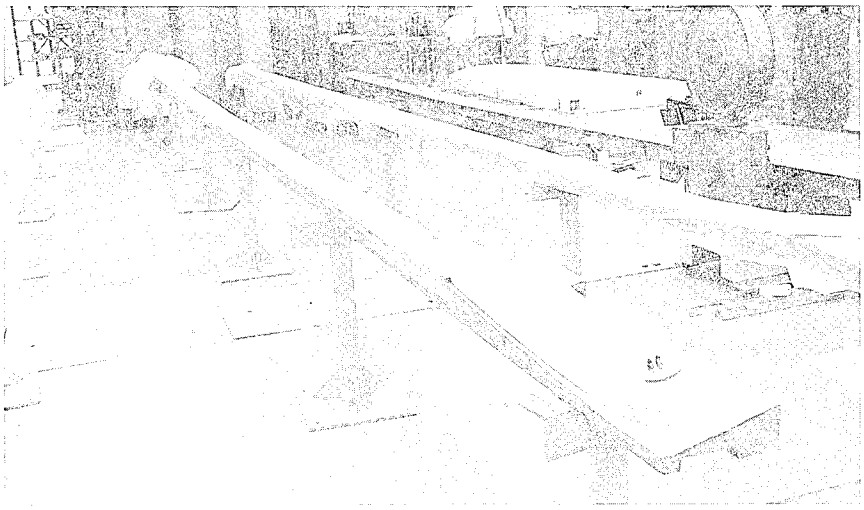


Figure 10. Hand-laid fiberglass straps for HLH blade.

crease lay-up rates to the 100–200-pound-per-hour level which would virtually eliminate tape lay-up of spar straps as a calculable cost. A technique was developed which provides an answer to all these objectives (Figure 11). Investigation with the preimpregnated-fiberglass tape demonstrated that tape packs could be laid up as simple vertical wraps without the horizontal-to-vertical transition (Figure 11A); after the complete pack is laid, it is then brought to the lay-up mandrel which has the necessary transition built into it (11B); the pack is then laid about the pin and simply wiped down against the mandrel (11C). The preimpregnated-fiberglass material offers little resistance to this technique and remains in this final location awaiting assembly and cure.

With this technique available, spar material can be laid automatically without transitioning, which significantly reduces the machine complexities. Furthermore, it presents the opportunity to lay up the straps in multiples of each lug height (Figure 12), which insures that rates of 100 and 200 pounds per hour will be achieved with these simple machines (see Acknowledgment). The unindirectional fiberglass material can be laid in the most convenient width for the lay-up machine consistent with the available handling equipment (a roll of fiberglass prepreg 24 inches wide by 500 yards long weighs approximately 260 pounds). The pack is then automatically slit into the required lug-height packs either for storage in this form or immediate use.

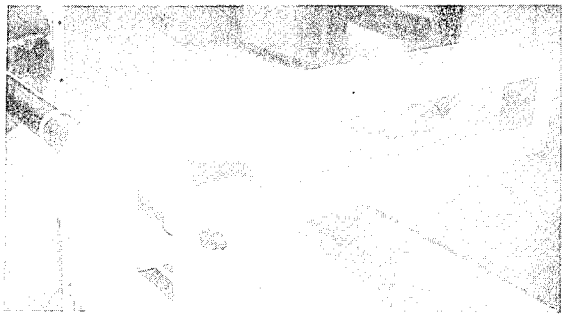
An example of the capability of this technique is shown in Figure 13, wherein 16 straps or 4 blades of CH-46 configuration could be laid in 1.6 hours, or less than a half hour per blade to lay up all of the unidirectional spar-pack material.

Since the selection of the vertical-wraparound concept, actual full-scale components have been fabricated for the UTTAS, HLH, and CH-47 (Figures 14, 15, and 16). Fatigue and static testing of both UTTAS and HLH specimens has been conducted which verified all of the structural, safety, and maintainability objectives stated previously.

The initial testing on the root end was a static and dynamic strain survey. This survey verified the load distribution between lugs and the wraparound-loop stress-concentration factor.

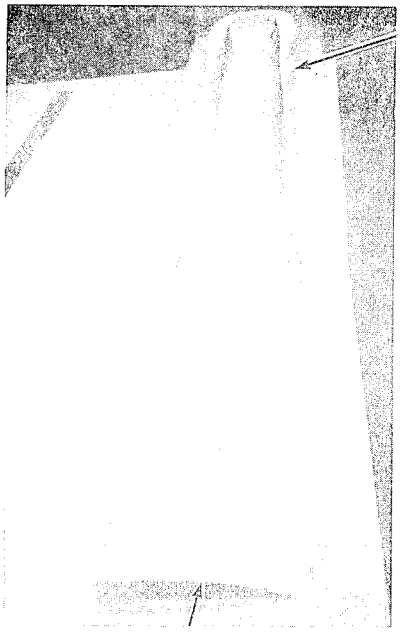
The fatigue testing of root ends includes a combination of flap and chord bending, centrifugal force, and torsional loads. The tests are run considerably above normal flight loads in order to induce earlier failures or to verify the required life in a minimum amount of test time.

The fatigue testing of the multiloop, vertical-wraparound configuration in the HLH size did not produce a failure in the fiberglass even at the elevated load levels; however, the metal sleeves and bushings within the lug loop did fail. These bushings and sleeves were designed as secondary elements to act as wear interfaces with the hub-retention hard-



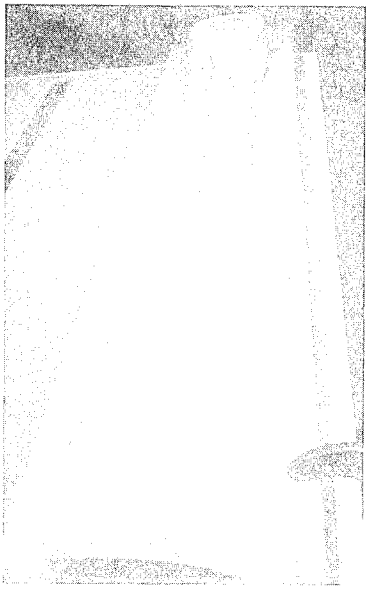
A

INDIVIDUAL STRAP OF UNIDIRECTIONAL MATERIAL LAID WITHOUT SPAR-TO-LUG ROTATION



STRAP BEFORE SHAPING

B MANDREL WITH CONTOUR



C STRAP AFTER SHAPING ON MANDREL

Figure 11. Construction sequence for shaping vertically wrapped strap.

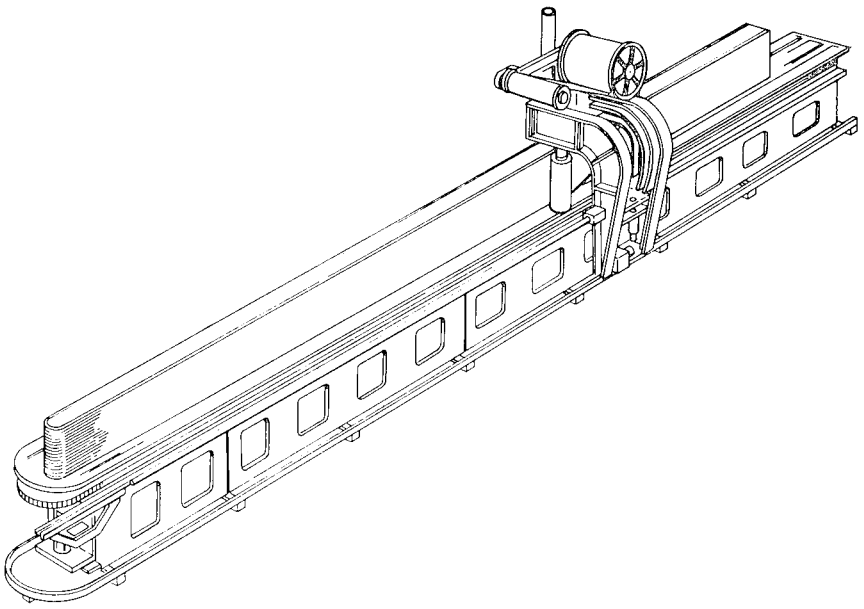


Figure 12. Automated spar-strap lay-up machine.

ware. Since all the fiber in the loop is circumferential, there is very little stiffness to the loop radially. Investigation indicated that the bushing was stiffening the composite loop in a radial direction and prevented the normal loop deflection under load; the high-modulus bushing could not accommodate the deflections and failed. The metal fittings were modified to separate the bushing into a separate sleeve (which will be composite in its production configuration) and washer and further testing indicated that the solution was satisfactory. The lesson, however, is clear. Metal elements in a composite joint, even secondary structure, introduce a significant design consideration and cannot be taken for granted. The damaged sleeves were removed from the loop and a new set of modified hardware was installed and tested; this verified the excellent maintainability of the root concept.

During the testing of the single-lug UTTAS root end, there was a noticeable increase in torsional deflection after several million cycles. Although the blade still retained its full structural integrity, this change in stiffness was deemed a failure. The loads were dropped to high-speed, level-flight loads and the equivalent of 30 flight hours was run; no further degradation or propagation resulted. The loads were then returned to the original high level. The tests were stopped when blade deflections exceeded machine capacity. However, even here there was no structural

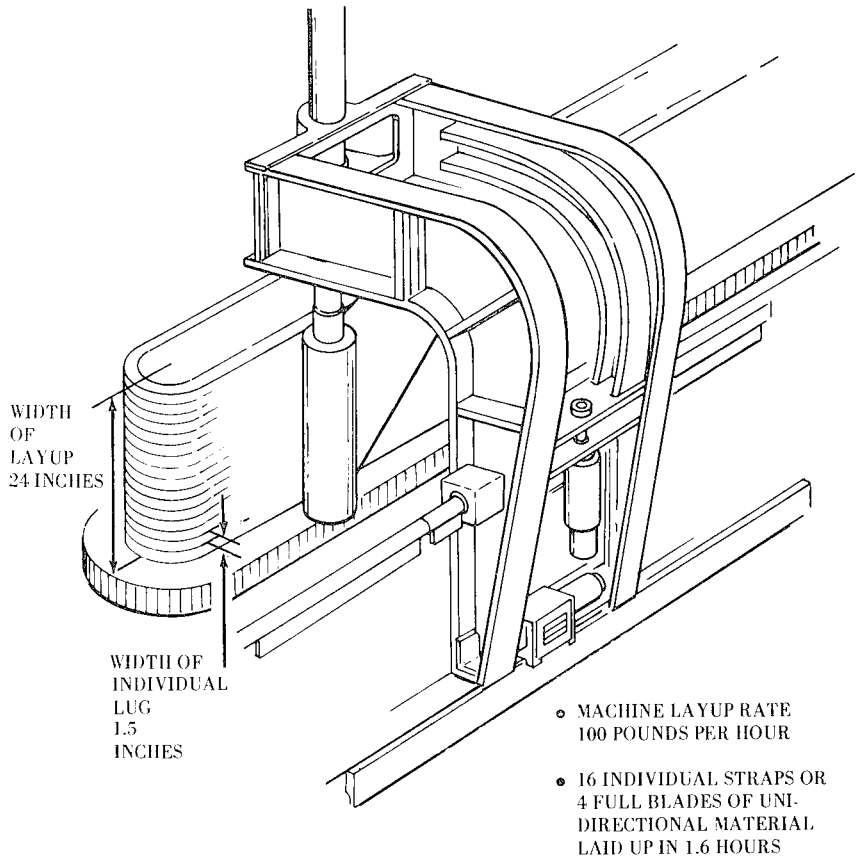


Figure 13. Example of multiple spar-strap lay-up for CH-46 multi-pin root end.

failure and the blade would have been safe to fly. Analysis showed that the vibration levels would have risen to a level noticeable to the pilot, but would still have been well within the safe operating range. Figure 17 shows the area of delamination which was visible after completion of the rest. This testing verifies in a full-scale specimen the soft, progressive failure characteristics of fiberglass. At this point in the testing, failure indication by both failure-detection system and vibration due to out-of-track will have occurred and the blade is still safe for flight.

A further demonstration of safety and damage tolerance was conducted on the unfailed HLH multilug configuration after the initial fatigue test. Damages were inflicted to three of the four major load paths and the specimen was tested for the equivalent of 200 flight hours at

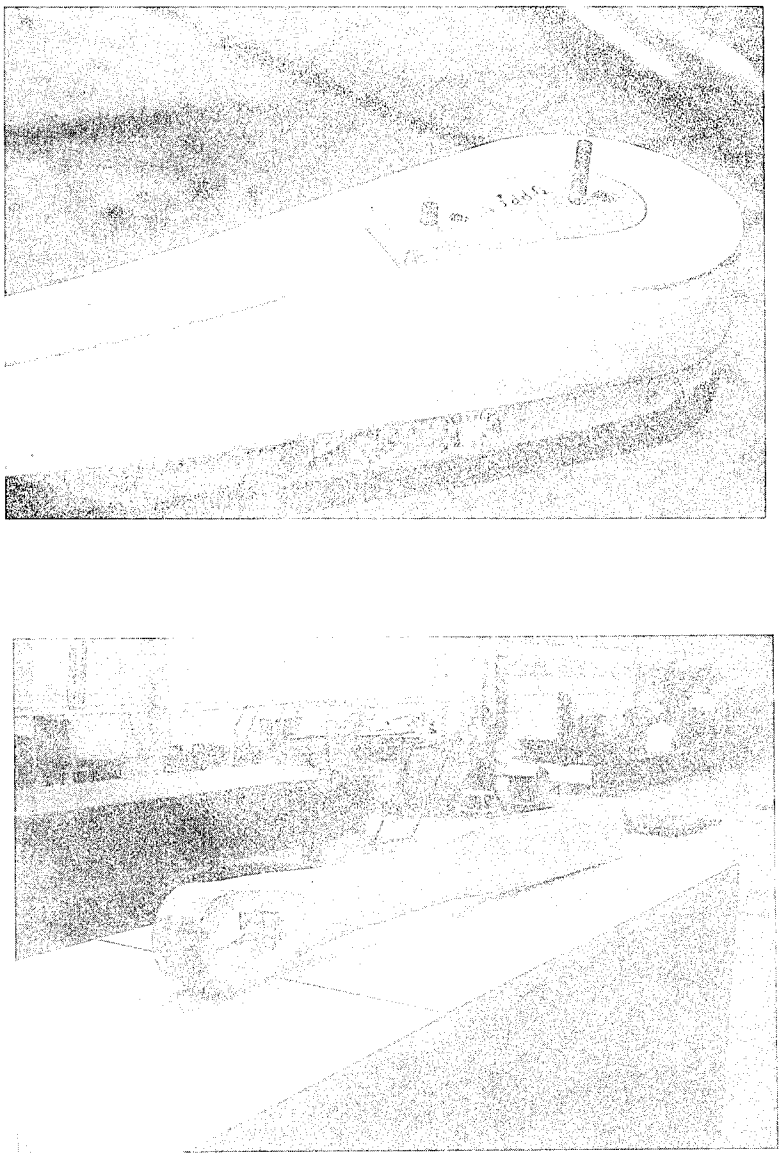


Figure 14. Root-end section of the UTTAS fiberglass blade.

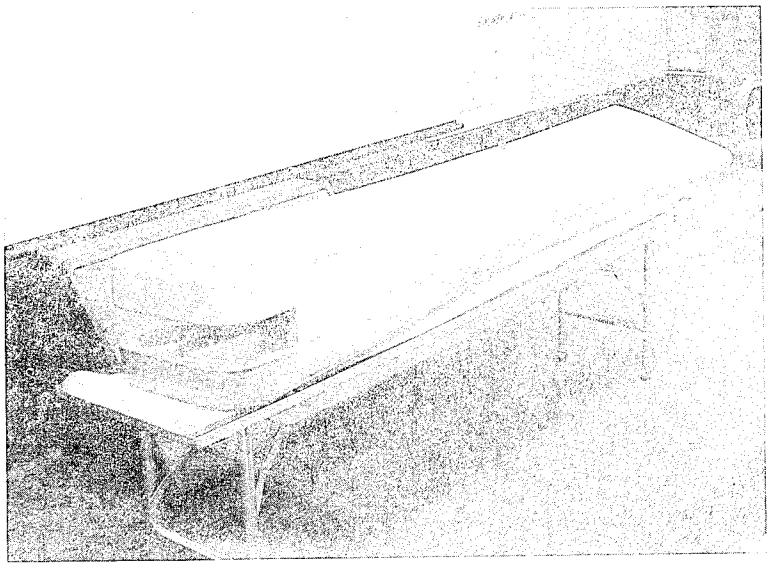


Figure 15. Root-end section of the HLH fiberglass blade.

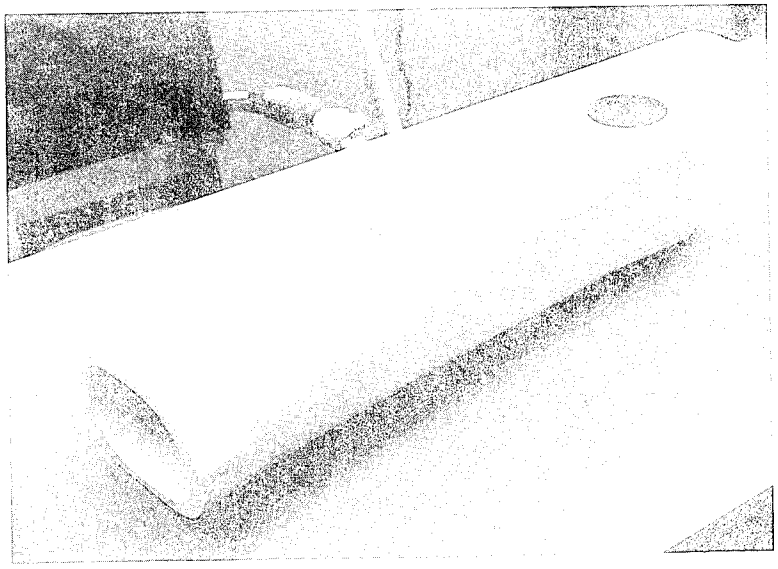


Figure 16. Root-end section of the CH-47 fiberglass blade.

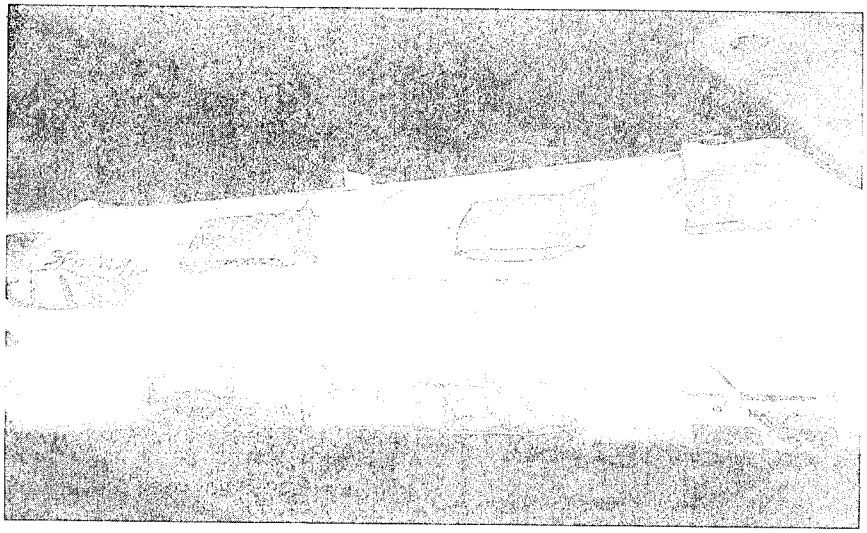


Figure 17. Delamination of the UTTAS blade shank after fatigue test.

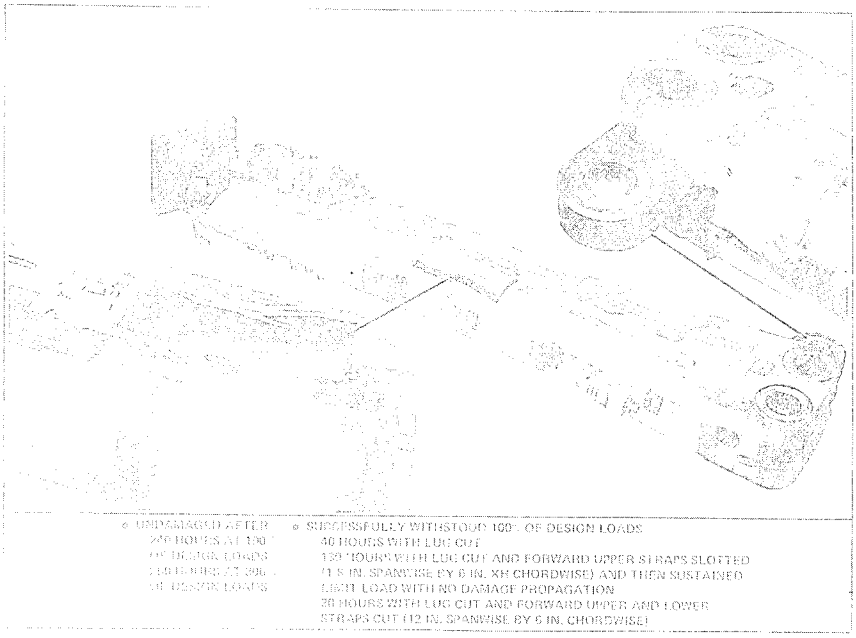


Figure 18. HLH root-end test demonstrates damage tolerance and survivability of fiberglass.

high-speed, level-flight loads. Figure 18 presents a summary of this testing and shows the level of damage that can be withstood by this fiberglass construction. At the section of the shank with the two large cutouts, the axial, flapwise, and chordwise stiffnesses have been reduced by 50 percent and the torsional stiffness has been reduced by 85 percent. This local reduction will generate an out-of-track-vibration condition which will provide an additional level of detectability and fail-safety.

SUMMARY

A trade study was conducted to select a root-end-retention concept for a family of helicopter composite rotor blades. The vertical-wrap-around-lug configuration was selected over the mechanically fastened, coke-bottle wedge, and horizontally wrapped concepts because of its superior structural efficiency, safety, and maintainability.

The complexity of the vertically wrapped lay-up was eliminated by the development of a simplified lay-up technique capable of automatic lay-up rates of 100–200 pounds per hour — a rate which reduces lay-up costs in production to less than 5% of total blade cost.

Static and fatigue testing of the full-scale root ends verified the analysis, strength, damage tolerance, and safety of the vertical-wraparound root-end concept.

ACKNOWLEDGMENT

We would like to acknowledge the contributions of Robert C. Huss, Senior Design Engineer; Raymond P. Belko, Senior Design Engineer; and Ed Frank, Senior Development Engineer, to the development of the reduced-cost tape lay-up technique which significantly simplified the fabrication of the vertical-wrap root-end design.

14. DESIGN PARAMETER CONSIDERATIONS FOR COMPOSITE SANDWICH BONDING

J. BRENTJES
Hexcel Corporation
Doublin, California

Selecting composite materials for honeycomb sandwich panels should be based on a variety of factors such as stress analysis, environmental exposures and special properties such as thermal, acoustical, or dielectrics. One very important area of design has often been neglected; edge members, closeouts, and joints. The intent of this chapter is to classify the different closeouts, corner joints, and fastener designs, and to point out how each can be defined by the fabrication technique as well as application. Also included are various factors to consider when designing doublers and reinforcement sections into a composite sandwich. In particular, the relative cost and ease of manufacture are two points stressed as the most critical parameters to consider for efficient designs.

Composites and adhesive-bonded parts are becoming more and more commonplace in all industries and designs. It took several years of experimenting with new adhesive formulations, cleaning and application techniques; and it required the development of new space-age materials such as titanium, graphite, and the various plastics. Above all, designers had to gain sufficient experience and confidence in the use of these materials. But now, cost savings are being realized for innumerable industrial and military applications. There is a simple reason; adhesives, when properly used, will provide better performance. Fatigue failure and crack propagations are reduced; higher strengths, better sealing, and corrosion barriers are provided; they reduce the number of fasteners required during assembly; maintenance and repair time can be minimized, hence, overall reliability can be improved.

Bonded honeycomb-sandwich panels are really an extension of the simple idea of joining two pieces of metal or plastic with glue. The process requires more insight and care, it involves proper selection of

core, facings, and adhesive, but in the long run can provide the cost savings and improved performance all of us are looking for. The largest helicopter in the United States, the XCH-62, presently being built by Boeing Vertol for the Army, has its entire fuselage made of honeycomb sandwich "resulting in 22.3% decrease in empty weight and an 86% reduction in rivets and other fasteners with the attendant reduction in installation cost."

The composite sandwich design depends on joining various selected materials into a structural unit which has to meet certain design requirements. The selection of these components are dictated by many considerations, some of which are listed below.

1. Stress analysis.
2. Service environment.
   A. Temperature exposure.
   B. Moisture/humidity.
   C. Other corrosive atmospheres.
   D. Impact and handling conditions.
   E. Flammability.
3. Heat transfer.
4. Acoustics.
5. Electrical transmission/shielding.
6. Facing-adhesive-core compatibility.
7. Producibility.
8. Value analysis.

Basically, a sandwich consists of two thin, strong facings separated by a low-weight core material which is bonded to these facings. When a bending load is applied, for example, this beam derives its strength from the facings, taking the tensile and compressive stresses while the core takes the resulting shear stresses.

Figure 1 lists the basic factors to consider in a sandwich panel. A structure can be subjected to a multitude of loading conditions ranging from uniformily distributed static loads to dynamic impact. Various facings and core types will react differently under such conditions, and certainly careful selection is important. However, the fact remains that unless the imposed stresses are properly transferred from the facings and core through the close-out or fastener to the substructure, all the advantages of the composite sandwich may well be lost. Hence, the proper design of the edge members or close-outs and means of fastening the panel requires careful planning and a certain degree of ingenuity.

In designing any kind of structure, one always has to consider "How is it going to be made?" This is particularly true of close-outs and fasteners. One has to think about the shape, size, and form of the part. Should it be machined, cast, extruded? What material? Can it be bonded

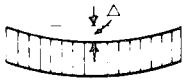
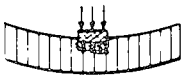
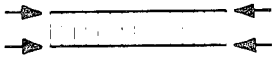
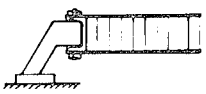
1	Facings to take tensile and compressive stresses.	
2	Honeycomb to take shear stresses.	
3	Sufficient rigidity to minimize deflection.	
4	Core to have sufficient compressive strength.	
5	Sandwich to take edge-wise compressive stresses.	
6	Adhesive to take tensile, shear and peel stresses.	
7	Close outs and fasteners to tie core and facings to substructure.	

Figure 1. Basic considerations for sandwich stress analysis.

with adhesives? Is it to be (if I may coin two new words) "co-fab" or "post-fab?" In other words, is it best to incorporate the edge shape right into the original panel bonding operation, or is it better to add the close-out afterwards? Figure 2 tries to illustrate this difference.

From the standpoint of structural stress analysis, the attachment can be categorized as a fixed or simple support. For a panel acting as a beam, for example, the formulas used to calculate deflection use different constants for different support conditions. The simple support being the most flexible, of course. Truly fixed supports are hard, if not impossible, to come by. All common designs fall somewhere between the two extremes. Consider the relative stiffness of the four supports shown in Figure 2, for example. For this reason, it is always a good idea to play it safe and design the structure as if it is simply supported.

As mentioned earlier, a good close-out provides a transfer path for the compressive and tensile forces from the facings to the attachment. Thus, the skins should be well joined to the edge member with a minimum amount of stress concentrations taking place at the interface. To accomplish this as gradually as possible, many structures use "doublers" or additional layers of facing material at the point of maximum stress concentration. Figure 3 shows how doublers can be classified as being external and internal as well as co-fab and post-fab. A typical helicopeter rotor blade can have many of these doublers built up at its attachment point (see Figure 4).

Film adhesives are normally used to bond the facings to the close-outs in co-fab designs. In fact, the same adhesive sheet is used to bond the honeycomb to the skins. In the post-fab designs, the member is usually bonded with a room-temperature curing two-part epoxy system. Pop rivets are sometimes used at a few locations to position the parts and apply pressure during the adhesive cure cycle. In either case, the adhesive joint should be as strong or stronger than the facings themselves. Again, this is to ascertain that this critical part is not the weakest link. Hence, as in every bonding process, make sure the parts can be and are cleaned, the adhesive is thoroughly mixed and put where it belongs, and that the peel, tensile, and shear stresses are well below the ultimate values reported for that system. However, don't over-kill. It shouldn't be necessary to make the part twice as heavy "just to be sure."

Shear stresses in honeycomb (or foam, or balsa wood) should be transferred to the edge members or fasteners wherever possible. Yet, it has been found that for lightly loaded panels with low-density/low-strength core, this is not always necessary. But my advice is: bond the core where loads are expected to be transferred. There are foaming splice adhesives which can be used for co-fab and two-part epoxies (with

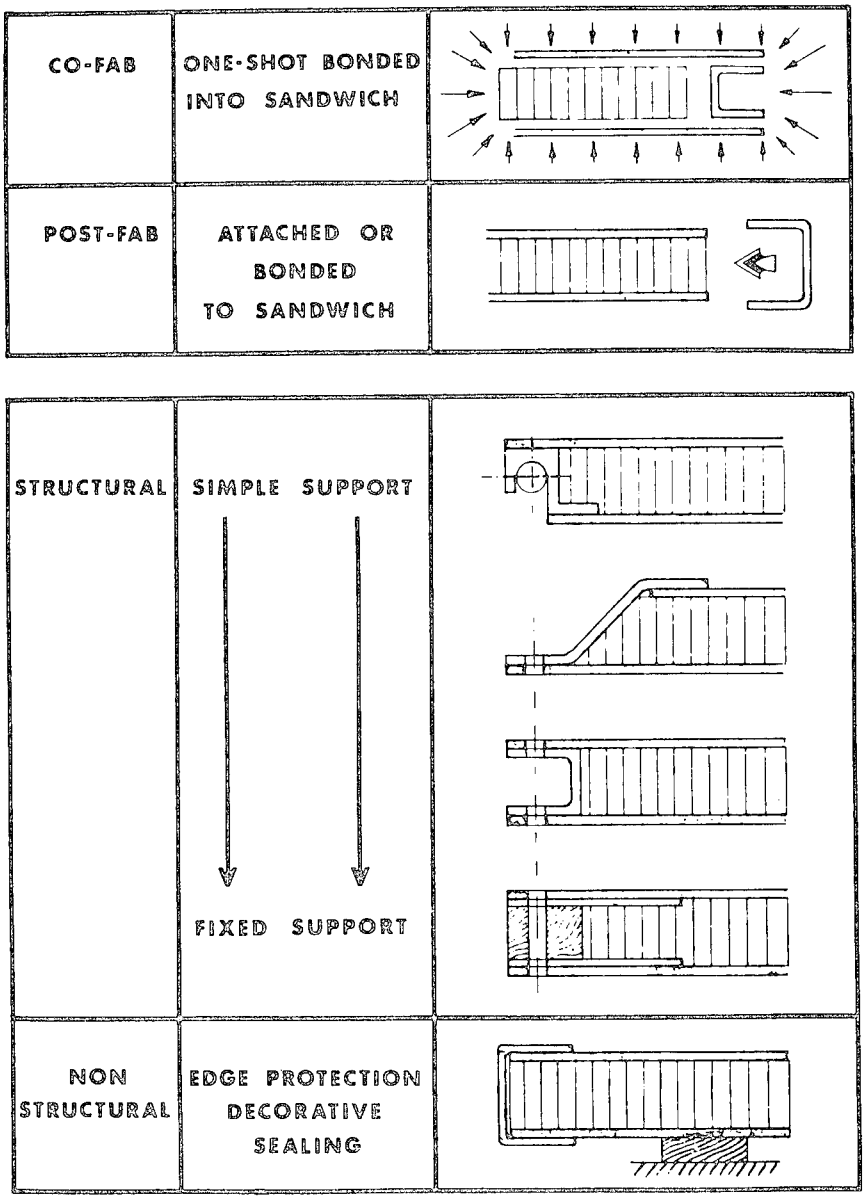


Figure 2. Close-outs as defined by the fabrication technique as well as end use.

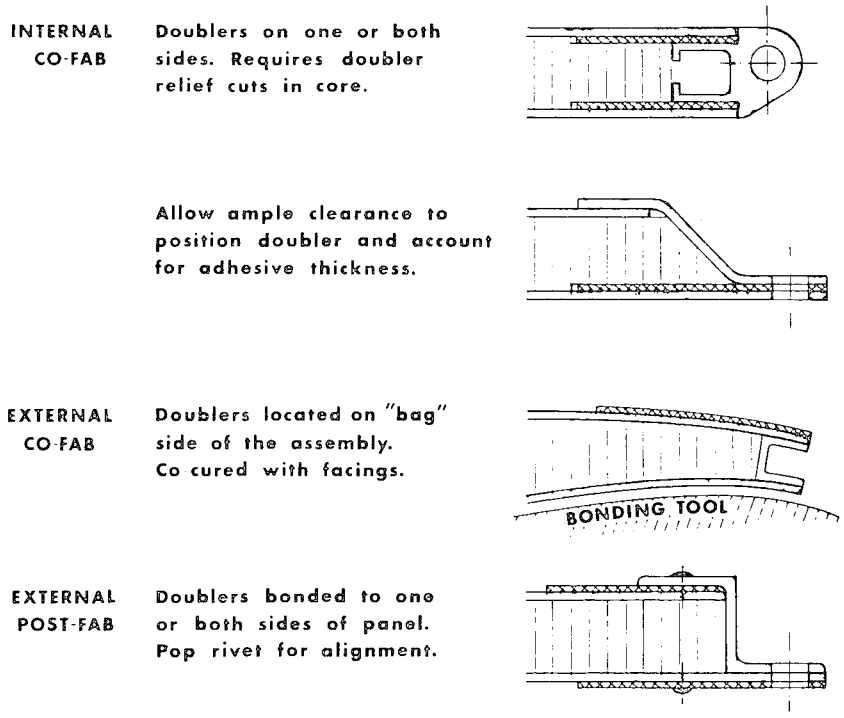


Figure 3. Doublers in a sandwich panel.

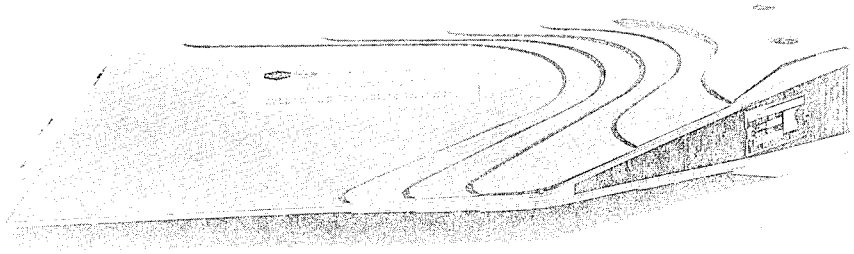


Figure 4. Helicopter tail rotor section showing buildup of external/co-fab doublers.

microballoons to keep the weight down) for post-fab close-out/fastener designs.

Some panels are subjected to loads which are complex and combinations of edgewise compressive or tensile loads, torsional, and racking forces. If at all possible, try to break out the components and consider your design for each and all. In the case of edgewise compressive loads introduced through an edge member, make sure the loads can be distributed equally to both facings, otherwise the facing with the higher stress level could fail prematurely. For torsional loading, the sandwich facings impose an awkward combination of shear, tensile, and peel stresses on the adhesive joint. In a rectangular panel, this stress will vary from corner to corner. Thus, close-outs or other attachments which have to carry a significant load should be analyzed as to the types of stresses they experience and best way they can be handled.

Quite frequently a panel close-out is not intended to carry a load. It acts primarily as a seal or edge member to prevent localized damage. In other words, the loads are taken out through an internal fastener or the panel may simply rest on support brackets. In this case, the closure member can be a very inexpensive channel bonded to the panel with R. T. cure epoxy adhesive. Several other simple shapes can be produced, but keep in mind how it is to be installed, how to fit the corners, etc. One interesting approach which provides a clean, smooth design is shown in Figure 5, second from the top. The close-out is actually of a post-fab design in that the extrusion is bonded to the panel after slotting the honeycomb with a special two-bladed router. The small lip on top and bottom provides a recess for the facings and prevents the facings from being peeled off easily. After the adhesive is cured, a light sanding will blend and feather this edge very nicely.

Some designs require two or more flat panels to be joined in a straight line or at right angles to each other. At first glance, this may appear to be a relatively simple situation. Many different approaches have been suggested and used. Some are shown in Figures 6 and 7. In each case, many factors have to be considered; cost of the shape, cost to install, relative strength and stiffness, moisture–corrosion barrier, weight, permanent or replaceable, cosmetics. One has to be careful when looking at two-dimensional drawings like this. For example, a very neat approach is the H-shaped extrusion to join flat panels. Slipping the extrusion into one panel is easy enough; however, trying to align and slide the second panel into its slot may be quite tricky for sheets that are 4×8 feet or larger (especially when handling sticky adhesive in a field installation). Maybe a simpler approach could be as shown in Figure 8. This design is used by Hexcel in assembling panels to form a trailer hopper. During assembly, the bottom extrusion (with adhesive applied)

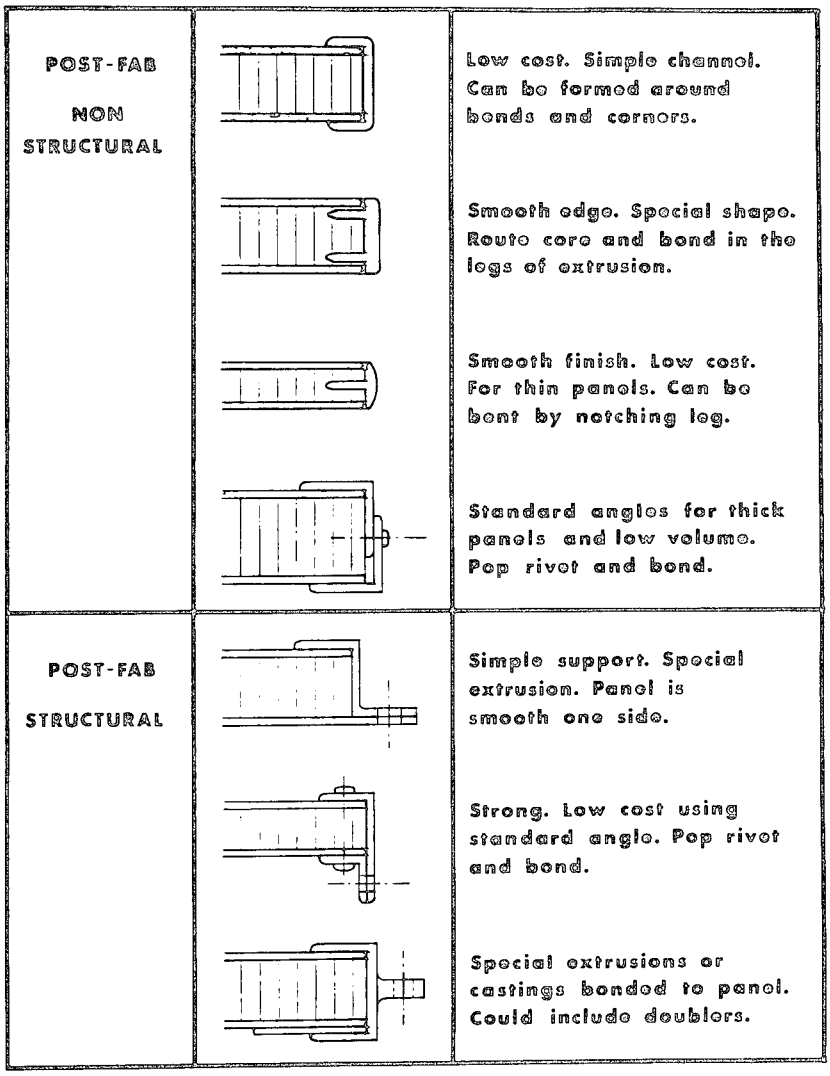


Figure 5. Typical panel close-out designs.

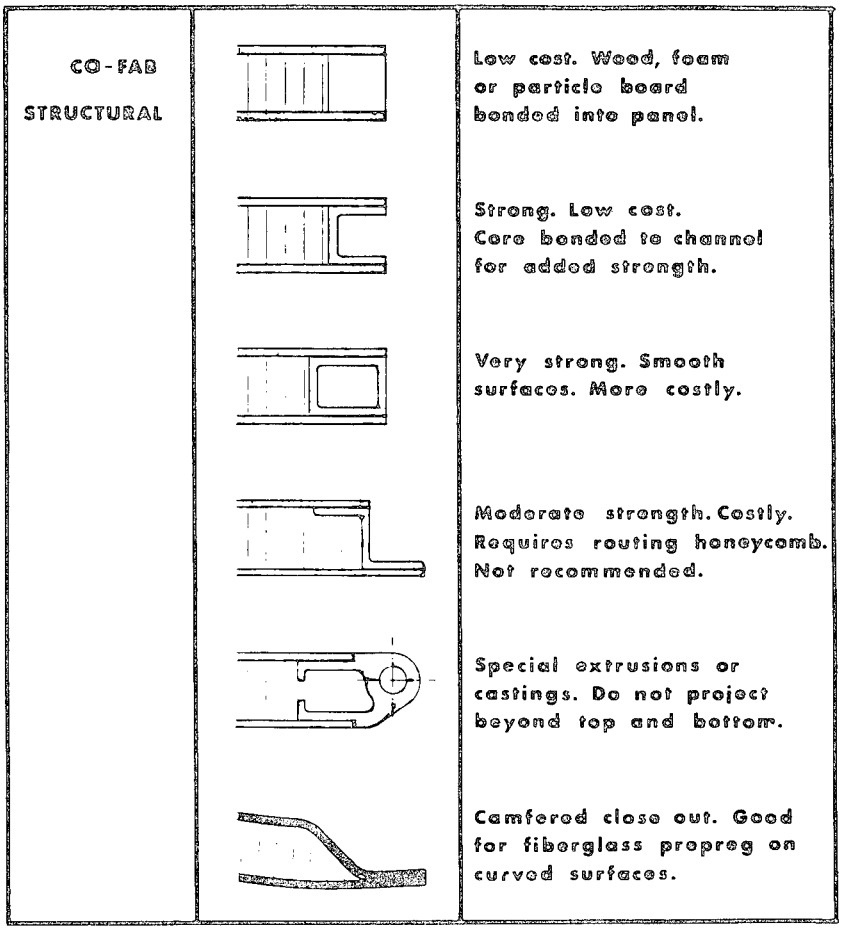


Figure 5. (Continued)

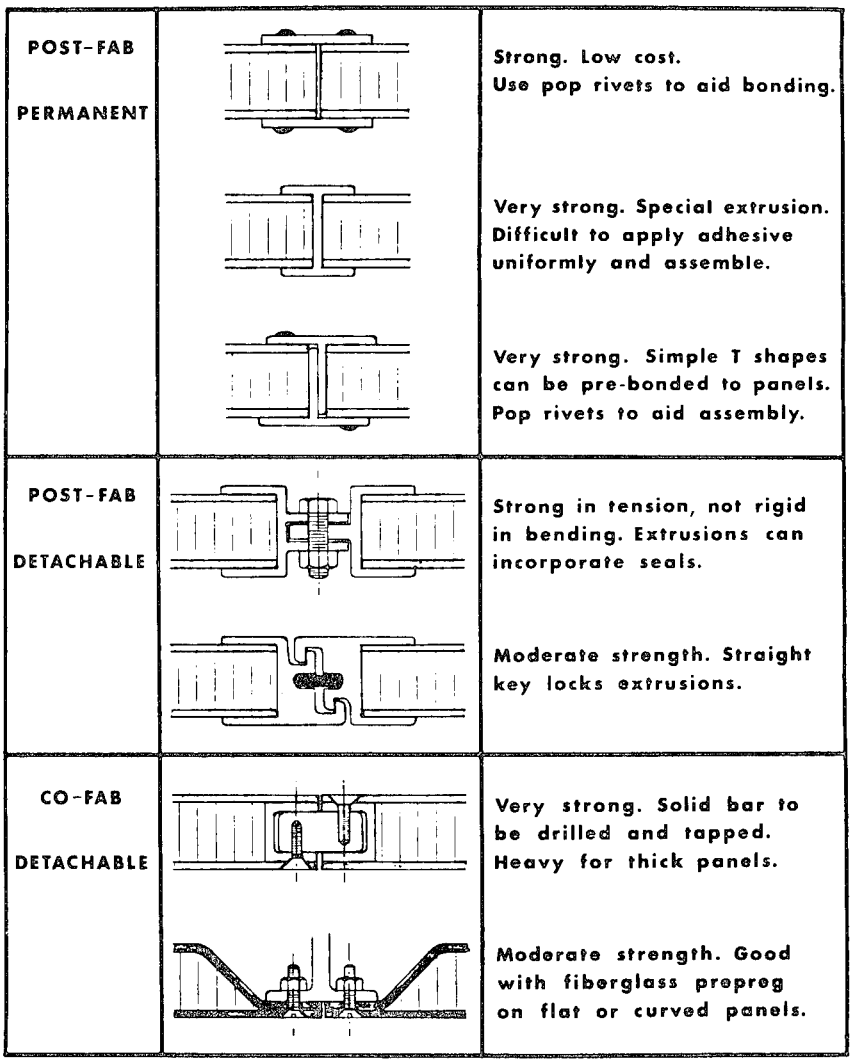


Figure 6. Straight joint designs.

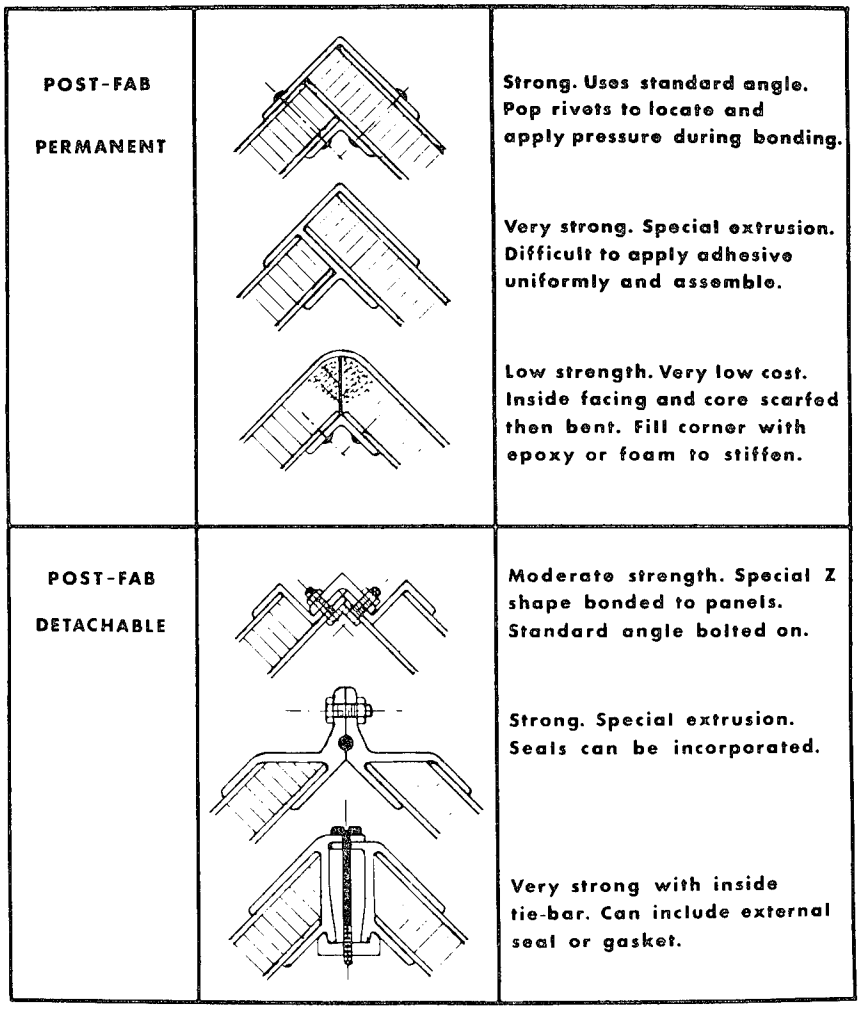


Figure 7. Corner joint designs.

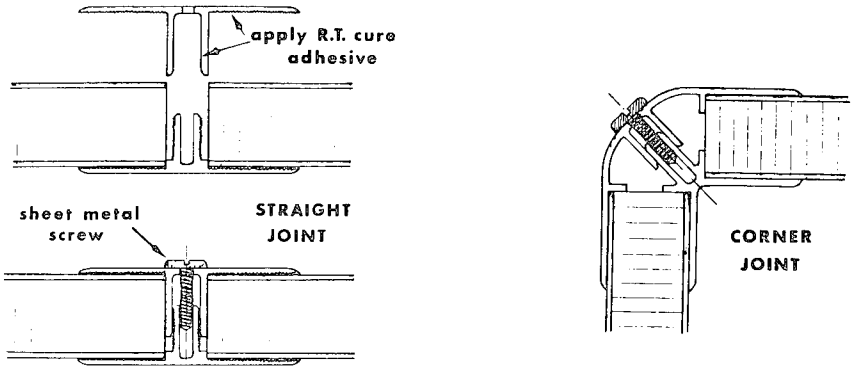
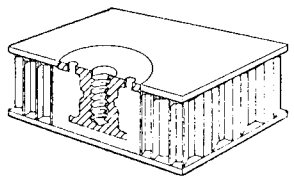


Figure 8. Special two-part extrusions for sandwich joints.

is slipped into the slot. Pressure is applied with sheet-metal screws every 12–16 inches. The added benefit of this system is that the adhesive is not smeared away and close tolerances on slot width are not needed. This two-piece joint is also used for corners at 90° and 120°.

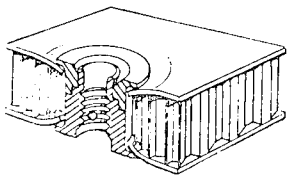
Partitions, shelves, containers, and many other applications require a means of attaching brackets or other subassemblies directly to the honeycomb panel. A wide variety of fasteners have already been designed and are commercially available for installation into sandwich panels. These post-fab inserts can go through the panel or are recessed part way; they can be crimped to the facings or potted in place with epoxy; some are threaded, some have floating nuts for easy alignment. Figure 9 shows some examples. This is one area where a few companies have a lot of expertise, and it would be well advised to contact these fastener manufacturers with your design requirements.

Panels which have concentrated loading conditions away from an edge or close-out may need provisions to take high compressive forces. This can be accomplished by incorporating higher density honeycomb or other core materials using specially shaped extrusions or castings, or densifying the honeycomb with foams or resin. Figure 10 again provides some examples. You'll note that in these situations, the majority need to be co-fab or included during the sandwich bonding. In many cases, this may not be a problem, if the proper tooling and fixtures are used to locate these points. However, if the area cannot be located in advance, or if a flat panel is cut from a larger sandwich section, it may be necessary to drill or remove part of one facing to be able to densify the area. In such cases, it is best to consider an epoxy-type filler. This way the core can be stiffened and at the same time the hole(s) can be covered with a doubler, the attachment fixture, or simply more epoxy resin.



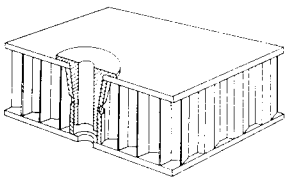
Molded-in

Molded-in fasteners will provide the best structural strength since the adhesive bonds the fastener to both facings and core. They add more weight to the panel (approx. 6 grams) and are more time consuming to install.



Mechanical Grommet

Grommet type fasteners consist of a plug and sleeve which are installed from opposite sides of the panel. They may be force fitted or mechanically locked to one or both facings. They are not as strong at the molded-in type. Typical weights per fastener is approx. 2 grams.



Mechanical Sleeve

Sleeve type fasteners consist of two parts, both of which are installed from one side of the panel. They lock mechanically to the top facing only. Hence, this type will not carry high loads in shear or torque. Tension loads should be applied primarily in one direction. Weight is about 1.5 grams.

Figure 9. Typical sandwich panel fasteners.

Particularly in these areas of post-fab design, one has to be careful to keep the number of steps and operations to a minimum. Drilling, cutting, carving, and a lot of fitting and hand work can skyrocket the part price. Buttering on some adhesive or potting compound may sound like a simple, low-cost method, but for reasonable volume quantities, a simple extrusion or casting can often reduce the installation cost. All of these factors point out the importance of a close liaison between designers and production people, and this should not be a one-way street either. Many times tool designers and production personnel can do a better job or suggest improvements or alternatives if they know why that particular design was chosen and how the part is used. In either case, the object is to consider ways of producing an acceptable part at the lowest cost.

What about the price of honeycomb and sandwich panels? They are not the run-of-the-mill type of item you buy in a hardware store. Be-

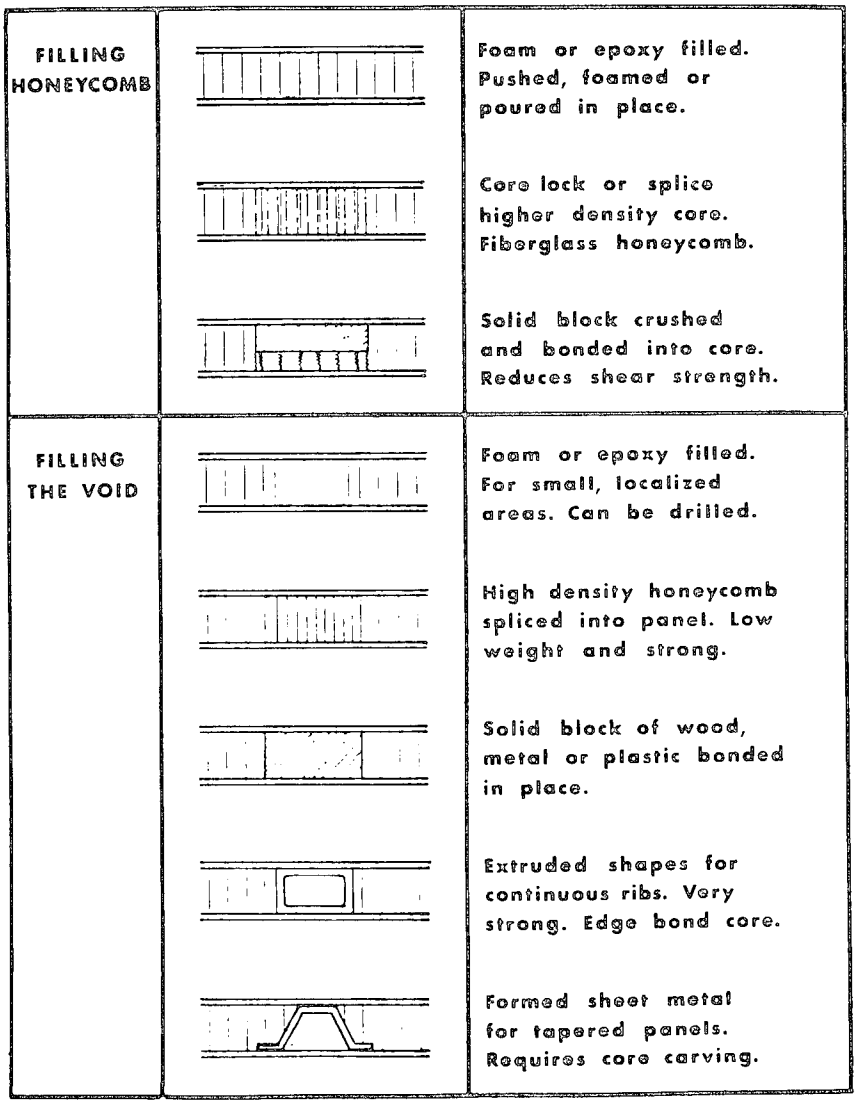


Figure 10. Panel reinforcements for concentrated loads.

cause of the infinite combinations of materials, shapes, and sizes, it is difficult to put a price tag on it. Certainly a sheet of plywood (despite its price increases in the last few years) is cheaper than a honeycomb panel of the same thickneess, and if plywood does everything you want it to do — fine! However, gross estimated sales of $30,000,000 in honeycomb alone for the United States in 1974 would not justify a statement that the honeycomb sandwich concept is too expensive. This kind of volume is probably due to the many successful designs which made use of the advantages this approach offers.

SESSION V

STRESS ANALYSIS

MODERATOR: E. M. LENOE
Army Materials and Mechanics Research Center

15. THERMOMECHANICAL ANALYSIS OF WELDED JOINTS AND STRUCTURES

H. D. HIBBITT
Marc Analysis Research Corporation
Providence, Rhode Island

The prediction of residual stress and distortion in a welded structure is a problem of great interest, both as a complex problem in structural mechanics and because of its practical impact. This paper summarizes work done to date on the development and application of numerical analysis via the finite-element method in this area. The analysis consists of separate heat-transfer and stress-history predictions, the former providing the input description for the latter. Both phases are dominated by severe nonlinearities. Radiation and phase-change effects must be modeled adequately for the heat transfer, and elastic–plastic creep models must be incorporated into the stress analysis. Application to sample welding problems indicates that it is currently possible to obtain quantitative predictions of temperature and stress/deformation history throughout the weld process, and hence the residual state following welding. Probably the most fruitful area of application of the models in the near future is the examination of the criticality of various weld and material parameters through sensitivity studies.

INTRODUCTION

The welding process is one of the most widely used structural fabrication techniques, and has therefore received much study as a mechanical process. The objective of such work is the identification of problems associated with welding, and among these the residual stresses and distortions resulting from the extreme thermal conditions during welding are some of the most important subjects. The residual state of stress has a strong influence on the strength and life of the resulting structure, and welds are usually the critical determinants of the overall structural integrity. The greater part of the information currently available in this area results from experimental work. Both experimentally and analytically,

the problem poses severe difficulties, and in spite of the extent of the experimental effort, there have been few direct studies of the residual stresses in a weld. Analytically most of the available work is one-dimensional, and uses a line solution for the thermal analysis. A survey of this work was prepared in 1970 by Masubuchi.[1]

The point of view of the work summarized in this chapter is to approach the problem of analytic prediction of weld effects from a completely numerical standpoint. The problem is seen as one too complex to admit sufficient simplification to allow a nonnumerical approach. Thus, the objective of the work is to build as complete a numerical model as possible, allowing as much generality as may be needed in all aspects of the analysis — the geometric modeling, thermal boundary conditions, and both thermal and mechanical material response. The basic model then provides a very general predictive capability. In particular cases simplifications can be incorporated to economic advantage, such as the use of generalized plane strain or axi-symmetric modeling where appropriate. More significantly, the models are readily extended to include new data, such as improved material characterization at high temperature. The brunt of this work is thus the identification of the dominant physical phenomena which govern the welding process, the development of adequate numerical models for these effects, and finally the synthesis of the complete weld model. The only inputs required for such a model are the constitutive definition of the material, the geometric configuration and the fundamental welding parameters (type of weld apparatus, weld speed and energy and material input rates, pre- and post-weld treatments and thermal boundary conditions). The model is then capable of predicting the temperature and subsequently the stress and distortion throughout the joint (including the detailed distribution in the weld filler itself) and throughout the time history of the weld.

Such a model as described in the paragraph above was first developed and applied by Hibbitt and Marcal.[2,3] Comparison with available experimental work was made, with gross quantitative agreement. The same model was used by Nickell and Hibbitt,[4] who compared temperature results (including the prediction of fusion zone) with a well-instrumented experiment on a complex geometry (an omega seal) with good accuracy. A similar model has been developed by Friedman,[5] who studied butt welds without experimental comparison. Buyukozturk and Hibbitt[6] applied the technique to a large, multipass butt weld, again without experimental comparison. In all these cases the authors reported that their main difficulty and source of possible error was the lack of basic material and parametric data. In fact, these models have the ability to assess the criticality of the various parameters through sensitivity studies, and so it is possible to direct the experimental effort into the most rewarding areas of study.

TECHNICAL APPROACH

The numerical models are based on the finite-element method, which by now is a well-established technique for modeling continua and structures.[7,8] There has been considerable application of the method to nonlinear problems, so that the welding problem may be viewed (with the assumptions described below) as a rather complex application of the method. The finite-element method allows complicated geometric modeling, since the structure is discretized into individual elements which may take various shapes. In the work done to date on welding problems, straight- and curved-sided quadrilateral elements have been used, allowing good detail in geometric modeling.

The most fundamental assumption incorporated in the analysis is the uncoupling of the thermal and mechanical analysis phases. It is readily shown, by order-of-magnitude arguments, that the energy equation during welding is dominated by thermal fluxes, and that strain energy and plastic dissipation do not contribute significantly to the balance.[2,9] Thus, the thermal analysis may be performed first, defining the temperature field throughout the history of the weld. Then the stress analysis is based on this temperature history. In the following, the governing assumptions and methods of these two parts of the analysis are discussed.

THERMAL ANALYSIS

The thermal problem associated with welding requires consideration of three mechanisms:

1. Heat input to the joint.
2. Heat transfer and storage mechanisms in the material itself.
3. Boundary heat transfer from the structure to its surroundings.

The mechanisms involved in (1) are extremely complex, and the physics of the weld arc are not fully understood. The common assumption,[10] adopted in the work described here, is that the heat of the arc may be related to electrical input:

$$Q = \varepsilon V I \tag{1}$$

where

Q is the net heat flux into the weld
ε is the "efficiency" parameter
V is the electrical input voltage

and

I is the electrical input current

Typically values of 70–90% are used for ε. The distribution of flux on the facing surface is assumed to be normal and radially symmetric. That is,

$$q = q_0 e^{-cr^2} \tag{2}$$

where q_0 and c are chosen based on the radius of the welding electrode.

In most welds it is readily shown that the arc speed (*i.e.*, deposition speed) is large compared to heat transfer rates, so that the heat transfer parallel to the line of motion of the electrode may be neglected. That is, the temperature history of any section normal to the line of motion of the weld head is the same as that of any other such section, except for a shift in time. This is an important consideration, since it allows a reduction from a three-dimensional to a two-dimensional (either plane or axisymmetric) thermal analysis. In this case equation (2) gives

$$q\,(s,t) = q_0 e^{-cs^2} e^{-cv^2(t-t_0)^2} \tag{3}$$

where

- s measures distance, on the surface, from the centerline of the weld electrode,
- v is the electrode velocity (normal to the plane of the analysis model), and
- t_0 is the time of peak heating for this section, chosen so that the analysis begins before any significant heating of this section can occur.

The unknown parameters in equation (3) are q_0 and c. The latter is assessed by comparison of the normal distribution with the electrode size, and the former is related, through the integral of equation (3), to the "efficiency" parameter. The most effective method of obtaining these two parameters is from a well-instrumented test, as was done in Reference 4.

The mechanism which carries the heat applied to the surfaces described above, into the bulk material of the filler and base material adjacent to the joint is that of conductive heat transfer. The Fourier law

$$q_i = -k_{ij} T_{,j} \tag{4}$$

governs this mechanism, where $k_{ij}(T)$ is the conductivity.

In addition, specific and latent heat effects must be included, since the problem is a transient one, with melting and resolidification occurring in the material. Since both the specific heat (rate of energy release with respect to decrease in temperature) and the conductivity [defined in equation (4)] are known to vary with temperature, it is necessary to have their values available for the complete temperature range of the analysis.

Usually the investigators must resort to extrapolation of known data, since high temperature values are difficult to measure experimentally.

The latent heat of solidification has been treated in some detail by several of the investigators,[2,11] although it is not clear whether a detailed and accurate evaluation of this effect is of first-order importance to the analysis. Most welds are made in alloy materials, where latent heat is released over a range of temperature, and the energy release rate per temperature may not be grossly different within this range than outside it. In fact the finite-element method as conventionally applied to heat-transfer problems is not well suited to latent heat calculations. The reason for this is that the method is based on the assumption of a local solution:

$$T = \phi^N(X)\, t^{-N} \tag{5}$$

which is assumed C^1 continuous on the interior of the elements. When phase change takes place at a unique temperature (as in a pure phase) the latent heat requires a discontinuity in the temperature gradients. Such discontinuities are only admitted at the element interfaces, so that it is not realistic to resolve the fusion front any finer than the element dimension. For alloys where the phase change occurs over a temperature range, the effect is smoothed and Friedman[11] shows a somewhat better resolution.

The third mechanism of importance in the heat transfer is the surface boundary conditions. Two heat-transfer mechanisms are usually considered here: radiation effects dominate at higher temperatures, but late in the cool-down history the primary mechanism is convection. The difficulty in the latter case is the large variation in convection coefficient depending on surface conditions and air flow. As in the case of defining the heat input, the analyst must use considerable judgment, or more realistically obtain values by comparison with well-instrumented tests.

The above three mechanisms define the heat-transfer model. The Galerkin finite-element method provides the geometric modeling, and the only other aspect of the analysis is a time-stepping procedure. All the work to date uses a central difference (Crank–Nicolson) or backward difference operator. The time step is usually held constant over some period of the solution. Time-step choice is based on solution accuracy, usually by repeating critical parts of the solution with shorter steps to demonstrate convergence. Numerical stability of the time-integration operator is rarely a consideration. Both of the above operators are unconditionally stable for the linear diffusion equation, and instabilities caused by the nonlinearities discussed above will not occur if accuracy is sought.

In any numerical model it is of great importance to assess solution accuracy. This is done in two ways — by comparison with known theoretical solutions, and by comparison with experiment. Comparison with known solutions can be misleading, since closed-form solutions tend to be over-simple compared to an actual problem. In Reference 2, Hibbitt compares one- and two-dimensional Stefan problems with other solutions, as well as the one-dimensional alloy cast problem of Weiner (Figures 1–3). Friedman[11] also shows results for the two-dimensional Stefan problem (Figures 4 and 5). These results all indicate the quality of results available for phase-change problems with the finite-element method. Friedman's solution in Figure 5 shows improvement over Hibbitt as a result of the introduction of an iterative technique. Such a technique should not be necessary for practical alloy melting problems, where high accuracy in the fusion-front prediction is not of great importance. The accuracy to be expected is well illustrated in Figures 2 and 3, since realistic material properties are used.

In Reference 4, Nickell and Hibbitt provide a comparison of thermal analysis predictions with experiment. The problem is shown in Figure 6 — an omega seal is completed by the insertion of a T-shaped ring, which is melted in place by heating from a weld torch passed above it. The experiment was well instrumented with thermocouples, and in addition the structure was sectioned and etched subsequent to welding to show the extent of fusion. Typical comparisons are illustrated in Figure 7 and Figures 8 and 9. In Figure 7 the predicted temperature history at a particular location is compared to the experimentally measured history. There is excellent agreement in peak temperature values, and good accuracy is maintained throughout the history, although the predicted cooling rate is underestimated at low temperatures, indicating that the surface convection was underestimated for the analysis. Remarkably good agreement was also shown between the experimentally measured fusion zone (Figure 8) and the predicted fusion zone (Figure 9). This analysis provides strong evidence for the conclusion that the heat-transfer techniques and assumptions provide an accurate model for that phase of the weld analysis.

STRESS AND DISTORTION ANALYSIS

The stress analysis also utilizes a finite-element geometric model and piecewise linear time stepping. The input for this phase of the analysis is the temperature history defined throughout the joint region by the previous thermal analysis.

In most cases the geometric model must be modified for the stress analysis. This is because the thermal analysis is a very local solution.

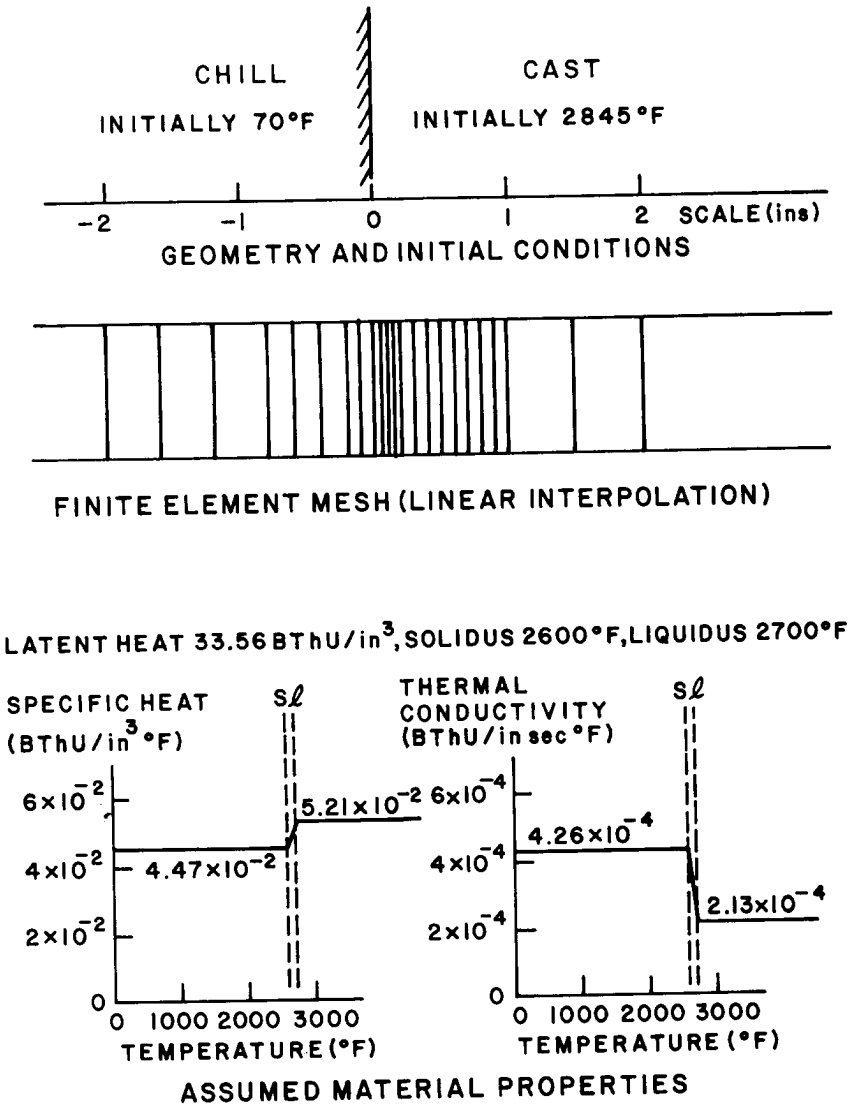


Figure 1. Weiner problem (one-dimensional steel solidification).

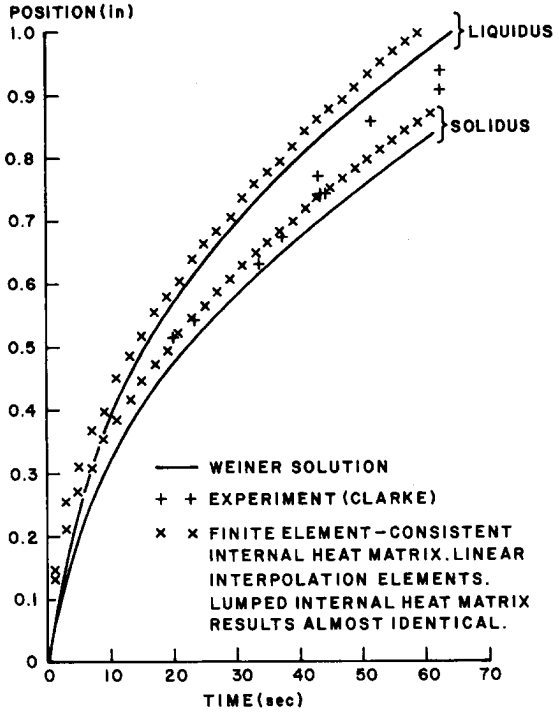


Figure 2. One-dimensional steel solidification problem (Weiner problem).

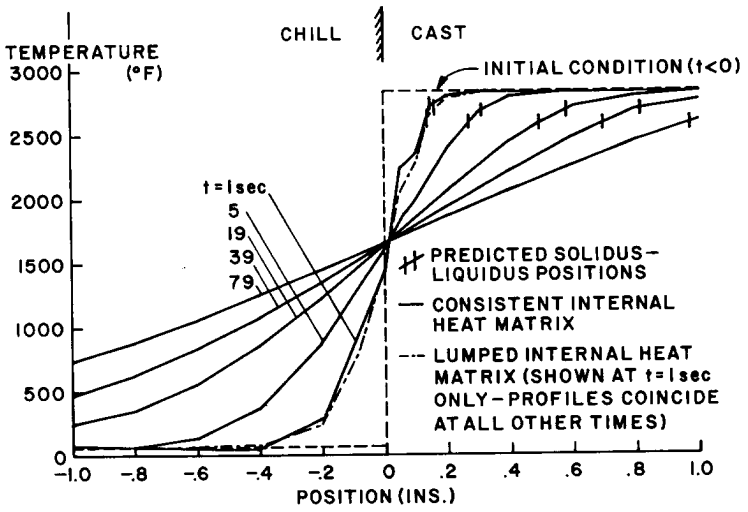


Figure 3. Weiner problem. Finite element predictions of temperature profiles.

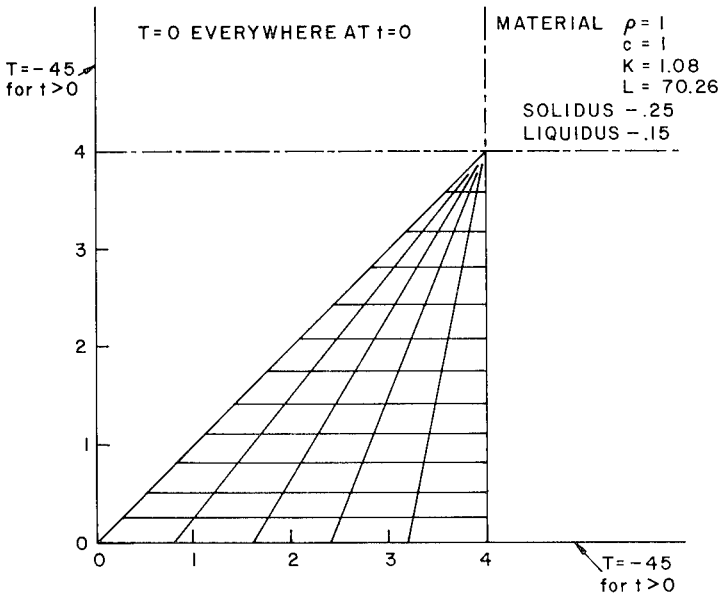


Figure 4. Finite element mesh for 2-D fusion problem.

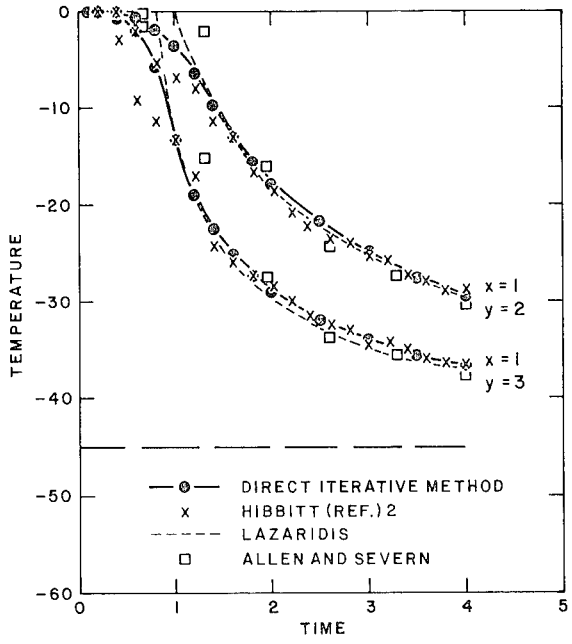


Figure 5. Square plate fusion-temperature vs time predictions.

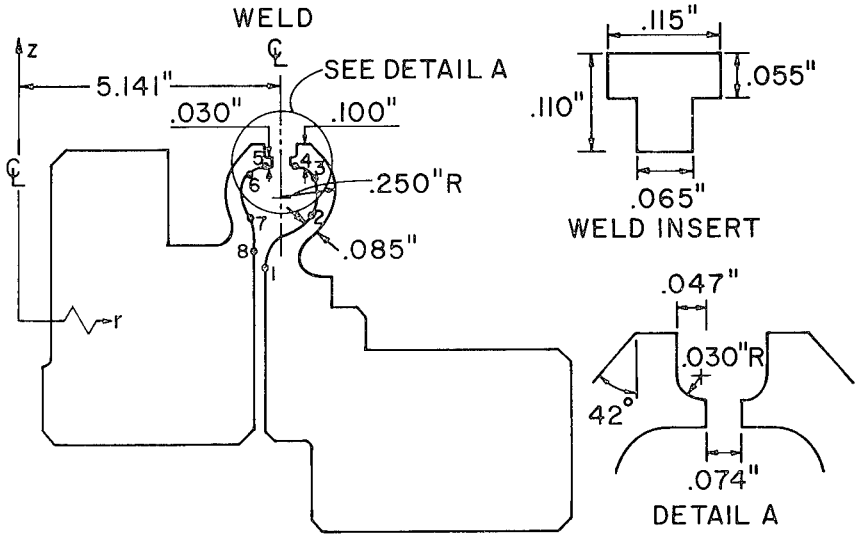


Figure 6. Omega seal geometry and thermocouple placement.

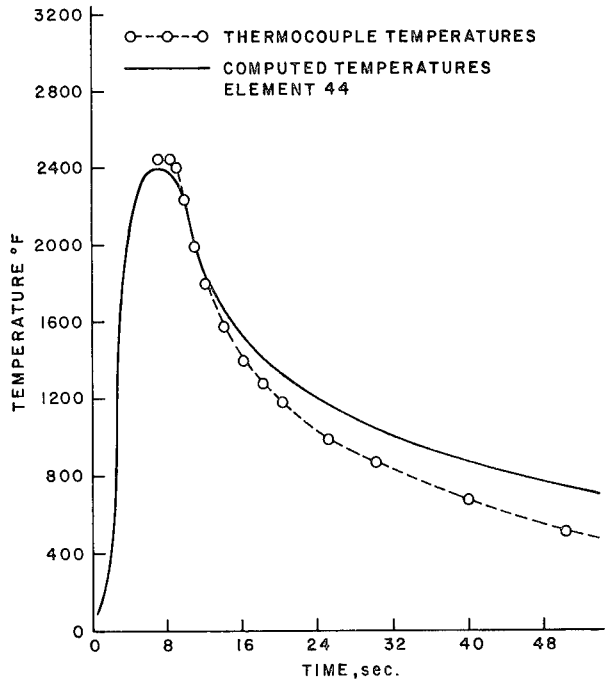


Figure 7. Thermocouple comparison, heat-affected zones.

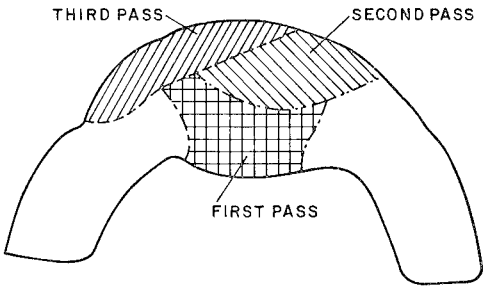


Figure 8. Observed melt regions (from photograph) omega seal.

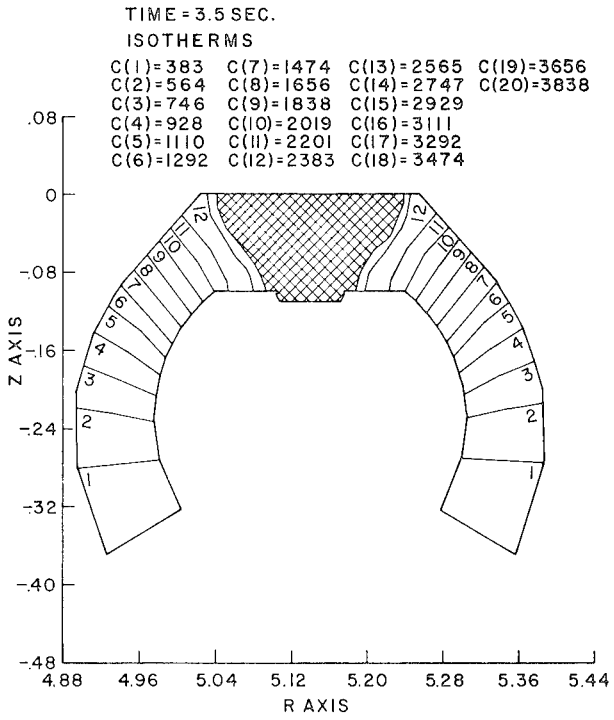


Figure 9. Predicted melt region, first pass, omega seal.

Extreme temperature gradients are present over a very small area around the fillet, and cool-down occurs quite rapidly compared to characteristic diffusion times. In order to predict residual stress and distortion accurately, it is important to model the flexibility of the rest of the structure, since the constraint provided by this structure outside the region in the immediate neighborhood of the joint plays a significant part in the growth of residual stress. Thus in Reference 6 the authors use a fine, local mesh for thermal analysis of a butt joint in a thick pressure vessel, but they model the whole vessel for stress and distortion studies. Spatial interpolation of the thermal analysis results onto the stress analysis mesh is therefore frequently necessary.

The residual stresses result from inelastic response of the material to the extremely severe thermal history of the joint. Constitutive characterization of the material is difficult since all temperatures from room temperature to well above the melting point are present. In addition, both spatial and temporal temperature gradients are extreme. In all the work to date the assumption is made that the material may be treated as a time-independent elastic–plastic material during welding, with temperature-dependent yield and elastic moduli. This characterization was justified in Reference 2 by the argument that welding times are short (of the order of several seconds at high temperature) so that any time-dependent behavior is restricted to sharp primary creep effects of extremely short characteristic times, which cannot be distinguished easily from yield in a material characterization experiment. Thus, it is likely that measured yield values correspond aproximately to the behavior under weld conditions, because of the similarity in time scales. This argument is difficult to support by experiment, because of the lack of materials data at the extreme temperatures involved. However, it seems reasonable to say that at temperatures where the measured yield stress is small (say less than 1/10 of the room-temperature yield) any constitutive model would predict large strains but little stress and material damage. At lower temperatures where the yield strength is significant (say above 1/2 of the room-temperature yield) it is possible to conduct creep experiments and isolate the time-dependent and time-independent behavior, and hence demonstrate experimentally that the times involved in the welding process itself are indeed too short for significant creep effects to occur. From the above discussion it would therefore appear that the use of time-dependent elastic–plastic analysis is a reasonable mechanical model.

An interesting aspect of the weld process is the presence of sharp temporal temperature gradients. The material cools so rapidly that it is clear that unstable material phases must be present, so that the material properties in regions where this happens must be quite different from

those of the bulk material. This point has never received attention in the welding analyses that have been performed, except in Reference 6, where the authors use a different material characterization in the heat-affected zone, based on post-weld surface-hardness measurements.

The use of the finite-element method for nonisothermal elastic–plastic analysis is by now a routine procedure, and the weld problem is merely a rather severe example of such an analysis. All of the authors cited use tangent modulus methods, whereby the system stiffness matrix is reformed at each step in order to account for active plastic loading, or elastic unloading from such a state. The formulation uses a piecewise linear approximation for the classical equations of plasticity,[2] and some scheme is always used to process the thermal analysis results to ensure sufficiently small steps in the stress analysis to satisfy this linearization requirement. This is akin to choosing the step size in the thermal problem to ensure accurate accounting for the nonlinear phenomena occurring there. In the case of the stress problem, time steps are subdivided or merged as dictated by the incremental strains generated. Advantage is taken of the time-independence of the constitutive theory.

The stress history during thermal gradient loading, such as occurs in welding, is quite complex, as is illustrated in Figures 10 and 11. These show the residual stress and the stress history in a plate of large dimensions relative to its thickness, cooling from a high temperature by con-

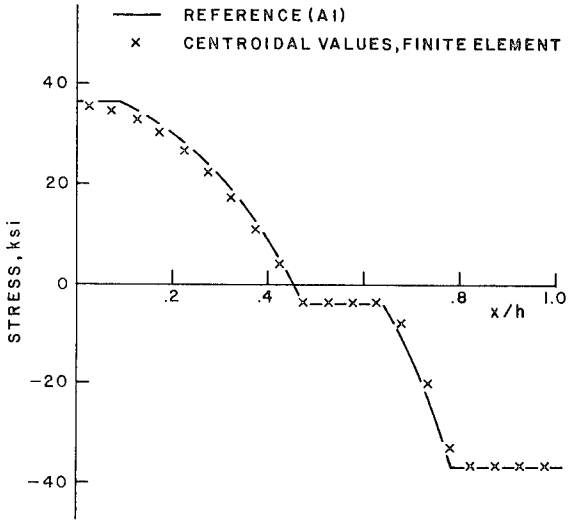


Figure 10. Residual stress in cooled plate.

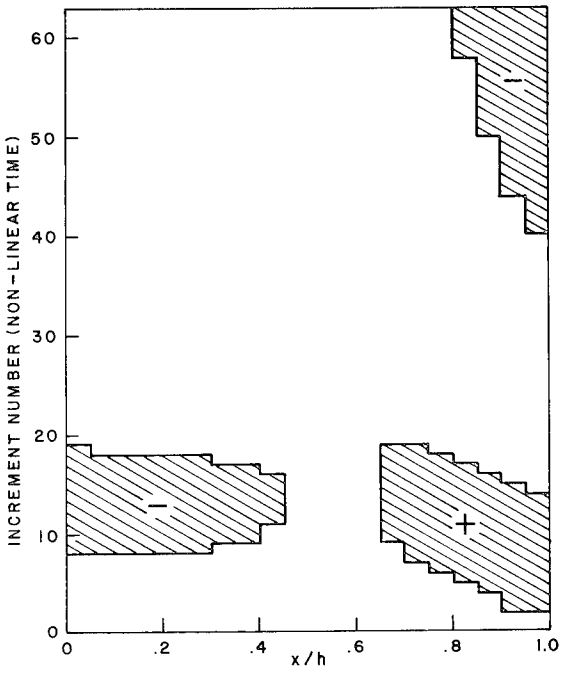


Figure 11. Cooled plate: development of yielding zones. (Sing of stress indicated by + and −).

stant convection. Time-independent elastic–plastic behavior with a temperature dependent yield stress is the material model. It is of significance to note that in Figure 11 there is active plasticity followed by unloading and again plasticity at the opposite side of the yield surface at most points through the thickness of the plate. This problem demonstrates admirably the complexity of the stress history during a rather simple thermal history, and indicates the order of difficulty which may be expected (and of course occurs) in a weld analysis.

STRESS RESULTS

The complexity anticipated above is well illustrated in the case of butt weld in Figures 12–14, taken from Friedman.[5] Figure 12 shows the geometry of a single-pass butt weld. The profile of accumulated plastic strain is shown in Figure 13. The stress histories at various positions are shown in Figure 14. These figures show the stress reversals so commonly seen in a weld analysis, and the characteristic peak plastic strains at

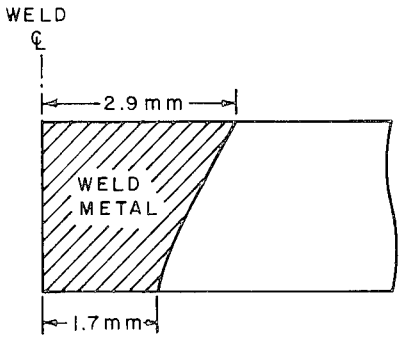


Figure 12. Weld metal zone.

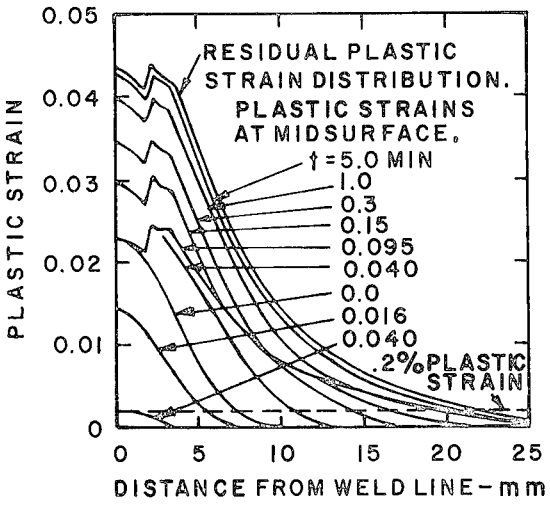


Figure 13. Transient and residual generalized plastic strain distributions.

the fillet–base metal interface, approaching 5%. Another analysis response is shown in Figures 15–20, where the experiment of Corrigan[12] was analyzed. Figure 15 shows the weld geometry. A fillet is added into a V-notch on a thick disc. Figures 16 and 17 show residual hoop and radial stress profiles. The experimental comparison is difficult, since the experiments used the Sachs boring technique, assuming conditions of plane stress. Stress contours are shown in Figures 18–20 which clearly indicate the lack of validity of the experimental measurement assump-

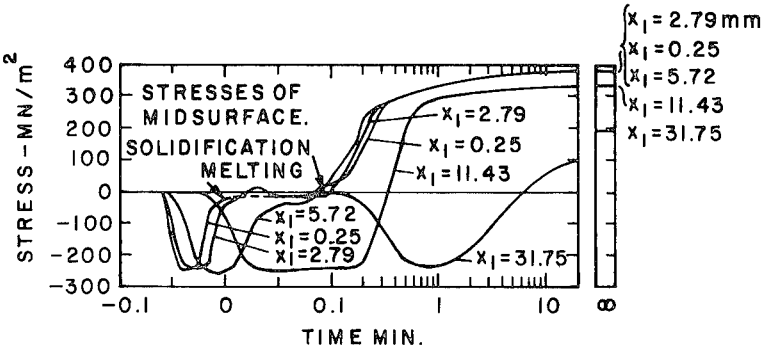


Figure 14. Longitudinal stress histories at various distances from the weld centerline.

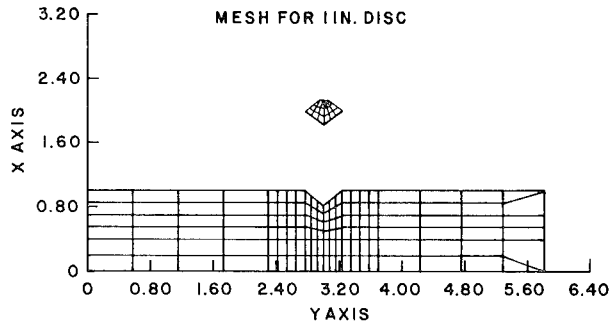


Figure 15. Mesh for 1″ disc.

tion. It is interesting to note the state of high hydrostatic tension at the root of the weld fillet. Such an observation was also made in Reference 6, where the authors reported residual hydrostatic stresses three times yield in the weld fillet. In this case a stress-relief analysis was also performed, based on classical stress-dependent creep theory. The interesting observation here is shown in Figures 21 and 22, where it is seen that the equivalent deviatoric stress is relieved rapidly during high-temperature stress relief, but the residual hoop stress (representative of the hydrostatic stress) is only reduced by 50%. In fact, although the peak deviatoric stress was reduced to 15% of its post-weld value by stress relief, the peak hydrostatic stress was only reduced to 65% of its post-weld value. This must be directly associated with the purely deviatoric character assumed for all the inelastic response (no dilatational creep is allowed), since hydrostatic stress can then only relieve itself through sec-

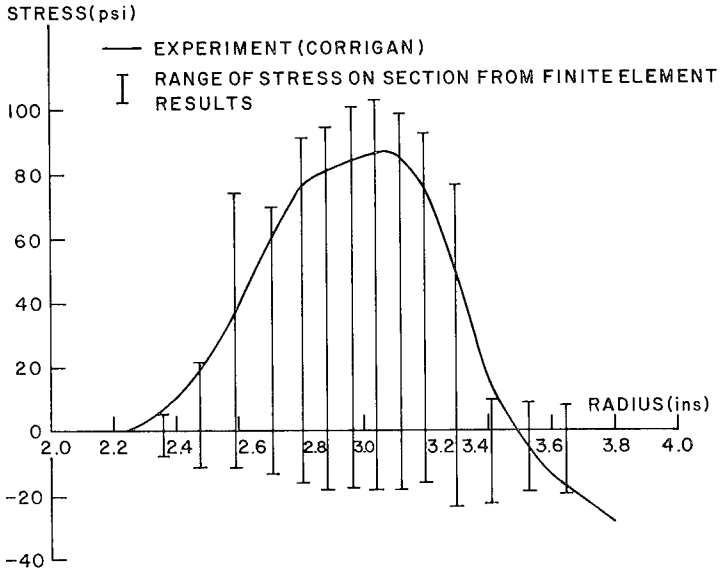


Figure 16. As welded tangential stress, HY80, 1″ disc.

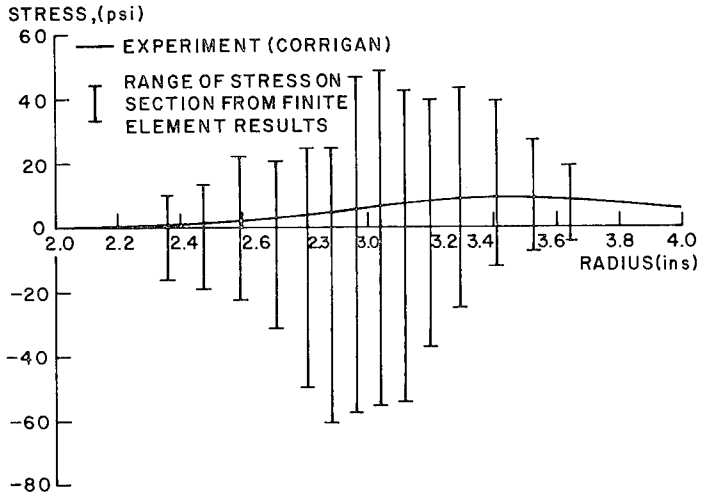


Figure 17. As welded radial stress, HY80, 1″ disc.

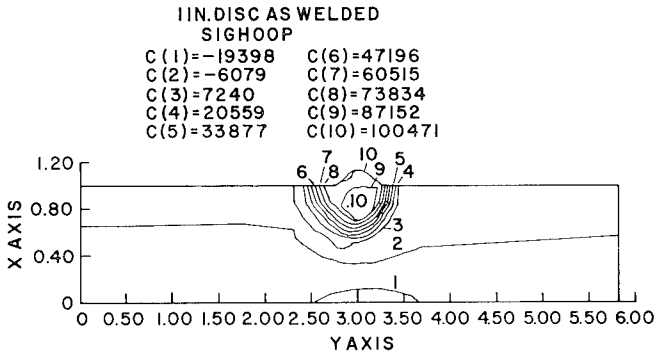


Figure 18. 1″ disc as welded SIGHOOP.

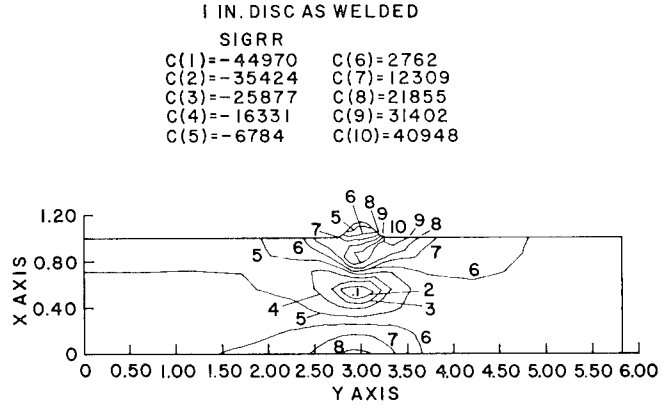


Figure 19. 1″ disc as welded SIGRR.

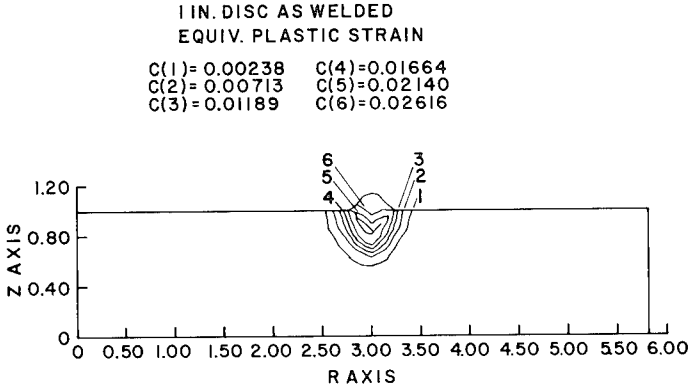


Figure 20. 1″ disc as welded equiv. plastic strain.

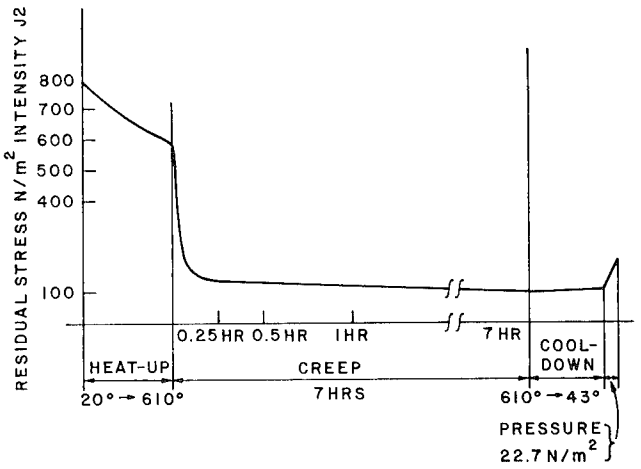


Figure 21. Equivalent stress variation during stress relief and subsequent hydrostatic testing.

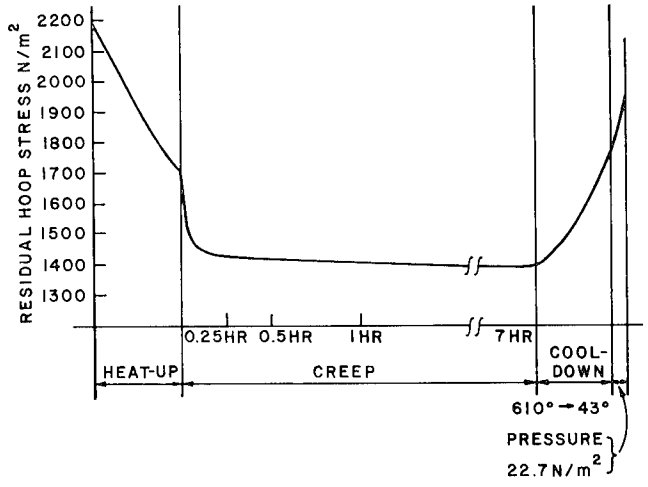


Figure 22. Hoop stress variation during stress relief and subsequent hydrostatic testing.

ondary (equilibrium) mechanisms. If this is indeed the case — that is, if the creep theory is at all accurate — this would suggest that current stress-relief practice, based on uniaxial relaxation date, does not provide the desired (and assumed) level of relief. This point deserves further study, since most steels would exhibit void-growth mechanisms at such levels of hydrostatic stress.

CONCLUSIONS AND RECOMMENDATIONS FOR FURTHER WORK

This chapter has discussed the numerical models and theories adopted for detailed weld analysis. In all the examples where experimental correlations were possible, quantitative comparison is good, and there is sufficient evidence to indicate that post-weld residual stresses and distortions may be adequately predicted by these techniques. Clearly, rather few comparisons have been made, and it would be desirable to have available more correlation studies. The necessary ingredient for such studies is carefully instrumented experimentation, which is extremely difficult because of the extreme temperatures involved.

One of the most interesting predictions of the numerical models is the high hydrostatic tension in the weld fillet in several cases. This hydrostatic stress is of significance in terms of fracture, and its slow decay under stress relief is disturbing. The applicability of the hydrostatically independent inelastic response theories used in these analyses should be examined for these stress levels. Additional constitutive refinement may be found from including temperature rate effects in the model, to allow for the nonequilibrium phase properties which result in regions of high cooling rate.

REFERENCES

1. Masubuchi, K., "Control of Distortion and Shrinkage in Welding," *Weld. Res. Counc. Bull.*, No. 149, April 1970.
2. Hibbitt, H. D., "A Numerical, Thermo-Mechanical Model for the Welding and Subsequent Loading of a Fabricated Structure," unpublished Ph. D. dissertation, Brown University, 1972.
3. Hibbitt, H. D. and Marcal, P. V., "A Numerical, Thermo-Mechanical Model for the Welding and Subsequent Loading of a Fabricated Structure," *Comput. Struct.*, **3** (1973), 1145–74.
4. Nickell, R. E. and Hibbitt, H. D., "Thermal and Mechanical Analysis of Welded Structures," *Nucl. Eng. Des.*, **32**, No. 1 (1975), 110–20.

5. Friedman, E., "Thermomechanical Analysis of the Welding Process Using the Finite Element Method," *Trans. ASME, Ser. J., J. Pressure Vessel Technol.*, **97** (1975), 206–13.
6. Buyukozturk, O. and Hibbitt, H. D., "Prediction of Residual Stresses and Distortion in Large Multi-Pass Welds," Marc Analysis Research Corporation, Providence, R. I., Report No. TR-75-3, June 1975.
7. Zienkiewicz, O. C., *The Finite Element Method in Engineering Science*. London and New York: McGraw-Hill Book Company (1971).
8. Oden, J. T., *Finite Elements of Nonlinear Continua*. New York: McGraw-Hill Book Company (1972).
9. Boley, B. A. and Weiner, J. H., *Theory of Thermal Stresses*. New York: John Wiley & Sons, Inc. (1960).
10. Pavelic, V., Tanbakuchi, R., Uyehara, O. A., and Myers, P. S., "Experimental and Computed Temperature Histories in Gas Tungsten-Arc Welding of Thin Plates," *Weld. J.*, **48** (1969), 295s–305s.
11. Friedman, E., "Direct Iteration Method for the Incorporation of Phase Change in Finite Element Heat Conduction Programs," Bettis Atomic Power Laboratory, Pittsburgh, Pa. U.S. Atomic Energy Commission Contract Report No. WAPD-TM-1133, March 1974.
12. Corrigan, D. A., "Thermo-Mechanical Effects in Fusion Welding of High Strength Steels," unpublished Ph. D. dissertation, Massachusetts Institute of Technology, 1966.

16. SURVEY OF MECHANICALLY FASTENED SPLICE-JOINT ANALYSES

I. U. OJALVO
Grumman Aerospace Corporation
Bethpage, New York

The critical need for detailed stress information in the design of mechanically fastened joints is discussed, and significant contributions in the field of bolted and riveted splice joints are reviewed. The types of structural analyses which have been performed are grouped into three general categories and their interrelationships are cited. These three categories are: (1) one-dimensional splice analyses, which are primarily aimed at determining the load carried by each mechanical fastener in single or multiple shear; (2) two-dimensional planar analyses, which seek to establish load-deflection characteristics and the detailed stress distributions in the material surrounding a fastener-loaded hole; and (3) three-dimensional analyses, which are used to establish through-the-thickness effects upon fastener and plate stresses as well as overall joint compliance.

The potentially important role of joint friction, both between pin and hole and the plate faying surfaces, is explored. Theoretical and experimental evidence is cited to guide further studies in this area. Recommendations are also made regarding the development of special purpose computer programs to accommodate nonlinear material behavior, three-dimensional effects and multiple hole configurations.

INTRODUCTION

It has been said that 95% of all reported metal structural failures are fatigue failures,[1] a large portion of which result from stress concentrations introduced at mechanically fastened joints. The failure rate at joints in composite structures is also significant, since the benefits of increased material allowables are generally offset by greater stress concentrations around fastener holes in fiber-reinforced laminates.[2] As will be shown, one of the major causes for such failures is that an accurate

splice analysis contains more important variables than one is likely to consider, and many of which are too difficult to include in all but the most complex analyses. Hence, the design of structural joints has required the use of extensive testing to verify accompanying incomplete analyses.

The purpose of this effort is to review the types of splice-joint analyses which have been performed and to discuss their interrelationships. In so doing we shall cite a number of important contributions in the field, identify the major problem areas, and make recommendation for future work.

PROBLEM STATEMENT AND ANALYSIS PROCEDURES

An accurate splice-joint analysis involves a determination of the load carried by each fastener, and the detailed stresses surrounding each fastener hole. For points in which plate bending exists, or when a splice-plate thickness approaches, or surpasses, the fastener diameter, three-dimensional considerations also become important.

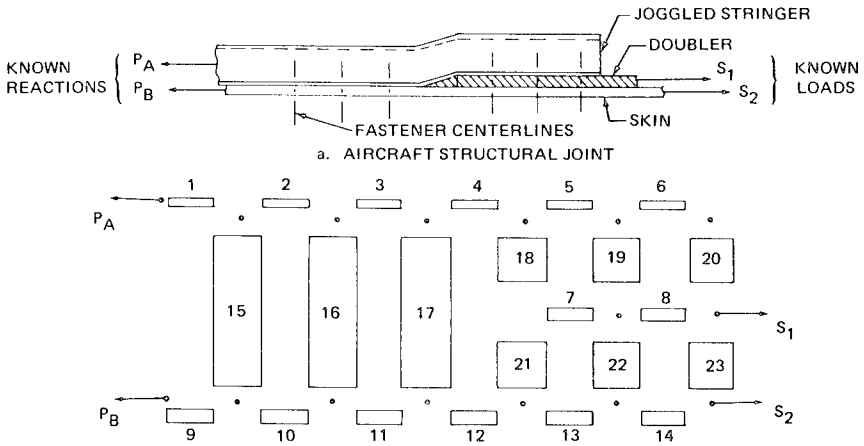
The usual procedure employed to attack the overall problem has been to segment it into three subproblems, as follows: (1) a one-dimensional analysis, which is used to determine the load carried by each fastener; (2) a two-dimensional planar analysis which is aimed at determining detailed stress distributions in the material; and (3) an analysis which seeks to evaluate the effects of certain factors upon stress variation through the plate thickness (*e.g.*, fastener bending and shear, the ratio of diameter to plate length, and head rotation). Interrelationships among these analysis types are discussed after reviewing the complexities, results, and solution potential within each category.

One-Dimensional Analyses

One-dimensional redundant structural analyses are commonly used to determine the load carried by each row of fasteners in a complex joint. The idealizations employed are based upon gross engineering assumptions (Figure 1) regarding the plate flexibility between successive fastener rows, the bolt flexibility due to shear and bending effects, and the local flexibility associated with the complex stress and deflection pattern in the immediate vicinity of the hole. Generally speaking, these analyses are based upon either the force or stiffness method of structural analysis. Until recently, when the situation was changed, material and geometric linearity was assumed. Such analyses relied rather heavily

upon empirical data obtained from load-deflection tests upon single fastener specimens.

An early version of the one-dimensional type of linear analysis was presented by Tate and Rosenfeld,[3] who refer to the combined fastener and local hole deformation as the "bolt constant." Switzky, Forray, and Newman[4] considered nonuniform thermal expansion effects and presented tables to assist in performing numerical calculations for joints with up to 10 similar rows of fasteners. McCombs, McQueen, and Perry[5] and Gehring and Maines[6] considered nonlinear load deflection characteristics of the structural elements by the finite element force method. A nonlinear finite-element analysis capability based upon the stiffness method was developed by Torczyner.[7] Gatewood and Gehring[8] extended the nonlinear type of analysis to include thermal as well as mechanical loadings. A elaborate program named JOSEF (JOint SEverity Factor), based upon work by Jarfall,[9] not only determines the load carried by each fastener, but is also concerned with converting the fastener loads to stress factors which predict fatigue life.



a. AIRCRAFT STRUCTURAL JOINT

b. STRUCTURAL IDEALIZATION OF JOINT

Figure 1. Typical structural joint and engineering idealization used to obtain load carried by each fastener.

Two-Dimensional Planar Analyses

By far the greatest number of papers and reports encountered in the field surveyed dealt with two-dimensional analyses of loaded plates with single holes. Among all these, two major plate-solution categories emerged: (1) the hole boundary loaded with a force resultant, and (2) the plate in uniaxial tension with no resultant hole force. Variations of these categories exist depending on whether the hole contains a fastener with clearance or interference, or fits neatly within the unloaded plate. The general problem encountered in realistic situations is a combination of these two (*i.e.*, a loaded hole with bypass loading, Figure 2). Unfortunately, its solution is not obtainable through a superposition of the previous two cases. This is caused by the fact that the stress state is usually nonlinear due to either material plasticity effects, or the development of a variable contact surface between hole and fastener.

Plates with Loaded Holes. Bickley[10] solved the problem of an infinite plate with a hole loaded with either a $\cos\theta$, or a uniform pressure distribution over half the hole, or a concentrated radial force. The next step towards solving a more realistic problem was taken by Knight,[11] who treated the finite-width plate. These studies were followed with experimental work performed by Frocht and Hill.[12] Their tests were performed on oversize strain-gaged aluminum specimens and small photoelastic models. They pinloaded the plate holes with varying amounts of clearance, thus simulating a true fastener loading more realistically. Theocaris[13] attempted to account analytically for pin effects also, through a solution of a finite-width-strip problem with a semicircular slit (Figure 3). This erroneously assumed a contact angle between pin and hole of 180° in addition to no slip friction and identical material properties for the pin and plate.

The work cited in References 10–13 was performed during the "precomputer" era and so was limited to techniques of classical elasticity. More recently the development of efficient computer programs permitted the numerical solution of complex fastener problems through iteration on the pin-hole contact angle. Using finite-element methods, Harris, Ojalvo, and Hooson[14] considered the nonlinear contact problem associated with a plate loaded by a clearance-fit rigid pin, as well as plasticity effects for loaded plates with open holes and for unloaded plates with interference-fit fasteners. They obtained elastic stress results for various consistent load levels and contact angles for different clearances (Figure 4). This work was followed by Oplinger and Gandhi,[15] who solved the problem of an initially neat-fitting rigid pin in an orthotropic material, using a least-squares boundary point-matching (collocation) approach.[16] This solution procedure was also used by Waszczak and Cruse,[2] except

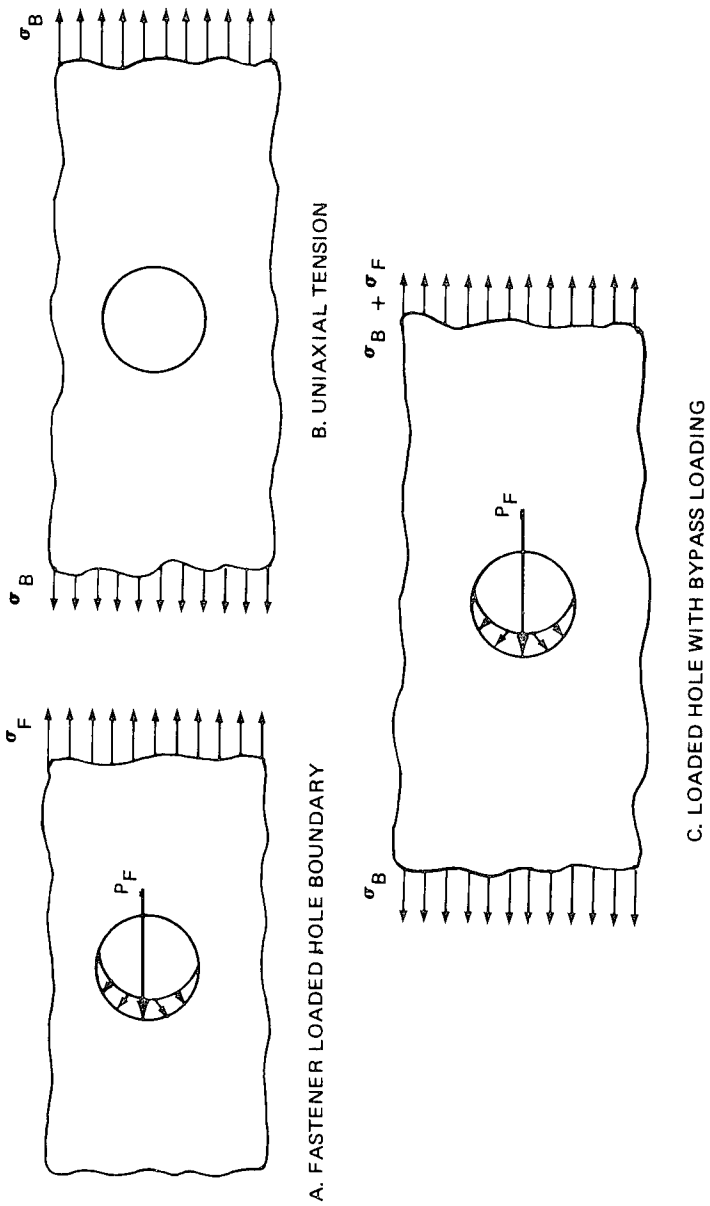


Figure 2. Two-dimensional idealizations of a loaded plate with a single hole.

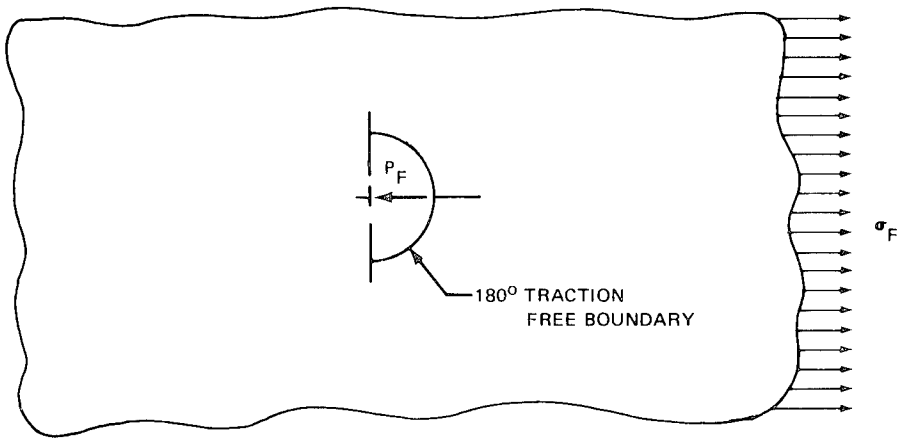


Figure 3. Structural idealization used to simulate pin loaded hole.[13]

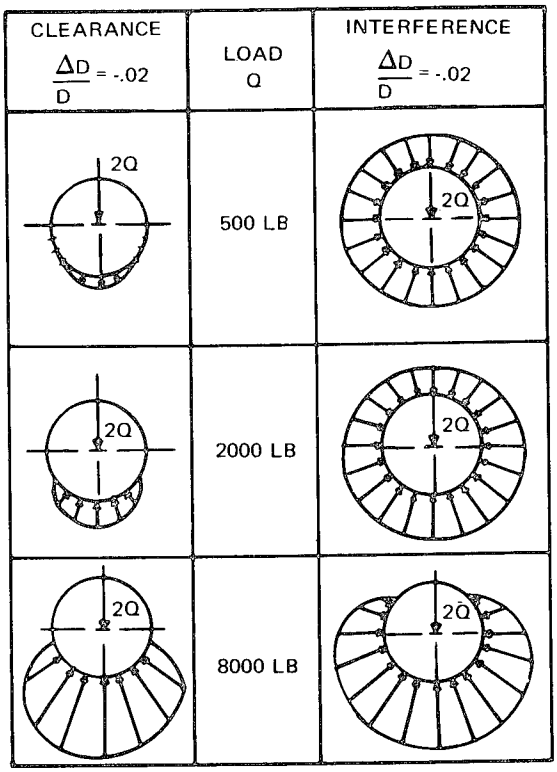


Figure 4. Load distribution around a fastener for a typical pin-loaded plate.[14]

that they replaced the pin with a cosine pressure distribution and termed the method BIE (Boundary Integral Equation).

In References 14, 15, 16 a smooth pin was assumed. However, Oplinger and Gandhi[17] followed their original work by considering two limiting cases with pin friction. These cases correspond to: (1) no-slip over the entire contact region, and (2) continuous slip over the entire contact region (where the boundary shear stress equals the product of the contact pressure and the coefficient of friction and opposes the relative motion between sliding surfaces). The true case consists of a combination of these two, *i.e.*, a region of no-slip and a region of slip.

Axially Loaded Plates with an Unloaded Hole, Open or Filled. The problem of a free boundary hole in a thin infinite plate, loaded in tension, was first solved by Kirsch[18] and extended to finite plates by Howland.[19] Some time later, Sternberg and Sadowsky[20] were able to extend Kirsch's work to include three-dimensional effects near the hole boundary.

Attempts at treating the interaction associated with a fastener-filled hole followed Goodier's solution[21] for the case where the stretched plate contains a circular elastic inclusion with perfect adhesion (*i.e.*, the pin and hole boundary are assumed in perfect no-slip contact over 360°. Crews[22] assumed an initial interference fit between fastener and hole and was able to determine the stress distribution in the plate and the applied load at which a gap would be initiated for the extreme conditions of a no-slip interface and a frictionless interface.

Stippes, Wilson and Krull[23] solved the contact stress problem of an unloaded frictionless elastic disk, with no initial interference, in an infinite stretched plate (Figure 5). They found that the contact angle is independent of the elastic properties as long as the pin and plate are of the same material. Results for the circumferential stress at the hole, when disk and plate have identical properties, are presented in Figure 6. This work was extended by Hussain and Pu,[24] who considered the effect of friction at the interface between the plate and an initially neat-fitting pin. Their solution yields three regions around the hole (Figure 7): a region of contact and no-slip, a second region of contact and slip, and a third region of no contact. Some typical results they generated for varying coefficient of friction (μ) reveals that for $\mu < 1$, the region of slip is much larger than that of no-slip (Figure 8), and that the presence of friction tends to lower the tangential stresses and increase the radial stresses around the hole (Figure 9).

Recently, the nonlinear material aspects of the stretched-plate-with-a-hole problem have been approached by the finite-element method. Harris, Ojalvo, and Hooson[14] treated tapered plates with loading which

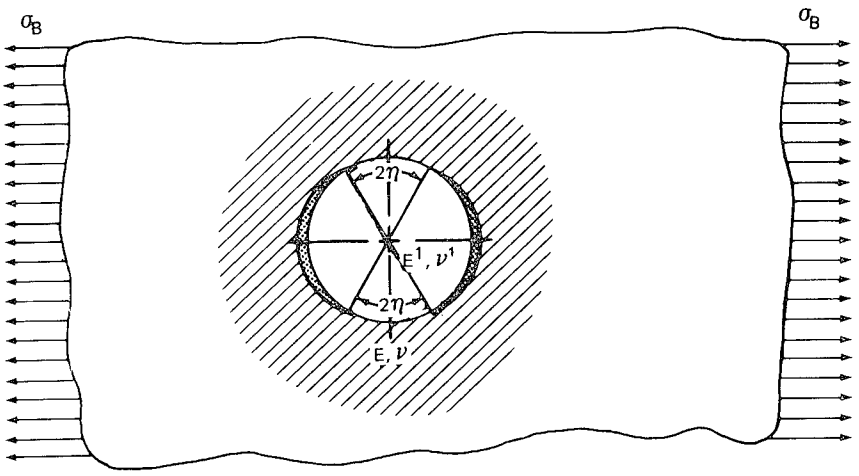


Figure 5. Contact stress problem of an initially neat fitting elastic pin in a stretched plate with no friction.[23]

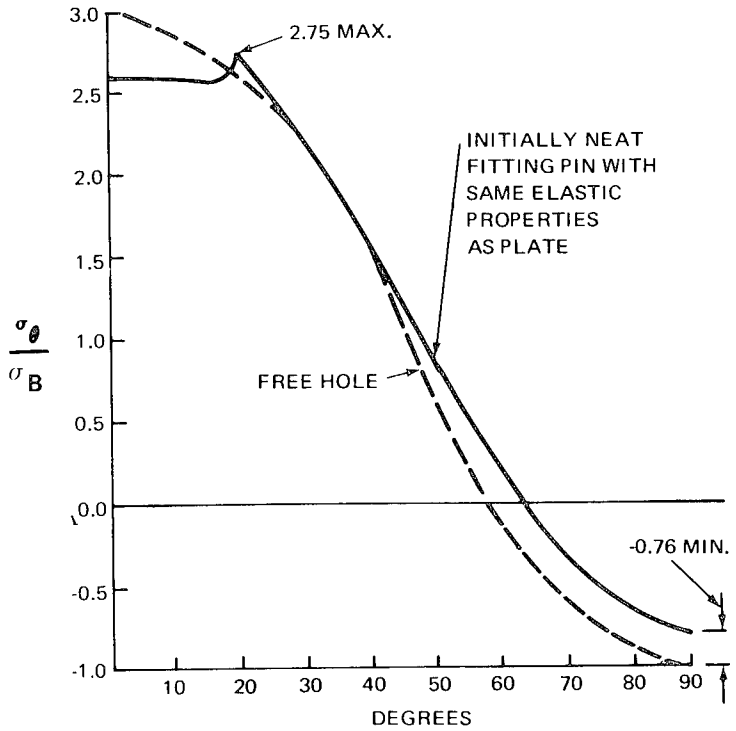


Figure 6. Circumferential plate stress, σ_θ around the hole boundary for a free hole and a stretched plate, σ_B with a frictionless pin.[22]

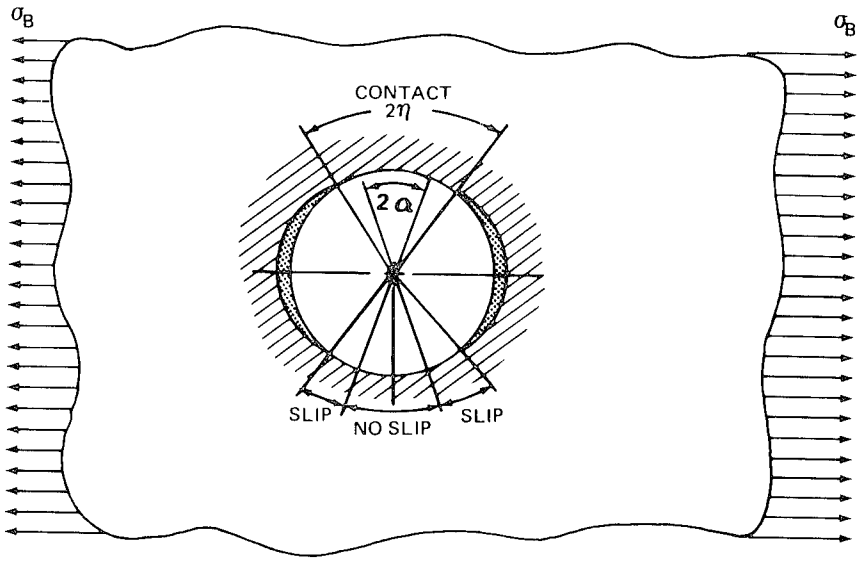


Figure 7. Contact stress problem of an initially neat fitting elastic pin with friction in a stretched plate.[24]

carried the material into the plastic regime. This was followed by Brombolich[25] who discussed a general finite-element program capable of considering an elastic–perfectly plastic material, load sequence effects (*i.e.*, the order in which the different types of loads are applied), and fastener interference or clearance (*i.e.*, the nonlinear contact problem). Allen and Ellis[26] considered a similar problem for a strain hardening material. However, they did not include the importance of load sequencing in problems with plasticity. This effect has been treated and shown to be important by Ghadiali, *et al.*[27] and Crews.[28] Adler and Dupree[29] have also developed an elasto-plastic finite-element program which they used to display the improved fatigue life of prestressed plate holes prior to assembly and loading.

Three-Dimensional Analyses

There does not appear to have been a serious attempt at attacking the precise three-dimensional equations for a fastener in a plate by either analytic or numerical methods. However, it would appear that the stiffness method, based upon modern three-dimensional finite elements, is capable of handling this situation.

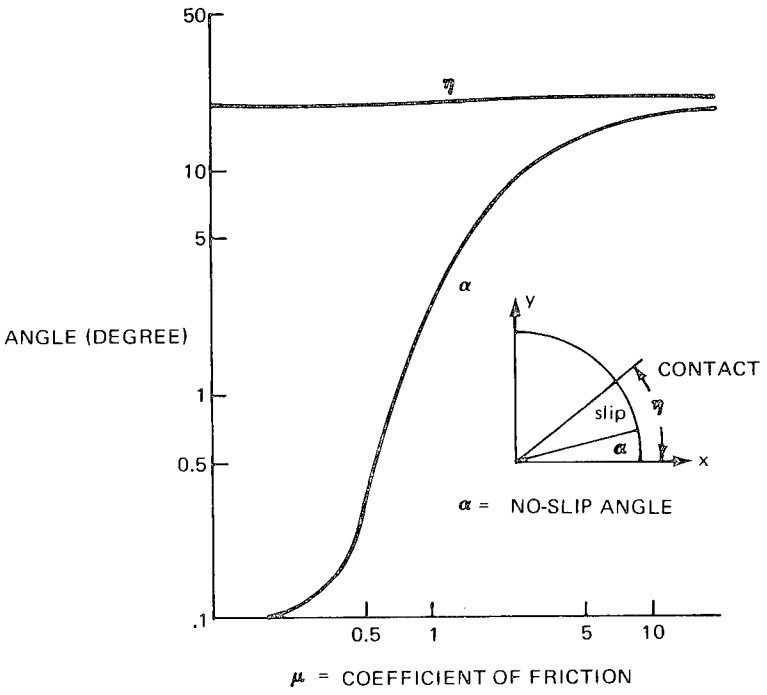


Figure 8. Variation of n as a function of coefficient of friction μ for the case that both inclusion and outer body have the same elastic constants.[24]

As an approximation to this problem, this author proposed a simplified approach[14,30] in which the fastener is idealized as a short beam on an elastic foundation (Figure 10) and the foundation modulus, k, is obtained from the planar analysis (Figure 11). Such a model is capable of accounting for fastener flexibility, head rotation, and countersink effects, as well as stress variation and nonuniform foundation modulus through the plate thickness (Figures 12 and 13). Although preliminary indications are that the idealization appears valid (Table 1), the implicit assumption of the method, *viz*: that the shear stresses through the plate thickness are of secondary importance, should be explored further.

Interrelationship of the Simplified Analyses

The interaction among the one-, two-, and three-dimensional types of analyses discussed is probably best described by Figure 14. Arbitrarily starting with a one-dimensional analysis of a joint, in which gross

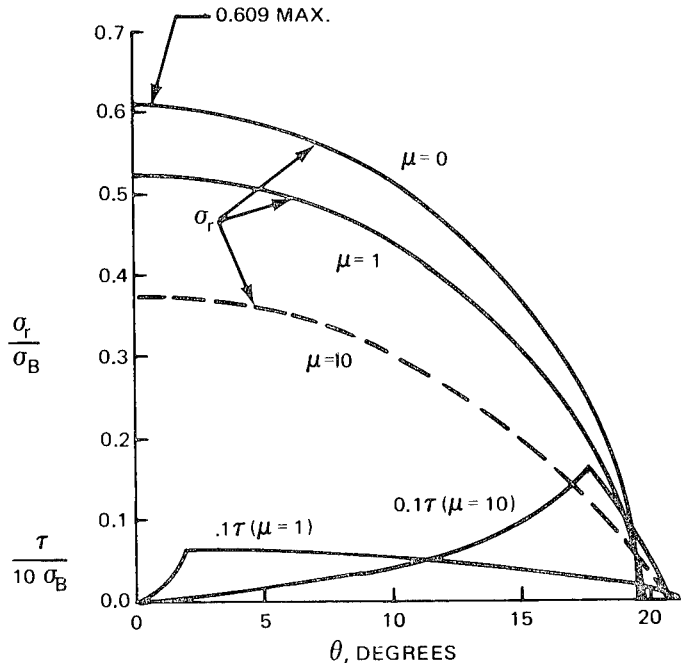


Figure 9. Compressive radial (σ_r) and tangential (τ) stresses for a 0, 1 and 10 coefficient of friction between pin and stretched plate of identical elastic constants.[23,24]

engineering assumptions regarding plate and fastener stiffnesses are made, the load carried by each fastener may be computed. These loads, in turn, may be used as input to perform a two-dimensional stress analysis and to obtain load-deflection data for a single fastener. This information may next be used to estimate through-the-thickness stress-concentration effects and to improve upon the single-fastener load-deflection ratios, employed initially, to permit a reanalysis via the one-dimensional analysis. This process may be repeated in an iterative manner until convergence is achieved. Alternately, one could start the process by using the two-dimensional and simplified three-dimensional solutions at each fastener to develop nonlinear load-deflection curves. A nonlinear one-dimensional analysis could then be used to determine bolt-load distribution in a multifastener joint using this nonlinear load-deflection data. With the resulting load distribution for each fastener, local peak stress could be calculated using the two-dimensional and simplified three-dimensional solutions.

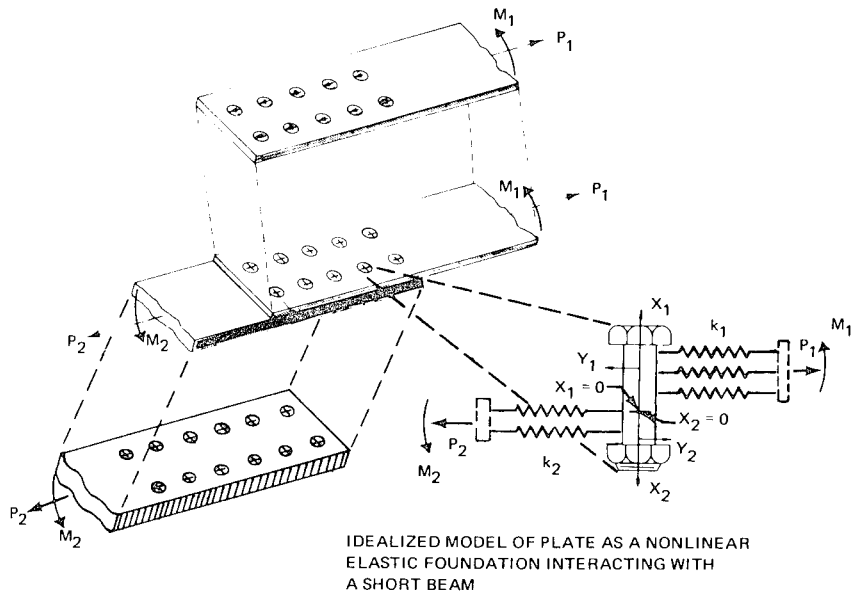


Figure 10. Short beam on elastic foundation modeling scheme for through-the-thickness effects.[30]

For the linear elastic case,[9] the plate stress-state surrounding a fastener is the nominal stress σ_0, associated with the bypass stress, σ_B, plus fastener load stress, σ_F, where $\sigma_0 = \sigma_B + \sigma_F$ (Figure 2), multiplied by the appropriate two-dimensional, K_{2D}, and three-dimensional, K_{3D}, stress-concentration factors, *i.e.*,

$$\sigma^{\max}_{\text{elastic}} = \sigma_F \circ K_{2D_F} \circ K_{3D_F} + \sigma_B \circ K_{2D_B}$$

If the material surrounding the fastener is not entirely elastic, the stress is governed by a two-dimensional elasto-plastic solution which varies with loading at each level through the thickness. Therefore, the individual solutions cannot be combined by superposition. In performing these nonlinear-type two-dimensional analyses, the strains are governed by the fastener and bypass loads, computed from the one-dimensional analysis, multiplied by the amplification factors associated with the three-dimensional solution.

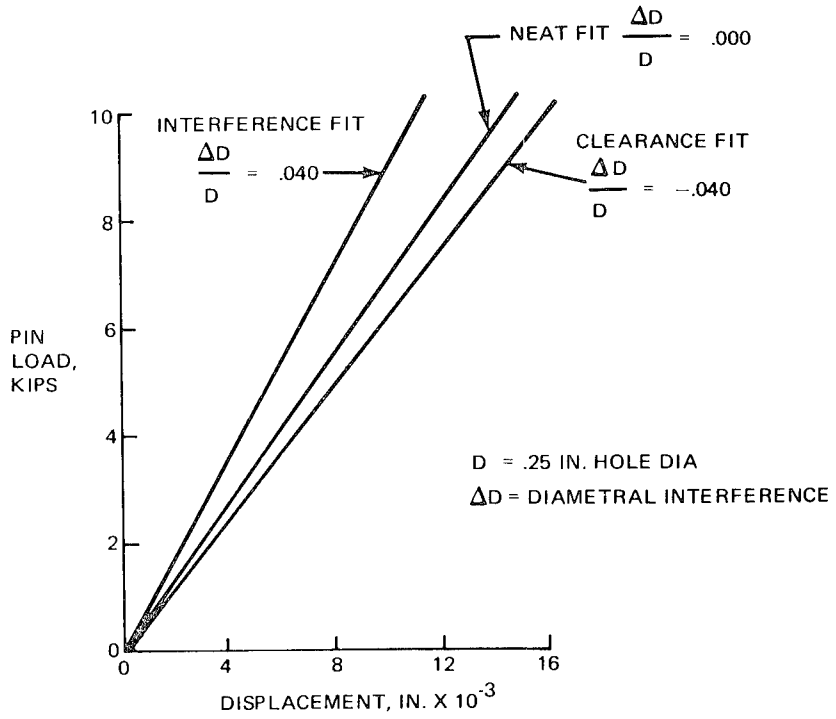


Figure 11. Computed load-deflection curves for a typical aluminum plate.[30]

RECENT APPLICATIONS

Although the underlying phenomenon governing fatigue, fretting, and crack growth in metals, and delamination and bearing-type failures in composites is not well understood, it is generally agreed that accurate stress analyses around fastener holes are highly useful tools in predicting structural life.

For fatigue, the alternating component of stress intensity is a dominant factor in determining fatigue life.[31,32] In recent works based upon elastoplastic finite-element programs,[25,27,28] the desirable effects of interference-fit fasteners in reducing the alternating stress has been numerically demonstrated. Adler and Dupree[29] have also shown, by a finite-element procedure, that cold working a fastener hole introduces beneficial residual compression stress at the hole. In a similar manner, Harris, Armen, and Pifko[32] have demonstrated the benefits of squeeze rivets in obtaining residual stresses which improve fatigue life.

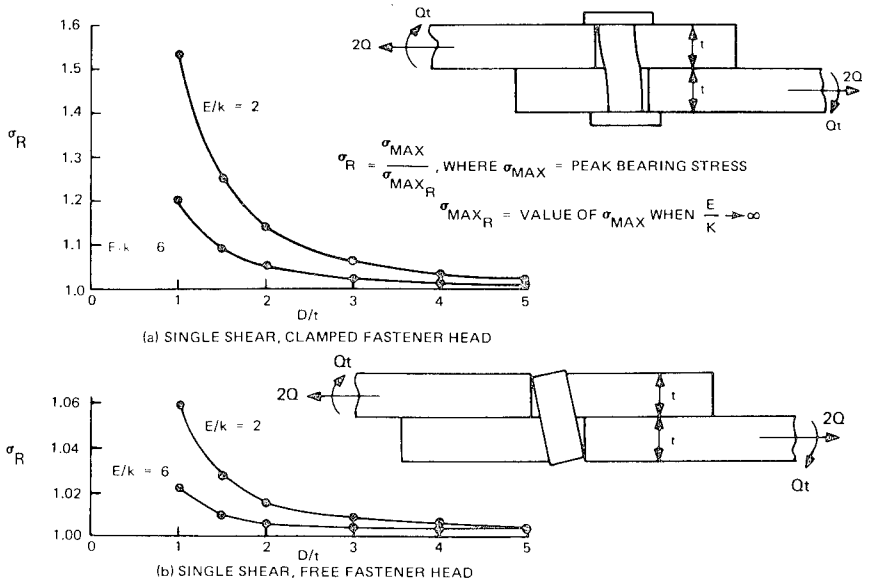


Figure 12. Effect of fastener stiffness on peak bearing stress in single shear lap joints.[30]

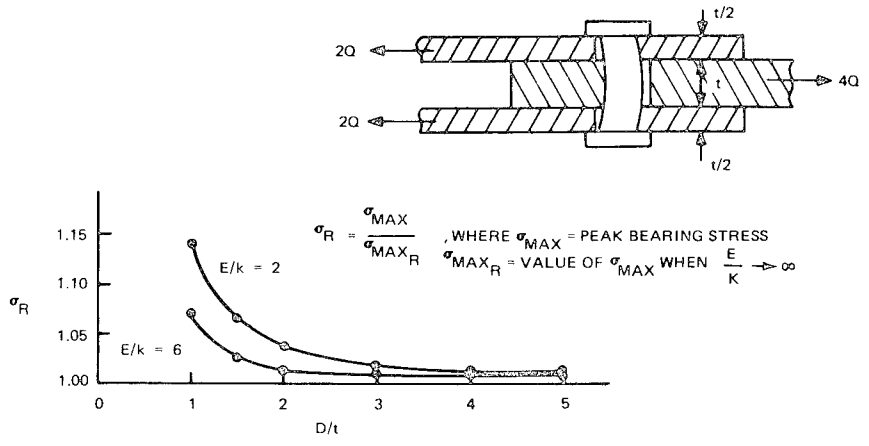


Figure 13. Effect of fastener stiffness on peak bearing stress-double shear case with arbitrary fastener head end conditions.[30]

Table 1. Analytical and Experimental Results for the Double Lap Joints Tested (Reference 30)

Type Fit	k Plate Stiffness $\times 10^{-6}$ psi	Overall Joint Stiffness $\times 10^{-6}$ lb/in.		
		Analysis	Test	Analysis for a Rigid Fastener
Loose	4.255	0.416	0.420 (avg. of 12 tests)	0.535
Perfect (Neat)	5.330	0.610	——	0.670
Interference	6.966	0.778	0.803 (avg. of 3 tests)	0.876

With regard to crack growth, the crack propagation rate, dc/dN, is proportional to K^{α},[1] where K (stress-intensity factor) is strongly dependent upon the local stress-concentration factor, and $2<\alpha<5$. Thus, any reduction in the stress-concentration factor, such as that reported by Harris and Ojalvo[30] when working with smaller clearances between fasteners and fastener holes (Figure 15), significantly impacts the crack-growth rate and structural life.

Bolted joints in composite laminates present particularly complex stress distributions and multiple, possibly interacting, failure modes which are not adequately understood. Boron and graphite–epoxy laminates exhibit a quasi-brittle reduction of static strength in the presence of stress concentrations.[33–35] Unlike metals, crack nucleates in composites do not appear to grow through the thickness.[33] However, examination of delamination and bearing failures indicate that three-dimensional and sometimes nonlinear phenomena are involved. Thus, it is evident that improved splice-joint stress analyses are required for a better understanding of failure modes in composite joints.

FRICTION EFFECTS

The potentially significant effect of friction between the pin and hole in reducing two-dimensional stress-concentration effects has been demonstrated experimentally by Lambert and Brailey[36] and analytically

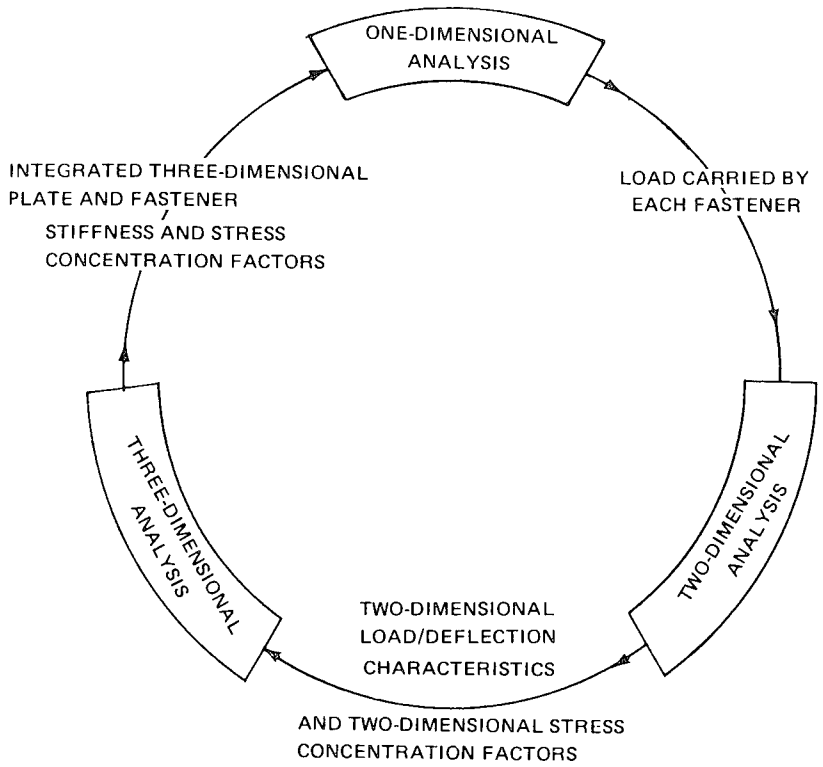


Figure 14. Input/output flow diagram depicting the interrelationship among the one-, two- and three-dimensional type analyses.

by Hussain and Pu[24] for the tension-loaded neat-fit fastener (Figure 9); Crews[22] for the interference-fit fastener (Figure 16); and Oplinger and Gandhi[17] for the pin-loaded hole (Figure 17). However, the equally important friction effect between plate surfaces, resulting from fastener clamp-up, has not been adequately treated in the literature.

As evidence of the importance of clamp-up force (resulting from bolt tightening) in relieving the joint load transmitted by fastener shear, we cite the experimental work of Wittmeyer and Smode[37,38] and the survey report by Munse.[39] In recent fatigue tests upon aluminum dog-bone specimens with steel Huck rivets in single-shear, Hooson and Baker[40] reported a significant plate fretting failure not at the fastened hole, but outside the regime of peak clamp-up pressure between plates (Figure 18b). A similarly fastened plate which did fail at the hole (as predicted by analyses which do not include friction), was one for which the rivet was improperly seated and so did not provide proper clamp-up force

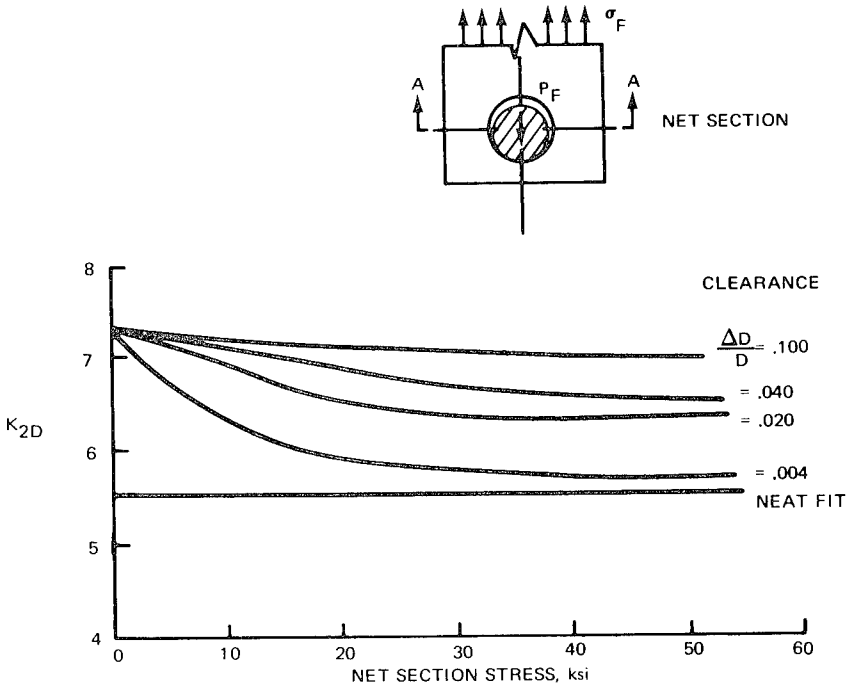


Figure 15. Variation of stress concentration factor with increasing net-section stress.[30]

(Figure 18c). It was also noted that the fatigue lives of the clamped-up fastener specimens were significantly longer (at least three to four times longer) than for the one which was not joined tightly.

As a first step in including the effect of friction in the faying plate surfaces, a knowledge of the clamp-up pressure is required. Cullimore and Upton,[41], employing a finite-difference scheme, obtained the axisymmetric pressure distribution between plates as a function of fastener-head radius, plate thickness, and hole radius (Figure 20). Similar studies by Gould and Mikic[42] and Cullimore and Eckhart[43] have also been performed using finite-element methods. Some typical results are presented in Figures 19 and 20.

CONCLUSIONS AND RECOMMENDATIONS

A comprehensive review of mechanically fastened splice-joint analyses has been attempted. In preparing this chpater, a number of noteworthy survey and reference works[44–51] were encountered which focus

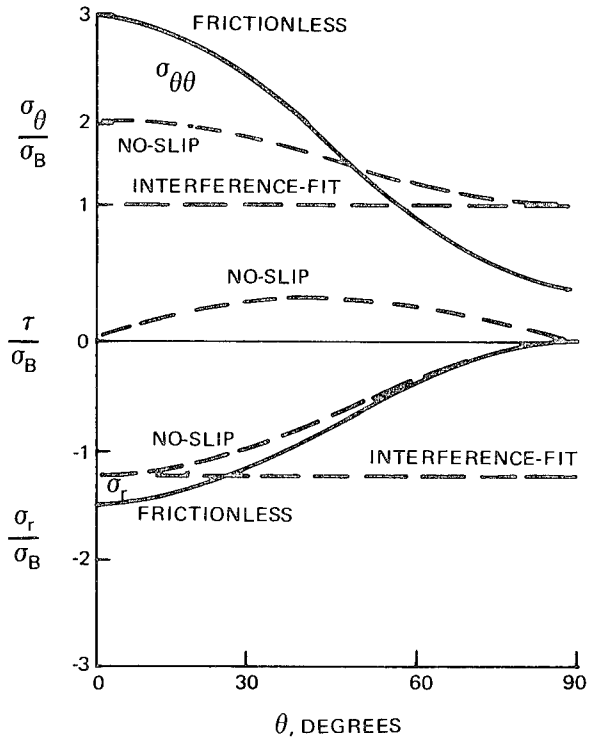


Figure 16. Elastic stresses along the hole boundary in a stretched sheet with a frictionless and a no-slip interference-fit fastener of the same material.[22]

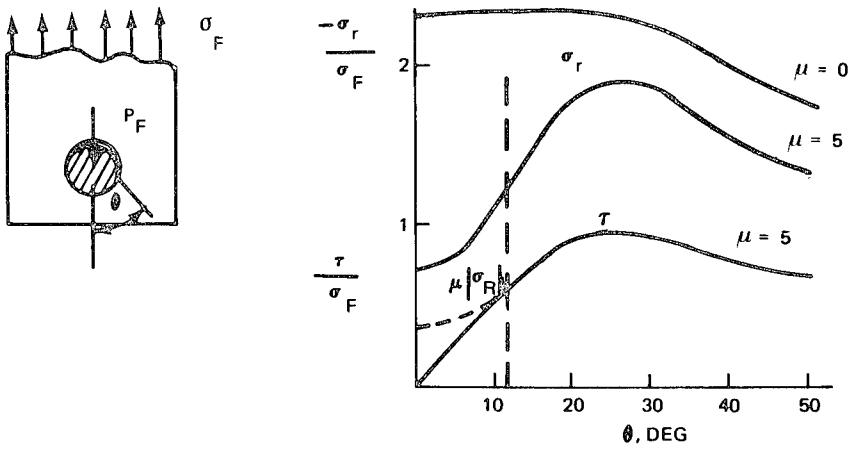


Figure 17. Effect of friction on contact radial and shear distribution around pin loaded hole of a graphite-epoxy plate.[17]

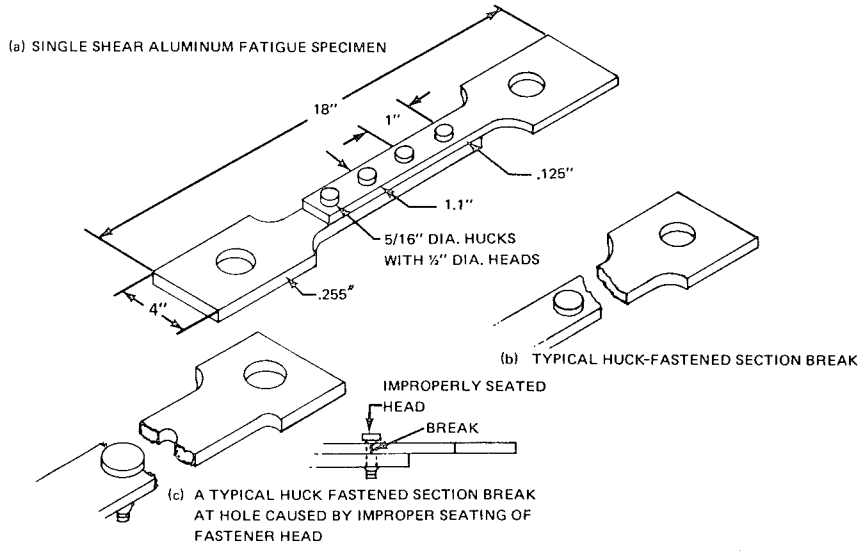


Figure 18. Fatigue test of cap joint specimen with typical and atypical failures.[37]

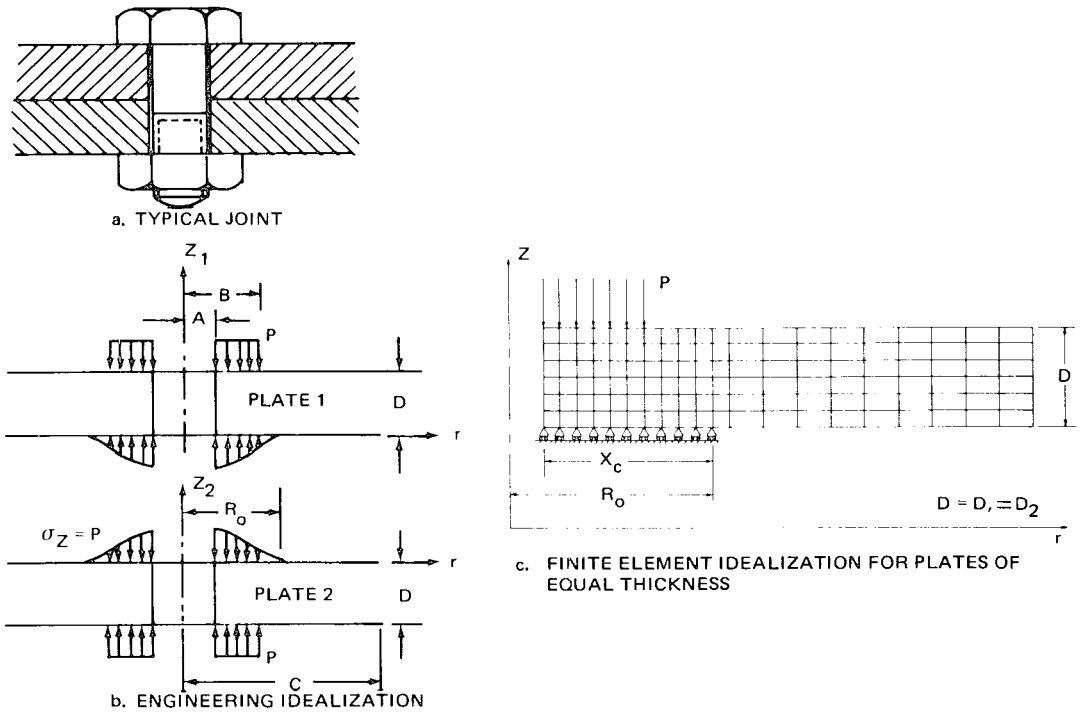


Figure 19. Idealization of tightly bolted joint to determine contact pressure between plates of equal thickness.[39]

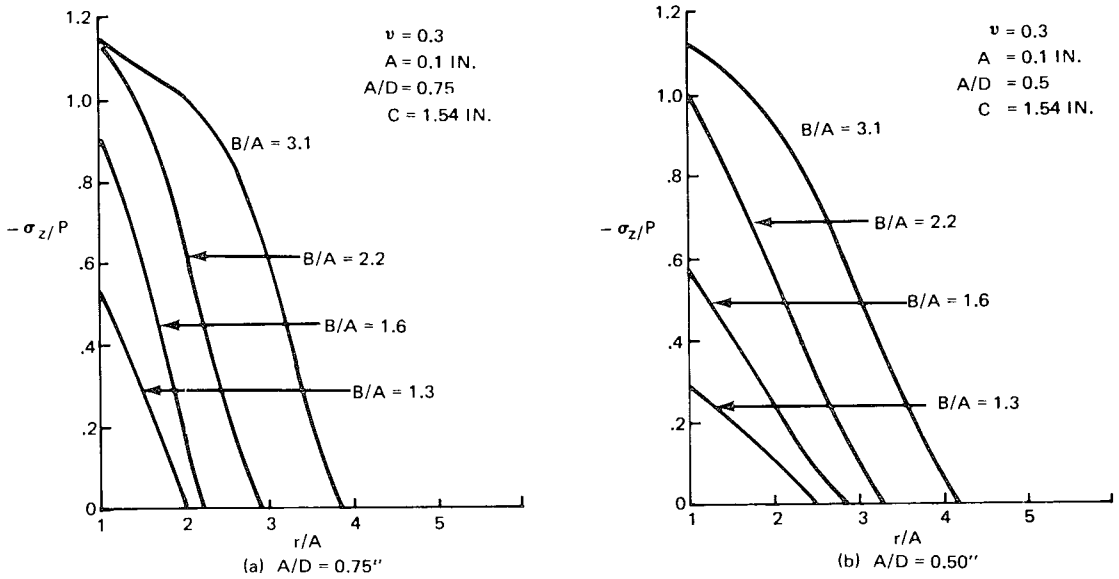


Figure 20. Contact pressure between tightly joined plates of equal thickness $\nu = .3$, $A = 0.1''$, $C = 1.54''$. (See Figure 19 for explanation of notation.)

on related areas. Since some of these may be of interest to the typical reader of this effort, they are noted here.

REFERENCES

1. Freudenthal, A. M., "Fatigue Mechanisms, Fatigue Performance and Structural Integrity," in Proceedings of the Air Force Conference on Fatigue and Fracture of Aircraft Structures and Materials, held at Miami Beach, Fla., 15–18 December 1969. Air Force Flight Dynamics Laboratory Report No. AFFDL-TR-70-144 (September 1970), 9–14. (AD 719 756)
2. Waszczak, J. P. and Cruse, T. A., "A Synthesis Procedure for Mechanically Fastened Joints in Advanced Composite Materials, Vol. II," Carnegie-Mellon University, Pittsburgh, Pa. Air Force Materials Laboratory Contract Report No. AFML-TR-73-145-Vol. 2, September 1973. (AD 771 795)
3. Tate, M. B. and Rosenfeld, S. J., "Preliminary Investigation of the Loads Carried by Individual Bolts in Bolted Joints," National Advisory Committee for Aeronautics, Washington, D.C., Report No. NACA-TN-1051, May 1946.
4. Switzky, H., Forray, M. J., and Newman, M., "Thermo-Structural Analysis Manual," Republic Aviation Corporation, Farmingdale, N.Y., Wright Air Development Division Contract Report No. RAC-679-1A, August 1962. (AD 286 908)
5. McCombs, W. F., McQueen, J. C., and Perry, J. L., "Analytical Design Methods for Aircraft Structural Joints," LTV Aerospace Corp., LTV Vought Aeronautics Division, Dallas, Tex. Air Force Flight Dynamics Laboratory Contract Report No. AFFDL-TR-67-184, January 1968. (AD 831 711)
6. Gehring, R. W. and Maines, C. H., "A Redundant-Force Method for the Inelastic Analysis of Mechanically Fastened Joints," North American Aviation, Inc., Columbus, Ohio. Naval Air Engineering Center, Aeronautical Structures Laboratory Contract Report No. NAEC-ASL-1103, January 1967. (AD 656 057)
7. Torczyner, R. D., "Computerized Method for Calculating Load Distributions in Multiple Fastener Joints," Grumman Aerospace Corporation, Bethpage, N.Y. Report No. ADRO2-01-71.3, June 1971.
8. Gatewood, B. E. and Gehring, R. W., "Inelastic Mechanical Joint Analysis Method with Temperature and Mixed Materials," in *Proceedings of the Army Symposium on Solid Mechanics, 1974: The Role of Mechanics in Design — Structural Joints*, Army Materials and Mechanics Research Center, Watertown, Mass., Report No. AMMRC MS 74-8 (September 1974), 193–210. (AD 786 543)
9. Jarfall, L., "Fatigue Cycling of Riveted or Bolted Joints," Aeronautical Research Institute of Sweden, Stockholm, Report No. HF-1239, June 1969. (N71-22508)
10. Bickley, W. G., "Distribution of Stress Round a Circular Hole in a Plate," *Phil. Trans. Royal Soc., London*, Ser. A, **227** (1928), 383–415.

11. Knight, R. C., "Action of a Rivet in a Plate of Finite Breadth," *Phil. Mag.*, Ser. 7, **19** (1935), 517–40.
12. Frocht, M. M. and Hill, H. N., "Stress Concentration Factors Around a Central Circular Hole in a Plate Loaded Through a Pin in the Hole," *J. Appl. Mech.*, **7** (1940), 5–9.
13. Theocaris, P. S., "The Stress Distribution in a Strip Loaded in Tension by Means of a Central Pin," *J. Appl. Mech.*, **23** (1956), 85–90.
14. Harris, H. G., Ojalvo, I. U., and Hooson, R. E., "Stress and Deflection Analysis of Mechanically Fastened Joints," Grumman Aerospace Corp., Bethpage, N. Y. Air Force Flight Dynamics Laboratory Contract Report No. AFFDL-TR-70-49, May 1970. (AD 709 221)
15. Oplinger, D. W. and Gandhi, K. R., "Stresses in Mechanically Fastened Orthotropic Laminates," in *Proceedings of the Conference on Fibrous Composites in Flight Vehicle Design*, Dayton, Ohio, 21–24 May 1974. Air Force Flight Dynamics Laboratory Contract Report No. AFFDL-TR-74-103 (September 1974), 811–42. (AD-B000 135L)
16. Ojalvo, I. U. and Linzer, F. D., "Improved Point-Matching Techniques," *Quart. J. Mech. Appl. Math.*, **18** (1965), 41–56.
17. Oplinger, D. W. and Gandhi, K. R., "Analytical Studies of Structural Performance in Mechanically Fastened Fiber-Reinforced Plates," in *Proceedings of the Army Symposium on Solid Mechanics, 1974: The Role of Mechanics in Design — Structural Joints*. Army Materials and Mechanics Research Center, Watertown Mass., Report No. AMMRC MS 74-8 (September 1974), 211–40. (AD 786 543)
18. Kirsch, G., "Die Theorie der Elastizitat und die Bedurfmisse der Festigkeitslehre," *Z. Ver. Deut. Ing.*, **42**, 1898.
19. Howland, R. C. J., "On the Stresses in the Neighbourhood of a Circular Hole in a Strip Under Tension," *Phil. Trans. Roy. Soc., London*, Ser. A, **229** (1929–30), 48–86.
20. Sternberg, E. and Sadowsky, M. A., "Three-Dimensional Solution for the Stress Concentration Around a Circular Hole in a Plate of Arbitrary Thickness," *J. Appl. Mech.*, **16** (1949), 27–38.
21. Goodier, J. N., "Concentration of Stress Around Spherical and Cylindrical Inclusions and Flaws," *J. Appl. Mech.*, **1** (1933), 39–44.
22. Crews, J. H., "An Elastic Analysis of Stresses in a Uniaxially Loaded Sheet Containing an Interference Fit Bolt," National Aeronautics and Space Administration, Langley Research Center, Langley Station, Va., Report No. NASA-TN-D-6955, October 1972. (N72-33914)
23. Stippes, M., Wilson, H. B. Jr., and Krull, F. N., "A Contact Stress Problem for a Smooth Disk in an Infinite Plate," in *Proceedings of the Fourth U.S. National Congress of Applied Mechanics*, Vol. 2. New York: American Society of Mechanical Engineers (1962), 799–806.
24. Hussain, M. A. and Pu, S. L., "Slip Phenomenon for a Circular Inclusion," *Trans. ASME, Ser. E, J. Appl. Mech.*, **38** (1971), 627–33.

25. Brombolich, L. J., "Elastic-Plastic Analysis of Stresses Near Fastener Holes," AIAA Paper 73–252, January 1973.
26. Allen, M. and Ellis, J. A., "Stress and Strain Distribution in the Vicinity of Interference Fit Fasteners," General Dynamics, Convair Aerospace Division, Fort Worth, Tex. Air Force Flight Dynamics Laboratory Contract Report No. AFFDL-TR-72-153, November 1972. (AD 760 570)
27. Ghadiali, N. D., Hopper, A. T., Sampath, S. G., and Simonen, F. A., "Elastic-Plastic Analysis of Interference Fit Fasteners," in *Proceedings of the Army Symposium on Solid Mechanics, 1974: The Role of Mechanics in Design — Structural Joints*, Army Materials and Mechanics Research Center, Watertown, Mass., Report No. AMMRC MS 74-8 (September 1974), 61–74. (AD 786 543)
28. Crews, J. H., "An Elastoplastic Analysis of a Uniaxially Loaded Sheet with an Interference-Fit Bolt," National Aeronautics and Space Administration, Langley Research Center, Langley Station, Va., Report No. NASA-TN-D-7748, October 1974. (N74-35304)
29. Adler, W. F. and Dupree, D. M., "Stress Analysis of Coldworked Fastener Holes," Bell Aerospace Company, Buffalo, N.Y. Air Force Materials Laboratory Contract Report No. AFML-TR-74-44, July 1974. (AD 784 920)
30. Harris, H. G. and Ojalvo, I. U., "Simplified Three-Dimensional Analysis of Mechanically Fastened Joints," in *Proceedings of the Army Symposium on Solid Mechanics, 1974: The Role of Mechanics in Design — Structural Joints*, Army Materials and Mechanics Research Center, Watertown, Mass., Report No. AMMRC MS 74-8 (September 1974), 177–92. (AD 786 543)
31. Smith, C. R., "Interference Fasteners for Fatigue-Life Improvement," *Exper. Mech.*, **5**, No. 8 (1965), 19A–23A.
32. Harris, H. G., Armen, H., and Pifko, A. B., "A Method for Determining the Stress Distribution in Plates with Squeeze Rivets," Grumman Aerospace Corporation, Bethpage, N.Y. Report No. 000-STMECH-029, April 1969.
33. Halpin, J. C., Jerina, K. L., and Johnson, T. A., "Characterization of Composites for the Purpose of Reliability Evaluation," in *Analysis of the Test Methods for High Modulus Fibers and Composites*. Special Technical Publication 521. Philadelphia: American Society for Testing and Materials (1973), 5–64.
34. Whiteside, J. B., Daniel, I. M., and Rowlands, R. E., "The Behavior of Advanced Filamentary Composite Plates with Cutouts," Grumman Aerospace Corporation, Bethpage, N.Y. Air Force Flight Dynamics Laboratory Contract Report No. AFFDL-TR-73-48, June 1973. (AD 764 362)
35. Whiney, J. M. and Nuismer, R. J., "Stress Fracture Criteria for Laminated Composites Containing Stress Concentrations," *J. Composite Mater.*, **8** (1974), 253–65.
36. Lambert, T. H. and Brailey, R. J., "The Influence of Coefficient of Friction on the Elastic Stress Concentration Factor for a Pin-Jointed Connection," *Aeronaut. Quart.*, **13** (1962), 17–29.

37. Wittmeyer, H. M. and Smode, F. E., "Fatigue Resistant Fastener," in *Aircraft Structures and Materials Application*, Proceedings of the 1st National SAMPE Technical Conference, Seattle, Wash., September 9–11, 1969. Azusa, Calif.: Society of Aerospace Material and Process Engineers (1969), 261–69.
38. "Conference Digest — Joints That Resist Fatigue," *Mach. Des.*, **42** (January 1970), 136–40.
39. Munse, W. H., "Riveted and Bolted Structural Joints," University of Illinois, Urbana, Structural Series Report No. 365, August 1970.
40. Hoosan, R. E. and Baker, M., "Spectrum Fatigue of Single Shear Lap Joints," Grumman Aerospace Corporation, Bethpage, N.Y. Test Report No. MPLR 45-74-95, October 1974.
41. Cullimore, M. S. G. and Upton, K. A., "The Distribution of Pressure Between Two Flat Plates Bolted Together," *Int. J. Mech. Sci.*, **6** (1964), 13–25.
42. Gould, H. H. and Mikic, B. B., "Areas of Contact and Pressure Distribution in Bolted Joints," *Trans. ASME, Ser. B, J. Eng. Ind.*, **94** (1972), 864–70.
43. Cullimore, M. S. G. and Eckhart, J. B., "Distribution of the Clamping Pressure in Friction-Grip Bolted Joints," *Struct. Eng.*, **52** (1974), 129–31.
44. Peterson, R. E., *Stress Concentration Design Factors*. New York: John Wiley & Sons, Inc. (1953).
45. Neuber, H. and Hahn, H. G., "Stress Concentration in Scientific Research and Engineering," *Appl. Mech. Rev.*, **19** (1966), 187–99.
46. Savin, G. N., *Stress Concentration Around Holes*. New York: Pergamon Press (1961).
47. Murphy, M. M. and Lenoe, E. M., "Stress Analysis of Structural Joints and Interfaces — A Selective Annotated Bibliography," Army Materials and Mechanics Research Center, Watertown, Mass., Report No. AMMRC MS 74–10, September 1974. (AD 786 520)
48. Newman, J. B., "Analysis of Problems Involving Nonlinear Boundary Conditions and Nonlinear Material Properties," in *Numerical Solution of Nonlinear Structural Problems*, ed. by R. F. Hartung. New York: American Society of Mechanical Engineers (1973), 51–65.
49. Tuba, I. S., "An Analytical Method for Elastic-Plastic Solutions," *Int. J. Solids Struct.*, **3** (1967), 543–64.
50. "Data Sheets on Fatigue," Royal Aeronautical Society, London, October 1963.
51. "Engineering Sciences Data," Royal Aeronautical Society, London, Aeronautical Series, Structures Sub-Series, **5**, 1967.
52. Pifko, A., Levine, H. S., Armen, H., and Levy, A., "PLANS — A Finite Element Program for Nonlinear Analysis of Structures," ASME Paper 74-WA/PVP-6, 1974.

17. STRESS ANALYSIS OF COMPOSITE JOINTS

D. W. OPLINGER
Army Materials and Mechanics Research Center
Watertown, Massachusetts

Stress analyses of adhesive and mechanically fastened joints in composite structures are discussed. In adhesive joints analyses of single and double lap joints as well as more advanced configurations including scarf joints and step-lap joints are described. Effects of laminate configuration, through-the-thickness deformations, nonlinear response, thermal stresses, and fracture mechanics considerations are treated. In mechanically fastened joints the effect of fastener configuration and composite material parameters on stress concentrations is described. Approaches to failure prediction are discussed, and the need for improved concepts for predicting failure is pointed out, based on experimental evidence which also suggests that nonlinearity in the laminate must be allowed for. The need for three-dimensional analysis is also covered.

INTRODUCTION

One of the more difficult aspects in the design of composite structures is that of joints. Joints tend to introduce a considerable amount of shear loading in the structural elements being joined, a mode of loading in which composites, especially organic matrix composites, tend to be weak. The role of stress analysis in the area of joints is to provide an understanding of the factors controlling joint strength and realiability, insight into the level of strength to be expected from a given type of joint, and a means of selecting directions in joint design which tend to provide improvement in joint performance.

The present chapter covers two generic types of joints, adhesive bonded joints and joints involving mechanical fasteners such as bolts or rivets. Adhesive joints are potentially the more desirable joining approach. Uncertainty in the reliability of bonded joints under fatigue and

other adverse environments and excessive thermal stresses in some material combinations used in the adherends makes the complete reliance on bonded joints difficult. In addition, many joints entail the need for component disassembly, mechanically fastened joints being a natural requirement in such cases.

In the case of adhesive joints, analyses have involved either closed-form or finite-element approaches. Closed-form analyses have used classical beam models for adherend response or simple modifications of these to allow for transverse shear and thickness normal deformations. More elaborate analyses based on two-dimensional continuum analyses are not readily available for the case of composite joints. Analyses of particular interest have treated single- and double-lap joints as well as scarf and step-lap configurations. Generalized laminate theory, treatment of thermal stresses and nonlinear response, and the application of fracture-mechanics approaches to growth of damage in adhesive joints are aspects of adhesive joint analysis given attention in the ensuing discussion.

In the case of mechanically fastened joints, both finite-element and two-dimensional elasticity analyses have been performed. Here the joint configuration is modeled in terms of arrays of circular inclusions representing the fasteners embedded in orthotropic plates representing the composite elements being joined. Of principal interest in the results discussed are stress concentrations as a function of fastener configuration and material parameters of the composite, and the relation between stress level and failure. While the prediction of stresses in fastened joints has been readily performed, some deficiencies have been found in currently available failure rules. Much of the work remaining to be done centers around the development of improved concepts for describing failure. The application of three-dimensional stress analyses and analyses which allow for nonlinear material behavior in the laminate appear to be essential for an adequate treatment of failure.

LIST OF SYMBOLS

B_ℓ, B_u	Stretching stiffnesses of lower and upper adherends, adhesive joint
C_ℓ, C_u	Bending tension coupling coefficients of lower and upper adherends, adhesive joint
C_v	Parameter in adhesive joint stress solution; $E_a/2G_a \equiv 1 + \nu_a$
D_ℓ, D_a	Bending stiffnesses of lower and upper adherends, adhesive joint

E_a	Young's modulus of adhesive layer
E'_ℓ, E'_u	Modified axial moduli of adhesive joint adherends; $E_{x\ell}/(1 - \nu_{x\ell}\nu_{y\ell}), E_{xu}/(1 - \nu_{xu}\nu_{yu})$
$E_{x\ell}, E_{xu}$	Axial Young's moduli of lower and upper adherends
$E_{z\ell}, E_{zu}$	Young's moduli of lower and upper adherends, thickness direction
e	"Edge-distance" parameter of pin-loaded plate, Figure 11(A)
G_a	Shear modulus of adhesive
$G_{xz}^{u}, G_{xz}^{\ell}$	Out-of-plane shear moduli of lower and upper adherends, adhesive joint
h_k	Location of upper surface of k^{th} ply in multilayer laminate
K_a	Parameter related to response of adhesive layer; E_a/τ_a
K'_B, K'_{NS}, K'_{so}	Stress concentration factors of pin-loaded hole with regard to: bearing (B); net section (NS); and shear-out (so) stresses
k_E, k_G	Parameters defining degree of orthotropy in laminate; E_1/E_2 $E_1/2G_{12}(1 + \nu_{12})$
ℓ	Overlap length of lap joint
ℓ_{eff}	"Ineffective length" of lap joint; MAX $\{3t_u/\lambda)\ 3t_u/\Lambda\}$
ℓ_p	Plastic portion of adhesive joint overlap
M_ℓ, M_u	Moments in lower and upper adherend
N_ℓ, N_u	Axial stress resultant of lower and upper adherend
N_0	Applied axial load per unit width on lap-joint adherends
ΔN	Increment of load developed in adherend in region of adhesive plasticity
s	"Side distance" parameter of pin-loaded plate, Figure 11(A)
t	Adherend thickness, general
t_a	Adhesive layer thickness
t_ℓ, t_u	Lower and upper adherend thickness
u, v, w	Displacement components in x, y, z directions, respectively
V_ℓ, V_u	Transverse shear force in lower and upper adherend
x, y, z	Rectangular coordinate; in adhesive joint x = axial, y = in-plane lateral, and z = thickness direction
α_ℓ, α_u	Thermal expansion coefficient of adherends
β	Parameter in adhesive joint equations (7)
γ_e, γ_p	Elastic and plastic shear strain in adhesive

γ_{xz}	Out-of-plane shear strain in adherend
ε_x	Axial strain
ε_{xp}, ε_{yp}, ε_{zp}	Plastic strains in adhesive joint elements
ζ	Dimensionless thickness direction coordinate, z/t_u in adherend
$\eta_k (k = 1,4)$	Constants in adhesive joint equations modified for plastic response
λ, Λ	Parameters in equations (7), differential equations for adhesive-joint response
ρ_{ep}	Adhesive ductility ratio, γ_p/γ_e
ρ_u	Characteristic adhesive joint parameter, $(E_a t_u/E'_u t_a)^{1/2}$
σ_A	Gross section stress in pin-loaded joint
σ_a	Peel stress in adhesive layer
$(\sigma_a)_{\max}$	Maximum adhesive peel stress
σ_B, σ_{NS}	Peak bearing and net section tensile stress in pin-loaded joint
τ_a	Adhesive shear stress
$(\tau_a)_{\text{ave}}$	Average adhesive shear stress
$(\tau_a)_{\max}$	Maximum adhesive shear stress
τ_{so}	Peak shear-out stress in pin-loaded joint

ANALYSIS OF ADHESIVE JOINTS

Much of the pertinent analytical literature on behavior of adhesively joined composite structures is discussed in the state-of-the-art review by Murphy and Lenoe.[1] In addition, a review of work up to 1969 is treated extensively in an annotated bibliography by Kutscha and Hoffer,[2] while more recent work is discussed by Sharpe and Muha.[3]

The aim of the following discussion was to treat the behavior of adhesive joints from the standpoint of physical phenomena controlling their behavior, rather than to give a comprehensive description of the body of analytical effort which has been devoted to them. It was intended, therefore, to give a description of the effects which play a role in the structural performance of adhesive joints and how these are typically incorporated in analyses which have been performed. The work which is cited is representative rather than all-inclusive.

General Observations

The role of analytical effort in connection with adhesive joints is to provide an understanding of how the shear and peel stresses in the adhesive are developed and how they may be controlled by varying material and geometric parameters of the joint as well as the overall joint configuration. Figure 1 taken from Reference 4 summarizes the main considerations which may be called into play in analysis of adhesive joints. Note that in general the load capacity of the adherends is controlled by adherend thickness which reflects load-bearing area in tension. Superimposed on the general trend of increased adherend load capacity with thickness are various strength cut-offs which reflect localized adherend stresses as well as stresses in the adhesive. The lowest cut-off occurs in the single lap joint, due to the load eccentricity associated with this configuration which results in peeling stresses as well as adhesive shear-

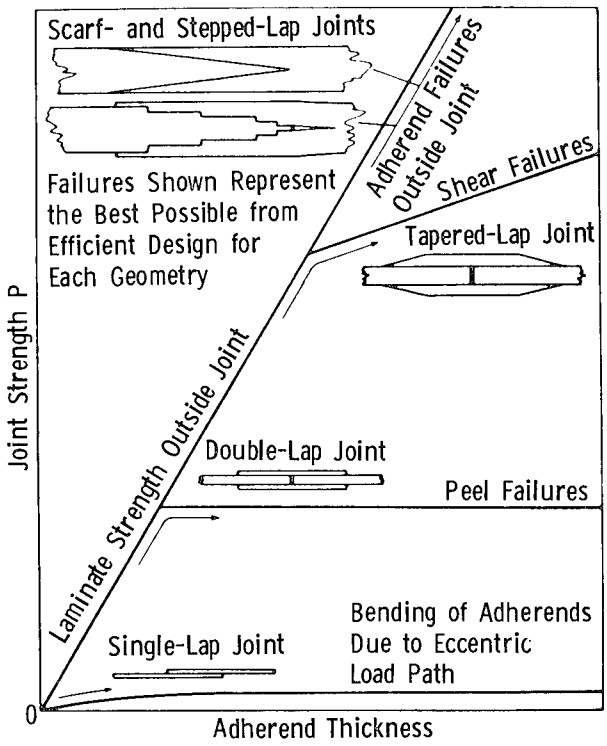


Figure 1. Failure condition vs configuration in adhesive joints (Hart-Smith[4]). Reprinted with permission of the Society for the Advancement of Material and Process Engineering.

stress concentrations. In the double-lap joint the situation is more favorable. While peel stresses were still the limiting factor, these may be eliminated from consideration by tapering the adherends near the end of the overlap, thereby softening them with respect to bending; at this point adhesive shear-stress concentrations become the limiting factor on joint strength. Changing the configuration to a scarf or step-lap joint helps to eliminate the "ineffective length" phenomenon associated with single or double-lap joints, making it possible to use long overlaps to effectively reduce the peak level of adhesive shear strength. ("Ineffective Length" — see discussion concerning equation (11) in section on Single- and Double-Lap Joints, Elementary Approaches.)

The above discussion describes considerations that are common to joints in general. Superimposed on these considerations are the effects of non-linear material response in both the adherends and the adhesive, and effects characteristic of composite adherends including that of inhomogeneity of fiber-reinforced materials and curing stresses developed during fabrication, in addition to thermal stresses. In the case of through-the-thickness inhomogeneity of fiber-reinforced adherends, although exact analyses would require detailed representation of fiber and matrix portions of the composite, practical considerations restrict the representation of the fiber-reinforced material to that of equivalent homogeneous orthotropic plates. At the same time, the simplest orthotropic plate theories may not be adequate, and higher order theories allowing for transverse shear and thickness normal deformations often are desirable.

Single- and Double-Lap Joints

The single- and double-lap joint configurations (Figure 2) are representative of a number of joint systems used in actual structures as well as in test specimens. In the case of joints in which composite adherends are present, the analyses have primarily used strength of materials approaches, with the adherends treated as Euler beams-on-elastic foundations. In the Euler-beam approach, transverse shear and thickness normal deformations in the adherend are ignored. In the most simplified analyses such as that of Volkersen,[5] the adherend is treated as a membrane in which only stretching deformations are considered, while in the well-known treatment by Goland and Reissner[6] adherend bending effects are included. In a series of reports dealing with scarf and step-lap joints as well as with single- and double-lap joints, Hart-Smith[7–9] developed a number of results using the Volkersen membrane response approach for the adherends in conjunction with nonlinear response in the adhesive. Erdogan and Ratwani[10] carried out similar studies with the adhesive

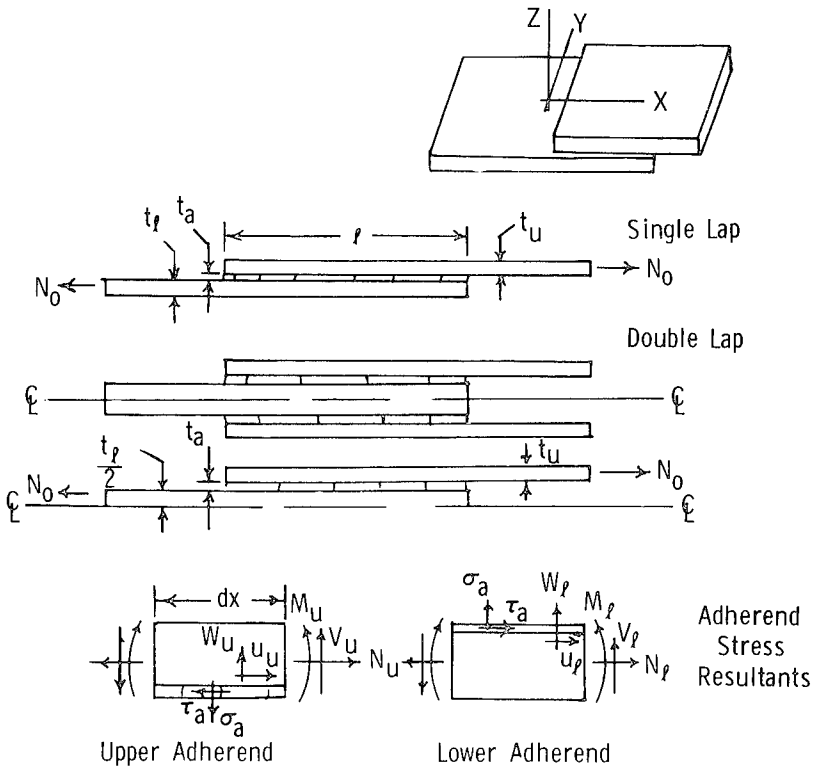


Figure 2. Nomenclature for single- and double-lap joints.

restricted to elastic response. Recently, more elaborate treatments of adherend deformation have been given by Renton and Vinson[11] and by Dickson *et al.*[12] These studies provided formulations in which transverse shear and thickness normal deformation in the adherends were provided for.

Elementary Approaches. Figure 2 shows the notation which applies to the following discussion. In the most elementary treatments[5,6] of single- and double-lap joints the axial strain, du/dx, in the adherend is either constant over the adherend thickness:

$$\frac{du}{dx} = \varepsilon_x = \frac{N}{B} \tag{1}$$

or a linear function of z:

$$\varepsilon_x = \frac{N}{B} + \left(z - \frac{t}{2}\right)\frac{M}{D} \tag{2}$$

where N and M are the in-plane stress resultant and moment:

$$N = \int_0^t \sigma_x dz \qquad M = \int_{-t/2}^{t/2} z\sigma_x dz \tag{3}$$

while

$$B = \int_0^t \frac{E_x}{1 - \nu_x \nu_y} dz \qquad D = \int_{-t/2}^{t/2} \frac{zE_x}{1 - \nu_x \nu_y} dz \tag{4}$$

(equations (1)–(4) apply to either adherend, and may be specialized for a particular adherend by adding subscripts u or ℓ). Equations (4) are written with the axial modulus and Poisson's ratio under the integral sign to allow for variations of layer properties in a laminate as a function of thickness coordinate z. When equation (1) or (2) is combined with the adherend equilibrium equations:

$$\frac{dN_u}{dx} + \tau_a = 0 \quad ; \quad N_\ell + N_u = N_0$$

$$V_u = \frac{t_u}{2}\tau_a - \frac{dM_u}{dx} \quad ; \quad V_\ell = \frac{t_\ell}{2}\tau_a - \frac{dM_\ell}{dx} \tag{5}$$

$$\frac{dV_u}{dx} = \sigma_a = -\frac{dV_\ell}{dx}$$

where the V's are adherend shear forces, together with adhesive stress–strain relations:

$$\frac{t_a \sigma_a}{E_a} = w_u - w_\ell \quad ; \quad \frac{t_a \tau_a}{G_a} = u_u - u_\ell \tag{6}$$

where the u's and w's are axial and out-of-plane displacements in the adherends, a pair of ordinary differential equations in the adhesive stresses τ_a and σ_a is obtained:

$$\frac{d^3\tau_a}{dx^3} - \frac{\lambda^2}{t_u^2}\frac{d\tau_a}{dx} - \frac{\beta^2}{t_u^3}\sigma_a = 0 \tag{7.1}$$

$$\frac{d^4\sigma_a}{dx^4} + \frac{4\Lambda^4}{t_u^4}\sigma_a - \frac{2C_\nu \beta^2}{t_u^3}\frac{d\tau_a}{dx} = 0 \tag{7.2}$$

where, letting

$$K_a = \frac{E_a}{t_a} \quad ; \quad C_\nu = \frac{E_a}{2G_a} = 1 + \nu_a$$

the parameters λ, Λ, and β are given for the single and double lap by:

Single Lap

$$\frac{\lambda^2}{t_u^2} = \frac{K_a}{2C_\nu}\left[\left(\frac{1}{B_u} + \frac{1}{B_\ell} + \frac{t_u^2}{4D_u} + \frac{t_\ell^2}{4D_\ell}\right)\right] \quad ;$$

$$\frac{\Lambda^4}{t_u^4} = \frac{K_a}{4}\left[\frac{1}{D_u} + \frac{1}{D_\ell}\right] \quad ; \tag{9}$$

$$\frac{\beta^2}{t_u^3} = \frac{K_a}{2C_\nu}\left(\frac{t_u}{2D_u} - \frac{t_\ell}{2D_\ell}\right)$$

Double Lap

$$\frac{\lambda^2}{t_u^2} = \frac{K_a}{2C_\nu}\left(\frac{1}{B_u} + \frac{2}{B_\ell} + \frac{t_u^2}{4D_u}\right) \quad ; \quad \frac{\Lambda^4}{t_u^4} = \frac{K_a}{4D_u} \quad ;$$

$$\frac{\beta^2}{t_u^3} = \frac{K_a}{4C_\nu}\frac{t_u}{D_u} \tag{10}$$

Using standard approaches, solutions of equations (7) are exponential functions of the form $\tau_{a0}e^{\pm\eta x}$ and $\sigma_{a0}e^{\pm\eta x}$, when η is the root of a sixth-degree polynomial derived from equations (7). For a large class of joints in which adherend bending deformations are small with respect to axial stretching deformations, two roots are approximately given by $\pm\lambda$, while the remaining four are approximated by $\pm\Lambda(1 \pm i)$ where $i = (-1)^{1/2}$. (For the identical adherend, single-lap case these are exact.) We are particularly interested in the peak stresses in the adhesive, $(\tau_a)_{\max}$ and $(\sigma_a)_{\max}$ for these cases. These will be given for long overlaps corresponding to $\lambda\ell/t_u \geq 3$ or $\Lambda\ell/t_u \geq 3$, whichever is longer. As shown in Figure 3, $(\tau_a)_{\max}$ decreases with increasing ℓ, but the decrease is limited to a lower bound governed by the long overlap criterion on ℓ just given. A similar type of behavior is encountered with $(\sigma_a)_{\max}$, in both cases the maximum stress values occurring at the end of the overlap. The ineffective length ℓ_{eff}, given by

$$\ell_{\text{eff}} = \text{MAX}\left\{\frac{3t_u}{\lambda}, \frac{3t_u}{\Lambda}\right\} \tag{11}$$

determines the lap length beyond which an increase in ℓ is ineffective in reducing peak adhesive shear and peeling stresses. In both cases a parameter ρ_u given by

$$\rho_u = \frac{E_a t_u}{E_u' t_a} \quad ; \quad E_u' = \frac{E_{xu}}{1 - \nu_{xu}\nu_{yu}} \tag{12}$$

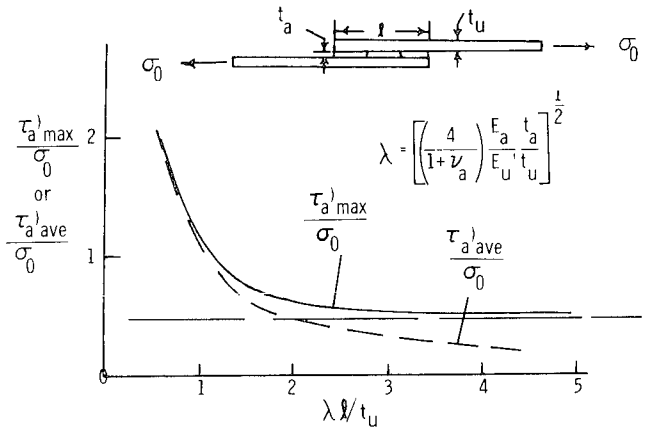


Figure 3. Variation of peak adhesive shear stress with overlap length.

figures prominently in the results. Note that λ and Λ are related to ρ_u for the special cases considered here by:

Single Lap, Identical Adherends

$$\lambda = 2\left(\frac{\rho_u}{C_\nu}\right)^{1/2} \quad ; \quad \Lambda = (6\rho_u)^{1/4}$$

Double Lap, $B_\ell = 2B_u$

$$\lambda = \left(\frac{5\rho_u}{2C_\nu}\right)^{1/2} \quad ; \quad \Lambda = (3\rho_u)^{1/4} \tag{14}$$

The peak stresses in the adhesive are then given by

Single Lap, Identical Adherends ($\ell \geq \ell_{\text{eff}}$)

$$\frac{(\sigma_a)_{max}}{\sigma_{u0}} = \frac{k}{2}\Lambda^2 + 2k'\frac{t_u}{\ell}\Lambda \quad ; \quad \frac{(\tau_a)_{max}}{\sigma_{u0}} = \left(\frac{1+3k}{8}\right)\lambda + 3(1-k) \tag{15}$$

where

$$\sigma_{u0} = \frac{N_0}{t_u}$$

while

$$k = \frac{\cosh\mu}{\cosh\mu + 2\sqrt{2}\sinh\mu} \quad ; \quad k' = \sqrt{2}\,k\mu$$

with

$$\mu = \frac{\ell}{2t_u}\sqrt{\frac{3}{2}(1 - \nu_{xu}\nu_{yu})\frac{N_0}{B_u}} \tag{16}$$

while for the double lap

Double Lap, $B_\ell = 2B_u\,(\ell \geq \ell_{\text{eff}})$

$$\frac{(\tau_a)_{\max}}{\sigma_{u0}} = \frac{\lambda}{2} \quad ; \quad \frac{(\sigma_a)_{\max}}{\sigma_{u0}} = \left(-\frac{1}{2} + \frac{\Lambda}{\lambda} + \frac{\lambda^2}{2\Lambda^2}\right)\left(\frac{4\Lambda^4}{4\Lambda^4 + \lambda^4}\right)\frac{\lambda^2}{2} \tag{17}$$

The parameters k and k' appearing in equations (15) and (16) reflect the bending of the single-lap configuration due to the introduction of load eccentrically. The results for the double lap are approximations hinging on the assumption that the term in equation (7.1) involving β^2 can be neglected, while that in (7.2) containing $d\tau_a/dx$ acts as a body force term and introduces a particular solution into the results. Note that peel stresses are not usually associated with the double-lap configuration because of its symmetry. As indicated in Figure 4, however, peel stresses are required in the outer adherends to equilibrate the moments introduced by the shear stresses which represent loads applied eccentrically to the outer adherends.

Using equations (13) and (14), the maximum adhesive stresses can be expressed in terms of ρ_u:

Single Lap

$$\begin{aligned} \frac{(\tau_a)_{\max}}{\sigma_{u0}} &= \left(\frac{1 + 3k}{4}\right)\left(\frac{\rho_u}{C_\nu}\right)^{1/2} + 3\,(1 - k) \quad ; \\ \frac{(\sigma_a)_{\max}}{\sigma_{u0}} &= \frac{k}{2}\,(6\rho_u)^{1/2} + 2k'\,\frac{t_u}{\ell}\,(6\rho_u)^{1/4} \end{aligned} \tag{18}$$

Double Lap

$$\frac{(\tau_a)_{\max}}{\sigma_{u0}} = \left(\frac{5}{8}\,\rho_u\right)^{1/2} \tag{19}$$

$$\frac{(\sigma_a)_{\max}}{\sigma_{u0}} = \left[\frac{5}{2 \cdot 3^{1/2} C_\nu}\rho_u^{1/2} + \left(\frac{2 \cdot 3\,C_\nu}{5}\right)^{1/2}\frac{1}{\rho_u^{1/4}} - \frac{1}{2}\right]\left(\frac{\dfrac{5}{4C_\nu}\rho_u}{\dfrac{25}{12C_\nu^2}\rho_u + 1}\right)$$

In both cases the peak shear stress varies as $\rho_u^{1/2}$. The peeling stresses for the single-lap case vary as $\rho_u^{1/4}$ for small ρ_u and as $\rho_u^{1/2}$ for large ρ_u. For the double-lap joint the peeling stresses vary as $\rho_u^{1/4}$ for small ρ_u, while again varying as $\rho_u^{1/2}$ for large ρ_u.

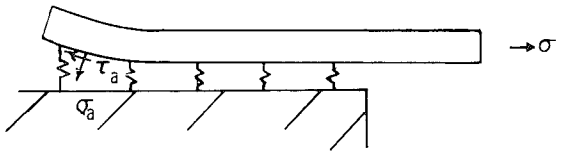


Figure 4. Mechanism of peeling stress development.

The dependence of the peak adhesive stresses on ρ_u suggests that ρ_u should be made as small as possible to avoid adhesive failure at a given adherend load. From the expression for ρ_u given in equation (12) this implies that continual increases in adhesive thickness are beneficial, although in practice a small adhesive-to-adherend thickness ratio is found to be optimum. In thin adhesives the effect of restraint of in-plane adhesive deformation by the adherend may have a beneficial effect on adhesive performance by tending toward a hydrostatic stress state. This has not been accounted for in the above analysis. The effect of thickness-normal and out-of-plane shear deformations in the adherends, which is discussed below, would also tend to modify the behavior of the adhesive. The elementary Goland–Reissner or Volkersen analyses, while bringing out the effect of the parameter ρ_u which expresses the effect of the modulus and thickness ratios between the adherend and adhesive, apparently ignore several effects that need closer attention.

The results given above apply to isotropic (*i.e.*, metallic) and "homogeneous" orthotropic adherends, the latter including orthotropic laminates not containing coupling terms between in-plane stresses and bending or twisting deformations. The moment and axial stress resultant for such laminates, expressed in terms of the middle-surface displacements are

$$N_u = B_u \frac{du_u}{dx} \quad ; \quad M_u = D_u \frac{d^2 w_u}{dx^2}$$

For more general laminates we have relations of the form

$$\begin{aligned} N_u &= B_u \frac{du_u}{dx} + C_u \frac{d^2 w_u}{dx^2} \\ M_u &= C_u \frac{du_u}{dx} + D_u \frac{d^2 w_u}{dx^2} \end{aligned} \tag{20}$$

together with a similar pair of equations for the lower adherend. The coefficients B_u and D_u are again given by equations (4) when the latter

are applied to the upper adherend. The cross-coupling coefficient is given by

$$C_u = \int_{-t_{u/2}}^{t_{u/2}} \frac{zE_{xu}\,dz}{1 - \nu_{xu}\nu_{yu}} \tag{21}$$

For N-layered adherends with stepwise variation of elastic constants, the following expressions hold:

$$B_u = \sum_{k=1}^{N} C_{11}^{u(k)} (h_k - h_{k-1})$$

$$C_u = \frac{1}{2} \sum_{k=1}^{N} C_{11}^{u(k)} (h_k^2 - h_{k-1}^2) \tag{22}$$

$$D_u = \frac{1}{3} \sum_{k=1}^{N} C_{11}^{u(k)} (h_k^3 - h_{k-1}^3)$$

where h_k is the distance of the "upper" surface of layer k (the surface of largest z) from the adherend middle surface, while

$$C_{11}^{u(k)} = \frac{E_x^{(k)}}{1 - \nu_x^{(k)}\nu_y^{(k)}} \tag{23}$$

is the axial modulus of layer k under uniaxial (in-plane) strain. When equations (20) together with the corresponding expressions for the lower adherend are combined with equations (5), a pair of ordinary differential equations in τ_a and σ_a of the same order as equations (7) again results, with appropriate changes in coefficients. The method for obtaining solutions is again straightforward.

Transverse Shear and Thickness Normal Deformations. In organic matrix composites the ratio of axial Young's modulus E_x to transverse shear modulus G_{xz} tends to be as high as 30 for uniaxial materials, as opposed to ratios on the order of 3.0 for metals and other isotropic materials. Since the effect of out-of-plane shear deformations becomes more important as E_x/G_{xz} increases, the necessity for considering the effects of such deformations is greater in joints containing composite adherends than those with metal adherends. Formulations taking transverse shear

and thickness normal deformations into account, were based on the well-known treatment by Whitney[13] for bending and stretching of laminated plates and given by Renton and Vinson[11] and by Dickson, Hsu, and McKinney.[12] The formulation given in References 11 and 12 applies to general laminates in which properties vary from layer to layer. It is instructive to consider a restricted version in which the adherends are generally orthotropic but essentially homogeneous, *e.g.*, a unidirectional laminate. The shear-stress distribution given in References 11 and 12 then reduces to a parabolic distribution in each adherend corresponding to the shear-stress distribution encountered in classical beam theory. For the upper adherend we have

$$\tau_{xz}^{u} = (1 - 4\zeta + 3\zeta^2)\,\tau_a + \frac{6}{t_u}(\zeta - \zeta^2)V_u \tag{24}$$

where

$$\zeta = \frac{z}{t_u}$$

and

$$V_u = \int_0^{t_u} \tau_{xz}^{u} dz$$

with a similar expression resulting in the lower adherend. On substituting equation (24) into the equilibrium equation $\frac{\partial \tau_{xz}^{u}}{\partial x} + \frac{\partial \sigma_z}{\partial z} = 0$ and integrating with respect to z, an equation for normal stress in the z-direction is obtained:

$$\sigma_z^{u} = -(\zeta - 2\zeta^2 + \zeta^3)t_u \frac{d\tau_a}{dx} + (1 - 3\zeta^2 + 2\zeta^3)\,\sigma_a \tag{25}$$

where use is made of the next-to-last of equations (5). On forming expressions for shear and extensional strains $\gamma_{xz}^{u} = \frac{\tau_{xz}^{u}}{G_{xz}^{u}}$, $\varepsilon_{xz}^{u} = \frac{\sigma_z^{u}}{E_z^{u}}$ corresponding to τ_{xz}^{u} and σ_z^{u} and performing appropriate integrations with respect to z, corrected expressions for axial strain ε_x^{u} and out-of-plane deformation w_u are obtained. On forming the corresponding corrected expressions for the distribution of axial stress and substituting into equations (3), corrections for shear-stress resultant N_u and moment M_u result:

$$N_u = N_u^0 + \frac{1}{12}\frac{E_u'}{G_{xz}^{u}} t_u^2 \frac{d\tau_a}{dx} + \frac{1}{2}\frac{E_u'}{G_{xz}^{u}} t_u \sigma_a + \frac{1}{60}\frac{E_u'}{E_{zu}} t_u^4 \frac{d^3\tau_a}{dx^3} - \frac{1}{60}\frac{E_u'}{E_{zu}} t_u^3 \frac{d^2\sigma_a}{dx^2}$$

$$M_u = M_u^0 - 0.00831 \frac{E'_u}{G^u_{xz}} t_u^3 \frac{d\tau_a}{dx} + \frac{1}{10} \frac{E'_u}{G^u_{xz}} t_u^2 \sigma_a + 0.00437 \frac{E'_u}{E_{zu}} t_u^5 \frac{d^3\tau_a}{dx^3} - 0.0310 \frac{E'_u}{E_{zu}} t_u^4 \frac{d^2\sigma_a}{dx^2} \tag{26}$$

where N_u^0 and M_u^0 are equivalent to N_u and M_u obtained for conventional laminate theory corresponding to equations (20). Similar expressions involving σ_a and τ_a are obtained for the lower adherend. On combining these with equations (5) and (6), a modified form of equations (7) is obtained which reduces to an eighth-order equation in either σ_a or τ_a, in contrast to the sixth-order system resulting from equations (7). The form of the equation obtained for general laminates where ply-to-ply property variations are allowed for is given as equation (75), p. 37 of Reference 12.

An estimate of the magnitude of the correction terms in equations (26) defining the difference between N_u and N_u^0, as well as between M_u and M_u^0, is of interest since it essentially determines the values of t_u and t_ℓ beyond which the corrections are significant. This can be obtained by using expressions for τ_a and σ_a obtained from uncorrected Goland–Reissner type of formulations and substituting the corresponding derivatives into equations (26). For the double-lap joint, for example, the expression for peak shear stress given in equation (17) corresponds to

$$\tau_a \cong \frac{\lambda}{2} \sigma_{u0} e^{-\lambda \frac{x}{t_u}} \tag{27}$$

which holds in the vicinity of $x = 0$ when $\ell > \ell_{\text{eff}}$. From this the first correction term in the first of equations (26) reduces to

$$\left(\frac{1}{12} \frac{E'_u}{G^u_{xz}}\right) t_u^2 \frac{d\tau_a}{dx} \sim -\left(\frac{1}{12} \frac{E'_u t_u}{G^u_{xz}}\right) \frac{\lambda^2}{2} \sigma_{u0} e^{-\lambda \frac{x}{t_u}} \sim -\frac{5}{24 C_\nu} \left(\frac{G_a}{G^u_{xz}} \frac{t_u}{t_a}\right) \left(t_u \sigma_{u0}\right) e^{-\lambda \frac{x}{t_u}} \tag{28}$$

where the first of equations (14) is noted and G_a is substituted for $\frac{E_a}{2C_\nu}$.

The significance of equation (28) is determined chiefly by the magnitude of the factor

$$\frac{5}{24} \left(\frac{G_a}{G^u_{xz}}\right) \left(\frac{t_u}{t_a}\right)$$

which, because of the fact that G^u_{xz} may easily be close in magnitude to G_a in organic matrix composites, grows rapidly with t_u for the small values of t_a encountered in practical bond layers. Similar estimates may be made for other correction terms appearing in equations (26).

Higher order approaches to the effect of transverse shear and thickness normal deformations can be formulated by replacing equations (24) with higher order polynomials in ζ. The need for providing such further improvements to the theory becomes important primarily for excessively thick adherends or where abrupt changes in adherend thickness occur.

An additional modification to the theory is required when obliquely oriented plies are present in the adherends, since the stresses τ_{xy}, σ_y, and τ_{yz} are then introduced, along with corresponding deformations in the y-direction. For certain laminate configurations, simple polynomial expressions for τ_{yz} will provide for corrections to the stress prediction through an approach similar to the one considered here for τ_{xz} and σ_z.

Results obtained from the formulations of References 11 and 12 were incorporated into the Air Force funded computer codes, BOND4 and BONJOI, as discussed by Muha and Sharpe.[3] As noted in the latter reference, boundary conditions on the shear stress as well as the shear force, V, can be applied at the adherend end, resulting in a distribution of τ_a which goes to zero at the overlap ends. In contrast, the elementary theories provide only for $V = 0$ at adherend free ends and lead to nonzero shear stresses at those locations.

Scarf and Step-Lap Joints

Typical adhesive shear and peel strengths are on the order of 5–10 ksi, while composite adherend tensile strengths are typically on the order of 50–200 ksi. The ratio of peak adhesive shear stress to adherend tensile stress is thus on the order of 0.025 to 0.2. A joint design for which

$$\frac{(\tau_a)_{\max}}{\sigma_{u0}} \leqq 0.025 \text{ to } 0.2$$

is desirable.

From the results obtained previously for single- and double-lap joints, the ratio of $(\tau_a)_{\max}$ to σ_{u0} cannot be reduced to less than about $\lambda/2$; *i.e.*, for the specialized cases treated above

$$\frac{(\tau_a)_{\max}}{\sigma_{u0}} > \frac{1}{2}\left(\frac{5}{2}\frac{\rho_u}{C_\nu}\right)^{1/2}$$

because of the ineffective length phenomenon which prevents the interior region of the overlap from contributing to the load transfer between adherends. The quantity

$$\left(\frac{\rho_u}{C_v}\right)^{1/2} = \left(\frac{G_a t_u}{E'_u t_a}\right)^{1/2}$$

being on the order of unity or greater for typical joints, the peak adhesive shear stresses cannot easily be reduced to values comparable to adhesive strength values when the adherends are fully loaded. Scarf and step-lap joints provide efficient use of the full overlap length by allowing the peak adhesive stresses to be continually reduced as the overlap length increases, thus avoiding the ineffective length difficulty.

As shown in Figure 5, a thin bond line between identical adherends cut at an angle α to the axial direction is subjected to shear and normal stresses which may be calculated from transformation relations describing stresses in a coordinate system rotated an angle $\frac{\pi}{2} - \alpha$ from the vertical direction, leading to adhesive shear and peak stresses τ_a and σ_a given by

$$\frac{\tau_a}{\sigma_0} = -\frac{\sin 2\alpha}{2} \tag{29}$$

$$\frac{\sigma_a}{\sigma_0} = \sin^2 2\alpha$$

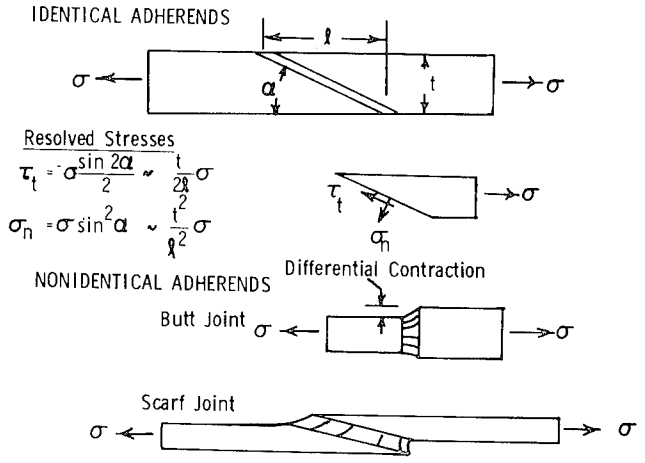


Figure 5. Relations for stresses in scarf joints.

Note that the angle α can be related to the ratio of lap length to adherend thickness by

$$\tan \alpha = \frac{t}{\ell} \; (\cong \sin \alpha \text{ for small } \alpha) \tag{30}$$

whence

$$\frac{\tau_a}{\sigma_0} \cong -\frac{t}{\ell} \quad ; \quad \frac{\sigma_a}{\sigma_0} \cong \frac{t^2}{\ell^2} \tag{30}$$

Through equations (30) the overlap length can be selected to give a "taper ratio" $\frac{t}{\ell}$ which will limit the stress ratios in (30) to the corresponding strength ratios. While these relationships are close to exact for identical adherends, for nonidentical adherends the difference in axial strain in the two adherends for a given stress, *i.e.*, the modulus difference, will cause some local intensification of adhesive stresses near the ends of the overlap as the adhesive is strained to provide for adherend incompatibility. For a butt joint (Figure 5, lower sketch) which can be viewed as a scarf joint with $\alpha = \frac{\pi}{2}$ it can be seen that the incompatibility is due to lateral contraction differences, *i.e.*, Poisson effects, while for a scarf joint with α close to zero, the incompatibility is primarily due to differences in axial moduli. The main result of scarf-joint analyses is the manner in which joint stresses are affected by adherend incompatibility.

In the case of the step-lap configuration, somewhat similar considerations apply. If the step lap is properly designed, one would assume that the stresses across the joint should be relatively uniform for similar adherends, although the cases for which analytical results have been given tend to show rather peaky distributions of shear stresses. Figure 6 shows the stress in a five-step joint between aluminum and boron epoxy obtained by Erdogan and Ratwani.[10] Since the analysis is based on the Volkersen approach for each section, it appears that shear-stress peaks are the result of making the section lengths greater than the ineffective length of a given section. The overall geometry of the joint, in particular the total length ℓ, can be roughed out by letting t/ℓ be related to the adherend–adhesive strength ratio as in the case of the scarf joint. At the same time, the peakiness has to be designed out of the stress distribution to make the scarf-joint analogy effective. The use of smaller "tread" lengths and correspondingly smaller "risers" (thickness increments between adjacent sections) would help to keep each section shorter than its ineffective length, thereby insuring a smoother shear-stress distribution. Practical considerations such as large filament diameter in the case of

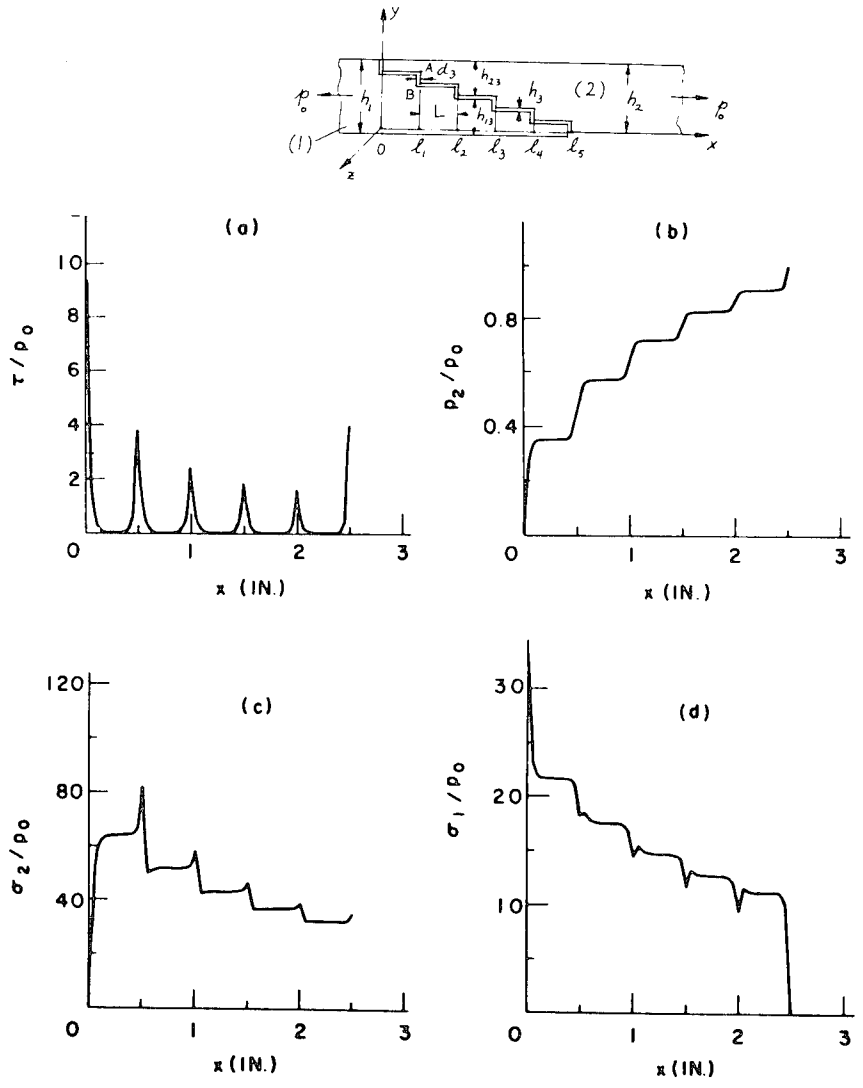


Figure 6. Stresses in aluminum–boron epoxy step joint:[10] (a) adhesive shear stress distribution; (b) force distribution in boron-reinforced adherend; (c) stress distribution in boron-reinforced adherend; (d) stress distribution in aluminum adherend. Reprinted with permission of Technomic Publishing Company.

boron may make small risers difficult to manufacture. However, qualitative design concepts such as these need to be explored to develop the full potential of the step-lap joint.

Analyses of scarf and step-lap joints have included the closed form solutions by Hart-Smith[7] and by Erdogan and Ratwani,[10] together with a number of finite-element approaches.[12,14] In particular, comparisons of finite-element results with the closed-form results of Reference 10 are discussed by Barker and Hatt.[14] Figures 7–10 show results discussed in Reference 14 for a single step joint and a scarf joint between boron epoxy and aluminum. Table 1, based on the results given in Reference 14, is a comparison of the peak shear stresses produced in various joints with that in a single-lap joint as predicted by the Volkersen analysis. The results here confirm that in general the step-lap and scarf joints give reduced stresses with respect to those in the single lap. Moreover, for the scarf joint considered here, the shear-stress concentration is relatively independent of lap length, which means that the ineffective length handicap of single-lap joints is surmounted. Potentially, the step-lap configuration should be capable of similar results.

The use of closed-form analyses for step-lap joints raises questions of adequacy because of the likelihood that abrupt changes of section thickness cause stress distributions to depart considerably from the form assumed in the analysis; namely, that the axial stress in each section is uniform and proportional to the inverse of section thickness. It would be useful to explore with the finite-element approach to what extent this assumption is violated in actual joints. Such an investigation does not appear to have been made. Furthermore, the presence of a sharp interior corner such as that occurring at the junction of "treads" and "risers" is known[15] to give rise to stress infinities in continuum mechanics formulations. These would appear to be natural sites of fatigue-damage initiation and further investigation of their effect appears warranted.

Thermal Stresses

Adhesive joints are often fabricated at adhesive curing temperatures on the order of 250–350°F. In applications, the resulting structure may experience much lower temperatures, as low as −67°F for example. If the adhesive is cured to a comparatively rigid state at 250–350°F, adherend thermal strain differences corresponding to differences in thermal expansion coefficients have the effect of adding a fictitious load to the joint at temperatures below the cure temperature. (Above the cure temperature it might be expected that softening of the adhesive would eliminate the generation of thermal stresses.) On the basis of a Volkersen analysis[5] applied to a single-lap joint, it can be shown that the following

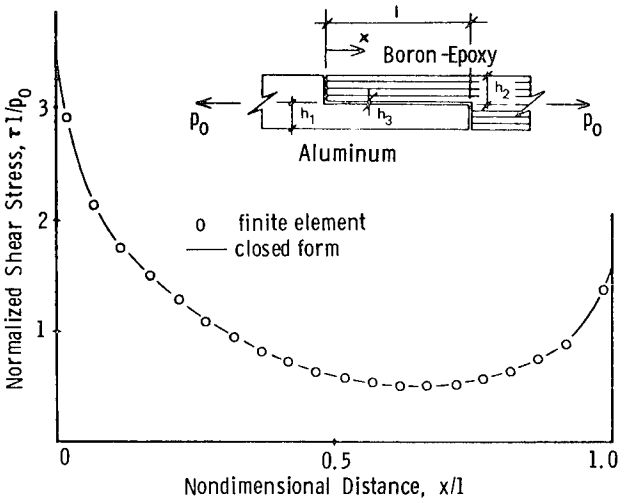


Figure 7. Shear-stress distribution in single-step joint, aluminum–boron epoxy.[14] $h_1 = h_2 = 0.1\ell$; $h_3 = 0.01\ell$.

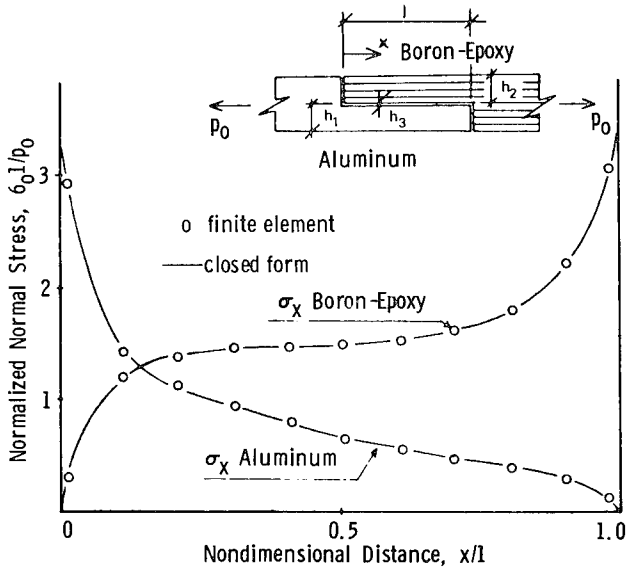


Figure 8. Normal stress in single-step joint, aluminum–boron epoxy.[14] $h_1 = h_2 = 0.1\ell$; $h_3 = 0.01\ell$.

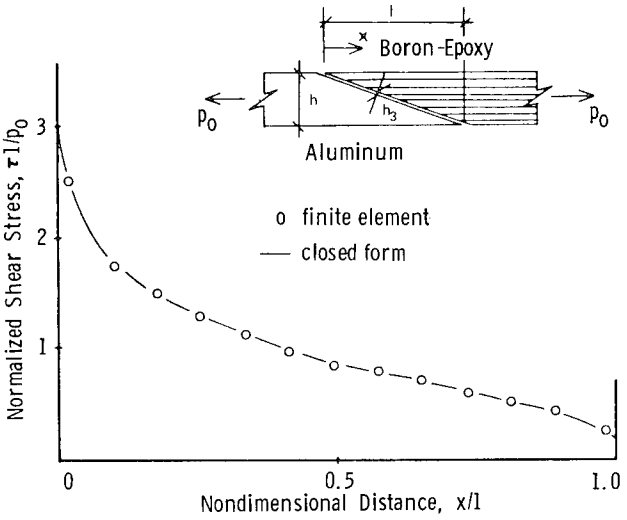


Figure 9. Adhesive shear-stress distribution in aluminum–boron epoxy scarf joint.[14] $h = 0.21\ell$; $h_3 = 0.001\ell$.

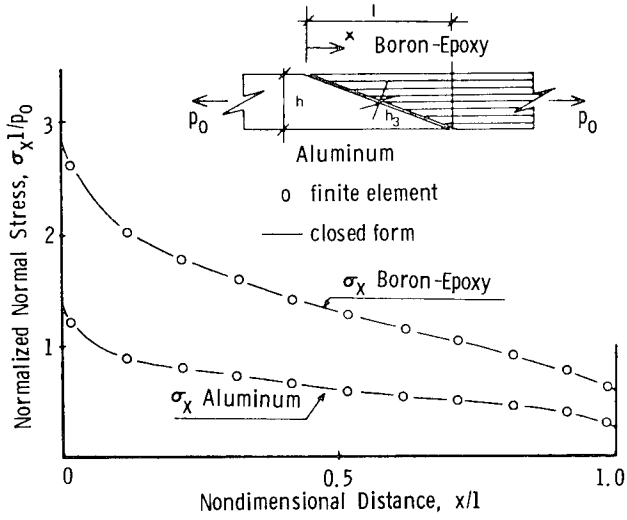


Figure 10. Normal stress distribution in aluminum–boron epoxy scarf joint.[14] $h = 0.21\ell$; $h_3 = 0.001\ell$. Figures 7–10 Reprinted with permission of the American Institute of Aeronautics and Astronautics.

expression for adhesive shear stress results when thermal mismatch of the adherends is taken into account:

$$\tau_a = \lambda \left[(\sigma_{u0} - \sigma_{\ell T}) \frac{B_u}{B_u + B_\ell} \frac{\cosh \frac{\lambda}{t_u}(\ell - x)}{\sinh \frac{\lambda}{t_u}\ell} + \left(\frac{B_\ell \sigma_{u0} + B_u \sigma_{\ell T}}{B_u + B_\ell} \right) \frac{\cosh \frac{\lambda}{t_u} x}{\sinh \frac{\lambda}{t_u}\ell} \right] \tag{31}$$

where $\sigma_{\ell T} = E'_\ell (\alpha_u - \alpha_\ell) \Delta\theta$, α_u and α_ℓ being thermal expansion coefficients while $\Delta\theta$ is the difference in temperature from the curing temperature (or more particularly, the temperature at which the adhesive becomes rigid). Maximum values of τ_a occur as before at $x = 0$ and $x = \ell$. For nonidentical adherends the $(\tau_a)_{\max}$ values without thermal mismatch effects for $\frac{\lambda \ell}{t_u} > 3$ are:

$$(\tau_a)_{\max} \begin{pmatrix} x = 0 \\ \theta = 0 \end{pmatrix} = \frac{B_u}{B_u + B_\ell} \lambda \sigma_0 \; ; \; (\tau_a)_{\max} \begin{pmatrix} x = \ell \\ \theta = 0 \end{pmatrix} = \frac{B_\ell}{B_u + B_\ell} \lambda \sigma_0 \tag{32}$$

in contrast with the results for identical adherends given in equation (18). With thermal mismatch present we get

$$\begin{aligned} (\tau_a)_{\max} (x = 0) &= (\tau_a)_{\max} \begin{pmatrix} x = 0 \\ \theta = 0 \end{pmatrix} \left(1 - \frac{\sigma_{\ell T}}{\sigma_0} \right) \; ; \\ (\tau_a)_{\max} (x = \ell) &= (\tau_a)_{\max} \begin{pmatrix} x = \ell \\ \theta = 0 \end{pmatrix} \left(1 + \frac{B_u}{B_\ell + B_u} \frac{\sigma_{\ell T}}{\sigma_0} \right) \end{aligned} \tag{33}$$

The maximum shear stress is increased at $x = \ell$ by a fraction $\left(1 + \frac{B_u}{B_\ell + B_u} \frac{\sigma_{\ell T}}{\sigma_0} \right)$ and decreased at $x = 0$ by a fraction $\left(1 - \frac{\sigma_{\ell t}}{\sigma_0} \right)$, assuming that $\sigma_{\ell t} > 0$. For identical adherends the maxima are

$$\frac{(\tau_a)_{\max}}{\sigma_0} = \frac{\lambda}{2} \left(1 \pm \frac{\sigma_{\ell T}}{\sigma_0} \right)$$

Effect of thermal mismatch on the peel stresses may be evaluated in a similar manner.

The effect of creep at high temperatures in providing for relaxation of the thermal stresses has been discussed in Reference 8. The need for investigating the adhesive viscoelastic properties to identify approaches to joint fabrication (*i.e.*, time and temperature programming associated

with the curing cycle) which will minimize thermal stresses at typical temperatures for which the structure is intended is obvious. Valuable guidance for selecting desirable adhesive characteristics based on such a study may be obtained. If the structure is used over a wide range of temperatures, it may be difficult to avoid detrimental thermal stress buildup, in which case redesign of the joint to provide greater flexibility may be necessary.

Nonlinear Response

Nonlinear analyses of adhesive joints have been carried out by Hart-Smith,[7–9] by Dickson *et al.*,[12] and by Grimes *et al.*[16] The approach taken by Hart-Smith, while based on a relatively elementary extension of the Volkersen analysis, gives a good feeling for the impact of adhesive nonlinearity on joint performance. In the double-lap joint analysis Hart-Smith[8] bases the bulk of his results on the assumption of an elastic-perfectly plastic stress–strain curve for the adhesive in shear, while assuming linear response in the peeling mode. The shear stress–strain curve is made up of an elastic part in which the linear relation

$$\tau_a = G_a \gamma_a \tag{34}$$

holds up to an ultimate stress τ_p, corresponding to yield strain γ_e:

$$\gamma_e = \frac{\tau_p}{G_a} \tag{35}$$

beyond which τ_a is constant. The adhesive is assumed to fail at an ultimate strain γ_p; the ratio ρ_{ep},

$$\rho_{ep} = \frac{\gamma_p}{\gamma_e} \tag{36}$$

is called the ductility. Due to the fact that τ_a is constant (*i.e.*, $\tau_a = \tau_p$) in the plastic zone the equilibrium equation

$$\frac{dN_u}{dx} = \tau_a$$

integrates to give a change of adherend load, ΔN_u,

$$\Delta N_u = \ell_p \tau_p \tag{37}$$

where ℓ_p is given by

$$\frac{\ell_p}{t_u} = \frac{(2\rho_{ep})^{1/2}}{\lambda} \tag{38}$$

in which

$$\lambda = \left(\frac{G_a t_u}{E'_u t_a}\right)^{1/2} \left(1 + \frac{E'_u t_u}{E'_\ell t_\ell}\right)^{1/2}$$

is obtained from the Volkersen analysis for elastic response. Corresponding to ΔN_u, the increase in upper adherend extensional stress, $\Delta\sigma_{u0}$, occurring in the plastic zone, after appropriate algebra, is found to be

$$\Delta\sigma_{u0} = \frac{\sqrt{2E'_u \frac{t_a}{t_u}}\sqrt{\tau_p \gamma_p}}{\sqrt{1 + \frac{E'_u t_u}{E'_\ell t_\ell}}} \tag{39}$$

Note the appearance of the plastic strain energy $\tau_p\gamma_p$ as a factor controlling the adherend stress increment $\Delta\sigma_{u0}$. The similar contribution of plastic strain energy to the total stress σ_{u0} was pointed out by Hart-Smith. In connection with peeling stresses, Hart-Smith discussed an approximate form of analysis in which τ_a is purely plastic (equal to τ_p) while the peeling stress is governed by the elastic equation

$$\frac{d^4\sigma_a}{dx^4} + 4\Lambda^4 \sigma_a = 0 \tag{40}$$

obtained from equation (7.2) when $d\tau_a/dx$ is set equal to zero. The peeling stress then has the form

$$\sigma_a = C \cosh \Lambda \frac{x}{t_u} \cos \Lambda \frac{x}{t_u} + D \sinh \Lambda \frac{x}{t_u} \sin \Lambda \frac{x}{t_u} \tag{41}$$

where C and D are determined so as to equilibrate the moment and shear force V, induced at the adherend end by the presence of τ_p in the adhesive. The peel stress is found to have a peak value given by

$$\frac{(\sigma_a)_{\max}}{\sigma_{u0}} = \left[\frac{3}{2}(1 + \lambda)(1 + \nu_a)\frac{E_a t_u}{E'_u t_a}\right]^{1/4} \frac{\lambda}{(2\rho_{ep})^{1/2}} \tag{42}$$

where it is noted that a large adhesive ductility has the effect of significantly reducing $(\sigma_a)_{\max}$. Equations (39) and (42) demonstrate the importance of ductility in allowing large adherend stress to be developed for a given ultimate shear stress in the adhesive, and in reducing $(\sigma_a)_{\max}$.

The Hart-Smith formulation, although providing important insight into the role of adhesive plasticity, does not appear completely consistent because of the assumption of elastic response of the adhesive in

peeling in combination with elastic-plastic response in shear. Dickson *et al.*[12] and Grimes *et al.*[16] give what appears to be a more consistent approach in which the peel and shear stress are combined in the yield criterion in the form of an effective stress, $\bar{\sigma}$:

$$\bar{\sigma} = (3\tau_a^2 + \sigma_a^2)^{1/2} \tag{43}$$

which is used in conjunction with a Ramberg Osgood law to calculate the following plastic strains:

$$\varepsilon_{xp} = -\frac{1}{2}\frac{\bar{\varepsilon}_p}{\bar{\sigma}}\sigma_a$$

$$\varepsilon_{zp} = \frac{\bar{\varepsilon}_p}{\bar{\sigma}}\sigma_a \tag{44}$$

$$\gamma_{xzp} = 3\frac{\bar{\varepsilon}_p}{\bar{\sigma}}\tau_a$$

where the ratio $\bar{\varepsilon}_p/\bar{\sigma}$ is given in terms of $\bar{\sigma}$ by

$$\frac{\bar{\varepsilon}_p}{\bar{\sigma}} = \frac{1}{7G_a}\left(\frac{\bar{\sigma}}{\sigma_0}\right)^{n-1}$$

in which σ_0 and $n - 1$ are constants derived from the experimental stress–strain law for the adhesive. The result of adding the plastic adhesive strains to the corresponding elastic strains, $\varepsilon_{xe} = -\frac{\nu_a}{E_a}\sigma_a$, $\varepsilon_{ze} = \frac{\sigma_a}{E_a}$, and $\gamma_{xze} = \frac{\tau_a}{G_a}$ gives rise to a set of equations identical to equations (7) with the replacement of zero on the right-hand side by

$$\eta_1\frac{d^2\gamma_{xzp}}{dx^2} - \eta_2\frac{d^3\varepsilon_{zp}}{dx^3} \tag{45}$$

in equation (7.1) and

$$\eta_3\frac{d^2\gamma_{xzp}}{dx^2} - \eta_4\frac{d^3\varepsilon_{zp}}{dx^3}$$

in equations (7.2), where η_k's are constants related to differences in the elastic constants of equations (4) for the upper and lower adherends. An iterative method for solving the resulting system is described in Reference 13. The set of equations obtained in Reference 12 is the eighth-order system in σ_a and τ_a allowing for transverse shear and thickness normal deformations in the adherends with the addition of the terms in expressions.[45] In both cases the iterative approach is started with the elastic formulation given by equation (7) or the analogous higher order system obtained in[11,12] providing initial solutions. In Reference 13 the

exponential functions obtained from the elastic solution are multiplied by functions of x determined from a standard approach, the "method of variation of constants," used to obtain particular solutions for ordinary differential equations.

Fracture-Mechanics Considerations

Fracture in adhesive-joined composite structures tends to occur either in the adhesive layer or between plies adjacent to the bond. Under fatigue the bond failure or ply separations tend to propagate in the manner of cracks in homogeneous structures. Application of fracture-mechanics approaches as a means of predicting crack-growth rates in fatigue appears desirable.

Observations on the nature of adhesive failure in bonded joints are discussed by Mostovoy *et al.* in Reference 17. Williams discussed fracture-mechanics approaches appropriate to adhesive joints.[18] A simplified approach which appears attractive in keeping with the strength-of-materials approaches treated here was that of DeVries *et al.*,[19] who used the Goland–Reissner approach to predict energy release rates as a function of unbond length in metallic joints. An application of this type of approach to analysis of composite joints would give a first-cut picture of crack propagation which would be useful for life-prediction applications when judiciously combined with appropriate experimental results. Allowance for adherend thickness normal and shear deformations would probably be desirable in such analyses. This would entail an appropriate extension of the Goland–Reissner approach such as that in References 11 and 12. An important part of such analyses is that of separating energy release associated with peel stress from that associated with shear stress. The simultaneous presence of these stresses gives rise to combined failure modes. Available test data on adhesives have been primarily for Mode-I (peel stress) failures, although some experimental results have suggested that failure under pure shear is really a form of Mode-I (cleavage) failures, since cracks tend to run at 45° to the bond layer, zigzagging back and forth after reflecting off the adherends. For shear loading, the 45° direction corresponds to the direction of principal stress and as such would govern the direction of cleavage failure.

A variety of contiuum approaches have been directed toward unbonds between dissimilar materials, analogous to a bond failure. Keer,[20] for example, used an integral equation formulation which was solved numerically using the Gauss–Chebyshev approach of Erdogan and Gupta.[21] Numerical formulations of this type may be fruitfully combined with finite-element or collocation approaches.

ANALYSIS OF MECHANICALLY FASTENED JOINTS

Ojalvo[22] has reviewed the state of the art of analysis of mechanically fastened structural joints. Other pertinent literature is discussed by Murphy and Lenoe[1] and by Kutscha and Hoffer.[2] Until recently, the bulk of the analytical results which have been available for bolt and pin-loaded structures have been classical two-dimensional elastic analyses of isotropic plates containing inclusions. The work of Bickley,[23] Knight,[24] Howland,[25] and Theocaris[26] are representative of such efforts. In the case of composite materials, Waszczak and Cruse[27] discussed the application of finite-element methods to pin-loaded composite strips in which the effect of the pin was represented by a "half-cosine" radial pressure distribution. Results consisted of a description of failure modes predicted by the finite-element approach using a distortional energy failure rule in conjunction with the assumption that first damage to any ply represents final failure. Modifications of the analysis allowing for progressive damage were also discussed. Waszczak[28] described a superposition approach in which stresses around an unloaded hole in a finite strip were combined with stresses in an infinite plate loaded by a pin. In Reference 28 as in Reference 27 the assumption of a half-cosine radial pressure distribution was used to represent interaction between the pin and the plate. The infinite case was treated by an analytical function approach, while corrections for finite geometry were made by use of the boundary integral equation (BIE) method of Cruse.[29] Oplinger and Gandhi[30,31] made extensive use of analytic function approaches in conjunction with least squares boundary collocation to treat single pins in finite strips and infinite plates as well as rows of uniformly spaced fasteners located a finite distance from the unloaded edge of the plate. These efforts featured a displacement boundary condition corresponding to rigid displacement of the fastener at the region of fastener–plate contact, as opposed to the half-cosine pressure distribution used in References 27 and 28. The effect of pin friction was discussed in Reference 31.

Two aspects of the analytical work on mechanically fastened joints are of interest: the prediction of stress concentrations and the description of conditions governing failure in terms of the resulting stresses. In regard to the stress concentration aspect, the effect of both fastener configuration and material parameters of the composite plate being joined are of interest. The subsequent discussion is organized along the lines of these considerations.

Stress Concentrations

Stress analysis of pin-loaded composite plates to date has been restricted[27,28,30,31] to two-dimensional elastic analyses of homogeneous

orthotropic plates used to represent typical laminate configurations. Although three-dimensional effects such as thickness deformation related to bearing failures and interlaminar shear resulting from ply-to-ply displacement incompatibilities probably play a significant role in joint performance, these have not received attention to date. Furthermore, it is reasonable to suspect that plastic deformation in many types of laminates has a sizable effect on stresses and failure conditions. Recent experimental results obtained from moiré surface strain measurements on pin-loaded 0/90° fiberglass strips by the author and his colleagues have supported this contention. Again, this type of behavior has been neglected in analytical work to date.

Figure 11 shows the fastener configurations which have been treated analytically. Waszczak and Cruse[27] considered the single fastener in a finite-width strip, Figure 11(A). Waszczak[28] dealt with the same configuration and in addition treated the single fastener, Figure 11(C), and a three-hole configuration, Figure 11(D), in an infinite plate, the latter being considered with tension at infinity and unloaded holes. Oplinger and Gandhi,[30,31] in addition to configurations (A) and (C) of Figure 11, dealt with a long row of equally spaced fasteners, Figure 11(B), loaded perpendicular to the line of centers.

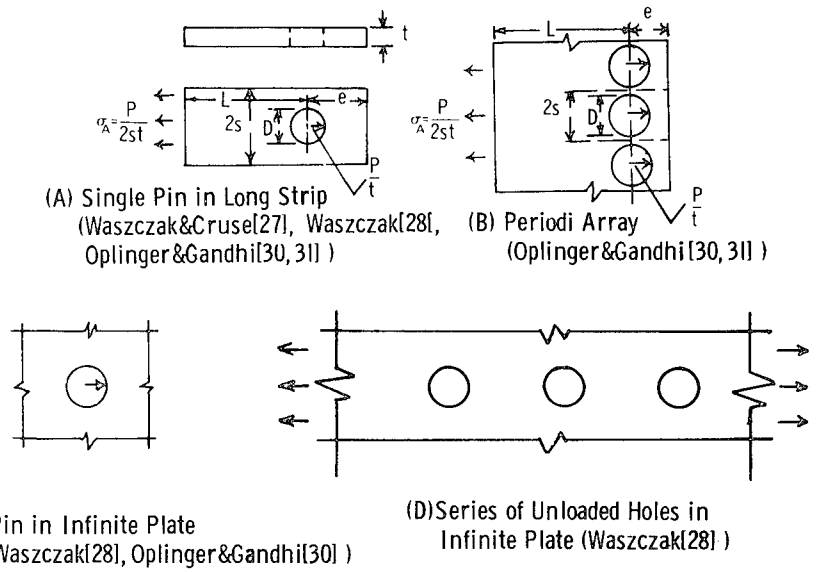


Figure 11. Mechanically fastened joints subjected to 2*D* elasticity solution.

As noted above, results obtained in References 27 and 28 were based on the assumption of a half-cosine radial pressure distribution at the edge of the hole. A more realistic definition of the mode of interaction between the pin and plate appears to be that of a displacement condition corresponding to rigid displacement of the pin in the region of contact together with a condition of zero radial pressure outside the contact region, the determination of the length of the contact region being part of the solution. The results of References 30 and 31 were based on this description of pin–plate interaction, an iterative method for determining the contact length being used. Results described in Reference 30 were for the friction-free case, while in Reference 31 results were included which described the effect of Coulomb friction between the pin and plate. Figure 12 shows distributions of radial pressure for several different situations treated in References 30 and 31 and illustrates the fact that in many cases the half-cosine distribution is not too far from reality. In one case (curve labeled with square symbols) corresponding to a small value of edge distance, e, significant departure from the half-cosine distribution occurs. A similar departure occurs in the case shown in Figure 13, where friction is taken into account. The departure is even more marked in the case of fasteners in series [Figure 11(D)] where the load exerted on the plate is only partly taken up by a given fastener. Figure 14 shows results obtained from the approach of References 30 and 31 on the radial pressure distribution for a strip in which part of the load is transmitted to the right-hand side of the strip which is assumed to com-

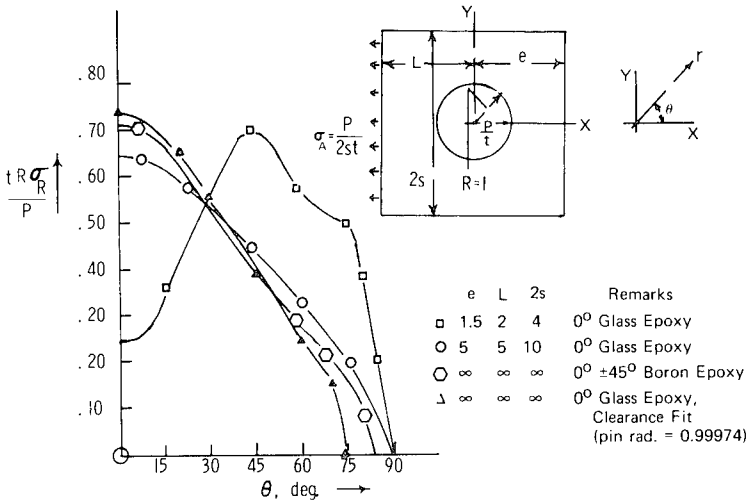


Figure 12. Radial stress distributions around fastener.[30]

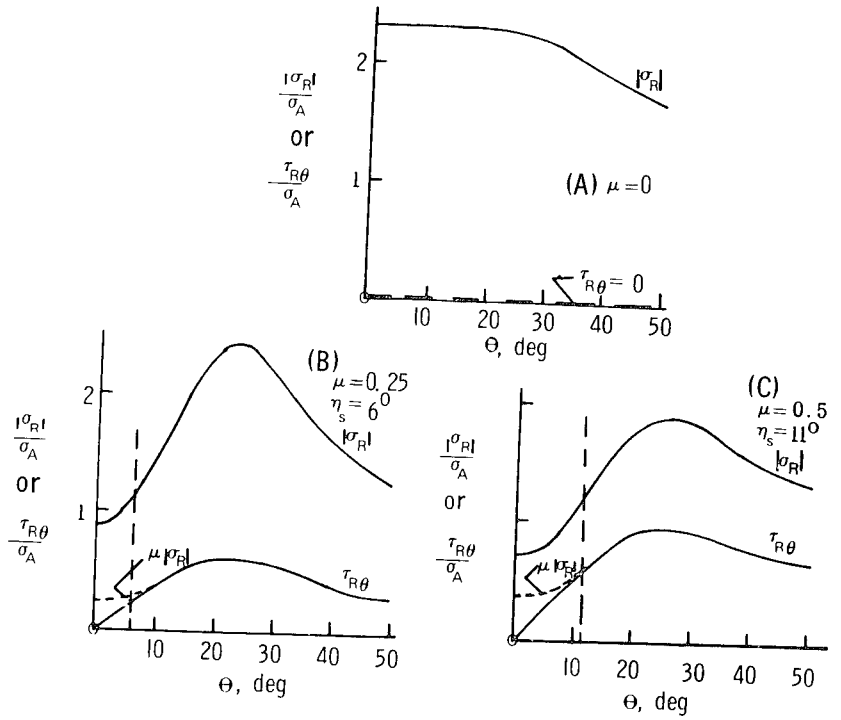


Figure 13. Effect of friction on radial and shear-stress distribution around fastener hole.[31] $0_2 \pm 45$ Graphite Epoxy $e/D = 4, s/D = 1$ (multipin).

municate with an adjacent fastener. As P_R/P_L increases toward unity, the radial pressure at $\theta = 0$ decreases until the contact region becomes split into two portions. In References 27 and 28 it was suggested that departures from the half-cosine pressure distribution do not seriously affect the overall stress state around the pin. However, it is clear that the prediction of bearing failures, and possibly of shear failure, requires an accurate description of the radial pressure. It is probably true that tensile stress at the 90° point (see Figure 15), the so-called peak "net section" stress, σ_{NS}, is not much affected by variations in the pressure distribution. The need for treating friction effects as well as for accurately determining the pressure distribution suggest that the use of a displacement condition at the pin is preferable to assuming the half-cosine pressure distribution, although the latter may be more convenient for making parametric studies on some aspects of joint design.

Geometric Effects. Figure 15 illustrates the definition of stress-concentration factors, K'_{NS} (net section tension), K'_{so} (shear-out), and K'_B

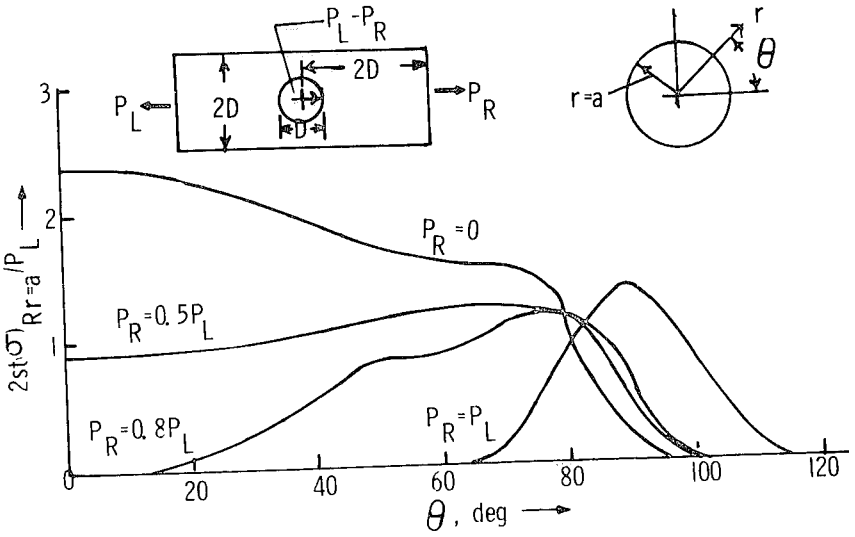


Figure 14. Radial stress distribution around partially loaded fastener $0_2 \pm 45$ Fiberglass Epoxy, $e/D = 2$.

(bearing) discussed in References 30 and 31. Note that these assume a nominal stress equal to the gross section stress given as σ_A in Figure 11(A),(B). The effect of side distance s [Figure 11(A), (B)] and edge distance e [Figure 11(A), (B)] on each of these stress-concentration factors is of considerable interest since they all may have a strong bearing on load-to-failure in various composite materials. In metals, on the contrary, the most important quantity is usually K'_{NS} since this controls maximum principle stress, failure initiation, and yielding. Figure 16 shows the variation of the three SCF's of interest as a function of s with e fixed in a typical laminate configuration. Note that Figure 16 applies to the periodic array configuration, Figure 11(B), and in this case s represents half the fastener spacing.

Similar trends are believed to hold for a single-fastener coupon, Figure 11(A), in which case s is half the width of the strip. The presence of minima in the K'_{NS} and K'_{so} curves is highly significant since it suggests the occurrence of an optimum fastener spacing given by $s/D = 1$. Larger s values produce higher values of all three SCF's while for s values smaller than D, the K'_{NS} and K'_{so} factors are again greater. It should be noted that the date of Theocaris[26] used to derive the curves given by Petersen[32] for the isotropic case gives a similar minimum in the K'_{NS} versus s/D curve at $s/D = 1$. The effect of edge distance on the SCF's is shown in Figure 17, with e normalized in terms of s for various values of

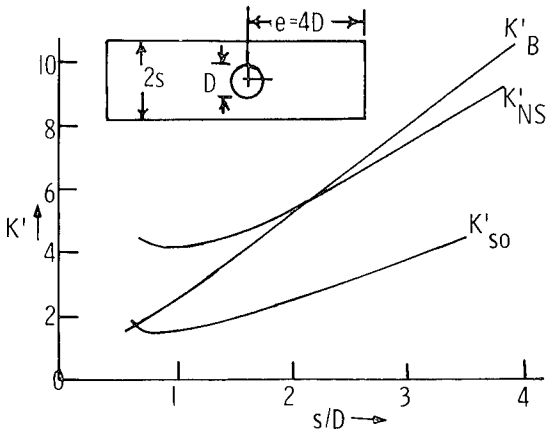


Figure 15. Definition of stress-concentration factors.

s/D. This mode of normalization of e is significant in that all curves reach a plateau at about the same value of e/s, independent of the value of s/D. This, in turn, means that if s/D is increased, the value of e/D beyond which the joint stresses become independent of e will increase proportionally. In such laminates as the 0/90° configuration where nonlinearity of shear response is significant, the curves of Figure 17 will be modified considerably. When this is not the case, the results of Figures 16 and 17 may be combined to provide the rule-of-thumb design for rows

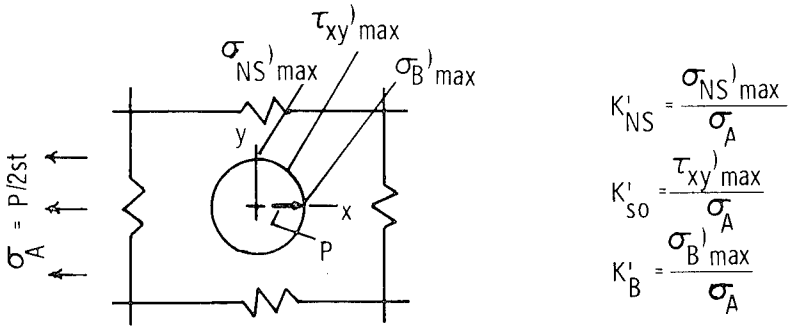


Figure 16. Effect of lateral fastener spacing, s, on stress concentrations.[30,31] Periodic array (Fig. 11(B)), $0_2 \pm 45$ Graphite Epoxy.

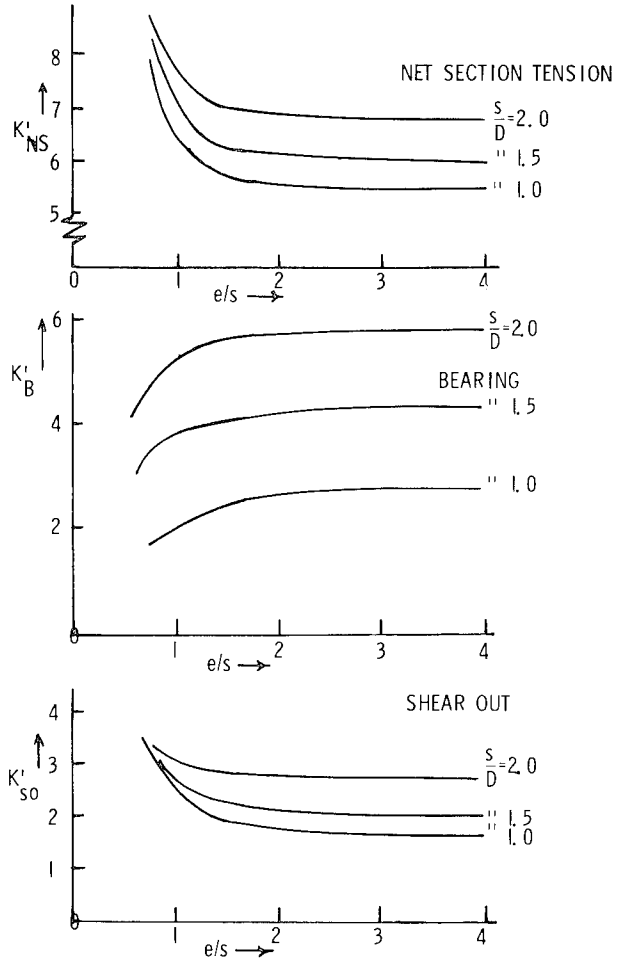


Figure 17. Effect of edge distance, e, on stress concentrations.

of fasteners, namely, that maximum joint strength is achieved by making $s/D = 1$ and $e/D = 2$. Larger values of e, while not reducing joint strength, entail excess joint material — which corresponds to a weight penalty. Where shear nonlinearity is present, e/D considerably larger than 2 may be required to achieve full-strength capability of the joint.

In addition to the above, differences between the single fastener [Figure 11(A)] and row configurations [Figure 11(B)] were explored in References 30 and 31. The net section tension is found to be higher and the shear-out and bearing stresses lower in the single-fastener configuration, which is often used for material evaluation and may therefore give

strength results somewhat at variance with performance of the laminate in a structure containing fastener rows. For $0_2 \pm 45$ graphite–epoxy laminates with $e/D = 4$, $s/D = 1$, K'_{NS} was 10% higher for the single-fastener coupon than for the row configuration, while K'_{so} was 13% lower and K'_B was 22% lower. Analogous fastener interference effects were considered in Reference 28 for column configurations [Figure 11(D)]. Results were given in the form of corrections to the distribution of hoop stress around the hole, the shear stress $\tau_{R\theta}$ being zero (frictionless case) and the radial pressure being given by the half-cosine distribution. Figure 18 gives a plot of the data presented in Reference 28 on the variation of σ_{NS} at the center fastener versus fastener separation in a three-hole configuration. In this case, as in that of the row configuration, fastener interactions cause a reduction of K'_{NS} from that occurring with widely spaced holes.

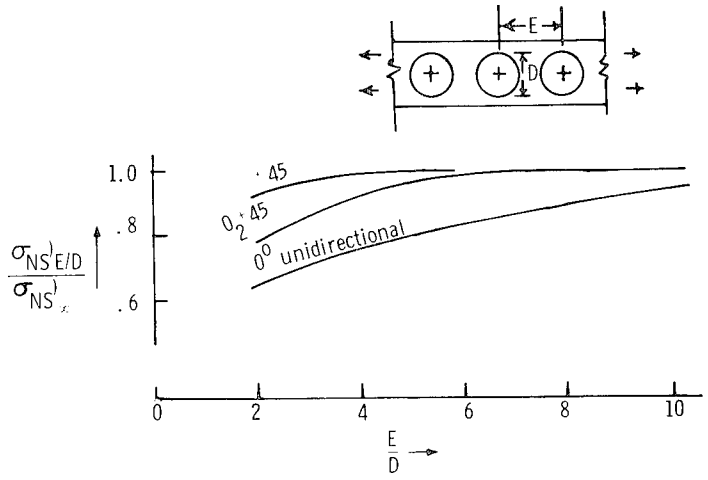


Figure 18. Effect of axial spacing of fastener holes on peak net section tension.[28] 0 ± 45 Boron Epoxy Laminates.

Effect of Material Parameters. The effect of material parameters on the three SCF's of interest is shown in Figure 19 for a fixed-geometry row configuration of fasteners. Here it is visualized that departure of the laminate from isotropy is due either to: (1) an unbalance in the Young's moduli in the 0° and 90° directions described in terms of the ratio $k_E = E_0/E_{90}$; or to (2) a departure of the shear modulus G_{xy} from the isotropic relationship $2G/E = 1/(1 + \nu)$, where ν is Poisson's ratio. In the latter case, E_0 and E_{90} are assumed to be equal and anisotropy is characterized by the parameter $k_G = 2G(1 + \nu)/E$. At the top of the two sets of curves

of Figure 19 are listed laminate configurations which would produce specific values of k_E or k_G lying on the horizontal axis. It is seen that over the range of k_E and k_G considered in Figure 19, K'_{NS} and K'_{so} vary by a factor of 2 to 3. While K'_B is relatively independent of material properties in the upper set of curves of Figure 19, it varies by about a factor of 3/2 in the lower set. As might be expected, K'_B and K'_{NS} are highest for 0/90° and 0° unidirectional laminates, while K'_{so} is highest for ± 45° laminates. Since laminate strength tends to vary much more rapidly with laminate configuration than the SCF's, high values of a given SCF as a function of the elastic constants do not necessarily indicate lowering of joint strength. As is generally necessary with composite structural analysis, it is essential to introduce anisotropic failure criteria along with stress-analysis results to draw valid conclusions about structural performance.

Failure Considerations

Failure predictions in laminates are often made by combining laminate stress predictions with one of the various failure rules (max stress, max strain, distortional energy) which have been suggested for unidirectional laminates. These are applied on a layer-by-layer basis by using appropriate laminate-analysis methods[33] to relate layer stresses to laminate stresses. In References 27 and 28 the Tsai–Hill distortional energy failure rule[34] was used for layer-failure predictions while in References 30 and 31 a modified form of this approach given by Hoffman[35] was used. The Tsai–Hill criterion is segmentally quadratic in the layer stresses normalized in terms of unidirectional laminate strengths, with changes in the normalizing factors corresponding to whether the extensional stresses which are present are tensile or compressive. The Hoffman criterion[35] is a modified quadratic rule which allows for changes in extensional stress from compression to tension in a continuous manner. Referring to the failure modes described in Figure 20, which represent typical failures in pin-loaded laminates, results based on the Tsai–Hill criterion[27] which illustrate the use of distortional energy contours (referred to as THC due to the connection to the "Tsai–Hill criterion") in predicting specific failure modes are given in Figure 21. An alternative method of presenting the failure-prediction data is shown in Figures 22 and 23.[31] Here the pin load which is predicted to cause failure at various points around the edge of the pinhole is plotted for different layers of a given laminate as a function of polar angle. Failure modes, not described in these figures, are determined by an auxiliary step involving consideration of individual stress components relative to corresponding unidirectional ply strengths. For example, in Figure 22 the low value of failure

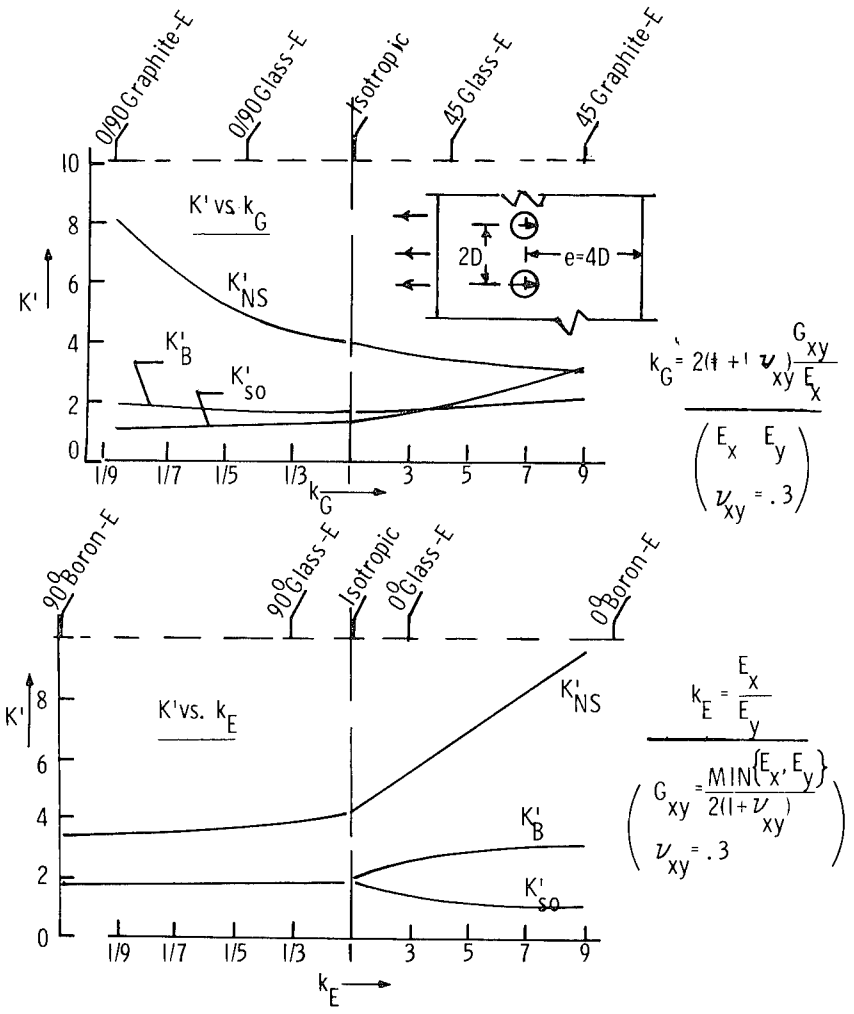


Figure 19. Effect of laminate elastic constants on stress concentrations, fastener geometry fixed [Periodic Array, Fig. 11(B)].

load in the 0° layer at $\theta = 0°$ is found to be due to hoop stresses which tend to produce cleavage. In the results shown in Figure 23, which represent the introduction of pin friction, cleavage failure in the 0° layer is suppressed (reflected in an increase in the failure load at $\theta = 0°$). In Reference 31 it was shown that pin friction tends to reduce hoop tension in the laminate to zero at $\theta = 0°$. The lowest failure load then falls in the +45° layer at about $\theta = 65°$, which would be expected to show up in the

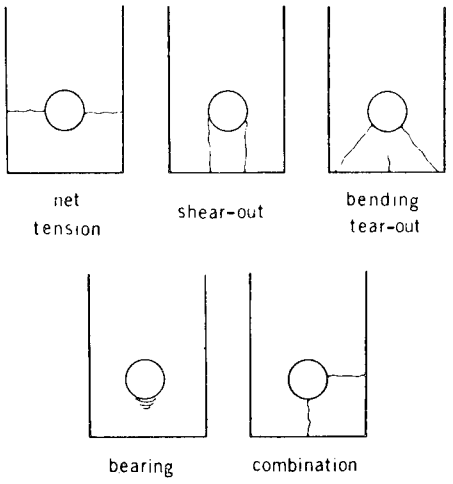


Figure 20. Failure modes in pin-loaded strip.

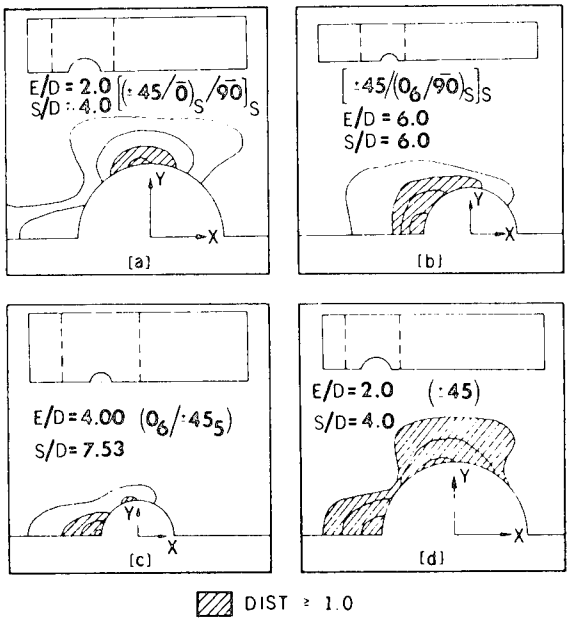


Figure 21. Distortional energy plots for bolt bearing specimens.[27] Reprinted with permission of Technomic Publishing Company.

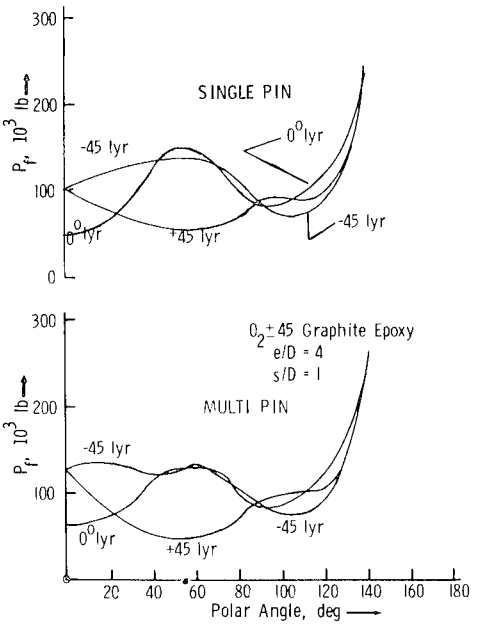


Figure 22. Failure load distribution around fastener hole, frictionless case.[31]

laminate as a shear-failure mode, since it is associated primarily with large τ_{xy} values.

Difficulties arise in universally applying the approaches just described, since they assume that failures will grow in a given layer under the same combination of stresses which the layer is embedded in a laminate or standing alone. In actuality, fibers in layers adjacent to an initially damaged ply may bridge the cracks and thus prevent growth of a predicted mode. Development of three-dimensional crack-stress analyses would be required to treat the effect of layer interaction. As an alternative, it may be feasible to treat incipient damage as a form of local softening analogous to plasticity. Figure 24 shows failed specimens of 0/90° fiberglass which were considered in AMMRC experimental studies. Moiré strain analysis results obtained on one such specimen at a load level below failure are shown in Figure 25. Severe distortion of the fringes in the upper part of the figure was found in preliminary evaluation of the displacement field to reflect nonlinear shear response. Figure 26 shows a comparison of the predicted shear strain obtained from the elastic analysis of References 30 and 31 with approximate strains evaluated from Figure 25, the approximation hinging on the assumption that

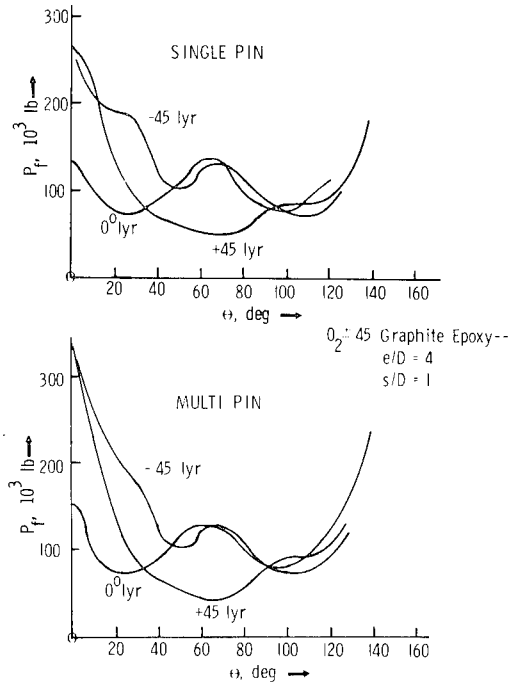


Figure 23. Failure load distribution around fastener hole, friction present.[31]

only the axial displacement gradient du/dy contributes to the shear strain. Further studies are underway to test this assumption by providing measurements of the V-displacement field. Note that the shear strains are given along the locus of maximum τ_{xy} (*i.e.*, the location of peak τ_{xy} when the latter is plotted as a function of y for a fixed x) indicated in the upper sketch of Figure 26. The fact that the observed strains shown in Figure 26 fall off much less sharply than the predicted strains based on elastic response gives a definite indication that nonlinearity in shear is present. Stress–strain curves for ± 45° glass–epoxy laminates strongly suggest the presence of shear nonlinearity in 0° and 0/90° laminates. Furthermore, the failure rule applied to the elastic analysis indicated that shear failure should occur at about 25% of the load which caused failure in the specimens shown in Figure 24. Shear failure in an individual ply would amount to the type of softening referred to above, being bridged by fibers of the adjacent plies. Nonlinear stress analyses are definitely called for to give more realistic predictions of stress-field development and ultimate failure.

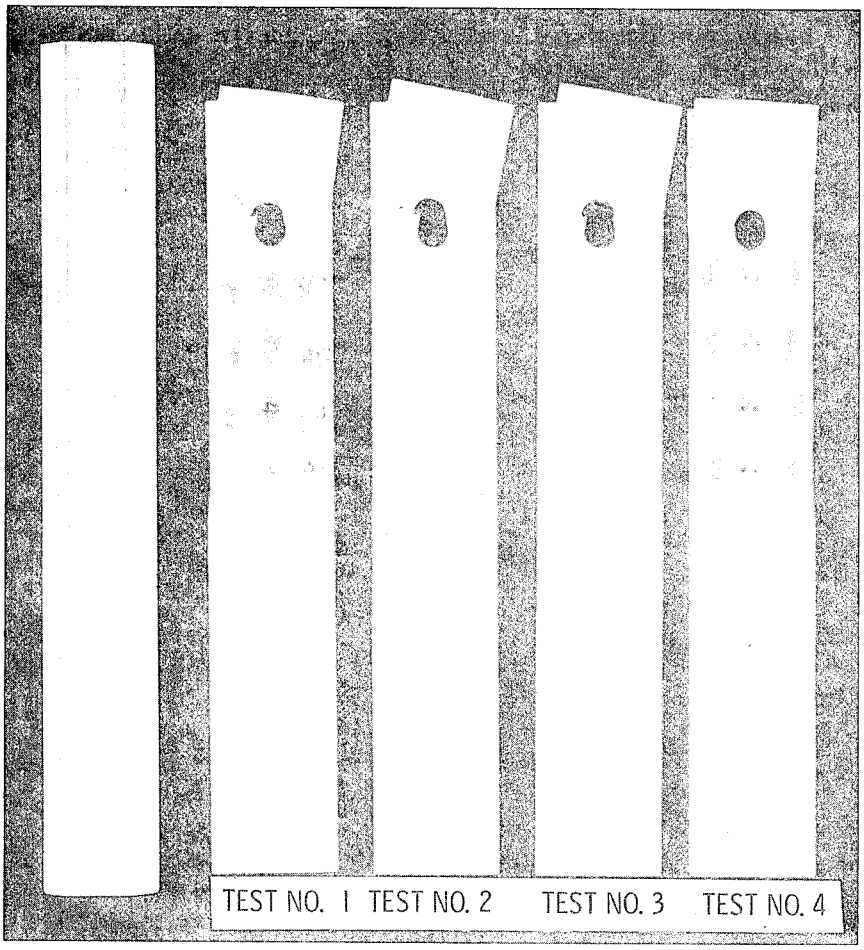


Figure 24. Failed pin-loaded fiberglass epoxy specimens 0/90 "Scotchply"* SC1002, 13 layers. (*Tradename, 3M Company)

Additional features in the failures shown in Figure 24 need attention. Specimens 1 and 3 illustrate a tendency for development of failure surfaces emanating from the hole at 45° to the specimen axis. The net tension failure shown in specimen 4 is more in line with what might be expected, based on where maximum tensile stresses in the 0° fibers are predicted by the two-dimensional elasticity analysis of References 30 and 31. Thus, there are apparently two available failure paths of nearly equal probability. The mechanism responsible for the 45° path is not apparent.

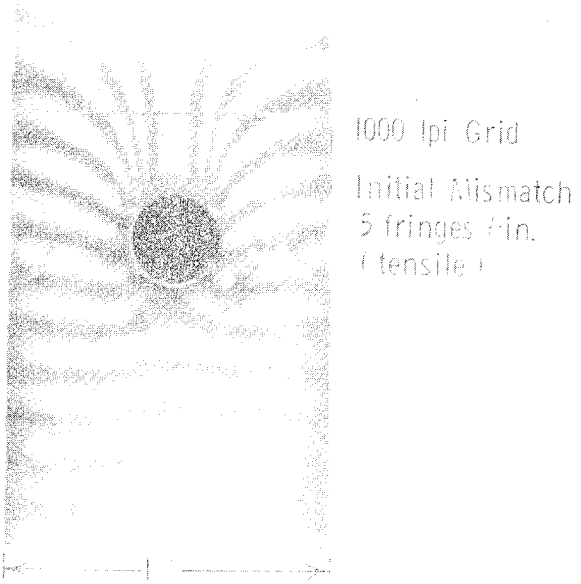


Figure 25. Moire fringe pattern (axial displacement fringes) in pin-loaded fiberglass epoxy strip. SC1002 $[(0/90)_6\bar{\emptyset}]_s$ stacking sequence (13 layers, 0.133" tk), 1000-lb load.

The presence of bearing damage at loads prior to final failure was a persistent feature in the tests. Bearing failure is indicated by a crazed appearance on the loaded side of the hole in Figure 24. Bearing failure may be associated with three-dimensional response, *i.e.*, out of plane-shear strains associated with Poisson expansion of the laminate due to in-plane compressive stress. Alternatively, bearing damage may correspond to failure obtained in uniaxial compressive strength tests. Three-dimensional analysis is necessary to investigate this type of failure as well as delamination associated with out-of-plane shear stresses in angle-ply laminates.

Joint Design Approaches

In addition to prediction of stresses and failure conditions around individual fasteners, methods are required for incorporating these results into a joint design. Invariably the presence of fasteners causes a local reduction of laminate strength which prevents loading of the laminate to its full capacity. Laminate strength can be recovered either by using

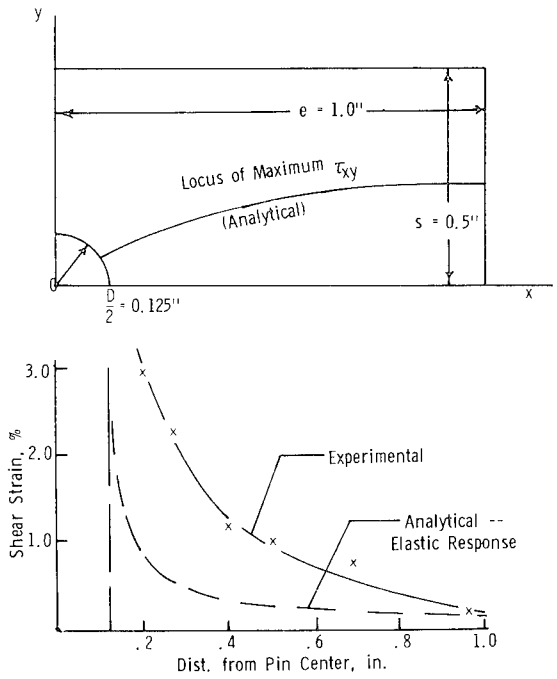


Figure 26. Experimental vs predicted shear-strain distribution in 0/90 fiberglass epoxy pin-loaded specimens.

multiple rows of fasteners or by thickening the laminate in the vicinity of the fasteners. Either approach results in an unavoidable weight penalty and careful attention to the design is required to minimize this.

A design synthesis approach for multirow fastener configurations is discussed in Reference 28. In addition to determination of stress concentrations and failure modes, the design process requires a determination of load distribution among various fastener rows. Simple redundant structural analyses have been frequently used to perform this step. Once the displacement field around an individual fastener is known in terms of load transmitted to the fastener and its neighbors, the stiffness array required for completing such an analysis can be generated. Kutscha and Hoffer[2] review a number of methods for pursuing the load-distribution analysis. A version which ignores the effect of deformations in the fastener is used by Waszczak.[28] As pointed out by Ojalvo,[22] accurate completion of the analysis requires a solution of the single-fastener problem using the displacement-type boundary condition around the hole to allow for the effect of variation of contact angle with load. The results shown in Figure 14 are representative of such an approach.

SUMMARY

Adhesive Joints

Stress analyses of adhesive joints have been made available for advanced geometries such as scarf and step joints as well as for the classical single- and double-lap configurations with uniform thickness adherends. Although finite-element treatments are readily available, valuable understanding of the role of various geometric and material parameters on joint strength can be obtained with closed-form analyses. For organic matrix composites with relatively low E_z and G_{xz}, the use of the more sophisticated closed-form analyses allowing for thickness normal and out-of-plane shear deformations is generally advisable. Even so, the rudimentary Volkersen membrane analysis modified to allow for variations in adherend thickness gives important insight into geometric design aspects of scarf, stepped, and other advanced joint configurations.

Thermal and curing effects in joints have received considerable attention in joint-stress analyses but may bear further investigation in regard to the details of how viscoelastic response of the adhesive varies throughout the curing cycle. Detailed experimental knowledge of the mechanical properties of the adhesive during this period is essential for carrying out such an investigation. Investigations which allow for nonlinear response in adhesive joints should be extended to give greater attention to adherend nonlinearity which is likely to be as important in organic matrix adherends as in typical adhesives. Few, if any, attempts at applying fracture mechanics to composite adherend joints have been made to date. Such work is needed to provide a clearer picture of factors controlling joint damage tolerance. Fracture-mechanics studies of composite joints should allow for the possibility of failures in plies adjacent to the adhesive as well as in the adhesive itself.

Mechanical Joints

Two-dimensional elastic stress analyses provide reasonably good understanding of design requirements for mechanically fastened composite joints. About the only aspect of joint design which has not been investigated by this route to date is that of staggered row configurations, which intuition suggests are the optimum type of configuration for a multirow array. An understanding of the role of pin friction is important for accurate failure-mode prediction in some laminates. In general the use of displacement boundary conditions at the fastener hole is preferable over assumed pressure distributions such as the half-cosine distribution.

Nonlinear response which seems to be present in certain laminate configurations should be given future attention. Improved failure rules providing alternatives to the "first ply failure" approach are desirable, in particular to allow for bridging of cracks by adjacent plies. Where shear failures are predicted by the "first ply failure" approach it seems especially important to determine whether the prediction is valid in the light of effects obviously produced by crack bridging.

Three-dimensional treatments are needed for assessing the role of bearing failure and for interlaminar shear failures.

Table 1. Comparison of Peak Shear Stresses for Various Joints (t = 0.033 in.)

	Single Lap (Volkersen Analysis)	5-Step Lap[10]		Scarf Joint[14]
$\lambda = \left(\frac{E_a t_u}{E_u' t_a}\right)^{1/2}$	0.8136	0.8136	1.4163	1.4163
$\frac{\ell}{t}$	75	75	54	90
$\frac{(\tau_a)_{max}}{(\tau_a)_{ave}} = \frac{\ell}{t}\frac{(\tau_a)_{max}}{\sigma_0}$	30.51	23.25	2.88	2.76
$\frac{(\tau_a)_{max}}{\sigma_0}$	0.4068	0.3063	0.0527	0.03036

REFERENCES

1. Murphy, M. M. and Lenoe, E. M., "Stress Analysis of Structural Joints and Interfaces — A Selective Annotated Bibliography," Army Materials and Mechanics Research Center, Watertown, Mass., Report No. AMMRC MS 74-10, September 1974. (AD 786 520)
2. Kutscha, D. and Hofer, K. E. Jr., "Feasibility of Joining Advanced Composite Flight Vehicle Structures," IIT Research Institute, Chicago, Ill. Air Force Materials Laboratory Contract Report No. AFML-TR-68-391, January 1969. (AD 690 616)
3. Sharpe, W. N. Jr. and Muha, T. J. Jr., "Comparison of Theoretical and Experimental Shear Stress in the Adhesive Layer of a Lap Joint Model," in *Proceedings of the Army Symposium on Solid Mechanics, 1974: The Role of Mechanics in Design — Structural Joints*. Army Materials and Mechanics Research Center, Watertown, Mass., Report No. AMMRC MS 74-8 (September 1974), 23–45. (AD 786 543)

4. Hart-Smith, L. J., "Advances in the Analysis and Design of Adhesive-Bonded Joints in Composite Aerospace Structures," in *New Industries and Applications for Advanced Materials Technology*, Proceedings of the 19th National SAMPE Symposium and Exhibition, Buena Park, Calif., 23–25 April 1974. Azusa, Calif.: Society for the Advancement of Materials and Process Engineering (1974), 722–37.
5. Volkersen, O., "Die Nietkraftverteilung in zugbeanspruchten Nietverbindungen mit konstaten Laschenquerschnitten," *Luftfahrt. Forsch.*, **15** (1938), 41–47.
6. Goland, M. and Reissner, E., "The Stresses in Cemented Joints," *J. Appl. Mech.*, **11** (1944), 17–27.
7. Hart-Smith, L. J., "Adhesive-Bonded Scarf and Stepped-Lap Joints," Douglas Aircraft Company, Inc., McDonnell-Douglas Corporation, Long Beach, Calif., National Aeronautics and Space Administration Contract Report No. NASA-CR-112237, January 1973. (N74-13197)
8. Hart-Smith, L. J., "Adhesive-Bonded Double-Lap Joints," Douglas Aircraft Company, Inc., McDonnell-Douglas Corporation, Long Beach, Calif., National Aeronautics and Space Administration Contract Report No. NASA-CR-112235, January 1973. (N74-13195)
9. Hart-Smith, L. J., "Adhesive-Bonded Single-Lap Joints," Douglas Aircraft Company, Inc., McDonnell-Douglas Corporation, Long Beach, Calif., National Aeronautics and Space Administration Contract Report No. NASA-CR-112236, January 1973. (N74-13196)
10. Erdogan, F. and Ratwani, M., "Stress Distribution in Bonded Joints," *J. Composite Mater.*, **5** (1971), 378–93.
11. Renton, W. J. and Vinson, J. R., "The Analysis and Design of Composite Material Bonded Joints Under Static and Fatigue Loadings," University of Delaware, Newark, Air Force Office of Scientific Research Contract Report No. AFOSR-TR-73-1627, August 1973. (AD 766 932)
12. Dickson, J. N., Hsu, T-M., and McKinney, J. M., "Development of an Understanding of the Fatigue Phenomena of Bonded and Bolted Joints in Advanced Filamentary Composite Materials, Vol. 1. Analysis Methods," Lockheed-Georgia Company, Marietta, Air Force Flight Dynamics Laboratory Contract Report No. AFFDL-TR-72-64-Vol. I, June 1972. (AD 750 132)
13. Whitney, J. M., "The Effect of Transverse Shear Deformation on the Bending of Laminated Plates," *J. Composite Mater.*, **3** (1969), 534–47.
14. Barker, R. M. and Hatt, F., "Analysis of Bonded Joints in Vehicular Structures," *AIAA J.*, **11** (1973), 1650–54.
15. Williams, M. L., "On the Stress Distribution at the Base of a Stationary Crack," ASME Paer 56-A-16, 1956.
16. Grimes, G. C., Greimann, L. F., Wah, T., Commerford, G. E., and Blackstone, W. R., "The Development of Nonlinear Analysis Methods for Bonded Joints in Advanced Filamentary Composite Structures," Southwest Research Institute, San Antonio, Tex., Air Force Flight Dynamics Laboratory Contract Report No. AFFDL-TR-72-97, September 1972. (AD 905 201L)

17. Mostovoy, S., Ripling, E. J., and Bersch, C. F., "Fracture Toughness of Adhesive Joints," *J. Adhes.*, **3** (1971), 125–44.
18. Williams, M. L., "Stress Singularities, Adhesion, and Fracture," in *Proceedings of the Fifth U.S. National Congress of Applied Mechanics*. New York: American Society of Mechanical Engineers (1966), 451–64.
19. DeVries, K. L., Williams, M. L., and Chang, M. D., "Adhesive Fracture of a Lap Shear Joint," *Exper. Mech.*, **14** (1974), 89–97.
20. Keer, L. M., "Stress Analysis for Bonded Layers," *Trans. ASME, Ser. E, J. Appl. Mech.*, **41** (1974), 679–83.
21. Erdogan, F. and Gupta, G. D., "On the Numerical Solution of Singular Integral Equations," *Quart. Appl. Math.*, **29** (1971–72), 525–34.
22. Ojalvo, I., "Survey of Mechanically Fastened Splice-Joint Analysis," in *Advances in Joining Technology*, ed. by J. J. Burke and A. E. Gorum. Chestnut Hill, Mass.: Brook Hill Publishing Company (1976).
23. Bickley, W. G., "Distribution of Stress Round a Circular Hole in a Plate," *Phil. Trans. Roy. Soc., London, Ser. A*, **227** (1928), 383–415.
24. Knight, R. C., "The Action of a Rivet in a Plate of Finite Breadth," *Phil. Mag., Ser. 7*, **19** (1935), 517–40.
25. Howland, R. C. J., "On Stresses in Flat Plates Containing Rivet Holes," paper presented at 3rd International Congress of Applied Mechanics, 1930.
26. Theocaris, P. S., "The Stress Distribution in a Strip Loaded in Tension by Means of a Central Pin," *J. Appl. Mech.*, **23** (1956), 85–90.
27. Waszczak, J. P. and Cruse, T. A., "Failure Mode and Strength Predictions of Anisotropic Bolt Bearing Specimens," *J. Composite Mater.*, **5** (1971), 421–25.
28. Waszczak, J. P. and Cruse, T. A., "A Synthesis Procedure of Mechanically Fastened Joints in Advanced Composite Materials, Vol. II," Carnegie-Mellon University, Pittsburgh, Pa., Air Force Materials Laboratory Contract Report No. AFML-TR-73-145-Vol. 2, September 1973. (AD 771 795)
29. Cruse, T. A., "Application of the Boundary-Integral Equation Method to Three Dimensional Stress Analysis," *Comp. Struct.*, **3** (1973), 509–27.
30. Oplinger, D. W. and Gandhi, K. R., "Stresses in Mechanically Fastened Orthotropic Laminates," in *Proceedings of the Conference on Fibrous Composites in Flight Vehicle Design, Dayton, Ohio, 21–24 May 1974*. Air Force Flight Dynamics Laboratory Report No. AFFDL-TR-74-103 (September 1974), 811–42. (AD-B000 135L)
31. Oplinger, D. W., "Analytical Studies of Structural Performance in Mechanically Fastened Fiber-Reinforced Plates," in *Proceedings of the Army Symposium on Solid Mechanics, 1974: The Role of Mechanics in Design — Structural Joints*. Army Materials and Mechanics Research Center, Watertown, Mass., Report No. AMMRC MS 74–8 (September 1974), 211–42. (AD 786 543)
32. Peterson, R. E., *Stress Concentration Factors*. New York: John Wiley & Sons, Inc. (1974), 135–36.

33. Ashton, J. E., Halpin, J. C., and Petit, P. H., *Primer on Composite Materials: Analysis*. Stamford, Conn.: Technomic Publishing Company, 1969.
34. Tsai, S. W., "Strength Characteristics of Composite Materials," Annual Report January 1964–January 1965, Aeronutronic, Newport Beach, Calif. National Aeronautics and Space Administration Contract Report No. NASA-CR-224, April 1965. (N65-21641)
35. Hoffman, O. J., "The Brittle Strength of Orthotropic Materials," *J. Composite Mater.*, **1** (1967), 200–06.

SESSION VI

FRACTURE MECHANICS AND NDT

MODERATOR: W. S. HYLER
Battelle Columbus Laboratories

18. THE CONSIDERATION OF DAMAGE TOLERANCE IN THE DESIGN OF JOINTS

R. L. CIRCLE
Lockheed-Georgia Company
Marietta, Georgia

The total concept of damage tolerance is discussed — what is meant by the term "damage tolerance" and why it is important. A review of some general design requirements is presented along with a brief discussion of the latest approach to achieving a satisfactory damage tolerance design in aircraft.

Special problems are associated with achieving damage tolerance in joints. These problems are a result of inherent complexity, inspectability, and associated analytical requirements. These problems are discussed with some specific examples.

Design practices, both good and bad, as related to the damage tolerance of a joint are discussed. For example, minor design changes that can make a joint inherently damage tolerant are shown.

The influence of the damage tolerance of many things that are inherent to a design such as thickness, eccentricity, fastener pattern load transfer, and fastener interference is discussed. Specific examples of these effects on safe crack-growth time and critical crack length are shown, and emphasis placed on the factors that can be controlled in design.

INTRODUCTION

Damage tolerance can be described as the ability of a structure to sustain an injury. This injury, or damage, can come from many sources. Some of the more obvious sources are battle damage, corrosion, and fatigue cracking. It matters very little what the source is, but it matters a great deal what are the immediate and longer term results. A rising incidence of dangerous, costly, and unexpected failures in aircraft, pressure vessels, ship hulls, bridges, etc., is testimony enough that too many structures do not possess an adequate level of damage tolerance. Increasing demands on materials and structures to fill expanding perfor-

mance requirements while holding costs to a minimum have contributed to the failure problem. The documentation of failures is probably best recorded in the aircraft industry because of the catastrophic consequences involved. An excellent review can be found in Reference 1. In another tabulation by Kirby[2], only two out of 18 failures reviewed are not associated with some type of joint. It is relatively easy to conclude from this and other similar tabulations that if we could only get rid of joints we could get rid of most of our problems.

A structure should possess certain characteristics to be truly and effectively damage tolerant. One of the most important is inspectability. It matters little if some initial damage can be endured if that damage remains undetected until subsequent damage causes final failure.

Another characteristic required of damage-tolerant structure is to have an acceptably slow rate of crack growth and long critical crack lengths. This is the area where fracture mechanics has been of great help in evaluating a design. Materials selected to best meet crack-growth and critical length requirements will generally not be the material desired to best meet the static strength requirements, as pointed out by Krupp and Hoeppner[3] and many others who have observed the inverse relationship between yield strength and fracture toughness. High-strength steels are classic examples of this paradox where compromise must be reached by the designer.

So, for a structure to be truly damage tolerant it must possess a satisfactory ability to sustain damage, but be inspectable enough so damage can readily be found, plus have an adequate combination of slow growth and long critical lengths so that it will endure long enough for the damage to be discovered. Joints involving special problems in meeting these objectives will be discussed.

DESIGN REQUIREMENTS

Specific design requirements are needed to assure that damage tolerance objectives are met. Civil transport aircraft have been designed for many years to meet a form of damage tolerance, referred to as "fail-safe," and defined by Reference 4. Some companies such as the Lockheed-Georgia Company have internal design policies specified to achieve a level of damage tolerance.

The Air Force has recently published, after several years in the development, a most detailed and comprehensive specification[5] in order to ensure that future Air Force flight structures will be damage tolerant. The philosophy, background, and many of the Air Force requirements are contained in publications by Wood[6] and Tiffany.[7] These design re-

quirements were developed largely as the result of structural problems in nondamage tolerant designs that resulted in unacceptable cost in lives, vehicles, and maintenance.

The general approach taken by the Air Force design requirements is to assume that flaws exist in any new structure from the beginning and these flaws will then grow in service. While the requirements do cover all primary fracture critical structure, the interpretation of the requirements in joints involves the most detailed and interesting application and will be discussed.

The size of flaw to be assumed depends to some extent on the amount and type of inspection done during fabrication, in other words, what size flaw might be missed. Also three different design concepts are defined within which the designer may choose to show compliance with requirements, and the flaw assumptions depend on the concept chosen. These concepts are Slow Crack Growth, Fail-safe Multi-Load Path, and Fail-safe Crack Arrest. An example of the flaws to be assumed in a typical joint, at holes, are illustrated in Table 1. As footnoted in the table, smaller values may be used if special inspection techniques are employed and substantiated. Also, if special joint preparation is used, smaller values of flaw may be approved. Good examples of special joint preparation are high clamp-up, cold working, and high fastener interference. These have been shown to give marked improvement in joint life.[8]

Table 1. Air Force Damage Tolerance Requirements at Holes in Joints

Structural Concept	Flaw at Critical Hole*	Flaw at Other Holes
Slow Crack Growth	0.05 radius corner	0.005 radius corner
Fail-safe, multiload path	0.02 radius corner	0.005 radius corner
Fail-safe, crack arrest	0.02 radius corner	0.005 radius corner

*Smaller values may be used subsequent to demonstration of better inspection technique and/or benefits of special joint preparation.

If the designer chooses to meet the damage tolerance requirements with a multi-load-path type of structure, in addition to the intial damage assumptions of Table 1, the critical load path must be assumed failed. Subsequent to this load-path failure, the structure must be shown to survive for a specified period that depends on how easily the failure can be detected. Figures 1 and 2 illustrate the damage assumptions to be made in a typical multi-load-path joint. If the inspectability of the joint is such that a special close visual inspection would be required to find the dam-

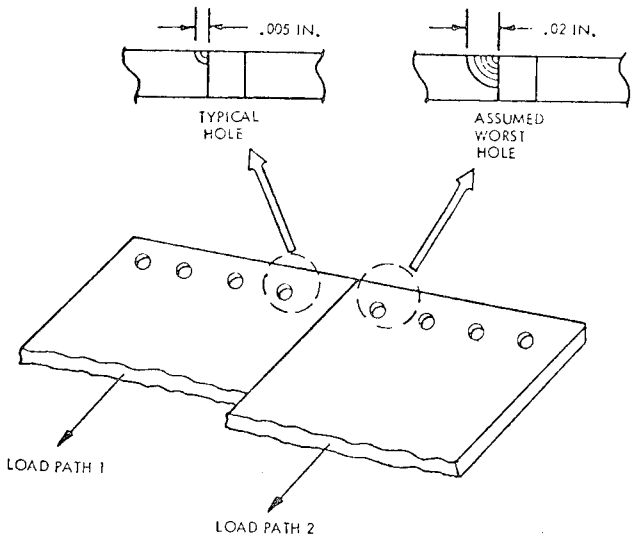


Figure 1. Assumed initial damage in new structure per mil-a-83444.

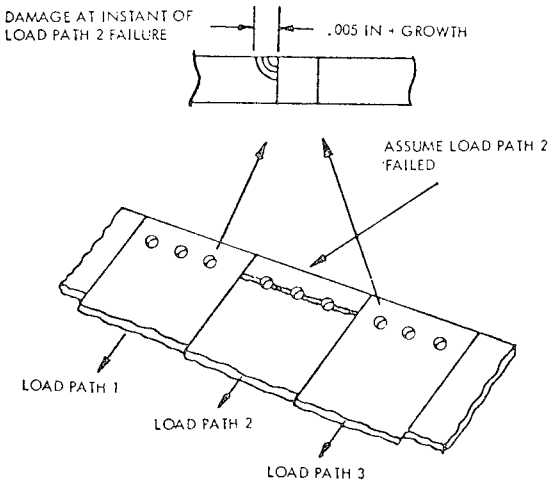


Figure 2. Multiload path failure assumption.

age shown in Figure 2, the joint must survive this damage for not less than two years. Other inspectability levels have different survival time period requirements. An important factor in these requirements is the concept that at the time load path 2 (in the example of Figure 2) fails, small damage is already present in the adjacent structure growing from the initial 0.005 in. flaw. This is a very brief review of the Air Force thinking on damage-tolerance requirements as applied to joints.

Design requirements can take other approaches but they should be specific and recognize the inspectability of the joint.

SPECIAL DAMAGE TOLERANCE PROBLEMS WITH JOINTS

As has been previously pointed out, the vast majority of structural problems occur at joints. Something then must be special about joints as compared to the more typical nonjoint areas. The complexity of joints is basically what brings on most of the problems, as well as the fact that these complexities are many times not understood or else present analytical problems beyond the capability of conventional analysis techniques to handle.

Along with complexity normally comes reduced inspectability. Overall damage tolerance is adversely affected by reduced inspectability as has previously been discussed. Figure 3 illustrates some joint designs where inspectability is difficult. You will note that in each example at least one part is hidden from view by another part. If corrosion, manufacturing defect, or fatigue were to damage the hidden part, total failure of the buried member could occur without warning. The damage tolerance of these joints can only be assured with an inspection involving disassembly of the joint or a special and extensive NDI procedure. Such inspections are not normally desirable and should be avoided. Consideration of inspectability as part of a good damage-tolerant design requires anticipation of probable cracking modes and providing a design where detection of such modes will be obvious. Many times a design that is very inspectable also automatically provides improved fail-safe or crack-arresting features. Figure 4 is a simple illustration of how this can work. The joint shown in Figure 4 will do the same job as the joint (a) in Figure 3. However the advantages from a damage-tolerance viewpoint are that (1) a crack in the basic plank will be observable between the tangs of the splice plate, and (2) a crack in a tang will be automatically arrested at the edge of the tang. This is a simple example to illustrate a point, but the improved damage tolerance afforded by the Figure 4 design probably would not be forthcoming unless the designer had in mind the requirements of inspectability and crack arrest.

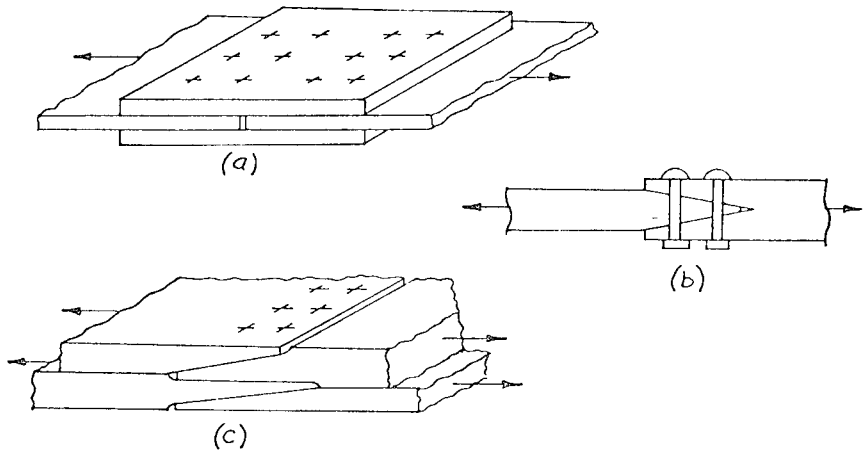


Figure 3. Typical joints with buried members.

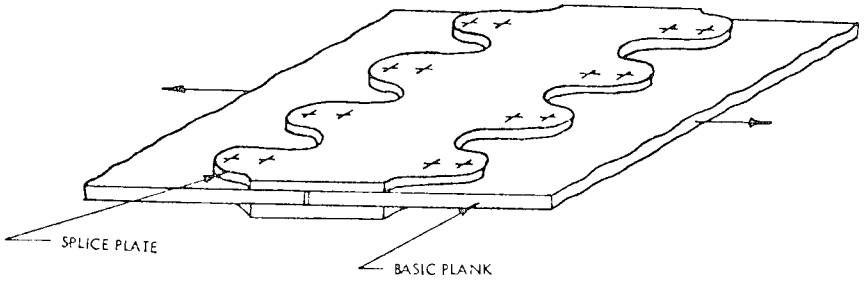


Figure 4. Scarfed type splice plate.

In addition to inspectability problems, the inherent complexities of joints present many analytical problems that must be dealt with. Among the things that present analytical problems are eccentricities, effects of load transfer, complex loading, and high stress gradients. The affect of eccentricity on damage-tolerance predictions can be dramatic. Figure 5 shows a joint where extensive machining and joggling was done in the design to minimize eccentricities. However, some eccentricity remained and was discovered by a strain survey on the actual hardware. The eccentricity resulted in local stresses in the critical area of the joint approximately 50% higher than that predicted. The curves of Figure 5 illus-

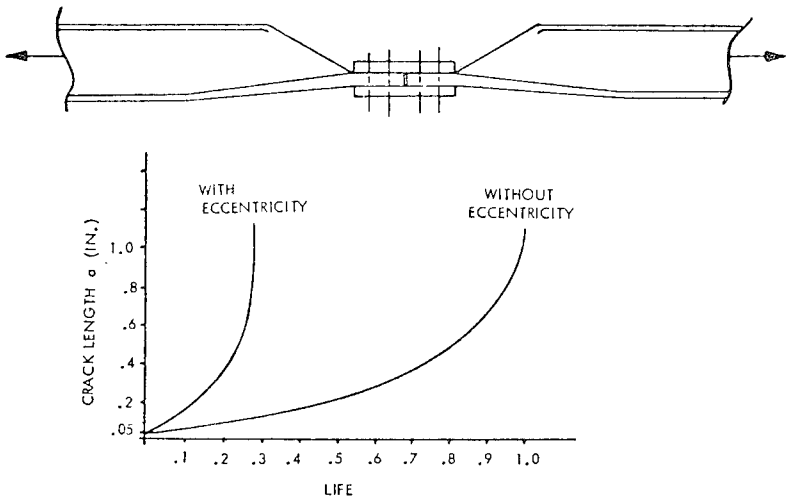


Figure 5. Influence of joint eccentricity on life.

trate the influence of this additional stress on crack-growth life. If possible, eccentricities should be avoided and the joint structural efficiency kept high. However, if some eccentricity is unavoidable, its effect should be accounted for in the damage-tolerance analysis.

Another special problem associated with most bolted joints is the effect of load transfer at the bolts. In order to predict accurately the damage tolerance of a joint, these load-transfer effects should be accounted for. The primary effect of bolt-hole load transfer is illustrated by Figure 6. Note that the load transfer by a bolt creates a local crack-opening force (or prying force) that can accelerate failure. This adds a level of analytical complexity above that required for simple static-strength analysis, however the increase in crack-tip stress intensity at cracks near loaded bolt holes can be dramatic. Grant[9] and Sih[10] have reported methods to account for this effect on crack-tip stress intensity. A method has also been developed at the Lockheed-Georgia Company[11] to account for load transfer. Figure 7 illustrates an example of the increase in crack-tip stress intensity that can result from joint load transfer. This example assumes a joint with two rows of bolts each side of the joint, the diameter of the bolts is equal to the thickness of the basic member, and the bolt hole is filled by the bolt without clearance or interference. Also shown in Figure 7 is predicted crack-growth life with and without consideration of load transfer. Obviously such an influence should not be overlooked in a good damage-tolerance design.

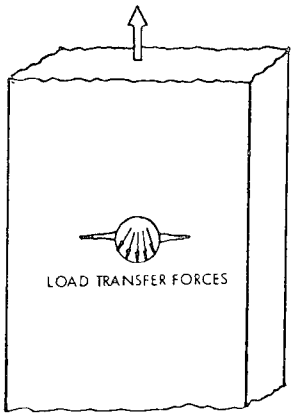


Figure 6. Effect of load transfer on damaged hole.

Critical crack lengths are an important factor in damage tolerance of joints. It has previously been pointed out that in a good damage-tolerant design the critical lengths should be sufficiently long to be readily detected. Since design loads normally cannot be reduced, an increase in critical crack length requires a reduction in stress. Most of the time a reduction in stress is achieved by an increase in thickness; however, this can result in what would be referred to as a "thickness paradox." Within a

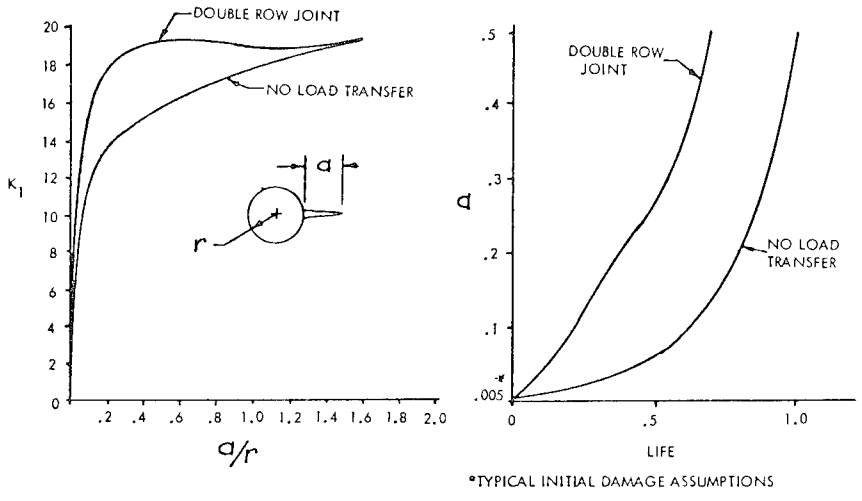


Figure 7. Influence of load transfer on stress intensity and on life.

thickness range between relatively thin and relatively thick material is a thickness range called "transitional." This means a transition from plane stress (thin material) to plane strain (thick material). A typical curve of fracture toughness versus thickness is shown in Figure 8, taken from Reference 12. Note that the fracture toughness of the thin material is

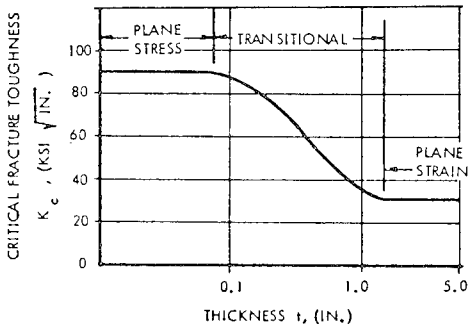


Figure 8. Critical stress intensity factor vs thickness for 7075-T76 al alloy.

300% of that in thick material. If thickness is increased in the transitional range to reduce stress and increase critical crack lengths, the allowable fracture toughness drops. With lower fracture toughness more increase in thickness is required and around and around we go. Kirkby has even suggested[13] that in some materials a thickness reduction may improve damage tolerance in some materials. Figure 9 shows a plot of critical

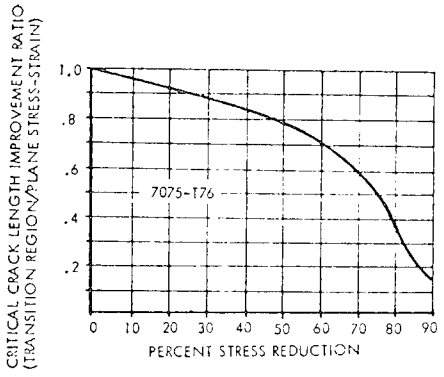


Figure 9. Critical crack length improvement vs percent stress reduction.

crack-length improvements in the transitional region and the plane stress–plane strain region as a function of stress reduction. This example curve is based on the Figure 8 fracture-toughness data and the stress reduction from a baseline thickness of 0.10 inches and is typical of aluminum alloys. The comparison will of course vary with material characteristics and thickness range of comparison. The example does illustrate that care should be taken to know the effects of thickness on material properties being used in designs where damage tolerance and fracture toughness requirements are to be met. Note that for a 50 percent stress reduction only 79 percent of the critical length improvement in the plane stress–plane strain is obtained when in the transitional region.

Serious consideration should be given to improvements in design configuration as a means to achieve damage tolerance as opposed to simple thickness increase when it is discovered that the design is influenced by this thickness paradox.

DESIGN PRACTICES

It has previously been pointed out that joints are rather special design problems due to inherent complexities and that these complexities demand careful analysis and/or clever design. Design practices must reflect consideration of damage tolerance — it is unlikely that good damage tolerance will be achieved by accident. The desirability of having defined damage-tolerance requirements has been discussed, and is indispensable as part of a set of good design practices. One of the best design practices is to limit the number of joints to an absolute minimum. But aside from these overall guidelines, what specifically can be done?

Probably the simplest and best approach to practical damage tolerance is to design multielement structure. Care must be taken here to not degrade the inspectability of the joint, but sometimes both can be improved as demonstrated by the scarfed splice plate in Figure 4. Another simple example is shown in Figure 10. In this example, the joint is parallel to the primary loading direction. Both joints are multielement, and therefore damage in one major member can be arrested and contained by the adjacent member. However, configuration (B) is superior in several respects to (A). Note that the major members are overlapped at the joint in (A) but not overlaped in (B). Part of one member in (A) is therefore hidden from view and cannot be inspected from the side with ready access. Both major members in (B) are in full view even in the joint. Also, the stiffener in (A) at the joint covers the tab that could not be inspected from the accessible side so that it cannot be inspected even from the side with difficult access. This problem does not exist in (B)

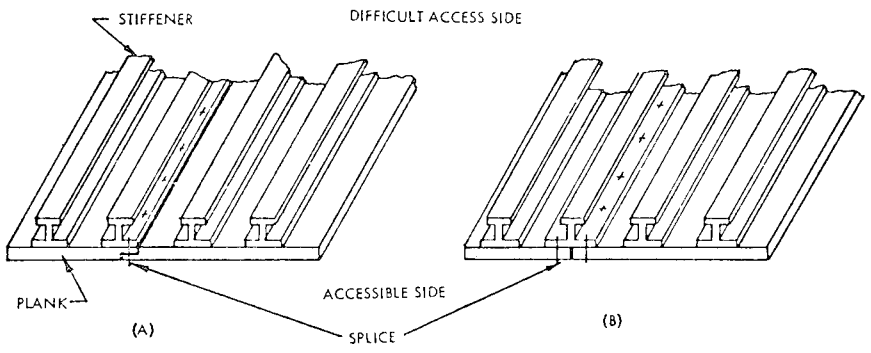


Figure 10. Joint damage tolerance design example.

since the major members can be readily inspected from one side and the splicing stiffener from the other side. Another difficulty with configuration (A) is that a poor quality hole will effect both major members. This is because operations related to joining such as drilling and reaming are conducted on both major members of (A) at the same time due to the overlap. This commonality of construction does not effect two major members in configuration (B) — only one major member and one stiffener. The probability of damage being present in two major members at the same location and possibility of failure of both members is therefore higher in (A) than in (B). This is a simple example, but illustrates how consideration of damage tolerance during design can significantly improve the design.

The detrimental effect of eccentricities within a joint have been illustrated. Careful attention to detail and adequate analysis will go a long ways toward improving these problems. The influence of load transfer in a joint in accelerating damage growth has also been pointed out. The development of ultra-high-strength fastener systems in recent years have tempted designers to use smaller diameter bolts for better joint static-strength efficiencies. The higher local bearing stresses these small diameter fasteners present must be considered in light of damage-tolerance requirements and careful compromise be maintained.

There are currently several special joint preparation techniques being used in aircraft joint design to improve damage tolerance. These techniques are illustrated in Figure 11. Clamp-up benefits to damage tolerance are achieved by the frictional forces resisting crack-opening displacements. These built-in frictional forces act to reduce the effective stress intensity due to applied loads. In other words, the crack cannot open without being restrained by the adjoining part to which it is clamped. These frictional forces also reduce the bearing stress at the

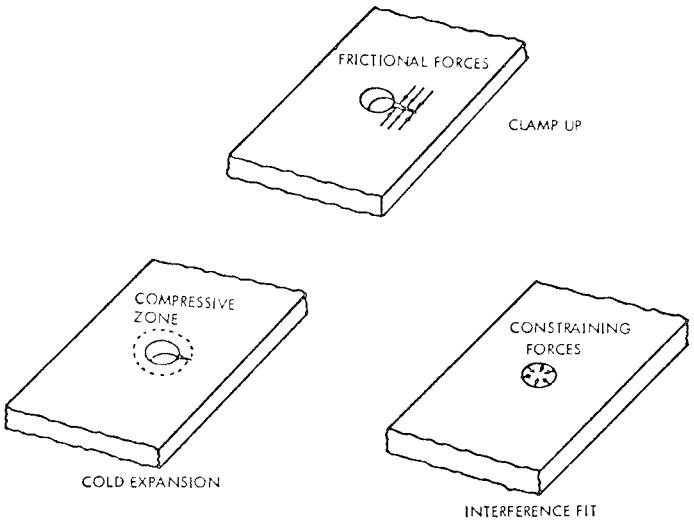


Figure 11. Special joint preparation techniques.

hole due to load transfer by allowing the joint loads to be transferred directly by friction.

The second joint-preparation technique to improve damage tolerance is cold expansion of holes. The dramatic improvement in flaw growth rate has been reported in Reference 8. Several techniques are available to accomplish the required expansion into the yield zone. Upon removing the expanding force, the surrounding elastic material forces the yielded area into compression. Subsequent applied loadings to the joint then result in a reduction in stresses within the compressive zone below those that would be the case without the cold expanding process. This effective stress reduction improves the damage tolerance of small damage within the compressive zone.

Another joint-preparation technique that is in use to improve damage tolerance is interference fit fasteners. When high interference is used, the hole is constrained, the effective stress concentration is reduced, and improved joint damage tolerance results.

Any of these special joint-preparation techniques require extensive testing to quantify the benefits obtained for a particular material, joint configuration, and loading. There are practical considerations to be made also when counting on any benefits demonstrated by test when applied in actual production. For example, can a method be implemented in production to ensure that the expected clamp-up, cold expansion, or interference is built in to each joint? Also, what are the realistic long-

term benefits that can be expected in service — will clamp-up, compressive zone, interference deteriorate with time? Finally, the possible detrimental effect of high compression overloads on the cold expansion compressive zone has been suggested and should be investigated.

The potential benefits of special joint preparation are important enough to be thoroughly explored. The latest Air Force damage-tolerance requirements[5] allow a limit on these benefits equivalent to a reduction in damage assumptions from 0.05 initial damage to 0.005 initial damage. This amount of benefit must be substantiated by test. The difference in damage-tolerance life for these two initial damage assumptions is illustrated in Figure 12.

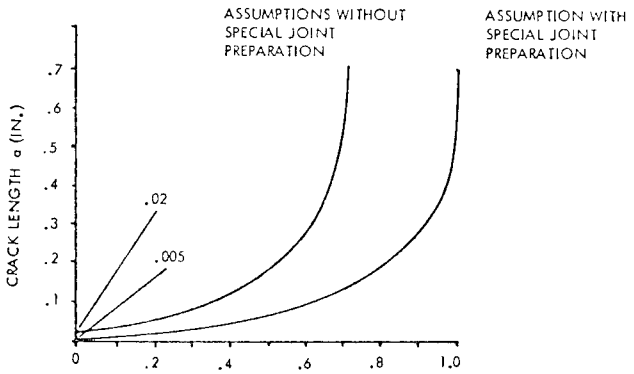


Figure 12. Potential effect of special joint preparation on damage tolerance life.

SUMMARY

Damage tolerance has been described as the ability of a structure to sustain an inquiry that might come from a variety of sources. Many failures result from a lack of adequate damage tolerance. It is unlikely that adequate damage tolerance will be achieved by accident.

Detailed damage-tolerance design requirements are necessary to define what specifically are the damage-tolerant objectives. These requirements can take many forms, and the latest Air Force specification is an example that assumes damage even in new structure. The basic factors that need to be defined in the requirements are:

1. Extent of damage present to be tolerated.
2. How inspectable the design should be.

3. Growth-rate limits.
4. Load level to be sustained with damage present.

Joints present special damage-tolerance problems because of inherent design complexities. The complexities present difficult inspectability and analysis problems. Among the analysis problems that need to be addressed are load-path eccentricities and high bearing stresses resulting from load transfer. Both of these factors can greatly effect the damage tolerance of a joint.

Good design practices are a necessity in achieving a damage-tolerant design. One of the best practices is to design multi-load-path structure with inherent damage-arresting characteristics.

Several techniques such as high clamp-up, cold expansion, and interference fit fasteners can be used to improve joint damage tolerance. These techniques should be used with care and with intensive production controls if quantitative improvements are to be assumed.

ACKNOWLEDGMENT

The author would like to express his gratitude for the assistance received in preparing this manuscript by R. W. Black and H. D. Allen, and especially to Joyce Clayton for typing support.

REFERENCES

1. Gran, R. J., Orazio, F. D. Jr., Paris, P. C., Irwin, G. R., and Hertzberg, R., "Investigation and Analysis Development of Early Life Aircraft Structural Failures," Universal Technology Corporation, Dayton, Ohio. Air Force Flight Dynamics Laboratory Contract Report No. AFFDL-TR-70-149, March 1971. (AD 884 790)
2. Kirkby, W. T., "Examples of Aircraft Failure," in *Fracture Mechanics of Aircraft Structures*, ed. by H. Liebowitz, Advisory Group for Aerospace Research and Development, Paris, Report No. AGARD-AG-176 (January 1974), 8–13. (N74-23413)
3. Krupp, W. E. and Hoeppner, D. W. "Fracture Mechanics Applications in Materials Selection, Fabrication Sequencing and Inspection," *J. Aircraft*, **10** (1973), 682–88.
4. "Airworthiness Standards: Transport Category Airplanes," Federal Aviation Regulations, Vol. III, Pt. 25, June 1974.
5. "Airplane Damage Tolerance Requirements," Military Specification MIL-A-83444 (USAF), 2 July 1974.
6. Wood, H. A., "Fracture Control Procedures for Aircraft Structural Integrity," Air Force Flight Dynamics Laboratory, Wright-Patterson AFB, Ohio, Report No. AFFDL-TR-71-89, July 1971. (AD 731 565)

7. Tiffany, C. and Haviland, G. P., "The USAF Structural Integrity Program," AIAA Paper 73–18, 1973.
8. Petrak, G. J., and Stewart, R. P., "Retardation of Cracks Emanating From Fastener Holes," *Eng. Fract. Mech.*, **6** (1974), 275–82.
9. Grandt, A. F. Jr., "A General Stress Intensity Factor Solution for Fastener Holes," Air Force Materials Laboratory, Wright-Patterson AFB, Ohio, Technical Memorandum No. AFML-TM-LLP-73-7, 1973.
10. Sih, G. C., *Handbook of Stress Intensity Factors*. Bethlehem, Pa.: Institute of Fracture and Solid Mechanics (1973).
11. Allen, H. D., "Analysis of Cracks Emanating from Fastener Loaded Holes," Lockheed-Georgia Company, Marietta, Ga., Report No. LG74ER0029, 1974.
12. "Fracture Mechanics Methodology and Analytical Procedures," Stress Memo Note 366, Lockheed-Georgia Company, Marietta, Ga., 1972.
13. Kirkby, W. T., "Heavy Sections," in *Fracture Mechanics of Aircraft Structures*, ed. by H. Liebowitz. Advisory Group for Aerospace Research and Development, Paris, Report No. AGARD-AG-176 (January 1974), 288–93. (N74-23413)

19. DAMAGE TOLERANCE ANALYSIS OF AN AIRCRAFT STRUCTURAL JOINT

S. H. SMITH and F. A. SIMONEN
Battelle Columbus Laboratories
Columbus, Ohio

The new U.S. Air Force specification, MIL-A-83444, on damage-tolerance requirements was applied to a typical structural joint on the wing structure of a military cargo aircraft. Detailed structural analysis of a chordwise structural joint was performed considering load transfer and finite-element structural models. Work energy and crack-surface-displacement methods of linear elastic-fracture mechanics were used to determine the variation of crack-tip stress-intensity factors with crack size. The initial damage size and fatigue-crack-growth behavior under spectrum loading were based on multiple cracking of single structural elements of the joint. Load-transfer effects on crack extension were considered in the fracture-mechanics analysis.

Fatigue-crack-propagation behavior analysis of the full-scale fatigue-test spectrum and reported flight-by-flight service usage spectrum was determined for the structural joint. Flight-by-flight stress spectra were generated based on 14 mission stress profiles for various logistics and training missions. From initial assumed corner crack sizes at the fastener holes, the fatigue-crack-propagation behavior analysis was utilized to establish the required inspection intervals for depot- or base-level inspection. In addition to the required inspection intervals, the structural crack-growth lives to clean-up size at holes of the structural joint were determined.

INTRODUCTION

The U.S. Air Force specification, MIL-A-83444, "Aircraft Damage-Tolerance Design Requirements,"[1] specifies that aircraft inspections are to be established for military aircraft based on certain initial damage-size assumptions and crack-growth calculations. The damage can result from initial material flaws, manufacturing defects, or inadvertent damage due

to service handling and operation. In aircraft structural joints, the most likely location of initial damage is at the edges of fastener holes.

With the ever-increasing developments of linear-elastic fracture-mechanics technology,[2-6] the fracture-mechanics analysis of complex structural joints can be performed. Because of the complex structural boundary conditions and load transfer associated with aircraft structural joints, finite-elment structural analysis coupled with fracture-mechanics analysis was utilized in an analysis of a multifastener structural joint.

Spectrum fatigue-crack-growth behavior of aircraft structural components is being oriented more to flight-by-flight type of crack-growth analysis and experimentation.[7,8] In this damage-tolerance analysis of a cargo aircraft structural joint, comparative fatigue-crack-growth analysis was conducted using flight-by-flight reported usage data from the Air Force Individual Aircraft Structural Life Monitoring Program (IASLMP). The service aircraft analyzed represented a sample of five aircraft with various fatigue damage, flight times, and usage behavior. Comparative analysis was conducted with the full-scale fatigue-test spectrum which was developed as a composite spectrum representative of anticipated service usage. The remainder of this chapter deals with a technical discussion of the analysis methods and results as applied to a typical joint of an aircraft wing structure. The context of this chapter is based on the results of an extensive study by the authors on several joints of a wing box structure. The full results of this study are reported in Reference 7.

FINITE-ELEMENT/FRACTURE-MECHANICS METHODS

Detailed structural stress analysis of the joint and surrounding structure was based on currently acceptable finite-element stress analysis techniques and modeling. Battelle's two-dimensional finite-element program, AXISOL, was used for the purpose of calculating the stress and displacement fields in the cracked and uncracked structural configurations. The following discussion describes details of the finite-element models and how these models were used to calculate crack-tip stress-intensity factors as a function of crack length. Extensive plots of the stress-intensity factors utilized in the crack-growth predictions are presented.

Structural Models of Chordwise Splice Joint

The chordwise splice joint located on the lower surface of the wing box is the main structural joint which attaches the outer and inner wing

Fastener Diameter = 0.250 inch

Fastener Spacing = 1.25 inches

Cover Plate Thickness = 0.25 inch

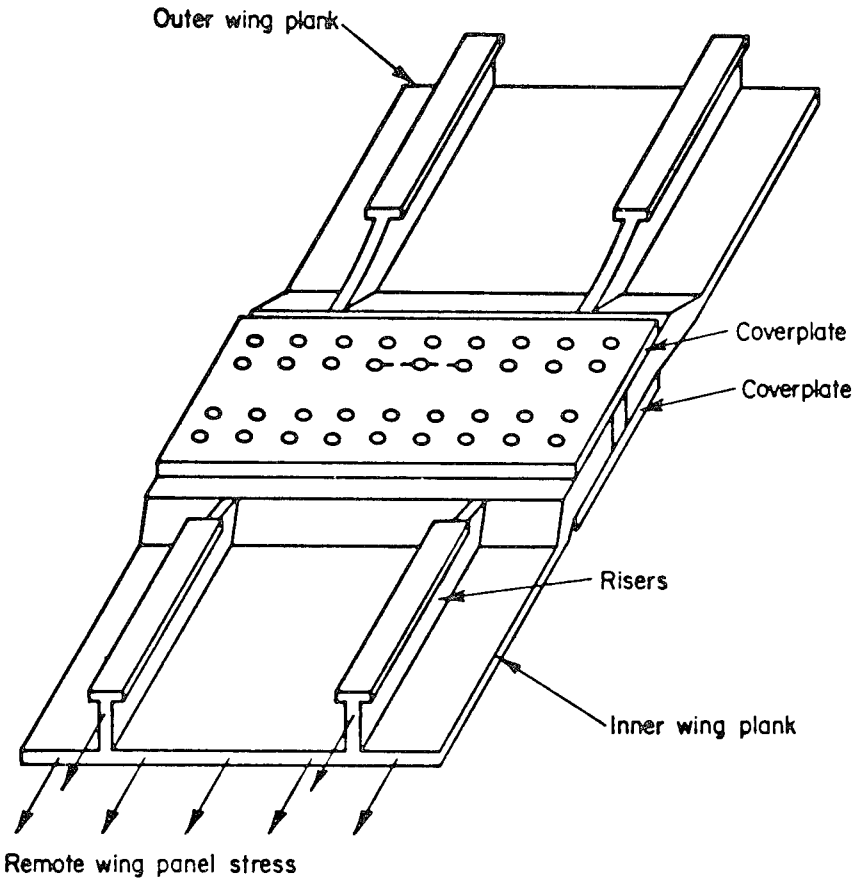


Figure 1. Sketch of chordwise splice joint.

sections. A three-dimensional sketch of this joint is shown in Figure 1. The chordwise splice consisted of two cover plates 0.250-in. thick which joined the 0.454-in.-thick main integral stiffened wing planks. The mechanical fasteners were two rows of 1/4-in. titanium taper-Lok fasteners on each side of the joggled plank splice line. Panel and riser runouts were configured so that a nominal 10,000 psi wing-bending tension stress resulted in 6236 psi local stress for the reinforced panel section at the fastener location. The riser spacing in the panels was 3.85 in.

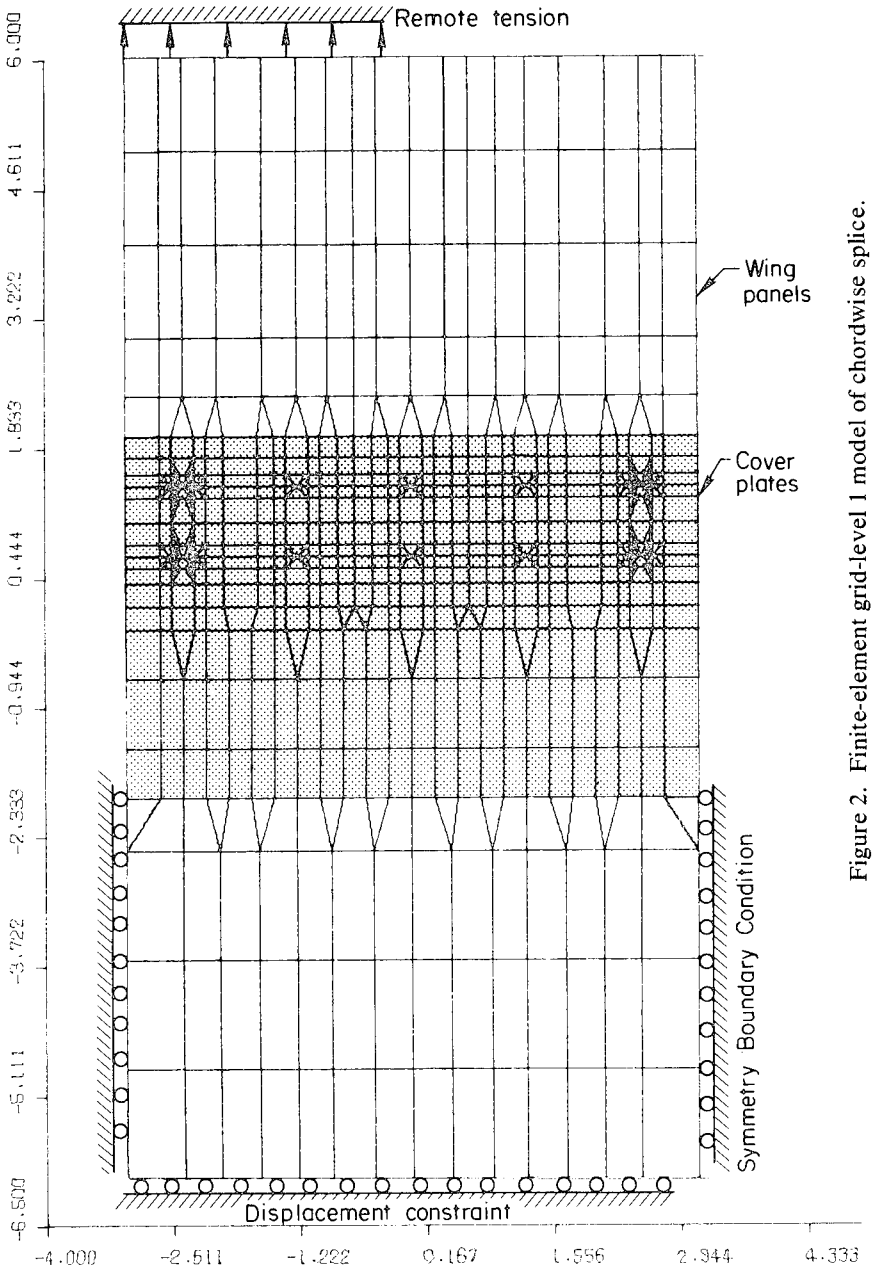


Figure 2. Finite-element grid-level 1 model of chordwise splice.

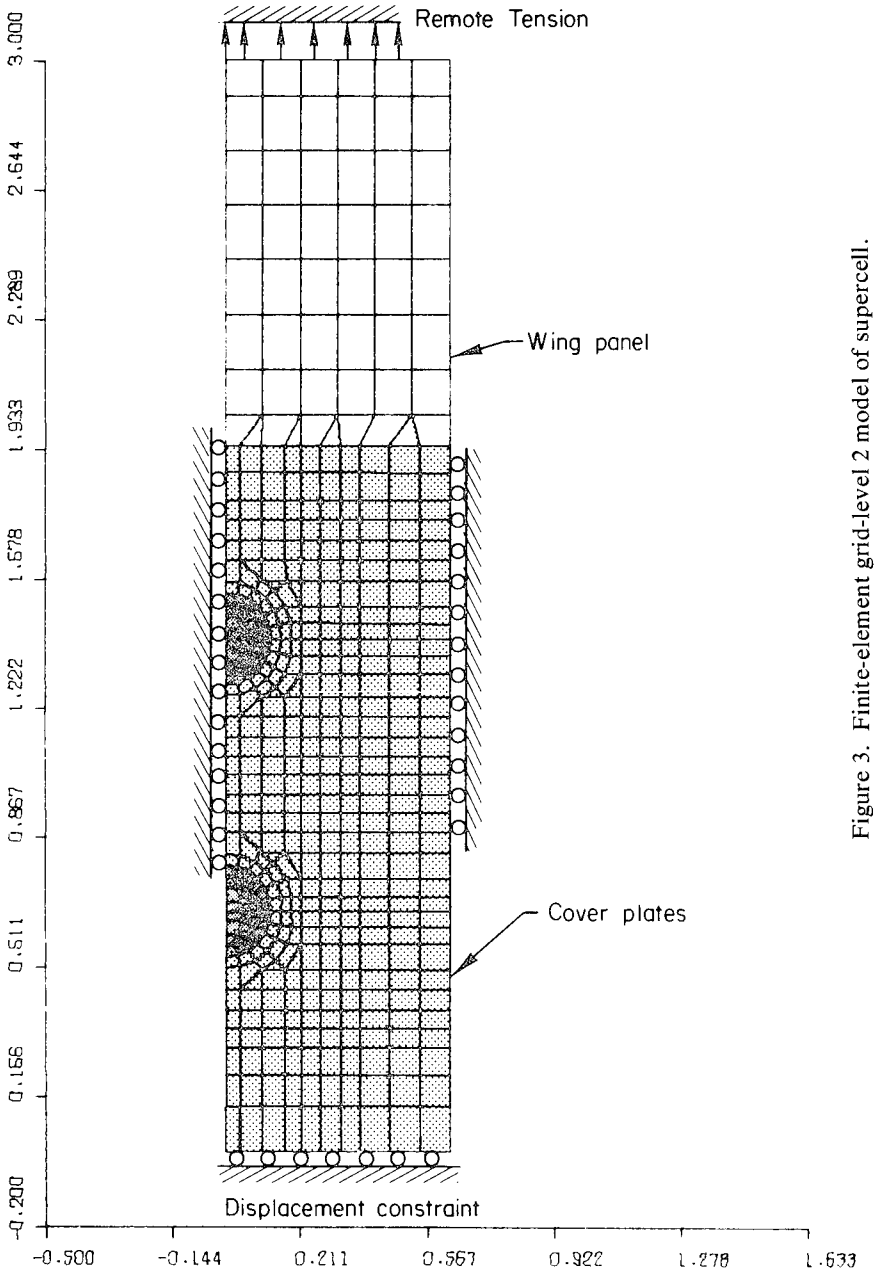


Figure 3. Finite-element grid-level 2 model of supercell.

Figures 2 and 3 show the level 1 and level 2 finite-element models of the chordwise splice. The level 1 model of Figure 2 consisted of 1668 nodal points and 1420 elements. A total of five fasteners in each row along the width of the joint were modeled to account for load transfer behavior. In this level 1 model, three layers of overlayed planar grids were used to represent the planks and cover plates with load transfer simulated at the fastener locations. These overlayed grids were free to deform independently except where they were joined by displacement constraints at the fastener locations. Along the lower two rows of fasteners, as shown in Figure 2, the members of the joint were joined by a simple rigid connecting element at the center of each fastener location. Along the upper two rows of fasteners, a more refined representation was used since the analysis was to consider cracking along these lines of fasteners. Double sets of nodes were used to simulate cracking along either the inner or outer rows of fasteners and in either the main plank or cover plates of the joint.

Properties of the 7075-T6 aluminum of the planks and cover plates consisted of an elastic modulus of 10×10^6 psi and Poisson's ratio of 0.30. For the titanium fasteners, a modulus of 15×10^6 psi and a Poisson's ratio of 0.30 were used.

The remote stressing applied to the joint was a tensile stress of 10,000 psi and displacement constraints were applied along the edges of the panel as shown in Figure 2. The lower edge of the model was fixed to react to the applied tension stress. The two edges of the modeled regions perpendicular to the joint were constrained to represent a symmetrical boundary condition and a large adjacent section of the wing by stiffness simulation. The edges were assumed to remain straight, resulting in a zero total load along these edges. However, self-equilibrating stresses were permitted to develop in members along the longitudinal direction of the joint.

A factor that was not considered was bending of the panels and fasteners in the joint area. The finite-element program used is inherently a planar analysis, and as such treated the wing panels and cover plates as superimposed within a single plane in space for which bending effects do not occur. However, bending in this space is minimized due to its design, since the joint is joggled such that the centroid of load path does not change as it crosses the joint.

The rows of nodes along the lines joining the two upper rows of fasteners (where cracking was to be simulated) were represented in the wing planks and cover plates by a double set of nodes. For the analysis of the uncracked structure, these nodes were rigidly connected by special connecting elements. For crack surface simulation, the coupling stiffness of the joint connecting element was uncoupled or "unzipped"

to build in the proper cracked structure stiffness and load transfer to the adjacent fasteners. This permitted the analysis of different crack lengths by progressive uncoupling of connected double nodes along the line of expected crack extension. Fracture mechanics analysis of cracks located in the wing planks or the cover plates was performed. Also, multiple cracking originating from different fasteners could be treated with the cracks being of unequal length, if desired.

The finite-element grid of Figure 3 represents a highly detailed second-level model of a single cell of the joint. The loadings, constraints, member thicknesses, and material properties were the same as for the level 1 model. Consisting of a typical unit cell of the joint configuration, the refined grid of the model was capable of accurately analyzing stresses in the uncracked or cracked structural condition. This second-level model consisted of 949 nodes and 790 elements, and both the cover plates and a segment of the plank were modeled. If all of the fastener locations were to be cracked in an identical manner, then the cracked structure was analyzed by imposing symmetrical boundary conditions as shown in Figure 3. For cracking at only a finite number of fastener locations and cracks of unequal length, the imposed boundary conditions were along the edges of the unit cell. These boundary conditions were obtained from the level 1 model of the cracked structure.

In the level 2 model, the fasteners of each row as modeled in the unit cell were represented as separate structural components. The boundary conditions between the fasteners and surrounding plates simulated a neat-fit pin situation. The bearing contact conditions imposed consisted of coupled radial displacement of the fastener and plate. However, the fastener boundary was allowed to rotate in a circumferential direction.

In the fracture-mechanics analysis of structural joints, the most important structural parameter to evaluate is fastener-load transfer during crack extension. The load transfer resulting from the level 1 model analysis was imposed on the level 2 model. This was accomplished by transfer of fastener nodal-point displacements of the level 1 model to the centroid of the fastener structural element of the level 2 model. Both fastener displacements resulting in the main plank and cover plates were transferred. In addition, the clearance on the diametrically opposite side of the fastener-plate bearing side was allowed to open up along the unloaded areas of the fastener hole in each member.

Stress-Intensity-Factor Solutions

Being a numerical approach, the finite-element modeling techniques applied to the joint can incorporate details of structural configurations

and loadings that are beyond the scope of purely analytical methods. The requirement for the flaw-growth analysis is the expression of the results of the finite-element solutions in terms of stress-intensity factors. Since standard finite-element formulations do not treat singular stress behavior, special procedures were utilized.

Two basic approaches to obtain stress-intensity factors from finite-element analysis have been rather extensively studied in the literature and were applied in this analysis. These are the crack-opening-displacement method and the work-energy concept applied to the crack-closure integral. The basic concepts of the methods as applied to finite-element results are discussed below.

Crack-Opening-Displacement Method. The continuum relationships involving opening and edge-sliding stress-intensity factors and the displacement field surrounding the crack tip were derived by Paris and Sih based on the stress function involving the stress-intensity factor and Westergaard's stress-analysis method.[2] From discrete nodal-point displacements in the vicinity of the crack tip, the stress-intensity factors can be determined by fitting the analytical forms for crack-tip displacement as described by Chan *et al.*[3] In this analysis, the opening mode stress-intensity factor was determined at discrete nodal points along the crack surface. In applying the crack-surface displacement method, the following relationships were used:

$$K_I = \Delta V G \left[\frac{\gamma}{2\pi}\right]^{1/2} \left(\frac{1+\nu}{2}\right) \tag{1}$$

$$K_{II} = \frac{\Delta U G}{2} \left[\frac{\gamma}{2\pi}\right]^{1/2} \left(\frac{1}{\nu - 1}\right) \tag{2}$$

where ΔV and ΔU are the relative opening and edge-sliding displacements of adjacent points on the crack surface, γ is the distance from the crack tip to the nodal points on the crack surface, and G and ν are modulus of rigidity and Poisson's ratio, respectively.

Work-Energy Method. The work-energy method is a numerical technique for evaluating stress-intensity factors based on Irwin's equation.[8] It has received little attention. The energy method is based on the work needed to close the crack surface and thus is called the work-energy method. The application to finite-element/fracture-mechanics analysis is similar to the procedure discussed by Dixon and Pook[9] and by Mowbray.[10] The procedure is to generate a series of finite-element solutions for a range of crack lengths and to determine stress intensities from relationships between strain energy and crack length for an extending crack.

In equation form, the energy absorbed in the crack-extension process and the equivalency of the work required to close the crack to its original length is as follows in terms of opening and edge-sliding deformations:

$$\mathcal{G}_I = \lim_{\Delta c \to 0} \frac{1}{2\Delta c} \int_0^{\Delta c} \sigma_{yy} (\Delta c - \gamma, 0)\, V(\gamma, \pi)\, d\gamma \tag{3}$$

$$\mathcal{G}_{II} = \lim_{\Delta c \to 0} \frac{1}{2\Delta c} \int_0^{\Delta c} \tau_{xy} (\Delta c - \gamma, 0)\, U(\gamma, \pi)\, d\gamma \tag{4}$$

where $\mathcal{G}_I$ and $\mathcal{G}_{II}$ are the energy release rates for modes I and II and are related to the stress-intensity factors K_I and K_{II} for plane-stress conditions. That is,

$$K_I = \sqrt{E\,\mathcal{G}_I};\ K_{II} = \sqrt{E\,\mathcal{G}_{II}} \tag{5}$$

where E is Young's modulus. The crack-closure concept of the work-energy method has been applied extensively by Rybicki and Kanninen[11] in

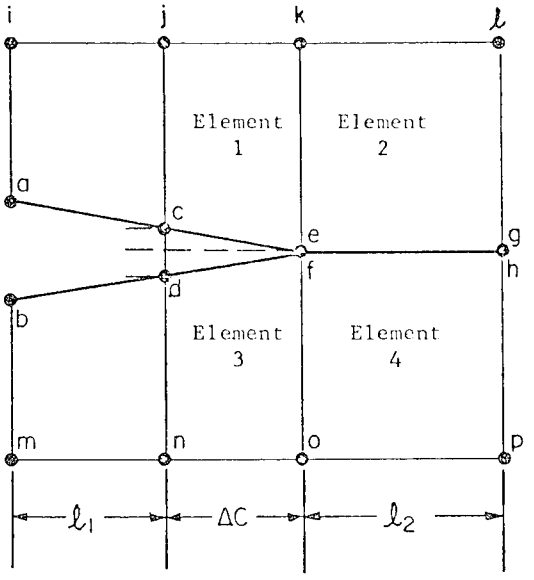


Figure 4. Finite-element nodes near crack tip.

finite-element analysis and they have found a good correlation with classical fracture-mechanics solutions. An explanation of the method as related to finite-element/fracture-mechanics modeling is given in terms of Figure 4. The physical interpretation of the integrals of equations (3) and (4) is the amount of work required to close the crack an amount Δc. In terms of the finite-element representation, this is one-half the product of the forces at nodes c and d required to close these nodes. In equation form, the expressions for $\mathcal{G}_I$ and $\mathcal{G}_{II}$ are

$$\mathcal{G}_I = \lim_{\Delta c \to 0} \frac{1}{2\Delta c} F_c \cdot (V_c - V_d) \tag{6}$$

$$\mathcal{G}_{II} = \lim_{\Delta c \to 0} \frac{1}{2\Delta c} T_c \cdot (U_c - U_d) \tag{7}$$

The values of F_c and T_c are taken as the y and x forces required to hold nodes c and d together. These forces vary as the normal and shear stresses near the tip of the crack and vary as $1/\sqrt{\gamma}$. Thus, the force over a length Δc is given by

$$F(\Delta c) = A_1 \int_0^{\Delta c} \frac{d\gamma^{1/2}}{\gamma} = 2A_1 \Delta c^{1/2} \tag{8}$$

Special attention must be given to unequally spaced elements. In this case, the forces can be estimated using the following equations:

$$F_c = \left[\frac{\Delta c}{\ell_2}\right]^{1/2} F_e \tag{9}$$

$$T_c = \left[\frac{\Delta c}{\ell_2}\right]^{1/2} T_e \tag{10}$$

The forces at the crack tip F_e and T_e are obtained by placing very stiff springs between points e and f and evaluating these forces in terms of the coupling spring stiffness.

Results as Applied to the Chordwise Joint. The two methods described above were applied to the chordwise joint. The finite-element modeling and analysis results provided the nodal-point displacements along the crack-opening displacement and work-energy methods.

Figures 5 through 8 present calculated stress intensities as a function of crack length for the lower surface chordwise joint at a remote wing-panel stress of 10,000 psi. Separate plots are given to clearly indicate the results for small and large crack regions. Most of the fatigue-

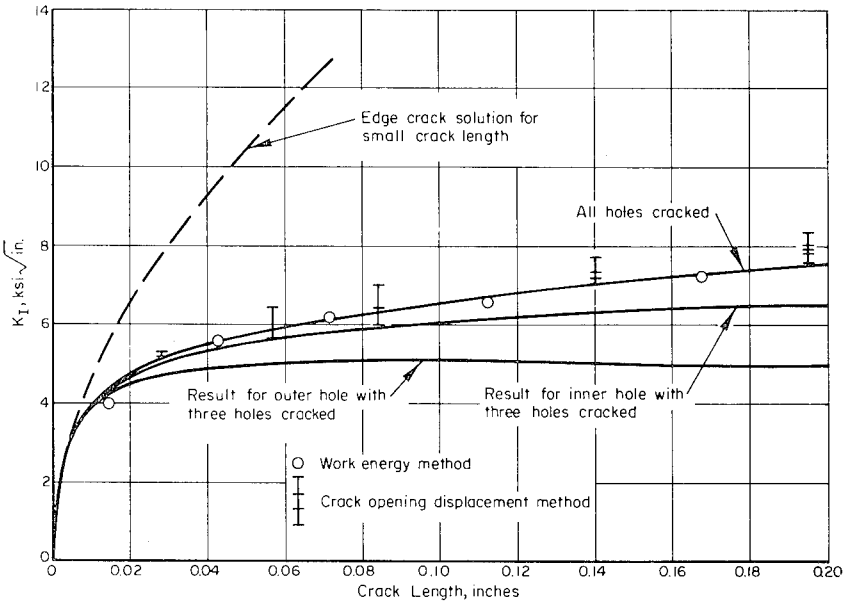


Figure 5. Variation of stress-intensity factor with crack length for small cracks in plank of chordwise splice joint.

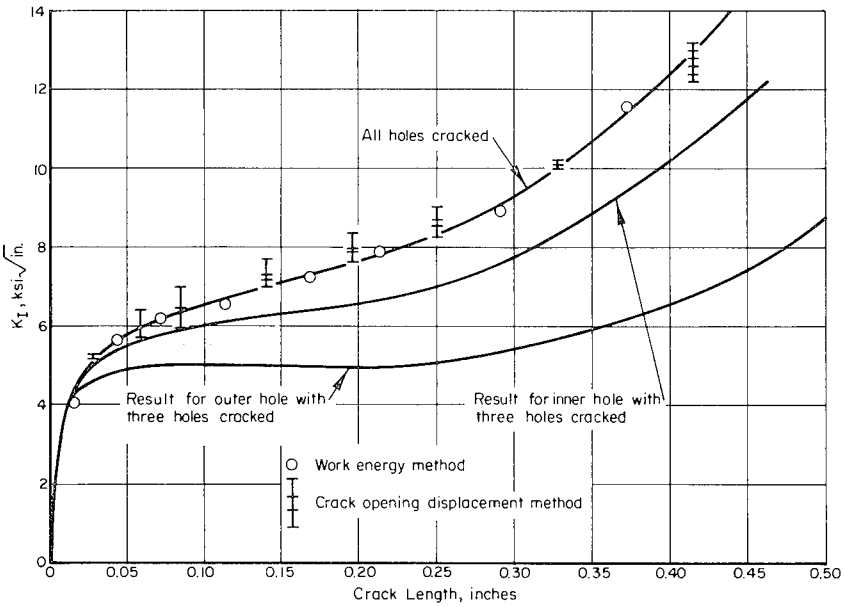


Figure 6. Variation of stress-intensity factor with crack length for large cracks in plank of chordwise splice joint.

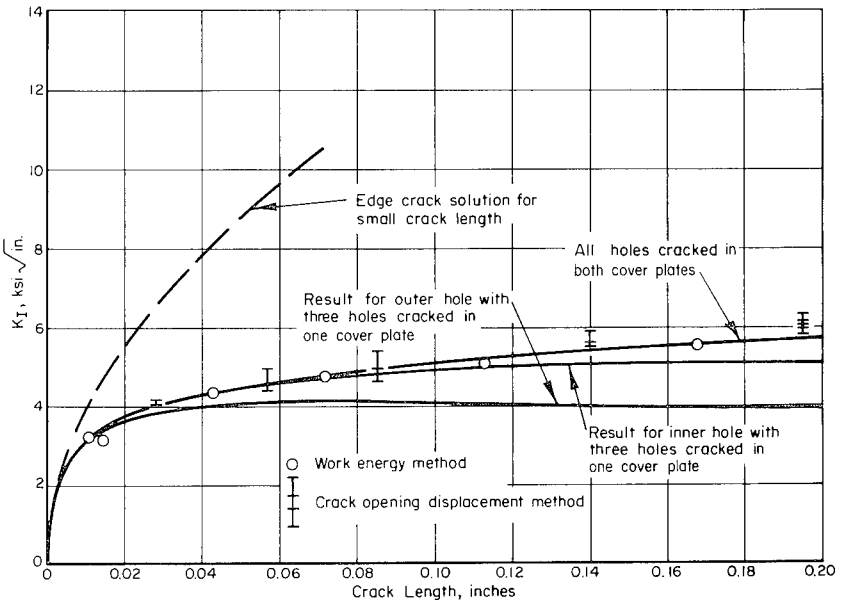


Figure 7. Variation of stress-intensity factor with crack length for small cracks in cover plate of chordwise splice joint.

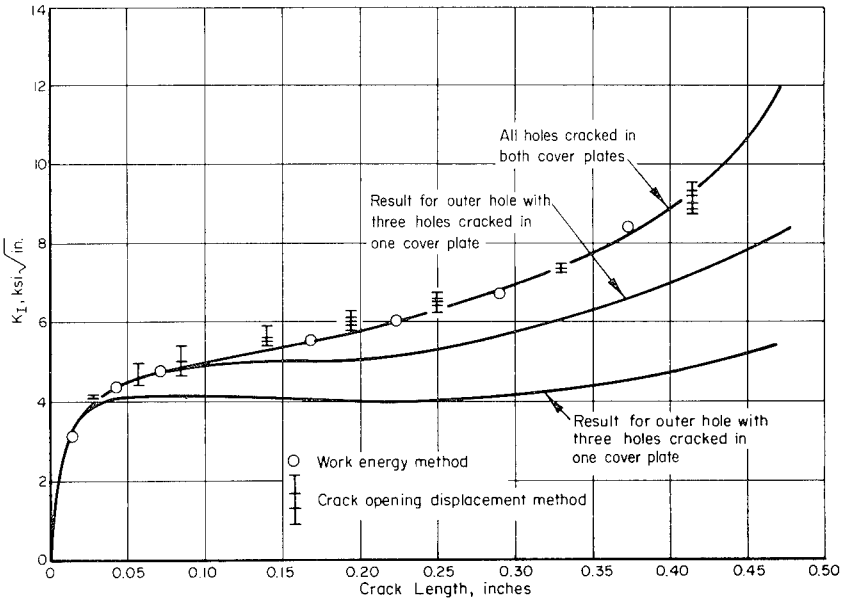


Figure 8. Variation of stress-intensity factor with crack length for large cracks in cover plate of chordwise splice joint.

crack-growth analysis was concerned with the smaller cracks (*i.e.*, 0.005–0.10 in.); whereas, the effects of load transfer became predominant only for relatively longer cracks. However, for small cracks, the loaded-hole effect was slightly higher in comparison to a filled or open hole. It is seen that the crack-opening-displacement method resulted in a band of possible stress-intensity values, with the end of the band corresponding to the smallest crack lengths approaching the curve developed by the work-energy method.

The uncracked stress and load-transfer analyses showed that the highest stresses and fastener loads occurred at the first row of fasteners in the plank. The highest stresses and fastener loads occurred at the second row of fasteners in the cover plate. Therefore, these areas were considered as the fracture critical locations of the chordwise joint.

Figures 5 and 6 show the stress-intensity factors for cracking of a main plank of the wing joint. For very small cracks, less than 0.005 in., the uncracked stress field as determined from the level 2 finite-element model was used in conjunction with the analytical solution for an edge crack to determine the limiting trend of the behavior.

The trend for larger cracks was first determined by cracking both sides of the hole of the level 2 model. This solutuon applies to the situation where all fastener holes in the joint undergo equal cracking. For the situations of interest in the crack-growth study, only three holes were to be involved in the cracking mode. For these results, the level 1 model was applied. Stress intensities were not calculated directly from the level 1 model because of the relative coarseness of the grid. Rather, the relative magnitudes of crack-opening displacements were determined using this model for all holes cracked and then for only three holes cracked. These stress-intensity ratios then were applied to the absolute magnitudes of the level 2 analysis to obtain the results plotted in Figures 5 and 6.

For small cracks (less than 0.05 in.) the stress intensities for the inner and outer holes were very nearly equal, as seen in Figure 5. However, for long cracks (shown in Figure 6), the stress intensity at the outer holes was significantly lower than for the cracks emanating at the inner hole. This indicates the extent of load-transfer effects in the joint. It is seen that the values of stress-intensity factor became relatively insensitive to crack length as the crack grew away from the local stress field associated with the loaded fastener hole. Only as the net section of the uncracked ligament became significantly reduced did the stress intensity begin to rapidly increase with crack length.

Figures 7 and 8 show the results obtained for cracking of cover plates. When both cover plates were cracked, the stress intensities were found to differ little from those for the case of plank cracking. However,

when only one of the two cover plates was cracked, the stress intensities were noticeably reduced.

The open-hole Bowie solution[12], when compared to the results of the joint, demonstrates a slightly lower stress-intensity versus crack-length behavior.

JOINT FATIGUE-CRACK-PROPAGATION ANALYSIS

The detailed fatigue-crack-propagation analysis of the chordwise structural joint considered the full-scale fatigue test spectrum and the flight-by-flight mission stresses as reported from service information. The full-scale fatigue-test spectrum was a composite spectrum comprised of several missions to evaluate the fatigue-crack-growth damage at an accelerated rate beyond the actual flight-by-flight fatigue-crack-growth damage rates. The following discusses the various spectra and fatigue-crack-propagation results.

Stress Spectra for Analysis

The full-scale fatigue-test spectrum consisted of 18 segments with a total of 60,800 cycles. Figure 9 shows the stress spectrum at the chordwise joint location of the wing box. The spectrum represents two passes in which the first part of the spectrum was reversed in application. At the end of the fifth pass, an additional 1595 ground-air-ground cycles were applied to produce the required fatigue damage accumulation. One pass of the spectrum represents 6000 hours of flight time. All compression stresses were truncated to zero for fatigue-crack-propagation analysis.

Flight-by-flight fatigue-crack-propagation analysis involved the generation of mission stress spectra. The mission stresses were generated based on the 14-mission stress profiles which involved various logistics and training missions. From Air Force-furnished segmented mean level wing-bending moment data at the chordwise joint location and use of the power spectral density equation for loading occurrences, the maximum and minimum stress histories of each of the 14 missions were generated. The flight profile with respect to sequencing of stresses for taxi, climb, cruise, gust, maneuver, descent, landing, and taxi was retained for crack-propagation analysis. Tables 1 and 2 show examples of typical logistics and training missions in which the compression stresses have been truncated to zero for fatigue-crack-propagation analysis.

The primary analysis conducted in this study was fatigue-crack-propagation analysis of flight-by-flight behavior of five service aircraft.

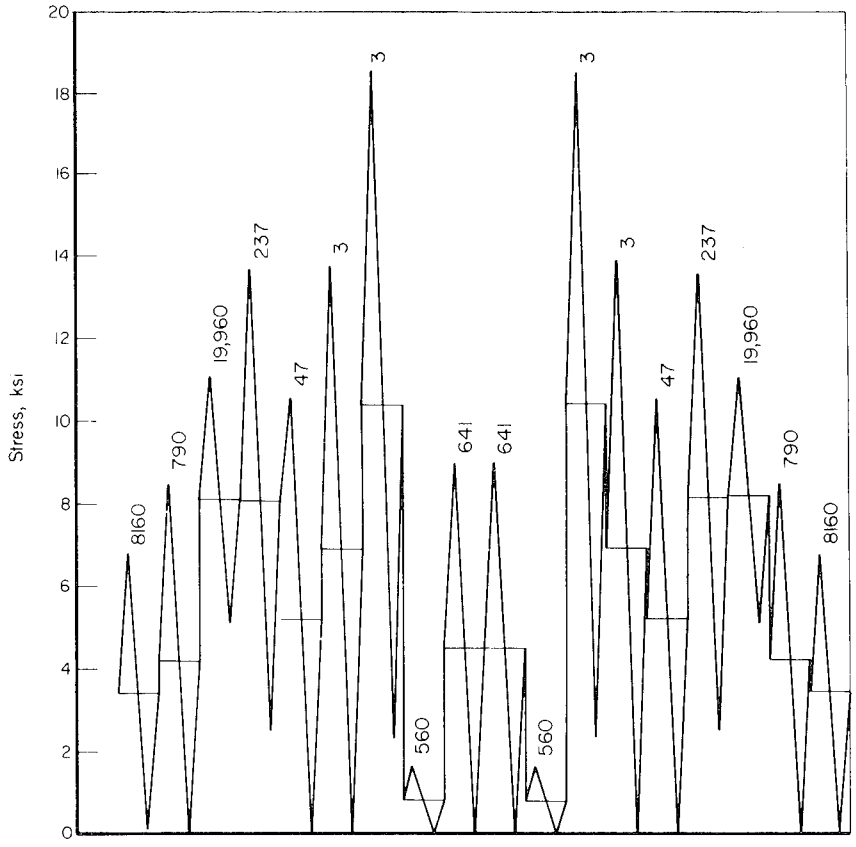


Figure 9. Full-scale fatigue-test spectrum.

Table 1. Stress Spectrum for Typical Logistics Mission

Layer	Maximum Stress	Minimum Stress	Cycles per Layer	Cumulative Cycles
1	9775.000	8775.000	17.000	17.000
2	10775.000	7775.000	2.000	19.000
3	10258.000	9258.000	7.000	26.000
4	11258.000	8258.000	1.000	27.000
5	9369.000	8369.000	19.000	46.000
6	10369.000	7369.000	4.000	50.000
7	11369.000	6369.000	1.000	51.000
8	9849.000	8849.000	6.000	57.000
9	10849.000	7849.000	1.000	58.000
10	8780.000	7780.000	6.000	64.000
11	9780.000	6780.000	1.000	65.000
12	9258.000	8258.000	2.000	67.000
13	9101.000	8101.000	7.000	74.000
14	10101.000	7101.000	1.000	75.000
15	9570.000	8570.000	1.000	76.000
16	8390.000	7390.000	57.000	133.000
17	9390.000	6390.000	17.000	150.000
18	10390.000	5390.000	5.000	155.000
19	11390.000	4390.000	2.000	157.000
20	8844.000	7844.000	6.000	163.000
21	9844.000	6844.000	1.000	164.000
22	9281.000	8281.000	11.000	175.000
23	10281.000	7281.000	2.000	177.000
24	9295.000	8295.000	2.000	179.000
25	9094.000	8094.000	54.000	233.000
26	10094.000	7094.000	10.000	243.000
27	11094.000	6094.000	2.000	245.000
28	9318.000	8318.000	6.000	251.000
29	10318.000	7318.000	1.000	252.000
30	8238.000	7238.000	18.000	270.000
31	9238.000	6238.000	4.000	274.000
32	10238.000	5238.000	1.000	275.000
33	8678.000	7678.000	3.000	278.000
34	9678.000	6678.000	1.000	279.000
35	8614.000	7614.000	47.000	326.000
36	9614.000	6614.000	10.000	336.000
37	10614.000	5614.000	2.000	338.000
38	11614.000	4614.000	1.000	339.000
39	9057.000	8057.000	15.000	354.000
40	10057.000	7057.000	3.000	357.000

Table 1. (Continued)

Layer	Maximum Stress	Minimum Stress	Cycles per Layer	Cumulative Cycles
41	11057.000	6057.000	1.000	358.000
42	5569.000	4569.000	78.000	436.000
43	6569.000	3569.000	6.000	442.000
44	7569.000	2569.000	1.000	443.000
45	5999.000	4999.000	49.000	492.000
46	6999.000	3999.000	5.000	497.000
47	7999.000	2999.000	1.000	498.000
48	5559.000	4559.000	16.000	514.000
49	6559.000	3559.000	1.000	515.000
50	5988.000	4988.000	10.000	525.000
51	6988.000	3988.000	1.000	526.000
52	8750.000	3966.000	1.000	527.000
53	9366.000	0.000	1.000	528.000

Figures 10 and 11 show the flight histories of five aircraft with respect to flights and flight hours over an 11-year time span. Actual flight-by-flight history data as reported from the IASLMP program for each quarter year were utilized in the fatigue-crack-propagation analysis.

The techniques used in fatigue-crack-propagation evaluation of the structural joint were based on linear-elastic fracture-mechanics technology. AFFDL's computer program, "CRACKS II", was utilized to analytically grow the fatigue cracks under spectrum and flight-by-flight stresses. The program used was a modification of the original AFFDL-CRACKS program developed by Engle.[13]

The basic fatigue-crack-growth-rate equation utilized in this study was the Forman equation,

$$da/dN = \frac{C(\Delta K)^n}{(1-R)K_c - \Delta K} \tag{11}$$

where

da/dN = fatigue-crack-growth rate, in./cycle
ΔK = cyclic range of stress-intensity factor, psi$\sqrt{\text{in.}}$
R = cyclic stress ratio
K_c = critical stress-intensity factor, psi$\sqrt{\text{in.}}$
C = constant, in./cycle/(psi$\sqrt{\text{in.}}$)$^{n-1}$
n = exponent

Table 2. Stress Spectrum for Typical Training Mission

Layer	Maximum Stress	Minimum Stress	Cycles per Layer	Cumulative Cycles
1	0.000	0.000	1.000	1.000
2	6344.000	5344.000	21.000	22.000
3	7344.000	4344.000	1.000	23.000
4	6778.000	5778.000	8.000	31.000
5	7778.000	4778.000	1.000	32.000
6	6326.000	5326.000	75.000	107.000
7	7326.000	4326.000	4.000	111.000
8	6627.000	5627.000	31.000	142.000
9	7627.000	4627.000	2.000	144.000
10	6307.000	5307.000	36.000	180.000
11	7307.000	4307.000	2.000	182.000
12	6608.000	5608.000	15.000	197.000
13	7608.000	4608.000	1.000	198.000
14	2916.000	1916.000	414.000	612.000
15	3916.000	916.000	20.000	632.000
16	4916.000	0.000	1.000	633.000
17	3207.000	2207.000	180.000	813.000
18	4207.000	1207.000	14.000	827.000
19	5207.000	207.000	1.000	828.000
20	6799.000	1700.000	1.000	829.000
21	2374.000	0.000	1.000	830.000
22	6183.000	5183.000	16.000	846.000
23	7183.000	4183.000	1.000	847.000
24	6484.000	5484.000	7.000	854.000
25	7484.000	4484.000	1.000	855.000
26	6138.000	5138.000	57.000	912.000
27	7138.000	4138.000	5.000	917.000
28	6495.000	5495.000	33.000	950.000
29	7495.000	4495.000	4.000	954.000
30	8495.000	3495.000	1.000	955.000
31	6106.000	5106.000	9.000	964.000
32	7106.000	4106.000	1.000	965.000
33	6403.000	5403.000	4.000	969.000
34	2785.000	1785.000	29.000	998.000
35	3785.000	785.000	1.000	999.000
36	3069.000	2069.000	13.000	1012.000
37	4069.000	1069.000	1.000	1013.000
38	6617.000	1657.000	1.000	1014.000
39	5866.000	0.000	1.000	1015.000
40	6042.000	5042.000	7.000	1022.000

Table 2. (Continued)

Layer	Maximum Stress	Minimum Stress	Cycles per Layer	Cumulative Cycles
41	6414.000	5414.000	3.000	1025.000
42	5995.000	4995.000	9.000	1034.000
43	6995.000	3995.000	1.000	1035.000
44	6293.000	5293.000	4.000	1039.000
45	5527.000	4527.000	9.000	1048.000
46	6527.000	3527.000	2.000	1050.000
47	5974.000	4974.000	9.000	1059.000
48	6974.000	3974.000	1.000	1060.000
49	5182.000	4182.000	7.000	1067.000
50	6182.000	3182.000	1.000	1068.000
51	6089.000	5089.000	3.000	1071.000
52	7089.000	4089.000	1.000	1072.000
53	5137.000	4137.000	121.000	1193.000
54	6137.000	3137.000	16.000	1209.000
55	7137.000	2137.000	2.000	1211.000
56	5762.000	4762.000	54.000	1265.000
57	6762.000	3762.000	13.000	1278.000
58	7762.000	2762.000	3.000	1281.000
59	8762.000	1762.000	1.000	1282.000
60	5039.000	4039.000	13.000	1295.000
61	6039.000	3039.000	2.000	1297.000
62	5925.000	4925.000	5.000	1302.000
63	6925.000	3925.000	2.000	1304.000
64	5748.000	4748.000	40.000	1344.000
65	6748.000	3748.000	6.000	1350.000
66	7748.000	2748.000	1.000	1351.000
67	6131.000	5131.000	26.000	1377.000
68	7131.000	4131.000	3.000	1380.000
69	2661.000	1661.000	36.000	1416.000
70	3661.000	661.000	2.000	1418.000
71	2939.000	1939.000	15.000	1433.000
72	3939.000	939.000	1.000	1434.000
73	2672.000	1672.000	18.000	1452.000
74	3672.000	672.000	1.000	1453.000
75	2950.000	1950.000	8.000	1461.000
76	3950.000	950.000	1.000	1462.000
77	6247.000	1842.000	1.000	1463.000

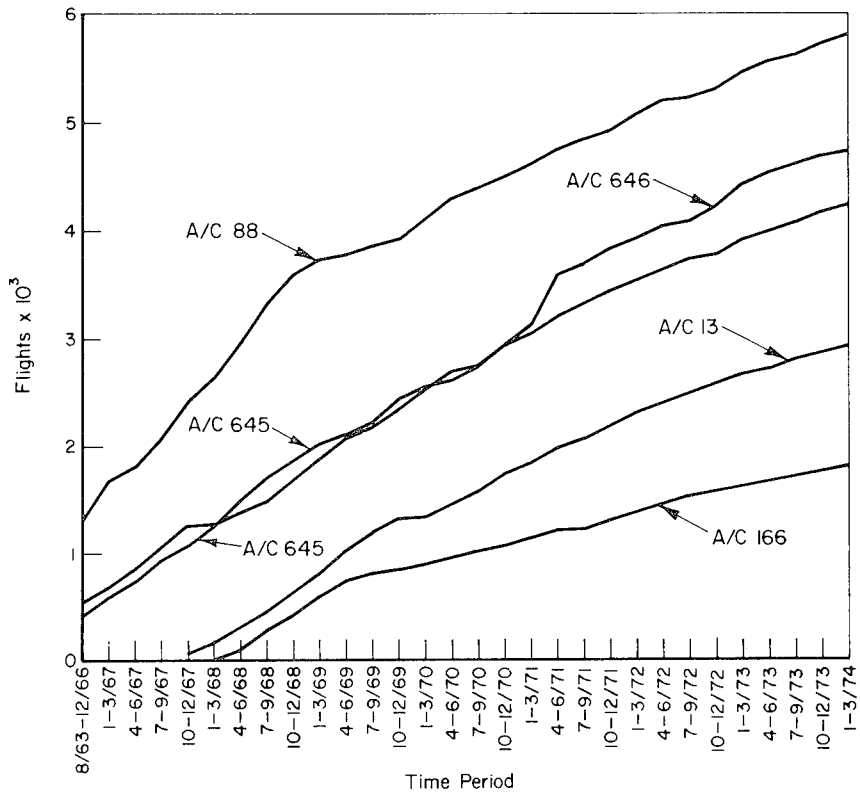


Figure 10. Cumulative flights vs. time period.

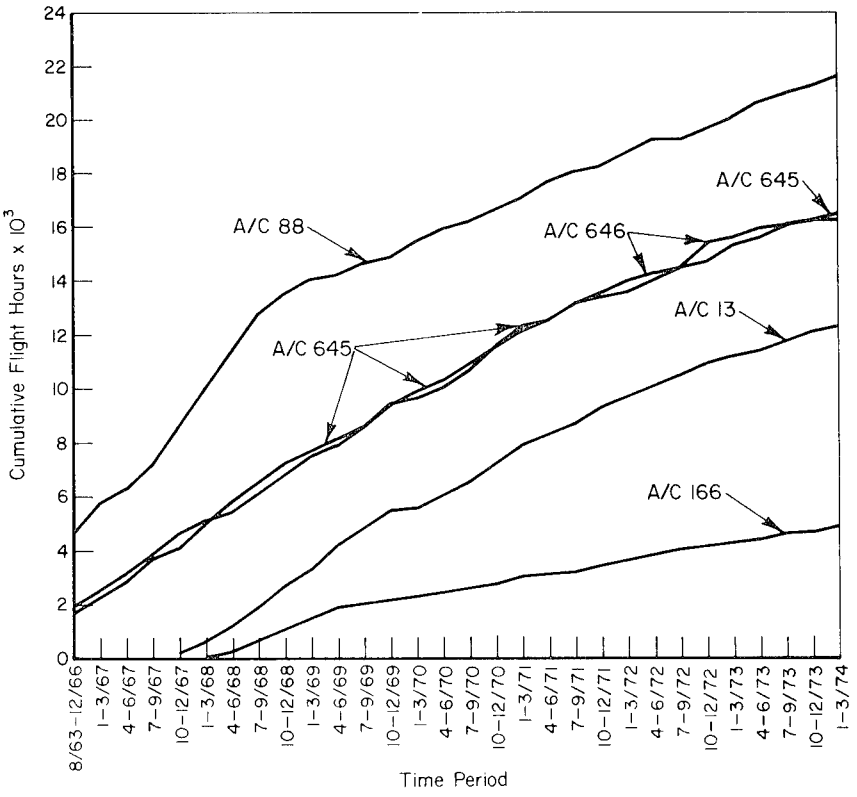


Figure 11. Cumulative flight hours vs. time period.

The constant C, and exponent n, utilized for 7075–T6511 extrusions are listed in Table 3. In this analysis, the upper-bound wet values were extensively utilized for conservatism and in a previous study of the C-5A flight-by-flight crack growth this approach was shown to bracket flight-by-flight test data.[14]

The main concern of the fatigue-crack-propagation behavior of cracks located in the structural joint is fatigue cracks located in the main planks under the cover plates, which cannot be inspected. In addition, the replacement due to failure of a main plank is much more costly than failure and replacement of cover plates. Therefore, the fatigue-crack-propagation analysis of the chordwise splice joints was based on corner cracks emanating at edges of holes in the main plank.

The stress-intensity-factor solution for the corner cracks emanating at holes was arrived at in the following fashion. From the finite-element/fracture-mechanics analysis described previously, Beta factors were derived for the through-the-thickness cracks at the three centrally located holes of the chordwise splice. Next, the corner crack geometrical shape was determined by considering a surface flaw of aspect ratio equal to a corner crack (*i.e.*, $a/2c = ½$). Therefore, the total stress-intensity factor was

$$K_I = \frac{\beta_3 \sigma_g \sqrt{\pi a} M_k}{Q^{½}} \tag{12}$$

where

β_3 = finite-element stress-intensity-factor solution for structure
σ_g = applied stress level, ksi
a = corner crack radius, in.
M_k = back surface magnification factor
$Q = \left[\Phi^2 - 0.212\left(\frac{\sigma_g}{\sigma_{ys}}\right)^2\right]$
σ_{ys} = yield strength, ksi
Φ = complete elliptical integral of second kind (function of crack aspect ratios).

The above stress-intensity solution was utilized with the crack aspect ratio remaining constant. That is, the corner flaw shape remained a corner flaw as growth occurred in a radial direction and toward the back surface of the thickness. Further, progression of the crack from a corner flaw to thickness breakthrough was a through-the-thickness crack.

Both linear and retardation fatigue-crack-propagation analyses were performed in the study. The Willenborg effective-stress-retardation

Table 3. Constants Utilized in Forman's Crack-Growth Equation, 7075–T6511 Extrusion

Environment	Scatter Band	C, in./cycles/ $(\text{psi}\sqrt{\text{in.}})^{n-1}$	n	K_c ($\text{psi}\sqrt{\text{in.}}$)	K_Q ($\text{psi}\sqrt{\text{in.}}$)	Yield Stress (psi)
Dry	Lower	5.0×10^{-13}	3.0	68,000	68,000	83,000
Dry	Upper	1.00×10	3.0	68,000	68,000	83,000
Wet	Lower	4.60×10	4.0	50,000	50,000	83,000
Wet	Upper	2.74×10	4.0	50,000	50,000	83,000

model was selected as the model to be applied. Previous crack-growth analysis of various mission mixes of the C-5A cargo transport[14] demonstrated that this model adequately predicted flight-by-flight fatigue-crack-growth behavior of laboratory specimens.

In the fatigue-crack-propagation analysis, fatigue-crack growth was calculated on a cycle-by-cycle basis for each layer or segment of stresses within a flight. This is referred to in the results as flight-by-flight crack growth.

Retarded fatigue-crack-propagation behavior was determined with a high yield-strength value for 7075–T6511 extrusion. This strength level was selected because of the strength/fracture-toughness trade-off behavior of 7000-series aluminum alloys.[15] This was also selected because the wing planks of the fleet probably contain some high-strength material. The use of high-yield-strength value associated with the Willenborg effective-stress model resulted in smaller crack-tip yield zones and less retardation. Therefore, the behavior of the fleet was covered in a realistic way.

The limiting critical crack length was established at limit stress. This limiting condition was utilized in establishing required inspection intervals from initial damage sizes according to MIL-A-83444.[1] Both plane-strain and plane-stress stress states existing around the crack front were considered in determining the mode of failure and critical crack lengths. For shallow corner cracks, the failure mode is plane strain and governed by the K_{Ic} property of the material. Experimental results of Broek[16] showed that this residual-strength criterion applies for corner cracks emanating at the edge of holes. In the case of deep corner cracks which are past mid-thickness in depth and in the transitional state, the residual strength is governed by the transitional K value for that condition. Through-the-thickness crack instability is governed by the K_c property of the material. For high-yield-strength 7075–T6511 extruded material, the properties utilized were $K_{Ic} = 25\ \text{ksi}\sqrt{\text{in.}}$ and $K_c = 50\ \text{ksi}\sqrt{\text{in.}}$

Fatigue-Crack-Propagation Behavior Results

Several integration methods are utilized to predict fatigue-crack-extension behavior under complex block spectra or flight-by-flight spectra. These methods have been discussed by Engle and Rudd[17] and Gallagher and Stalnaker[18]. The integration procedures are usually based on some integration interval such as layers, flights, or cycle-by-cycle. In this analysis, the integration was performed on a layer-by-layer interval.

The fatigue-crack-propagation behavior of the full-scale fatigue test spectrum for this joint is shown in Figure 12. The behavior has been plotted as crack length versus flight hours. The cracks considered emanated from the inner hole of the three-hole pattern of the main plank. Analysis was performed based on two initial damage sizes — 0.005- and 0.02-in. corner cracks emanating from the load-transfer holes. As expected, a longer fatigue-crack-propagation life resulted from the smaller assumed damage size. For this full-scale fatigue stress spectrum, the retardation fatigue-crack-growth behavior showed a slightly longer crack growth than the linear life. Transitional crack-growth behavior occurred at this location with continuing crack growth. However, the continued crack-growth life was almost negligible since multiple cracks were assumed from a 0.005-in. initial damage length, and eventually crack joining resulted.

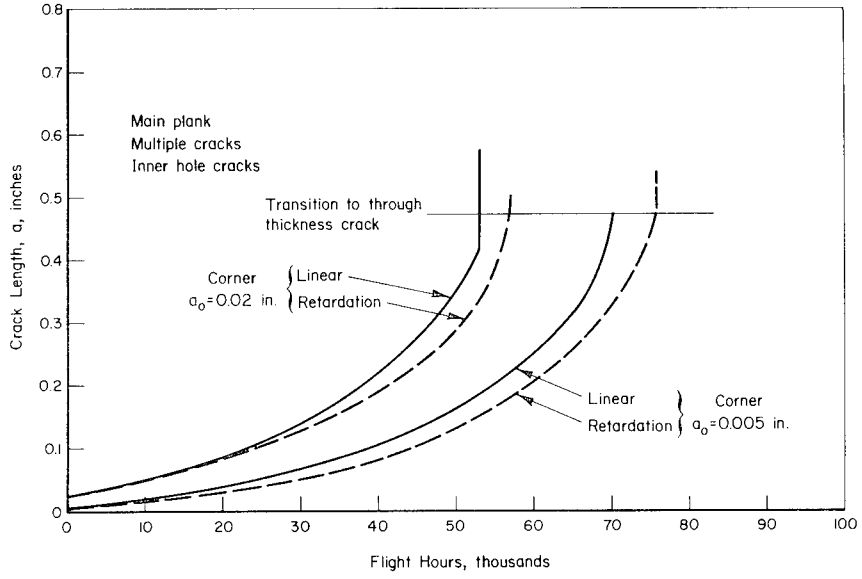


Figure 12. Fatigue-crack-growth behavior of cracks in splice, full-scale fatigue-test spectrum.

The flight-by-flight fatigue-crack-propagation behavior of the five fleet aircraft is shown in Figures 13 and 14. The behavior has been plotted as crack length versus flight hours and a nomograph representation of flight hours has been shown for comparison purposes. Due to the lengthy flight spectra and the magnitude of the 1-g stress levels on this aircraft, retardation-crack-growth behavior was handled in a special way because of economical reasons and excessive requirements of large computer runs.

A retardation factor for each aircraft history was determined for growth from an initial corner crack length of 0.02 in. The computer-run time was limited to 1200 seconds. The retardation factors established for each aircraft are shown in Table 4. The retardation fatigue-crack-growth behavior was determined from 0.005- and 0.02-in. initial corner crack sizes, using the appropriate factor for each aircraft flight history.

The flight-by-flight fatigue-crack-growth behavior as determined by a linear analysis (Figure 15) showed that the crack-growth behavior fell in a very tight scatter band and was slower than the full-scale fatigue-test spectrum behavior. However, the retardation fatigue-crack-growth behavior of each aircraft shows a large variation from aircraft to aircraft.

The fatigue-crack-propagation results generated in this analysis can be used in establishing reliable inspection periods for the chordwise

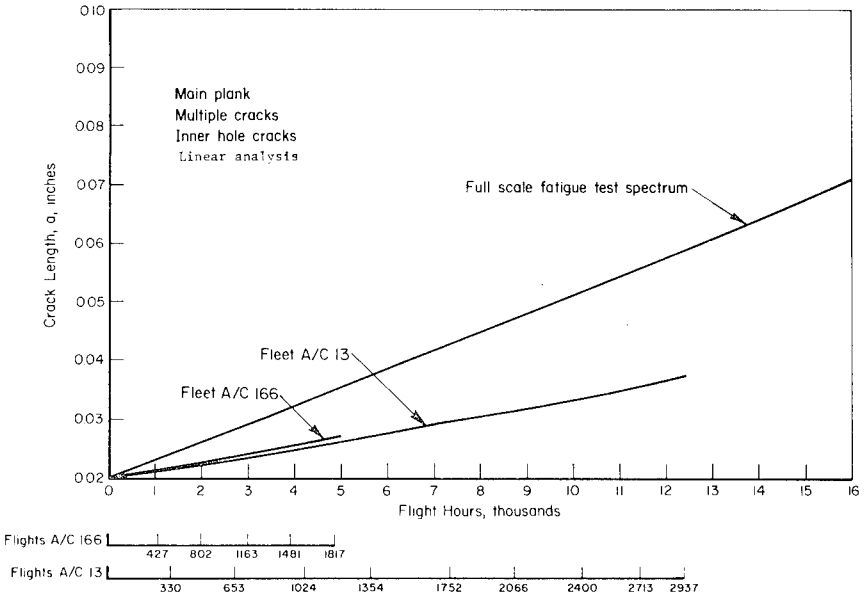


Figure 13. Fatigue-crack-growth behavior of cracks for AC 13, 166 (a_0 = 0.02 in.).

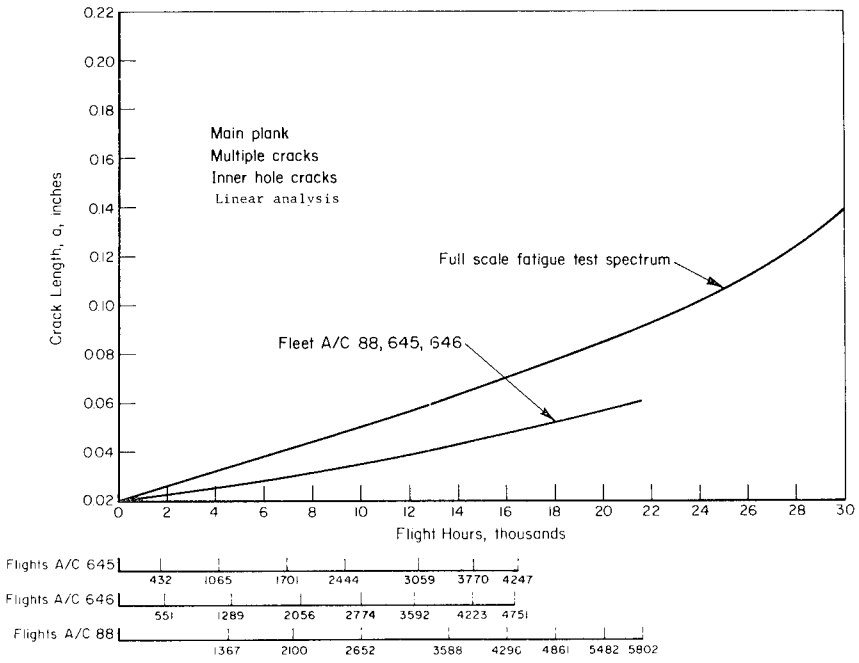


Figure 14. Fatigue-crack-growth behavior of cracks for AC 88, 645, 646 ($a_0 = 0.02$ in.).

splice of the wing box. In applying the requirements of MIL-A-83444, several aspects of the inspection techniques already used, the expected maximum loads that will occur, and the details of the structure with respect to inspectability had to be considered.

First of all, the loading levels that the aircraft may encounter during the design lifetime or inspection interval must be considered. The particular military cargo aircraft considered in this study is expected to reach a lifetime of 40,000 flight hours. According to the specification, the residual strength of the structure is specified by the minimum internal load, P_{xx}. For a one-lifetime span, this load level is limit load times a dynamic magnification factor of 1.15. This applied to noninspectable structure. If the structure is inspectable, then P_{xx} depends on the load level that could occur during a specified inspection interval and depends on the degree of inspectability.

For fail-safe structures, there is a requirement that a minimum load, P_{yy}, must be sustained prior to load-path failure as well as being able to sustain P_{xx}. The P_{yy} load is not less than P_{xx} if the incremental loading is taken as design limit load.

Table 4. Retardation Factors for Lower Surface (a_0 = 0.02 Inch)

Aircraft Number	a, inch	Cycles, Linear	Cycles, Retardation		Factor
013	0.02122	87,500	161,215		1.84246
013	0.02188	162,000	213,516		1.31800
013	0.02239	195,000	295,730		1.51656
013	0.02265	212,000	319,123		1.50530
				Average	1.45435
088	0.02087	72,891	96,151		1.31911
088	0.02173	140,144	166,756		1.18989
088	0.02215	153,700	192,500		1.25244
088	0.02300	193,015	244,921		1.26892
				Average	1.25769
166	0.02052	104,944	210,317		2.00409
166	0.02084	156,149	339,425		2.17372
				Average	2.08890
645	0.02162	104,000	130,984		1.25946
645	0.02225	131,342	231,965		1.76611
645	0.02243	140,000	285,182		2.03701
				Average	1.68754
646	0.02112	81,890	98,000		1.19672
646	0.02226	134,330	185,000		1.37721
646	0.02254	145,000	260,000		1.79310
646	0.02261	150,000	276,244		1.84162
				Average	1.55216

Based on the assumption that a cargo aircraft is depot or base-level inspectable, the degree of inspectability had to be considered. The reported techniques and inspection flaw sizes reported by WRALC defined the degree of currently utilized reliable techniques. These flaw sizes are 0.25 in. resulting from experience with eddy-current and X-ray inspection techniques. These flaw sizes for the joint are in accordance with the in-service inspection flaw assumptions of MIL-A-83444 for structure without component or fastener removal. Therefore, inspection intervals based on crack growth from initial 0.25 in. corner cracks to failure would provide the required inspection intervals for this criterion. However, the length of flaw must be an inspectable uncovered length.

It became obvious that the above criterion could not be applied for cracks located in the joint and particularly the main planks. The critical crack lengths calculated for plane-strain-fracture instability were rela-

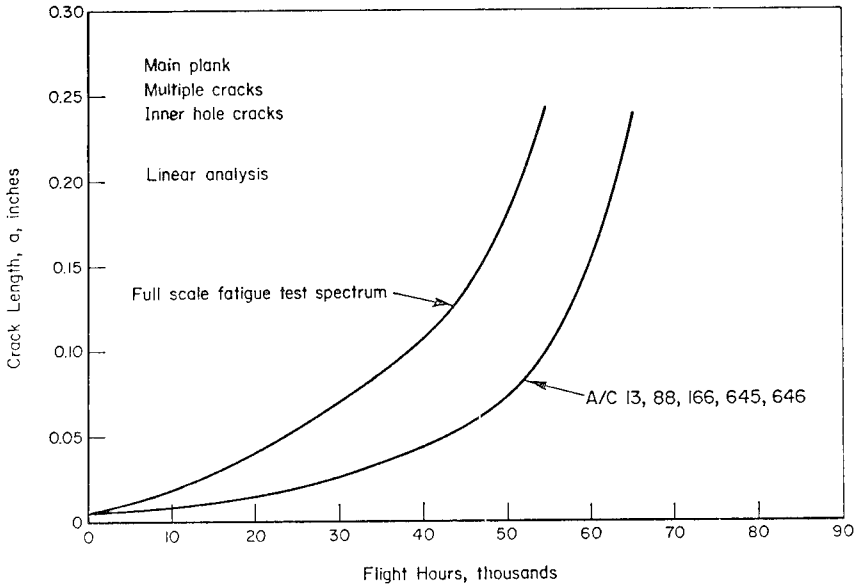


Figure 15. Fatigue-crack-growth behavior of cracks in chordwise splice ($a_0 = 0.005$ in.).

tively small at limit stress so the obvious inspection intervals to be applied would be associated with the uninspectable type of structure. Therefore, for each location, the fatigue-crack-growth results from 0.005- and 0.02-in. initial flaw sizes were used to establish inspection intervals. The limiting crack size for growth was the critical flaw at limit load application, P_{yy}.

Table 4 lists the linear and retardation total flight hours to critical crack size for each aircraft based on initial 0.02-in. corner cracks according to fail-safe multiload-path type of structure. Table 4 also lists the linear and retardation total flight hours to critical crack size for each aircraft based on initial 0.005-in. corner cracks according to the fastener policy for aircraft structure.

From these results, the required inspection intervals for base or depot-level inspection were calculated by applying the factor of 2 requirement to the retarded crack-growth lifetimes of Table 5. These results are listed in Table 6 and the minimum flight hour value of the high crack-growth-damage airplane can be assessed from Table 6. For this joint, the inspection interval is 42,880 hours.

The assumptions of the analysis, the requirements of MIL-A-83444, the service-inspection requirements, and methods of nondestructive inspection define the structure to be uninspectable. Therefore, the only

Table 5. Flight Hours to Critical Crack Length at Limit Load (a_f = 0.475 in.)

Aircraft Number	a_0 = 0.02 in.		a_0 = 0.005 in.	
	Linear Flight Hours	Retardation Flight Hours	Linear Flight Hours	Retardation Flight Hours
013	59,000	85,760	84,000	122,140
088	59,000	94,163	84,000	105,646
166	59,000	123,226	84,000	175,470
645	59,000	99,530	84,000	141,750
646	59,000	91,450	84,000	130,380
FSFT	53,000	55,500	70,000	76,000

Table 6. Required Inspection Intervals for Base or Depot-Level Inspections

Aircraft Number	Flight Hours (a_0 = 0.02 in.)	Flight Hours (a_0 = 0.005 in.)	Linear* Flight Hours	Retardation* Flight Hours
013	42,880	61,070	32,000	46,539
088	47,080	52,820	32,000	40,243
166	61,613	87,700	32,000	66,845
645	49,760	70,875	32,000	53,984
646	49,760	60,190	32,000	49,664
FSFT	27,750	38,000	16,000	22,000

*Interval to crack clean-up size (a = 0.03 in.).

approach that can be used for inspection is a fastener-pulling inspection and the use of eddy-current or some other more reliable technique to find cracks in the fastener holes.

Of particular importance in any fatigue-crack-growth study involving an aircraft program is the crack-growth lifetime-to-clean-up size. This is associated with cracks emanating at the edges of holes and the maximum extent to which the crack can grow and be cleaned up by drilling and reaming of oversize holes. The clean-up size selected was 0.03 in. Table 6 shows the results of each aircraft based on an initial damage size of 0.005 in. For the fleet aircraft, this flight aircraft time is 40,423 hours for aircraft No. 88. However, it should be pointed out that hole quality due to drilling and fastener installation could change the effective initial damage size to a value larger than 0.005 in. This would result in a smaller aircraft flight time to clean-up size.

CONCLUSIONS

Based on the results of this analytical study, the following conclusions are presented:

1. The analytical results, using the finite-element method of structural analysis, demonstrated that finite-element techniques can be applied in analyzing load-transfer joints. The overlaying of two-dimensional grid systems and fastener nodal connecting provides an approach in accounting for load-transfer effects.

2. Fracture-mechanics/finite-element analyses were performed in deriving the stress-intensity-factor variation with crack size from the finite-element models. The approach involved two levels of models with the second-level model a supercell of the first. Structural crack stiffness was accounted for by successive double nodal point "unzipping" of the models. Fastener load-transfer effects were accounted for in the second level models and resulting stress-intensity-factor calculations.

3. Two approaches, the work-energy and crack-opening displacement methods, were utilized in calculating the variation of stress-intensity factor with crack size for a structural joint. The crack-opening-displacement approach demonstrated a scatter band in values of stress-intensity factors. However, the stress-intensity factors were in agreement as derived by the two methods. The work-energy method was selected as the approach to apply in calculating stress-intensity factors.

4. The results of the fatigue-crack-propagation analysis from initial corner cracks at the joint and for the five aircraft of the fleet demonstrated that the fleet behavior fell within a relatively narrow band. This is attributed to the mission usage of predominantly three missions of the 14-mission profile. However, when considering a fleet of some 250 aircraft, the fatigue-crack-growth results of other aircraft demonstrating high time and high fatigue damage should be compared to the banded behavior as demonstrated by these five aircraft.

5. The calculated flight hours from initially assumed damage sizes were performed based on conservative assumptions. These assumptions were the boundary conditions of neat-fit fasteners in the joints, the upper end of the scatter band on da/dN, and the high-yield-strength low-fracture toughness material properties used in retardation and critical-crack-length calculations. However, these assumptions provide a realistic approach against loss of aircraft in establishing reliable inspection intervals.

6. The required inspection intervals for base or depot level inspections were established for each aircraft. For the chordwise joint, this was determined to be 42,880 hours. The corresponding calculated flight

hours from an initial damage size of 0.005 in. to a crack clean-up size of 0.03 in. were 40,243.

7. The stringent requirements of fracture-mechanics technology and residual-strength approaches demonstrated that the predominant failure mode of critical cracks was in the plane-strain region. This, in turn, resulted in critical crack sizes at limit load which are reasonably inspectable by current nondestructive methods for in-place structure. However, because of the covered length of crack, a bolt- or fastener-pulling inspection will have to be performed.

ACKNOWLEDGMENT

The results presented in this chapter are based on those of a much larger study conducted for Warner Robins Air Logistics Center under Government Contract F09603-74-C-1232. The authors express their gratitude to Capt. Ronald Hardy, the Project Engineer, during this study.

REFERENCES

1. "Airplane Damage Tolerance Requirements," Military Specification MIL-A-83444 (USAF), 2 July 1974.
2. Paris, P. C. and Sih, G. C. M., "Stress Analysis of Cracks," in *Fracture Toughness Testing and Its Applications*, Special Technical Publication 381. Philadelphia: American Society for Testing and Materials (1965), 30–83.
3. Chan, S. K., Tuba, I. S., and Wilson, W. K., "On the Finite Element Method in Linear Fracture Mechanics," *Eng. Fract. Mech.*, **2** (1970–71), 1–17.
4. Hall, L. R., Shah, R. C., and Engstrom, W. L., "Fracture and Fatigue Crack Growth Behavior of Surface Flaws and Flaws Originating at Fastener Holes," Boeing Aerospace Company, Seattle, Wash. Air Force Flight Dynamics Laboratory Contract Report No. AFFDL-TR-74-47-Vol. 1, May 1974. (AD-A001 597)
5. Newman, J. C. Jr., "Finite-Element Analysis of Fatigue Crack Propagation — Including the Effects of Crack Closure," unpublished Ph. D. dissertation, Virginia Polytechnic Institute and State University, 1974.
6. Broek, D., *Elementary Engineering Fracture Mechanics*. Leyden, Netherlands: Noordhoff International Publication Company (1974).
7. Smith, S. H., Simonen, F. A., and Hyler, W. S., "C-141 Wing Fatigue–Crack Propagation Study," Battelle Columbus Laboratories, Ohio, Warner Robins Air Logistics Center Contract Report No. G-2954-0001, February 1975.
8. Irwin, G. R., "Fracture," in *Encyclopedia of Physics*, Vol. 6, *Elasticity and Plasticity*, ed. by S. Flugge. Berlin: Springer-Verlag (1958), 551–90.

9. Dixon, J. R. and Pook, L. P., "Stress Intensity Factors Calculated Generally by the Finite Element Technique," *Nature*, **224** (1969), 166–67.
10. Mowbray, D. F., "A Note on the Finite Element Method in Linear Fracture Mechanics," *Eng. Fract. Mech.*, **2** (1970–71), 173–76.
11. Rybicki, E. F. and Kanninen, M. F., "A Finite Element Calculation of Stress Intensity Factors by a Modified Crack-Closure Integral," *Eng. Fract. Mech.*, to be published.
12. Bowie, O. L., "Analysis of an Infinite Plate Containing Radical Cracks Originating at the Boundary of an Internal Circular Hole," *J. Math. Phys.*, **35** (1956–57), 60–71.
13. Engle, R. M. Jr., "Cracks, a FORTRAN IV Digital Computer Program for Crack Propagation Analysis," Air Force Flight Dynamics Laboratory, Wright-Patterson AFB, Ohio, Report No. AFFDL-TR-70-107, October 1970. (AD 717 150)
14. Smith, S. H., "Fatigue-Crack Growth Behavior of C-5A Wing Control Points," Battelle Columbus Laboratories, Ohio. Aeronautical Systems Division Contract Report No. ASD-TR-74-18, May 1974. (AD-A002 553)
15. Anderson, W. E., "Design and Purchase Expectations for Fracture Resistance of 700-Series Aluminum Airframe Alloys," Battelle Columbus Laboratories, Ohio. Aeronautical Systems Divisions Contract Report No. ASD-TR-74-16, January 1974. (AD-A002 522)
16. Broek, D., Nederveen, A., and Meulman, A., "Applicability of Fracture Toughness Data to Surface Flaws and to Corner Cracks at Holes," National Aerospace Laboratory, Amsterdam, Netherlands, Report No. NLR-TR-71033-U, January 1971.
17. Engle, R. M. and Rudd, J. L., "Analysis of Crack Propagation Under Variable Amplitude Loading Using the Willenborg Retardation Model," AIAA Paper 74-369, 1974.
18. Gallagher, J. P. and Stalnaker, H. D., "Methods for Analyzing Fatigue Crack Growth Rate Behavior Associated with Flight-by-Flight Loading," AIAA Paper 74-367, 1974.

20. APPLICATION OF NDT TECHNIQUES FOR DETECTING FLAWS IN JOINTS

W. D. RUMMEL
Martin Marietta Corporation
Denver, Colorado

Assessment of critical defects must be included in any structural design analysis. Critical defects occur most frequently in structural joints and are therefore of primary concern in such analysis. Fracture-mechanics analysis provides an analytical tool for predicting critical flaw sizes. Flaws can be detected and characterized by nondestructive testing techniques and may therefore provide assurance of structral design integrity. Common nondestructive testing techniques include radiography, ultrasonic, eddy current, liquid penetrant, magnetic particle, and acoustic emission. This chapter discusses recent analyses and applications of nondestructive testing for detection of flaws in joints.

INTRODUCTION

Nondestructive testing (NDT) has been used as a critical tool in the prevention of structural failure. Fracture-mechanics design principles assume the presence of flaws in load-carrying structures and provide a quantitative prediction of flaw behavior in service. The challenges of applying fracture-mechanics design principles to nondestructive testing technology are to (1) reliably detect critical flaws, (2) accurately describe the size and shape of flaws detected, and (3) precisely describe the location and orientation of the flaws detected.

Nondestructive testing technology has been historically challenged to describe the "smallest flaw that can be detected" by a given technique. The new challenges are to describe the "largest flaw that can be missed" by a given technique. The reliability of the technique must therefore be established in terms of critical flaw characteristics.

The majority of fracture-mechanics data concerns behavior of cracks in wrought forms of common structural metal alloys. It was therefore logical to determine flaw-detection reliability for various non-

destructive testing techniques using wrought metal alloy specimens containing cracks of various sizes. Several programs have been conducted to establish detection reliabilities for smooth, flat specimens.[1,2,3] In a program conducted by the author and his coworkers, 328 fatigue cracks of varying sizes and geometries were introduced in 118 aluminum alloy panels. These panels were then systematically evaluated by various nondestructive testing techniques to determine detection reliability as a function of crack length and depth.[4] Figure 1 is an example of the reliability data generated by this technique. As hardware geometry varies from the simple flat surface to complex shapes, additional analysis must be completed to determine flaw-detection reliability.

When simple hardware configurations are joined to form complex structures, considerable design attention is given to joints. Since joints are often made under varying conditions, more attention is in order for nondestructive testing and evaluation. A prerequisite to design analysis and to nondestructive analysis is the identification of critical defects in the joint.

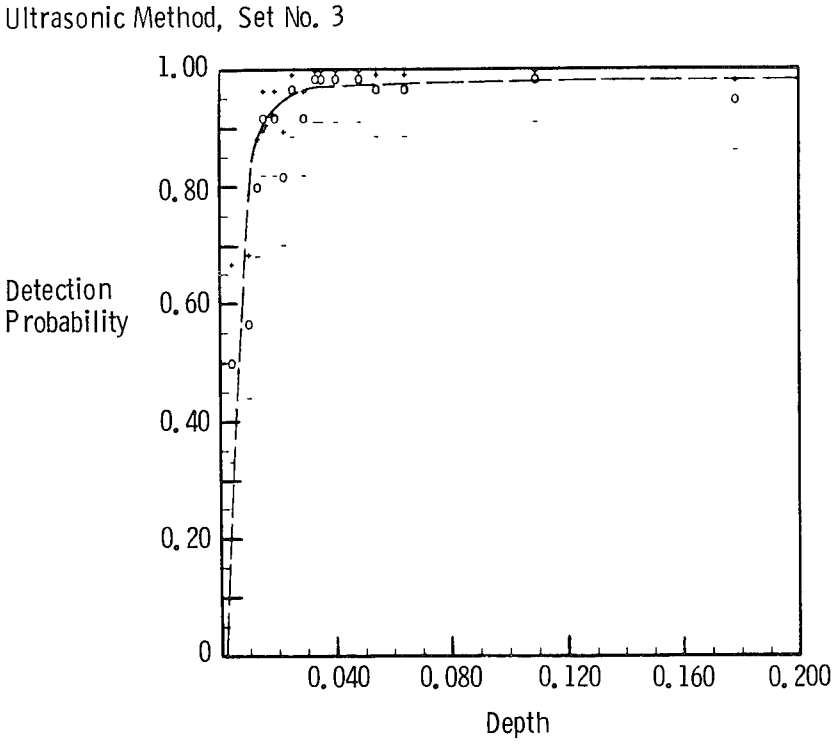


Figure 1. Fatigue crack detection at 95% reliability and 95% confidence level.

WELDED JOINTS

A common joint in wrought metal structures is a fusion-welded joint. In this case, a crack or crack-like defect are the most probable critical flaws. A welded joint requires fracture analysis for flaws in various geometries and conditions and also requires more complex analysis of potential nondestructive testing techniques. Figure 2 illustrates some possible flaws in a butt-fusion-welded joint. Nondestructive test techniques used for evaluation of welded joints include X-radiography, liquid penetrant, ultrasonic, eddy current, magnetic particle, and accoustic emission.

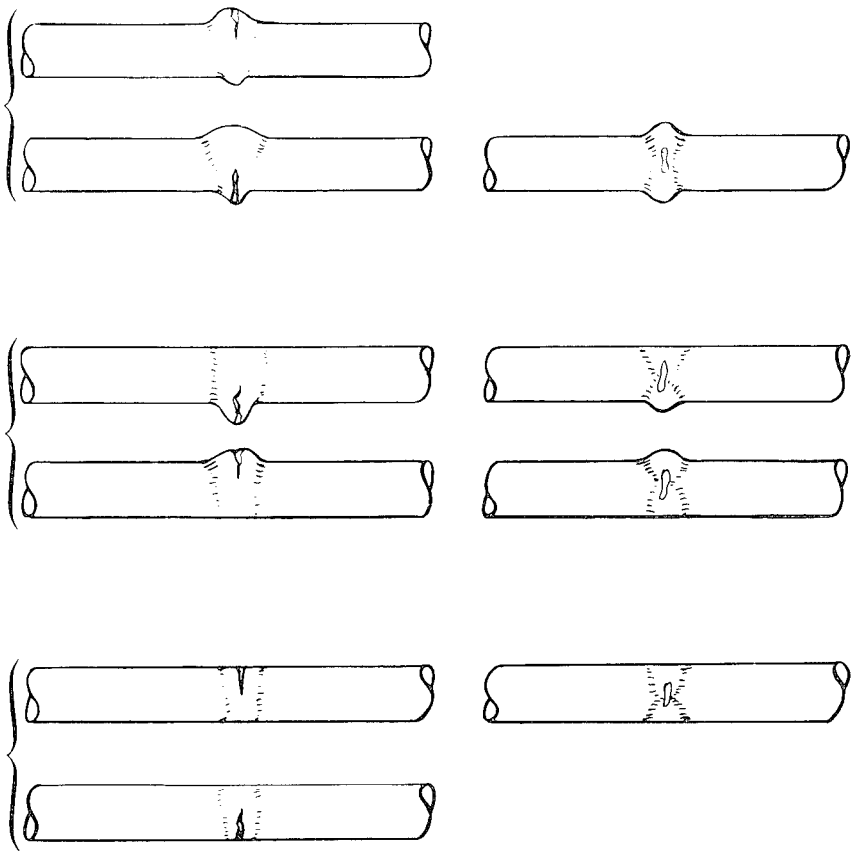


Figure 2. Flaw configurations (end view) for a butt fusion-welded joint.

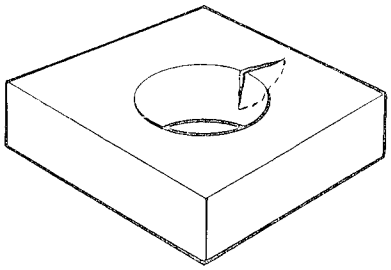
OTHER METALLURGICAL JOINTS

Resistance-welded, electron beam-welded, inertially welded, explosively welded, diffusion-bonded, and brazed joints constitute a partial list of the metallurgical joints used in industry. In some cases a critical flaw in the joint may be cracklike in nature and therefore amenable to analysis by fracture-mechanics techniques. A metallurgical variation such as shear or peel strength in a spot weld may be the dominant failure mode in a structure as fabricated. In service, crack initiation and propagation from a metallurgical variation is a usual mechanism for joint failure and therefore may be amenable to fracture-mechanics analysis. The task for nondestructive evaluation is therefore twofold: (1) detection of critical metallurgical variations in as-fabricated structures, and (2) detection of cracks initiated by such variations in service. The two NDT problems are quite different and must be separated to enable successful analysis and evaluation of a joint.

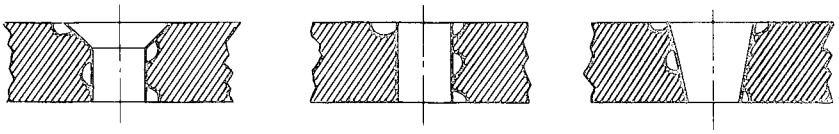
MECHANICALLY FASTENED JOINTS

Mechanically fastened joints also present dual problems of crack initiation and crack propagation. Since cracks emanating from fasteners constitute the major mechanism for structural degradation in aircraft structures, considerable emphasis is being placed on using nondestructive testing methods for their detection. Typical configurations for cracks in mechanically fastened joints are shown in Figure 3. Visual inspection and liquid-penetrant inspection are the usual methods for examining the outer surface layer of such joints, and X-radiography is the usual method for examining subsurface layers. Cracks must be initiated and must propagate outside the fastener-head area to be detected by these methods. Cracks of considerable size may therefore be "missed" on NDT evaluation. Common aircraft maintenance practices have been to (1) periodically remove fasteners in critical structural joints, (2) evaluate the internal bore of the joint by visual and eddy-current methods, (3) remove cracks detected by reaming and/or component replacement, and (4) reinstall a fastener. This practice is expensive and therefore limited to critical joints.

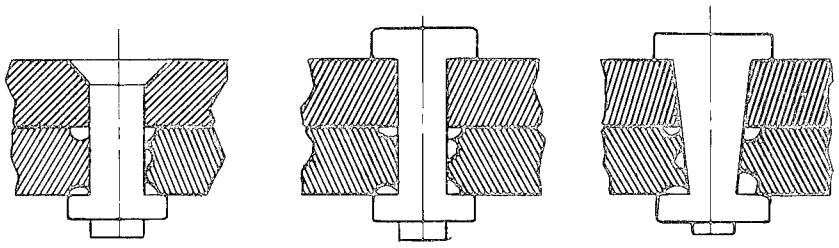
The Boeing Commercial Airplane Company has recently evaluated ultrasonic techniques for detection of cracks under installed fasteners and has developed an inspection system for examination of the outer layer in a joint.[5] Battelle Columbus Laboratories is currently investigating an eddy-current technique for examination of subsurface layers in a joint with fasteners in place.[6] Much work remains to provide reliable and economical detection of critical flaws in such joints.



Fastener Hole Showing Typical Crack Location



Typical Crack Locations within a Fastener Hole Crossection



Typical Crack Locations in the Second Layer of a Joint

Figure 3. Typical configurations for cracks in mechanically fastened joints.

ADHESIVELY BONDED JOINTS

Adhesively bonded joints present a unique challenge to fracture mechanics and nondestructive testing technology due to the nature of the joint. Critical flaws are initiated and propagate in an adhesive material in which material properties are continually varying. If precise bonding-process control is assumed, the task of analyzing flaw propagation is

greatly simplified. Nondestructive evaluation does not, however, benefit to the same extent since flaw initiation is normally the result of local variation in material properties and such variations affect the nondestructive technique used in evaluation. Nondestructive evaluation is again separated into two test problems — flaw initiation and flaw propagation.

Local failure of a weak bond is a primary mechanism for flaw initiation in a bonded joint. Considerable work has been done to nondestructively evaluate bond strength in adhesively bonded joints. A thorough state-of-the-art review of this work was provided by Cagle.[7] A more recent review and analysis has been provided by Curtis *et al.*[8] The complexity of the problem may be appreciated by analyzing the constituents and possible variations in adhesively bonded joint as shown schematically in Figure 4. Out-of-tolerance variation in any layer of the bonded joint may result in flaw initiation.

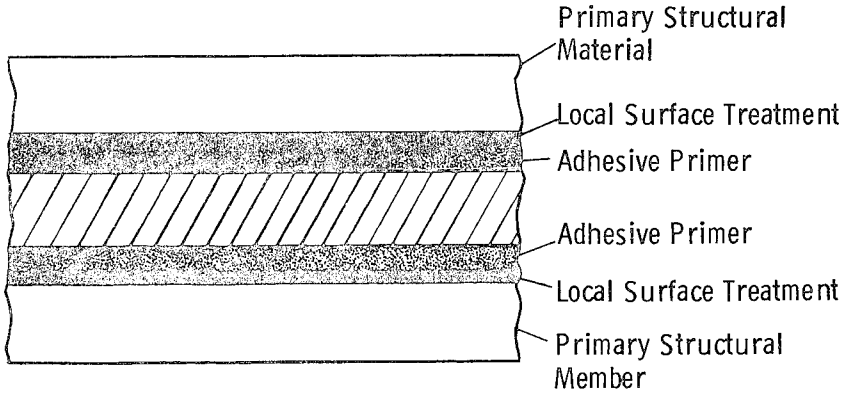
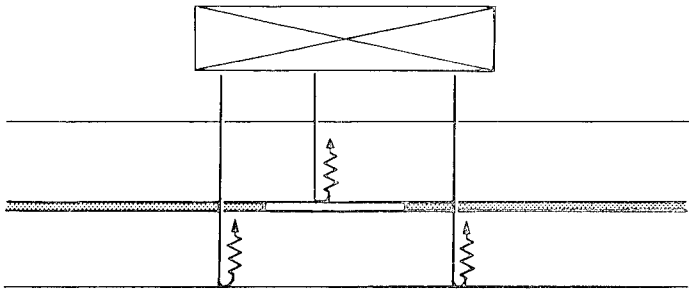
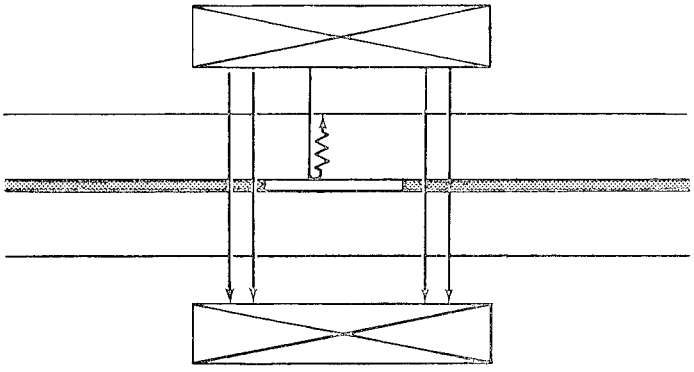


Figure 4. Schematic cross-section view of an adhesively bonded joint.

If primary structural material failures caused by joint design are neglected, lack of bonding (unbonded or debond) at the joint interface is the critical flaw type that must be detected. The nondestructive test methods that are applied to this flaw type are: (1) reflected or transmitted energy methods such as sonic, ultrasonic, radiographic, and thermal techniques; and (2) strain analysis by visual, brittle coating, birefringent coating, holographic, and strain-gage techniques. The application of reflected energy and transmitted energy techniques is shown schematically in Figure 5. Although nondestructive methods are used routinely for adhesive bond evaluation, little quantitative data concerning detection re-



Pulse Echo Technique



Through Transmission Technique

Figure 5. Schematic view of the reflected energy and transmitted energy methods for bond evaluation.

liabilities are available. Continuing challenges to fracture mechanics and nondestructive testing technologies are:

1. Establishment of methods to analyze and predict critical flaw sizes.
2. Establishment of quantitative data and analysis techniques for nondestructive flaw detection reliability.

COMPOSITE STRUCTURES

Composite material structures provide one of the most difficult challenges to nondestructive testing technology. The ability to "build a material" with varying properties in different directions provides previously unattainable flexibility in structural design and in structural load-carrying efficiencies. At the same time, varying material properties increase the difficulty in analyzing and applying nondestructive techniques to detect defects. Nondestructive evaluation methods have a significant role in determining and assuring the uniformity of such material properties as density, modulus, fiber–matrix ratio, etc. (Figure 6). Local variation of such properties may result in flaw initiation, for example local cracking or unbonding. Once a flaw is initiated, methods used in detecting flaws in metals are applicable.

Considerable variation in joint design is possible due to varying material properties and many joint configurations have been used. Examples of some typical joints are shown in Figure 7. Variations in joint configurations require analysis and evaluation of each specific joint configuration to select the optimum nondestructive testing techniques. Passive techniques that have been applied include visual, liquid penetrant, ultrasonic, radiographic, and thermal methods. Active techniques include visual, brittle coating, birefringent coating, holographic, acoustic emission, and strain-gage techniques.

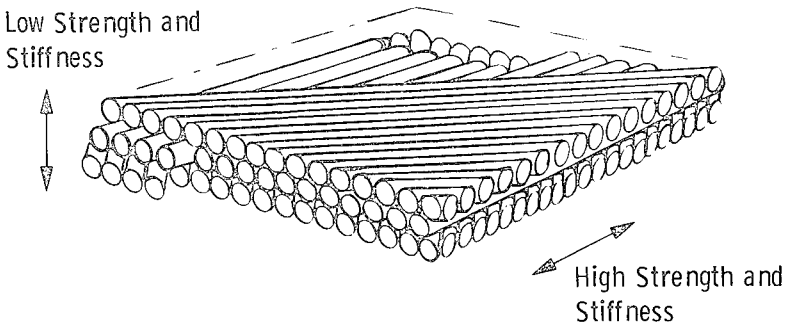
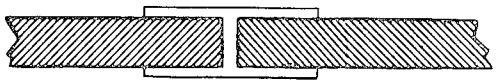
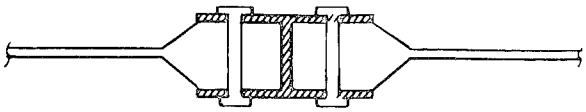


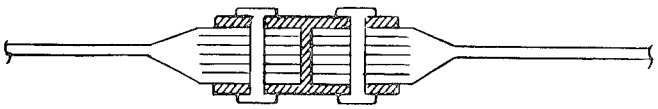
Figure 6. Composite material having nonhomogeneous material properties.



Single and Double Adhesively Bonded Joint



Local Reinforcement for Installation of
Mechanical Fasteners



Local Reinforcement by Interleaving Metal
Strips at a Mechanical Joint

Figure 7. Typical composite material joint configurations.

SUMMARY

In summary, although nondestructive evaluation techniques are used extensively in industry to assess the integrity of structures, little quantitative data is available to establish critical flaw detection sensitivity and reliability. Fracture mechanics has provided a major challenge and tool for establishing such data. It is apparent that numerical approaches to establishing detection reliabilities for the variety of materials, configurations, and flaw types are beyond the economic resources available. Analytical approaches must be developed to predict detection reliabilities. In the meantime, numerical data generated will be used as a tool for evaluating current NDT performance and as a basis for establishing analytical models. Fracture-mechanics analyses will continue to

be a major analytical tool in defining critical defects. Nondestructive test analyses will define reliable detection sensitivities for the variety of structural configuration and test conditions involved in practical application.

REFERENCES

1. Packman, P. F., Pearson, H. S., Owens, J. S., and Marchese, G. B., "The Applicability of a Fracture Mechanics–Nondestructive Testing Design Criterion," Lockheed-Georgia Company, Marietta, Ga. Air Force Materials Laboratory Contract Report No. AFML-TR-68-32, May 1968. (AD 832 042)
2. Pettit, D. E. and Hoeppner, D. W., "Fatigue Flaw Growth and NDI Evaluation for Preventing Through-Cracks in Spacecraft Tankage Structures," Lockheed California Company, Burbank. National Aeronautics and Space Administration Contract Report No. NASA-CR-128560, September 1972.
3. Anderson, R. T., DeLacy, T. J., and Steward, R. C., "Detection of Fatigue Cracks by Nondestructive Testing Methods," General Dynamics, San Diego, Calif. National Aeronautics and Space Administration Contract Report No. NASA-CR-128946, March 1973. (N73-24901)
4. Rummel, W. D., Todd, P. H. Jr., Frecska, S. A., and Rathke, R. A., "The Detection of Fatigue Cracks by Nondestructive Testing Methods," Martin Marietta Corporation, Denver, Colo. National Aeronautics and Space Administration Contract Report No. NASA-CR-2369, February 1974. (N74-17285)
5. Raatz, C. F., Senske, R. A., and Woodmansee, W. E., "Detection of Cracks Under Installed Fasteners," Boeing Commerical Airplane Co., Seattle, Wash. Air Force Materials Laboratory Contract Report No. AFML-TR-74-80, April 1974. (AD A-004 458)
6. Hyler, W. S., private communication.
7. Cagle, C. V., *Adhesive Bonding: Techniques and Applications*. New York: McGraw-Hill Book Company (1968), 229–72.
8. Curtis, G. J., Joinson, A. B., and Lloyd, P. A., "The Role of Transient Spectrum and Damping Analysis in Assessing the Strength of Polymeric Adhesive Metal Bonding," Atomic Energy Research Establishment, Harwell, Eng. Air Force Materials Laboratory Contract Report No. AFML-TR-74-280, January 1975. (AD A009 172)

SESSION VII

LIFE PREDICTION AND FACTORS INFLUENCING THE BEHAVIOR OF JOINTS

MODERATOR: E. J. MCQUILLAN
Naval Air Development Center

21. A NORMALIZATION SCHEME FOR DESCRIBING CRACK-GROWTH BEHAVIOR

J. P. GALLAGHER and R. M. BADER
Air Force Flight Dynamics Laboratory
Wright-Patterson AFB, Ohio

A crack-growth normalization scheme has been suggested as a basis for tracking the structural life of the F-4 aircraft. The scheme offers the potential of monitoring in an accurate and simplified manner all critical structural locations on the aircraft of a given force. The normalization schedule is developed, the associated advantages and disadvantages are discussed, and its sensitivity to the various parameters affecting crack growth is evaluated. The application of these normalized curves in inspection and modification scheduling is described.

INTRODUCTION

The rate of accumulating fatigue damage among aircraft of a given force varies considerably. The economical approach to life management requires tracking of aircraft and its critical locations on an individual basis to insure that inspections are accomplished on time and that structural modifications are installed at the opportune time. Monitoring the damage for all critical locations in an individual aircraft presents a potentially monstrous aircraft instrumentation, data-gathering, and data-analysis job since most critical locations will have different rates of accumulating damage. Aircraft flight parameters or structural measurements are required to determine the stress or strain at the critical locations in order to calculate the accumulated structural damage. The potential magnitude of the tracking effort required is illustrated by the product of the number of critical locations in each aircraft, the criteria for determining inspection and modification times, the number of aircraft in the force, and the past and/or anticipated usage of the aircraft.

This chapter provides in the following section a general description of the F-4 Tracking Program procedure which was developed during a recent F-4 aircraft structural evaluation accomplished by a team of

McDonnell and Air Force engineers. Thereafter the chapter focuses attention on the normalized crack-growth curve, the basic element used to transfer crack-growth behavior information between critical locations throughout the structure. The advantages and potential deficiencies of the normalized crack-growth-curve approach are noted following a sensitivity study which identifies principal variables. The use of normalized crack-growth curves for planning inspections or modifications to aircraft is also outlined.

BACKGROUND

When the crack-growth curves associated with the different structurally critical locations of the F-4 were examined, it was noted that normalizing the crack-growth curves to the forms illustrated in Figures 1 and 2 provided a strong indication of similarity from location to location. Figure 1 describes a life normalization scheme in which the ordinate expresses the crack size (a_i), between specified initial size (a_0) and the final size (a_f), and the abscissa expresses the percent of total life expended in growing the crack to a_i. This scheme was used to determine modification schedules. Figure 2 presents a second normalized life scheme in which the ordinate is nondimensionalized to express the percent of growth from the initial crack size to the final crack size. The Figure 2 scheme was employed to determine inspection schedules.

Using the normalized life procedure and considering the critical area selected as the control or monitoring point, less than 10 percent varia-

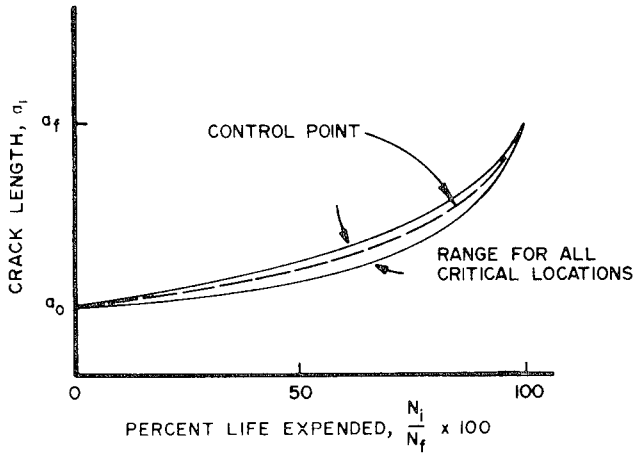


Figure 1. The family of normalized curves (modification).

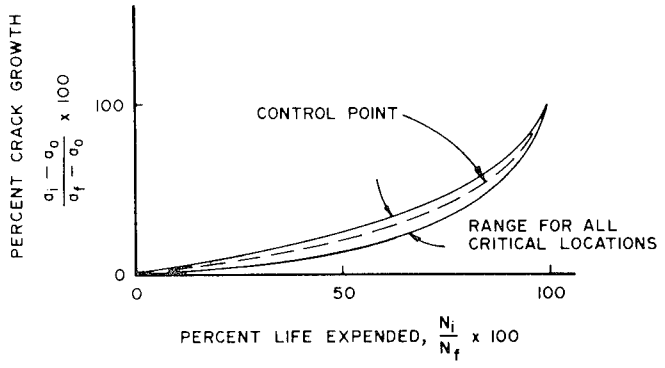


Figure 2. The family of normalized curves (inspection).

tion is expected in the predictions of the inspection and modification times for any individual F-4 aircraft. It was concluded that the crack-growth behavior for any single location (the control point) on an aircraft could be monitored and the crack growth at all locations of interest could be determined. The life normalization scheme was also determined to be valid for collapsing crack-growth curves generated using various stress spectra representative of F-4 airframe usage. Thus, the advantage of the life normalization scheme is that only one structural life (crack growth) calculation need be performed per aircraft (for the control point). The measure of airframe structural life expended, called the damage index, can be calculated for the control point and then the normalized curve can be used to predict the condition of other critical locations on the airframe.

The damage index (DI) for any given aircraft is defined by the expended life ratio (N_i/N_f) associated with the control point; referring to the control point in Figure 1, the aircraft allowable damage index of 1.0 is associated with a modification requirement. However, since at other designated critical positions the structure will no doubt have different allowable lives (N_f) for the same usage, the allowable damage indices (ADI) for the other critical points will differ from 1.0. The ADI for these points is given by

$$\text{ADI} = \frac{N_f(\text{critical point})}{N_f(\text{control point})} \tag{1}$$

The expended life fraction at other critical points is then obtained by the ratio of DI to ADI. An example illustrating the procedure for determining the modification time follows:

Critical Location	Modification Time, N_f (hrs)	Allowable Damage Index, ADI
Control Point, Location A	4000	1.0
Location B	2000	0.5
Location C	6000	1.5
etc.		

Thus, if an aircraft has flown, say 2,500 hours of average usage, the calculated damage index is $\frac{2500 \text{ hrs}}{4000 \text{ hrs}}$ or 0.625. (The 4000 hours is the assumed modification time in average flight hours for the control point.) Location B should have been modified since the allowable has been exceeded. Each structurally critical location has a calculated allowable damage index for the modification or inspection time. As the damage index increases, the maintenance manager can compare the aircraft damage index with the allowable damage indices for the critical locations and plan for the opportune scheduling for modifications and inspection.

The F-4 method of developing the damage index for each aircraft in the fleet is now outlined. The DI is a measure of the accumulated crack growth at the control point, and as such is a function of service history. To obtain the DI, the ratio of accumulated in-service stress cycles to the allowable number of cycles must be formulated. Counting accelerometers are installed on F-4 aircraft and a large amount of data describing past aircraft usage is available for deriving information of in-service stress cycles. Additionally, the availability of service-stress data provided the opportunity to study crack growth behavior generated under typical service-stress spectra in the laboratory. Coupling counting accelerometer data with crack-growth data was then accomplished as schematically illustrated in Figure 3. Figure 3(a) describes the relationship between N_z (g levels) and stress at the control point. Thus, knowing the N_z counts directly provides the counts of the corresponding stresses. Figure 3(b) describes the relationship between applied stress and allowable number of stress cycles associated with extending the crack between the specified crack sizes (a_0 and a_f). Figure 3 provides three curves, each associated with a specific usage, *e.g.*, fighter or reconnaissance mission types that are associated with configuration or weight changes.

Given that the type of usage for a particular aircraft is known, the change in the DI, defined by $\Delta \frac{N_i}{N_f}$ can be determined for an increment in service time (Δt) using the stress counts and the specific usage defined S–N curve such as described in Figure 3. The incremental damage

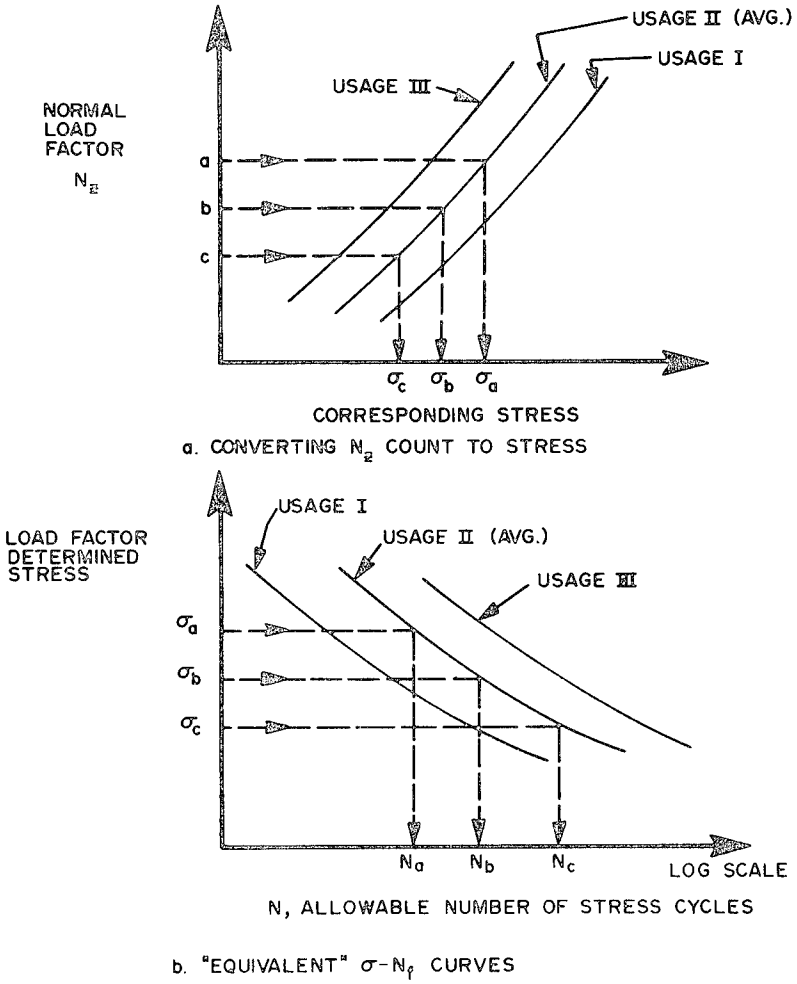


Figure 3. Calculating the damage index.

index is obtained by summing of individual stress counts to corresponding stress cycle allowable ratio:

$$\Delta \frac{N_i}{N_f} = \sum_{j=a}^{m} \frac{n_j}{N_j} \text{ for } \sigma_j \tag{2}$$

for the control point. The number of cycles Δn_a for the a accelerometer count is divided by the N_a cycle allowable associated with the σ_a stress to give its contribution to the incremental damage increment. A sum of the other counted cycles to allowable cycles ratio is performed as idicat-

ed by equation (2) to yield the incremental damage index for the service time increment (Δt). The current damage index at time t is the sum of the previous damage index ($t_o = t - \Delta t$) and the incremental damage index

$$\left.\frac{N_i}{N_f}\right|_t = \left.\frac{N_i}{N_f}\right|_{t_0} + \Delta \frac{N_i}{N_f} \tag{3}$$

The current DI, such as given by equation (3), can be used in conjunction with the number of flight hours accumulated (N_i) on the structure to estimate the modification time (N_f), *i.e.*,

$$N_f = N_i/\mathrm{DI} \tag{4}$$

which must be associated with continued service usage that is similar to past usage. When N_f at the control-point position is available for any given specified usage, the modification times for other critical locations can be estimated by inverting equation (1). The technique for determining the rate of change in damage as described by Figure 3 represents only one of a group of conceived methods that could be used in conjunction with equations (3) and (4).

If an aircraft has many critical locations with differing modification and inspection times, a severe scheduling problem for the maintenance manager and operational commands is imposed if the procedure described is followed exactly. It is envisioned that the required modifications could be assembled into groups for installation to minimize the impact on the maintenance facilities and the operational commands. The procedure, however, does provide the insight or background so that intelligent decisions may be made concerning the life management of a force of aircraft.

THE NORMALIZED CRACK-GROWTH CURVE

The normalized crack-growth curve shown in Figure 4 can be developed utilizing crack-growth data of the type shown in Figure 5. Figure 5 describes crack-growth data that are obtained under steady-state loading conditions. Steady-state loading conditions are normally associated with constant-amplitude loading, but such conditions would also apply to those spectra which can be divided into a series of statistically identical loading subblocks which produce a quasi-stationary cracking process at the crack tip.[1] A demonstration of the normalized crack-growth curve concept for steady-state spectrum loading conditions is conducted using the laboratory-generated crack-growth data which were collected by

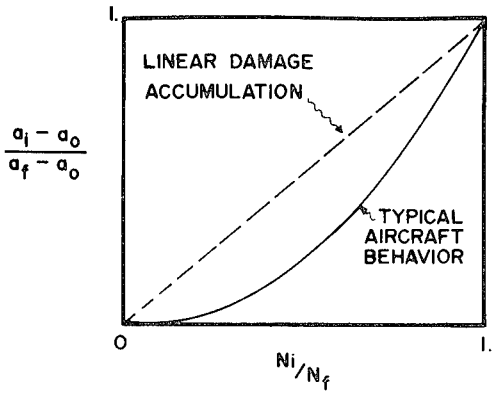


Figure 4. Schematic of normalized crack-growth curve.

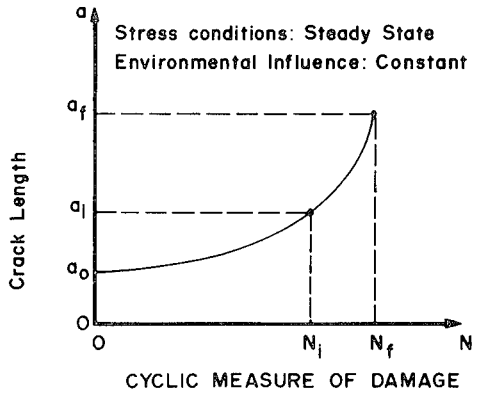


Figure 5. Schematic of a typical crack-growth curve.

Potter *et al.*[2] using two similar F-4E(S) wing spectra. These two F-4E(S) spectra were developed from the bending-moment spectra applied at Load Reference Station (LRS) 140 of a F-4E static test aircraft, and are described by their exceedance curves (scaled to a maximum stress of 36 ksi) shown in Figures 6 and 7. As can be noted by these figures, the spectra are the same except for the count of low-level stresses.

The crack-growth test data shown in Figures 8 and 9[2] were developed using 7075–T6511 aluminum specimens containing a radial corner crack emanating from a 0.250-in.-diameter hole, in a 1.0-in.-wide and 0.5-in.-thick cross section. Both Figures 8 and 9 show the influence of

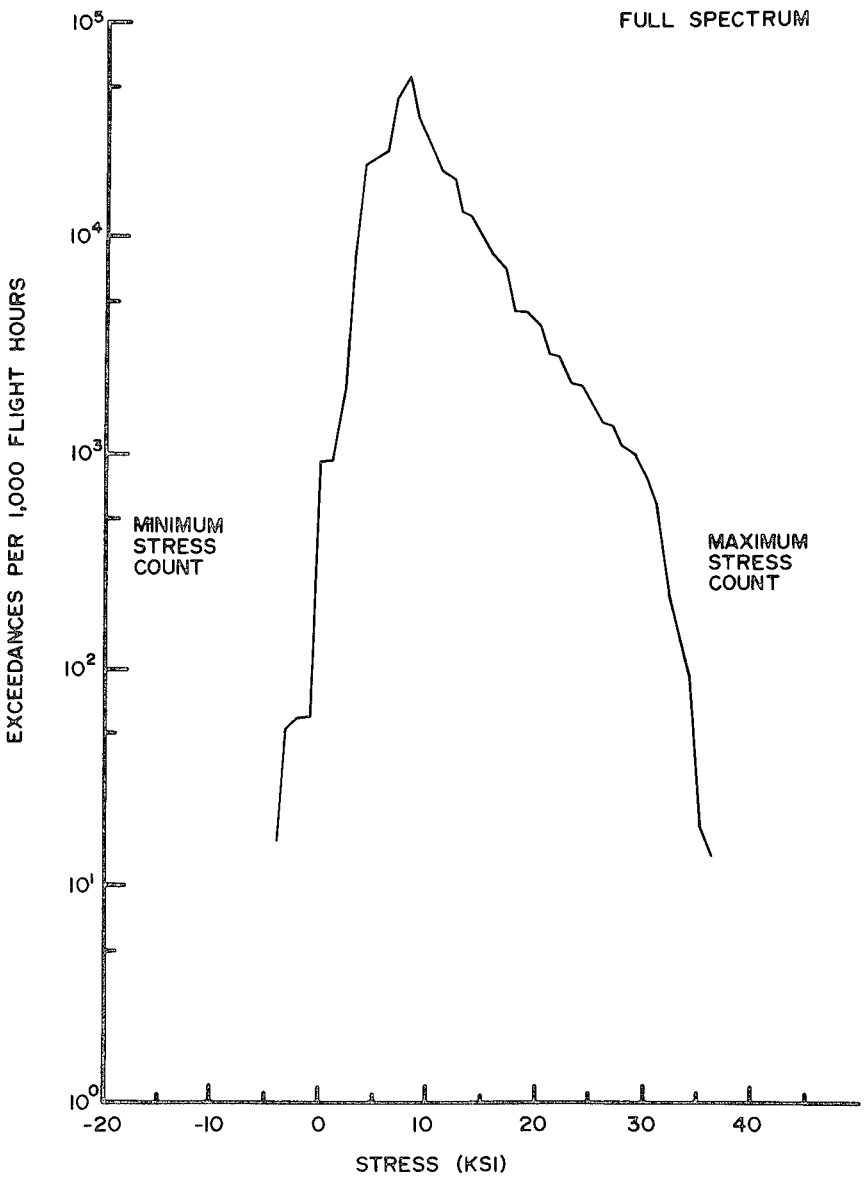


Figure 6. Exceedance data for a F-4E(S) wing spectrum scaled to a design limit stress of 36 ksi.

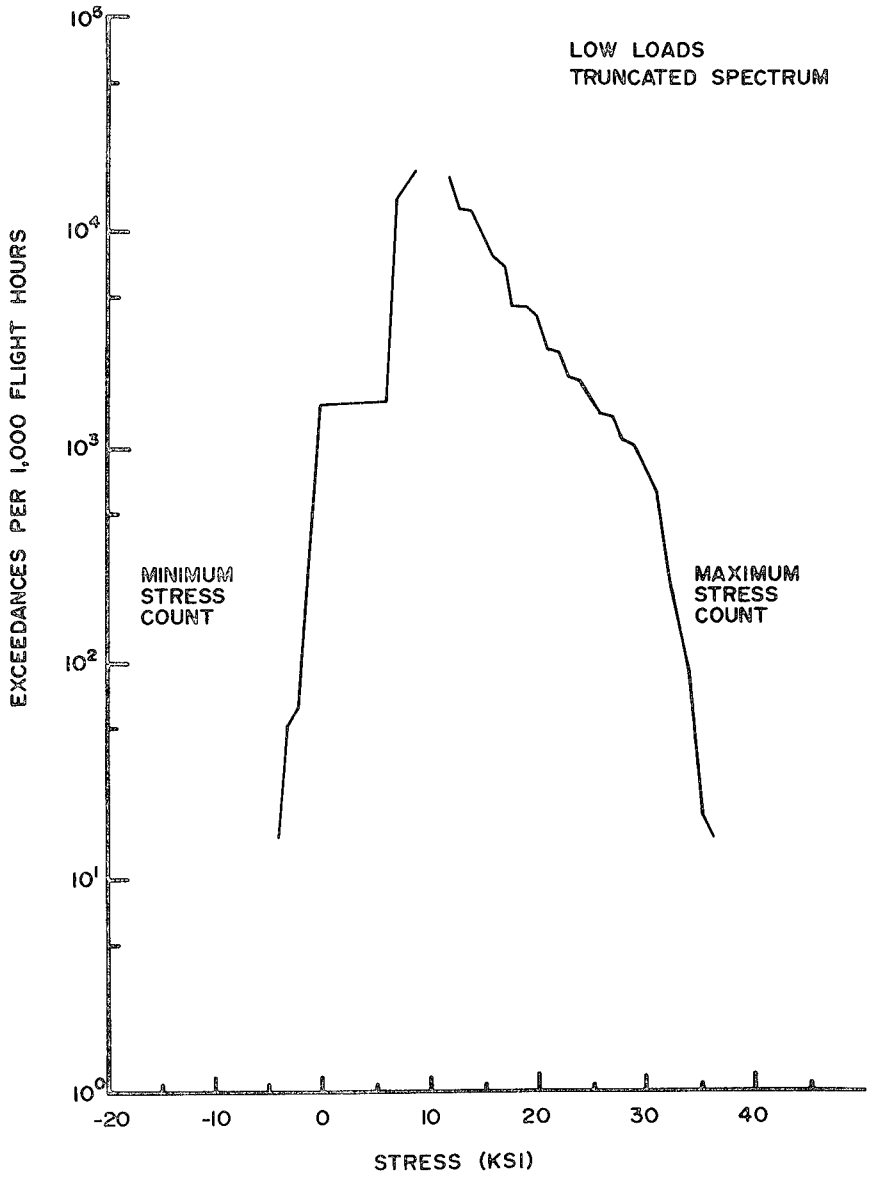


Figure 7. Exceedance data for a low loads truncated version of the spectrum described by Figure 6.

stress magnification within a spectrum. To achieve the 30.5 ksi maximum stress spectrum, all loads in the 36 ksi maximum stress spectrum were multiplied by the ratio (30.5/36). As shown by Figures 8 and 9, stress magnification (compare 30.5 to 36 ksi results) can produce significant life differences. Taking the data given in Figures 8 and 9 and choosing the normalized crack length interval to be $0.025 \leq a_i \leq 0.300$ in. results in the normalized curve given in Figure 10. The choice of a_0 (= 0.025 inch) and a_f (= 0.300 in.) was dictated by the availability of crack-growth data obtained from the four spectrum tests. Note that the test data shown in Figure 10 are tightly scattered about the mean curve, suggesting that minor spectrum differences and stress-level magnifications can be suppressed using a normalized crack-growth-curve concept. The results presented in Figure 10 indicate that spectrum-load-induced crack-growth results can be normalized.

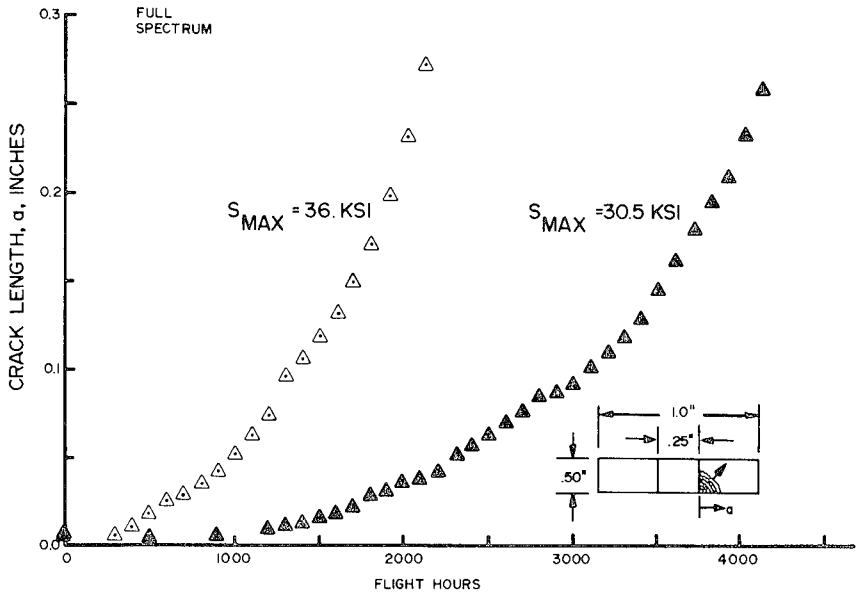


Figure 8. Corner crack-growth behavior generated by the F-4E(S) (full) spectrum described by Figure 6. Two stress magnifications considered.

DERIVATION OF NORMALIZED CURVE

The normalized crack-growth curve shown in Figure 4 can be generated either by utilizing crack-growth data of the type shown in Figure

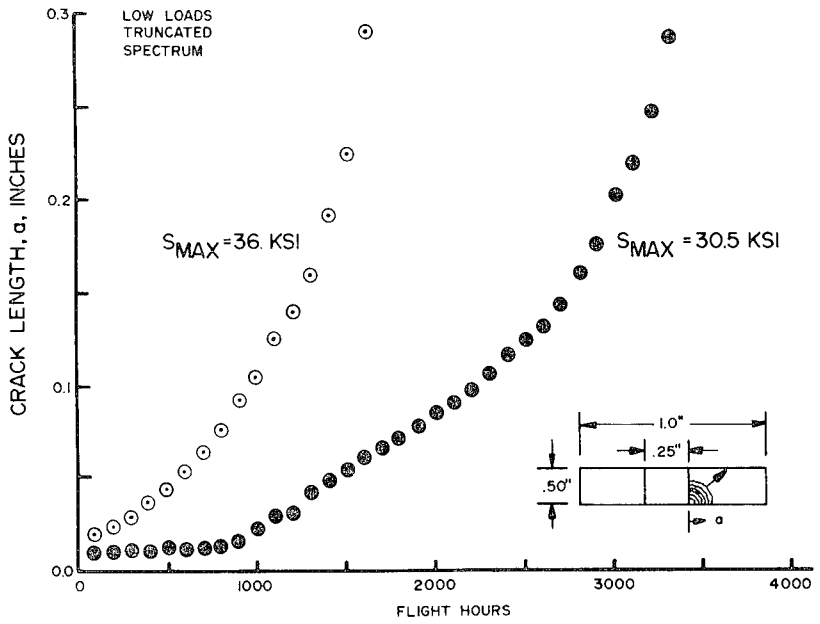


Figure 9. Corner crack-growth behavior generated by the F-4E(S) (low loads truncated) spectrum described by Figure 7. Two stress magnifications considered.

5 as described in the previous section or by utilizing an analysis of the type described below. The crack-growth lives (N_i and N_f) can be determined using integral equations [such as equations (5) and (6)] from which the abscissa of the normalized curve (N_i/N_f) can be formulated.

$$N_i = \int_{a_0}^{a_i} \frac{da}{C\,(\Delta K)^p} \tag{5}$$

$$N_f = \int_{a_0}^{a_f} \frac{da}{C\,(\Delta K)^p} \tag{6}$$

The integrands in equations (5) and (6) assume that the crack-growth process can be described with a power-law equation. The inference which results from combining equations (5) and (6) to form the life ratio N_i/N_f is that

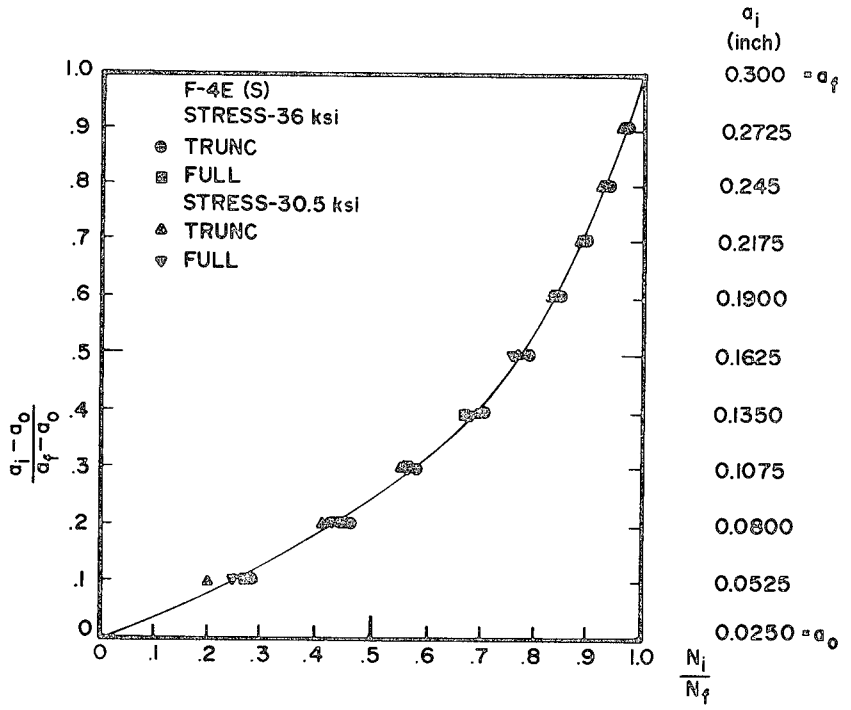


Figure 10. A normalized crack-growth curve for crack-growth behavior generated under spectrum loading (see Figures 8 and 9 for raw data).

$$\frac{N_i}{N_f} = f(a_0, a_i, a_f, C, p, \frac{K}{\sigma}, \Delta\sigma), \tag{7}$$

a generalized function of many interacting variables. Several reasonable assumptions will be suggested to simplify equation (7). These assumptions directly facilitate identification of major variables.

Stress Influence

Curves of the type shown in Figure 5 can be generated under constant amplitude loading conditions, *i.e.*, with

$$\begin{aligned} \Delta a &= \text{constant} \\ \sigma_{\max} &= \text{constant} \end{aligned} \tag{8}$$

If the stress-intensity factor coefficient is expressed in the following form

$$\frac{K}{\sigma} = \beta \sqrt{\pi a} \tag{9}$$

so that

$$\Delta K = \Delta\sigma \left[\beta \sqrt{\pi a} \right] \tag{10}$$

then the ratio N_i/N_f based on equations (5) and (6) becomes

$$\frac{N_i}{N_f} = \frac{\displaystyle\int_{a_0}^{a_i} \frac{da}{(\beta\sqrt{a})^p}}{\displaystyle\int_{a_0}^{a_f} \frac{da}{(\beta\sqrt{a})^p}} \tag{11}$$

where the constants ($\Delta\sigma$, $\sqrt{\pi}$, and C) common to equations (5) and (6) were eliminated prior to writing equation (11). Equation (11) directly shows that the life ratio is independent of the stress required to achieve a_i when $a_0 \leq a_i \leq a_f$. The major implication of equation (11) is that curves such as that given in Figure 5 can be normalized and thereby be used for predicting crack-growth response developed under stress conditions independent of those used to derive the normalized curve. When test-coupon data can be generated for those crack geometries which are difficult to describe with accurate stress intensity factor calibrations [equation (9)], the resulting normalized crack-growth curve may provide reasonably accurate remaining life estimates for structures.

SENSITIVITY STUDY

Direct Integration of Equation (11)

Several crack geometries have stress-intensity-factor coefficients [equation (9)] for which

$$\beta = \text{constant} \tag{12}$$

This class of crack geometries includes the wide panel center (through-thickness) crack geometry, the small edge (through-thickness) crack geometry and the small thumb-nail (semielliptical) crack with constant

Q.[3,4] When equation (12) is specified, equation (11) can be directly integrated to yield (for $p \neq 2$)

$$\frac{N_i}{N_f} = \frac{a_i^x - a_o^x}{a_f^x - a_o^x} \tag{13}$$

where

$$x = \frac{2 - p}{2} \tag{14}$$

and unnecessary common constants associated with the integration have been eliminated from equation (13).

The simplicity of equation (13) allows the reader to observe that the cyclic ratio N_i/N_f (for $a_i = D(a_f - a_0) + a_0$) is a constant whenever the ratio of initial and final crack lengths are the same. Equation (13) is presented graphically in Figures 11–13 to show the influence of (1) the exponent p, (2) the initial crack size a_0 ($a_f = 0.100$ in., $p = 4$), and (3) the final crack size a_f ($a_0 = 0.010, p = 4$), respectively.

Figure 11 shows that the crack-growth rate constant p can markedly affect the shape of the normalized crack-growth curve. The implication obtained from this observation is that the normalized growth curves are material specific. Any load, metallurgical, or environmental changes which affect the crack-growth rate equation exponent p will induce changes in the shape of the normalized crack-growth curve. Indiscriminate use of normalized curves obtained using one material may result in incorrectly predicted structural life fractions for other materials.

Figures 12 and 13 are provided to show the reader the substantial influence that assumed initial crack size (a_0) and final crack size (a_f) can have on the shape of the normalized curve. In general, normalized crack-growth curves should be developed and used only for specific initial and final crack-length values. Shape changes in Figures 11–13 can be accompanied with substantial changes in total usage allowed (*i.e.*, life).

Numerical Integration of Equation (11)

When the stress-intensity factor coefficient requires that β vary with crack length, *i.e.*, equation (12) does not apply, equation (11) then must be integrated numerically. Two such crack geometries which are of interest to aircraft designers are the corner and through-the-thickness cracks at the edge of a hole. The Bowie radial through-the-thickness crack has a β function described by[5,6]

$$\beta = \beta_B \left(\frac{a}{r}\right) = 0.6762 + 0.8733/\left(0.3245 + \frac{a}{r}\right) \tag{15}$$

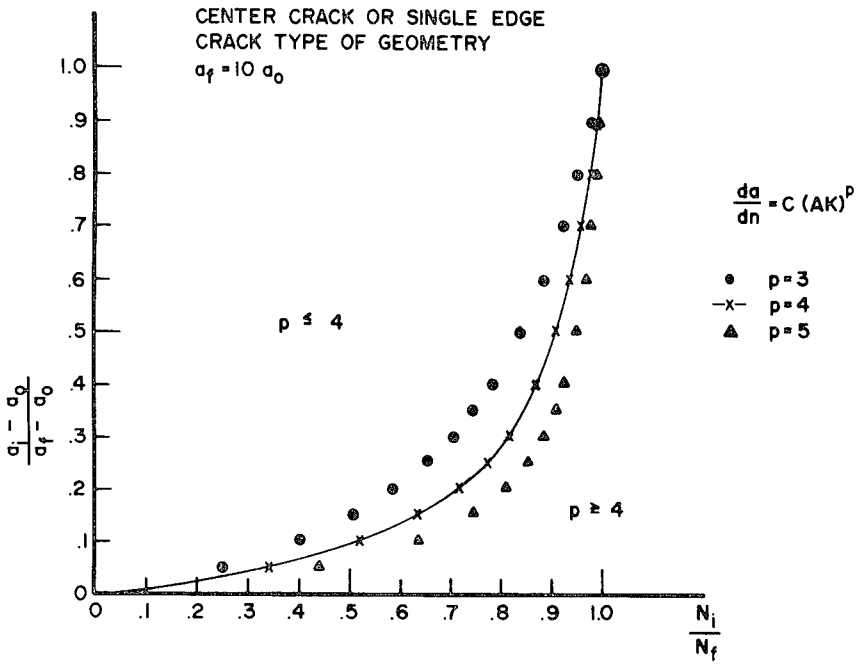


Figure 11. Influence of the Paris power law slope.

for an open hole having a radius of r.

Liu[7] provided an estimate of the quarter-circular corner crack at a hole using

$$\beta = \beta_L\left(\frac{a}{r}\right) = 1.12\frac{2}{\pi}\beta_B\left(\frac{a^*}{r}\right) \tag{16}$$

with $a^* = a/\sqrt{2}$; the crack length a expressed in both equations (15) and (16) is measured from the hole. Shown in Figure 14 are graphical presentations of equations (15) and (16). Equation (11) was evaluated numerically for these two β functions by dividing the total interval of integration into 2000 equal subintervals and summing the cycle count associated with the individual crack movements through the successive subintervals such as indicated in equation (17).

$$N_i = \sum_{j=0}^{k} \frac{1}{(\beta_j)^p} \int_{a_j}^{a_j + \Delta a} \frac{da}{a^{p/2}} \tag{17}$$

where β_j was β evaluated at $a_j + \frac{\Delta a}{2}$ and k is the number of subintervals

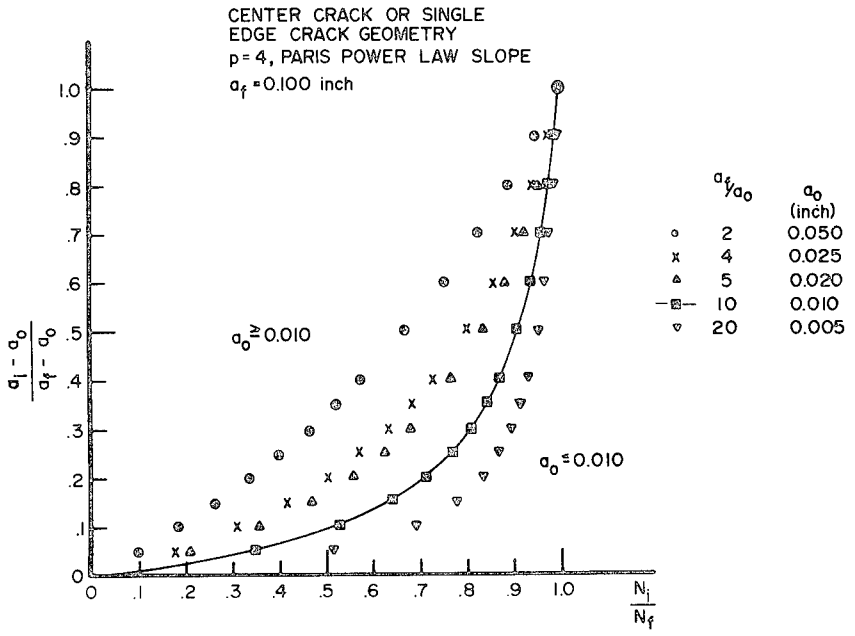


Figure 12. Influence of initial crack size (for constant final crack size).

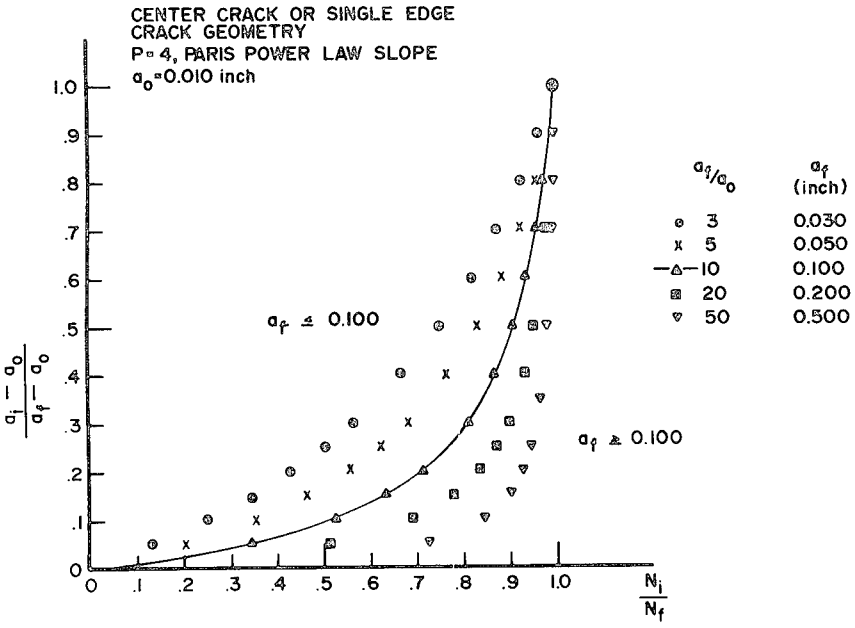


Figure 13. Influence of final crack size (for constant initial crack size).

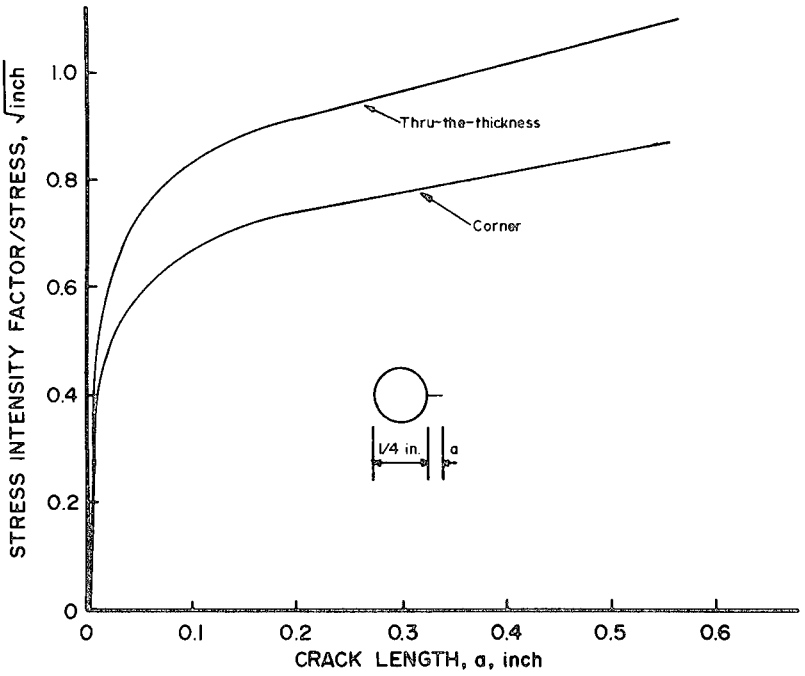


Figure 14. Stress-intensity factor coefficients for radial corner and through-thickness cracks compared.

integrated through ($1 \leq k \leq 2000$). Figure 15 shows the influence of crack geometry, as sensed by the β function. The small through-the-thickness (center) crack geometry that was chosen as baseline in Figures 11–13 is repeated in Figure 15. Substantial differences are noted between the baseline and the hole results; but, probably due to similar characteristics in the structure of the β functions, the two dissimilar (hole) crack geometries give results that are within 10% of each other.

THE TIFFANY–MASTERS LIFE SCHEME

Tiffany and Masters[8] developed a life prediction scheme which incorporated the use of fracture-mechanics tools as applied to pressure-vessel structures. Their approach, schematically shown in Figure 16, eliminated the influence of stress level through the use of the ratio of initial maximum stress intensity factor (K_{I0}) to the critical stress-intensity factor (K_{Ic}, the fracture toughness). The initial stress-intensity factor was calculated for the known conditions of stress and initial flaw size and shape. The ratio of K_{I0} to K_{Ic} eliminates the stress variable because it is the same for both the initial and final crack geometries.

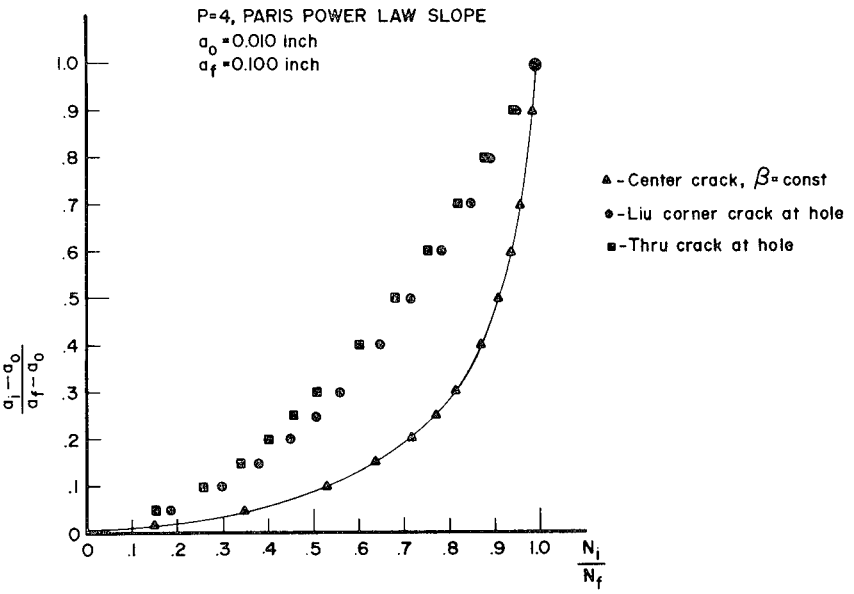


Figure 15. Influence of crack geometry.

Later, Hall and Finger[9] provided additional data which verified the approach but showed that derived stress normalized curves must be separately developed when any of the following variables change: crack configuration, stress ratio, fatigue-crack-growth properties (material), and rate of environmental attack. Schematically shown in Figure 17 is the influence of stress ratio on the Tiffany–Masters Life prediction diagram. As discussed by Hall and Finger,[10] the reason for the success of the approach is attributed to the third- or fourth-power dependence of crack-growth rates on the stress-intensity factor which predominates over influences due to differences in stress intensity-load-crack geometry relationships.

Life prediction diagrams of the type illustrated in Figures 16 and 17 can be best employed in design. Their application for field maintenance or inspection is complicated by the requirement that those using the approach must have the necessary fracture-mechanics background to understand the parameters and their influence on physical behavior. The life prediction diagram presented in this report eliminates this requirement through its direct presentation of physically obvious parameters.

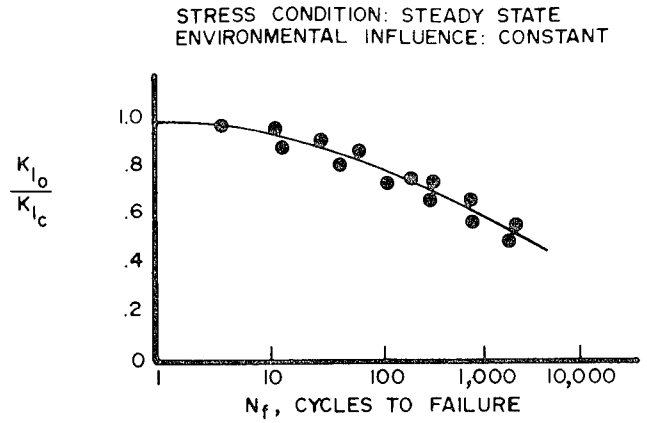


Figure 16. Tiffany–Masters scheme to eliminate stress variable (schematic).

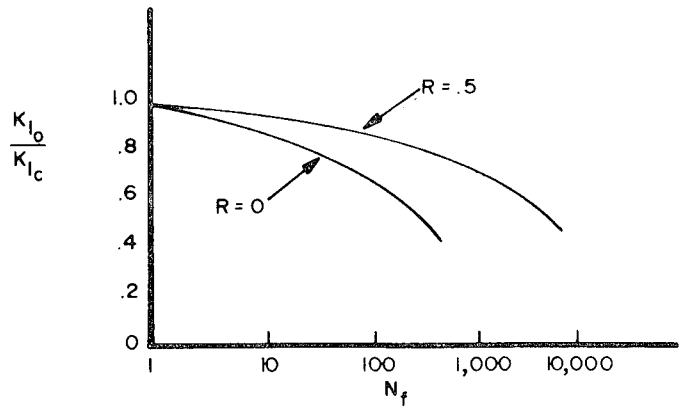


Figure 17. Influence of stress ratio on Tiffany–Masters diagram (schematic).

CONCLUSIONS

The normalized crack-growth curve concept has been applied in the F-4 Tracking Program and has the potential to be widely applied in individual aircraft tracking programs for planning inspections and modifications. This study has shown that the concept provides the capability for suppressing stress-level effects, whether associated with a typical aircraft-load spectrum or constant amplitude load spectrum. The sensitivity

study, based on constant amplitude spectrum analyses, indicates that part geometry, crack geometry, initial and final assumed crack sizes, as well as the power law exponent p will affect the shape of the normalized growth curve.

The normalized crack-growth method is sufficiently attractive to merit transfer of its application to other aircraft systems in the Air Force inventory. To support this effort, additional analytical/experimental investigations should be initiated to validate the approach for other airframe systems for which data are available. Such studies will provide the necessary information on advantages/disadvantages using the suggested approach to track crack damage under aircraft usage spectra.

SYMBOLS

a	crack length
a_0	initial crack length
a_i	intermediate crack length
a_f	final crack length
β	stress-intensity factor coefficient function
$\frac{da}{dN}$	cyclic crack growth rate
C, p	constants associated with Paris power law crack-growth rate equation, $\frac{da}{dN} = C\Delta K^p$
D	a specified fraction between 0 and 1
K	stress-intensity factor
K/σ	stress-intensity factor coefficient [see equation (9)]
K_{10}	initial K
K_{1c}	final K, fracture toughness
ΔK	range of stress intensity factor
N	cycles
N_i, N_f	cycles required to propagate the crack from a_0 to a_i and to a_f, respectively
σ	stress
$\sigma_{max}, \Delta\sigma$	stress maximum and stress range, respectively
x	exponent defined by equation (14).

REFERENCES

1. Gallagher, J. P., "Estimating Fatigue Crack Lives for Aircraft: Techniques," paper presented at the SESA Spring Meeting, Chicago, Ill., 16 May 1975.

2. Potter, J. M., Gallagher, J. P., and Stalnaker, H. D., "The Effect of Spectrum Variations on the Fatigue Behavior of Notched Structures Representing F-4E/S Wing Stations," Air Force Flight Dynamics Laboratory, Wright-Patterson AFB, Ohio, Technical Manual No. AFFDL-TM-FBE-74-2, January 1974.
3. Paris, P. C. and Sih, G. C., "Stress Analysis of Cracks," in *Fracture Toughness Testing and Its Applications*. Special Technical Publication 381. Philadelphia: American Society for Testing and Materials (1965), 30–83.
4. Clark, W. G. Jr., "Fracture Mechanics in Fatigue," *Proc. SESA*, **28** (1971), 421–28.
5. Bowie, O. L., "Analysis of an Infinite Plate Containing Radial Cracks Originating at the Boundary of an Internal Circular Hole," *J. Math. Phys.*, **35** (1956–57), 60–71.
6. Grandt, A. F. Jr. and Gallagher, J. P., "Developing an Infinite Life Design Procedure for Fastener Holes Utilizing Fracture Mechanics," Air Force Materials Laboratory, Wright-Patterson AFB, Ohio, Technical Memorandum No. AFML-TM-LLP-72-3, August 1972.
7. Liu, A. F., "Stress Intensity Factor for a Corner Flaw," *Eng. Fract. Mech.*, **4** (1972), 175–79.
8. Tiffany, C. F. and Masters, J. N., "Applied Fracture Mechanics," in *Fracture Toughness Testing and Its Applications*. Special Technical Publication 381. Philadelphia: American Society for Testing and Materials (1965), 249–89.
9. Hall, L. R. and Finger, R. W., "Fracture and Fatigue Growth of Partially Embedded Flaws," in *Proceedings of the Air Force Conference on Fatigue and Fracture of Aircraft Structures and Materials, Held at Miami Beach, Fla., 15–18 December 1969*. Air Force Flight Dynamics Laboratory, Wright-Patterson AFB, Ohio, Report No. AFFDL-TR-70-144 (September 1970), 235–62. (AD 719 756)

22. FATIGUE CRACK-GROWTH BEHAVIOR OF FASTENER-HOLE FLAWS

L. R. HALL
Boeing Aerospace Company
Seattle, Washington

An experimental investigation was undertaken to study the fatigue-crack-growth behavior of both uniform through-the-thickness and quarter-circular part-through cracks originating at fastener holes. Three alloys were tested including 2219–T851 aluminum, 9Ni–4Co–0.2C (190–210 ksi) steel, and 6Al–4V (ELI) beta annealed titanium. Test variables included hole condition (conventional reamed and cold worked), fastener type (close tolerance and Taper-lok), and initial crack shape (uniform through-the-thickness and quarter-circular part-through). Tests were conducted under constant amplitude cyclic loadings in air having a relative humidity of about 10%. Experimental results for close-tolerance and interference-fit fasteners were compared to calculated results with calculations based on engineering estimates of stress-intensity factors and crack-growth rate data obtained from tests of surface flaw specimens. Good agreement was obtained between experimental and calculated results.

INTRODUCTION

New design criteria[1] are being developed for military aircraft to minimize the possibility that cracklike defects in airframe components will result in component failures during a specified period of time. The criteria reflect the knowledge that metallic components can contain cracklike defects due to material imperfections or damage introduced during production and service. It is necessary to limit the maximum size of defects in any component at the outset of the specified operational period and to evaluate quantitatively the effects of aircraft loadings on the growth and stability of defects.

One of the most common sources of cracklike defects in airframe components is fastener holes,[2] and one of the most common causes of crack growth is fluctuating loads. Hence, this experimental program was

undertaken to study the fatigue crack-growth behavior of cracks originating at fastener holes. Three alloys were tested including 2219–T851 aluminum, 9Ni–4Co–0.2C (190–210 ksi) steel, and 6Al–4V (ELI) beta annealed titanium. Test variables included hole condition (conventional reamed and cold worked), fastener type (close tolerance and Taper-lok), and initial crack shape (uniform through-the-thickness and quarter-circular part-through). All tests described in this chapter were conducted under constant amplitude cyclic loadings in air having a relative humidity of about 10%. Experimental results for close-tolerance and interference-fit fastener tests were compared to calculated results with calculations based on engineering estimates of stress-intensity factors[3] and crack-growth rate data obtained from tests of surface-flaw specimens.

The tests described in this chapter were part of a program[4] sponsored by the United States Air Force to evaluate the fracture and fatigue crack-growth behavior of surface flaws and flaws originating at fastener holes. The program reported in Reference 4 was one of a series of programs[5–12] undertaken by the USAF to develop methods and data needed for design against fracture in military aircraft.

MATERIALS

The 2219–T851 aluminum alloy plates (1.0 × 36 × 72 in.) were purchased from Alcoa in the T851 condition per military specification MIL-A-8920A. The 9Ni–4Co–0.2C hot-rolled steel plates (0.50 × 27 × 36 in.) were purchased in the annealed condition from Republic Steel per North American Rockwell Specification ST0160LB0001. The plates were heat treated to the 190–210 ksi strength level by the Boeing Aerospace Company. The 6Al–4V standard ELI titanium alloy plates (0.60 × 55 × 129 in.) were produced by RMI per Boeing Material Specification XBMS7-174B. This specification requires an extra low interstitial grade and annealing above the beta transus. Chemical compositions and mechanical properties for the plate materials are listed in Tables 1 and 2, respectively.

A summary of fasteners used in this program is included in Table 3. Both close-tolerance and interference-fit fasteners were tested in conjunction with all three alloys. Table 3 lists alloy, tensile strength, head configuration, finish, lubrication, and supplier for each type of fastener.

Procedures

Test Specimens. All test specimens conformed to the configuration shown in Figure 1. For the titanium and steel alloys, each specimen

Table 1. Chemical Composition of Materials

Alloy		Alloy Element (% by Weight)																		
		Cu	Si	Mn	Mg	Fe	C	Co	Ni	Cr	Mo	P	S	V	N	O	H	Z	Ti	Al
2219-T851 Al Plate (Spec Limits)	Min.	5.80	—	0.20	—	—	—	—	—	—	—	—	—	0.05	—	—	—	0.10	0.10	Bal.
	Max.	6.80	0.20	0.40	0.02	0.30	—	—	—	—	—	—	—	0.15	—	—	—	0.25	0.20	Bal.
Ti-6Al-4VβA Plate	Min.	—	—	—	—	—	—	—	—	—	—	—	—	3.50	—	0.06	—	—	Bal.	5.50
	Max.	—	—	—	—	0.25	0.08	—	—	—	—	—	—	4.50	0.03	0.13	.0125	—	Bal.	6.30
Ni-4Co-0.2C Steel Plate	—	0.15	0.07	0.24	—	Bal.	0.19	4.58	9.32	0.78	0.96	.0007	.0003	0.09	—	—	—	—	—	—

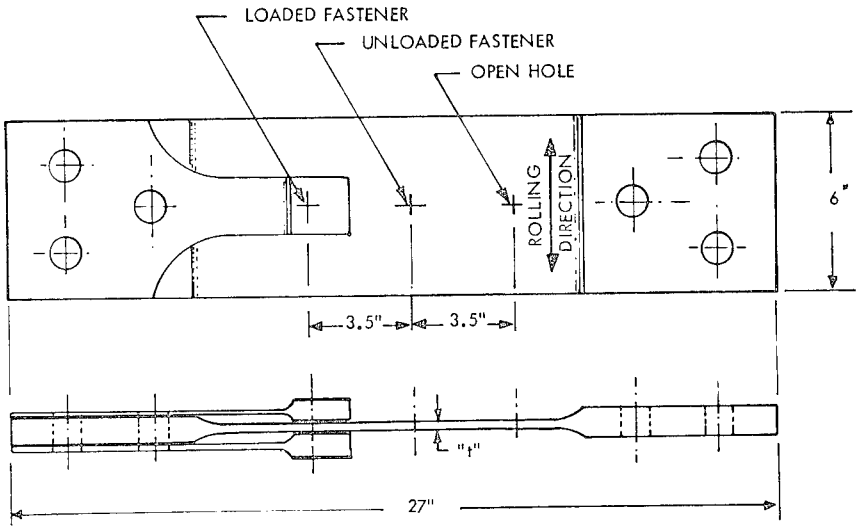
Table 2. Mechanical Properties of Materials

Alloy	Specimen Width x, Thickness (in.)	Grain Direction	Ultimate Tensile Strength (ksi)	0.2% Offset Yield Strength (ksi)	Elongation In 1.0 In. (%)	Elongation In 2.0 In. (%)	In Area (%)
2219-T851 Al Plate	0.50 × 0.25	Long. Trans.	66.1 66.3	52.6 51.3	16 15	11 11	28 25
Ti-6Al-4VβA Plate	0.50 × 0.25	Long. Trans.	138.4 138.6	125.3 128.0	16 16	10 11	26 25
9 Ni-4Co-0.2C Steel Plate	0.50 × 0.20	Long. Trans.	203.2 203.5	185.3 186.6	23 23	13 13	56 55

NOTE: All values are averages of two tests.

Table 3. Summary of Fasteners Used in Test Program

Plate Alloy	Fastener Details					
	Type	Alloy	Tensile Strength (ksi)	Head Configuration	Finish and Lubrication	Supplier
2219-T851 Aluminum	Taper Shank (3/8″ Dia.) Close Tolerance (3/8″ Dia.)	PH 13-8 Mo Steel PH 13-8 Mo Steel	220–240 220–240	Protruding Shear 100° Tension 12 Point	Passivated Cetyl Alcohol	Omark PBF Omark
Ti-6Al-4V Beta Ann.	Taper Shank (5/16″ Dia.) Close Tolerance (5/16″ Dia.)	Ti-6Al-4VSTA Ti-6Al-4VSTA	160 160	Protruding Shear 100° Shear 12 Point	Unplated Phos. Flouride Cetyl Alcohol	Omark PBF Dumont Av.
9Ni-4Co-0.2C and 4340 Steels	Taper Shank (1/4″ Dia.) Close Tolerance (1/4″ Dia.)	H-11 Steel PH13-18 Mo Steel	260–290 220–240	Protruding Shear 100° Shear 12 Point	Diffused Cd-Ni Lubeco #2123 Passivated Cetyl Alcohol	GD/FW Omark



ALLOY	"t" (IN)	BOLT DIA (IN)
Al - 2219-T851	0.45	0.375
Fe - 9Ni - 4Co	0.30	0.250
Ti - 6Al - 4V	0.38	0.313

Figure 1. Test specimens.

contained three cracked fastener holes including one hole filled with a loaded fastener and two additional holes including one filled with an unloaded fastener and one open hole. For the aluminum alloy, specimens contained only two holes including one hole filled with a loaded fastener and one open hole.

Fasteners were loaded using loading straps as shown in Figure 2. The position of the bearing block was adjusted by turning the cap screws until the block was snug against the fastener. The adjustable feature eliminated variations in loading from specimen to specimen due to small variations in the distance between the grip holes and loaded fastener hole. Furthermore, adjustments could be made through each test to keep the load transfer constant. Load transferred through the straps was measured using back-to-back pairs of uniaxial strain gages located as shown in Figure 2. The straps were precalibrated to determine relationships between strain output and load transfer.

Cold-worked fastener holes were produced using methods developed by the Boeing Commercial Airplane Company. Two expansion levels were used, with the lower value 25% less than the higher value. For the aluminum and titanium alloy high-expansion holes, a 0.355-in.-

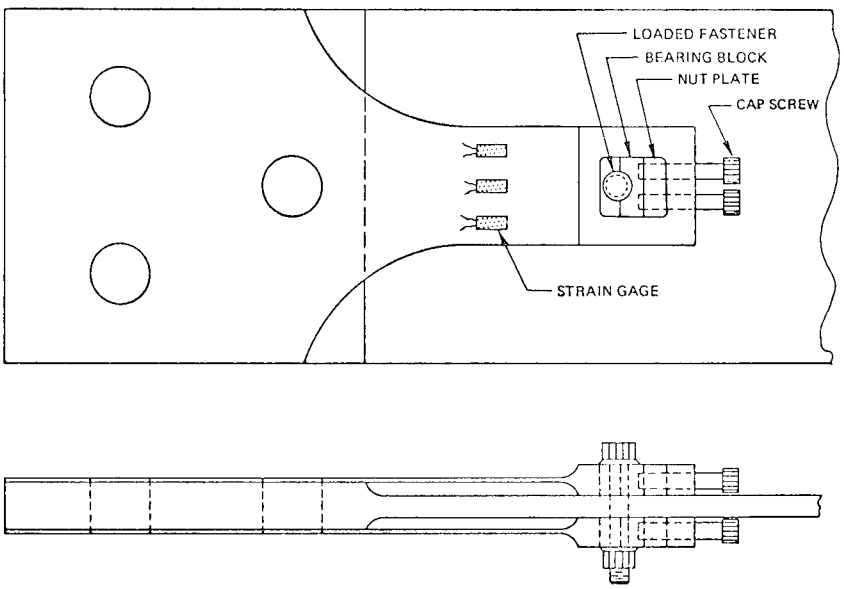


Figure 2. Test setup for loaded fasteners.

diameter hole was drilled and the required crack was introduced. The hole was then fitted with a lubricated split sleeve and a mandrel was drawn through the hole to cold expand it to a diameter of 0.375 in. After removal of the mandrel, the hole diameter decreased to 0.366 in. and was reamed to the final size of 0.375 in. For the 9Ni–4Co–0.2C steel alloy high-expansion holes, the initial hole diameter was 0.333 in. After the required crack was introduced, the hole was coated with a dry film lubricant (Fel Pro 300) and baked at 375°F for four hours. Cold working was accomplished by pushing a mandrel through the lubricated hole to cold expand it to a diameter of 0.358 in. The holes were then reamed to 0.375 in. The lower expansion levels were achieved by increasing initial hole diameter to 0.361 in. for the aluminum and titanium alloys and 0.339 in. for the steel alloy.

Flaw Preparation. All flaws were prepared by growing fatigue cracks from crack starters. Crack starters were introduced using an electrical discharge machine, kerosene dialectric, and 0.06-in.-thick circular electrodes. Fatigue cracks were grown from the periphery of the starter slots using loading cycles having a stress ratio of 0.06, cyclic frequency of 1800 cpm, and peak cyclic stresses of 10 ksi for the aluminum alloy and 25–30 ksi for the steel and titanium alloy specimens. The width of the precrack ranged from 0.02 to 0.05 in. All 9Ni–4Co–0.2C steel specimens

were baked at 400°F for four hours to remove any hydrogen that may have been introduced by electrical discharge machining.

Experimental. Tests were conducted in desicated air having a relative humidity of about 10%. This was accomplished by taping rectangular plexiglass containers containing a controlled amount of desiccant to the faces of all specimens. Test temperatures ranged from 69°F to 75°F. Cyclic loading profiles were all sinusoidal in shape with a stress ratio of 0.1 and cyclic frequency of 60 cpm.

Crack Propagation Life Calculations. Crack propagation life calculations were made by numerical integration of predicted crack-growth rates between the limits of initial and final crack dimensions.

Crack-growth rates were predicted by using stress-intensity factor versus crack-growth rate correlations for the specimen materials[4] and stress-intensity factors for the test specimens obtained from equations (1), (2), or (3). The transition from a part-through to a through-the-thickness crack was made by assuming that a part-through crack having a depth equal to the specimen thickness is equivalent to a uniform through-the-thickness crack of equal area. Through-the-thickness cracks having unequal crack lengths at each side of the specimen were assumed to be equivalent to uniform through-the-thickness cracks having a length equal to the arithmetic average of the surface lengths for the nonuniform crack.

All stress-intensity factors were calculated using solutions described in Reference 4. Results applicable to this program are included herein. Details of the solutions can be found in References 3, 4, and 13.

Stress-intensity factors for part-through cracks originating at open holes and holes filled with unloaded close-tolerance fasteners were calculated using the equation

$$K_1 = F_1 \cdot M_F \cdot M_B \cdot K_{Ie} \cdot \sqrt{\frac{2r + \pi ac/4t}{2r + 2\pi ac/4t}} \qquad (1)$$

where

F_1 and K_{Ie} are defined in Figure 3

$$M_F = \begin{cases} 1.0 + 0.12\,(1 - a/2c)^2 & \text{for } \beta < 90° \\ 1.11 & \text{for } \beta = 90° \end{cases}$$

M_B is defined in Figure 4

r is radius of the fastener hole

a and c are depth and length of crack measured along the side of the hole and specimen surface, respectively.

Stress-intensity factors for part-through cracks originating at holes containing loaded close-tolerance fasteners were calculated by adding

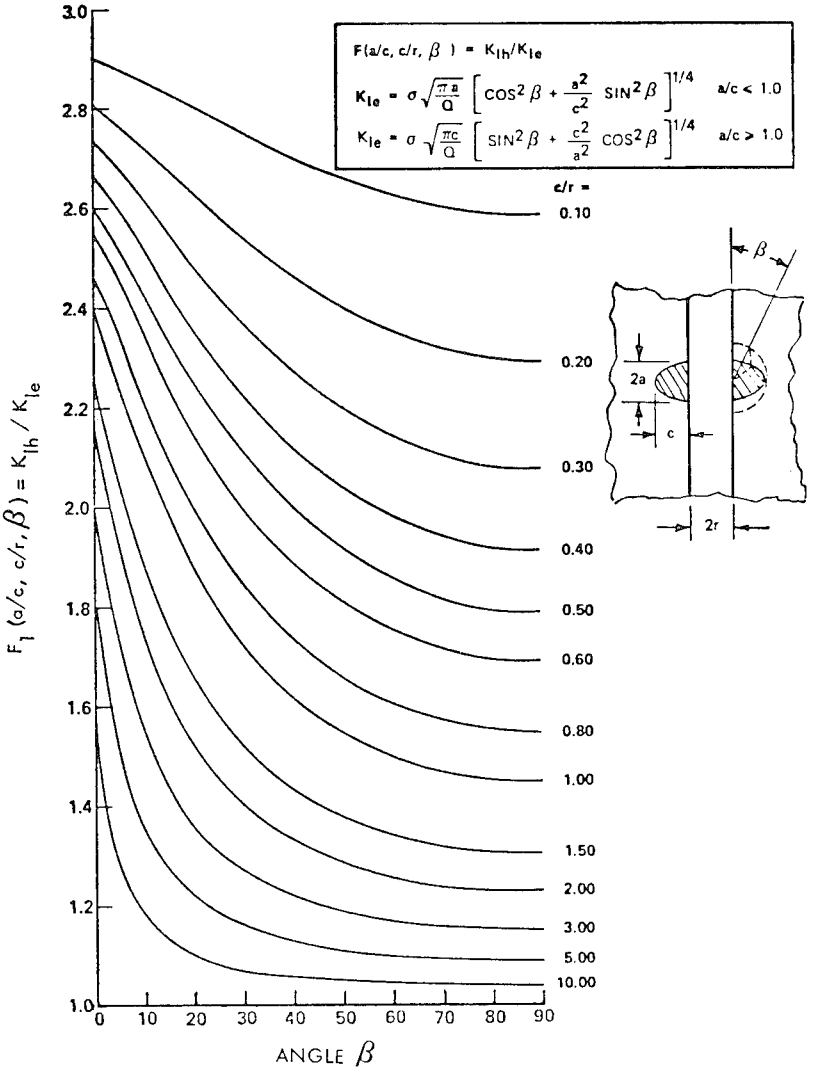


Figure 3. Nondimensionalized stress-intensity factors for two semi-elliptical cracks at a hole in a thick plate.

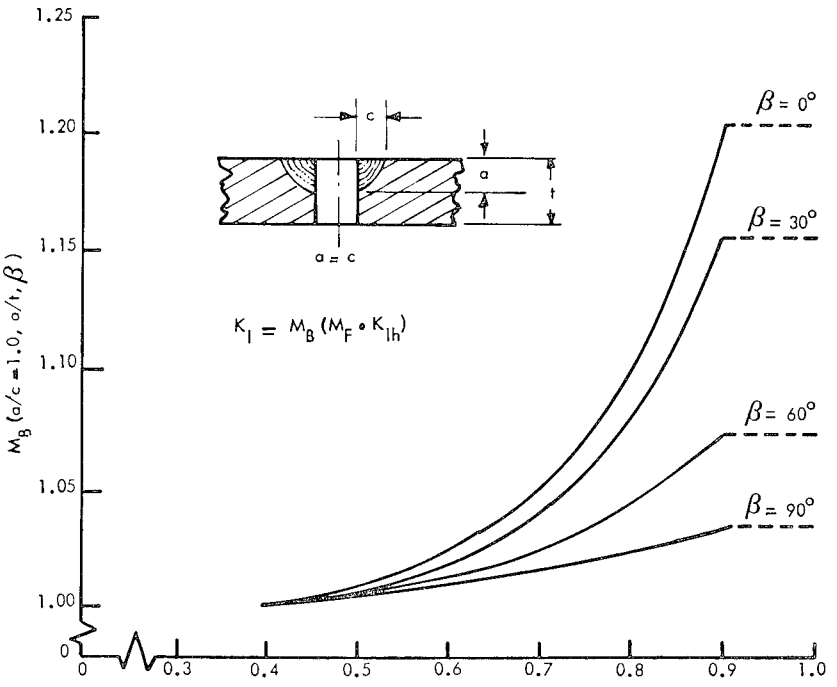


Figure 4. Assumed back surface stress-intensity magnification factor for quarter-circular part-through fastener hole flaws.

stress-intensity factors due to applied stress [given by equation (1)] and fastener load [given by equation (2) as follows]:

$$K_I = F_2 \cdot K_{Ieb} \cdot M_F \cdot M_B \cdot \sqrt{\frac{2r + \pi ac/4t}{2r + 2\pi ac/4t}} \qquad (2)$$

F_2 and K_{Ieb} are defined in Figure 5 and other variables were previously defined for equation (1).

Values of F_1 and F_2 at $\beta = 25°$ were used to determine effective stress-intensity factors and crack-growth rates for the depthwise direction. Because of the plastic flow and large stress-intensity factor gradient in the region defined by small values of β, it was anticipated that the peak stress-intensity factor at $\beta = 0°$ would not be the appropriate value to use in calculations of crack-depth growth rates. Prior static fracture test results[4] showed that $K_{I|\beta = 25°} \simeq K_{IE}$ (K_{IE} is fracture toughness determined from surface-flaw specimen tests) when fracture initiated at quarter-circular part-through cracks originating at open holes and holes containing loaded close-tolerance fasteners. Accordingly, $K_{I|\beta = 25°}$

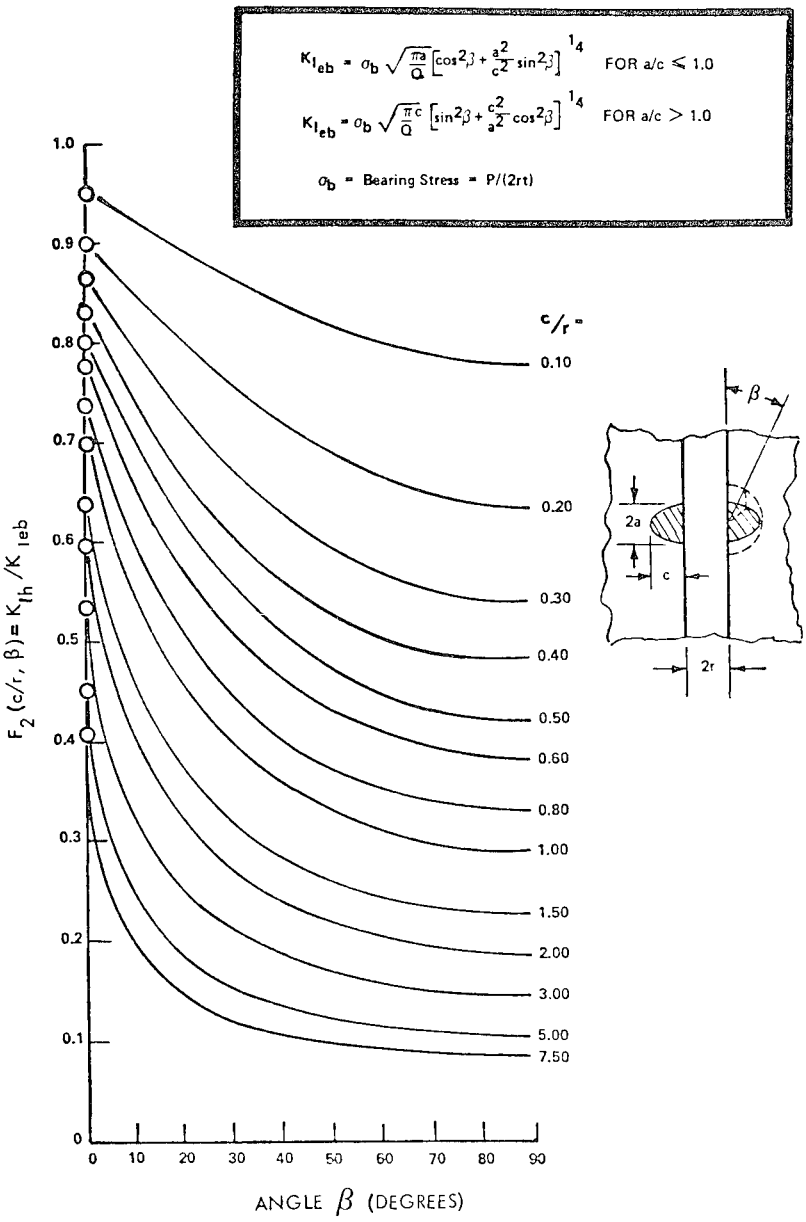


Figure 5. Nondimensionalized stress-intensity factors for two semi-elliptical cracks originating from a loaded close-tolerance fastener in a thick plate.

stress-intensity factor values were used to determine crack-depth growth rates in this program.

Stress-intensity factors for through-the-thickness cracks originating at holes containing unloaded interference fit fasteners were calculated using the following equations:

$$K_{I\,\mathrm{MAX}} = F_{1\sigma} \cdot \sigma_{ys} \cdot \sqrt{\pi c} \cdot \sqrt{\frac{2r + c}{2r + 2c}}$$
$$K_{I\,\mathrm{MIN}} = K_{I\,\mathrm{MAX}} - (\sigma_{\max} - \sigma_{\min}) \sqrt{\pi c} \sqrt{\frac{2r + c}{2r + 2c}} \tag{3}$$

where

$K_{I\,\mathrm{MAX}}$ is stress-intensity factor at the peak cyclic stress
$K_{I\,\mathrm{MIN}}$ is stress intensity factor at the minimum cyclic stress (if the calculated $K_{I\,\mathrm{MIN}} < 0$, $K_{I\,\mathrm{MIN}}$ is set equal to 0)
$F_{1\sigma}$ is defined in Reference 13
c is crack length
$\sigma_{\max}$ and $\sigma_{\min}$ are the maximum and minimum cyclic stresses, respectively.

Crack-growth rate data were obtained from Reference 4 in which tests of surface flaw and double cantilever beam specimens were used to acquire crack-growth rate data for the depthwise (T–S) and lateral (T–L) directions of the plate stock used in this program. Crack-growth rates for the two directions were found to be equal and were expressed as follows:

$$\frac{da}{dN} = \frac{dc}{dN} = C\,(K_{\max} - K_{\mathrm{th}})^m\,(\Delta K)^n$$

where

da/dN and dc/dN are crack-growth rates for the T–S and T–L directions, respectively
$K_{\max}$ is peak cyclic stress intensity factor (ksi $\sqrt{\text{in.}}$)
K_{th} is peak cyclic threshold stress intensity factor (assumed to be 1.5 ksi $\sqrt{\text{in.}}$ for aluminum alloy, 10 ksi $\sqrt{\text{in.}}$ for the steel alloy, and 5 ksi $\sqrt{\text{in.}}$ for the titanium alloy)
ΔK is stress-intensity factor range (ksi $\sqrt{\text{in.}}$)
C is a constant
m and n are exponents

Values of C, m, and n for each alloy are given below for $0 \leq R \leq 0.5$[4]:

Alloy	C (for rates in in./cycle)	m	n	Validity Range
Al–2219–T851	0.34×10^{-8}	0.84	2.40	$14 < K_{max} < 28$ ksi $\sqrt{\text{in.}}$
Fe–9Ni–4Co–0.2C	0.40×10^{-8}	0.57	1.76	$15 < K_{max} < 100$ ksi $\sqrt{\text{in.}}$
Ti–6Al–4V	0.33×10^{-8}	1.02	3.00	$20 < K_{max} < 60$ ksi $\sqrt{\text{in.}}$

RESULTS AND DISCUSSION

Crack Geometries

Changes in crack geometry with increase in crack size were different for all three fastening systems tested, particularly for the aluminum and titanium alloys. This is illustrated in Figure 6, where crack width is plotted against crack depth for both conventional and cold-worked close-tolerance fastener holes and for interference-fit fastener holes. All cracks were nominally quarter-circular in shape at the outset of each test. For conventional close-tolerance fastener holes, crack depth increased at a slightly faster rate than crack width, and the cracks remained nearly quarter-circular in shape until they penetrated the specimen thickness. For cold worked fastener holes, crack depth increased at a much faster rate than did crack width, resulting in the flaw shape illustrated in Figure 6(a). Interference-fit fasteners tended to retard crack-depth growth rate and resulted in the largest ratio of crack width to crack-depth growth of any of the three fastening methods tested; the maximum crack depth occurred a small distance away from the hole rather than at the wall of the hole, and the cracks first penetrated the specimens at the point of maximum depth. In the steel alloy specimens, crack-geometry changes were similar to those for the aluminum and titanium alloys but were much less pronounced. The high yield strength of the steel alloy probably contributed to the differences in crack geometry changes between the steel and aluminum–titanium alloy results.

Conventional Open and Close-Tolerance Fastener Filled Holes

Three specimens containing part-through cracks originating at open and close-tolerance fastener filled holes were tested. One specimen was tested for each alloy including 2219–T851 aluminum alloy specimen

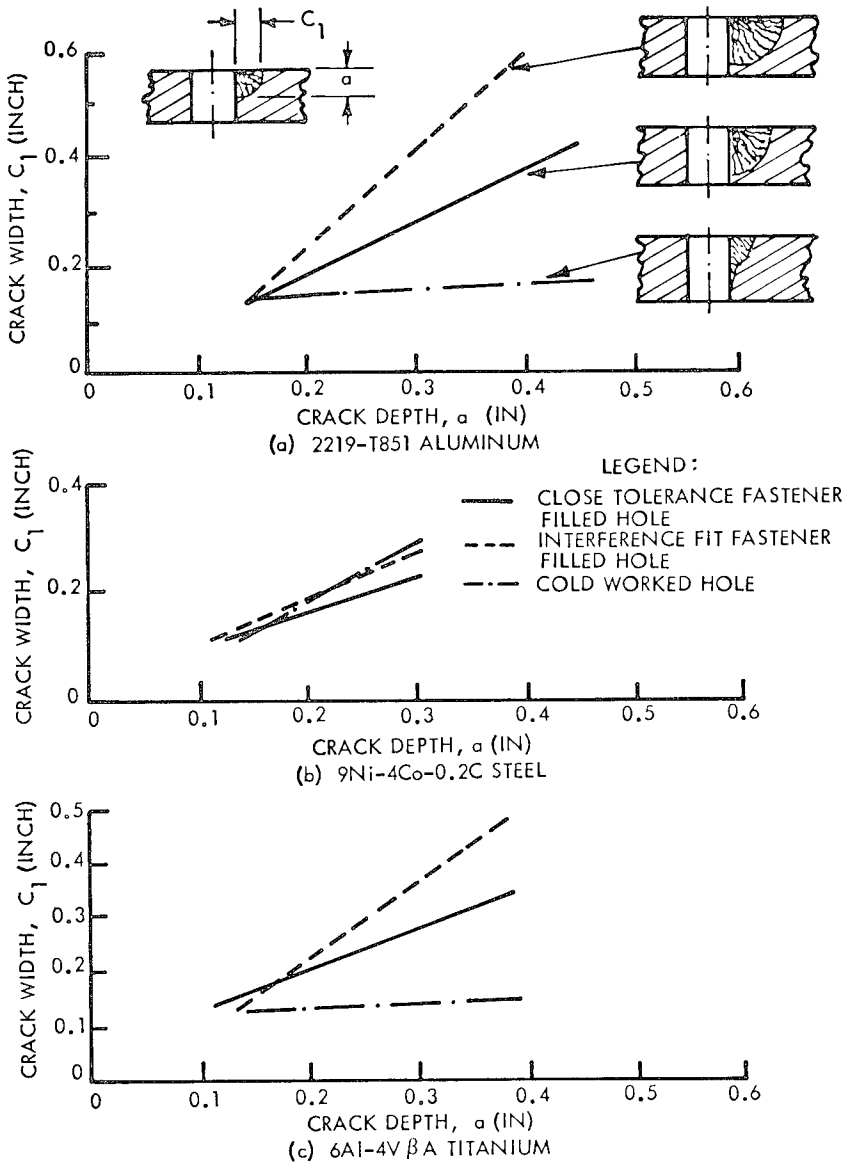


Figure 6. Comparison of growth characteristics for constant cyclic load tests of part-through cracks originating at fastener holes.

FUCTA-1, 9Ni–4Co–0.2C steel specimen FUCTS-1, and 6Al–4V βA titanium specimen FUCTT-1. Test details for each of the three specimens are listed in the uppermost lines of Table 4. Test data are plotted in Figure 7 on graphs of crack depth versus cycles until the flaw depth equals the specimen thickness; thereafter, values of the sum of specimen thickness and crack length at the back specimen face ($a + c_2$) are plotted against cycles. In all cases, cracks originating at loaded holes grew faster than cracks originating at open or filled holes, and there was essentially no difference between crack-growth behavior of open and filled holes.

A comparison was made between experimental and calculated cyclic lives for each flaw to evaluate the applicability of the previously described engineering estimates of stress-intensity factors in predicting cyclic life for cracked close-tolerance fastener holes. Two different methods were used to calculate the number of loading cycles required to grow the cracks through the specimen thickness. In one method, stress-intensity factors and crack-growth rates for the depthwise direction were used in a direct calculation. In the second method, stress-intensity factors and crack-growth rates for the lateral direction were used to determine the number of cycles required to grow the crack width from the initial value to the value that existed at the time the crack depth reached the specimen thickness.

Comparisons between calculated and experimental lives are illustrated in Figure 8. Agreement between calculations and experiment is good in all cases. Ratios of actual to calculated life ranged from a low of 0.75 for the aluminum alloy to a high of 1.63 for the titanium alloy. For the aluminum and steel alloys, there was very little difference between results of the calculations made for the depthwise and lateral directions. This result indicates that stress-intensity factors for both the depthwise and lateral directions were equally applicable. For the titanium alloy, the discrepancy between results of depthwise and lateral calculations was greater than that for the other two alloys. This result may have been due to the fact that crack-growth rates were more sensitive to stress-intensity factors for the titanium alloy than for the aluminum and steel alloys. Hence, small inaccuracies in stress-intensity factor could have resulted in reasonably large changes in calculated life for the titanium alloy specimens. Finally, ratios of calculated to actual life tended to be smaller for the loaded holes than for both open and filled holes.

For the range of parameters used in these tests, it was found that calculations of crack-propagation life for cracked fastener holes using stress-intensity factors calculated from equations (1), (2), and (3), and baseline crack-growth rate data obtained from surface-flaw specimens agreed well with test data. However, these tests were limited to simple loading profiles, part-circular cracks, one initial crack-depth-to-hole-di-

Table 4. Summary of Test Parameters for Close Tolerance Fastener Tests

Flaw Geometry	Alloy	Specimen Code	Fastener Hole			Fastener Load (lbs)	Initial Flaw		Peak Cyclic Stress (ksi)
			No.	Condition	Cold Expansion (in.)		Depth a, (in.)	Width c, (in.)	
t a d c Alloy d (in.) t (in.) Al 0.375 0.45 Fe 0.250 0.30 Ti 0.313 0.38	Al	FUCTA-1	1 2	As Reamed	0 0	4000 0	0.174 0.168	0.144 0.146	21
	Fe	FUCTS-1	1 2 3	As Reamed	0 0 0	3600 0 0	0.127 0.125 0.127	0.113 0.103 0.106	70
	Ti	FUCTT-1	1 2 3	As Reamed	0 0 0	3000 0 0	0.128 0.114 0.114	0.138 0.136 0.124	35
	Al	FUCCA-1	1 2	Cold Worked	0.019 0.019	4000 0	0.178 0.176	0.150 0.150	28
	Fe	FUCCS-1	1 2 3	Cold Worked	0.019 0.019 0.014	3600 0 0	0.125 0.140 0.122	0.104 0.103 0.090	90
	Ti	FUCCT-1	1 2 3	Cold Worked	0.019 0.019 0.014	3000 0 0	0.130 0.128 α	0.112 0.123 α	55

α could not be determined

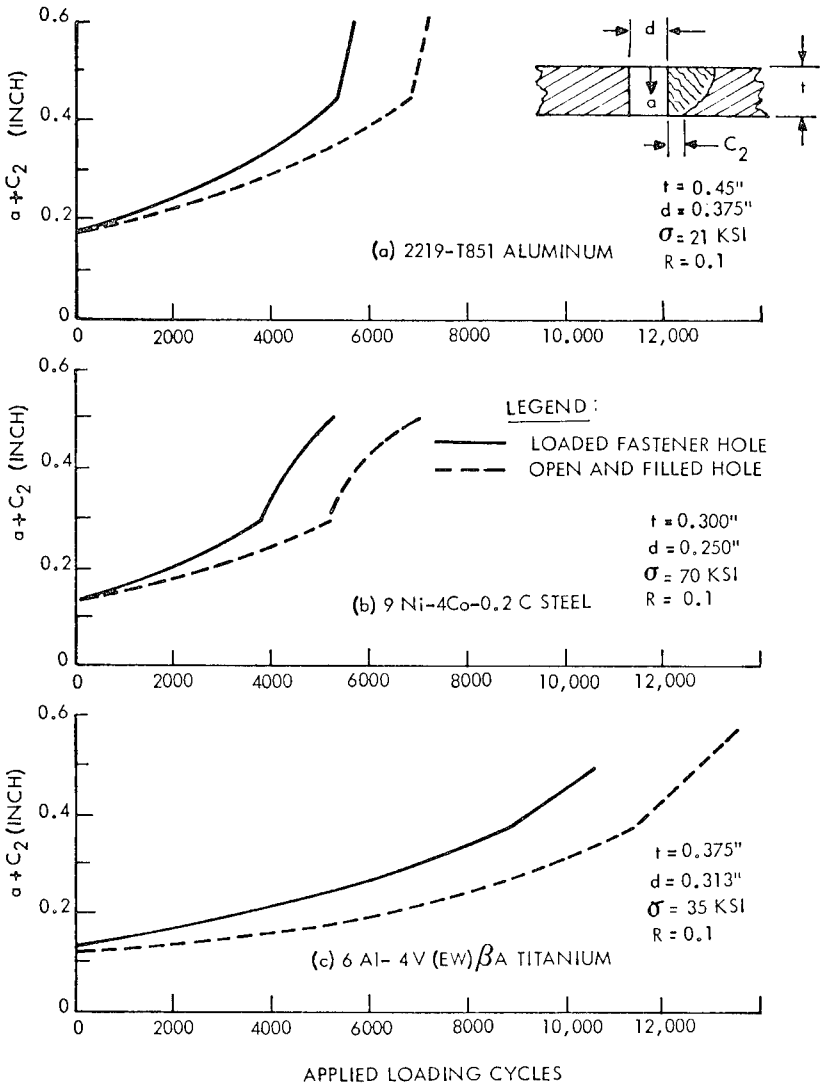


Figure 7. Crack depth growth behavior for flaws originating at close-tolerance fastener filled and open conventional holes.

Table 5. Summary of Test Parameters for Taper-lok Fastener Tests

Flaw Geometry	Alloy	Specimen Code	Fastener			Initial Flaw		Peak Cyclic Stress (ksi)
			No.	Interference (in.)	Load (lbs)	Depth a, (in.)	Width c, (in.)	
t d c Alloy d (in.) t (in.) Al 0.375 0.45 Fe 0.250 0.03 Ti 0.313 0.38	Al	FUCIA-1	1 2 3	0.0024 0.0060 0.0024	4000 0 0	0.160 0.151 0.156	0.138 0.140 0.145	24
	Al	FUCIA-2	1 2 3	0.0038 0.0038 0.0024	4000 0 0	0.160 0.144 0.136	0.139 0.130 0.144	24
	Fe	FUCIS-1	1 2 3	0.0030 0.0030 0.0036	3600 0 0	0.109 0.106 0.106	0.105 0.106 0.094	75
	Ti	FUCIT-2	1 2 3	0.0034 0.0034 0.0042	3000 0 0	0.141 0.129 0.120	0.128 0.124 0.115	50
t d c Dimensions d and t same as above	Al	FUTIA-1	1 2 3	0.0038 0.0038 0.0024	4000 0 0	— — —	0.080 0.078 0.090	24
	Fe	FUTIS-1	1 2 3	0.0030 0.0030 0.0036	3600 0 0	— — —	0.116 0.064 0.062	75
	Ti	FUTIT-1	1 2 3	0.0034 0.0034 0.0042	3000 0 0	— — —	0.075 0.082 0.009	50

ameter ratio, and either no load transfer or moderate load transfer. Hence, even though the results obtained herein are encouraging, further work is needed to investigate crack propagation behavior for cracks having smaller initial size to hole-diameter ratios and subjected to greater load transfer through the fastener.

Cold-Worked Open and Fastener-Filled Holes

Three specimens containing part-through cracks originating at cold-worked fastener holes were tested. One specimen was tested for each alloy including FUCCA-1 for the aluminum alloy, FUCCS-1 for the steel alloy, and FUCCT-1 for the titanium alloy. Each specimen contained one high-expansion hole filled with an unloaded close-tolerance fastener, and one open hole for which the amount of cold expansion was reduced by 25 percent. Test details for each of the three specimens are listed in Table 4.

Crack-depth growth rates for cold-worked holes were considerably slower than rates for conventional holes even though cold working resulted in accentuated crack growth along the face of the hole. This result is illustrated in Figure 9, where crack width is plotted as a function of loading cycles for both conventional and cold-worked open holes. There appears to be an initial period of very slow crack-growth rates for the cold-worked holes similar to crack-growth behavior observed after tensile overloads.

Since methods were not available for calculating stress-intensity factors for cold-worked hole specimens, experimental lives were compared to calculated lives for cracked conventional fastener holes having the same initial crack geometry as the cold-worked holes. Calculated lives were equal to the number of cycles required to grow the initial crack depth to the final crack depth observed in the cold-worked hole specimens. Shape change behaviors were assumed to be the same as those illustrated in Figure 6 for close-tolerance fastener-filled holes. Hence, the calculated final crack widths were larger than the actual crack widths in the cold-worked hole specimens. This procedure was selected to yield lower bound estimates for increase in crack propagation life due to cold working. Results of the calculations are summarized in Figure 10. The calculations indicate that cold working resulted in about a tenfold increase in crack propagation life except for the low-expansion open hole in the steel alloy specimen. In these tests, the titanium alloy responded most favorably to the cold working process but it is not known whether this result would be generally applicable. The effect of the amount of cold expansion was stronger in the steel alloy than in the titanium alloy. A 25 percent reduction in cold expansion resulted in de-

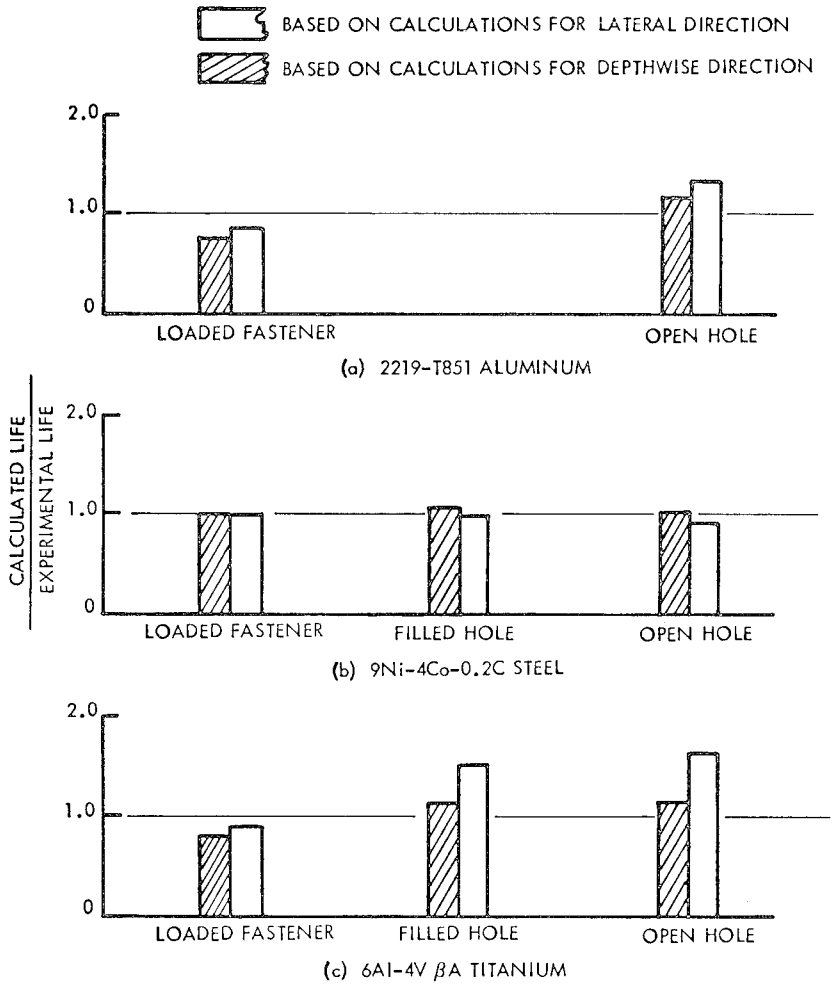


Figure 8. Comparison of calculated and experimental lives for part-through cracks originating at open and close-tolerance fastener filled holes.

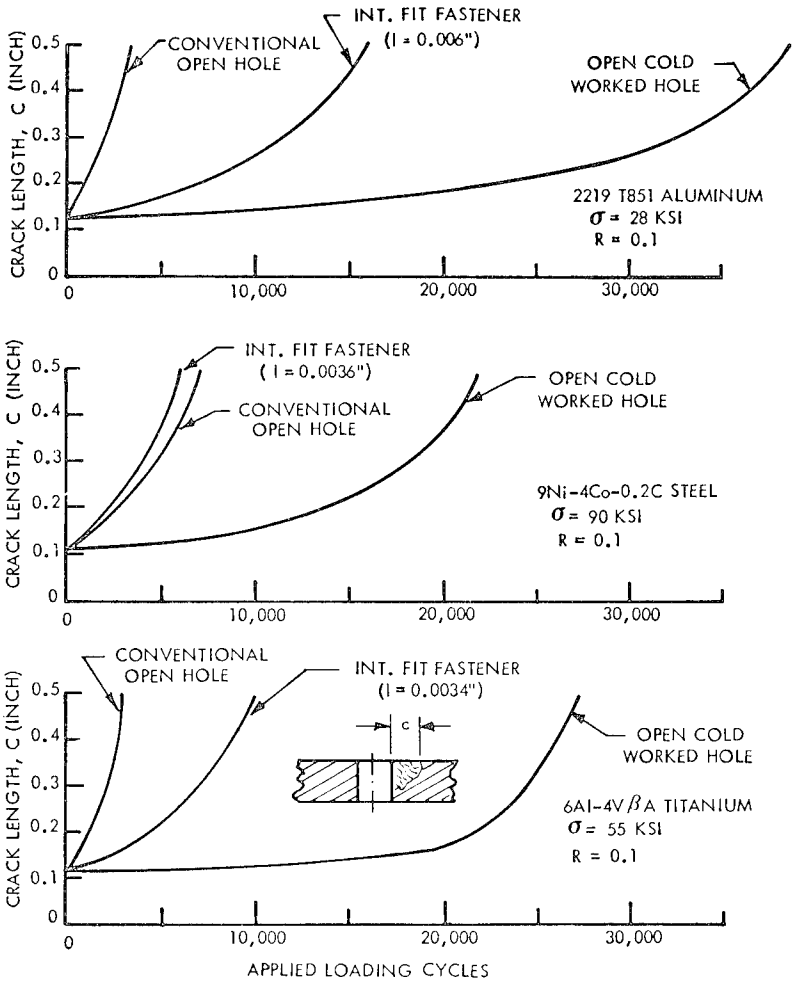


Figure 9. Crack length vs. cycles for part-through cracks originating at open conventional, open cold worked and interference fit fastener filled holes.

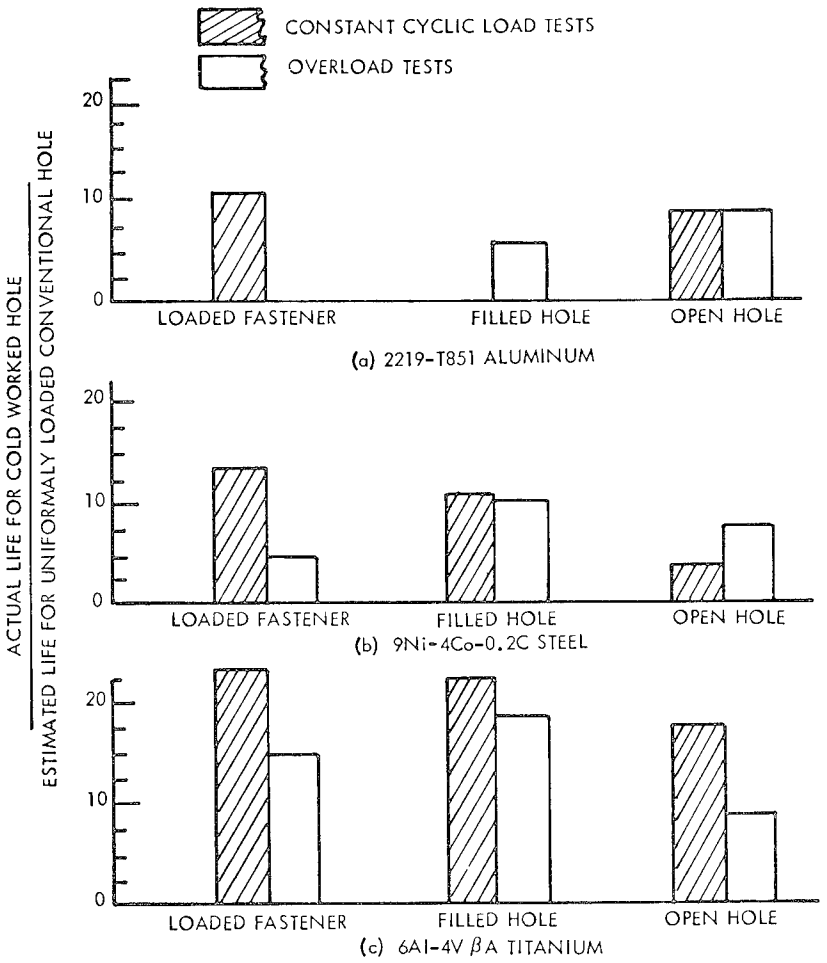


Figure 10. Comparison between crack propagation lives for part-through cracks originating at cold worked and conventional fastener holes.

creases in crack propagation life of about 70 percent for the steel alloy and about 20 percent for the titanium alloy. The effect of expansion level could not be determined for the aluminum alloy.

Stress-intensity factors applicable to cold-worked holes are not available and, hence, it is not possible to apply the results of this program to conditions that differ from those used in these tests. The effect of cold working on crack propagation life should depend on initial crack

shape, initial crack size, crack-size-to-hole-diameter ratio, and expansion level. Additional analyses and test data will be required to better characterize the effects of cold working of fastener holes on crack propagation life.

Interference-Fit Fastener Tests

Seven interference-fit fastener specimens were tested, including three specimens fabricated with uniform through-the-thickness cracks and four specimens fabricated with part-through quarter-circular cracks. Test details for all specimens are summarized in Table 5. In all but one specimen (aluminum alloy specimen FUCIA-1), one loaded and one unloaded fastener hole contained Taper-lok fasteners installed with an interference value midway between the maximum and minimum values for standard installations. Interference level for the remaining unloaded fastener was set at the minimum level for standard installations in the aluminum alloy specimens, and midway between the average and maximum values for standard installations in the steel and titanium alloy specimens. In aluminum alloy specimen FUCIA-1, interference values were set at the minimum level for standard installations for the loaded fastener and one unloaded fastener, and at the maximum value allowed by specifications for the Boeing 747 airframe for the second unloaded fastener.

Results for Through-the-Thickness Crack Tests

Test results for specimens fabricated with uniform through-the-thickness cracks are plotted on graphs of crack length versus cycles in Figure 11. For the aluminum alloy, a change from minimum to average interference levels almost doubled crack propagation life whereas fastener loading had only a very small effect. For the steel alloy, a 20% increase in fastener interference resulted in only a small increase in crack propagation life. The steel alloy fracture surface for the loaded fastener hole contained a distinct band of dull colored crack growth between the shiny bands of fatigue crack growth due to precracking and subsequent cycling. The source of this crack growth is not known. Similar growth was not observed at the other two fastener holes in the same specimen. For the titanium alloy, neither fastener load nor a 24% increase in interference level had a significant effect on crack propagation life.

Test results are compared to calculated results in Figure 12. For each unloaded fastener hole, two different calculations were made including one which accounted for and one which did not account for the

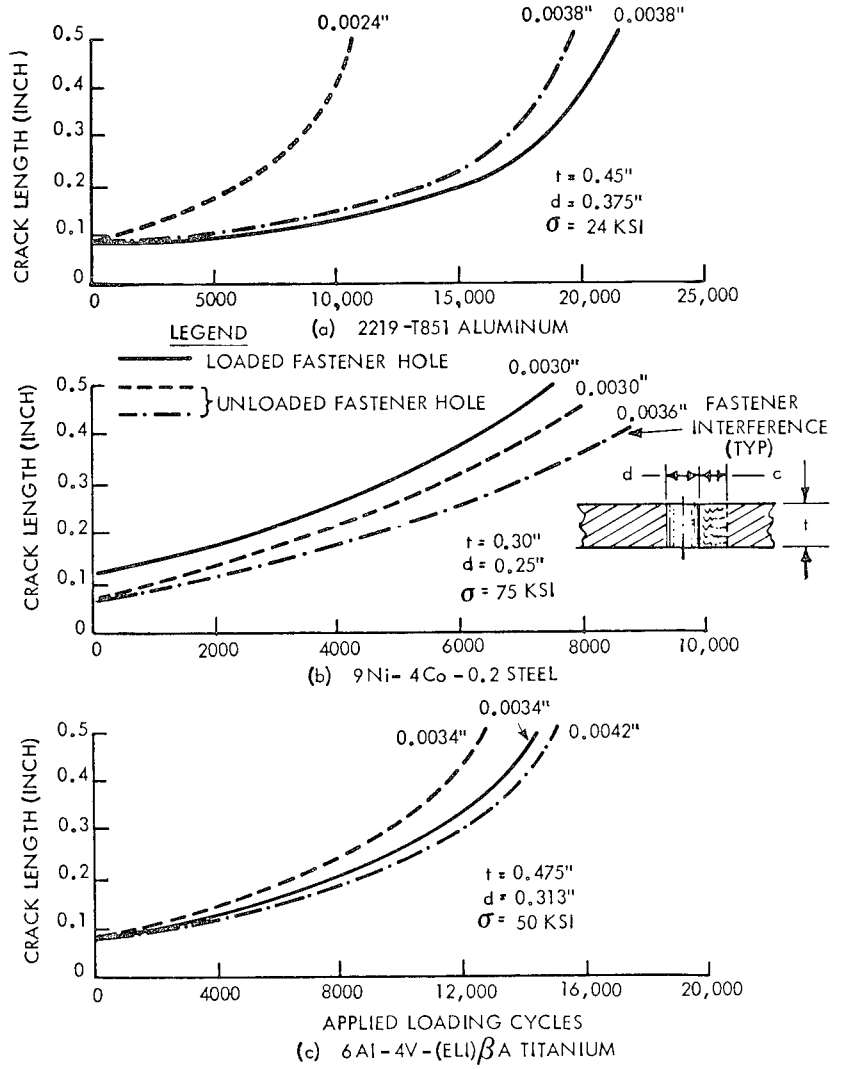


Figure 11. Crack growth behavior for through cracks originating at interference-fit fastener holes.

effects of interference on stress-intensity factors. The former calculation was made using equation (3) to evaluate stress-intensity factors. The latter calculation was made using the Bowie[14] and Shah[13] solutions for stress-intensity factors due to remote and fastener loading, respectively. For loaded fastener holes, methods for evaluating the effects of interference on stress-intensity factor were not available, and results were com-

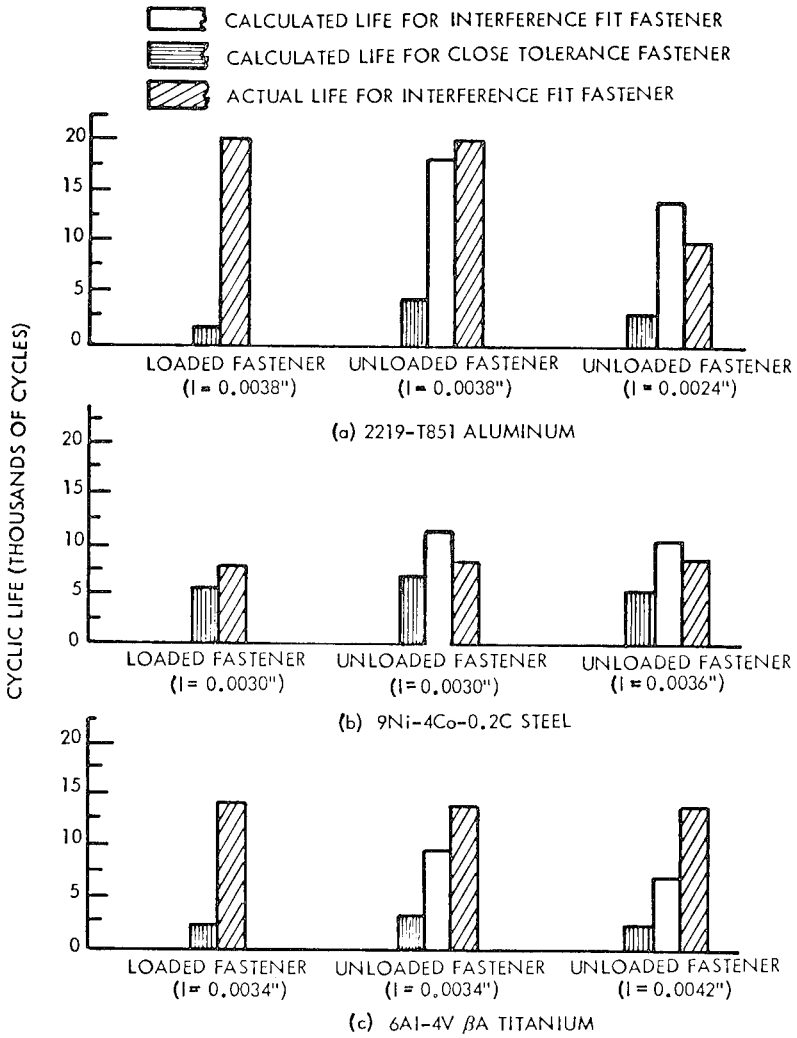


Figure 12. Comparison of experimental and calculated lives for uniform through cracks originating at interference-fit fastener holes.

pared only to calculations that did not account for interference effects. For the aluminum alloy, calculations that did not account for interference effects greatly underestimated crack propagation life, whereas calculations that did account for interference effects yielded calculated lives that were in reasonably good agreement with test results. For the steel alloy, interference-fit fasteners had only a small effect on crack

propagation life and both calculation methods yielded results that were in good agreement with experimental results.

Methods used herein to estimate the effects of interference on crack propagation life indicate that such effects should be quite sensitive to initial crack-length-to-hole-diameter (c/r) ratios. For very small c/r values, substantial improvements in crack propagation life should result from the use of interference-fit fasteners. For large c/r values, interference-fit fasteners would be expected to reduce crack propagation life. For some intermediate range of c/r values, interference fasteners should have little or no effect on crack propagation life. In this program, both calculations and experiment showed that initial c/r ratios for the steel specimens were in the range where interference-fit fasteners would not be expected to have a strong influence on crack propagation life.

Results for Part-Through Crack Tests

Test results for specimens fabricated with part-through cracks are plotted on graphs of crack depth versus cycles in Figure 13. For the aluminum alloy, an increase in interference level from minimum to average values seemed to have a greater effect on crack propagation life for loaded fasteners than for unloaded fasteners. For all alloys, neither fastener load nor moderate changes in unloaded fastener interference had a large effect on crack propagation life.

The effect of a wide range of interference levels on fatigue crack growth of part-through fastener hole flaws in aluminum alloy specimens is illustrated in Figure 14. The interference level of 0.0024 in. is the minimum permissible value for standard installations of 0.375-in.-diameter bolts. The interference level of 0.006 is slightly greater than the maximum specified value of 0.0054 in. for standard installations. Crack propagation life increased by a factor of about 2.5 when interference level was increased from minimum to maximum values. Crack propagation lives for Taper-lok fastener-filled holes ranged from 2 to 5 times comparable lives for open holes as interference level was increased from minimum to maximum values. The above results are not applicable to all interference-fit fastener installations since variables such as crack size, crack shape, and hole diameter will influence results. In general, it is believed that increase in crack propagation life due to interference-fit fasteners will increase with decreasing crack-size-to-hole-diameter ratios when interference to hole-diameter ratio is kept constant.

Methods were not available for computing stress-intensity factors for part-through cracks originating at interference fastener-filled holes. Hence, experimentally determined crack propagation lives were compared to calculated lives for geometrically identical close-tolerance fas-

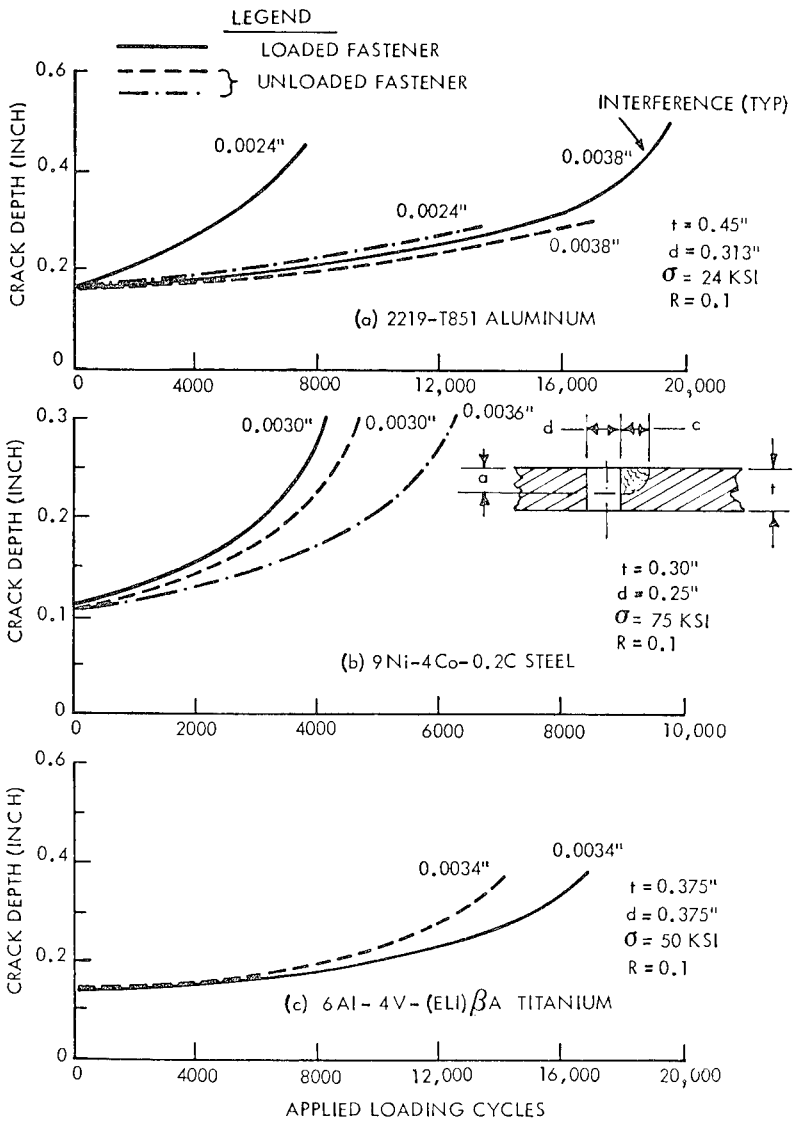


Figure 13. Crack depth growth behavior for part-through cracks originating at interference fit fasteners.

tener-filled holes. Results are summarized in Figure 15, where ratios of actual to calculated life are shown for specimens FUCIA-2, FUCIS-1, and FUCIT-1. For the aluminum and titanium alloy specimens, the cracked interference-fit fastener holes yielded cyclic lives ranging from 3

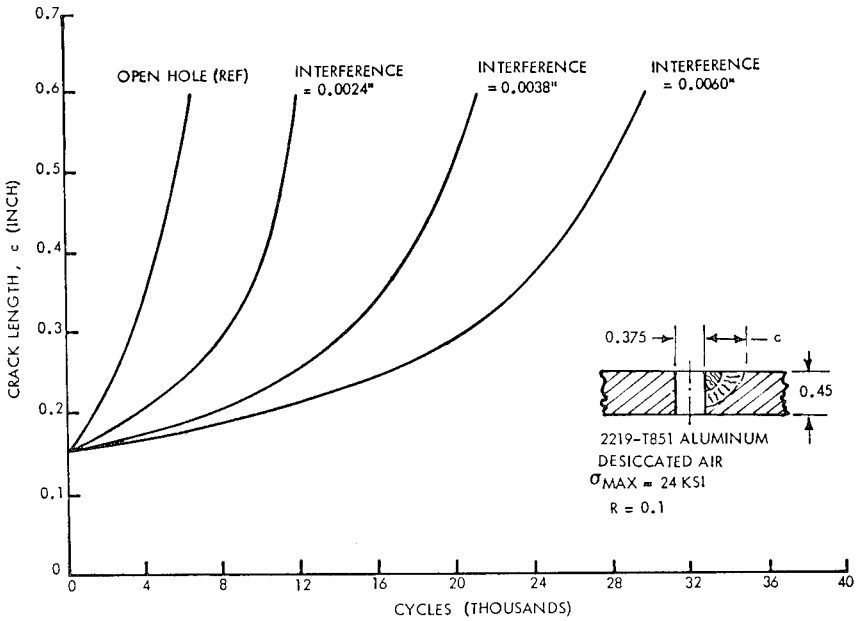


Figure 14. Effect of Taper-lok bolt interference on fatigue crack growth of part-through cracks in 2219-T851 aluminum alloy.

to 5 times the lives that would have been anticipated for comparable cracked close-tolerance fastener holes. For the steel alloy specimens, interference-fit fasteners had very little effect on crack propagation life. These results are similar to those obtained from the through-cracked specimen tests where all but the steel alloy specimens yielded beneficial effects of interference-fit fasteners on crack propagation life.

SUMMARY OF FINDINGS

This program provided both a quantitative and qualitative understanding of the crack-growth characteristics of fastener-hole flaws under uniform cyclic loadings. Both cold working of fastener holes and installation of Taper-lok fasteners were shown to influence the geometry of part-through cracks as the cracks grew through the specimen thickness. Initial part-circular cracks tended to remain nearly part circular when growing from conventional reamed holes. Cold working of holes tended to accentuate crack growth in the depthwise direction, whereas Taper-lok fasteners tended to accentuate growth in the lateral direction.

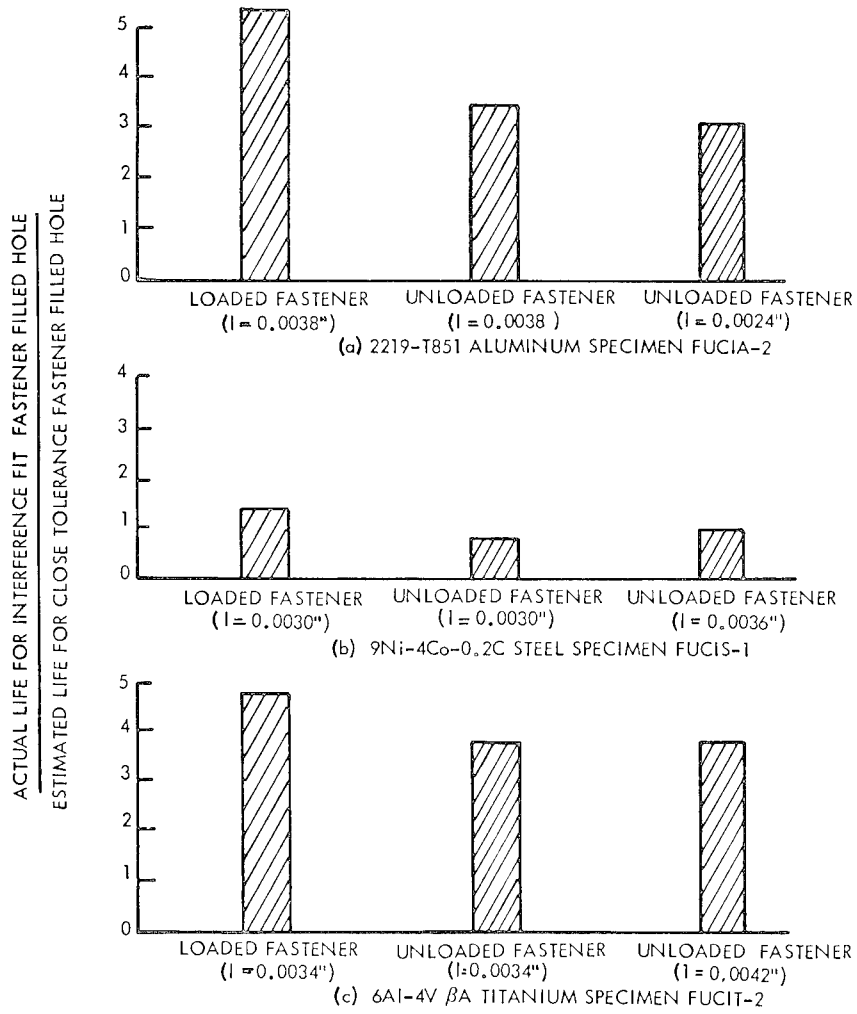


Figure 15. Comparison between crack propagation lives for part-through cracks originating at interference-fit and close-tolerance fastener filled holes.

Of the three fastening systems tested (close-tolerance fasteners in conventional reamed holes, close-tolerance fasteners in cold-worked holes, and Taper-lok fasteners in taper-reamed holes), close-tolerance fasteners in conventional reamed holes yielded the shortest crack propagation lives. In the 2219–T851 aluminum and 6Al–4V beta-annealed titanium alloy tests, Taper-lok fasteners installed using average interference values for standard installations yielded crack propagation lives ranging

from 3 to 5 times comparable lives for conventional reamed close-tolerance fastener holes. Fastener holes that were cold worked using the Boeing Airplane Company's high-interference split-sleeve process yielded crack propagation lives that ranged from 9 to 23 times comparable lives for conventional reamed fastener holes. In the 9Ni–4Co–0.2C steel alloy test, Taper-lok fasteners had only small effects on crack propagation lives. For the steel alloy through-cracked specimens, calculations indicated that the combination of variables used in this program were such that fastener interference could not exert a strong influence on crack propagation life. Cold working of fastener holes did result in substantial increases in crack propagation life in all steel alloy tests.

For the range of parameters used in this program, it was found that good estimates of crack propagation life for close tolerance fastener and open holes could be made using stress-intensity factors described in References 3, 4, and 13 and baseline crack-growth rate data obtained from surface-flaw specimens. Tests were limited to circular part-through cracks, one crack-depth-to-hole-diameter ratio ($\simeq 1.0$), and either zero or moderate load transfer. Ratios of calculated to experimental lives were lower for loaded holes than for either filled or open holes.

Methods developed to evaluate quantitatively the effects of fastener interference on crack propagation life for through-cracked fastener holes yielded calculated lives ranging from 0.5 to 1.4 times experimental lives. Methods for evaluating effects of fastener interference on crack propagation life for part-through cracked fastener holes were not available.

Agreement between experimental and calculated results obtained in this work was good. Tests were, however, limited to uniform cyclic loading profiles, two crack shapes, one hole diameter per alloy, and zero or moderate load transfer. Further work is needed to evaluate the applicability of the crack propagation life calculation methods used in this work to a broader range of conditions. In particular, smaller initial crack-to-hole-size ratios and larger values of load transfer should be investigated.

ACKNOWLEDGMENT

The author wishes to express his appreciation to the United States Air Force and, in particular, Mr. Howard A. Wood, who initiated and supported the work described in this paper through USAF contract F33615-72-C-1740. The author wishes to acknowledge the invaluable help of Dr. R. C. Shah who developed the analytical solutions, Mr. W. L. Engstrom who coordinated the tests, and Mr. A. A. Ottlyk who performed the tests.

REFERENCES

1. "Airplane Damage Tolerance Requirements," Military Specification MIL-A-83444 (USAF), 2 July 1974.
2. Gran, R. J., Orazio, F. D., Paris, P. C., Irwin, G. R., and Hertzberg, R., "Investigation and Analysis Development of Early Life Aircraft Structural Failures," Universal Technology Corporation, Dayton, Ohio. Air Force Flight Dynamics Laboratory Contract Report No. AFFDL-TR-70-149, March 1971. (AD 884 790)
3. Shah, R. C., "Stress Intensity Factors for Through and Part-Through Cracks Originating at Fastener Holes," paper presented at 8th National Symposium on Fracture Mechanics, Brown University, 26–28 August 1974.
4. Hall, L. R., Shah, R. C., and Engstrom, W. L., "Fracture and Fatigue Crack Growth Behavior of Surface Flaws and Flaws Originating at Fastener Holes," Boeing Aerospace Company, Seattle, Wash. Air Force Flight Dynamics Laboratory Contract Report No. AFFDL-TR-74-47-Vol. 1, May 1974. (AD-A001 597)
5. "Improved Finite Element Methods for Fracture Analyses," Bell Aerospace Company, Buffalo, N.Y., Air Force Flight Dynamics Contract No. F33615-72-C-1739, 1972.
6. "Development and Evaluation of Methods of Plane Stress Fracture Analysis," Northrop Corporation, Aircraft Division, Hawthorne, Calif., Air Force Flight Dynamics Laboratory Contract No. F33615-72-C-1796, 1972.
7. "Damage Tolerant Design Handbook. A Compilation of Fracture and Crack-Growth Data for High-Strength Alloys," Battelle Columbus Laboratories, Metals and Ceramics Information Center, Columbus, Ohio, Report No. MCIC-HB-01, December 1972. (AD 753 774)
8. Hall, I. R., Finger, R. W., and Spurr, W. F., "Corrosion Fatigue Crack Growth in Aircraft Structural Materials," Boeing Aerospace Company, Seattle, Wash. Air Force Materials Laboratory Contract Report No. AFML-TR-73-204, September 1973. (AD 916 695)
9. "Crack Growth Analysis for Arbitrary Spectrum Loading," Grumman Aerospace Corporation, Bethpage, N.Y., Air Force Flight Dynamics Laboratory Contract No. F33615-72-C-1744, 1972.
10. "Advanced Air Superiority Fighter Wing and Carrythrough Structure," General Dynamics, Fort Worth Division, Tex., Air Force Flight Dynamics Laboratory Contract No. F33615-72-C-1891, 1972.
11. "Advanced Air Superiority Fighter Wing Structures," Northrop Corporation, Aircraft Division, Hawthorne, Calif., Air Force Flight Dynamics Laboratory Contract No. F33615-72-C-1891, 1972.
12. "Advanced Cargo/Tanker Structures," Lockheed-Georgia Company, Marietta, Ga., Air Force Flight Dynamics Laboratory Contract No. F33615-72-C-2165, 1972.
13. Shah, R. C., "Stress Intensity Factors for Through and Part-Through Cracks at Unloaded and Loaded Open, Filled and Interface Fit Fastener

Holes," Boeing Aerospace Company, Seattle, Wash., Document No. D180-17951-1, 1974.

14. Bowie, O. L., "Analysis of an Infinite Plate Containing Radial Cracks Originating at the Boundary of an Internal Circular Hole," *J. Math. Phys.*, **35** (1956–57), 60–71.

23. THE EFFECT OF A CORROSIVE ENVIRONMENT ON THE STRENGTH AND LIFE OF GRAPHITE–EPOXY MECHANICALLY FASTENED JOINTS

M. S. ROSENFELD
Naval Air Development Center
Warminster, Pennsylvania

A galvanic corrosion problem exists when graphite–epoxy composites are coupled to aluminum alloys. The graphite composite–aluminum couple causes the aluminum to corrode faster and to generate more corrosion products than an all-aluminum structure when both are exposed to aqueous salt environments. The effect was studied quantitatively by testing mechanically fastened joints fabricated of these materials with and without corrosion protection applied to the materials.

INTRODUCTION

A galvanic corrosion problem exists when graphite–epoxy composites are coupled to aluminum alloys. The graphite composite–aluminum couple causes the aluminum to corrode faster and to generate more corrosion products than an all-aluminum structure when both are exposed to aqueous salt environments. Although this problem has been studied qualitatively, no quantitative study of its effect on joint mechanical properties has been conducted. Furthermore, the effect of incorporating conventional corrosion-control treatments in the fabrication of the joint is also unknown.

This program was initiated (1) to determine the order-of-magnitude effect of the corrosion on the static and tension–tension fatigue behavior of a simple mechanically fastened joint between a graphite–epoxy laminate and aluminum alloy, and (2) to determine if the conventional Navy corrosion-control treatment and/or simple material changes would alleviate the anticipated problem.

TEST SPECIMEN

The test specimen was a single-shear butt joint of graphite–epoxy laminate with a 7075–T73 aluminum alloy splice plate using 1/4-in.-diameter, 100° countersunk, flush-head fasteners. Geometric details of the specimens are contained in Figure 1. The joint was designed to represent a typical graphite–epoxy skin splice over aluminum alloy substructure. In the initial specimen design, the substructure was an extruded Tee section, but the initial tests indicated that the same results could be obtained using a flat splice plate to represent the substructure. To further simulate this type of joint, the grain of the aluminum alloy was kept transverse to the load direction; this makes the aluminum more critical since the principal stress is in the long transverse direction.

The specimens were fabricated of various combinations of materials; graphite–epoxy laminate, fastener system, and corrosion-protection system. They were subjected to two different environments prior to test. All tests were performed in the laboratory environment of 72°F ± 2°F and relative humidity of 50% ± 5%.

The specimen numbering system is keyed to the laminate and fastener system used, the corrosion protection applied, and the pretest environmental exposure. The first character, a letter, denotes the combination of laminate system and fastener system used; the second character,

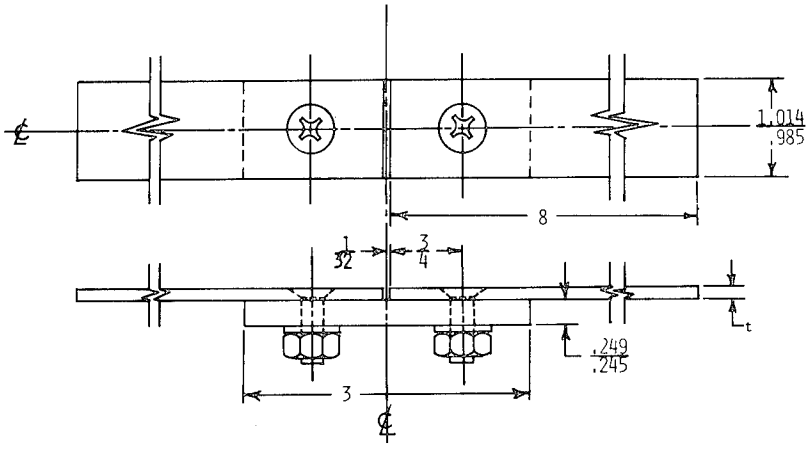


Figure 1. Test specimens.

a digit, denotes the corrosion-control system; and the third character denotes the environmental exposure. The numbers after the dash are serial numbers for the specimens within each group. The numbering system is shown in Table 1. Thus specimen A1X-3 is the third specimen of the group made from NARMCO 5209 Gr/Ep prepreg with the steel fastener system and corrosion-protection system 1 and exposed for 2 weeks prior to test to synthetic sea water with simulated stack gas.

The aluminum alloy splice plates were fabricated from 7075–T73 aluminum alloy with the holes reamed to size after sulfuric acid anodizing per MIL-A-8625C, Type II.

Both the NARMCO 5209 and NARMCO 5206 prepregs used the MODMOR Type II high-strength graphite fibers. The laminate lay-up sequence was 0°, −45°, +45°, +45°, −45°, 0°, repeated three times for all specimens. The C — and D — groups of specimens also had one layer of 7-mil 181-fiberglass fabric on the faying surface. The holes in the laminate were drilled using a 0.250-in. Master, 2-flute, carbide drill after 1/8 in. pilot drilling and were then countersunk using a 4-flute carbide countersink.

TEST METHOD

All tests were performed in a 20 kip M-T-S closed-loop hydraulic fatigue machine equipped with "Alignomatic" grips. The use of self-aligning hydraulic grips made it unnecessary to reinforce the specimen ends to preclude failure at the grips.

Three types of tests were performed for each group of specimens except for the B1X specimens: monotonic static tests, zero-to-maximum-tension fatigue tests, and residual-strength static tests. The static tests of the B1X specimens were omitted because these specimens were identical to the A1X specimens except for the use of the titanium fastener system in lieu of the steel fastener system.

Prior to exposure to the simulated marine environment, all sealed and painted specimens were preloaded for 10 cycles at 0.5 Hz between limits of zero and +1400 lbs, which corresponds to approximately 60% of the average static strength of the A — groups of specimens. This was done to crack the paint film and the sealant prior to exposure to the simulated marine environment. Typical appearance of the specimens after 2 weeks' exposure are shown in Figures 2 and 3. The latter photo also shows typical damage to the protective coating resulting from the preloading.

All static tests were performed at a constant loading rate of 8 lbs/sec. No data was recorded except for the failing load.

Table 1. Specimen Numbering System

Material System		Protection System	Exposure
Laminate	**Fastener**		
A — NARMCO 5209 Gr/EP $(0°, \pm 45°)_6$ balanced lay-up; MODMOR Type II high-strength graphite fibers.	MS-24694-599 100° C'S'K steel bolt w. Cd plate and chromate conversion coating. AN960D416 al. al. washers AN315-4 steel nut w. Cd plate & chromate conversion coating.	0 — no corrosion protection applied to laminate or splice plate	No letter–Normal laboratory environment.
B — Same as A	NAS 664V7 100° C'S'K Ti Al. bolt AN960C416 CRS washers TLN10001 CD^2-4 CRS nut	1 — MIL-P-23377 Epoxy Primer MIL-S-81733A (AS) Type 4 Chromate Inhibited Polysulfide sealant on faying surfaces and gap. MIL-S-81733A (AS) Type 1 Chromate Inhibited Polysulfide sealant on fasteners and over fastener heads. MIL-C-81773 Polyurethane topcoat.	X — Preloaded for 10 cycles from 0 to 1400 lbs. Then exposed to a continuous spray of synthetic sea water w. injections of SO_2 for 1 hr. every 6 hrs. for 2 weeks. pH = 2.5–3.0.
C — NARMCO 5206 Gr/EP Prepreg $(0° \pm 45°)_6$ balanced lay-up (same fibers as A) w. one layer of 7-mil 181-fiberglass fabric on faying surface	Same as A	2 — Same materials as in 1 above except that the sealants were thinned down and sprayed on. No sealant applied to fastener shank or underside of head.	
D — Same as C	Same as B		

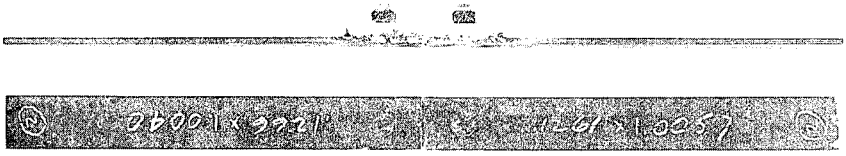


Figure 2. Unprotected specimen A0X–12 after two weeks sea-water spray.

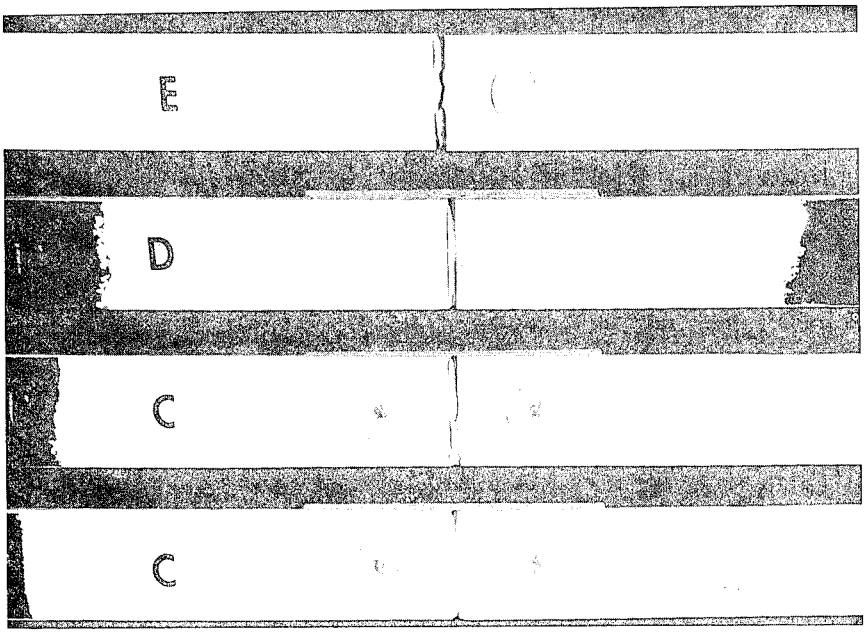


Figure 3. Typical protected specimens after two weeks' sea-water spray.

The fatigue-test specimens were loaded sinusoidally from zero to the maximum tension load at a frequency of 5 Hz. Testing was continued to complete failure.

The residual strength tests were performed on rebuilt fatigue specimens. Since almost all the fatigue failures occurred in the splice plate, a new splice plate was installed, keeping the bolts in the same position with respect to the laminate as they were for the fatigue tests and the bolts were retorqued to 40 in. lbs. The residual strength tests were run identically, to the monotonic static tests.

RESULTS

Static Tests

The static test data are summarized in Table 2. Except as noted in the table, all static failures occurred through the composite net section. Three of the five D2X failures were fastener failures through the section at the junction of the head and shank; these failures were caused by the reduction in shank area due to excessive Phillips' recess depth in the heads of the titanium alloy fasteners.

Fatigue Tests

The lives of the specimens not exposed to the sea-water spray are plotted in Figure 4 against the net section stress of the composite laminate. The almost horizontal line at 25 ksi represents the joint life based on the life of the composite laminate, and the intersecting curve above 20,000 cycles represents the joint life based on failure of the aluminum alloy splice plate. It is apparent that the standard corrosion-control treatment as applied to the A1 specimens had no effect on the life.

The lives of the NARMCO 5209 prepreg specimens exposed to the sea-water spray for two weeks prior to test are shown in Figure 5. These data show that the fatigue life of the specimens without the corrosion-prevention treatment was degraded by more than 50% from that of the specimens with the standard treatment. Furthermore, the use of titanium alloy fasteners (B1X specimens) in lieu of the steel fasteners (A1X specimens) had no effect on the fatigue life.

Figure 6 shows three modes of failure of the unprotected specimens exposed to the sea-water spray. Of 12 A0X specimens tested, 9 failed in the aluminum splice plate only, 1 failed at the bolt, and 2 failed in the laminate as a result of the aluminum failure. Close-ups of the failures are shown in Figure 7. The A1X and B1X failures were all in the aluminum

Table 2. Static Test Results

NARMCO 5209				NARMCO 5206 W. Glass			
Specimen No.	Failing Load (lbs)	Failure Stress (ksi) Gross	Net	Specimen No.	Failing Load (lbs)	Failure Stress (ksi) Gross	Net
A0–1	2224	16.21	24.23	C1X–1	2500	21.88	33.45
A0–2	2200	16.22	24.31	C1X–2	2392	20.64	31.49
A0–3	2192	16.30	24.39	C1X–15	2560	21.13	31.97
A0–4	2072	16.55	24.99	C1X–16	2880	23.63	35.79
Average	2172	16.32	24.48	Average	2583	21.82	33.18
A0X–1	2424	18.65	28.07				
A0X–2	2292	16.93	25.35	D2X–1*	2560	24.39	38.12
A0X–3	2388	19.10	28.93	D2X–3*	2772	25.05	38.59
A0X–4	2504	18.89	28.32	D2X–4	2812	24.50	37.55
Average	2402	18.39	27.67	D2X–16*	2536	22.20	34.08
				D2X–17	2820	24.33	37.05
				Average	2700	24.09	37.08
A1–3	2480	19.10	28.75				
A1–9	2380	17.90	26.85				
Average	2430	18.50	27.80				
A1X–1	2480	19.88	30.07				
A1X–2	2500	19.71	29.77				
A1X–3	2360	17.54	26.29				
A1X–4	2400	17.79	26.65				
Average	2435	18.73	28.20				

*Failure of bolt at junction of head and shank.

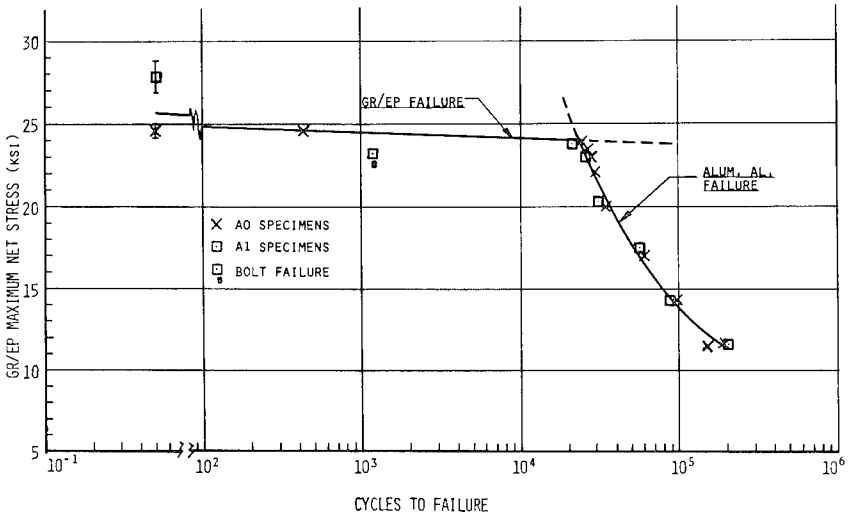


Figure 4. Life to failure, NARMCO 5209 prepreg, unexposed specimens.

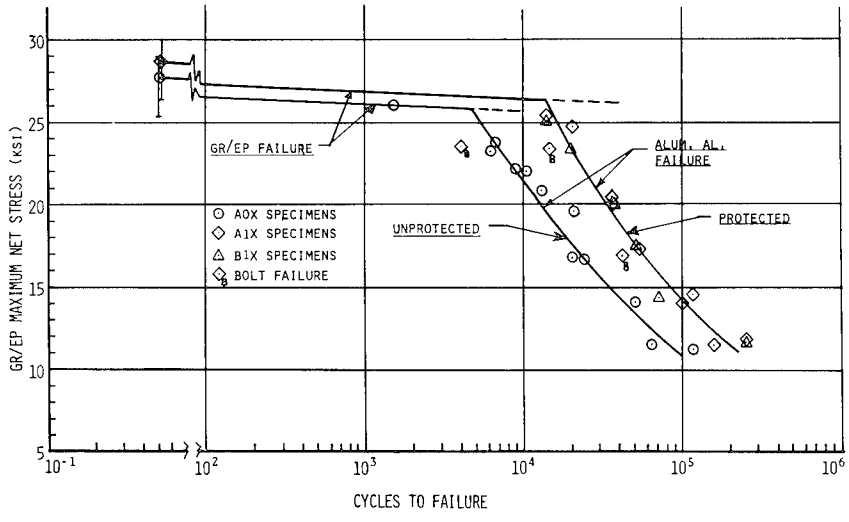


Figure 5. Life to failure, NARMCO 5209 prepreg, after two weeks' sea-water spray.

alloy splice plate except for 3 fastener failures in the A1X specimens. These fastener failures are attributed to over-hardening of the sealant under the fastener head prior to torquing the fastener, thus precluding proper seating of the fastener head in the countersink; this was evident

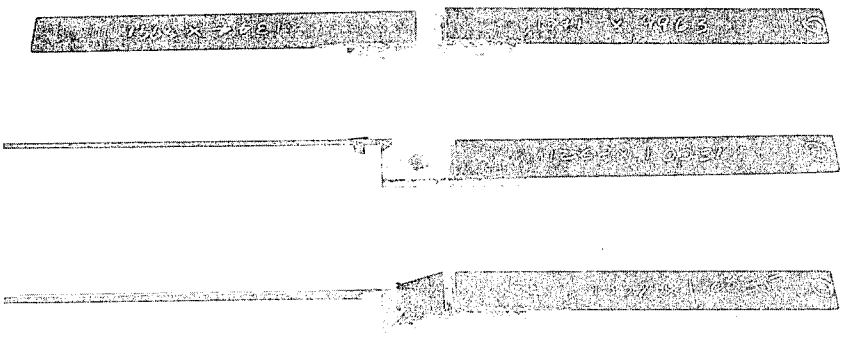
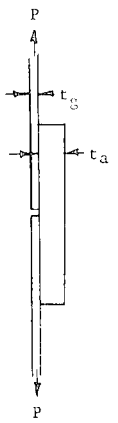


Figure 6. Typical failures of unprotected specimens.

by excessive relative deformation between the laminate and the fastener head prior to failure.

The results of the tests of the NARMCO 5206 prepreg are shown in Figure 8. There appears to be a consistent difference between the results of the two groups of specimens. However, this difference disappears when the effect of laminate thickness is considered and the data are plotted against the maximum stress in the splice plate as described below.

Direct comparison of the data from the NARMCO 5206 prepreg specimens with the data from the NARMCO 5209 prepreg specimens is not possible on the basis of the laminate net section stress because the difference in thickness of the two laminates affects the bending stress for the splice plate. The maximum stress at the surface of the splice plate is:



$$\sigma = \sigma_t + \sigma_b$$

$$= \frac{P}{A} + \frac{M}{I/C}$$

$$= \frac{P}{t_a w_a} + \frac{P \times 1/2\,(t_a + t_g)}{1/6\, t_a^2 w_a}$$

$$= \frac{P}{t_a w_a}\left[1 + \frac{3}{t_a}(t_a + t_g)\right]$$

$$\sigma = \sigma_{a_{gr}}\left(4 + 3\frac{t_g}{t_a}\right)$$

where

w_a = splice-plate width

$\sigma_{a_{gr}}$ = splice-plate gross area direct

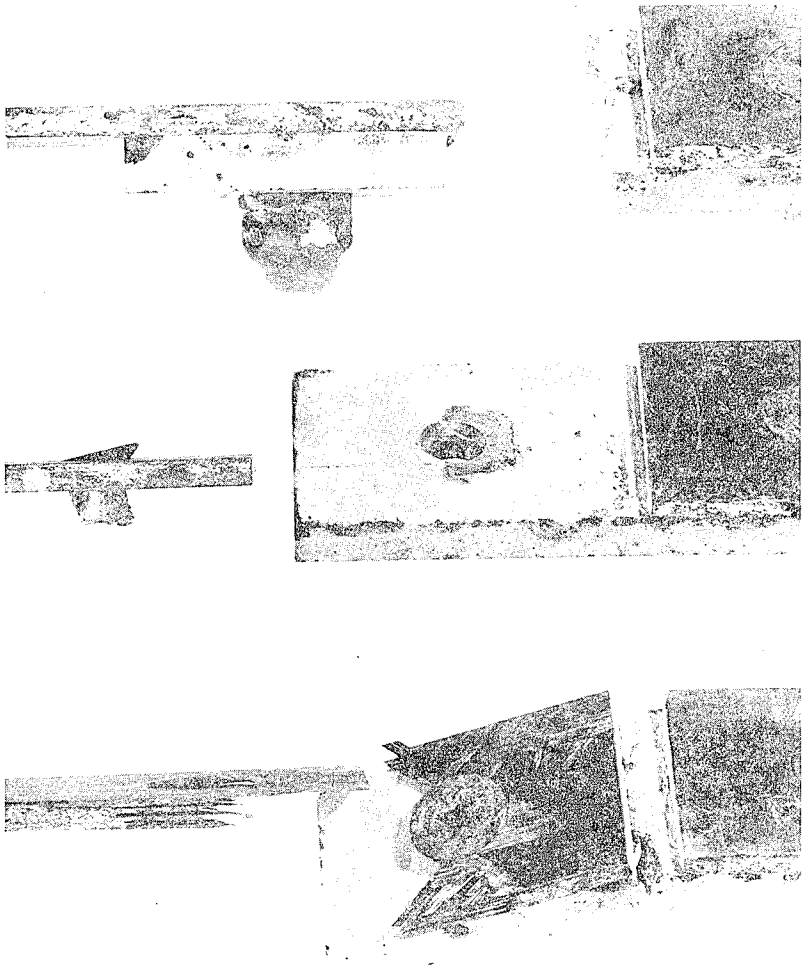


Figure 7. Close-ups of typical failures of unprotected specimens.

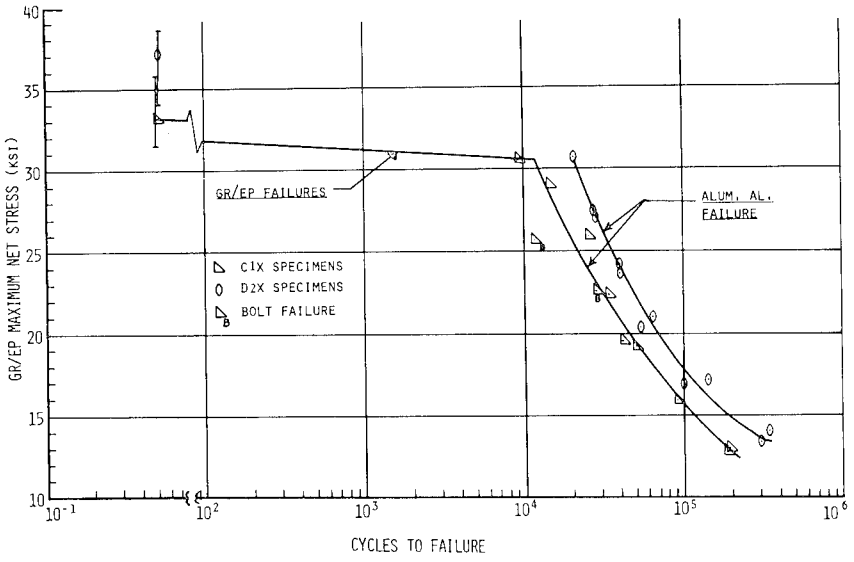


Figure 8. Life to failure, NARMCO 5206 prepreg, after two weeks' sea-water spray.

The lives of all specimens exposed to the salt spray are plotted in Figure 9 against this calculated stress. The data for both the NARMCO 5206 and NARMCO 5209 prepreg laminates lie along the same curve, thus demonstrating that the use of the fiberglass layer at the faying surface and the use of titanium alloy fasteners were unnecessary for corrosion prevention. The unexposed specimen data are also included to show that the corrosion-control treatment did not affect the fatigue characteristics. The life degradation resulting from corrosion of the unsealed and unpainted joint specimens exceeds 50% as previously noted.

Residual-Strength Tests

Since almost all failures occurred in parts other than the graphite laminate, the specimens were rebuilt by replacement of the splice plate. These rebuilt specimens were loaded monotonically to determine the residual strength and to investigate the effect of prior cycling and the sea-water spray on the residual strength. The results, shown in Figure 10, fall into two bands, one for the NARMCO 5209 prepreg and one for the NARMCO 5206 prepreg. The points plotted at zero cyclic stress represent the original average static strength for each group of specimens. The ± 10% band widths are typical of static-strength data.

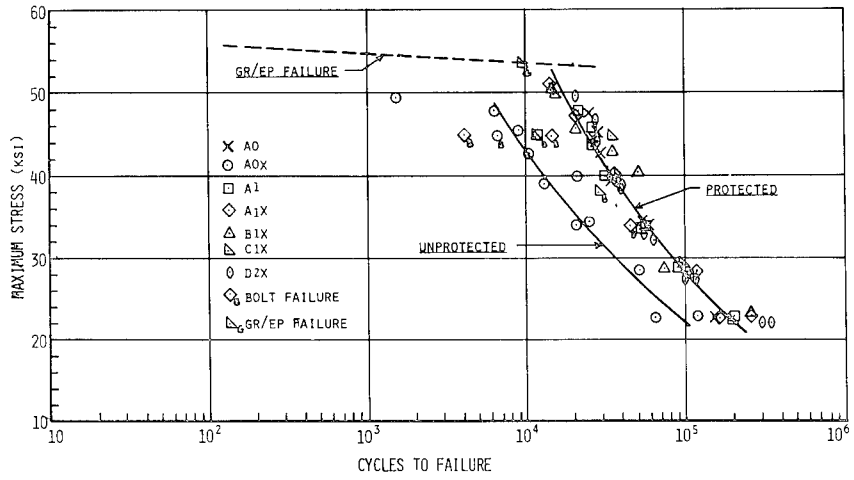


Figure 9. Life to failure, aluminum alloy splice plate.

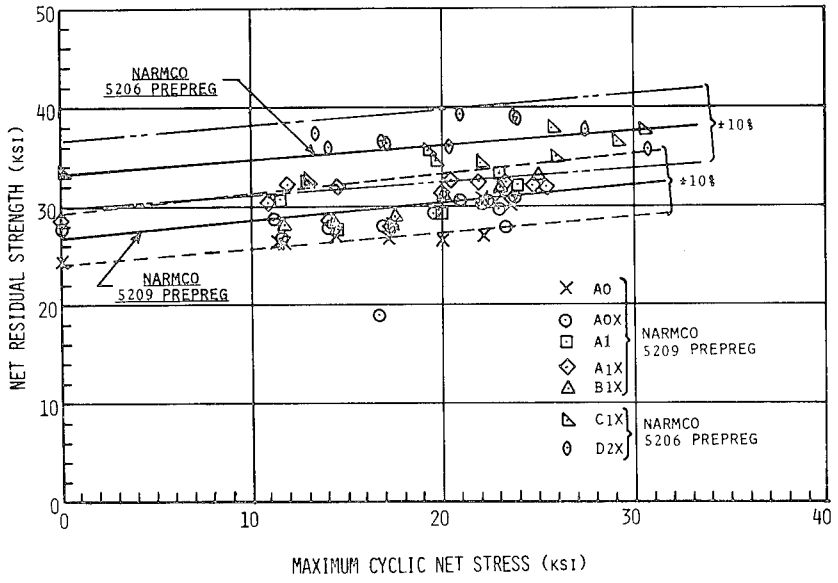


Figure 10. Residual strength of graphite–epoxy laminates.

The data show that the static strength of the graphite laminate was not affected by the sea-water exposure even for the unprotected A0X specimens. There is a definite increase in static strength with increase in the cyclic stress; however, the increase is not sufficiently large to warrant consideration, and it should merely be concluded that the static strength does not degrade as a result of cyclic loading.

CONCLUSIONS

This program was initiated to investigate the effect of a simulated marine environment on the static and fatigue behavior of a simple mechanically fastened joint between a graphite–epoxy laminate and aluminum alloy. The efficacy of some simple corrosion-control procedures and material substitutions were also evaluated.

The results of this investigation showed the following:

1. There was no change in static strength due to exposure.
2. The unprotected specimens exposed to the corrosive environment had their fatigue life degraded by more than 50% from the base line specimens.
3. The protected specimens showed no evidence of corrosion after exposure and the fatigue life was identical to the base-line specimens.
4. The residual strength of the exposed specimens was not reduced from the base-line specimens.

Therefore, it is concluded that graphite–epoxy can be used in structures in juxtaposition with aluminum alloy provided that the conventional Navy corrosion protection is applied to the structures during fabrication.

SUMMARY

Static, constant amplitude (R = 0) fatigue, and residual-strength tests were performed on a simple mechanically fastened joint between a graphite–epoxy laminate and 7075–T73 aluminum alloy. Various corrosion-control treatments were used to protect the specimens from the simulated marine environment to which the specimens were subjected prior to the tests. The test results demonstrated that graphite–epoxy can be used in structural applications in juxtaposition with aluminum alloy provided that the conventional Navy corrosion-control protection is applied to the components during fabrication.

24. DETECTION OF ADHESIVE BOND-LINE FLAWS BY NEUTRON RADIOGRAPHY

D. H. PETERSEN and W. E. DANCE
Advanced Technology Center, Inc.
Dallas, Texas

The design and fabrication of adhesively bonded structures for service under severe fatigue and environmental exposure conditions assumes that there exist adequate nondestructive inspection techniques for quality assurance and durability assessment. Research results are presented demonstrating a technique by which neutron radiography can be applied as an NDI/NDT method for detection of defects within adhesive bondlines as well as for prediction of lap shear strength. The use of neutron-absorbing additives in adhesive systems is shown to greatly enhance the contrast in neutron radiographs of bonded joints. Flaws such as voids and inclusions as small as 0.01 in. were readily detected and located nondestructively within adhesive bondlines. The lap shear strength of a joint made with an adhesive modified with a gadolinium oxide neutron-absorber additive could be easily estimated based on visual inspection of the neutron radiograph for void content within the bond lines. The technique described appears readily applicable to durability assessment of adhesively bonded primary structures through correlation of bond-line defect size and location with the critical load distribution stress analysis.

INTRODUCTION

The increasing emphasis on adhesively bonded metallic structures, both as primary and secondary structures in aircraft design, has led to the requirement for advanced NDT techniques specifically tailored to evaluate the integrity of such structures. The substantial differences in material volume and density of structural adhesives and the bonded metallic members, and the complexity of geometries, at rib/spar–skin interfaces, for example, serve to limit the effectiveness of the more conventional NDT techniques in evaluating the integrity of the bondlines in

many practical situations. The difficulty in evaluating adhesively bonded structures is further increased with the use of multilayer laminates.

The use of thermal neutron radiography in the evaluation of bondlines in such structures appears promising as a technique for augmenting and complementing the information acquired through presently employed NDT techniques based on X-ray, ultrasonic, and thermal phenomena. The potential advantage is due to the unique capacity of neutrons to image, by selective absorption, the hydrogenous adhesive material located within dense metal structures. A technique is discussed in which gadolinium oxide powder addition to the adhesive shows promise for extending the resolution and sensitivity of the standard neutron radiography approach to bond-line defect detection.

EXPERIMENTAL

Technical grade (99%) gadolinium oxide powder was blended by hand at room temperature into XA-3455 epoxy adhesive (a product of 3M Company). In order to remove the air which became entrained during blending, the Gd_2O_3–modified adhesive was degassed for 30–60 minutes in a vacuum oven (29″ Hg) at 60°C. Noticeable viscosity increase occurred during this procedure but there was no noticeable change in bonding characteristics or the environmental resistance (Table 1). Air bubbles were admixed with the modified epoxy resin just prior to bonding for preparation of the void-containing bond lines.

Except for the salt-spray exposure tests, all adherends were 0.063-in.-thick unprimed FPL-etched 2024-T3 aluminum alloy. The test specimens were prepared by bonding 4 × 9-in. aluminum sheets together with

Table 1. Lap Shear Strength of Gadolinium Oxide–Modified XA-3455 Bonded Joints

Adhesive Modification	Environmental Exposure	Mean Lap Shear Strength (psi)	Standard Deviation (psi)
None (control)	75°F, 40% RH	6100	320
5% Gd_2O_3	75°F, 40% RH	5720	320
5% Gd_2O_3	75°F, 100% RH, 14 days	6040	280
None*	90-day salt spray	5900	360
5% Gd_2O_3*	90-day salt spray	6030	170

*BR-127 primed surfaces, edge protection, MIL-5-810B.

a 1/2-in. overlap. The bond-line thickness was maintained at 0.005 ± 0.002 in. All the bonded panels were cured in air at 250–260°F for 2 hours and were cooled under pressure. Each panel was radiographed before cutting into 1-in.-wide lap shear test specimens. The laps were identified as to specific location within the panel for visual verification of the void distribution, if any, after lap shear strength tests were performed on the specimen.

Two types of environmental exposure testing were conducted. The data are presented in Table 1. Lap shear specimens made with unprimed adherends were exposed to 100% humidity at 75°F for 14 days. No loss in strength was observed. In fact, there appeared to be a room-temperature post-cure improvement. Salt-spray exposure for 90 days (MIL-5-810B) was also employed to verify that the Gd_2O_3 additive was inert in the epoxy resin. BR-127 primed adherends were used for this test and edge sealing was employed. The data show that the gadolinium-modified adhesive retains the environment resistance of the original epoxy-resin systems. Overall, the mean lap shear strength of the Gd_2O_3–modified adhesive lap shear specimens was within approximately 1σ of the control specimen, where σ is the standard deviation.

Neutron radiography was performed using the Advanced Technology Center, Inc., 3.0 Mev Van de Graaff accelerator. A flux of approximately 10^6 n/cm^2/sec at the sample surface was generated from a beryllium target using the $^9Be(d,n)^{10}B$ reaction. Eastman Kodak SR-54 (single emulsion) film was used with a neutron beam collimation ratio of L/D = 18.

Lap shear strength measurements were made using a MTS 120,000 lb tensile machine. The load rate was approximately 450 lbs/min. X-Y recordings of load-versus-strain were made for all tests.

FLAW RECOGNITION AND STRENGTH PREDICTION

Neutron radiography is capable of distinguishing between materials with different neutron mass absorption coefficients. For a bond line of uniform thickness, variations in the radiograph film contrast indicate variations in absorber uniformity. Such variation could be the result of voids or inclusions. Voids may in fact be fissures or bubbles extending from adherend to adherend or may be localized within a portion of the glue line, such as an unbond at one adherend surface. Inclusions may have absorption coefficients either greater or less than that of the adhesive. Low coefficients will cause the inclusion to appear as a void; inclusions which have high absorption coefficients are readily recognized as such.

Voids were easily detected in bond lines prepared with a uniformly doped adhesive. They appear as light areas in a neutron radiograph positive. Non-bonds are more difficult to define unless good contrast enhancement was achieved. As in the case of X-radiography, detection of hairline cracks is orientation dependent and is subject to the resolving power of the technique. In the radiographs taken in this study, the resolution was slightly better than 0.01 in. One-mil resolution could be achieved by use of a higher beam collimation ratio with the resultant increase in exposure times.

The radiographs of three uncut panels and (0.5 × 9-in. bond lines) and the photographs of the tested lap joint bond line surfaces are shown in Figures 1, 2, and 3. The bond line in Figure 1 was prepared using unmodified adhesive. The bond line is only barely visible and the edge filleting is evident only immediately adjacent to the overlap edge. Figures 2 and 3 are radiographs and corresponding photographs of bond lines prepared from the 5% Gd_2O_3–modified epoxy. Figure 3 is an extreme case of void content. Obviously, this is atypical of bonding overall. However, defects such as this are all too common on a localized basis in laminate structures. The bond line in Figure 3 was prepared by

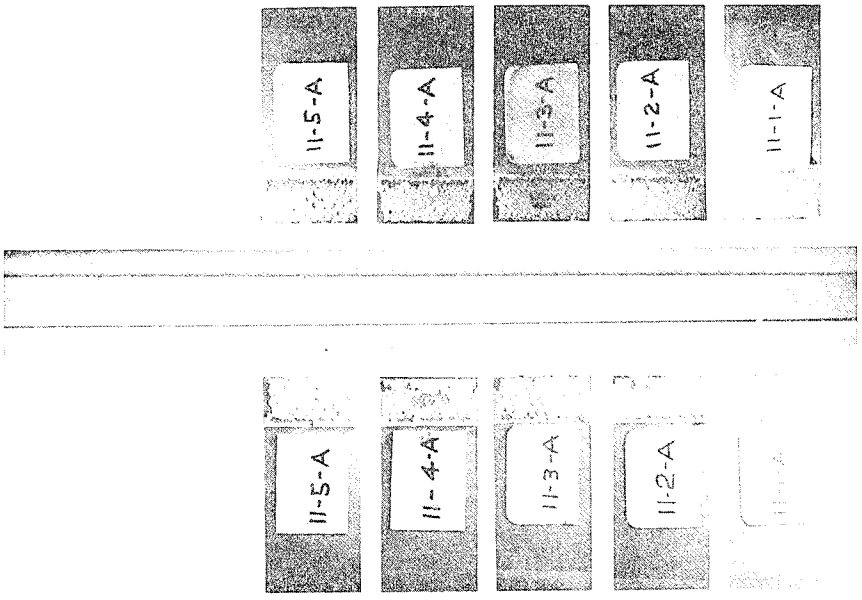


Figure 1. Comparison of neutron radiograph of undoped adhesive joints before failure tests (center strip) with photographs of adhesive surfaces after failure.

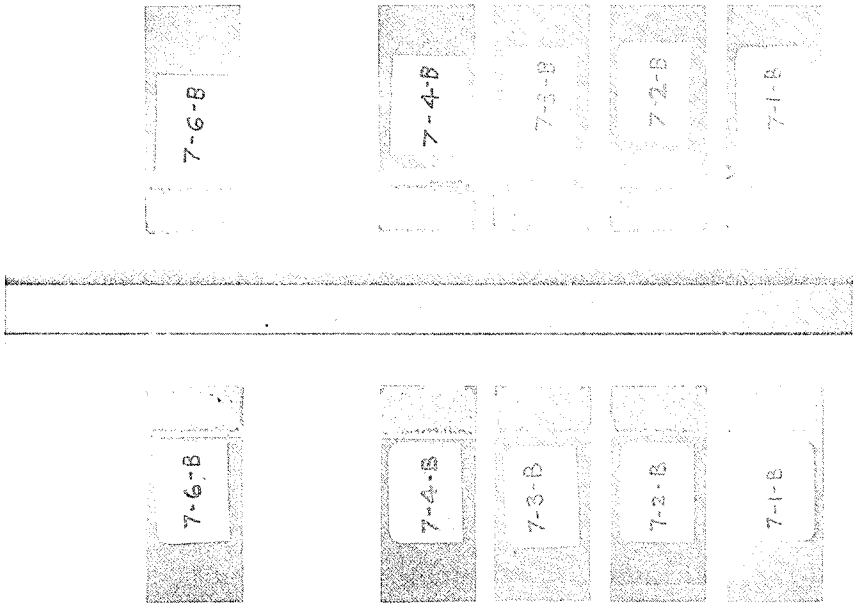


Figure 2. Comparison of neutron radiograph of Gd_2O_3-doped adhesive joints before failure tests (center strip) with photographs of adhesive surfaces after failure.

admixing air with the uncured epoxy resin prior to lay-up in order to simulate a void defect. The dark areas at the overlap edges are due to filleting of the adhesive. The light areas indicate voids. There are no dark spots or other patterns. The photographs of both faces of the bond show patterns of dark spots which appear qualitatively to correspond to the light spots on the radiograph. With the exception of the specimens shown in Table 2, discussed below in detail, the percent void area was usually obtained by a qualitative visual estimate of the percentage light area in the radiograph. As is described below, visual estimation was usually valid within ± 5%.

A meticulous quantitative analysis of specimen 5-1-B (Table 2) was made to demonstrate the effect of void area on failure strength. The portion of the radiograph of the panel shown in Figure 3 corresponding to the bond line of specimen 5-1-B was enlarged photographically to a magnification of 9:1. The enlarged radiograph is shown in Figure 4. The void fraction in this bond line was determined graphically to be 34% (0.261 $in.^2$ bond area). Minimum void size included in this analysis was approximately 0.015 in. If the value of 34% is used to predict the failure

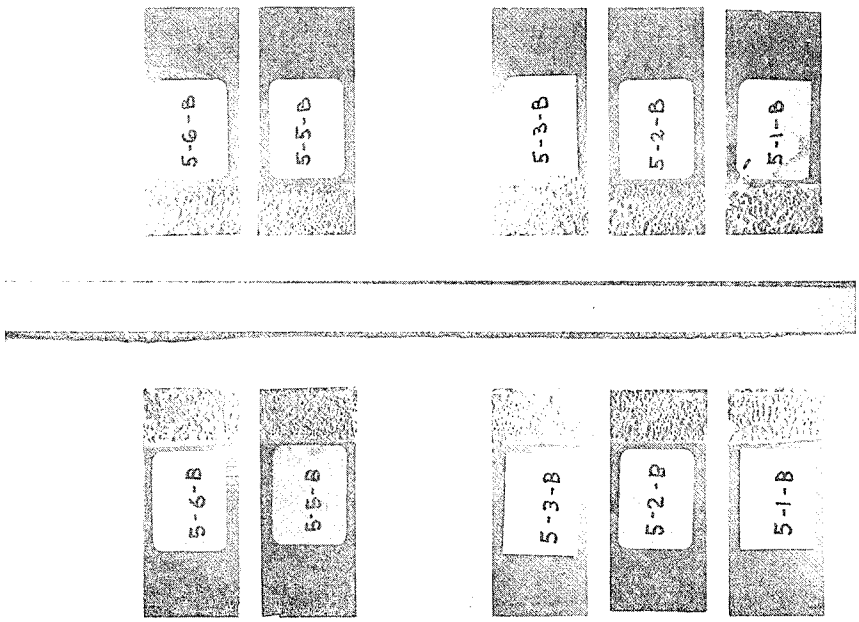


Figure 3. Comparison of neutron radiograph of Gd_2O_3-doped adhesive joints before failure tests (center strip) with photographs of adhesive surfaces after failure.

Table 2. Predicted vs. Actual Shear Failure Loads of Flawed Bond Lines*

Specimen Identification	Estimated Bonded Area (in.^{2})	Predicted Failure Load (lbs)	Actual Failure Load (lbs)	Error (lbs)	Error (%)
5-1-B	0.261	1490	1500	10	0.7
5-2-B	0.267	1530	1590	100	4
5-3-B	0.270	1540	1590	50	3
5-5-B	0.326	1860	2070	210	10
5-6-B	0.235	1340	1350	10	0.7
14-3-B	0.446	2550	2640	90	3
14-4-B	0.451	2580	2650	70	3

*Nominal 0.5 in.^{2} overlap.

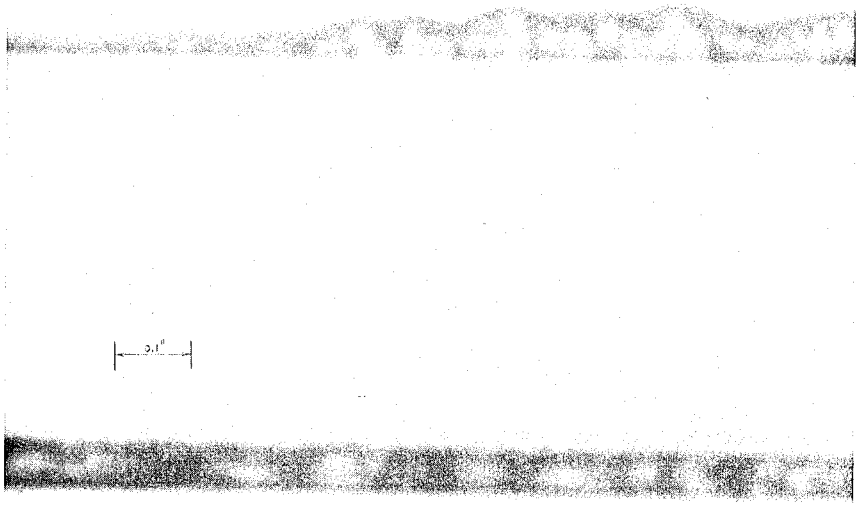


Figure 4. Enlargement (9X) of neutron radiograph of bond line in Gd_2O_3-doped specimen 5-1-B, showing extreme case of high void content.

load for this specimen, based on the mean shear strength of the doped specimens which had little or no voids, a value of 1492 lbs is obtained, which is very close to the observed value. Table 2 lists the predicted and actual failure loads for 7 flawed specimens. Errors in predictions are given in pounds and percent of actual failure load. The reference shear strengths were taken as the mean shear strengths of specimens having estimated void areas of 1% or less (Table 1). These values are 5720 psi for the gadolinium-oxide-modified epoxy and 6100 psi for the unmodified adhesive system.

Figure 5 graphically illustrates the technique for prediction of lap shear failure loads by neutron radiography using two specimens, one with no voids and one with approximately 50% bond-line void area. The figure shows the correlation between the void area, as imaged in the neutron radiographs before test, and the respective ultimate shear loads. Based on the 2860-lb ultimate shear failure load observed for the control, one would predict that at 50% bond-line void content the flawed specimen should fail at about 1430 lbs. The observed failure load was 1350

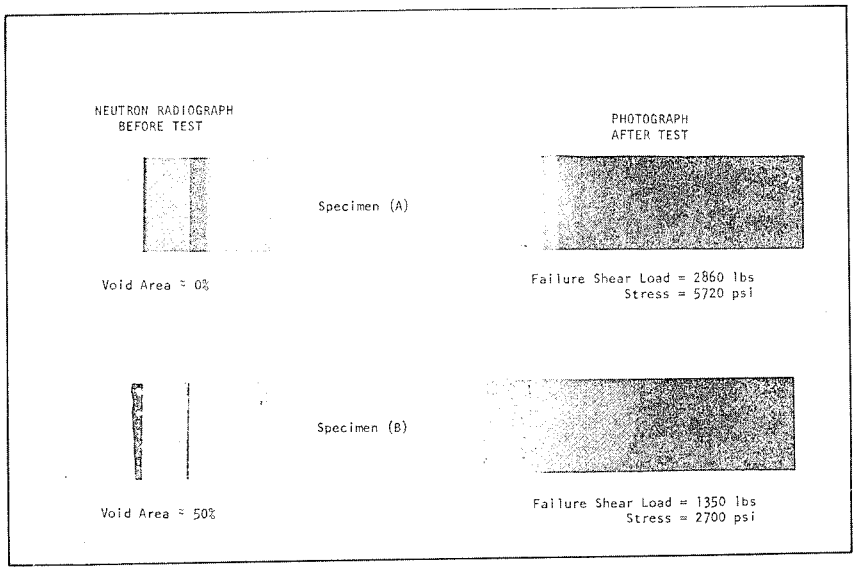


Figure 5. Adhesive joint failure predicted by neutron radiography. Gd_2O_3-doped adhesive was used in these specimens.

pounds, which is within 5% of the prediction and is certainly well within the typical scatter of lap joint shear strength test measurements. On more critical inspection, using graphical techniques, this specimen 5-6-B of Table 2 was found to have 0.235 in.^{2} bonded area which calls for a prediction of 1343 lbs ultimate shear load. Obviously, visual inspection is convenient, simple, and adequate, but when more accurate bond-line strength prediction is desired, graphical techniques are preferable.

A number of research efforts are now in progress investigating the effects of bond-line defects such as voids on adhesively bonded joint durability under simple as well as complex loading. These will soon result in a clear definition of defect size limit as functions of joint configuration, adhesive toughness, and loading condition for safe life prediction. Obviously, this will also establish the NDI/NDT criteria for quality assurance.

Ultrasonic and X-ray procedures could be used to investigate void content and predict bond strength in a manner similar to that described here for neutron radiography. However, only neutron radiography tends to be independent of metallic adherend thickness and number of bond-line layers. Specific shielding procedures for neutron radiography are well established and portable neutron sources based on californium-252 are being developed. It is obvious that NDI/NDT techniques such as

have been described here offer a great promise for the inspection of bonded structures both in the laboratory and in the field.

SUMMARY

The contrast in neutron radiographs of adhesive bond lines is greatly enhanced by incorporating into the resin system a special neutron-absorbing additive such as gadolinium oxide. Flaws such as voids and inclusions are accurately imaged and located nondestructively within the adhesive bond overlap joint. Voids as small as 0.01 inch were easily detected with exposure times of 30–40 minutes. The gadolinium oxide additive appeared essentially inert in the XA-3455 adhesive system investigated, and no change in humidity or salt spray exposure resistance was observed. The strength of lap joints made with the gadolinium oxide–modified adhesive could be easily and accurately estimated based on the bonded area as interpreted from the neutron radiographs. This technique can be applied to a wide variety of adhesives and joint configurations. The neutron radiographic procedures described in this study are readily applicable to adhesively bonded structure durability assessment when combined with critical defect size criteria and structural load-distribution analysis.

ACKNOWLEDGMENT

Although the results discussed here were obtained using the Advanced Technology Center, Inc., 3.0-Mev Van de Graaff accelerator for neutron production, the authors wish to acknowledge the support provided earlier by the U.S. Atomic Energy Commission (U.S. Energy Research and Development Administration) through the loan of a 2.0-milligram ^{252}Cf neutron source, with which a portion of the early feasibility experiments was conducted. Loan of this source was through the USAEC Californium-252 Evaluation Program under Contract AT(38-1)-684.

SESSION VIII

PANEL DISCUSSION, IMPACT OF JOINING METHODS ON MATERIALS SELECTION AND DESIGN

MODERATOR: B. R. NOTON
Battelle Columbus Laboratories

25. ALUMINUM-BRAZED TITANIUM DESIGN

R. H. HAMMER
Boeing Commercial Airplane Company
Seattle, Washington

The recent development of the aluminum-brazed titanium system, when combined with innovative design techniques, offers the design engineer a new cost- and weight-effective choice in the design of elevated temperature structure.

INTRODUCTION

Brazing, as an aircraft structures production joining system, has traditonally been limited to high-temperature, high-cost, engine-related components such as thrust reverser doors and tailpipes.

Two notable exceptions to this statement are the North American B-70, which extensively utilized silver-brazed steel sandwich wing skins, but developed into a very expensive research, instead of production, aircraft; and the Boeing SST, which of course never developed at all but did provide the impetus for the development of aluminum-brazed titanium. This material-joining system has now been developed into a cost-effective, production-qualified, nonproprietary material-joining system.

DEVELOPMENT

During the early design states of the SST, titanium was selected as the primary structural material. Early design studies showed that, due to the large delta wing configuration of the aircraft, the wing skin end loading was considerably lower than a conventional wing skin end loading. Because of this lower end loading, a sandwich panel was the optimum design configuration. At this point it became mandatory that an efficient, cost-effective titanium sandwich joining system be developed. At that time, the two leading candidate systems for titanium sandwich panels were diffusion bonding and resistance welding. The resistance-welding method presented formidable problems in edge-member configurations

and in tailoring the panels to accept concentrated loads. The diffusion-bonded method, while it could be tailored for varied loading conditions, was excessively costly. Because of these shortcomings, a program was initiated to develop a brazed titanium system. At first aluminum was not seriously considered as the braze alloy because of suspected galvanic corrosion problems when the aluminum was coupled with titanium.

Thorough laboratory and service testing proved there was no galvanic corrosion problem. Specimens of bare aluminum-brazed titanium panel sections exposed to a standard 5% salt spray for 250+ days showed only limited corrosion damage. For comparison, military specification requirements for salt spray testing of protective coated structural aluminum alloys require only 7–20 days exposure. The results of these tests exceeded all expectations.

The belief that the system strength properties would degrade with increasing temperature at the same rate as that of the aluminum-braze alloy was also disproved. The testing results showed, as illustrated in Figure 1, that the actual temperature degradation was between that of aluminum and titanium.

After the cancellation of the SST, The Boeing Company, under a Department of Transportation SST follow-on contract, did extensive work to develop and document mechanical and physical properties, design allowables, nondestructive testing techniques, and producibility techniques of the aluminum-brazed titanium process. These documents are listed in the Reference Section.

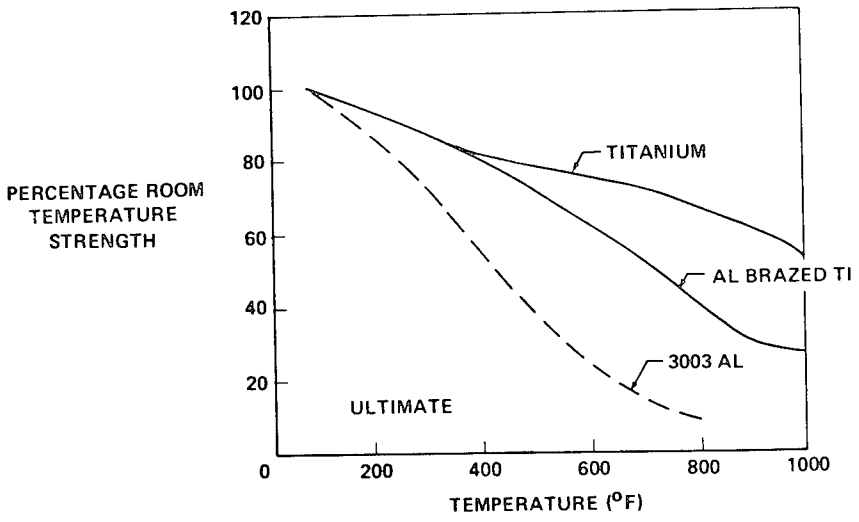


Figure 1. Temperature degradation.

DESIGN

The results obtained from this extensive testing and further development work eliminated the need for many precautionary requirements placed on the designer, such as hermetically sealing all panels or restricting contour to no more than 20° from horizontal. These test and development results, together with advances made in developing design techniques unique to the aluminum-brazed titanium system, have substantially improved the producibility and cost effectiveness of this material system. An actual example of application of these unique design techniques, which resulted in reduction of the unit cost of the assembly by more than 50%, is a wedge assembly shown in Figure 2.

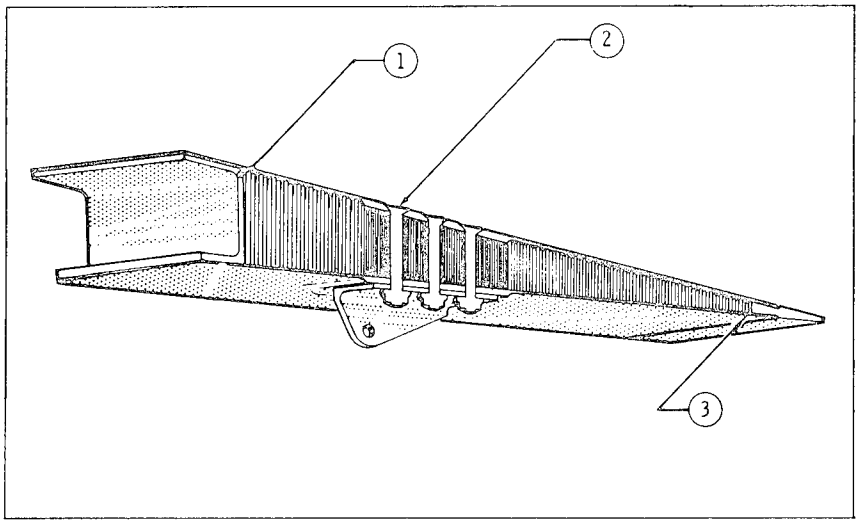


Figure 2. Conventional honeycomb wedge design.

The proposed design was very conventional and was based on current adhesive bonded design techniques. The major cost drivers in the assembly are:

1. The titanium hogout front spar must be machined to exceedingly close tolerances in height to ensure a minimum mismatch between the core and spar. Even with the close-tolerance machining, it is often necessary to hand hone the core to ensure proper mismatch control.

The spar also dictates faying surface braze joints which require a prebraze spotwelding operation to ensure proper gap control.

The lay-up of the core to the spar web requires hand spot tacking of each individual core wall to the spar web. This operation is costly and time consuming and becomes increasingly more difficult as the spar height increases.

2. The requirement for through-bolts and a smooth aerodynamic outer surface resulted in an internal pad in the outer skin to accommodate the countersunk bolt head. This inner pad dictated a machine sculpturing of the core which is extremely expensive and a constant source of braze quality problems.

3. The machine trailing edge member and side closure members present the same problems as the front spar described above.

The redesign of this wedge assembly, as shown in Figure 3, has taken advantage of the unique properties of the aluminum-brazed titanium system and looks quite unconventional. The major design changes are:

1. No front spar. The separate front spar of the original design has been replaced with a band of small cell, high density core which provides adequate shear and peel strength.

2. No through-bolts. The extremely high face tension and peel allowables of aluminum-brazed titanium combined with blind fasteners through the inner skin eliminated the requirement for the internal skin pad and resultant core machine sculpturing.

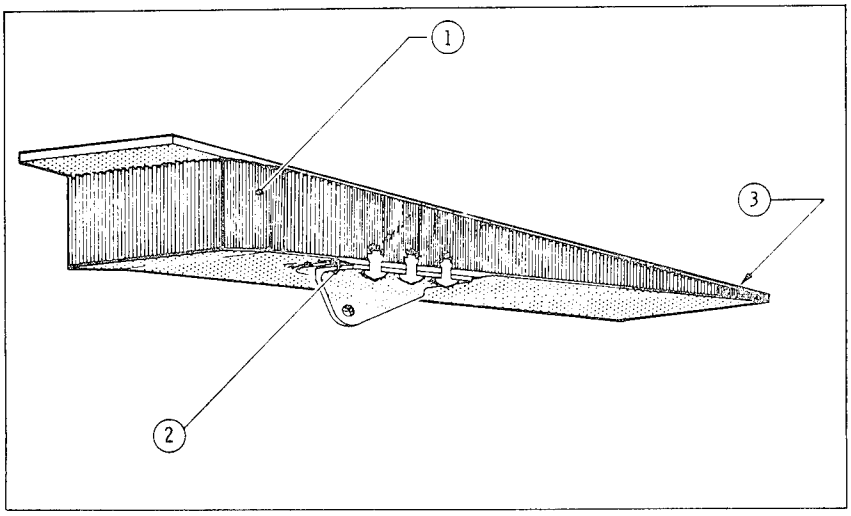


Figure 3. Wedge design for aluminum-brazed titanium honeycomb system.

This particular design concept has been tested both statically and in fatigue quite successfully.

3. No trailing edge or side closure members. As described for the front spar, the addition of the band of small cell core around perimeter eliminated the requirement for a trailing edge or side closure members.

The cost and producibility aspects of the changes made in this redesign are quite obvious, namely:

1. Elimination of all machined edge members.
2. Simplification of core blanket machining by eliminating sculpturing and core close tolerance requirements.
3. Elimination of all faying surface brazes and their prebraze operations.

Another example of redesigning to take full advantage of aluminum-brazed titanium's properties is the edge details for the SST skin panels as shown in Figure 4.

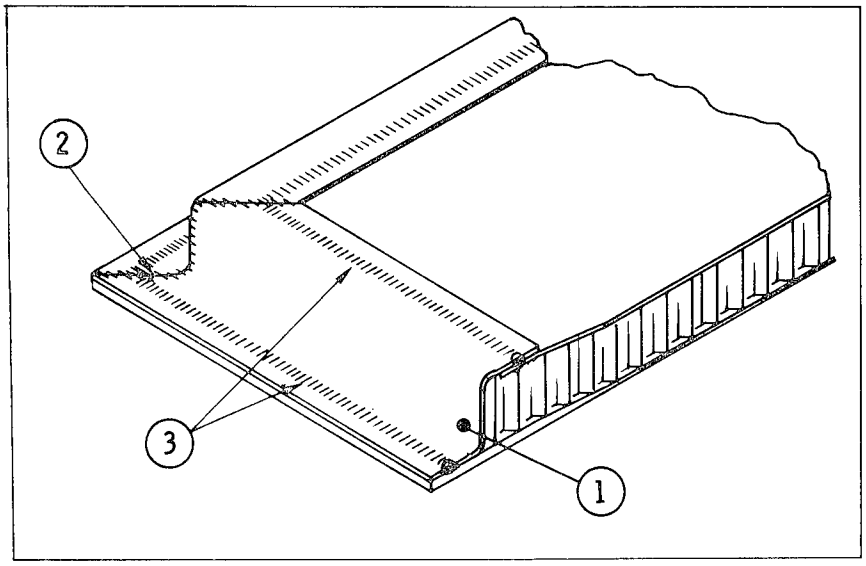


Figure 4. SST skin panel edge design.

The design features of this configuration which are major cost drivers are:

1. Hot sized sheetmetal or machined titanium edge zee closure members.

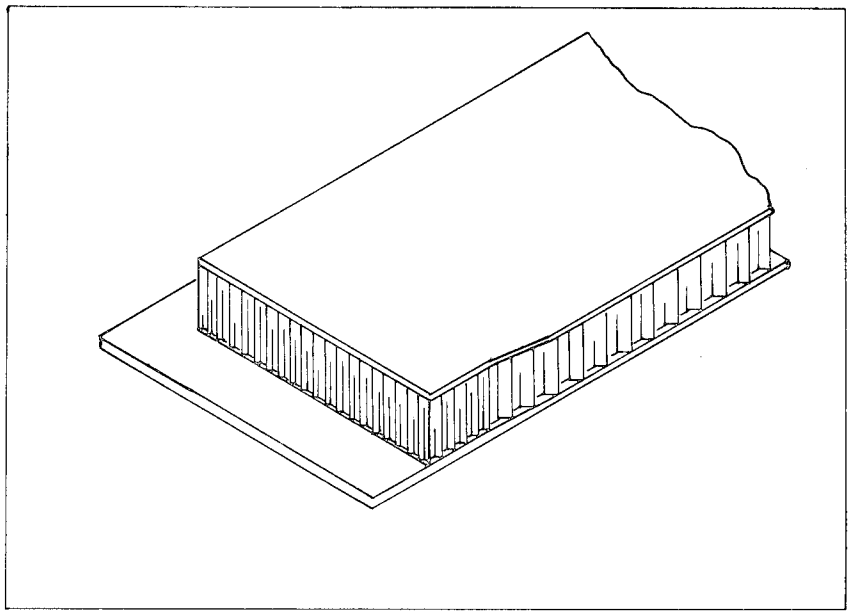


Figure 5. Open edge core design concept.

2. Fusion-welded corners.
3. Prebrazed seam welds to seal the panels hermetically.

If these panels were to be designed today, they would probably look like the design in Figure 5.

The reduced cost and improved producibility aspects of this redesign are again quite obvious.

These concepts are not developmental and unproven. Figure 6 illustrates four examples which use the aluminum-brazed titanium open edge core concept.

Although aluminum-brazed titanium is normally used in elevated temperatures to be economically competitive, there are examples where the system has been proved superior on a cost/weight relationship to aluminum conventional structure. An example of this is the rotary missile launcher (Figure 7) designed and fabricated by Aeronca for the Rockwell B-1 bomber. The maximum temperature for the launcher is 265°F, well within the structural limits of aluminum. The development of being able to braze 360° conical sections and the structural weldability of titanium produced a part which was superior in weight/cost relationship to aluminum construction.

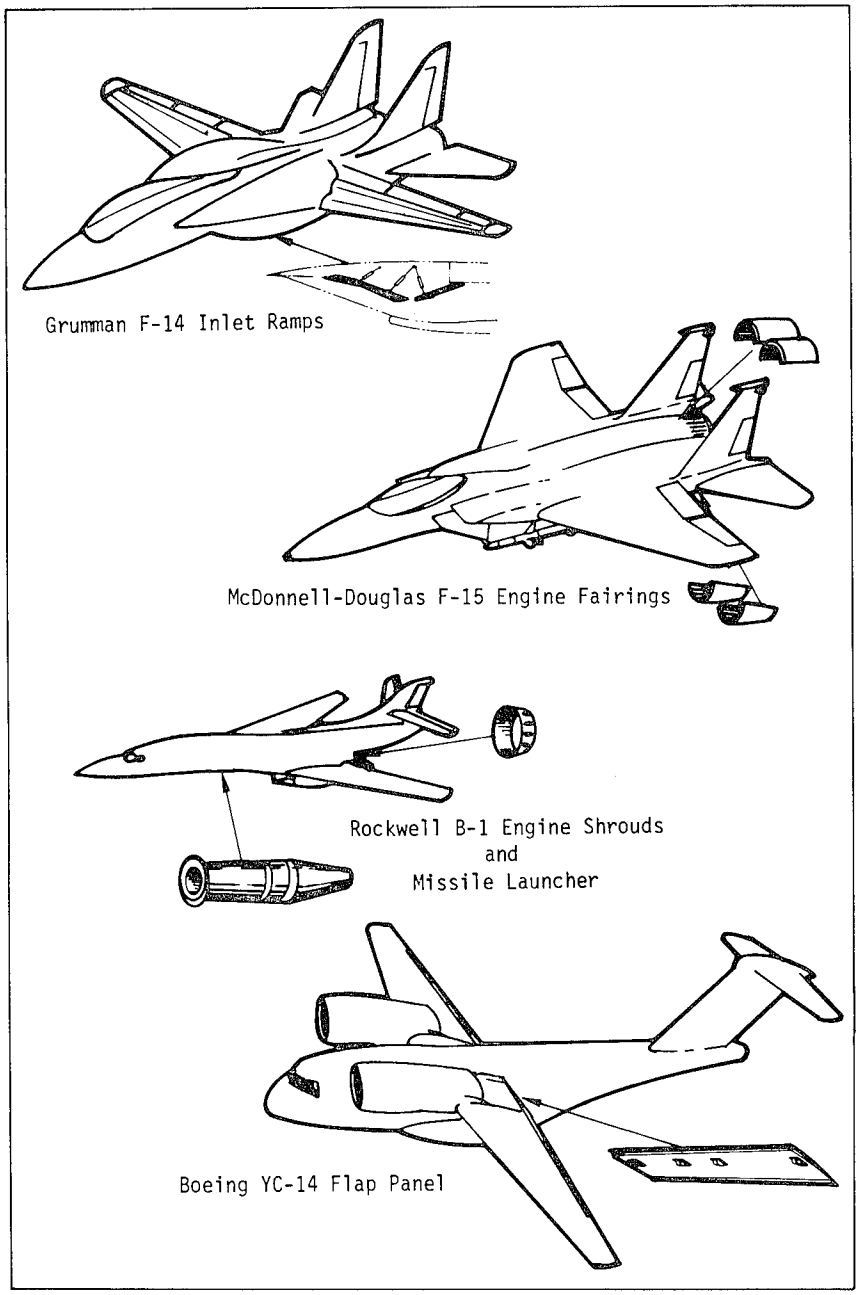


Figure 6. Applications of aluminum-brazed titanium open edge core design.

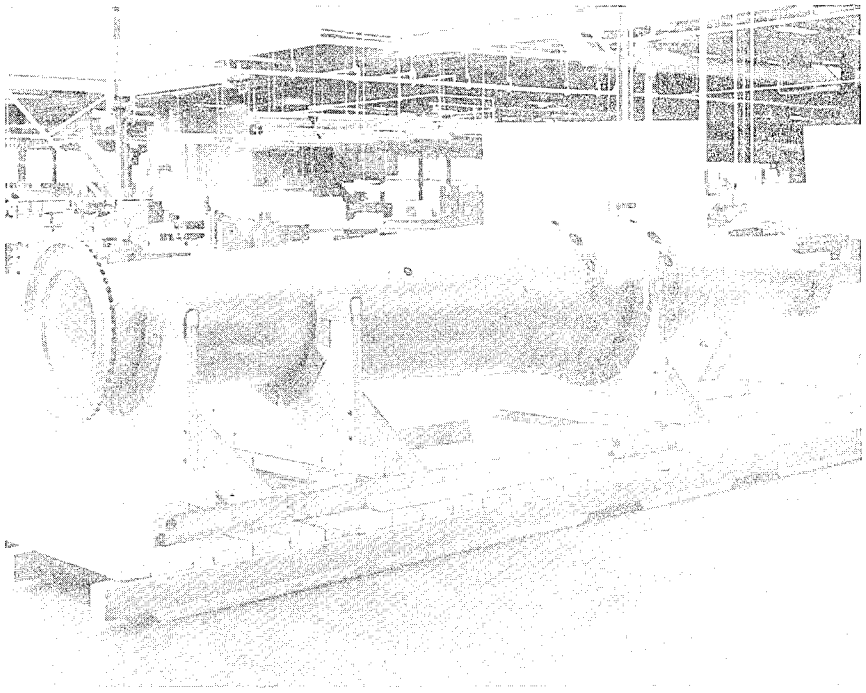


Figure 7. Rotary missile launcher.

CONCLUSION

These are just a few examples of applications of this relatively new material system. Generally, if the designer will use ingenuity in his design and will seriously and persistently question the requirements or need for high-cost detail items, aluminum-brazed titanium sandwich structure will be superior in a cost/weight relationship to any other material system or design configuration in the 400°F to 800°F temperature environment.

REFERENCES

1. Elrod, S. D. and Lovell, D. T., "SST Technology Follow-On Program, Phase I. Development of Aluminum-Brazed Titanium Honeycomb Sandwich Structures," Boeing Company, Commercial Airplane Group, Seattle, Wash. Department of Transportation Contract Report No. FAA-SS-72-03, July 1972. (AD 902 453L)
2. Bay, B. F. and Eichenberger, T. W., "SST Technology Follow-On Program, Phase I. Aluminum-Brazed Titanium Sandwich Allowables," Boeing Com-

pany, Commercial Airplane Group, Seattle, Wash. Department of Transportation Contract Report No. FAA-SS-72-10, July 1972. (AD 902 461L)

3. Elrod, S. D. and Moji, Y., "SST Technology Follow-On Program, Phase I. Creep and Corrosion Testing, Aluminum-Brazed Titanium Honeycomb Sandwich," Boeing Company, Commerical Airplane Group, Seattle, Wash. Department of Transportation Contract Report No. FAA-SS-72-14, July 1972. (AD 902 465L)
4. Elrod, S. D. and Lovell, D. T., "SST Technology Follow-On Program, Phase II. Development and Evaluation of the Aluminum-Brazed Titanium System. Volume 1. Program Summary," Boeing Commercial Airplane Company, Seattle, Wash. Department of Transportation Contract Report No. FAA-SS-73-5-1, May 1974. (AD 920 794L)
5. Boyer, R. R., Elrod, S. D., and Lovell, D. T., "SST Technology Follow-On Program, Phase II. Development and Evaluation of the Aluminum-Brazed Titanium System. Volume II. Process R and D," Boeing Commerical Airplane Company, Seattle, Wash. Department of Transportation Contract Report No. FAA-SS-73-5-2, May 1974. (AD 920 795L)
6. Taylor, R. Q., Elrod, S. D., and Lovell, D. T., "SST Technology Follow-On Program, Phase II. Development and Evaluation of the Aluminum-Brazed Titanium System. Volume III. Scale-Up Technology," Boeing Commercial Airplane Company, Seattle, Wash. Department of Transportation Contract Report No. FAA-SS-73-5-3, May 1974. (AD 920 796L)
7. Lindh, D. V., Elrod, S. D., and Lovell, D. T., "SST Technology Follow-On Program, Phase II. Development and Evaluation of the Aluminum-Brazed Titanium System. Volume IV. Material Properties," Boeing Commercial Airplane Company, Seattle, Wash. Department of Transportation Contract Report No. FAA-SS-73-5-4, May 1974. (AD 920 797L)
8. Cheng, A. S. and Fogleman, J. W., "SST Technology Follow-On Program, Phase II. Development and Evaluation of the Aluminum-Brazed Titanium System. Volume V. Structural Verification," Boeing Commercial Airplane Company, Seattle, Wash. Department of Transportation Contract Report No. FAA-SS-73-5-5, May 1974, (AD 920 798L)
9. Cotton, W. L., Moji, Y., Elrod, S. D., and Lovell, D. T., "SST Technology Follow-On Program, Phase II. Development and Evaluation of the Aluminum-Brazed Titanium System. Volume VI. Corrosion Resistance," Boeing Commercial Airplane Company, Seattle, Wash. Department of Transportation Contract Report No. FAA-SS-73-5-6, My 1974. (AD 920 799L)
10. Barton, R., Taylor, R. Q., Elrod, S. D., and Lovell, D. T., "SST Technology Follow-On Program, Phase II. Development and Evaluation of the Aluminum-Brazed Titanium System. Volume VII. Producibility and Costs," Boeing Commercial Airplane Company, Seattle, Wash. Department of Transportation Contract Report No. FAA-SS-73-5-7, May 1974. (AD 920 800L)
11. Elrod, S. D. and Lovell, D. T., "SST Technology Follow-On Program, Phase II. Development and Evaluation of the Aluminum-Brazed Titanium

System. Volume VIII. Process Specification," Boeing Commerical Airplane Company, Seattle, Wash. Department of Transportation Contract Report No. FAA-SS-73-5-8, May 1974. (AD 920 801L)

12. Lindh, D. V. and Lovell, D. T., "Titanium Structures Technical Summary, DOT/SST Phase I and Phase II," Boeing Commercial Airplane Company, Seattle, Wash. Department of Transportation Contract Report No. FAA-SS-73-27, October 1974. (AD-B000 291L)

26. AEROSPACE ADHESIVE BONDING

B. L. REYNOLDS
Boeing Commercial Airplane Company
Seattle, Washington

Adhesives which have been used in the aircraft industry for over twenty years have had a profound influence on the design and performance of today's aircraft. Because of continually improving adhesive materials and processes, today's aircraft are better in performance, safety, durability, aesthetics, and environmental impact. However, years of field service have revealed some problems which have demanded improvements if adhesives are to continue influencing the design of aircraft as they have in the past. This chapter discusses the impact that adhesive bonding has had on aircraft design and makes some attempt to forecast future trends.

INTRODUCTION

Throughout the history of aircraft, there have only been a few breakthroughs of major significance. Generally, these have had a very dramatic impact on the aircraft industry. The introduction of aluminum monocoque structure, swept wings, pressurized fuselages, de-ice boots, and jet engines are prime examples of significant changes (see Figure 1). Less spectacular has been the application of adhesive-bonding technology because its development has been so gradual that few have realized the total impact.

During the decade of the sixties, the utilization of bonding increased to 65% of the total wetted area of the most recent Boeing aircraft (see Figure 2). Today bonding and plastics technology has been applied in structures, interiors, electronic devices, and sound-attenuating materials. Consequently, aircraft are lighter, last longer, and are more attractive, safer, and quieter.

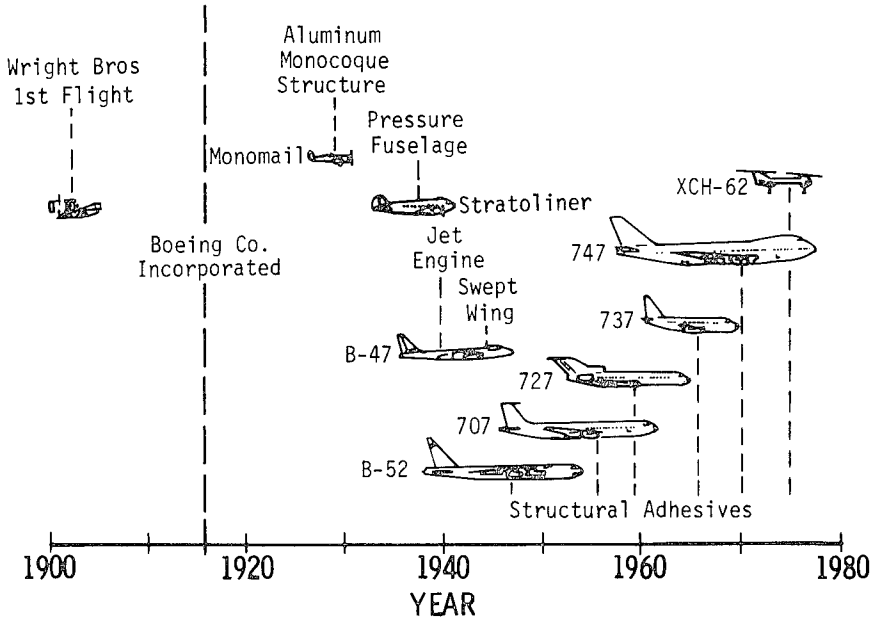


Figure 1. Major technology breakthrough applied to Boeing aircraft.

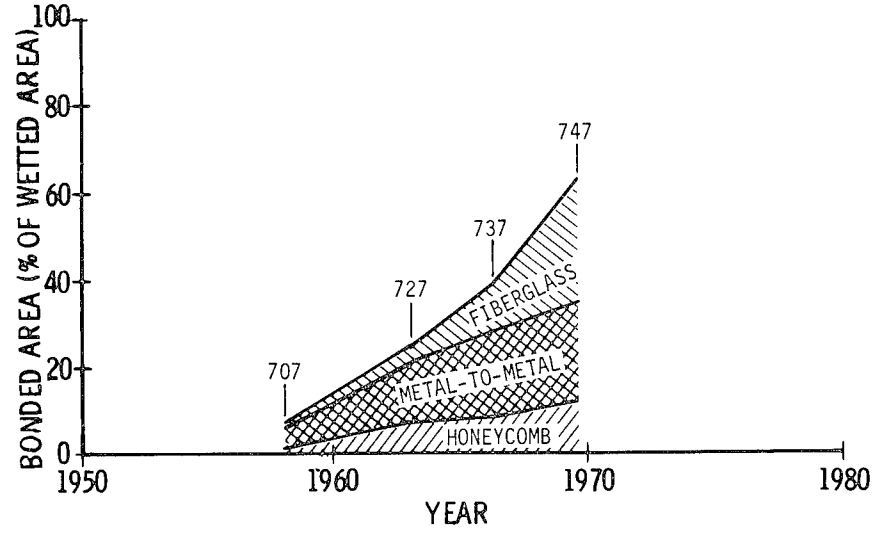
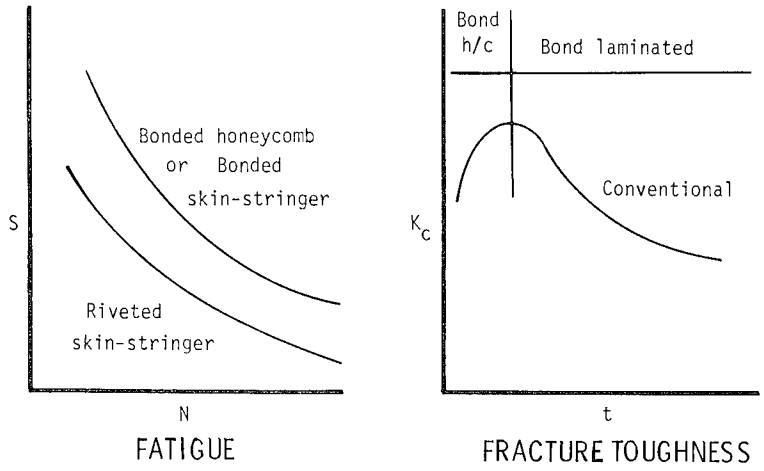


Figure 2. Usage of bonded structure, Boeing Commercial Airplane Company.

WEIGHT SAVINGS

Bonded metallic structures have contributed to weight reductions because of higher allowables, improved fatigue resistance, better fracture toughness, and reduced crack growth (Figures 3 and 4). Bonded



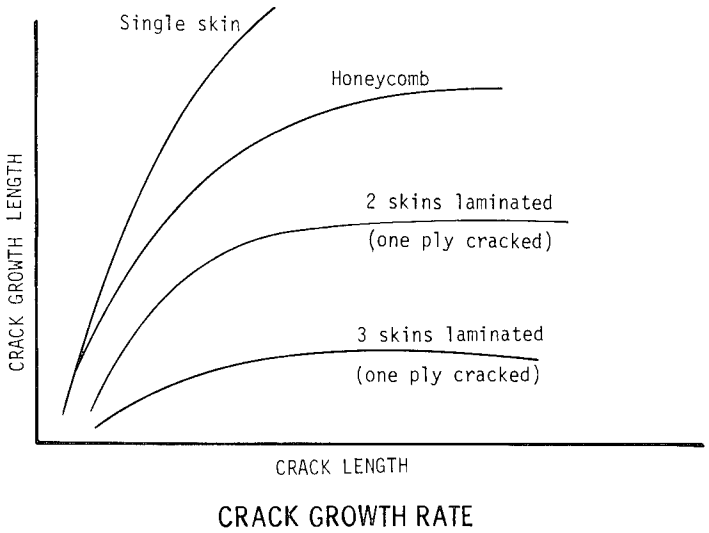


Figure 3. Characteristics of bonded structure.

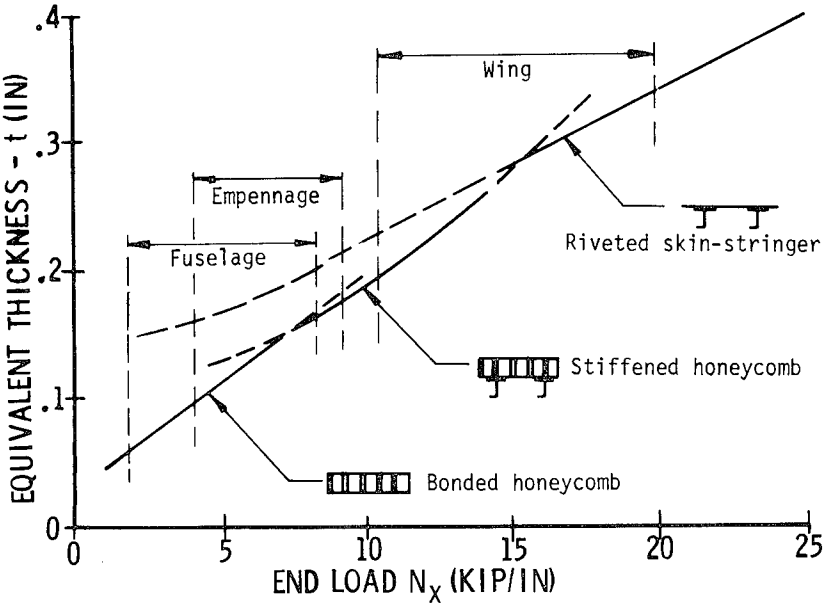


Figure 4. Weight saving, bonded structure.

tear stoppers have effectively reduced weight in fail-safe design (Figure 5). The weight of secondary structures has been pared down considerably because of the use of bonded honeycomb sandwich construction. Designers, however, have avoided extensive use of bonding for primary structures because of past experiences with corrosion. Recent advances in phosphoric acid anodize, corrosion-inhibiting primers, new adhesives, and corrosion-resistant honeycomb will lead to more primary structure applications in the future and, therefore, considerably greater weight reductions.

SAFETY

Over thirty years ago aircraft began flying with radar equipment. Without plastics it would have been impossible to cover the equipment with the necessary "transparent" radome. Similarly, plastics have entered the general field of electronics for aircraft communication and navigational systems providing more advanced equipment for safety of flight. Windshields are more impervious to birdstrike and hailstone impact because of bonded laminates with plastic layers.

Cracks in structures tend to be suppressed at bond lines, thus making a bonded structure a good fail-safe technique (Figure 5). Bonded laminates also tend to exhibit better damping characteristics than all-metal structures in mechanical or sonic vibration and, therefore, longer life can be expected. A deterent, from the safety standpoint, has been the flammability and toxicity of adhesives and plastics. Considerable research has resulted in reducing these factions.

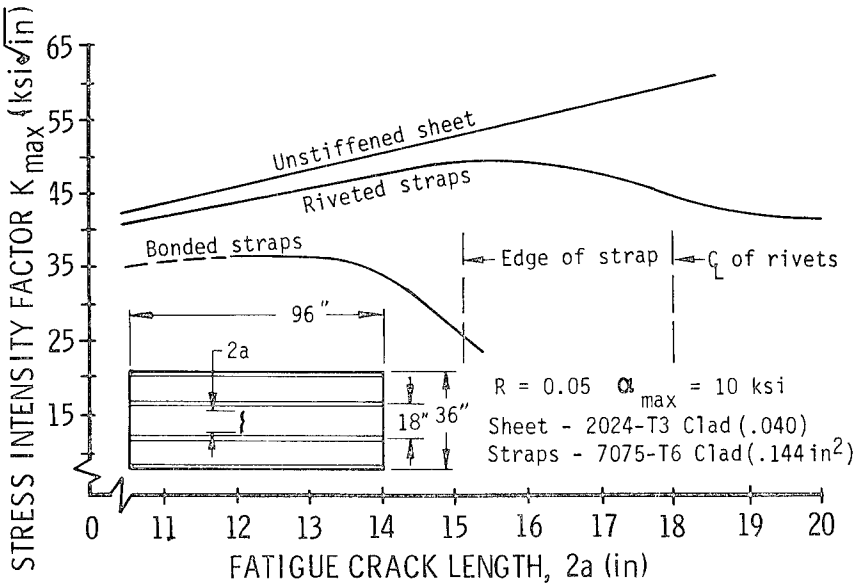


Figure 5. Effectivity of bonded vs. mechanically fastened straps.

APPEARANCE

Aircraft interiors have come a long way since the wicker seats and the cloth head lining. Plastics have added a new dimension in beauty and durability of aircraft interiors.

ENVIRONMENTAL IMPACT

Aircraft noise pollution was an irritant to the general public less than a decade back. Adhesive bonding has had an important role in suppressing noise around the inlets of jet engines. Sound-attenuating panels

are being made of porous sheets bonded to suppression cavities. Without adhesive bonding, noise suppression would have been an even greater challenge.

COST

Adhesive bonding reduces the number of mechanical fasteners and number of detail parts in aircraft structures. Both factors are important in lowering the cost of fabrication. Laminating the structure reduces machining and the waste of raw materials, which further contributes to cost savings.

AERODYNAMICS

Aerodynamic smoothness has been improved by adhesive-bonded structures. Because of the reductions of fasteners and method of tooling to outer contours, it has become easier to obtain a smooth aerodynamic shape.

Flutter-critical areas are frequently helped by the bonding process. Because of adhesive bonding, the designer can use honeycomb structures to reduce skin gages and lower the mass while the stiffness is increased. This design approach increases the critical flutter speed.

DISBOND AND CORROSION

The most disturbing detriment to bonded structure has been disbonding and corrosion. Considerable research has been directed to develop an understanding of the disbond and corrosion mechanisms and to find methods of combating them.

Boeing has examined examples of in-service failures and has determined that a majority of bond failures were interfacial due to ingress of moisture between the adhesive and the oxide surface on the aluminum. This interfacial failure mode is characterized by initiation at an edge and progressive failure under very low stresses. The corrosion failure mechanism was found to work in the following manner.

Moisture diffuses into and through the adhesive in all bonded structure. This moisture then reacts with the surface oxide film to form a hydrated oxide that exhibits poor strength characteristics (Figure 6). Under stress this oxide fails, with the failure initiating at an edge (location of maximum peel or shear stress). A crevice is formed as a result of

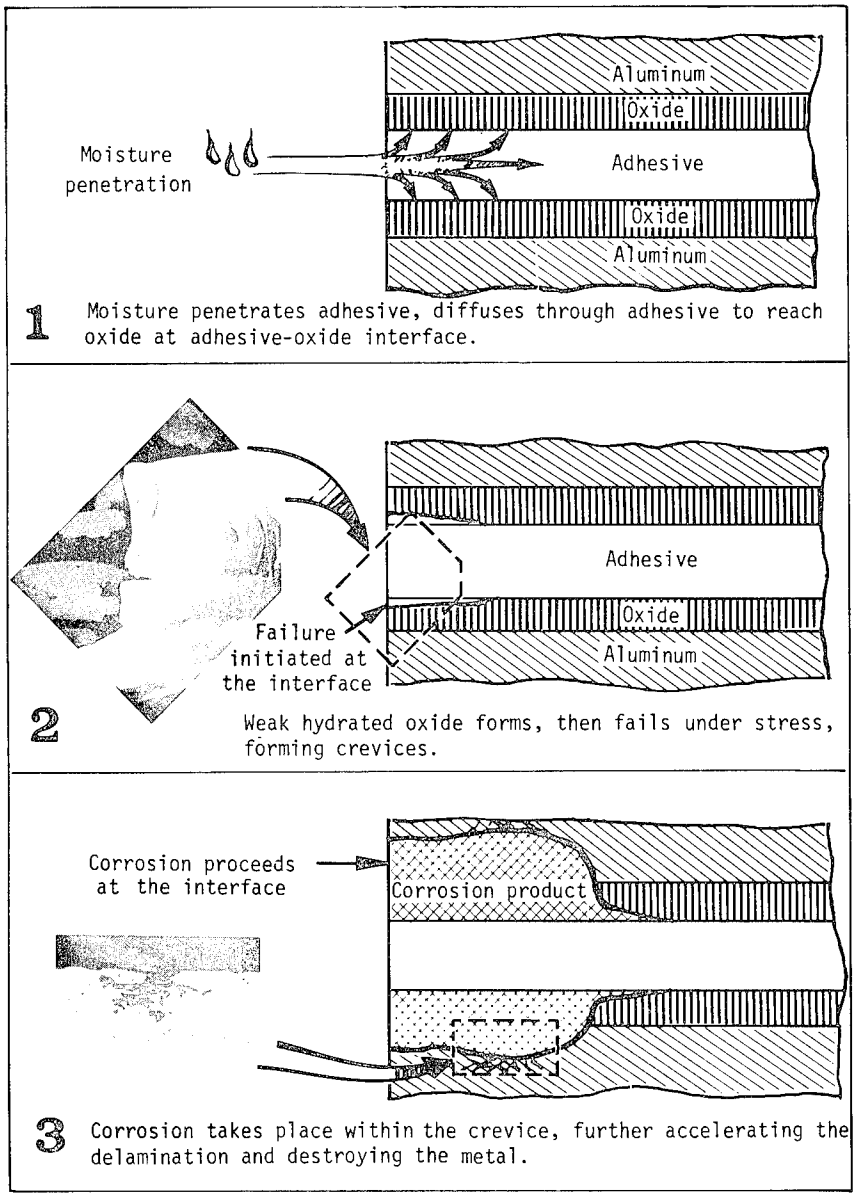


Figure 6. Mechanism of bond delamination and corrosion.

this failure, serving as a site of corrosion and subsequent acceleration of the delamination process. The delaminated structure, with the protective oxide film missing, is exposed to the environment and considerable corrosion results.

The key to the problem has proved to be the preparation of an adherent surface that is immune to hydration. Boeing has developed an anhydrous surface preparation which combats the interfacial corrosion shown in Figure 6. Advancements in corrosion-inhibiting primers and adhesion materials have also contributed to startling improvements in corrosion resistance. It has also been determined that clad surfaces in the bond line are detrimental to corrosion and therefore should be avoided.

Because of the vast improvements in corrosion resistance, adhesive bonding is currently advancing toward greater utilization in aircraft structures.

FUTURE TRENDS

The next major step for adhesive bonding will be the application to primary structures.

Boeing Vertol is building the prototype XCH-62 Heavy Lift Helicopter, which is the first U.S. helicopter to use bonded honeycomb material for all primary structures.

Currently the USAF Flight Dynamics Lab is developing an all-bonded aircraft fuselage using the YC-15 Advance Medium STOL Transport (AMST) as a base line. Douglas Aircraft is performing the work under the PABST (Primary Adhesive Bonded Structure) program. Ground test hardware will be fabricated and tested during the period of 1977–1979.

Boeing has developed a bonded honeycomb primary structure box in the horizontal and vertical stabilizers of the YC-14 AMST (see Figure 7). This bonded primary structure will be flying in 1976.

Boeing's preliminary designers are looking at an all-bonded, very large freighter capable of carrying payloads of a million pounds or more (Figure 8). These aircraft would be fabricated of honeycomb bonded panels to get the empty weight down and to reduce part count (cost).

Fully automated, continuous bonding facilities are being considered for these large aircraft. Honeycomb panels would be fabricated from coil stock and trimmed to size. While this may be considered a bit far-reaching, it must be recognized that an aircraft of this size and performance is only possible by the extensive use of adhesive-bonded structures. Any other structure would weigh so much that it would become prohibitive.

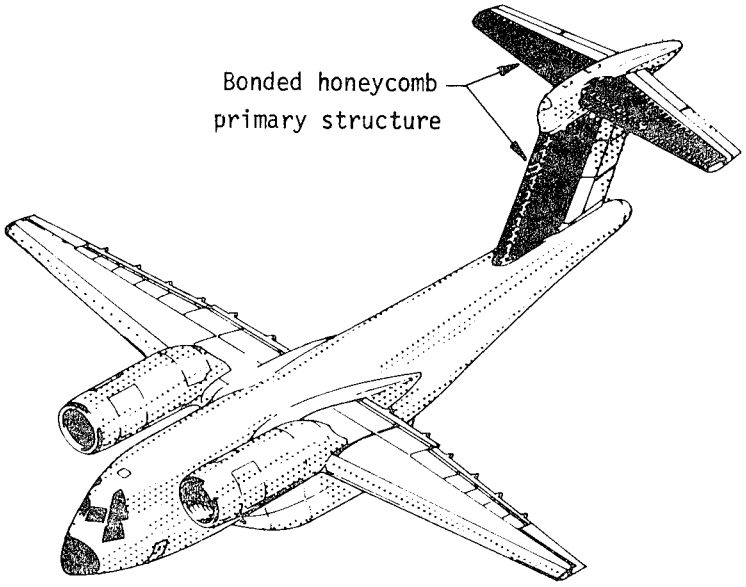


Figure 7. Boeing YC-14 AMST.

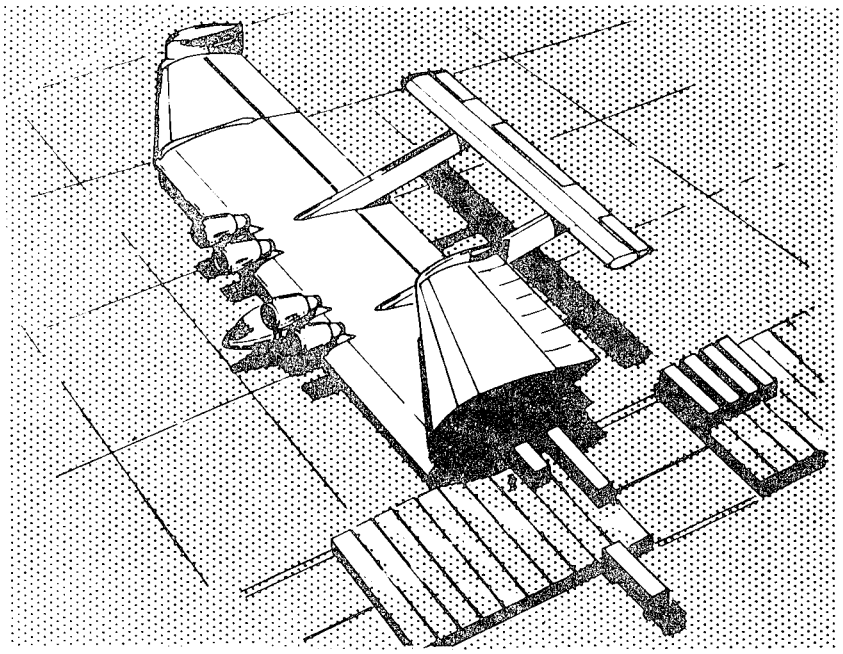


Figure 8. Large freighter.

CONCLUSIONS

Adhesive bonding and plastics have made a considerable impact on the aircraft industry. Problems which have been considered major deterents are gradually disappearing into the past and the next major step, *i.e.*, primary structure, is underway. Once adhesive bonding is accepted for primary structures, we will likely see the emergence of a new generation of very large lightweight cargo aircraft.

27. AEROSPACE WELD BONDING–RIVET BONDING

J. W. DALLEY and S. W. MCCLAREN
LTV Aerospace Corporation
Dallas, Texas

The reflective photoelastic technique was used to determine the relative stress levels in two typical lap joint configurations using five different joining techniques. The objective was to evaluate weld-bonded and rivet-bonded joints. A total of 10 specimens were used. The five types of joints tested were: adhesive only, adhesive with mechanical fastener(s), adhesive with spotweld(s), mechanical fastener(s) only, spotweld(s) only.

The loads were all normalized, and the corresponding photoelastic fringe orders were obtained across the width of the joint at a section which was observed to contain the maximum fringe order. Curves are presented showing the variation of fringe order across the width of each specimen at the section which included the maximum fringe order. Each fringe order (isochromatic) represented a particular value of either the difference in the principal stresses or the maximum shear stress at the point in question. If the static failing load causes the joint to fail according to the maximum shear-stress theory, the curves may be regarded as a presentation of relative joint strength. For areas in the joint in which it may be deduced that the minimum principal stress is small, the curves may be regarded as relative maximum normal stress curves which are significant in predicting fatigue life.

The data demonstrate that there is an appreciable advantage to be gained by using weld-bonded or rivet-bonded lap joints.

INTRODUCTION

With the development of advanced adhesive-bonding methods, rivet-bonded and weld-bonded joints in aerospace structures are not only cost effective, but their structural benefits are significant. The payoffs are in the areas of reduced joint stress and the probably longer fatigue life. In addition, joints of these types offer improved fracture

characteristics and a degree of redundancy in load paths. This chapter deals with a first-order determination of the characterization of rivet-bond and weld-bond joints and compares them with conventionally riveted or spot-welded joints, as well as all adhesive-bonded joints. The results are reduced to a simplified direct comparison of the maximum stress in each joint, so that potential benefits can be observed.

PHOTOELASTIC TEST PROCEDURE

The reflective photoelastic technique (Photostress) was used to determine the relative stress levels in two typical lap joint configurations using five different joining techniques. Ten different specimens were evaluated. Each lap joint tested consisted of two 1-in.-wide × 0.1-in.-thick strips of bare 7075-T6 aluminum. The two configurations tested consisted of a 1.0-in. and a 1.5-in. lap joint length. Table 1 describes each of the specimens. The adhesive used was Whittiker X-1093-3 (16 pts. aluminum flake to 100 pts. adhesive).

A strip of birefrigent plastic was bonded over the entire surface of one side of each of the lap joints, and sufficient axial load was applied to produce an optimum fringe pattern in the plastic. Fringe values were then read for selected sections (where the maximum stress occurred) across the width of the joint.

The maximum fringe values did not always occur on corresponding sections for each joint. For direct comparison purposes, the maximum

Table 1. Specimen Identification

Specimen No.	Type of Lap Joint	Length of Lap Joint
1	Rivet Bond (1 Fastener)	1.0 In.
2	Weld Bond (1 Spot Weld)	" "
3	Adhesive Only	" "
4	1 Spot Weld Only	" "
5	1 Fastener Only	" "
6	Rivet Bond (2 Fasteners)	1.5 In.
7	Weld Bond (2 Spot Welds)	" "
8	Adhesive Only	" "
9	2 Spot Welds Only	" "
10	2 Fasteners Only	" "

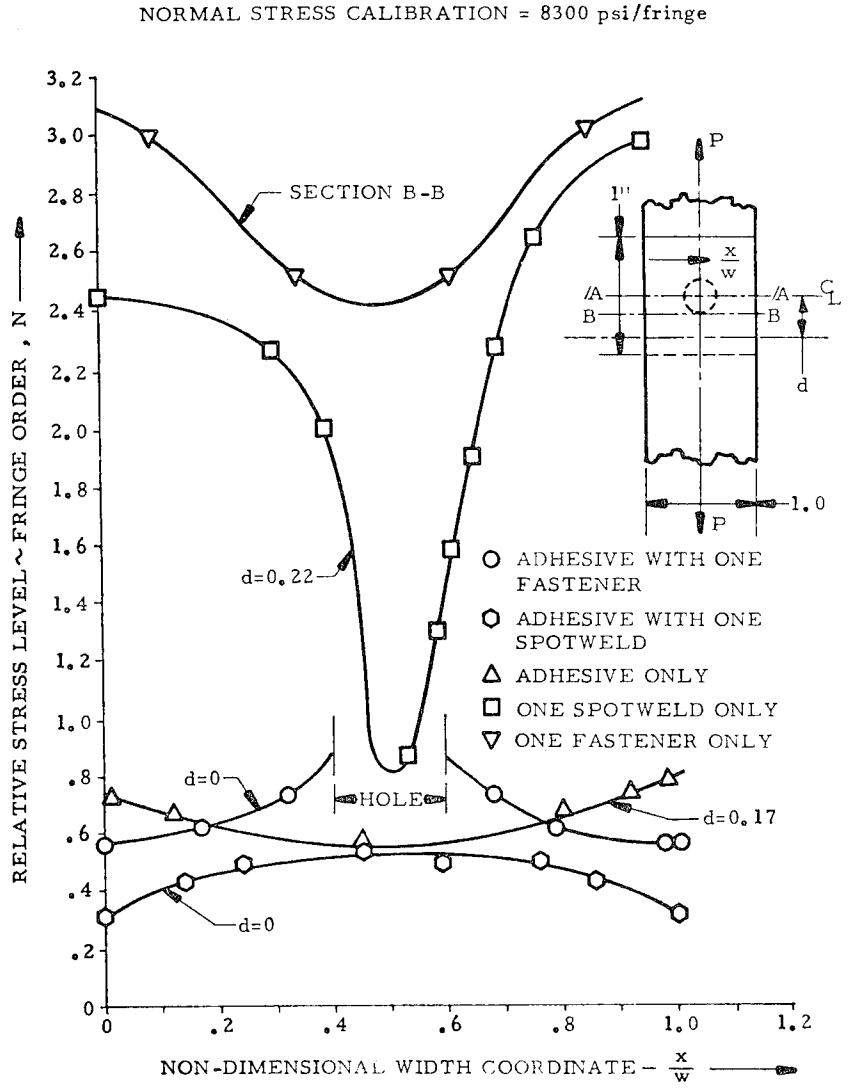


Figure 1. Relative stresses in various 1.0-in. lap joints.

stress for a given load was selected and used in Figures 1 and 2. Figures 1 and 2 are plots of the fringe value, N, (relative stress) across the width of each joint, at the section containing the maximum fringe value. The fringe values were all normalized to reflect the stress distribution for the same load (1000 lbs) in each joint. Figure 1 presents data for specimens

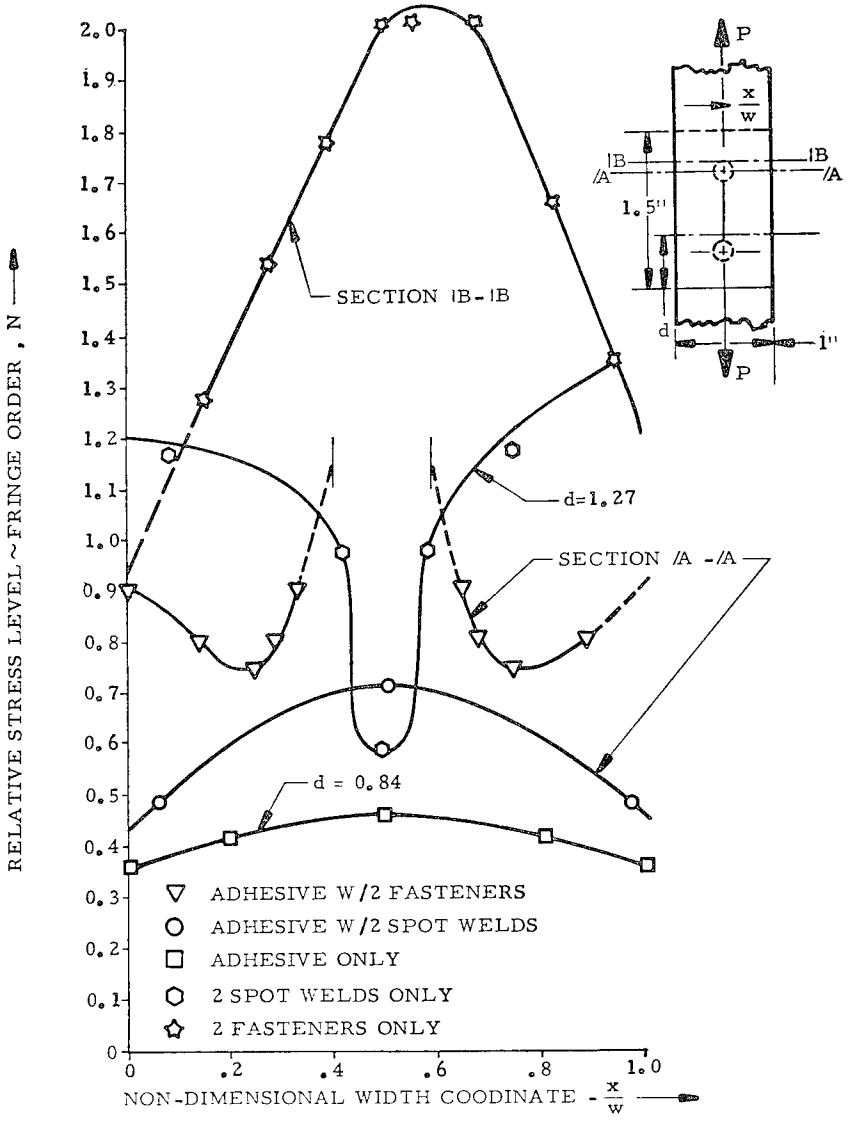


Figure 2. Relative stresses in various 1.5-in. lap joints.

1–5 (1.0-in. lap joint) and Figure 2 presents data for specimens 6–10 (1.5-in. lap joints).

DISCUSSION OF RESULTS

It is important to keep in mind that the plots represent either the relative magnitudes of the maximum shearing stress distribution (valid for $\sigma_{max} < 0 < \sigma_{min}$) or the relative magnitude of the difference in principal stresses at each point. If the joint were made from material that fails according to the maximum shear-stress theory, then Figures 1 and 2 can be interpreted as plots of the relative strengths of the joints. The results obtained are a first step toward an accurate quantitative evaluation of weld bonded–rivet bonded lap joints. This observation is indicated because the normalization of the loads in each joint to 1000 pounds for comparison purposes assumes all components of the joint to be linear. However, the adhesive used was slightly nonlinear at the applied stress levels. This may have some small effect on the normalized results.

Figure 1 illustrates that the joint with adhesive only and that with adhesive plus one spot weld have a rather uniform stress distribution with a relatively low maximum value. The latter (weld bond) exhibits smaller maximum fringe values than the former (adhesive bond only). A probable explanation for this is that a substantial portion of the load in the weld bond joint was transferred through a complex stress field in the weld nugget which was not reflected in the surface strains detected by the birefringent coating. The load transfers through the weld nugget primarily as the integrated shear stress π_{zx} (Figure 3). No shear stresses containing a z in the subscript are detected by the firefringent coating.

The maximum fringe values measured for the joint using adhesive with one fastener are only slightly greater than that using adhesive alone or weld bonding.

Further examination of Figure 1 demonstrates that the joint using a single fastener exhibited fringe values in excess of 3.6 times greater than the corresponding values for a rivet-bonded joint stress. An even larger difference exists between the maximum fringe value for the spot weld alone and that for the weld-bond joint. In this case the spot-weld joint stress exceeded the weld-bond joint stress by a factor in excess of 4.7.

Although the test was designed to load each joint symmetrically, it is apparent from Figure 1 that the joint with the spotweld only did not have a symmetrical stress field. No attempt was made to adjust the raw data to produce symmetry. On the contrary, the lack of symmetry obtained demonstrates the difficulty of transferring a load uniformly through a joint, even under laboratory conditions. In addition to the

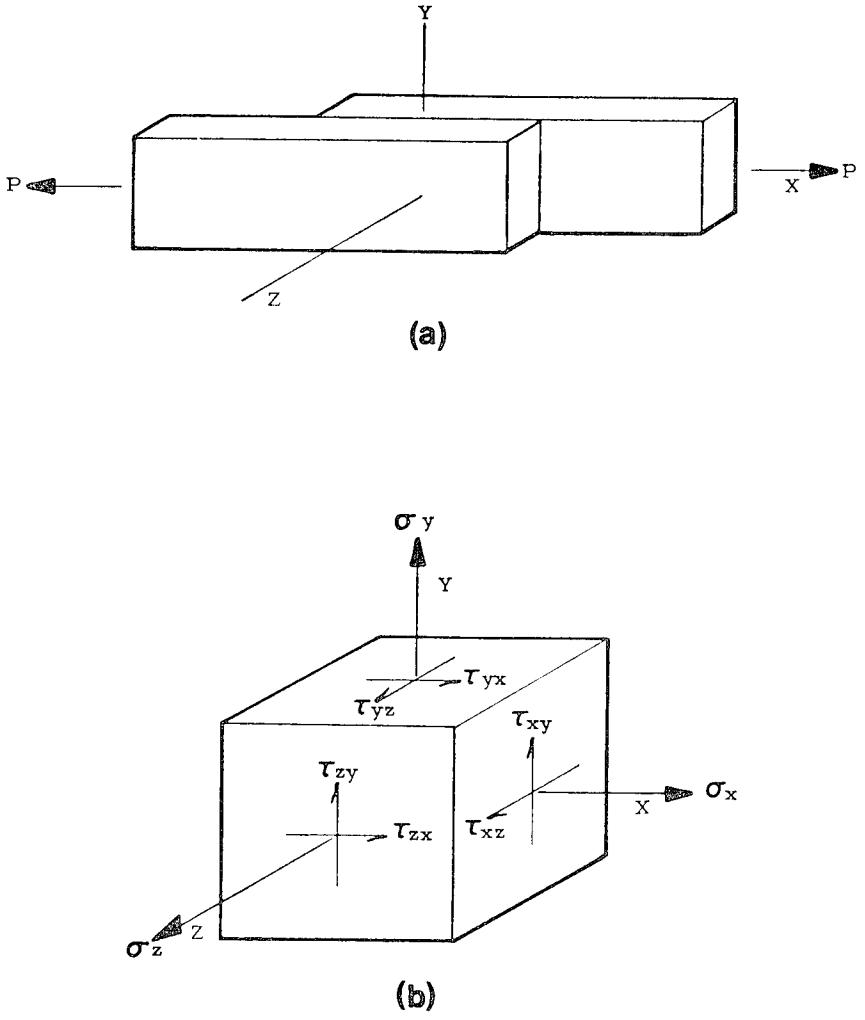


Figure 3. Reference axes and stress notation: (a) joint reference axes; (b) element showing stress notation.

presence of some eccentricity in load application, the weld nugget and/or adhesive may have contributed to some nonsymmetric characteristics.

Figure 1 clearly indicates that the fringe order in the joints using adhesive is substantially lower than in those using only a spot weld or mechanical fastener. Figure 2 is a plot of the same parameters as plotted in Figure 1 except they are for a 1.5-inch lap joint (specimens 6, 7, 9, and 10), and contain either two fasteners or spotwelds.

The curve for the joint with adhesive only in Figure 2 is concave down while the corresponding curve in Figure 1 is concave up. Both of these curves are fringe distributions across the approximate mid-length of the joint. The difference in shape can be attributed to the fact that the 1.5-in. joint is 50% longer than the 1.0-in. joint. In addition, the long joint was loaded to a higher value than the short joint.

The weld-bond joints are concave down in both Figures 1 and 2. The distribution of the surface stresses detected by the birefringent plastic is the difference in the secondary principal stresses, *i.e.*, the principal stresses in the x-y plane, (see Figure 3). Since $\tau_{\max} = \dfrac{\sigma_1 - \sigma_2}{2}$, it can be deduced that the maximum shear stresses observed act on planes whose normal lies in the x-y plane.

Load transferred through the joint by cross shear in either a weld nugget or a mechanical fastener is the integrated value of τ_{zx} over the shear area (Figure 3b). This stress is not detected by the birefringent coating as previously noted.

Differences in shape of the various curves in Figures 1 and 2 are due to the following:

1. Difference in joint length.
2. Difference in relative shear stiffnesses between the weld shear area(s) or mechanical fastener shear area(s) and the adhesive.
3. The fringe distributions for corresponding joints are not plotted for corresponding geometric sections but rather at sections observed to contain the highest (maximum) fringe order.

For example, the top curve in Figure 1 is for the 1.0-in. lap joint with one fastener. This curve is concave up and the data were obtained for a section tangent to the bearing side of the fastener. The corresponding joint in Figure 2 (the top curve) is for the 1.5-in. joint with two fasteners. This curve is concave down and also represents the distribution across a section tangent to the fastener on the bearing side.

The dip in the middle of the curve for spot weld(s) only in both Figures 1 and 2 is caused primarily by the fact that the middle portion is in the area of the weld nugget and the birefringent plastic is not sensitive to τ_{xz} stresses (Figure 3).

SUMMARY

Figures 1 and 2 demonstrate that the fringe order for a given load (and hence the maximum shear stress) is substantially less for the weld-bonded and rivet-bonded lap joints than for the corresponding joint joined only with a spot weld or a rivet. There is also evidence that the maximum normal stresses also follow this pattern. For example, at the free surface on each edge of the joint, the minimum normal stress is zero and the maximum normal stress is parallel to the joint edge and its magnitude is represented by the fringe order. The nature of the stress field is such that, away from discontinuities, the maximum stress is probably much larger than the minimum principal stress with a direction nearly parallel to the load (x axis) of the joint specimen as defined in Figure 3a. This indicates that the maximum normal stress is also less for weld-bonded and rivet-bonded lap joints. This leads to the conclusion that the weld-bonded and rivet-bonded lap joints should be superior to those with only spot weld(s) or rivet(s), both from static load and fatigue considerations.

It is recommended that additional tests be made using joints with a similar geometric configuration to check data repeatability. In addition, the directions of the principal stresses should be determined by using a plane polariscope and observing the isoclinics. The principal stresses should also be determined uniquely, using either the oblique incidence or shear difference method.[1] More than one specimen (a minimum of three is recommended) of each configuration should be tested to ensure consistent and repeatable data. Fatigue tests should be conducted obtaining the photoelastic data using stroboscopic light source. The results of these tests would provide the information necessary to assess more accurately the potential of weld-bonded and rivet-bonded lap joints.

REFERENCES

1. Dally, J. W. and Riley, W. F., *Experimental Stress Analysis*. New York: McGraw-Hill Book Company (1965), 235, 244.

28. SHIP STEEL WELDMENTS FOR LOW-TEMPERATURE SERVICE

H. I. McHENRY
National Bureau of Standards
Boulder, Colorado

The ship steels, welding practices, and weldment toughness requirements applicable to low-temperature (to −46°C) regions of liquefied-natural-gas (LNG) tankers are reviewed. In the construction of LNG ships, the principal welding productivity problem is the low deposition rate associated with the low heat input welding practices required to provide sufficient toughness in the weld heat-affected-zone (HAZ). A potential solution to this problem is to use improved steels which can be welded using efficient procedures and still provide satisfactory HAZ toughness. The steelmaking practices that contribute to low-temperature toughness are reviewed with respect to economic limitations associated with ship steels and to their potential for improving HAZ toughness.

INTRODUCTION

A large fleet of tankers is under construction for the marine transport of liquefied natural gas (LNG). In LNG ships, significant portions of the hull are cooled by the cryogenic cargo to temperatures ranging from 0 to −46°C. At these temperatures, many ship steels exhibit brittle behavior. Consequently, the U.S. Coast Guard (USCG),[1] the American Bureau of Shipping (ABS)[2] and comparable regulatory agencies around the world have established strict requirements on the ship steels and weld-procedure qualifications for weldments subjected to low temperatures. To meet these requirements, shipyards generally employ low-heat-input, multipass welding practices for welds in the low-temperature regions of the hull. As a result, welding productivity is being limited to a level far below the capability of the equipment and facilities.

The Maritime Administration (MarAd) was advised of the increased costs of welding LNG ship hulls by the Welding Panel of the Ship Pro-

duction Committee, a group of industry experts organized by the Society of Naval Architects and Marine Engineers to advise MarAd on how to improve shipyard productivity. In their efforts to reduce the cost of ship construction, MarAd requested the National Bureau of Standards to conduct a survey to establish the feasibility of improving the efficiency of welding ship steels for low-temperature service. The survey included visits to the shipyards involved in LNG construction, to the appropriate regulatory agencies, to the steel plate producers and to other companies engaged in fabricating structures for low-temperature service. These visits clarified the problem and the rules, and provided a review of the technology available for improving welding efficiency. The survey has been completed and the results are presented herein.

SHIPYARD PRACTICE

The LNG ships under construction in the United States are approximately 280 m long, 42 m wide, and 30 m deep and have a cargo capacity of 125,000 cubic meters. The ships are double-hull vessels with transverse bulkheads dividing the ship into several cargo bays as shown in Figure 1.[3] The cryogenic containment system fitted within each cargo bay consists of the cargo tank, the insulation, and a secondary barrier to contain the LNG in case of tank failure. Thomas and Schwendtner[4] have described eight types of containment systems in use or under consideration worldwide. In the U.S., three designs are under construction: the Conch freestanding prismatic tank, the Gazocean membrane prismatic

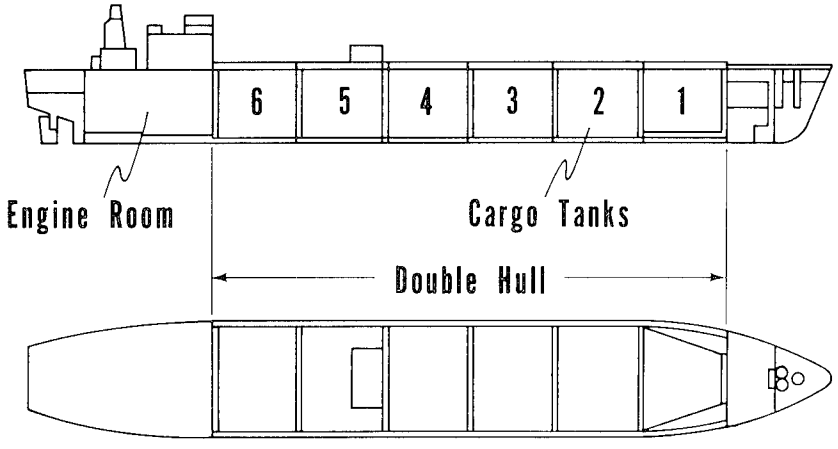


Figure 1. Structural arrangement of an LNG ship hull.[3]

tank, and the Kvaerner–Moss free-standing spherical tank. For each system, the insulation is sufficient to permit transport of the LNG at approximately −162°C and atmospheric pressure with boil-off rates less than 0.25% per day.

The temperature environment within the hull is a function of the ambient air and water conditions, the effectiveness of the insulation system, and the proximity of the cargo. For North Atlantic routes, the USCG specifies that the design temperatures be based on assumed ambient conditions of −18°C air, a 5 mph (2.33 m/s) wind and still water at 0°C. The inner hull, the transverse bulkheads, and the tank support structure are the principal areas cooled by proximity to the cargo. Minimum design temperatures in these areas range from 0°C to −46°C. The coldest locations are the inner side-shell above waterline and parts of the tank support structure.

Steel Selection

The chemistry, processing, and testing requirements of steels used in LNG ships being made in the U.S. are summarized in Table 1. These steel selections are generally in accordance with the proposed (1975) regulations of the International Maritime Consultive Organization (IMCO) as outlined in Tables 2 and 3. For temperatures below −10°C, fully killed, aluminum-treated, fine-grain, C–Mn–Si steels are used. For temperatures below −25°C, the steel must also be either normalized or quenched and tempered. The most commonly used steels are the ABS ordinary strength grades; CN is used for temperatures to −23°C, CS for temperatures to −34°C, and V-051 for temperatures to −46°C. For high-strength applications, ABS grade EH steel is commonly used for temperatures to −34°C and ASTM grades A537-A Modified and A-678A are used for temperatures to −46°C.

Approximately 28,000 metric tons of steel are required for the hull of a 125,000-cubic-meter LNG ship. The tonnage requirements for all grades of hull steel and for low-temperature steels are summarized in Table 4. These data are indicative of the total usage of low-temperature steels and include significant tonnage selected for improved toughness and used in parts of the ship not exposed to temperatures below 0°C.

Weld Procedure Qualification

For service temperatures less than −18°C, the welding procedures must be qualified in accordance with USCG and ABS requirements. Procedures are specific for each base metal, wire, and flux combination, and must be established for each welding process and position. The joint

Table 1. Specifications for Steel Plates Used in LNG Ship Hulls

	Ordinary Strength Grades			Higher Strength Grades	
	CN	CS	V-051	EH-36	A537-A, Modified
Minimum Design Temp, °C	**−23**	**−34**	**−46**	**−34**	**−46**
Chemical Composition, %	**(ABS 1972 Rules)**	**(ABS 1974 Rules)**		**(ABS 1974 Rules)**	**(ASTM 1970 Standards)**
C, Max	0.23	0.16	0.16	0.18	0.16
Mn	0.6–0.9	1.00–1.35	1.15–1.50	0.90–1.60	1.15–1.50
Si	0.1–0.35	0.10–0.35	0.10–0.35	0.10–0.50	0.15–0.50
P, Max	0.05	0.04	0.04	0.04	0.04
S, Max	0.05	0.04	0.04	0.04	0.04
Al	0.02–0.06	0.02–0.06	—	0.06 Max	—
Ni, Max				0.40	0.25
Cr, Max				0.25	0.25
Mo, Max				0.08	0.08
Cu, Max				0.35	0.35
Cb, Max				0.05	—
V, Max				0.10	0.08
Mechanical Properties					
Tensile, kg/mm²(KSI)	41–50(58–71)	41–50(58–71)	41(58), Min	50–63(71–90)	46(65), Min
Yield, kg/mm²(KSI)	—	24(34), Min	25(35), Min	35(51), Min	32(47), Min
Elongation in 50 mm	24%	24%, Min	24%, Min	22%, Min	22%, Min
Charpy Impact Requirements					
Test Temperature			−51	−40	−51
Energy, Min Avg. kg-m(ft-lb)			2.8(20)Transverse	3.5(24)Longitudinal	4.2(30)Longitudinal
No. of Specimens			3/Plate	3/Plate	3/Plate
Heat Treatment	All grades normalized				
Deoxidation	All grades aluminum killed, fine grain practice				

Table 2. IMCO Requirements for LNG Hull Steels

Minimum Design Temperature, T, °C	Plate Thickness, t, mm	Approved ABS Steel Grades
$T \geq 0$	—	Normal Practice
$0 > T \geq -10$	$t \leq 12.5$	B
	$12.5 < t \leq 25.5$	D
	$t > 25.5$	E
$-10 > T \geq -25$	$t \leq 12.5$	D
	$t > 12.5$	E
$-25 > T \geq -55$	—	See Table III

Table 3. IMCO Requirements for LNG Hull Steels for Design Temperatures of −25 to −55°C

Chemical Composition

C	Mn	Si	S	P
0.16% max	0.70–1.60%	0.10–0.50%	0.035% max	0.035% max

Optional additions:

Ni	Cr	Mo	Cu	Cb	V
0.80% max	0.25% max	0.08% max	0.35% max	0.05% max	0.10% max

Heat Treatment

Normalized or quenched and tempered.

Deoxidation

Fully killed, aluminum treated, fine-grain practice.

Toughness Requirements

Temperature: 5°C below design temperature
Specimens: Charpy V-notch-transverse
Energy, min. avg.: 2.8 kg m (20 ft-lb)
No. of Tests: 3 from each plate

Table 4. Usage of Low-Temperature Steels in LNG Ship Hulls

Ship Design	Steel	Weldment Test Temp, °C	Tonnage, long tons (1000 kg)	Applications
Gazocean	All Grades	—	29,573	Total hull plus scrap and spare
Membrane	ABS CS	−34	9,666	Inner bottom, web frames, gunwale, bilge
Prismatic	ABS V-051	−43	2,695	Inner side shell, transverse deck box
Conch	All Grades	—	17,810	Midbody (hull less bow and stern)
Free Standing	ABS CN	−23	6,058	Trans. Bulkhead, inner side shell, deck
Prismatic	ABS CS	−21 to −32	4,602	Inner bottom, gunwale, bilge
	ASTM A678-A	−45	418	Roll key
Kvaerner–Moss	All Grades	—	17,393	Midbody
Free Standing	ABS CN	−23	1,408	Inner hull
Spherical	ABS CS	−33	1,602	Transverse bulkheads
	ABS EH-36	−29	1,515	Deck girders
	ASTM A537 (Mod)	−51	1,185	Cylindrical tank support

preparation, preheat and interpass temperatures, root coping, and other aspects of the procedure must be representative of the procedures used in production. Generally, two qualifications are required to cover the range of plate thickness: $9.5 < t \leq 19$ mm and $t > 19$ mm. Test plates for these qualifications are usually 19-mm thick for the lower thickness range and the maximum thickness used in production for thicknesses greater than 19 mm. The test plates are oriented such that the weld axis is parallel to the rolling direction.

The qualification requirements include the room-temperature tensile and guided bend tests specified by ABS for all weld procedure qualifications plus a series of Charpy V-notch impact tests. The Charpy tests are conducted at 5.5°C below the minimum service temperature in accordance with ASTM A 370, using type A specimens. The specimens are cut transverse to the weld axis with the notches normal to the plate surface. Three specimens are tested for each of the following notch locations: centered in the weld metal; on the fusion line; and in the heat-affected zone (HAZ) 1, 3, and 5 mm from the fusion line. The impact specimen location requirements are summarized in Figure 2. The average Charpy value must equal or exceed 2.8 kgm (20 ft lb); the minimum value for one specimen is 1.9 kgm (13.3 ft lb).

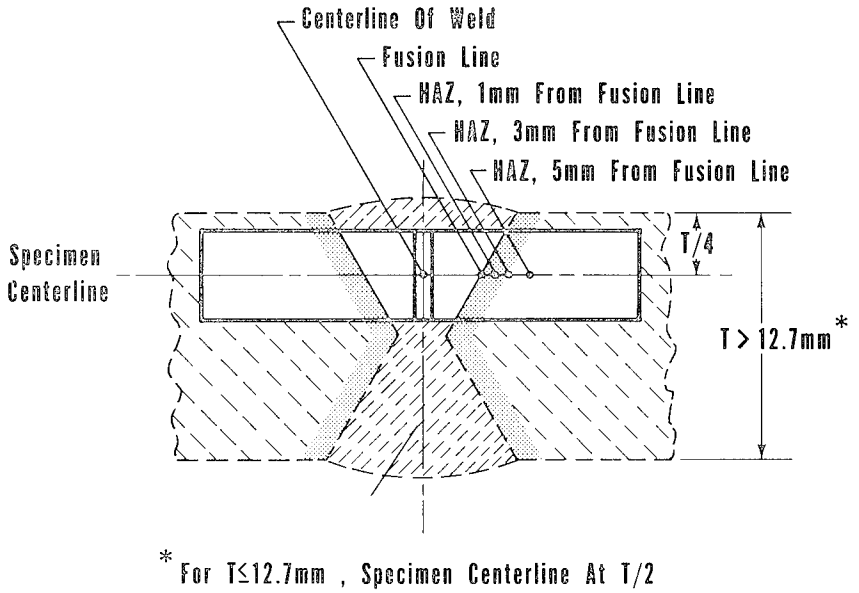


Figure 2. Charpy V-notch specimen locations for weld procedure qualification.[1]

Welding Processes and Consumables

Conventional shipyard welding practices are generally being used to fabricate low-temperature steels; however, the heat inputs are restricted in order to meet the Charpy impact requirements. Consequently, the deposition rates are far below the equipment capabilities. The principal welding processes are submerged arc (SA), shielded metal arc (SMA) and gas metal arc (GMA). For flat position welds and horizontal fillet welds, SA is the most efficient and reliable process, and therefore is widely used on automated panel-lines. Both SMA and GMA are used for most of the other welding; the selection of one process over the other varies widely from yard to yard. Variations of these processes such as one-sided welding, gravity welding, tandem arc and 3 o'clock subarc welding are used in specific instances depending on the capabilities of the shipyard. High-heat-input processes such as the electro-slag and electro-gas processes are not approved by ABS for use on low-temperature steels.

A wide range of wires, rods, and fluxes are used to weld ship steels for low-temperature service. For submerged arc welding, two approaches have been taken: (1) use a mild steel wire and an alloy flux, or

(2) use an alloy wire and a neutral flux. The mild steel wires conform to AWS specification AS.17-69 Class EM12K, and the alloy fluxes are of a proprietary nature. The alloy wires, which contain 1–2% Mn, 0.1–0.5% Mo, and 0.5–2.0% Ni, are welded with a neutral flux suitable for multipass welding. For SMA welding, the most common electrode is AWS E 8018-C3 which contains 1% Ni. In some cases, E 7018 electrodes, which contain 0.5% Mo, are used for moderately low temperatures and E 8018-C1 electrodes, which contain 2–2.75% Ni, are used for the lowest temperatures. Both solid and flux-core wires are used for GMA welding. The solid wires are alloyed with Mn, Mo, and Ni for low-temperature toughness and the cored wire generally has a mild steel sheath and a proprietary flux.

Low-heat-input welding practices are necessary to meet the USCG impact requirements in the HAZ of low-temperature ship plate weldments. This poses a significant productivity problem to the LNG shipyards because deposition rate is proportional to heat input, and their welding equipment is capable of far greater deposition rates than are possible using the low-heat-input practices. Consider, for example, the welding procedures that are representative for welding 19-mm plate. For X-ray quality welds in steels such as ABS grade B, the following conditions are recommended:[5]

Joint preparation: double V groove with an 8 mm land.

Backing weld: 850 amps, 33 volts, 16 in./min (0.68 cm/sec), 105 kJ/in. (41.3 kJ/cm).

Finishing weld: 1150 amps, 35 volts, 13 in./min (0.55 cm/sec), 186 kJ/in. (76.2 kJ/cm).

In contrast, 19-mm ship plate for low-temperature service must be multipass welded with the heat input limits ranging from about 40 to 80 kJ/in. (16 to 32 kJ/cm) depending on the particular combination of steel grade and service temperature. At heat input levels within this range, anywhere from 4 to 14 passes may be required to weld 19-mm plate.

Two approaches to solving the productivity problem are apparent: either change the weldment toughness requirements or improve the tolerance of the base metal to higher heat input welding practices. Changing the rules is not a viable solution to the problem, because strict requirements are appropriate for hazardous cargo such as LNG. In addition, the requirements have recently been adopted by IMCO as standards acceptable to all major shipping countries. Thus, any change in the existing requirements would probably be contingent upon agreement by both the USCG and IMCO, certainly a long-term proposition. The alternative solution would be to make available an economical steel which, when welded using efficient procedures, provides the required level of toughness. This potential solution is attractive because it is based on

steelmaking technology and shipyard economics instead of international agreements. The feasibility of this solution is addressed in the next section.

STEELMAKING TECHNOLOGY

Current steelmaking technology offers several methods for providing improved toughness at low temperatures. The methods include alloying, rolling practice, sulfide shape control, and heat treating. The extent to which the improvements are reflected in HAZ toughness of high heat input welds is not well documented. Nevertheless, there exists reason to believe that one or a combination of the available metallurgical treatments will permit higher heat inputs than currently being used. Whether or not the improvement will be economically justifiable depends on the cost increment added to the price of the steel and the extent of the improvement. Because of the large tonnages involved, the added cost of an improved ship steel will likely be limited to a maximum of $20 to $60 per ton, depending on the specific application.

Alloying

The use of additional alloying to improve ship steels is severely constrained by steel pricing practices. Steel prices are comprised of a base price and extras for the specification, plate dimensions, and quantity. There are two base prices; the carbon steel base and the alloy steel base, the latter of which is about 40% higher. The carbon steel base price is applicable to all the steels used in LNG ship hulls. The American Iron and Steel Institute (AISI) considers a steel to be an alloy steel when either: (1) the maximum of the range given for the content of alloying elements exceeds one or more of the following limits — Mn, 1.65%; Si, 0.60%; Cu, 0.60%; or (2) a definite range or a definite minimum quantity of any other element is specified to obtain a desired alloyed effect.[6] The chemistry specification for ABS EH 36 shown in Table 1 is typical of the degree of alloying permissible in carbon steels. Notice that there are no minimum requirements on alloying elements such as Cr, Mo, Ni, V, and Cb. Thus, the steelmaker has flexibility on how best to achieve the required tensile and impact properties. These pricing practices preclude the use of 0.4–0.8% Ni additions that are frequently specified for low-temperature applications by Japanese and European shipbuilders. However, the transition temperature of ship steels can be reduced by alloy adjustments within the AISI limits for carbon steels. As shown in Figure 3, the transition temperature is reduced by increasing the Mn content and by lowering C, Si, and N.[7]

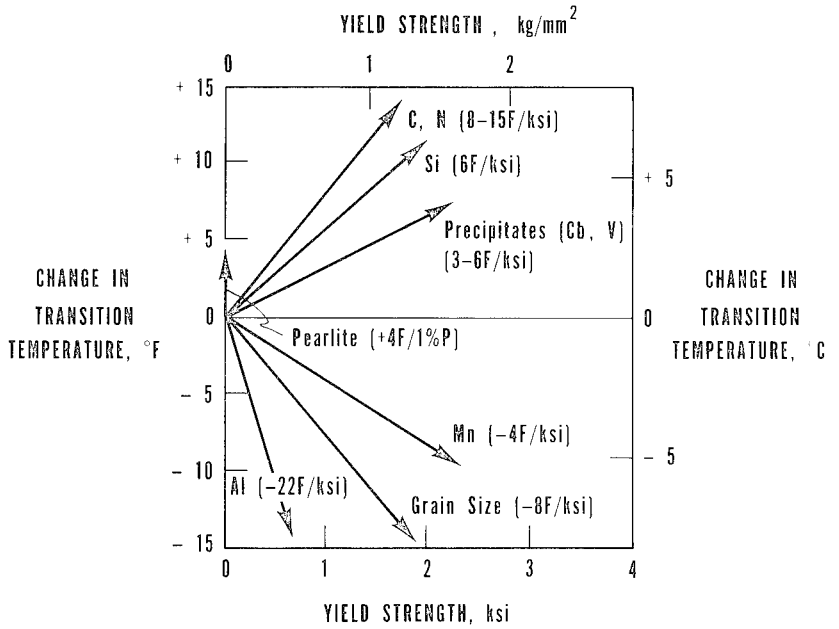


Figure 3. Strength toughness vectors for structural steels.[7] Reprinted with permission of the Welding Research Council.

Microalloying with Cb or V is an economical approach to providing strength and good low-temperature properties in the base plate, and is currently used in EH 36 and A537 Modified steels. Strengthening is provided by a combination of reduced grain size and precipitation hardening. The low-temperature toughness is improved because of the small grain size — an improvement that is only partially offset by the precipitation hardening effect shown in Figure 3. However, the HAZ toughness near the fusion line is adversely affected by grain coarsening and further reduced by the strengthening effect of carbonitride precipitation.[8,9] This embrittlement is almost always observed in simulated HAZ specimens, but is frequently not evident in Charpy specimens taken from weldments. The absence of embrittlement in high heat input weldments such as shown in Figure 4 suggests that the high-toughness material surrounding the embrittled region substantially reduces the embrittlement.[10] It is not clear at this time whether this can be attributed to an averaging effect, *i.e.*, the Charpy impact specimen samples a composite of high- and low-toughness material, or to a reduction of constraint provided by the ductile material surrounding the embrittled region. In either case, it appears that the problem of Cb or V embrittlement in the HAZ may not be as significant in real weldments as suggested by some investigators[8,9] on the basis of simulated HAZ studies.

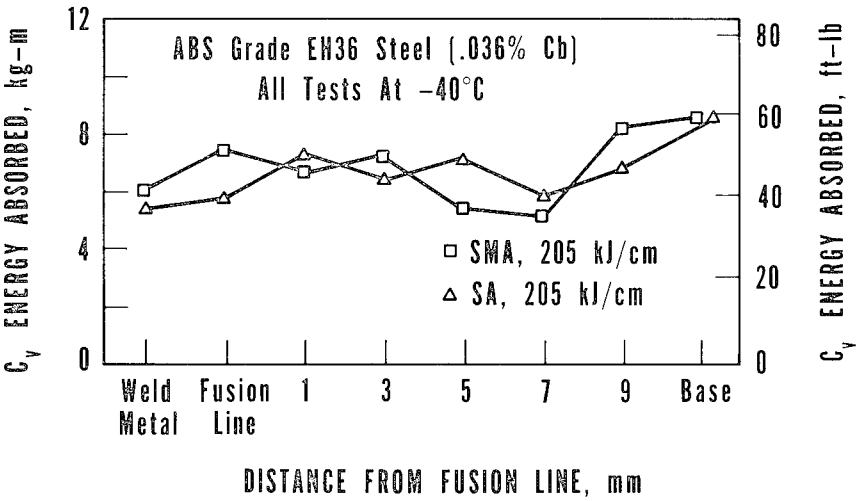


Figure 4. Charpy toughness traverse for Cb-treated EH-36 weldment.[10]

Inclusion Control

Nonmetallic inclusions are an intrinsic constituent of all steels. There are two main types of inclusions: (1) the indigenous inclusions which precipitate in the molten or solidifying metal due to decreased solubility of oxygen and sulfur upon cooling, and (2) the exogenous inclusions which are introduced into the steel from materials such as the refractories which come in contact with the molten steel. The indigenous inclusions are far more numerous and predictable in their behavior than the exogenous types, which occur sporadically. The principal types of indigenous inclusions are oxides and sulfides. In Al-killed steels, the dominate oxide is Al_2O_3, which precipitates as small refractory crystals that do not agglomerate and do not change shape appreciably during rolling operations.

The principal sulfide inclusion in C–Mn steels is MnS. In low-oxygen steels (*e.g.*, Al-killed), the MnS inclusions are quite plastic and tend to elongate during rolling. These stringer-shaped inclusions separate readily from the steel matrix, and have a higher surface-to-volume ratio and a shorter interparticle spacing than globular inclusions. Consequently, the MnS stringers serve as initiation sites for low-energy fracture when the steel is loaded transverse to the direction of rolling.

Sulfide shape control is rapidly emerging as a practical tool for eliminating stringers and thereby improving the transverse toughness of structural steels.[11] The process generally consists of lowering the sulfur content of the heat below 0.015% and then adding elements to the melt

which form refractory sulfides. The refractory sulfides take on a spherical shape in the liquid steel and tend to retain this shape upon solidification and during the rolling process. Several elements, including Ti, Zr, Ca, Mg, and the rare-earth metals, form refractory sulfides. Although practices vary widely, sulfide shape control by the ladle addition of rare-earth metal (REM) in the form of mischmetal, a mixture of rare earths containing about 50% Ce, appears to be gaining favor. The rare earths are preferred over Ti and Zr because, in addition to shape control, an appreciable reduction in sulfur content occurs due to the solution of rare-earth sulfides and oxysulfides in the slag. Calcium and magnesium are effective for both sulfide shape control and sulfur reduction; however, Mg is difficult to introduce into molten steel because of its high vapor pressure; and Ca, which is not soluble in liquid iron, does not mix readily enough to assure complete sulfide shape control. The influences of sulfur content and REM additions on toughness are shown in Figure 5.[12]

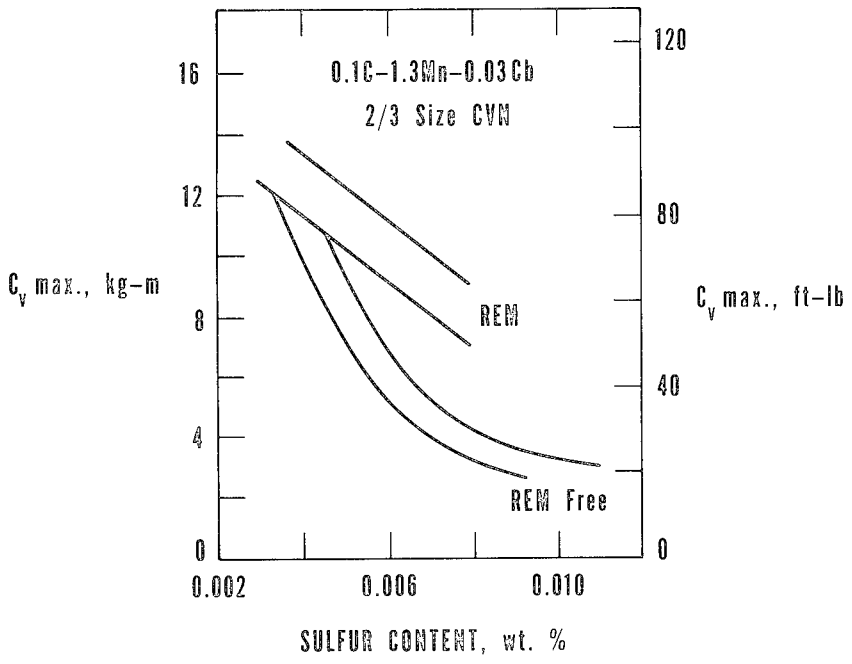


Figure 5. The effect of rare-earth metal treatments on the transverse shelf energy of low sulfur C–Mn Steel.[12] Reprinted with permission of the Metallurgical Society of AIME.

Rolling Practice

Significant toughness improvements can be obtained by altering the rolling practice. Cross rolling can improve transverse properties at a moderate increase in steel cost; however, substantial improvements require rolling ratios that approach unity. Steel specifications rarely include cross-rolling requirements; however, a guaranteed transverse Charpy requirement generally implies that cross rolling will be used. Thus, the principal use for cross rolling is to make moderate improvements in transverse properties to assure conformance to a transverse toughness guarantee.

Controlled rolling can improve strength and low-temperature toughness by substantially reducing the austenite grain size and the fineness and nature of the transformation products.[13] It involves a schedule of reductions at specified temperatures, sometimes coupled with controlled cooling between passes and after the final pass. Most commonly, controlled rolling is limited to performing the final reduction at a specified temperature which is lower than normally employed. As shown in Figure 6, the reduction below 900°C causes a significant decrease in transi-

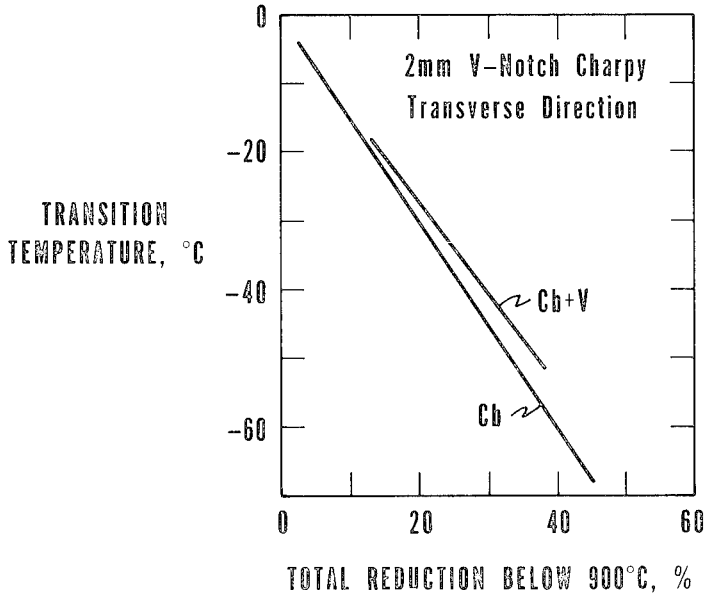


Figure 6. The effect of rolling reduction below 900°C on the fracture appearance transition temperature.[13] Reprinted with permission of the Metallurgical Society of AIME.

tion temperature. It is particularly useful for the production of line pipe, where the large tonnage involved permits optimization of the rolling schedules on an economical basis. For ship steels, the large variety of plate sizes, thickness, and grades, and the lack of facilities for producing controlled-rolled plates greater than 16-mm thick, limit the practicability of controlled rolling. In addition, the large variety of rolling schedules can lead to more scatter in the material properties than is associated with more easily controlled procedures such as normalizing. Due to these limitations, controlled rolling is not considered practical for improving the toughness of ship plate.

Heat Treatment

Nearly all of the ship steels used for low-temperature (to −46°C) applications are normalized. The typical normalizing heat treatment involves heating the as-rolled plate to 925 ± 25°C and air cooling to room temperature. As shown in Figure 7, the low-temperature toughness of these steels could be improved by a quench and temper (Q and T) heat

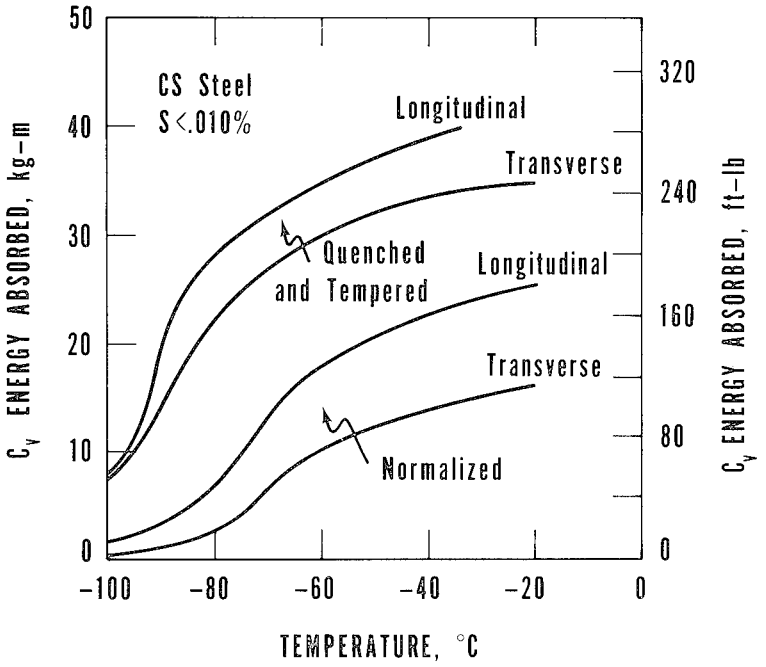


Figure 7. Charpy impact transition curves for normalized and for quenched and tempered CS steel.[14]

treatment.[14] For C–Mn steels such as ship plate, Q and T involves heating to 925 ± 25°C, quenching in water, and subsequently tempering at 650 ± 50°C. This heat treatment is nearly twice as expensive as normalizing. Although Q and T improves base plate toughness, it is not clear whether this benefit will be apparent in the heat affected zone of weldments. It is considered likely that the reheat treatment caused by the weld thermal cycle will impart the same toughness to the heat affected zone regardless of prior heat treatment. Thus, the extra cost of Q and T over normalizing ($30 to $40/metric ton) is not considered a cost effective means of improving heat-affected zone toughness.

WORK IN PROGRESS

On the basis of the shipbuilding and steel industry survey, MarAd requested NBS to conduct a follow-on program in cooperation with the LNG shipbuilders to evaluate improved ship steels for low-temperature service. In this program, the major steel companies are providing the LNG shipyards with production heats of ABS steels, modified to possess improved transverse fracture properties at the appropriate test temperatures. The shipyards will evaluate these steels by qualifying optimum weld procedures in accordance with the USCG requirements. A comparison of the optimized procedures with those currently employed will be indicative of the cost reduction possible through the use of improved steels. As a result, each participating shipyard will be in a position to make a rational decision regarding the cost effectiveness of premium quality steels. The program, currently in the formative stages, will be completed in mid-1976, and the results will be published shortly thereafter.

SUMMARY

A survey of the U.S. shipyards engaged in LNG ship construction, the major steel plate producers and the maritime regulatory agencies has been conducted to establish the feasibility of improving the efficiency of welding ship steels for low-temperature service. The results of this survey suggest that application of state-of-the-art steelmaking technology can substantially improve the low-temperature toughness of ship steels. A program is being conducted to determine if steels with improved toughness retain satisfactory toughness in the HAZ when higher heat input welding practices are used.

ACKNOWLEDGMENT

This work was sponsored by the U.S. Maritime Administration. The author wishes to acknowledge the many contributions of M. B. Kasen and R. P. Reed of NBS who collaborated on all aspects of the program described herein. The author also expresses appreciation to R. W. Schaffran of the U.S. Maritime Administration and W. C. Brayton of Bethlehem Steel Corporation who were responsible for initiating the program.

REFERENCES

1. "U.S. Coast Guard Marine Engineering Regulation," Subchapter F, CG-115, July 1970.
2. *Rules for Building and Classing Steel Vessels*. New York: American Bureau of Shipping (1974).
3. Emery, W. B., II, Sterrett, E. L., and Moore, C. F., "Alaskan Liquefication Plant to Supply Gas for Japanese Use," *Oil Gas J.*, **66**, No. 1 (1968), 55–59.
4. Thomas, W. D. and Schwendtner, A. H., "LNG Carriers: The Current State of the Art," paper presented at the Annual Meeting of the Society of Naval Architects and Marine Engineers, New York, 1971.
5. "Submerged Arc Welding Handbook," Linde Reference Library, Union Carbide Corporation, New York, 1974.
6. "Alloy Steel Plates," American Iron and Steel Institute, New York, April 1970.
7. Cordea, J. N., "Niobium- and Vanadium-Containing Steels for Pressure Vessel Service," *Weld. Res. Counc. Bull.*, No. 203, February 1975.
8. Hannerz, N. E., "Effect of Cb on HAZ Ductility in Constructional HT Steels," *Weld. J.*, **54** (1975), 162s–68s.
9. Hannerz, N. E. and Jonsson-Holmquist, B. M., "Influence of Vanadium on the Heat-Affected-Zone Properties of Mild Steel," *Metal Sci.*, **8** (1974), 228–34.
10. Alia, B. L., Stern, I. L., and Null, C., "Toughness Evaluation of Electrogas and Electroslag Weldments," Project Report, The National Shipbuilding Research Program, U.S. Maritime Administration, March 1975.
11. Korchynsky, M., "The Relationships Between Sulfide Composition Morphology and Distribution on Mechanical Properties of HSLA Steels," paper presented at the Interrnational Symposium on Sulfide Inclusions in Steel, American Society for Metals, Port Chester, N.Y., November 1974.
12. Kozasu, I. and Osuka, T., "Processing Conditions and Properties of Control-Rolled Steel Plates," in *Processing and Properties of Low Carbon Steel*, ed. by J. M. Gray. New York: The Metallurgical Society of AIME (1973), 47–67.

13. Gray, J. M., "Columbium (Niobium) as a Grain Refiner in Hot-Rolled Steels," in *Processing and Properties of Low Carbon Steel*," ed. by J. M. Gray. New York: The Metallurgical Society of AIME (1973), 225–42.
14. "N-Tuf, Low Temperature Steels," Nippon Steel Corporation, 1972.

INDEX

Adhesive bonding,
  adhesive application, 252–255
  adhesive selection, 237, 242, 244–247
  aluminum, 201–206, 271, 311–312
  bondability index, 242
  ceramics, 70–76, 106–107
  cohesive strength, 255–257
  corrosion, 608, 610–612
  curing, 224, 255–259, 263, 275–276
  fatigue properties, 305, 307–312, 607
  finite element method, 406, 424–426, 448
  fracture energy, 267, 269–271, 273–277, 279, 285–291, 293–298
  fracture of epoxy adhesives, 265–267, 273–298
  fracture mechanics, 431, 507–510, 607
  helicopters, 344–345, 350–351
  in aerospace, 605–614
  in thermoplastics, 228–232
  lap joints, 259–260, 305–316
  loading forces, 239–241, 244
  nondestructive testing, 507–510, 583–591
  outgassing, 255
  peel properties, 243–244, 258, 261, 266, 297, 409, 415–416, 427, 429–430
  piezoelectrics, 74–75
  polymers to ceramics, 207, 209–228, 231–232
  polymers to polymers, 237–263
  radomes, 73
  residual strain on lap joints, 310–312
  shear properties, 240, 251, 259–262, 314, 409, 414–415, 417–420, 422–427, 430
  stress, 240–244
  stress analysis, 405–406, 408–431, 448
  stress strain, 261–262
  surface treatment, 202–206, 212–228, 238, 247–252
  testing, 202–203, 242–244
  thermal stress, 424
  thickness, 283–287, 295–298, 306, 409, 422
  tire cords, 246
  windows, 71–72
ALCO/BLH, 25
Alumina,
  adhesive bonding, 71–76
  brazing, 83–85, 88–95
  cement and mortar, 77
  diffusion bonding, 155
  eutectic bonding, 186–187, 189–191
  fusion welding, 100–104
  hot pressing, 179–182
  mechanical fastening, 79–81
  solid state welding, 99
Aluminum and aluminum alloys,
  adhesive bonding, 201–206, 271, 311–312, 584, 616
  braze alloys for titanium, 595–602
  explosive welding, 52–53, 55, 59–65
  fatigue crack growth, 492–493, 504, 521, 524–525, 537–538, 549–551, 553
  fatigue failure, 574–580
  galvanic corrosion in couples to composites, 569–571, 580
  mechanical fastening to composites, 80, 569
  oxide coatings, 203–206
  properties, 476, 540–541, 596
  stress analysis of joints, 391, 423–427, 463
  thickness, 463
  2219, 539–542, 549–554, 556–565

Bearings,
  adhesive bonding, 73, 76

Beryllium ceramics,
brazing, 88–91
cracking, 187
eutectic bonding, 186–187, 189, 191
fusion welding, 100
oxides, 88–91, 100, 186–187, 189, 191
Boron/resin composites, 245, 254–255, 258–259
infrared absorbances, 254
stress analysis, 423–426, 439, 441
Boron ceramics, 96, 98, 100
Boron composites, 317, 322, 326–327
Brazing,
braze metals, 82, 84–89, 91, 595–596
ceramics, 80–95, 106–107
diffusion, 86, 88

Carcium oxide, 97
Carbon,
welding, 98, 101
Carbon-carbon composites,
mechanical fasteners for, 80
Cements and mortar,
for ceramics, 75, 77, 106–107
for firebrick, 75, 77
for thermocouples, 77
properties, 75
Ceramic joining, 69, 109
adhesive, 70–76, 106–107
brazing, 81–95, 106–107
cement and mortar, 75, 77, 106–107
cold pressing, 171–173
cost, 107
diffusion bonding, 155–160
eutectic bonding, 185–197
fusion, 99–108
hot pressing, 113–115, 130–151, 155, 160–176, 179
mechanical fasteners, 78–81, 106–107
slip cast bonding, 113–114, 120–131, 151
solid state, 96–99, 106–107
to stainless steel, 76
vacuum tightness, 106–108
Ceramic-polymer composites,
bonding, 207, 212–229, 255
Cerium oxide, 96–97
Chromium eutectics, 197
Coatings,
creep, 11, 27
electrode, 8–10, 27
filler effects on curing, 224
flexural strength, 217
silane, 213–231
tensile properties, 9–11
Volan, 213
water-resistant, 213–216, 218
Cobalt eutectics, 197
Columbium,
welding, 55, 63–65, 97–98, 101
Columbium carbide,
solid state welding, 98
Compatibility of ceramics, 171–172, 174
Constant-strain cold cracking test, 39–49
Coolant systems, 3, 5, 13, 19–21, 25–26
Copper and copper alloys,
brazing to alumina, 84–85, 95
eutectic bonding to ceramics, 185, 188–197
explosive welding, 55, 57, 59–65
Corrosion,
adhesive bonds, 608, 610–611
galvanic, 569–581, 596
of graphite/epoxy to aluminum joints, 569–571, 574–581
protection of aluminum, 204–296
stress cracking, 25
Coupling agents,
filler effects, 224, 231
for ceramic-polymer interfaces, 214–232, 248–249
models of, 218–220
titanates, 231–232
Cracking,
adhesives, 265–267, 271, 273–298, 607
beryllium oxide, 187
cold, 31, 39–50

crack growth, 457–461, 492–497, 506–507, 515–534, 537, 543–546
hot, 7, 31, 36–38, 40–50
hydrogen content, 42, 44–47
of glass, 112
plastic deformation of adhesives, 278–279, 281, 286, 297
propagation in fastened joints, 393
rare earth addition, 48
solid state welds, 99
stress corrosion, 25
stress intensity, 477–484, 520–534
test, 36–49
theory, 267–273, 478–480, 525–529
CRBRP, 13–14, 16, 18–20, 22–27
Creep ductility of stainless steel, 3, 9–12, 27
Cryogenic applications, 64, 91

Damage index, 517–519
Damage tolerance, 455–468, 471–501
Deformation of silicon nitride, 143, 149
Design of honeycomb, 339–353
Diamonds,
braze alloys for, 87–88
Diffusion bonding of ceramics, 155
Dislocations, 49
Dissimilar joints, 25–26, 53, 55, 80, 83–85
cold pressing, 171–173
diffusion bonding, 155
fusion welding, 99, 101, 104–105
hot pressing, 160–161, 163–165, 180–182
solid state welding, 97–98

Elasticity,
stress concentration in laminates, 441
Electrical/electronic applications, 180, 185
electron tubes, 155
eutectic bonding, 191–196
microelectronics, 91–92
microwave tubes, 85
Energy consumption, 3–4
Energy supply, 3–5
Epoxy adhesive additives, 265–267, 277–289, 584–591
Epoxy adhesive fracture, 265–267, 273, 275–298
elastomer-modified, 265–267, 277–289, 294–298
energy, 275–277, 279, 285–291, 293–298
temperature dependence, 285–289, 298
thickness, 283–287, 295–298
Eutectic joining,
bonding, 185–186
brazes, 91, 95
Explosive welding, 51, 53–66

F-4 aircraft, 515–534
Fail-safe design, 320, 323–325, 456–457, 459, 496, 608–609
Failure prediction in composite joints, 440–446
Fatigue,
cold worked fastener holes, 555, 557–559, 564–566
detection, 504
in aircraft, 471–472, 487–489, 494–501, 515–534, 607
in mechanically fastened joints, 471–472, 484, 499–501, 537–566, 574–580
mathematical models, 487, 492
of lap joints, 305, 307–312
stress spectrum, 485–489
FFTF, 15, 17–19, 21, 23, 26–27
Fiberglass, 317, 323–327, 330–332, 334–337, 579
Fiberglass/boron composite, 322, 327
Fiberglass/resin composite, 73, 436, 441, 444–447
Filler metals for stainless, 3
Flaw detection, 503–512, 583–591
Flexural strength,
lap joints, 315
polymers, 217, 229–231
silicon nitride, 134–135
Fracture,
detection, 503, 511–512

energy, 267, 269–271, 273–277, 279, 285–291, 293–298
finite element method, 472, 474–475, 480
flaw geometry, 552–554
of adhesive bonds, 431, 607
of epoxy adhesives, 265–267, 273–298
temperature dependence, 285–289, 298
theory, 267–273, 492–493, 544, 546
thickness, 283–287, 295–298, 462–464
Fusion welding, 99, 101, 104–108
Furnace firebrick,
cement joining, 75, 77
fusion welding, 101
mechanical fasteners, 78–79

Gadolinium oxide,
addition to epoxy adhesives, 584–591
Gas turbines, 96, 113–152
duodenisty rotors, 130–133, 146, 148–149
hub/blade ring, 137, 139, 141, 143–144, 146–147, 150
Glass,
adhesive bonding, 72, 232
brazing material, 91
cleaning, 212
welding of silicate, 95
wetting, 212–215
Gold,
explosive welding, 55
Graphite,
braze alloys for, 86–87
composites, 255, 397, 435, 437, 439, 441, 443, 569–572, 574–581
failure modes, 441, 443, 574–581
fusion welding, 101, 105
galvanic corrosion, 569–572

Heat exchanger, 13, 16–18, 22
Helicopters,
blades, 320–323, 330, 335–338, 342
fail-safe design, 320, 323–325
failure mode, 323, 334
honeycomb, 340–351
lap-up, 328–334, 338
rotors, 317–319, 344
spars, 329, 333–334
trade-offs, 322–328
Honeycomb, 612–613
design, 339, 342–353, 597–600, 608
stress analysis, 339–343
Hot press bonding,
microstructure, 138
refractories, 155, 160–171, 179–182
silicon nitride, 113–115, 130–151
Hybrid composites, 312–316
Hydrogen diffusion, 44–48

Impact properties, 628–629, 633–636
Injection molding of silicon nitride, 115–116
Insulation,
adhesive bonding, 73–74
Insulators, 75, 77
IR domes, 73
Iron,
eutectics, 197
solid state welding, 97

Lanthanum boride brazing, 95
Lithium fluoride,
solid state welding, 98
LMFBR, 3, 5–6, 13, 18, 26–27
LNG ships, 623–628

Magnesium,
explosive welding, 55
Magnesium oxide, 93, 96–100
additive to silicon nitride, 131, 133, 135, 145–146, 149
Mechanical fasteners,
crack propagation, 393, 506–507, 537–566
damage tolerance, 461–462, 465–466, 483, 500–501
design for composites, 446–447
effects of friction, 388–389, 393–395, 397, 435, 444

finite element analysis, 391, 395, 398–399, 406, 432, 474–480, 500
for ceramics, 78–81, 106–107
galvanic corrosion, 569–581
in aluminum plate, 391, 475, 542–543, 550–565
in cold worked holes, 555, 557–559, 564–566
in steel, 542–543, 550–563, 565
in titanium, 542–543, 550–563, 565
press, 79–80
stress analysis, 379–400, 405–406, 432–449, 462–463, 483, 544–549
stress distribution, 434–437, 441, 443
thickness, 462–463
Melting point of zirconium ceramics, 165
Metal matrix composites, 245, 254–255, 258–259
Metal to ceramic joints, 79–81, 92, 94, 312
eutectic bonds, 185
Molybdenum,
eutectics, 197
fusion welding, 101
slip casting, 125, 127
solid state welding, 98
Molybdenum ceramics, 125, 127

Neutron radiography, 583–591
Nickel alloys,
eutectics, 197
explosive welding, 55
hot cracking test, 38, 49
Inconel 600, 25
solid state welding, 97
stress corrosion, 25
Nickel oxide, 97
Noble metal brazes, 82–88
Nondestructive testing, 58–59, 503–512, 583–591
Nozzles, 80
Nuclear generators, 6
Nylon fabric, 249–250, 253

Oxidation of zirconium ceramics, 165

Photoelastic test, 616–619
Piezoelectrics,
adhesive bonding, 73–75
Pioneer Venus spacecraft, 88, 91
Piping,
cryogenic, 64
sodium, 3, 19, 22
Polymer-ceramic interface, 207–228, 231–232, 249
adhesive bonds, 209–232
flexural strength, 229–231
Polymer-polymer joints, 237–263
bondability index, 242
stresses, 239–241
Powder metallurgy,
particle size of zirconium ceramics, 157–161
silicon, 121–128, 133–134, 151
Pumps, 19–21

Radomes, 73, 78
Reaction sintering, 115
Reactor vessels, 13–15
Refractory brazes, 88–91, 94–95
Residual stress
in graphite composites, 579–580
in welds, 357
Rivet bonding, 615–622

Shear properties,
adhesive bonds, 240, 251, 259–262, 314, 409, 414–415, 417–420, 422–428, 584–590, 619, 621
composites, 251, 259, 314, 447, 449
mechanically fastened joints, 435, 446–447, 449
Ships,
low temperature applications, 623–637
Silica, 73–74, 189
Silicon, 98, 121–128
Silicon carbide, 100–101
Silicon nitride, 76, 88, 96
deformation, 143, 149
for gas turbines, 96, 113–115
forming, 115–120
hot press bonding, 131–151

magnesium oxide in, 131, 133, 135, 145–146, 149
microstructure, 138, 150
slip cast bonding, 120–132, 151
Silver, 55, 164, 197
Slip-casting of silicon nitride, 114, 116–132, 151
Solid state welding, 96–99, 106–107
Sonar, 74
Space Shuttle, 71–74, 78, 80
Spinel,
eutectic bonding, 189
Steam generator tubes, 3, 18, 25–26
Steel,
adhesive bonding to ceramics, 76
brazing to ceramics, 83
coatings, 9–10
cold cracking test, 40
composition, 626–627, 631–634
creep, 3, 7, 9–12, 27
defects, 13
explosive welding, 52–53, 55–59, 63–65
fatigue, 7, 537
heat treating, 636–637
hot cracking, 7, 38–39
HY-80, 34–36, 39–47, 49, 373
HY-130, 35
HY-150, 40
impact properties, 628–629, 633, 635–636
LNG tanker ships, 623, 625–628, 637
maraging, 38–40
reactor vessels, 13
rolling, 635–636
stainless 3, 7–14, 27, 55, 57–58, 64–65, 76, 83
stress analysis, 373
stress corrosion, 25
tensile properties, 9–12, 540–541, 626, 632
tubing, 25
welds, 3, 7–14, 23, 25, 34–36, 39–40, 52–53, 55–59, 63–65, 373, 623, 625, 628–631
2.25Cr-1Mo, 23
9Ni steel, 40, 537–543, 549–554, 556–563, 565
Stress analysis,
adhesive bonds, 405–406, 408–431, 448
coefficient of friction, 388–389
definitions, 406–408
in welds, 357, 362, 368–376
lap joints, 392–393, 420–425
mathematical models, 411–422, 427–430, 478–480
mechanically fastened joints, 379–400, 405–406, 432–449
of honeycomb composites, 339–343
Stress loading, 44–45, 462, 521–529, 544–547, 575, 616–618
Surface treatment,
aluminum, 203–206
infrared spectrum of solvent, 249
leaching, 225
polymer-ceramic interface, 207, 212–216
polymer-polymer bonding, 238, 247–252
porosity, 238

Tantalum, 55, 98, 101, 105
Tantalum carbide, 98, 101, 105
Tensile properties,
aluminum, 540–541, 596
elongation, 9–11
flexural strength of polymers, 217, 229–231
humidity effect, 251–252
of elastomer-modified epoxy adhesives, 281
steel, 540–541, 626–632
stress by mechanical fasteners, 78
temperature effect, 596
titanium alloys, 540–541, 596
9Ni steel, 540–541
Thermal expansion,
in ceramic brazing, 91
of elastomer-modified epoxy adhesive, 281
of zirconium ceramics, 160–164
Thermal shock, 155, 161, 165
Thermal stress,
creep, 427
of adhesive bonds, 424, 427–428

Thermomechanical analysis, 357–376
Titanium alloys,
  brazing, 84–86, 595
  composition of Ti-6Al-4V, 539
  explosive welding, 52–53, 55–57, 64–65
  fasteners, 473, 476, 541, 574, 579
  fatigue, 537–538, 549–554, 556–565
  properties, 540–541, 596
Titanium ceramics,
  borides, 155, 179–180
  carbides, 155, 179–180
  hot pressing, 179
  nitrides, 155, 179–180
  solid state welding, 98
transition temperature of epoxy adhesive, 281
Tubing welds, 18, 25, 27
Tungsten, 101, 105

Varestraint test, 36–39, 49

Weld bonding, 615–622
Welding in ships, 629–631
Welds,
  finite element method 359–367, 369, 373
  flaws, 505–506
  HAZ, 623, 628–629, 637
  modeling, 358–359
  plastic strain, 370–371, 375
  residual stress, 357, 368–371, 374–376
  steel, 3, 7–14, 23, 25, 34–36, 39–49, 52–53, 55–59, 63–64, 623, 625
  stress analysis, 357, 362, 368–376
  thermal analysis, 359–367
  zones, 31–35
Wetting,
  of aluminum for bonding, 202–203
  of ceramics, 82–84, 88, 91, 211–215, 221
  of polymer adhesives, 210–211, 239
  surface treatment, 212–214
Windows, 71–72, 78–79, 87, 91
Wings,
  damage tolerance, 471–473, 476–477, 496
  F-14, 521–523
  titanium brazing for, 595

Zirconium ceramics, 80, 97–98, 101, 105
  borides, 155–157, 159–167, 169–174, 176–182
  carbides, 155–158, 160–174, 176–182
  diffusion bonding, 155
  hot pressing, 160–176
  melting points, 165
  nitrides, 155–158, 160–161, 163–169, 171–174, 176–177, 179–182
  oxidation, 165–171
  oxides, 155–157, 159, 180–182
  particle size, 157–159
  rupture modulus, 165–166